बी एआरसी न्यूज़लैटर
BARC NEWSLETTER

ISSUE NO. 297 | OCTOBER 2008

DR. HOMI BHABHA CENTENARY YEAR - 2008-2009

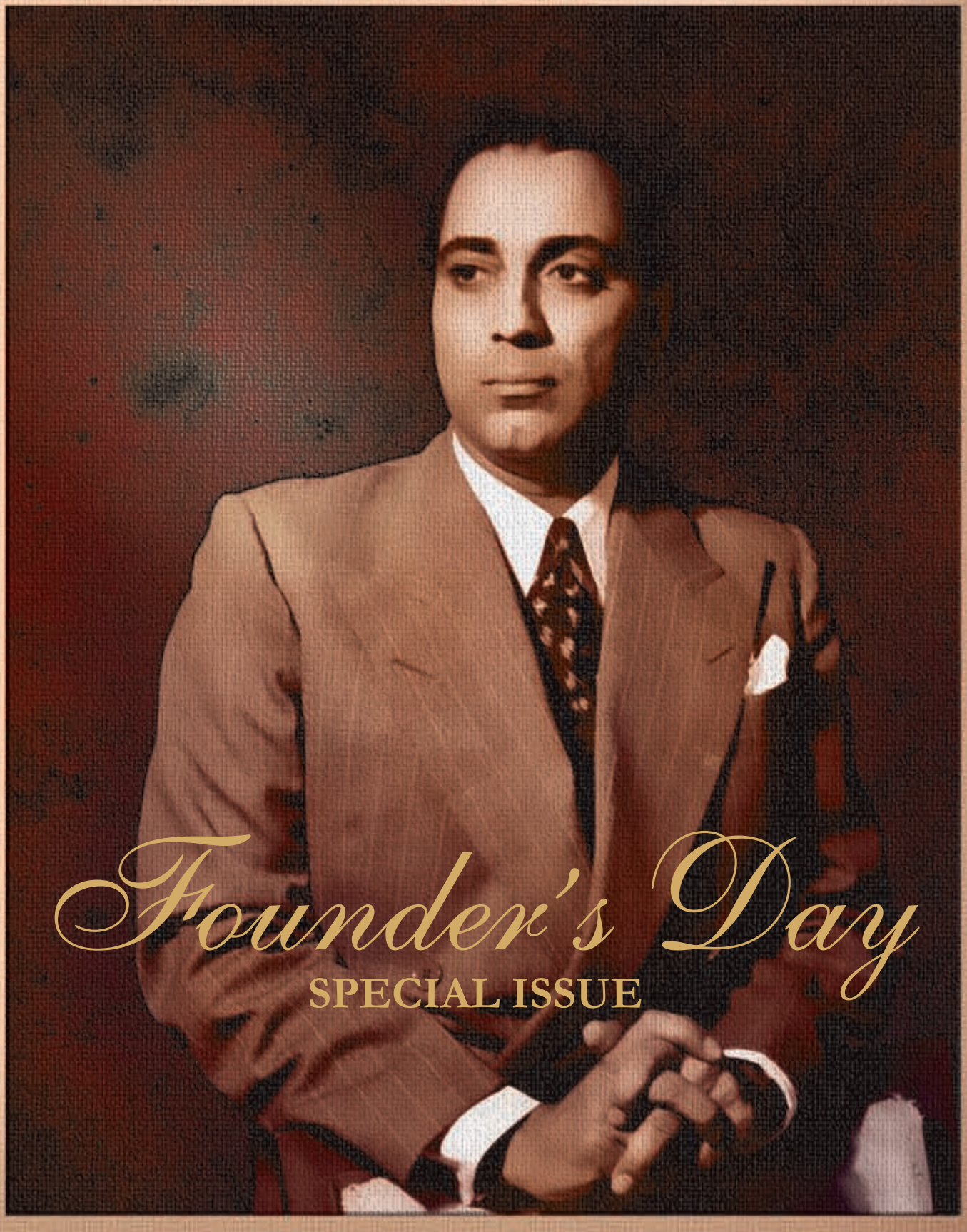

Founder's Day

SPECIAL ISSUE


BHABHA CENTENARY YEAR
OCTOBER 30, 2008 - OCTOBER 30, 2009
होमी भाभा जन्म शताब्दी वर्ष
Homi Bhabha Birth Centenary Year
३० अक्तूबर २००८ - ३० अक्तूबर २००९
30 October, 2008 - 30 October, 2009

बी एआरसी
न्यूज़लैटर

BARC
NEWSLETTER

Founder's Day

SPECIAL ISSUE

Government of India

भाभा परमाणु अनुसंधान केंद्र

Bhabha Atomic Research Centre

बीएआरसी न्यूज़लेटर
BARC NEWSLETTER

CONTENTS

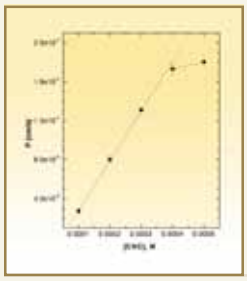

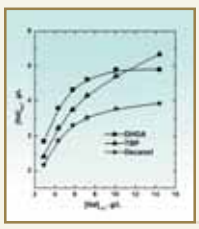

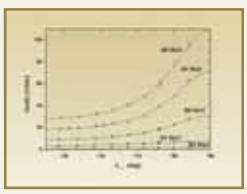

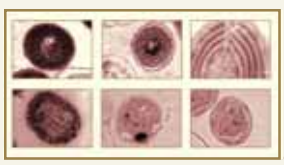

DEDICATED TO THE MEMORY OF

HOMI JEHANGIR BHABHA

(1909-1966)

Founder and Architect of the
Indian Atomic Energy Programme

बीएआरसी न्यूज़लेटर
BARC NEWSLETTER

HIGH POWER TUNABLE DYE LASERS FOR PHOTO-IONIZATION APPLICATIONS

Sucharita Sinha
Laser and Plasma Technology Division

Dr. Sinha is the recipient of the Homi Bhabha Science and Technology Award for the year 2006

ABSTRACT

In this paper, a brief review of results from our recent studies on design, development and operation of high power, high repetition rate, tunable dye lasers for photo-ionization applications is presented. Results of experimental investigations aimed towards achieving efficient and reliable, long term operation of such Copper Vapor Laser (CVL) pumped high power, high repetition rate, dye lasers are described. Theoretical models simulating the operation of such dye lasers, have also been developed. Time dependent analysis of rate-equation based models provide, not only an understanding of the dynamics of laser action, but also useful estimates for optimum operating parameters of such high power dye lasers and associated effects such as: extent of deterioration in laser performance with dye photo-degradation, optical non-linearities and laser beam distortion arising from induced thermo-optic effects in such high power dye laser systems.

Introduction

Organic dyes dissolved in suitable liquid solvents have found wide application in laser technology serving both as an active gain medium for generation of coherent tunable radiation and also for tailoring the laser radiation via Q-switching and modelocking. In addition to this, organic materials with large third order nonlinearities, exhibit an intensity-dependent refractive index and nonlinear transmission. These qualities make such material promising candidates, for various photonic applications. The search for materials with large and fast optical nonlinearities, has led to extensive investigation of nonlinear optical organic materials. In fact, nonlinear Fabry-Perot etalons exhibiting optical bistability have been widely studied, for their application as logical memory units with fast switching times in the field of optical computing.

Pulsed dye lasers can typically be pumped by various sources such as frequency doubled Nd:YAG lasers, excimer lasers, nitrogen lasers or flashlamps. However, Copper-Vapour-Laser (CVL) is the preferred pump source for high power dye lasers, particularly for applications requiring high average power and tunable laser output at high pulse repetition rates. Copper-Vapour-Laser pumped dye lasers, are often operated at very high average pump power levels, owing to the high repetition rate operation capability of CVLs (repetition rates of tens of kHz). Efficient and reliable

long-term operation of high power dye lasers is largely determined, among other factors, by the fluorescence yield and the photo-stability of the lasing dye solution. Various photo-chemical reactions initiated in the active dye solution under the action of the exciting radiation, result in the photo-degradation of the dye solution and also in the formation of new photo-products. Dye degradation results in bleaching of the dye solution that, in it's turn, leads to a loss of lasing dye molecules, deterioration of the laser efficiency and an appreciable reduction of the service lifetime of the laser.

An important phenomenon that determines the quality of the laser beam delivered by high power dye lasers, when operating at high pulse repetition rates, arises from the field induced refraction effects in the dye laser medium. Large optical field induced refraction in the dye laser medium can lead to severe wave-front distortion of the propagating optical beam, thus restricting the operation of high power dye lasers. A variety of physical mechanisms can result in intensity-dependent contributions to the refractive index. In liquids, a strong light field can lead to orientation of anisotropic molecules and as a result, the medium becomes anisotropic and the average refractive index is altered. In liquids consisting of isotropic molecules, the nonlinearity may arise from molecular redistribution or by electronic polarizability caused by distortion of electronic clouds or by resonance effects such as saturation or two-photon absorption. However, a large contribution to nonlinear refractive index can also occur, due to thermal effects.

Proper choice of solvent in which the lasing dye is dissolved and use of a dye circulation system that circulates the dye solution through the dye cell, can restrict field-induced laser beam distortion and ensure efficient long-life operation of high power, high repetition rate, dye lasers. Through circulation of dye, the active dye volume exposed to the pump laser is rapidly removed between successive pump laser pulses, a high clearing ratio resulting in extended dye lifetime. Therefore, dye-flow handling system considerations become a major concern for high power dye lasers operating at high repetition rates. Alcohol or other organic solvents, are commonly used as solvents for dyes, in dye lasers. Being volatile and inflammable, the handling and disposal of these organic solvents poses serious environmental hazards. Water is safe, environmentally friendly and in addition has several advantages over alcohol and other organic solvents, thus making it the solvent of choice for application in high-power, high-repetition rate dye lasers.

In this paper, we briefly review the results of some of our studies aimed towards achieving efficient and reliable, long term operation of CVL pumped high power, high repetition rate, tunable dye lasers.

Laser Operation with Heavy-water-based dye solutions

In spite of the positive qualities of water, use of water as a solvent in high power dye lasers, has been significantly restricted by the fact, that several commonly used laser dyes are not easily soluble in water. Even when dissolved in pure water (at typical concentrations necessary for laser operation), dye molecules exhibit a tendency to form non-fluorescent dimers and higher aggregates. Non-fluorescent dimers constitute an absorptive loss of pump power in dye lasers, leading to reduced laser efficiency. The suppression of dimer formation in aqueous solutions by addition of various organic compounds has been reported in literature. Organic solvents, in contrast, do not normally induce dye molecule aggregation and dimer formation.

Heavy water has been reported to have superior thermo-optic properties, in comparison with normal or ordinary water. We have reported a comprehensive study, evaluating the possibility of using heavy water as a solvent for high-average-power

dye-laser systems, suitable for copper vapour laser pumping. It compares the performance of normal water and heavy water as dye solvents, in terms of dye photo-stability and laser efficiency in high-power, high-repetition rate, dye lasers. Improved quantum yield of fluorescence, by addition of suitable de-aggregating agents, to aqueous dye solution using normal water and heavy water for three commonly used laser dyes Rhodamine-6G (Rh-6G), Rhodamine-B (Rh-B) and Kiton-Red (KR) are shown in Table 1.

Performance of normal and heavy-water-based pulsed Rh-6G dye lasers when investigated in two resonator configurations: a broadband resonator cavity and a narrow band tunable laser cavity, have been compared. Fig.1 shows typical tuning curves for laser action for Rh-6G solution in ethanol, normal water and heavy water, respectively. Our results indicate that a heavy-water-based dye laser performs nearly as efficiently as an ethanol-based system. Moreover, the peak laser efficiency value, achieved with a dye solution in heavy water, was higher than that obtained with a normal-water-based dye solution at similar levels of pump power.

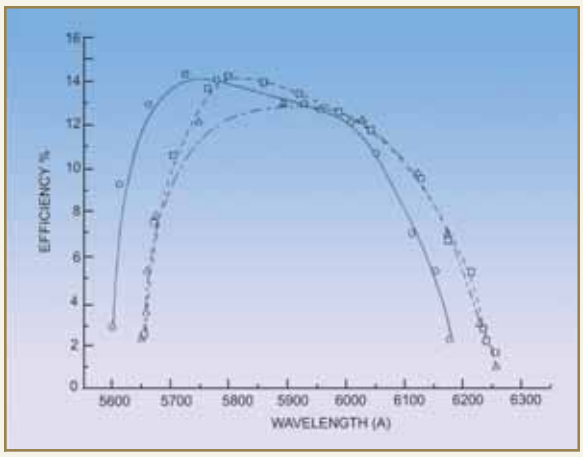

Fig. 1: Tuning curves for laser action in a Rh-6G dye solution when dissolved in ethanol (open circles and solid line); normal water (open triangles and dashed-dotted line); and heavy water (open squares and dashed line).

The photo-bleaching rate of organic dyes, has been observed to depend strongly on several factors such

Table 1: Quantum yield of fluorescence of dyes Rh-6G, Rh-B and Kiton-Red

Dye [a]	Solvent [b]	Fluorescence maximum λ_{max} (nm).	Relative quantum yield of Fluorescence[c]
Rh-6G	Ethanol	555.0	1.0
Rh-6G	Water + 40mM SLS	560	0.88
Rh-6G	Heavy Water + 40mM SLS	560.0	1.07
Rh-B	Ethanol	571	0.64
Rh-B	Water + 40mM SLS	587	0.5
Rh-B	Heavy Water + 40mM SLS	582	0.55
Kiton-Red	Ethanol	577	0.5
Kiton-Red	Water + 40mM SLS	593.5	0.4
Kiton-Red	Heavy Water + 40mM SLS	593.0	0.46

(a) Dyes used were commercially procured from Lambda-Chrome Laser Dyes.
(b) Spectroscopic grade Ethanol, ultra-pure normal water, 99.4% purity heavy water,and Fluka grade SLS.
(c) Quantum yield of fluorescence relative to Rh-6G in Ethanol

as: nature of solvent, temperature of dye solution and presence of special additives, in addition to pump wavelength and pump power. Extensive investigations studying photo-stability of commonly used laser dyes in different solvents such as ethanol, normal and heavy water, have been carried out. Our observations comparing aqueous solutions of dyes such as Rh-6G and Rh-B indicate, highest photostability of both dyes in a heavy water medium, followed by normal water and ethanol. Exhaustive photo-bleaching of laser dyes Rh-6G, Rh-B and KR under high repetition rate CVL irradiation suggest, that the photo-degradation of dyes occurs predominantly through excited-state intermolecular reactions involving the singlet state, rather than the process of nonlinear optical absorption in individual molecules. Our investigations also ascertained the extent to which the products generated during the process of photo-degradation would interfere with the lasing process of the unbleached dye molecules.

Dye Photodegradation and it's effect on Laser Operation

Although considerable insight can be gained into dye and solvent stability, from extensive data reported in literature, the detrimental effects of dye degradation on the laser efficiency are highly system-specific and need to be individually evaluated for the system under study. Detailed study of laser dye stability and the subsequent effects of photo-degradation products on laser operation have been carried out, for flashlamp pumped dye laser systems, where, in some optical cavities, absorption as low as 1% at laser wavelength, was seen to be sufficient to reduce the laser output by 50%. Therefore, it is of practical interest to investigate the extent to which photo-degradation products affect the fluorescence properties and therefore, the lasing action in dye molecules. In addition to experimental investigations of effect of dye photo-degradation on efficiency of Rh-6G dye laser oscillators, we have also developed a rate equation based theoretical model, simulating the effects of dye photo-degradation on the performance of such high power, high repetition rate, dye lasers. Our theoretical model provides theoretical estimates for the drop in output energy, when the laser oscillator is operated over an extended period of time. This data enables the dye laser user, to determine at what stage the degraded dye solution would need to be replenished and to what level the concentration of photo-products may be allowed to build up, without critically affecting the laser output. Close agreement of our experimental observations and theoretically estimated dependence of dye laser efficiency on the laser dye solution undergoing photo-degradation is evident from Fig. 2. Photo-degradation of the dye molecules and the subsequent reactions of the photo-products among themselves or with impurities, is a complex phenomenon. Our experimental and theoretical studies provide useful estimates for the deterioration in laser performance of high average power dye lasers on account of photo-degradation of active dye molecules. Recently, solid-state dye lasers in which an organic dye doped in a suitable solid matrix replaces the

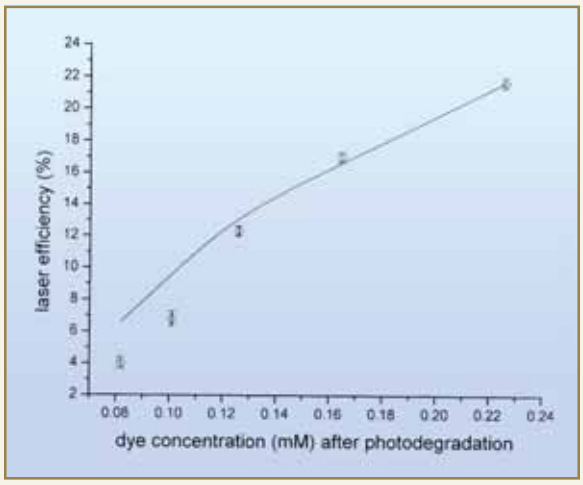

Fig. 2: Dye laser efficiency as a function of the concentration of the photodegraded dye solution for a frequency doubled Nd:YAG pumped pulsed dye laser. The solid line depicts the theoretically calculated dependence.

conventional liquid dye solution, has been extensively investigated. Studies reported so far suggest that rapid dye degradation is a critical issue severely limiting not only the lifetime, but also the laser beam quality and the high repetition rate operation capability of these solid-state dye lasers.

Optical Nonlinearity and Thermo-Optic Properties of dye laser medium

The thermo-optic properties of the dye solvents or the solid matrix in case of solid-state dye lasers, are significant parameters that determine field-induced optical non-linearities in the dye medium. The associated nonlinear refractive index of the dye medium, leads to distortions in the laser beam, delivered by a high average power dye laser when operating at high repetition rate. Thermal lensing in the active medium irradiated by a laser beam is a laser irradiance-dependent phenomenon, that is also a function of material parameters such as thermal diffusivity and thermal coefficient of refractive index (dn/dT), of the solvent or host material.

Nonlinear refraction resulting in thermal lensing, essentially arises from the phenomenon of non-radiative energy transfer from the dye molecules, either to the solvent or to the solid host. We have investigated the optical nonlinearity exhibited by an organic dye, Rhodamine-B when dissolved in various commonly used dye solvents using the Z-scan technique [15]. The Z-scan technique, based on the principle of spatial beam distortion arising from an optically-induced nonlinear refractive index, offers experimental simplicity, as well as very high sensitivity.

Analysis of our experimental data indicated, that the arge negative lensing observed in the Rh-B dye solution, induced by 40ns laser pulses at 510.6 nm is thermal in origin, resulting from energy transfer from the dye molecules to the solvent molecules and is therefore strongly dependent on the thermo-optical properties of the solvent. Using this scheme, the thermal properties of an aqueous dye solution were compared with that of a solvent comprising a water-surfactant mixture. The thermal figure of merit M_H that characterizes the solvent (also denoted by parameter $H = 1/M_H$), is given by $M_H = (\rho C)/(dn/dT)$, where ρ denotes the density of the medium and C it's specific heat. Our measurements on thermally-induced nonlinear refractive index, using Z-scan technique, provided direct estimates for the thermal figure of merit for various solvents.

The problem of thermal non-linearity may be substantially reduced, using solvents with high specific heat and operating at temperatures at which the variation of refractive index with temperature is low. The thermal characteristics of water make it an ideal solvent for high-power laser applications. However, heavy water has been reported to have superior thermo-optic properties as compared to normal water. The thermal characteristics of both normal and heavy water improve substantially as the solution is cooled. However, contrary to normal water, in the case of heavy water, the thermal lensing effect reduces to zero while it is still in the liquid phase.

Using the Z-scan technique, we have investigated non-linear refraction in aqueous solution of dye Rh-B when dissolved in normal and heavy water, respectively. The measured nonlinear refraction has been compared with thermal nonlinearity observed in a standard sample of ethanolic solution of the same dye. Analyzing our Z-scan data, we have obtained the figure merit of heavy water to be 1.414 times that of normal water, at an operating temperature of 20^0C. This compares well with the factor of 1.47, as reported in literature. Thus, the effect of thermal lensing is expected to be lower in heavy water than in normal water, thereby establishing it's suitability for use in high-average-power, high repetition rate dye lasers and amplifiers.

In case of solid-state dye lasers, an organic dye is doped in a suitable solid host and this dye-doped solid

matrix, serves as the active medium for laser radiation. However, high resistance to laser-induced photo-degradation and good thermo-optical properties of the dye doped solid matrix, are critical parameters which determine the performance and operating lifetime, as well as the high power, high repetition rate, operation capability of such solid state dye lasers. Although several solid hosts ranging from organic polymers to inorganic glasses and organic-inorganic composites have been investigated, material studies still continue towards development of solid matrices, that can satisfy all material requirements crucial for an ideal solid host for organic laser dyes. Of the available solid matrices, inorganic glasses exhibit better thermal properties (higher thermal conductivity and lower thermal expansion) and a higher damage threshold. Polymers on the other hand have better compatibility with organic dyes and superior optical homogeneity.

We have studied non-linear refraction in various poly (methyl methacrylate) (PMMA) solid hosts when doped with fluorescent organic dyes, commonly used as a laser active medium. The observed thermal lensing effect arising from optical nonlinearity, results from non-radiative energy transfer from the dye molecules to the solid matrix and is therefore, strongly dependent on the thermal properties and the material parameters of the polymeric host. The non-linear index of refraction, n_2, for each sample host has been measured, using the Z-scan technique and variation of refractive index with temperature (dn / dT) determined for various host materials. Estimation of dn / dT is crucial in determining the extent of thermal lensing in dye doped solid-state medium, that in turn determines the spatial quality and divergence of the generated laser beam, from a dye-doped, solid-state laser system. The samples investigated by us included either, Rhodamine-6G or Pyrromethene-567 fluorescent dyes, doped in a variety of polymeric hosts such as, polymethyl methacrylate (PMMA) and copolymers of methyl methacrylate (MMA) with 2-hydroxyethyl methacrylate (HEMA), or, pentaerythritol triacrylate (PETA), or ethylene glycol dimethacrylate (EGDMA), etc. Nonlinear refraction effects of thermal origin, observed with pulsed radiation can be approximated in a quasi-steady state regime, when the pulse duration, τ_p of the incident radiation satisfies the condition: $\tau_{resp} < \tau_p \tau_D$, where, τ_{resp} is the buildup time of the nonlinearity and τ_D refers to the relaxation time for induced nonlinear effect. The buildup time of nonlinearity is given by the time required for a sound wave to propagate across the beam, $\tau_{resp} \sim \omega_0 v_s$, where ω_0 is the $1/e^2$ beam radius and v_s is the velocity of sound, τ_D is related to the thermal diffusive coefficient D of the medium ($\tau_D = \omega_0^2/4D$). Under this deemed steady state regime, for a cumulative nonlinearity, having a decay time much longer than the pulse width of the incident radiation, the on-axis time-averaged nonlinear index change at the focal plane in the Z-scan configuration is given by $\Delta n_{0ss} = (\alpha F\, dn / dT)/2\rho C$, where α is the linear absorption coefficient of the nonlinear medium, F is the incident fluence of the laser beam, ρ is the density of the medium and C is the specific heat of the medium.

Analyzing our Z-scan data on the various samples of dye doped solids, the nonlinear index of refraction was estimated for each sample, following the standard Z-scan analysis. From the measured value of nonlinear index of refraction we also obtained the thermo-optic coefficient dn / dT for each polymeric host (Table 2). Estimates for dn / dT obtained from our measurements for a PMMA host compared well with the theoretical estimates calculated, assuming that, a change in temperature of the dye-doped solid host, primarily resulted in a change in it's density. As most physical and thermal properties, other than absorption of the dye-doped solid hosts, are governed predominantly by the host material, the variation of refractive index with temperature, dn / dT was determined as $dn / dT = (\delta n / \delta \rho)(\delta \rho / \delta T) = -\gamma \rho (\delta n / \delta \rho)$, where γ is the expansivity, $g = V^{-1}(dV / dT)$, V is the volume and the change in the index of refraction with density for the solid host, can be determined from the Lorenz-

Table 2: Measured value of dn / dT for dye-doped solid state polymeric media

Serial No.	Dopant (Organic Dye)	Solid Host	dn / dT (K^{-1})
1.	Rhodamine 6G	P[MMA:10% Ethanol]	$-(2.25X10^{-5}$ to $1.15X10^{-4})$
2.	Rhodamine 6G	P[MMA:HEMA: 1 % Ethanol]	$-1.2X10^{-5}$
3.	Rhodamine 6G	P[MMA:HEMA: 1 0% Ethanol]	$-(1.6X10^{-5}$ to $1.5X10^{-5})$
4.	Rhodamine 6G	P[MMA:EGDMA]	$-(1.5X10^{-5}$ to $2.48X10^{-5})$
5.	Pyrromethene 567	P[MMA:PETA:DABCO]	$-(2.5X10^{-5}$ to $1.27X10^{-5})$

Lorentz relation $\delta n / \delta \rho = \{[(n^2-1)(n^2+1)]/6n\rho\}$. For a PMMA host, using reported material data, values for dn / dT ranging between -5.73 X 10^{-5}/ ^{0}K to –3.87 X 10^{-5}/ ^{0}K have been estimated. This compares well with the value of dn / dT obtained from our Z-scan measurements.

Extended Tunability with Binary dye-mixture Laser

Photo-ionization and spectroscopic applications, often require narrow band dye lasers tunable over a specific wavelength range, that cover the absorption features of the sample being investigated. Tunable dye lasers operating with a mixture of lasing dyes, thus capable of producing extended tuning range, are ideal for such applications. Tunable dye lasers based on a mixture of dyes have been investigated with several different combinations of lasing dyes. The primary motivation for use of a mixture of dyes as the lasing medium, has been either an improvement in the laser performance or the possibility of multi-frequency operation. The operation of these lasers is based predominantly on the mechanism, of energy transfer between dye molecules, which provides an effective as well as simple method for the improvement of the laser efficiency and a wider spectral range of laser oscillation.

An extension of the tuning range from a laser, based on a mixture of dyes is also possible, when the constituent dyes absorb the same pump radiation but fluoresce over spectrally separated regions. We have studied such a binary mixture of dyes Rhodamine-6G (Rh-6G) and DCM pumped by radiation at 510.6 nm from a Copper Vapour Laser, resulting in laser emission tunable over an extended frequency region (Fig. 3).

Utilizing the two laser dyes dissolved in a common solvent, we have achieved improved laser performance and a desired shifting of the laser tuning range. We have also demonstrated how a judicious choice of the relative concentrations of the dye components in the mixture, allows optimum laser performance to be achieved at pre-selected wavelengths, within the fluorescence band of the dye mixture. Following a time-dependent analysis of a rate-equation model that closely describes the operation of such a laser, theoretical estimates for optimum dye concentrations and corresponding extension of the laser tuning range were also obtained.

The mixture of dyes leads to an extension of the tuning range, although the mixture does operate at a lower efficiency as compared to the individual components. This reduction in efficiency

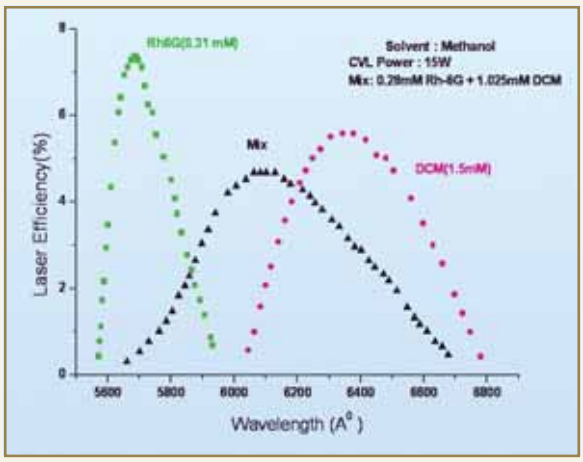

Fig. 3: Experimentally measured tuning curves depicting laser efficiency versus oscillation wavelength for individual dyes Rh-6G, 0.31mM (squares 0; DCM, 1.5 mM (circles); and a mixture of the two dyes Rh-6G, 0.28 mM and DCM, 1.025 mM (triangles).

is a consequence of the distribution of the total pump power between the two constituent dyes. Laser emission tunable over the wavelength range spectra ranged from 560 to 590 nm for Rh-6G and from 610 to 675 nm for DCM; all other experimental conditions remained unchanged.

Conclusion

In this paper, we have briefly reviewed results from our recent studies on design, development and operation of high-power, high repetition rate, tunable dye lasers for photo-ionization applications. Our efforts have been directed towards achieving efficient and reliable, long term operation of such CVL pumped high power, high repetition rate dye lasers. Theoretical models, simulating the operation of such dye lasers, have also been developed providing an understanding of the dynamics of laser action, extent of deterioration in laser performance with dye photo-degradation, as well as theoretical estimates for the optimum laser parameters and associated thermo-optic effects, observed in such high-power dye laser systems.

Acknowledgement

The author wishes to thank all her colleagues from Tunable Laser Section, Laser and Plasma Technology Division, for their active participation in these investigations.

ABOUT THE AUTHOR

Dr. (Ms.) Sucharita Sinha, is a Homi Bhabha awardee of the 26th Batch of BARC Training School. She has carried out extensive theoretical and experimental investigations on nonlinear optical phenomena in laser-atom interaction, photo-thermal properties of tunable-laser media and developed novel attractive means to improve the quality of high-average-power laser beams. The output from her research has been successfully implemented in the RIS programme, resulting in improved performance of the laser systems. She has modeled, designed and developed optically-pumped infrared molecular gas lasers producing output at 16 micron, a wavelength of interest for molecular Uranium isotope separation. Her work on theoretical analysis of quantum size effects in composite materials and semiconductor nanospheres resulting in tailored optical absorption spectrum is widely cited in literature.

Among her current research interests, in the field of laser material ablation process she has demonstrated a unique dry laser etching technique required for metallographic examination of nuclear fuel pellets. For the first time, Dr. Sinha has been able to demonstrate picosecond laser-based surface micro-structuring of electron emitters leading to vastly improved field-emission properties.

बीएआरसी न्यूज़लेटर
BARC NEWSLETTER

SOLID STATE CHEMISTRY: UNLIMITED OPPORTUNITIES

A. K. Tyagi
Chemistry Division

Dr. A.K. Tyagi is the recipient of the Homi Bhabha Science & Technology Award for the year 2006

ABSTRACT

In recent times, Solid State Chemistry has emerged as a truly multidisciplinary subject as it connects Chemistry with Physics and Materials Science. Further in view of the fast moving field of Materials Science, synthesis has assumed significant importance. The last decade witnessed a remarkable impact made by soft-chemical routes in the field of Materials Science. In fact, some metastable compounds, which have wonderful properties, can be synthesized only by soft-chemical routes. As a Solid State Chemist, one gets an opportunity to contribute to a wide range of materials. The aim of the present review article is to give a bird's eye view of some of the work carried out in our group during the last ten years. Examples have been taken from the fields of Nuclear Materials, Nanomaterials and Functional materials.

Research on Nuclear Materials

Phase relations and thermal expansion studies on thoria-based systems for Advanced Heavy Water Reactors (AHWRs)

Thorium has attracted considerable attention in the recent past, as it is expected to play an important role in the third stage of the Indian nuclear power generation programme. Since thorium itself is not a fissile material in the thermal region of neutrons, it is proposed to use about 2 to 6 % of fissile uranium and plutonium dioxides in the ThO_2 matrix, in the Advanced Heavy Water Reactor (AHWR). Unlike the urania-based fuels, thoria-based fuels are not well investigated. In view of this, a research programme on the investigation of various aspects of thorium-based mixed oxide systems was initiated by our group in 1998, as part of the Task Force on Thermodynamic Properties of Thoria-based Fuels for AHWRs. One of the mandates given to us was to investigate thermal expansion behaviour of different thoria-based systems relevant to AHWR. Thermal expansion is an important parameter governing the performance of a nuclear fuel-pin assembly.

Most of the thoria-based mixed oxides investigated in this study, were prepared by a solid state route. All the products were characterized by XRD. Thermal expansion behaviour was investigated by Dilatometry and High Temperature XRD. A summary of results follows:

ThO_2-UO_2 system

It was found that most of the thermal expansion studies in ThO_2-UO_2 system, are on solid solutions containing higher amounts of UO_2 i.e. ≥ 10 %. There were no reports of ThO_2 containing 2-6 wt. % UO_2, which is one component of the proposed fuel for AHWR. Therefore, thermal expansion of compositions ThO_2-2, 4 & 6 wt. % UO_2 was studied, by high temperature X-ray powder diffraction. The XRD patterns were recorded in the range $10 < 2\theta < 90^o$ from room temperature to 1623 K in vacuum. The unit cell parameters were determined, using a least squares refinement programme. The observed cubic lattice parameters at room temperature for ThO_2 and ThO_2-2 wt. % UO_2, ThO_2-4 wt. % UO_2, ThO_2-6 wt. % UO_2 were 5.599(1), 5.591(1), 5.589 (1), 5.585(1) Å, respectively. In order to study thermal expansion behaviour, the unit cell parameters were refined, as a function of temperature. The coefficients of average lattice thermal expansion (α_a) of ThO_2 and ThO_2 - 2, 4 and 6 wt. % of UO_2 are 9.67 x 10^{-6}, 9.82 x 10^{-6}, 10.09 x 10^{-6} to 10.37 x 10^{-6} K^{-1}, respectively. It was observed, that there was a systematic increase in the average thermal expansion coefficient, after the incorporation of UO_2 into ThO_2. This trend can be correlated to the higher melting point of ThO_2 as compared to that of UO_2.

ThO_2-CeO_2 systems

A review article on thermophysical and thermodynamic properties of ThO_2, $Th_{1-y}U_yO_2$ and $Th_{1-y}Pu_yO_2$ revealed that the mixed oxides in the ThO_2-PuO_2 systems are scantily reported in literature. The main difficulties while investigating PuO_2 based systems, are their high radioactivity and toxicity. One way to overcome this problem, is the use of CeO_2 as a surrogate material in place of PuO_2 as they both have quite similar physico-chemical properties viz. ionic size in octahedral and cubic coordination, melting points, standard enthalpy of formation and specific heat etc. CeO_2 is an ideal material to simulate thermophysical properties of PuO_2 and PuO_2-based systems.

About 10 compositions in the $Th_{1-x}Ce_xO_2$ system were prepared, by a ceramic route. The observed gradual decrease in the lattice parameter as a function of Ce^{4+} concentration in $Th_{1-x}Ce_xO_2$ series, can be attributed to the different ionic radii of Th^{4+} and Ce^{4+} (1.05 and 0.90 Å, respectively). The bulk and lattice thermal expansion behaviour of these solid solutions were investigated by dilatometery and high temperature-XRD, respectively. It was observed that the incorporation of CeO_2 into ThO_2 lattice has a noticeable effect on it's thermal expansion behaviour. The increase in average linear thermal expansion coefficient (α_l) on going from ThO_2 to CeO_2 can be attributed to a relatively higher α_l value of CeO_2.

Thermal expansion of $BaThO_3$ and $SrThO_3$

A large number of fission products are formed, during the fission of uranium. It is desired to study the chemical state of these fission products. The probability of the formation of oxides of fission products, is much higher in the case of thoria-based fuels as compared to that of urania-based fuels because unlike UO_2, ThO_2 lattice cannot accommodate oxygen at interstitials, due to it's fixed oxidation state. The existence of various compounds formed by the interaction of oxides of some of these fission products with ThO_2, is not well documented. In view of this, $BaThO_3$ and $SrThO_3$ powders were synthesized, by a self-propagating combustion technique. The powders resulted in highly dense pellets on sintering at 1923 K. It was observed that the average linear thermal expansion coefficients, α_l, values (293-1123 K) for $BaThO_3$, $SrThO_3$ and ThO_2 are 11.09 x 10^{-6}, 10.49 x 10^{-6} and 9.10 x 10^{-6} K^{-1}, respectively, which are about 21.9 and 15.3 %, higher than that of pure ThO_2.

Preparation of highly sinter-active thoria powders

Thoria has an inherent problem of poor sinter-activity. It is known that nano-ceramics have far superior

sinterability compared to their bulk counterparts. In view of this, nanocrystalline thoria powders were prepared, by a combustion process. The technique involves the exothermic decomposition of viscous liquid, prepared by thermal dehydration of the aqueous solution, containing thorium nitrate and glycine. Thoria powders of different crystallite size and surface area were prepared, by varying ocidant-to-fuel molar ratios (stoichiometric and fuel-deficient). The exothermic decomposition of viscous liquid, at about 200°C, containing thorium nitrate-to-glycine in molar ratio 1:1.2, yielded the well-crystalline nano-sized ThO_2 powder (15 nm), with surface area about 90 m^2/g). These thoria powders were highly sinter-active as dense pellets (≥ 93 % th.d.) could be obtained at relatively low sintering temperature of 1300°C for 3 hours. The sintered pellet's microstructure was investigated by SEM.

Research on Glasses for AHWR waste

AHWR waste will have additional constitutes like Th, Al and F. Thus, there is a need to modify the existing borosilicate glasses or to develop new glasses. In view of this, a collaborative research programme was initiated with Waste Management Division, BARC. Some of the representative results are discussed below.

Study of thorium solubility in barium borosilicate glass

In general, solubility of actinides in silicate glass matrix is low. In case of thorium, a maximum solubility of 2-6 wt% in borosilicate glasses quenched from near 1250°C has been reported. From the above data, it is clear that borosilicate glass matrix has low solubility of thorium and in all probability it may act as a 'waste load' limiting factor. In order to circumvent this problem, Th solubility limit assessment in Barium BoroSilicate (BBS) matrix was investigated.

Detailed study of the structural aspects of these glasses, using different techniques is desirable, to understand the bonding characteristics of Th^{4+} in the borosilicate network and their thermal stability. In view of this, barium borosilicate glass loaded with different amounts of thorium was prepared, which was investigated by X-Ray Diffraction (XRD), Differential Thermal Analysis (DTA), ^{29}Si and ^{11}B Magic Angle Spinning Nuclear Magnetic Resonance (MAS NMR), IR, EPMA to understand the structural features and location of Th^{4+} ions in these glasses. In addition to this, thermo-physical properties like glass transition temperature, microhardness, thermal expansion behaviour were also investigated. XRD and EPMA/WDS studies, carried out for barium borosilicate glasses containing different amounts of ThO_2 clearly revealed that about 15.87 wt% of ThO_2 can be incorporated in BBS glass. In case of glasses containing more than 15.87 wt% thoria, XRD studies showed the presence of crystalline phases (Fig. 1) identified as thorianite and thorite, which was further confirmed by EPMA.

^{29}Si and ^{11}B MAS NMR patterns of these glasses were recorded using a Bruker Avance DPX 300 machine and are presented in Fig. 2.

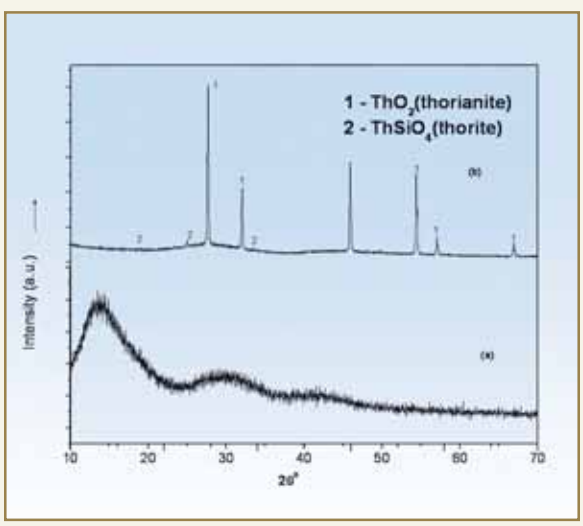

Fig. 1: XRD patterns of BBS glasses containing (a) 15.87 wt % of ThO_2 and (b) 23.75 wt % of ThO_2

It can be seen from ^{29}Si NMR patterns for all the samples, that an asymmetric peak placed at –89.5 ppm is observed. Deconvolution of this peak assuming a Guassian line shape, resulted in two peaks around –95 and –86 ppm. Based on the ^{29}Si MAS NMR studies of borosilicate glasses, the peak around –95 ppm, characteristic of Q^3 structural units of silicon and that around –86 ppm, is attributed to Q^2 structural units (where Q^n represents silicon structural units having 'n' bridging oxygen atoms). The relative concentration of Q^3 and Q^2 structural units and their chemical shift values are not affected by increasing ThO_2 concentration, establishing the fact, that the borosilicate network is unaffected by ThO_2 incorporation in the glass. Similarly, from ^{11}B MAS NMR patterns of the glasses, it can be seen, that intensity and the line shape of these spectra remained almost unchanged, with increase in ThO_2 contents, indicating that there is no interaction between ThO_2 and the boron structural units. Differential thermal analyzer studies also corroborate the above observations, as there is no change in glass transition

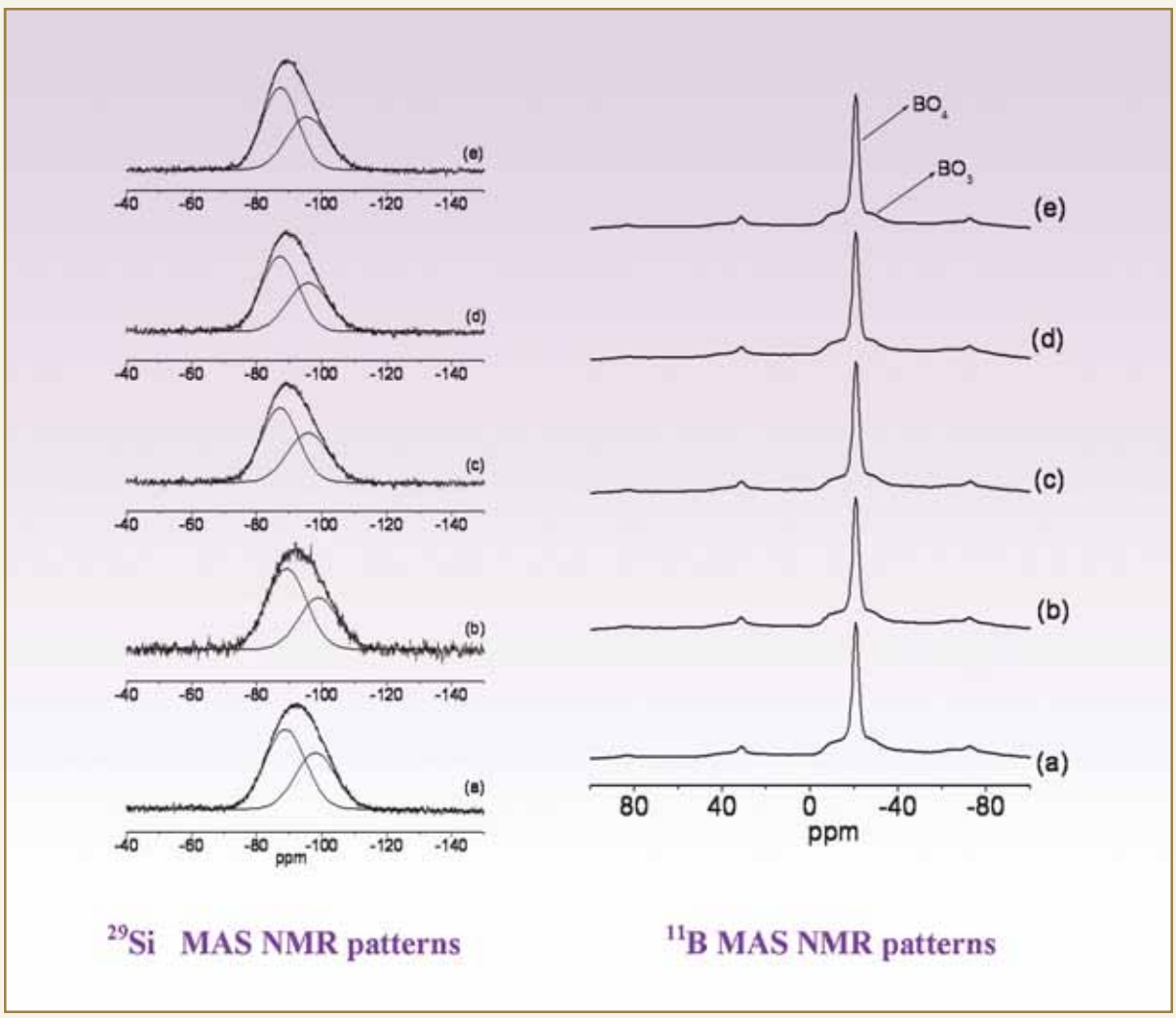

Fig. 2: MAS NMR patterns for barium borosilicate glasses containing (a) 0 wt % (b) 6.8 wt %, (c) 13.2 wt %, (d) 15.8 wt% and (e) 18.6 wt % of ThO_2.

temperature of BBS glass having different amounts of ThO_2.

Structural aspects of barium borosilicate glasses containing thorium and uranium oxides

It was felt worth while to study the structural aspects of borosilicate glasses, when both uranium and thorium oxides are incorporated in it. Barium borosilicate glasses containing a fixed concentration of ThO_2 (15.86 wt % i.e. the upper limit as shown in previous section) and incorporated with different amounts of uranium oxide (UO_3) and their structural aspects using ^{29}Si and ^{11}B MAS NMR and XRD techniques were studied. ThO_2 amount was kept at 15.86 wt. % as it is close to the optimum ThO_2 concentration that can be incorporated into the barium borosilicate glass without any phase separation. XRD patterns of barium borosilicate glass without any thorium and uranium oxides, showed a broad peak around 2θ value of 13° characteristic of amorphous borosilicate network. Above 7.5 wt. % uranium oxide incorporation, phase separation in the glass took place as revealed by the sharp peaks observed around 2θ values 27.53°, 31.89°, 45.77° and 54.25°, attributed to the presence of crystalline ThO_2 phase in the glassy matrix. ^{29}Si MAS NMR patterns (not shown) for barium borosilicate glasses containing 15.86 wt.% of thorium oxide and incorporated with varying amounts of uranium oxide were recorded, along with the glass sample without any thorium and uranium oxide incorporation. Barium borosilicate glasses without any thorium and uranium oxide, showed a broad asymmetric peak around –92 ppm. De-convolution based on a Guassian fit resulted in two peaks around –98 and –89 ppm, characteristic of the Q^3 and Q^2 structural units of silicon respectively, (where Q^n represents silicon structural units having "n" bridging oxygen atoms). With 15.86 wt.% incorporation of ThO_2 in the glass, the relative concentration of Q^3 and Q^2 structural units remained unaffected, suggesting that thoria incorporation does not result in the breakage of Si-O-Si linkages. However, with incorporation of 5 wt.% of uranium oxide in the thorium oxide incorporated glass, the ^{29}Si MAS NMR line shape changes and based on the de-convolution of the NMR pattern it can be seen that, the relative concentration of Q^2 structural units increases at the expense of Q^3 structural units. With further increase in uranium oxide concentration, the relative concentration of both Q^2 and Q^3 structural units and their chemical shift values remained unaffected. Identical chemical shift values for both Q^2 and Q^3 structural units of silicon, with increase in uranium oxide concentration suggest that, there is no direct interaction between silicon and uranium structural units and uranium ions probably occupy the sites, created by the significant number of non-bridging oxygen atoms, present in the glass (network modifying sites). There is no change in the ^{29}Si MAS NMR line shape, even after partial phase separation of ThO_2 from the glass matrix.

The above study clearly shows that the solubility limit of thoria in borosilicate matrices considerably increases, with addition of barium as network modifier in borosilicate glass. Uranium oxide incorporation is associated with the conversion of Q^3 to Q^2 structural units of silicon and the increased number of non-bridging oxygen atoms thus produced, favours the uranium ions to occupy the sites which are created by the non-bridging oxygen atoms in the glass. Above 7.5 wt. % of uranium oxide incorporation in the BBS glass with 15.87 wt% of ThO_2, resulted in phase separation of ThO_2 as revealed by XRD studies.

Inert Matrix Fuels

The development of uranium-free inert matrix fuel is of worldwide interest, as by using this concept, it is possible to annihilate the large stock of plutonium available from dismantled weapons and accumulated stock from the nuclear power plants and also to prepare targets for transmutation of minor actinides. In these fuels, an inert matrix serves as a support for the actinide phases, as does the non-fissile $^{238}UO_2$ matrix for PuO_2 in a typical fast breeder MOX fuel. An

inert matrix material has to satisfy a number of stringent conditions: for e.g. a good neutron economy, superior thermophysical properties, compatibility with the cladding material, stability against radiation and insignificant leachability etc. A number of host lattices are being considered, to act as inert matrices, viz., Multi-phase Ceramic-Ceramic composites (MCC) based on zirconia, alumina or magnesia, $MgAl_2O_4$, ROX (rock-like oxides), yttria-stabilized zirconia (YSZ)-Al_2O_3-$MgAl_2O_4$, YSZ-$MgAl_2O_4$, ThO_2-$MgAl_2O_4$, etc. have also been proposed. Thoria being a very stable oxide (chemically inert), could also be considered as a potential host for diluting and burning plutonia. In this context, it is considered worthwhile to investigate inert matrix coupled with thoria for plutonia burning. During the last few years, considerable research has been done by our group on exploring new materials, which could be potential Inert Matrix Fuels. About 500 compositions in CeO_2-ThO_2-ZrO_2, CeO_2-Gd_2O_3-ZrO_2, CeO_2-Gd_2O_3-ThO_2, CeO_2-Dy_2O_3-ZrO_2 and CeO_2-YSZ-ZrO_2 were prepared, by a solid state route and characterized by XRD. Ceria was used as a surrogate material in place of plutonia. Dysprosia and gadolinia with their high neutron absorption cross sections are potential burnable poisons. ThO_2 acts as a fertile additive which is relevant from the point of view of thorium utilization. Zirconia has high radiation stability and favourable neutronic properties, which makes it an ideal choice to act as inert matrix. Silicates with zircon structure have a high potential from the point of view of inert matrix fuel, because of their high melting point and highly stable structure. Also, in nature considerable amounts of uranium and thorium are locked in zircon lattices and therefore it is appropriate to do a sort of reverse engineering on zircon and related lattices like thorite etc. The phase relations / diagrams established in these studies, can be used to simulate the corresponding PuO_2-based systems.

Radiation stable materials

Disposition of minor actinides is one of the most pressing problems. One of the means of doing so, is Partitioning and Transmutation of minor actinides using ADSS or disposal in a geological repository. Among the many thermo-physical requirements for materials to serve the above application, radiation damage is one of the most important concerns. Radiation damage caused in materials is specified in terms of displacement per atom (dpa). Radiation damage is going to be much more severe in case of ADSS as compared to PHWR or PFBR. The radiation damage cane is usually simulated using ion accelerators in order to evaluate materials.

In view of this, work was initiated in collaboration with HPPD, BARC, to understand the radiation-induced material modifications in Pyrochlores ($A_2B_2O_7$), CeO_2 and ThO_2. Here some typical results for pyrochlores and CeO_2 are being summarized.

Pyrochlores ($A_2B_2O_7$) are being contemplated as potential host lattices, for accommodating minor actinides and hence their use as materials for storage of nuclear waste and also as inert matrix fuels for transmutation. We performed irradiation experiments using ions in the electronic stopping regime, to simulate the damage caused by fission fragments. The results show that the radiation susceptibility of these pyrochlores in the electronic stopping regime, strongly depends on the radius ratio of A to B cations and hence, on the energy required for formation of cation antisites and anion Frenkel pairs. X-ray diffraction (Fig. 3) on the irradiated materials indicate amorphization in $Gd_2Ti_2O_7$ at the lowest S_e used and a transition to anion-deficient fluorite (*Fm3m*) structure in $Nd_2Zr_2O_7$ and $Gd_2Zr_2O_7$ at higher S_e. In $Nd_2Zr_2O_7$ this is followed by amorphization, whereas, $Gd_2Zr_2O_7$ does not amorphize even at the highest S_e employed.

Raman spectra of $Gd_2Zr_2O_7$, irradiated with 120 MeV Au with 2.4×10^{13} ions/cm^2, show band broadening due to loss of translational symmetry, O-Gd-O band shifts towards higher frequencies indicating shortening of bonds. Most importantly, the T_{2g} band

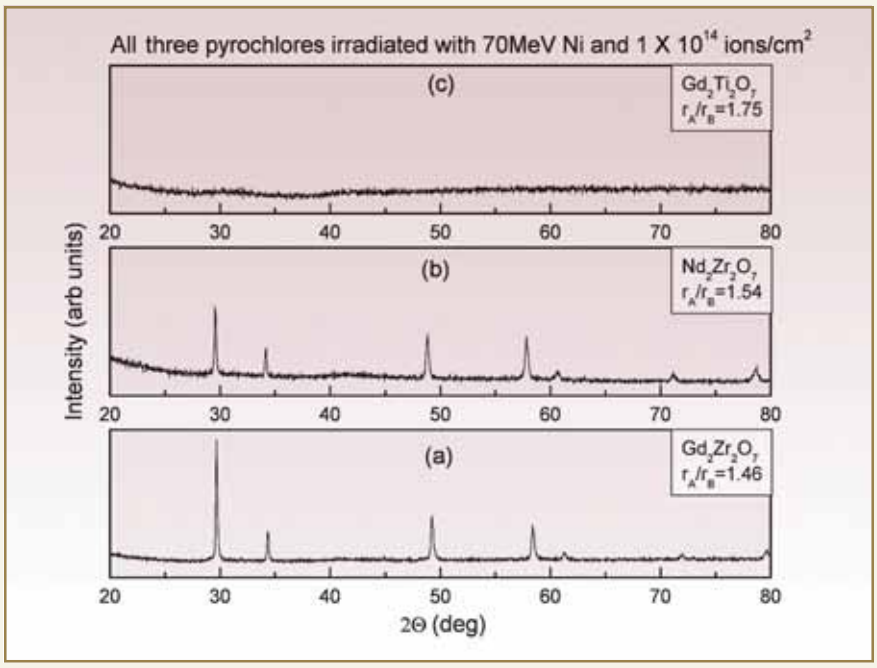

Fig. 3: XRD patterns of (a) $Gd_2Zr_2O_7$ (b) $Nd_2Zr_2O_7$ (c) $Gd_2Ti_2O_7$ irradiated by 70 MeV Ni with 10^{14} ions / cm^2

at 700 cm^{-1}, characteristic of the ZrO_6 octahedra in pyrochlore shifts towards lower frequencies with an increase in intensity, indicating an increase in the coordination of Zr from 6 to near 8 for fluorite structure. CeO_2 is envisaged as a potential inert matrix fuel candidate, for transmutation of Americium. In view of this, radiation stability of CeO_2 has been investigated in the nuclear stopping and electronic stopping regimes, in order to simulated/recoil and fission fragment damage. CeO_2 was irradiated with 300 keV Ar, 500 keV Xe ions and 100 MeV I, with varying ratios of nuclear to electronic energy loss at room temperature. X-ray diffraction measurements show a volume swelling and the maximum damage simulated in the present experiments, is about 300 dpa. CeO_2 shows exceptional stability with no signatures of amorphization; however damage caused in the electronic stopping regime seems to be more. The transmission electron microscopy results, show formation of ion tracks and large dislocation loops and the electron diffraction pattern shows no signatures of amorphization. These studies are likely to find application in the selection of a suitable host lattice for transmutation of minor actinides.

Research on Nano-materials

Nanomaterials (1-100 nm in size) owing to their potential for technological applications, have gained immense attention. Nano-materials exhibit improved properties as compared to conventional bulk materials and hence can be utilized for various applications for their electronic, ionic, thermal, optical and catalytic properties. In view of this, research on various nanomaterials is going on in our group. Some of the recent results are discussed in the following sections.

Nano-ceramics by combustion process

During the last ten years, a large number of ceramics such as CeO_2, ZrO_2, YSZ, ThO_2, yttria-doped-thoria, yttria-stablized-zirconia, Sr_2CeO_4, $SrCeO_3$, ZrO_2-CeO_2 based oxygen storage capacitors, barium polytitanates, Ca or Sr substitutes $LaCrO_3$, pyrochlores, multiferroic materials such as $YCrO_3$, $CeCrO_3$ etc. have been prepared by our group. Most of these samples were synthesized by combustion method. Various powder properties could be tailored by varying oxidant-to-fuel ratio. An important outcome of this work was preparation of highly sinter-active powders, for various applications such as Solid Oxide Fuel Cells.

The combustion technique is capable of producing nanocrystalline powders of oxide ceramics, at a lower calcination temperature, in a surprisingly short time.

The solution-combustion is a two-step process viz. (i) formation of a precursor and (ii) auto-ignition. The nature of the fuel and it's amount are important process parameters for getting the transparent viscous gel without any phase separation or precipitation. The two events, which occur during combustion are (i) generation of heat of combustion and (ii) gas evolution. Heat of combustion (or flame temperature) helps in crystallization and formation of the desired phase.

Combustion synthesis of nanocrystalline yttria: tailoring of powder properties

Yttrium oxide (Y_2O_3) represents a novel prototype for high temperature materials, for electrochemical applications. Owing to it's high chemical stability and refractory nature, it has a wide range of applications e.g. high - temperature chemical-resistant substrate, crucibles for melting reactive metals. In view of it's application, yttria, with tailored powder properties was synthesized by the combustion technique, using glycine as the fuel. The particle sizes of the calcined powders, with different oxidant-to-fuel ratios, were in the range of 8 to 30 nm. The best powder properties were observed for powders with glycine-to-nitrate ratio of 1:1. This product has a crystallite size of about 8 nm and a high surface area of about 165 m^2/g after calcination at 600 ^oC. The size of the primary crystallites, nature and extent of the aggregation, was also investigated by transmission electron microscopy. The sintered density obtained for this powder was about 97 % of the theoretical density. The sintered microstructure, as studied by scanning electron microscopy, revealed the presence of fine grains. A remarkable correlation between the oxidant-to-fuel ratio and the powder properties was established.

$YCrO_3$: an interesting multi-ferroic material

$YCrO_3$ is an important multi-ferroic material. It's synthesis in single-phasic form is of prime significance. The conventional solid state synthesis of $YCrO_3$ requires high temperatures and long annealing duration. Therefore, a facile low temperature synthesis of $YCrO_3$ was developed, using the solution glycine-nitrate combustion. It was observed that the phase pure orthorhombic $YCrO_3$ could be obtained using stoichiometric ratio, whereas, the combustion reaction performed in the fuel-deficient ratio resulted in the formation of zircon-type $YCrO_4$. The formation of phase pure $YCrO_3$ in the stoichiometric ratio, can be attributed to high exothermicity, generated during the combustion reaction. The average crystallite size of nano-crystalline $YCrO_3$, as found by Scherrer's formula was found to be 36 nm. The HRTEM micrographs of nano-crystalline $YCrO_3$ shows the presence of onion like structure made of concentric rings. Nano-crystalline $YCrO_3$ powder was also studied by SQUID between 5K to 300 K at 10 kOe, which revealed the presence of antiferromagnetism at 140 K, along with signatures of a weak ferromagnetism below 100K. The presence of hysteresis in magnetization curve (M vs H) further confirmed the ferromagnetic nature of $YCrO_3$ nano particles. Hence, nanocrystalline $YCrO_3$ exhibits features similar to those of canted antiferromagnetic system, which may be attributed to the nanostructured nature of the material. The dielectric measurements on sintered pellet of $YCrO_3$ indicated the presence of a relaxor type behaviour.

Ce-M-O system (M = Gd, Sm)

Ceria is an important rare-earth oxide that has been attracting ever-growing attention, due to it's varied applications in fuel cells, oxygen gas sensors and as catalysts at different technologically important processes etc. Pure CeO_2 alone as a catalyst is probably of little interest because of it's low textural stability under high-temperature condition, usually encountered in the exhaust gases. It has been observed, that ceria with suitable dopants improves it's stability towards sintering as well as the catalytic activity of the resulting catalysts. Addition of H_2O_2 during synthesis of Sm and Gd doped ceria from the corresponding nitrates,

results in better products. From XRD line broadening and TEM images, it has been found that the particle size obtained from the samples synthesized in presence of H_2O_2 are smaller than the samples prepared in the absence of H_2O_2. The histograms also indicate that particle size distribution is also wider in case of the samples prepared in the absence of H_2O_2. In Raman spectroscopic investigation it has been found, that a peak at 835cm^{-1} appears for the uncalcined samples prepared in the presence of H_2O_2. This peak is due to O-O stretching mode of peroxo (O_2^{2-}) linkage. It can be inferred that the peak at 835 cm^{-1} is due to η^2 peroxo (O_2^{2-}) linkage in precursors. It has been proposed that this band is observed when the metal ion (Ce^{4+}) is connected with peroxo linkage (η^2) in a sideways bonding configuration. During condensation, the precipitate eliminates H_2O and forms M-O-M network, whereas the samples prepared in the presence of H_2O_2 form have peroxo linkages, which hinder the formation of an infinite network. Again upon calcination, these O-O linkages also break down which ultimately leads to higher surface area. Correspondingly, this results in disappearance of the peak at 830 cm^{-1} from the Raman spectrum of both the compositions upon calcinations, which in turn results in materials having higher surface area and lower particle size. Interestingly, this sample showed the reduction in conversion temperature of CO to CO_2 , proving it to be a better catalyst.

Nano-crystalline neodymia doped ceria by the combustion route

Doped ceria (CeO_2) is an important material in view of it's potential application as a solid electrolyte for it's use in oxygen concentration cells and in solid oxide fuel cells. About 8 compositions in the system $Ce_{1-x}Nd_xO_{2-x/2}$ (0.0 ≤" x ≤" 0.50) were prepared, by the gel combustion process. The crystallite size of powders, as obtained by the line broadening method, was typically in the range of 7 to 16 nm. With successive increase of Nd concentration in the ceria matrix, the particle size and surface area decreased, but the agglomerate size increased systematically. In the case of 50 mol% Nd-doped ceria, the powder showed smallest crystallite size (7 nm), smallest surface area (10 m^2/g), and largest agglomerate size (22 mm), which has a strong bearing on sintering. The powders were sintered at 1200°C for 2 h to yield densities in the range of 80-95 % of theoretical densities. This difference can be attributed to the presence of different nature of agglomerates in these samples. These results amply demonstrate that sintering is governed not only by particle size and surface area, but also by agglomerate size. Ionic conductivity measurements were carried out on a few samples in the temperature range of 300 – 700°C. The conductivity values for pure ceria corresponding to grain and grain boundary were found to be 1.5563 x 10^{-2} Scm^{-1} and 0.1265 x 10^{-2} Scm^{-1} at 650°C, respectively. The activation energy (E_a) values of ceria were 0.76 eVand 1.25 eV for grain and grain boundary, respectively. In the case of 50 mol% doped ceria, total conductivity was calculated as the frequency response for the grain and grain boundary were too close to resolve. The conductivity of this sample was found to be 1.3672 x 10^{-2} Scm^{-1} and the activation energy was 1 eV at 650 °C.

Lanthanide-based Optical Nanomaterials

One of the major requirements for further development in solid state lighting, is the synthesis of efficient optical materials. Key contributory factors include quantum confinement of electrical carriers within nanoparticles, efficient energy and charge transfer over nanoscale distances and in many systems, a highly enhanced role of interfaces. Phosphors are composed of an inert host lattice and an optically excited activator, typically a 3d or 4f electron metal ion. Gadolinium oxide (Gd_2O_3) has been shown to be a good host for the luminescence of rare-earth ions. Gadolinium oxide host and europium /dysprosium / terbium-doped gadolinium oxide nanoparticles were synthesized using the sonochemical technique. Gadolinium oxide nano crystals were also co-doped with total 2 mol% of Eu^{3+}/Dy^{3+}, Eu^{3+}/Tb^{3+}, Dy^{3+}/Tb^{3+} and also Eu^{3+}/Dy^{3+}/Tb^{3+}

ions, by the same method. The nanoparticles obtained were characterized, using powder X-ray diffraction (XRD) and HRTEM.

In the triple doped Gd_2O_3 sample also, the total doping concentration was 2 mol%. In the first case, each of the rare-earth ions was doped equally, the doping level being 0.67 mol%. When doped with equal amounts of RE^{3+} (RE = Eu, Tb, Dy) ions, a weak green and strong red emission respectively of Tb^{3+}, Eu^{3+} along with weaker yellow emission of Dy^{3+} were observed. On excitation at 230 nm, the host absorbs and energy transfer takes place to all the lanthanide ions present, leading to these emissions. The PL intensity of Dy^{3+} ion in this equally doped sample, was found to be comparatively weak and was dominated by red emission from Eu^{3+} ion. Hence, a new sample was prepared, having a higher concentration of Dy^{3+} ions (1.5 mol%), keeping the total doping level at 2 mol %. In this case, the blue emission of Dy^{3+} ions (487 nm) was found to be doubly intense. Although the concentration of Tb^{3+} ions was decreased in this sample, intense green emission was clearly seen at 543 nm, suggesting a possible energy transfer from Dy^{3+} to Tb^{3+} ions, as was observed in the case of double-doped sample. Consequently, a third sample was prepared, wherein the concentrations of Eu^{3+} and Tb^{3+} ions were reduced drastically. It could be inferred that the triple-doped Gd_2O_3 phosphor can be fine-tuned to give PL emissions at selected wavelengths with desired intensities.

In continuation of this work, we have been successful in synthesizing a novel nanocrystalline Gd_2O_3:RE (RE = Dy, Tb) phosphor, which simultaneously emits blue and yellow light from it's active region on exciting the host and consequently has tremendous application in white light-emitting deep UV-LEDs. These phosphors have been synthesized using a sonochemical technique. The corresponding chromaticity diagram is shown in Fig. 4. The points I, II and III in the diagram, correspond to CIE coordinates, on excitation at 230 nm, 247 nm and 277 nm, respectively. In case of 230 nm excitation, the LED emission appeared predominantly yellow. The CIE chromaticity coordinates calculated for point II correspond almost exactly to the CIE coordinates of the balanced white light region of the chromaticity diagram, where x = 0.33, y = 0.33.

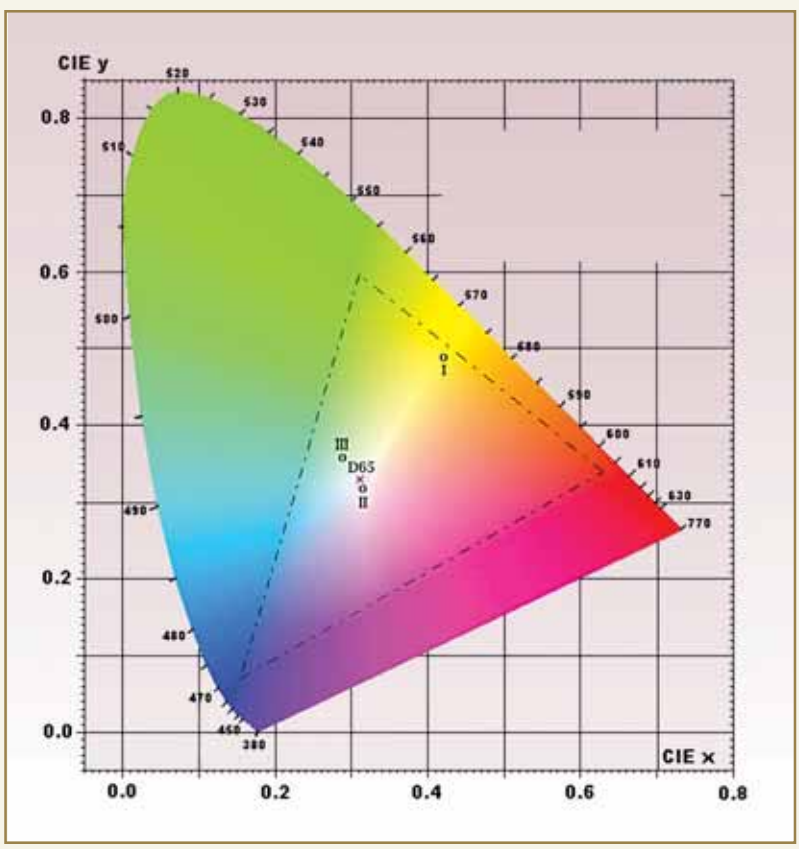

Fig. 4: CIE coordinates of Gd_2O_3: (Dy, Tb) phosphor

Nanomagnetic materials

Of late, considerable thrust is on nanomaterials with size-dependent

magnetism. Some typical results in this direction are discussed.

Spintronics materials

Transition Metal (TM) doped ZnO-based Diluted Magnetic Semiconductors (DMSs) are promising group of materials, for achieving Room Temperature Ferromagnetism (RTF). Soft-chemical routes have assumed an unprecedented significance in these materials, as the observation of ferromagnetism is found to be dependent on preparation conditions. In general, the conventional high temperature ceramics route, which often leads to the formation of secondary phases, does not yield intrinsic ferromagnetism.

In our group, various soft chemical routes such as combustion, coprecipitaion, template synthesis, sono-chemical route, single pot synthesis etc. are being employed, to prepare good quality spintronics materials. Mainly host lattices like ZnO, In_2O_3, CeO_2 etc. are being explored, to accommodate an optimum level of transition metal ions such as Fe, Co, Cr. The absence of parasitic phases is being ascertained by detailed HR-TEM investigations. The magnetic properties of these materials are investigated, using a SQUID magnetometer. Recently, yet another novel method of preparation of ZnO and Mn-doped ZnO particles at relatively high temperature (900 °C), using polystyrene (PS) as a template, was employed. The nano-particles of ZnO and Mn doped ZnO (5 at % Mn) were prepared, by infiltrating an aqueous solution of Zn^{2+} and Mn^{2+} ions mixture, into a dried aqueous solution of PS beads (630 nm sizes), followed by the removal of the template (PS) by rapidly heating to 900 °C in air. This is perhaps the first ever report of the observation of significantly enhanced room temperature ferromagnetism, in high temperature synthesized Mn doped ZnO particles, with Mn concentration above 2.2 at.% using PS as a template. The next step in research on spintronics materials, is to prepare thin films using a Piezo-electric based ink jet printer, for various applications.

Nano-crystalline $GdFeO_3$

$GdFeO_3$ belongs to the perovskite rare-earth ortho-ferrites. These materials form an important class with a wide range of applications such as ferroelectricity and magnetism. The synthesis of such ferrite materials is quite challenging because of the formation of garnet phase, which is thermodynamically more stable than the desired ferrite. Nano-crystalline $GdFeO_3$ powder was synthesized by a gel combustion technique, using glycine as the fuel and the corresponding metal nitrates as oxidants. It was observed that phase pure $GdFeO_3$ was obtained, only when the fuel content is increased to 1:1.2 as observed without any impurity phase. The crystallite sizes for the phase pure products after calcination at 600°C, were in the range of 40 to 65 nm. The magnetic hysteresis for $GdFeO_3$ at 5 K under FC condition (H_{FC} = 100 Oe) was studied. The coercivity (Hc) and remnance (Mr) were found to be 370 Oe and 0.4 emu/g), respectively. Furthermore, the hysteresis loop was found to be shifted slightly along the field axis i.e., loop is not symmetrical, which is an indication of the exchange interaction between different magnetic sublattices. One plausible explanation is the coupling between spin-canted structure of (weakly ferromagnetic) Fe sublattice and (antiferromagnetic) Gd sublattice. In nanoparticles, uncompensated surface spins (at steps or grain boundaries) are known to create interfacial exchange energy, with the core particles.

Nano-crystalline $HoCrO_4$: facile synthesis and magnetic properties

$RECrO_4$ materials, with zircon type structure, are expected to exhibit interesting magnetic properties. However, their synthesis is quite challenging due to the presence of Cr^{5+}, an unusual oxidation state. In fact, it is almost impossible to synthesize these materials by a solid state route, as it would require high pressure of oxygen to stabilize Cr^{5+} state. Recently, we developed a soft-chemical route for synthesis of these materials. Some typical results are being discussed. Nano / crystalline $HoCrO_4$ powder was synthesized by a combustion technique, using glycine and citric acid as fuels, in different oxidant-to-fuel ratios. Fuel-

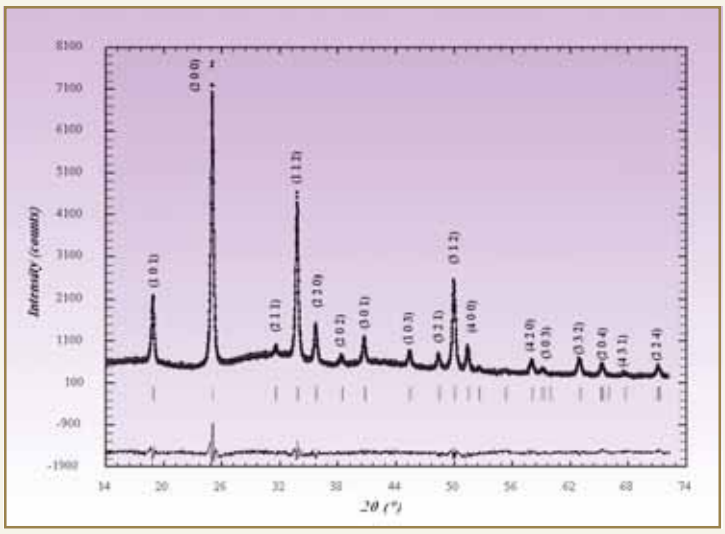

Fig. 5: XRD pattern of $HoCrO_4$ recorded using Cu-Kα

deficient glycine-nitrate combustion reaction, resulted in zircon type $HoCrO_4$ free from $HoCrO_3$ phase. The XRD pattern of the calcined $HoCrO_4$, having a tetragonal phase modification, is shown in Fig. 5. No detectable reflections attributable to the impurities such as Ho_2O_3, Cr_2O_3 or $HoCrO_3$ were observed, indicating the phase pure product. The crystallite size for the phase pure product after calcination at 575°C in oxygen atmosphere was found to be 34 nm by X-ray line broadening. The TEM observations showed highly porous structure. Magnetic measurements reveal the ferromagnetic nature of $HoCrO_4$ nano particles with Tc = 18 K. The compound shows high remnance of 30.4 emu.g^{-1} and low coercivity of -0.0343 T. The μ_{eff} of $HoCrO_4$ was found to be 10.32 μ_B per formula unit, which agreed reasonably well with the theoretically expected value of 10.74 μ_B per formula unit.

Research on Functional materials

Materials with tunable thermal expansion behaviour: role of structure

Thermal expansion is an important property for any material to be used in a thermal gradient. The detrimental effect of the thermal expansion on it's own or in coupled materials, needs extra precaution to withstand thermal stress. Tailored thermal expansion materials are likely to prevent unwanted thermal stress. It is well known that thermal expansion of any materials arises from the anharmonic vibration of atoms of chemical bonds. Thus, the thermal expansion of any material is related to the strength of the chemical bonds. It has been observed, that the solids with ionic or metallic bonds exhibit a higher thermal expansion as compared to those with covalent bonds, e.g. Si-O bond, shows an insignificant thermal expansion as due to strong covalent character.

In general, ceramic materials used in common applications, show significant thermal expansion due to the expansion of chemical bonds. However, there are also several previouly known low thermal expansion ceramic materials. In addition to this, materials showing a large negative thermal expansion have been reported in literature. Sleight and his group explained the large negative thermal expansion of ZrW_2O_8 from precise crystal structure analysis at various temperatures. Following this, a large number of exploratory studies in phosphates, tungstates, molybdates etc. resulted in newer materials with low or negative thermal expansion coefficients. From these studies it is well understood that the transverse vibration of bridging atoms of framework crystals, shows negative or low thermal expansion. Moreover there are several densely packed zircon-type materials also, which show low thermal expansion behaviour. The analysis of the thermal expansion of various materials, suggests the expansion trend and magnitude and is a manifestation of the crystal structure and bond strength. A large number of framework and non framework materials have been extensively studied by us by variable temperature diffraction and dilatometry methods and the results are presented in the following section.

$A_2B_3O_{12}$ ($A = Fe^{3+}$, Cr^{3+} and Al^{3+}) system

These trivalent metal ion molybdates, crystallize in monoclinic lattice made up of the AO_6 octahedra and MoO_4 tetrahedra. These polyhedra are connected at the corners giving a flexible structure. The dilatometric study on the sintered pellets, shows a significant positive thermal expansion initially, followed by a phase transition. Beyond the phase transition, all three studied materials show significant negative thermal expansion. The typical values of liner thermal expansion coefficients of the orthorhombic phases are: $-14.82 \times 10^{-6}\ K^{-1}$, $-9.39 \times 10^{-6}\ K^{-1}$ and $-2.83 \times 10^{-6}\ K^{-1}$, for $Fe_2(MoO_4)_3$, $Cr_2(MoO_4)_3$ and $Al_2(MoO_4)_3$, respectively. The presence of phase transition is further confirmed by DSC. To understand the nature of phase transition and expansion behaviour, HTXRD studies on them are carried out. Phase transition arises from the displacement of the polyhedral units to bring the symmetry change from $P2_1/n$ to Pbcn. The high temperature orthorhombic phase $A_2W_3O_{12}$ has also been observed in various heavier trivalent rare-earth ions. Dilatometric data in all cases shows significant negative expansion in these compounds. While the lighter rare-earth group tungstates, viz. $Nd_2W_3O_{12}$ crystallizes in scheelite related structures with cation vacancies and shows significant positive thermal expansion. The closely similar structure of the lighter and heavier rare-earth tungstate, opens a possibility to tune the thermal expansion by varying the composition. A series of compositions with different proportions of $Nd_2W_3O_{12}$ and $Y_2W_3O_{12}$ were prepared and studied by dilatometry. The typical linear thermal expansion coefficient for $Nd_2W_3O_{12}$ is about 7.9 ppm/K and that of $Y_2W_3O_{12}$ is -5.8 ppm / K. A gradation of thermal expansion coefficient from the positive to negative could be established by varying the composition in this series.

AMo_2O_8 ($A = Zr^{4+}$, Hf^{4+}) series

In view of significantly large negative thermal expansion coefficient for cubic ZrW_2O_8 (-8.8 ppm/K), and other analogues compounds, e.g. trigonal form of the $ZrMo_2O_8$ and $HfMo_2O_8$, were investigated by high temperature XRD. The crystal structures of these trigonal molybdates consist of layers made up with AO_6 octahedra and MoO_4 tetrahedral units. The layers are bonded together by a weak attraction (Fig. 6).

The thermal expansion behaviours of these molybdates, were found to be drastically anisotropic, with significantly large positive expansion, perpendicular to the layers as compared to small negative expansion along layers. Similar behaviour was also observed in the case of trigonal $HfMo_2O_8$. The coefficients of axial thermal expansion for $HfMo_2O_8$ are: $\alpha_a = \alpha_b = -6.42$ ppm / °C, $\alpha c = 56.6$ ppm / °C (in the range of 25-700 °C). The large positive thermal expansion along the c-axis is attributed to weak bonding interaction of the layers, while the rotation of the polyhedra, brings the negative expansion along the layer axes. Also, the thermal expansion of a closely packed $HfMo_2O_8$ (about 20 % higher density the trigonal form) prepared by high pressure and high temperature, was also studied by high temperature diffraction. This monoclinic form is a metastable and transforms to original trigonal form at above 600°C. The thermal expansion coefficients of the monoclinic phase ($\alpha_a = 1.3$, $\alpha_b = 15.6$, $\alpha_c = 10.7$ ppm /°C and $\alpha_{vol} = 21.9$ ppm/°C) are relatively lower than the trigonal phase, due to the strong bonding interaction in all directions.

Cristobalite type APO_4 ($A = Al^{3+}$, Ga^{3+} and B^{3+}) materials

Cristobalite, the high temperature modification of SiO_2, has been known for low thermal expansion coefficients. Several APO_4 type phosphates are known to crystallize in almost all modifications of SiO_2 structures and have half of the Si replaced by A and the other half by P atoms. The structure of these compounds contain both $[AO_4]^{3+}$ and $[PO_4]^{3-}$ tetrahedral units and the four oxygen of PO_4^{3-} are

connected to four metal ions. The cristobalite (orthorhombic) lattice for $AlPO_4$ and $GaPO_4$ is observed at elevated temperature, but can be retained at room temperature by annealing for a long time above the cristobalite transition temperature. A series of compositions $Al_{1-x}Ga_xPO_4$ have been prepared and studied by HTXRD and DTA in the temperature range of 25-1000°C. All these compositions undergo reversible displacive transition from low cristobalite (orthorhombic $C222_1$) to high cristobalite (Cubic F-43m) structure at higher temperature. The transition temperature increases gradually from $AlPO_4$ (202°C) to $GaPO_4$ (605°C). The phase transition is accompanied by a significant increase in the unit cell volume, leading to the formation of a low dense structure. The variation of unit cell volume with temperature, for each composition shows, that the orthorhombic phase has a significantly larger thermal expansion than the cubic (high temperature) phase. The coefficient of volume thermal expansion of the high cristobalite phase increases with increase in Ga^{3+} content in the unit cell, while that for the low cristobalite phase decreases with Ga^{3+} content. The phase transition temperatures and associated enthalpy are related to the change in unit cell volume and the orthorhombicity and strain in the lattice of the respective phosphates. Similar studies on BPO_4 which crystallize tetragonal lattice within high cristobalite structure shows significant anisotropic expansion along the a- and c- axes (12.9×10^{-6} and 2.1×10^{-6} / °C, respectively). The average volume thermal expansion coefficient is 28.2×10^{-6} / °C in the temperature range of 25-900 °C.

The variation of crystal structure with temperature suggests, that the M-O-P bond angle arising from the transverse vibration and tilting of tetrahedral units plays a crucial role in their thermal expansion behaviour. A comparison of the thermal expansion coefficient of various high cristobalite type phosphates revealed, that higher the M-O-P bond angle, lower is the thermal expansion coefficient, which can be represented as:

$$\alpha_V (/°C) = -191.32 + 4.33 \times [\theta] - 0.02 \times [\theta]_2$$

(where θ is the inter-polyhedral bond angle).

These studies reveal the role of inter-polyhedral bond angles in tailoring thermal expansion behaviour in a series of materials.

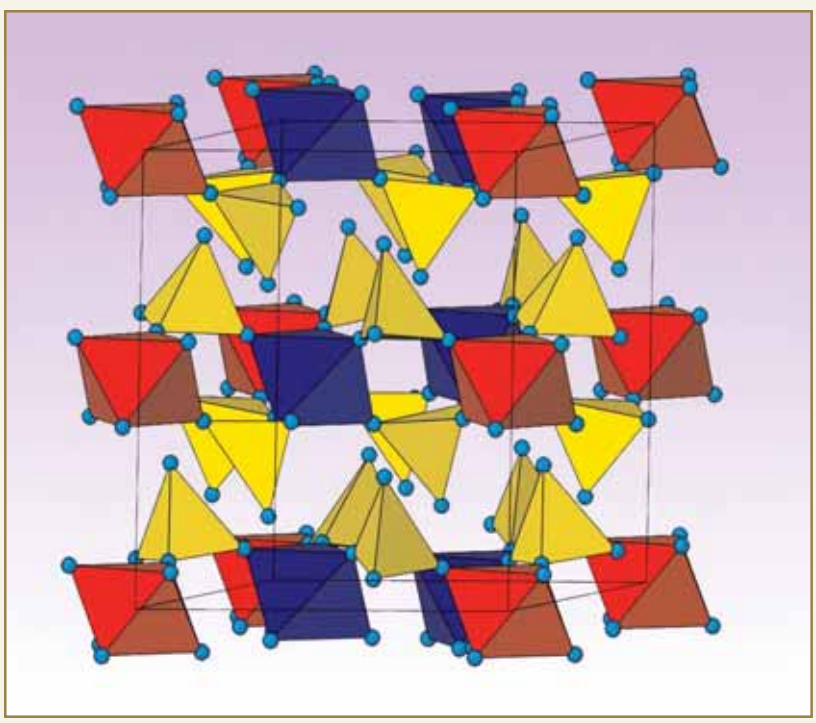

Fig. 6: Crystal structure of trigonal $HfMo_2O_8$ depicting HfO_6 octahedra and MoO_4 tetrahedra

$Gd_{2-y}Nd_yZr_2O_7$ Pyrochlores: Tuning of ionic conductivity guided by structure-property correlation

Pyrochlore structure is cubic with space group *Fd3m*, and the structural formula is $A_2B_2X_6Y$ where A is a trivalent rare-earth ion, but can also be a mono, divalent cation and B may be 3d, 4d or 5d transition element, having an appropriate oxidation state required for charge balance, to give rise to the composition $A_2B_2O_{7-}$.The pyrochlore structure is closely related to the fluorite-structure AX_2, except that there are two cation sites and one-eighth of the anions are absent. Pyrochlore-structured compositions have a wide range of technologically relevant properties, such as high radiation stability (discussed earlier) high ionic conductivity, luminescence etc. In view of this, there has been considerable research interest in studying the phenomena of order-disorder phase transition from pyrochlore ⇔ defect fluorite structure. In addition to fully ordered and fully disordered (defect fluorites) states, partial disorder state can also exist. Recently on the basis of Rietveld analysis of the XRD data and Raman spectroscopic studies on $Nd_{2-y}Gd_yZr_2O_7$ solid solutions, we showed that structural transitions from ordered pyrochlore to disordered pyrochlore take place from $y \geq 1.8$ onwards. The Raman spectra become broader with increase in disorder in the system. The qualitative features of the spectra remain unchanged till $Nd_{0.2}Gd_{1.8}Zr_2O_7$ beyond which the Raman spectra changes drastically. At $Nd_{0.15}Gd_{1.85}Zr_2O_7$, the existing set of modes completely disappears with a concomitant appearance of an altogether new set of modes with enormous broadening which match with phonon frequencies of defect fluorite structure.

In another series, $Nd_{2-y}Gd_yTi_2O_7$, it has been found that with increase in Gd content, structure transitions take place from layered monoclinic to cubic pyrochlore through a biphasic region. The impedance measurements on $Nd_{2-y}Gd_yZr_2O_7$ were carried out, over a frequency range of 100Hz to 15MHz at five different temperatures in the range 622K-696K.

The values of activation energy *E* were determined from the slopes of the linear fits to the σ_{dc} plots. It has been found that both the bulk conductivity σ_{dc} and it's activation energy *E,* show a dependence upon the Nd content. There exists an intermediate composition, at which the dc conductivity exhibits maxima at all temperatures studied in our experiments. Our results suggest that the conductivity of the $Gd_2Zr_2O_7$ system can be increased, by suitable doping at the Gd site by Nd. The activation energy for bulk conduction was found to steadily increase as Nd content decreases. We have also observed that the pre-exponential factor σ_0 of Arrhenius equation behaves in a manner similar to *E*. It steadily increases with decreasing Nd content, indicating that the effective number of mobile oxygen ions increases as Gd replaces Nd at the *A* site. This is consistent with the observation, that there is greater disorder upon incorporation of Gd in the lattice. The increase in s_0 would lead to an increase in conductivity, but the increase in *E* would hinder the oxygen ion migration. Thus the two processes are competing and we observe that the intermediate compositions ($y = 1.0$) show maximum conductivity.

Rare earth based-Inorganic fluorides

Inorganic fluorides find wide application as optical, ionic conducting materials and metallurgical processes. During the last few years, we have carried out extensive crystallographic studies of the rare-earth and alkaline-earth based mixed fluoride systems, to reveal correlation of the ionic radii of rare-earth ion and alkaline earth ions on the crystal chemistry of these systems. It may be noted that except for MgF_2, all alkaline earth fluorides (MF_2) and PbF_2 crystallize in the fluorite lattice. The crystal structure of rare-earth trifluorides can be grouped into the hexagonal tysonite group (LaF_3-PrF_3), orthorhombic YF_3 group (GdF_3-LuF_3) and rhombohedral ScF_3 group (ScF_3). Depending on the method of preparation, SmF_3 and EuF_3 can exist in both tyosnite or orthorhombic structure types. ScF_3 and fluorides of almost all trivalent transition metal ions and some p-group elements, crystallize in

rhombohedral modification. The typical mixed fluorides in MF_2-$M'F_3$ (M = Pb^{2+}, Ba^{2+}, Sr^{2+}, Ca^{2+} and Mg^{2+}; M' = Nd^{3+}, Eu^{3+}, Y^{3+} and Sc^{3+}) have been studied under short annealed condition. The variation of the crystal structure in MF_2-$M'F_3$ system has been revealed, from systematic structural analysis of the series of compositions. The phase fields MF_2-$M'F_3$ of various studied systems are summarized in the bar diagram in Fig. 7.

In all the MF_2-$M'F_3$ systems (except M = Mg^{2+}) the fluorite-type solid solution was commonly observed. (extreme left side of bar diagram). Structural analysis revealed that all the fluorite-type solid solutions have anion excess fluorite lattices. The fluorite-type solid solutions are formed with the random distribution of metal ions over the *4a* site of Fm3m. The anions occupy in the interstitial sites in addition to the normal fluorite anion sites. The formation of solid solution was often accompanied by either dilation or contraction of unit cell parameters. In the formation of fluorite-type solid solution of MF_2 and $M'F_3$, the average cation radius decreases, which contracts the unit cell volume, whereas the presence of extra anions in the lattice expand the unit cell, due to the repulsion of anions in the lattice. The overall unit cell volume of the fluorite-type lattice was explained, on the basis of these two opposite effects. Tysonite-type solid solutions are observed with LaF_3 group rare-earth fluorides. Similar to fluorite-type solid solutions, the tysonite-type solid solutions also show two contributing effects for their unit cell parameters.

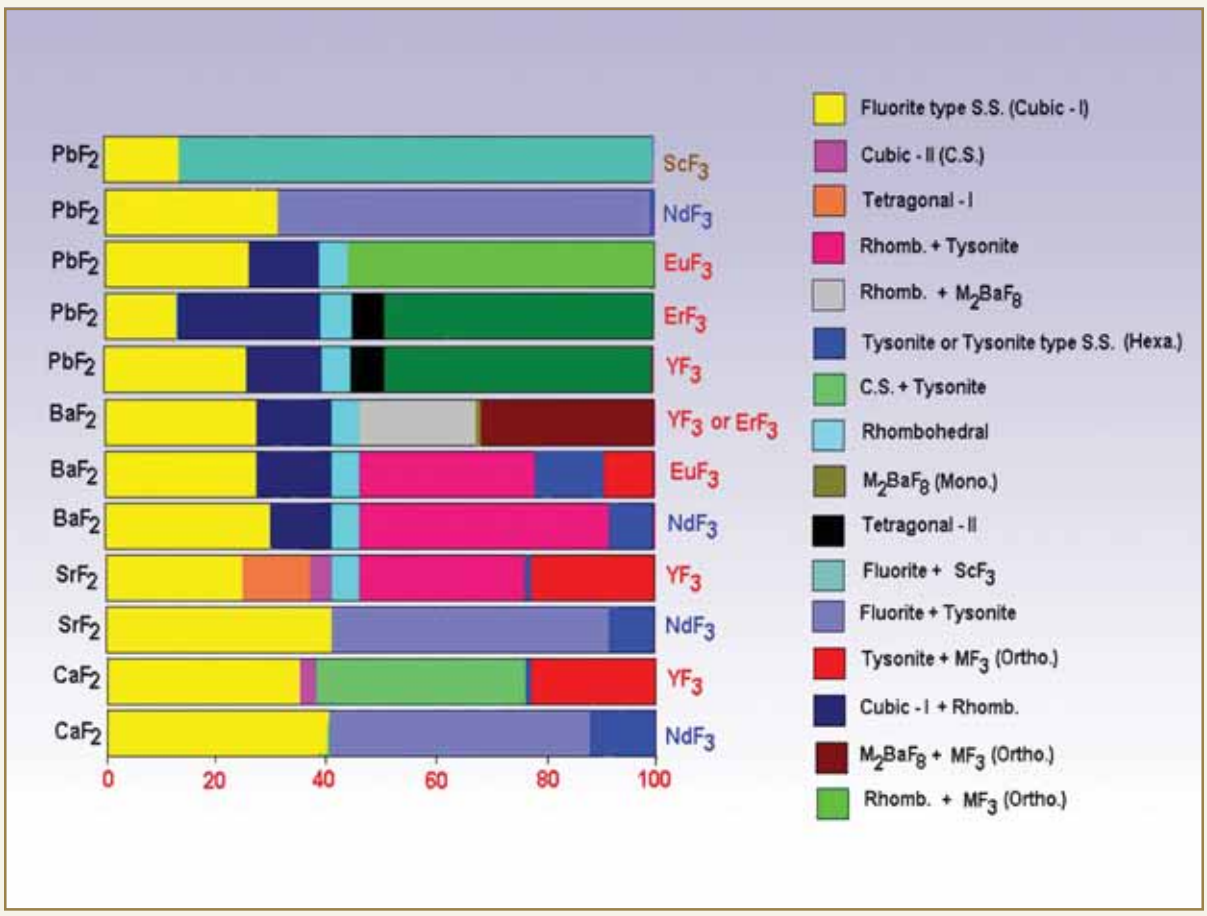

Fig. 7: Phase relation in MF_2-$M'F_3$ systems

Also, it was observed that the width of the solid solution depends on the difference in the ionic radii of the two metal ions.

Several fluorite related ordered phases, like tetragonal, cubic and rhombohedral phases were observed in these systems. A monoclinic $BaM_2'F_8$ ($M' = Y^{3+}$ or Er^{3+}) phase was formed, beyond the rhombohedral phase. A comparative analysis of these systems revealed that the ionic radii of the M^{2+} and M^{3+} ions plays a significant role on the structure of the ordered phase, in the excess anion in the lattice. It can be emphasized that all these structures can be related to either fluorite-type lattice or the rare-earth structures.

The fluorite related ordered structures are formed, with the transformation of the eight coordinated MF_8 cube to square antiprism. This arrangement results in a cluster of the M_6F_{36} cluster, which represents the unique structural entity in all the anion excess fluorite related structures. This M_6F_{36} structure can also be visualized as the cubo-octahedron of fluoride ions, with capping of metal ions on all the six square faces. An additional anion often occupied the inside of the cubo-octahedron cluster of the fluoride ions.

The ionic conductivity of these anion excess solid solutions was also investigated. In PbF_2-YF_3 systems, ionic conductivity gradually decreases accompanied with an increase in the activation energy, on increasing the yttrium content up to about 5 mol % and above which the trend is reversed. This unusual result was explained on the basis of a cumulative effect of the decrease in polarization and increase in concentration of interstitial anions, as a result of Y^{3+} incorporation in PbF_2 lattice.

Recently, a hitherto unkown compound, $LiScF_4$ with scheelite structure (Fig. 8) has been prepared by high pressure and high temperature technique. The crystal structure is built from LiF_4 tetrahedra and

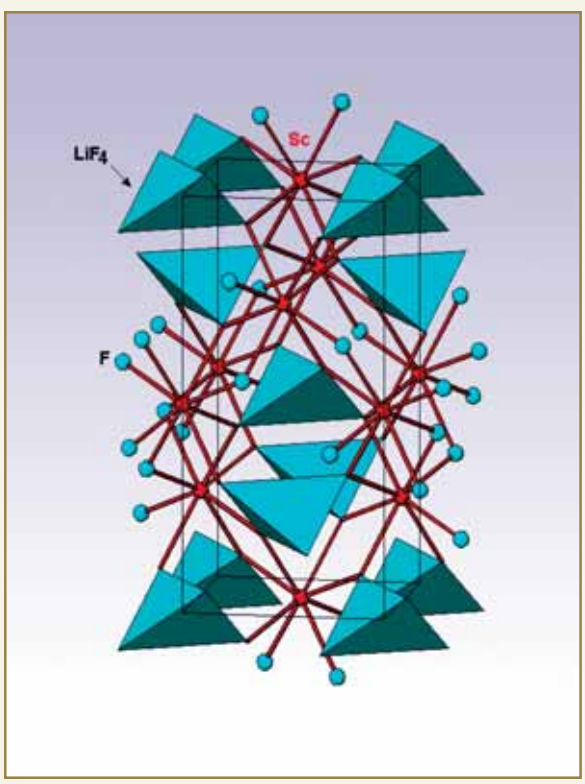

Fig. 8: Crystal structure of $LiScF_4$ (LiF_4 tetrahedra are shown)

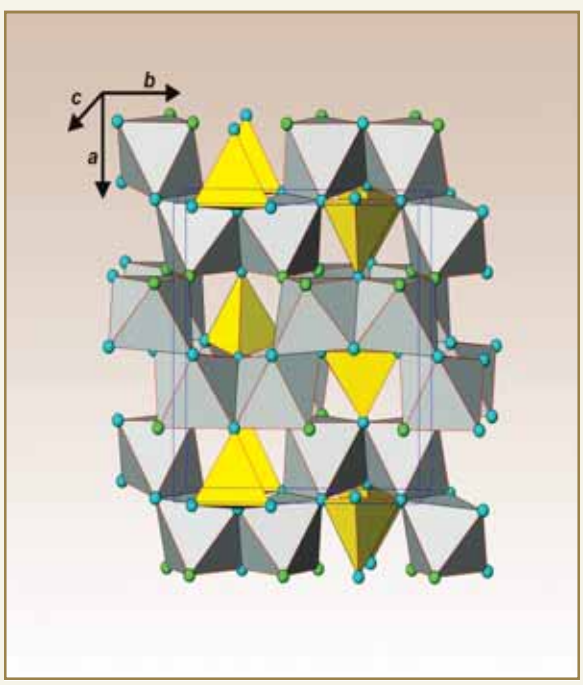

Fig. 9: Crystal structure of $V_2GeO_4F_2$ (VO_4F_2 octahedra and GeO_4 tetrahedra are shown).

ScF_8 bisdisphenoid. The unusual high coordination of Sc^{3+} could be stabilized by high pressure method. $LiScF_4$ showed intense luminescence in the far IR region, after Er^{3+} doping. A new topaz type oxyfluoride, $V_2GeO_4F_2$ was prepared and detailed crystal structure has also been investigated. The crystal structure of $V_2GeO_4F_2$ is formed with the edge and corner shared VO_4F_2 octahedra in a zigzag manner (Fig. 9). The one -dimensional anti-ferromagnetic diffused transition has been observed, in this material.

Thus, it can be inferred that rare-based fluorides have very rich crystal chemistry and these materials are endowed with several superior properties as compared to their oxide counterparts.

Conclusions

An attempt was made in this review article to provide highlights of some of the relevant and contemporary Solid State Chemistry programmes pursued by our group. The structure-property correlation was discussed by giving several examples. The importance of soft-chemical routes for preparation of technologically- important materials, was also emphasized. As mentioned earlier, it was a Herculean task to provide details of all these research activities in the present article, mainly due to space constraints. For further details, interested readers are requested to contact the author.

Acknowledgements

I place on record my sincere acknowledgements for the encouragement and support provided by Dr. D. Das, Head, Chemistry Division, BARC and Dr. T. Mukherjee, Director, Chemistry Group, BARC.

ABOUT THE AUTHOR

Dr. A. K. Tyagi, presently Head, Solid State Chemistry Section, Chemistry Division, joined BARC in 1986 from the 29th Batch of BARC Training School. Since then, he has been working in the field of Chemistry of Materials. In recognition of his seminal contributions in the field of Nuclear Materials, Nanomaterials and Functional materials, Dr. Tyagi was conferred with the Homi Bhabha Science & Technology Award 2006, which is the highest award in DAE, on the11 May, 2008 by Dr. A. P. J. Abdul Kalam, former President of India. He is a recipient of several other prestigious awards such as Dr. Laxmi Award by ISCAS, Rheometric Scientific-ITAS Award, Gold Medal of Indian Nuclear Society, MRSI Medal, CRSI Medal and IANCAS - Dr. Tarun Datta Memorial Award. He is a Fellow of the Maharashtra Academy of Sciences and National Academy of Sciences, India. He was a Max-Planck Fellow at MPI, Stuttgart, Germany during 1995-96. He is a recognized Ph.D. guide of the Mumbai University and the Homi Bhabha National Institute (HBNI).

बीएआरसी न्यूज़लेटर
BARC NEWSLETTER

BHABHATRON: AN INDIGENOUS TELECOBALT MACHINE FOR CANCER TREATMENT

K. Jayarajan, D.C. Kar, R. Sahu and Manjit Singh
Division of Remote Handling and Robotics

Mr. K. Jayarajan is the recipient of the Homi Bhabha Science and Technology Award for the year 2006

ABSTRACT

Cancer is a major health problem in India. Most of the cancer patients need radiation therapy during the course of their treatment. However, there is an acute shortage of radiotherapy facilities in the country, due to the high cost of radiotherapy machines. To meet the demand for affordable machines, Bhabha Atomic Research Centre has developed a telecobalt machine, called Bhabhatron. Compared to any imported telecobalt machines, the indigenous machine is cheaper and superior in features. Now, Bhabhatrons are installed in many cancer hospitals in the country.

Introduction

In India, there are about 20-25 lakh cancer patients. The number will nearly double by the year 2015. Every year, about eight lakh new cancer cases are detected and over five lakh patients die due to this dreaded disease. Established methods of cancer treatment are radiotherapy, surgery and chemotherapy. A majority of the patients need radiotherapy during the course of treatment. In a developing country like India, teletherapy using cobalt-60 is the most cost-effective and relevant method of treatment.

Although, telecobalt machine is one of the essential equipment needed in a cancer hospital, the number of machines available in the country is only about 260. As per WHO, a developing country should have at least one teletherapy machine for a population of one million. Therefore, India has to increase the number of machines four-fold. Many of the operating telecobalt machines are old and need immediate replacement. Most of the existing cancer treatment facilities are located in urban areas, while the vast rural areas remain untouched. More than 80 % of the districts in the country do not have any teletherapy machine. Non-availability of affordable telecobalt machines is the cause of this alarming shortage and urban-centric distribution of the machines.

Considering the growing demand for affordable cobalt-60 teletherapy machines, BARC has taken up indigenization of telecobalt technology. It has resulted in Bhabhatron, a high performance telecobalt machine at a much lower price. The first unit of Bhabhatron

was installed at the Advanced Centre for Treatment, Research and Education in Cancer (ACTREC), Navi Mumbai. Later, BARC developed an improved version of the machine, Bhabhatron-II. Bhabhatrons are installed in many cancer hospitals in India.

Bhabhatron is an isocentric, external-beam radiation therapy machine, using cobalt-60 isotope as radiation source. High-energy gamma rays emitted from the source are directed to the cancer site to destroy cancerous cells. Normal cells are also affected by radiation, but they recover faster from the radiation effects than the cancerous cells. Bhabhatron has a high capacity of 250 RMM (Roentgen per minute at one metre). The challenge in Bhabhatron development is to make a system that delivers required high radiation dose to the cancerous site, while protecting adjacent parts of the body from harmful radiation. In addition to the safety of the patient, safety of hospital staff and the public is also a concern during design.

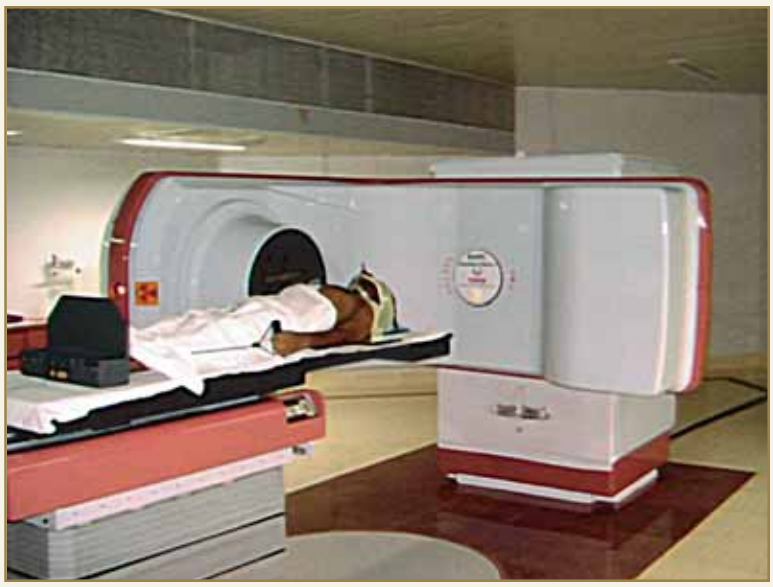

Fig. 1: A patient being treated on Bhabhatron at ACTREC

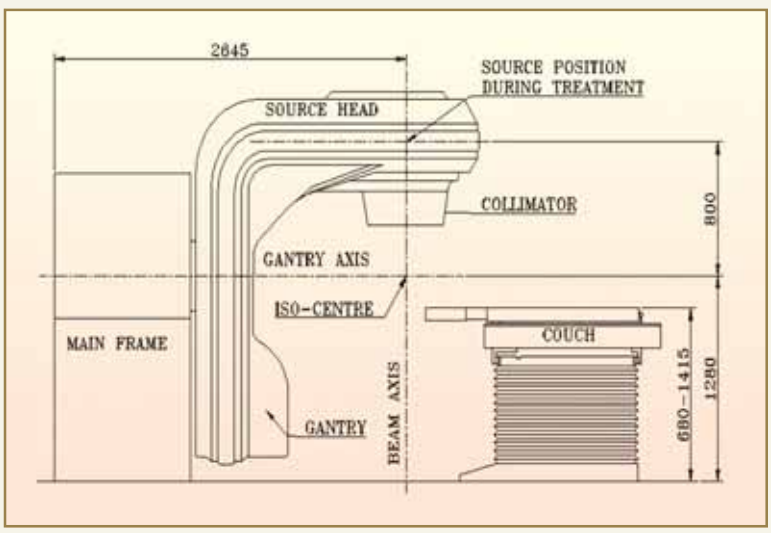

Fig. 2: Parts of Bhabhatron

Parts of Bhabhatron

Bhabhatron houses a Cobalt-60 source of high activity in a well-shielded containment. For treatment, the source is moved from shielded position to treatment position and the radiation beam is directed to the cancerous site, after controlling the beam to desired size, shape and differential attenuation. Major components of the machine are radioactive source, source drawer, source head, collimator, gantry, base housing, patient support system and control console.

Cobalt-60 Source

Cobalt-60 isotope of high specific activity is used as a gamma source in Bhabhatron. Cobalt-60 emits

high-energy gamma rays of 1.17 MeV and 1.33 MeV. Bhabhatron has the capacity to load a 15 kilocurie source.

Source Drawer

The source is assembled in a source drawer. The pneumatically driven drawer moves the source between shielded (beam-off) position and treatment (beam-on) position. The cylinder will withdraw the source automatically to beam-off position, in case of any emergency. In beam-off position, the shape, size and location of the radiation beam can be visualized using a light beam.

Source Head

Source head is a heavily shielded container, housing the source drawer. Depleted uranium and lead are used as shielding materials in the source head. Low source-to-skin distance of 80 cm is achieved, by compact design of the source head and the collimator.

Collimator

The collimator assembly controls the size, shape and orientation of the radiation beam exposed to the patient. *One of the unique features of Bhabhatron is it's fully closable collimator.* During any emergency, the collimator closes fully, protecting the patient from over-exposure. Two sets of trimmers are provided to reduce the penumbra of the beam.

Beam Shaping and Modifying Devices

The system has accessories like wedge filters, breast cone and shielding blocks, to modify the beam shape or beam attenuation. They are placed on the machine between the collimator and the patient. Shielding blocks protect vital organs in the path or near the

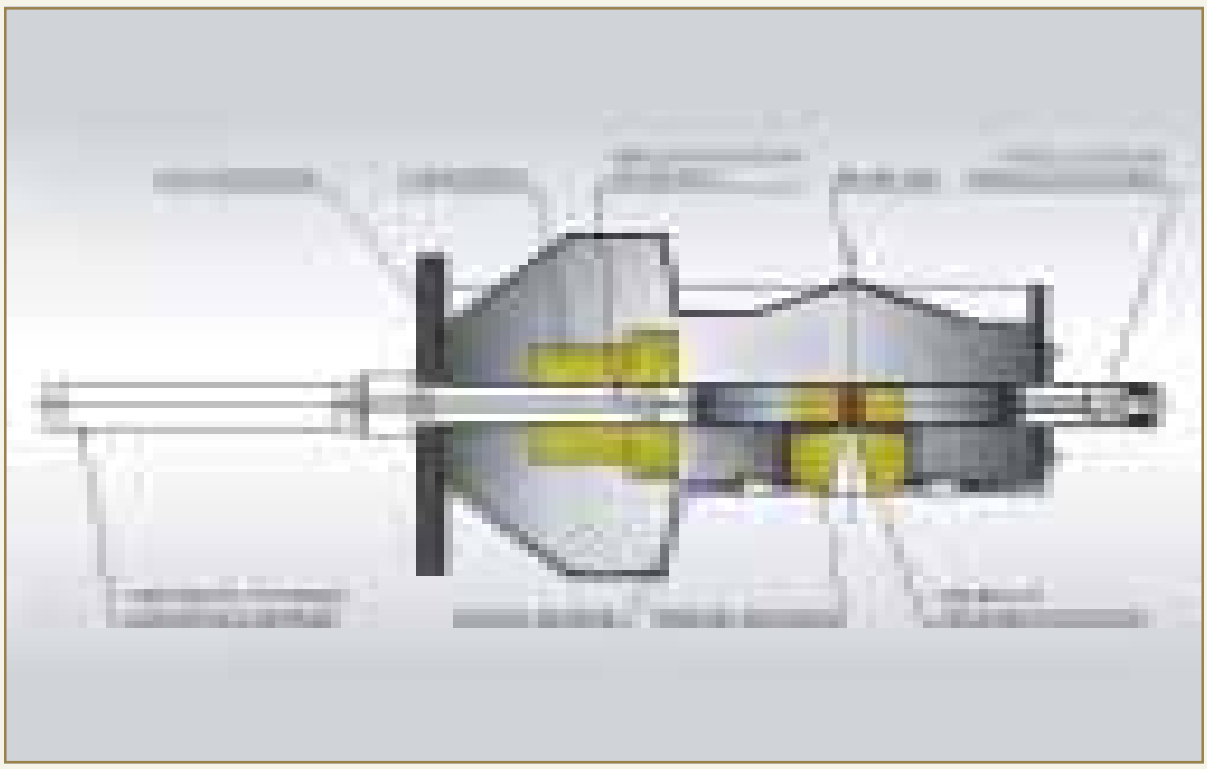

Fig. 3: Radiation head, Shielding, Source drawer, Source, etc.

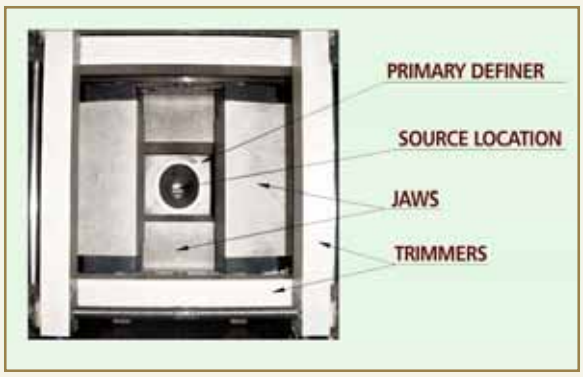

Fig. 4: Collimator

Fig. 5: Shielding blocks

radiation field. Wedge filters generate ramped dose distribution of radiation field.

Gantry, Mainframe and Base

Gantry holds the source head and counter weight. It can rotate around the patient on a horizontal axis by ±180°, allowing source positioning at any point on a circle of 80 cm radius. The gantry is mounted on the mainframe. The entire unit is mounted on a steel base below floor level. The base supports the mainframe and the couch.

Patient Support System

The patient positioning table or couch consists of a turntable mounted eccentrically with the isocentre. The couch has four motorized motions: isocentric rotation and translations in longitudinal, lateral and vertical directions. The motions are controlled through keypads attached on either side of the couch body. Salient features of the couch are high stability, noise-free motions and high precision. The couch top is made of lightweight, radio transparent carbon-fibre sheet. Patient restraining straps and universal metal clamps are provided for immobilization of the patient.

Fig. 6: Couch of Bhabhatron-II

Controls and Indicators

Bhabhatron controller is fully computerized. Data of treatment session registered on hard disk can be retrieved for control and analysis. Many safety interlocks are provided, to prevent the patient from over-exposure to radiation. For example, treatment room door interlock prevents or terminates treatment when the room door is open; gantry fault interlock terminates treatment in case of any error in gantry motion; and source drawer movement interlock prevents treatment when the drawer fails to move in the desired manner. Controls and indicators are installed in mainframe, gantry, door, power panel, operator's panel, couch and on the wall of the operational room. To provide additional security, access to modification of patient data and treatment data is limited to authorized staff, by password protection.

Operator's Panel

Main interaction between the operator and the machine is through computer monitor, keyboard and mouse.

Fig. 7: Control station of Bhabhatron

Fig. 8: Couch control panel

A key switch and an emergency switch are also provided near the operator's panel.

Control console displays the status of AC power, battery charge level, emergency switch, door closure, correctness of wedge, presence of key and air pressure. Treatment can start, only when all of the above parameters are within the acceptable range. The console also displays collimator opening, collimator orientation, gantry orientation and couch configuration. Source position, whether it is in shielded, transit or exposed position, is also displayed. During treatment, it displays set time, exposed time and remaining time.

Couch Control Panel

Keypads and emergency switches are mounted on either side of the couch. An operator can quickly position the patient on the couch using the keypads. He can also control the motions of the gantry and collimator using the keypads. Patient positioning lasers, optical distance indicator, field light and room lights can be controlled, using the buttons on the keypads.

Field Light and Optical Distance Indicator

Field light is used to visualise the collimated radiation field in the beam-off position of the source. The field light system consists of an external projector employing a quartz halogen bulb and a concave mirror to direct a light beam along the passage of the source drawer. Optical Distance Indicator (ODI) displays the distance between the source and the patients' skin. The scale of the ODI is projected on the patient's skin.

Patient Positioning Lasers

Patient Positioning Lasers are used, for accurate patient positioning. Two cross lasers and one sagittal laser are mounted on the wall of the treatment room. The intersection of these three laser beams represents the isocentre, which is the key reference of the machine.

CCTV Camera System

Using two CCTV cameras mounted in the treatment room, the operator at the control console can continuously monitor the patient, during treatment.

Wall Mounted Display

A unit parameter display in the treatment room displays the configurations of the gantry, collimator and couch.

Other Controls and Indicators

Many emergency switches are provided at main frame, couch, door and operator's panel, to terminate treatment in case of any emergency. A mandatory T- rod is provided, for withdrawing the source manually to the fully shielded position, in the unlikely event of the failure of automatic source return system. Status

lights to indicate the source position are provided on the gantry and access door.

Fig. 9: Wall mounted display inside the treatment room

Quality Assurance

The main objective of quality assurance is to ensure consistency and accuracy in dose delivery as prescribed by the radiation oncologist, minimal dose to normal tissue, minimal exposure to occupational workers and adequate patient monitoring. In addition to radiological safety, the machine has to meet stringent regulatory requirements for mechanical safety and electrical safety.

Electronics Regional Test Laboratory (South), Thiruvananthapuram, conducted the regulatory evaluation of the machine as per IEC standards for the Safety of Medical Electrical Equipment and certified the machine for electrical safety.

AERB, with assistance from RP&AD and RSSD of BARC, evaluated the machine for radiological safety and conformity of the machine to IEC standards, IEC 601-1 and IEC 60601-2-11. Parameters verified include radiation leakage at various locations in different conditions; accuracy of beam parameters and various components; and functionality of safety interlocks and other sub-systems.

Important Features

Important features of Bhabhatron are listed in Table 1. Many of them are unique to Bhabhatron.

Status of the Technology

Bhabhatron - I

The first unit of Bhabhatron was installed at ACTREC in March 2005. More than 50 patients were treated daily on the machine for various anatomic sites, such as head and neck, cervix, brain, pelvis and chest wall. The Cancer Research Institute used the machine for basic research in cancer. Blood banks were also using the machine, for blood irradiation in leuko-depletion.

Bhabhatron - II

Based on the operating experience of Bhabhatron at ACTREC, an advanced version of the machine, called Bhabhatron-II was developed. Bhabhatron-II has battery backup for six-hour operation, for use in rural areas, where there is power shortage. Other major enhancements include optimization of uranium shielding, reduction of source to skin distance and improvements in user interface. In December 2006, Honourable President of India, Dr A. P. J. Abdul Kalam dedicated the Bhabhatron-II to the cancer patients of the country at the Indian Red Cross Society Cancer (IRCS) Hospital, Nellore.

Fig. 10: Bhabhatron-II installed at the IRCS Hospital, Nellore

Table 1: Important features of the Bhabhatron

1. High Capacity	Bhabhatron is designed to house 15 kilo curie cobalt-60 source.
2. Motorized motion	All the motions of the main unit and treatment couch are motorised to reduce the patient setup time.
3. Computer controlled	The computer continuously monitors all the vital system parameters. It terminates treatment, if any parameter exceeds the acceptable limits. Patient and treatment database are maintained.
4. Improved radiation Safety	During power failure or other emergency conditions, the source automatically gets withdrawn to beam-off position. In addition, the collimator closes fully to reduce unwanted exposure to the patient. Many safety interlocks are provided to protect the patient and the operator from unwanted exposure.
5. Enhanced security	Through password protection, access to operation of the machine, machine parameters, patent data and treatment data are limited only to authorised staff.
6. Battery backup	The machine consumes only 1.5 kW power. A battery backup for six hours of continuous operation is provided to make it suitable for rural Indian conditions.
7. User friendly	All vital parameters are displayed in the computer screen. The operator can interact with the machine, using mouse and keyboard. Two ergonomic backlit keypads on the patient couch enable faster patient setup. Machine parameters and patient specific notes are displayed on a wall-mounted display in treatment room.
8. More spacious	Heavy counter weight of the gantry is located on the rear side of the machine, operator behind a wall to enhance safety. It also provides more space for the operator to setup the machine.

Transport Container

BARC has recently developed a container for transporting high capacity telecobalt sources of Bhabhatron and other telecobalt machines. After the drop test, fire test, radiological tests and necessary analysis, AERB awarded type B(U) approval to the container, for international transportation of Cobalt 60 sources.

Machine Installations

Eight machines are installed in various cancer hospitals in the country. More machines are under fabrication, based on orders from cancer hospitals.

Conclusion

Development of indigenous cobalt-60 teletherapy machine, Bhabhatron is completed. The machine has superior features in terms of safety, user-interface and security. Moreover, the cost of Bhabhatron is significantly lower than imported machines of similar capacity. The technology for this machine is already transferred for mass production. Bhabhatron development is improving the access of cancer patients to treatment facilities and reducing treatment cost.

Acknowledgement

The authors wish to thank all DRHR staff, Mr. B. C. Pal (retd.) and Mr. M. G. Radke (retd.) for their involvement in the development. We also thank Dr. Anil Kakodkar, Chairman AEC; Dr. S. Banerjee, Director, BARC; Mr. R. K. Sinha, Director, RDDG and DMAG; and Dr. K. A. Dinshaw, Director, Tata Memorial Centre for their guidance, support and encouragement.

ABOUT THE AUTHORS

Mr. K. Jayarajan joined the Division of Remote Handling and Robotics, after completion of training from the 28th Batch of BARC Training School. Mr. Jayarajan has developed and installed many mechanical master slave manipulators, servo manipulators, automation systems and special purpose remote handling tools for radioactive material handling. The first sets of servo manipulators installed in Indian hotcells were developed by him. He has also developed and supplied many remote handling systems to defence sector for handling hazardous materials. Another successful area of his work is development of Bhabhatron, the first indigenous teletherapy machine for cancer treatment.

Dr. D.C. Kar after graduating from BARC Training School in 1990 joined the Division of Remote Handling and Robotics. He is working on design and development of robots, telemanipulator systems and specialized remote handling equipment for nuclear and other hazardous applications. Dr. Kar was actively associated with the development of the Indigenous Cobalt Teletherapy Machine Bhabhatron. He has successfully developed the Teletherapy Source Transportation Flask for transporting cobalt teletherapy source capsules. Presently he is working for the development of Radiotherapy Simulator, a remotely-operated diagnostic machine, useful for localization of cancer-affected regions prior the radiation therapy. He is also involved with the development of Robotic Assistant for Minimally Invasive Surgery.

Mr. Ramakant Sahu after training from the 38th Batch of BARC Training School, joined the Division of Remote Handling and Robotics of BARC in 1995. His broad area of work includes development of remote handling tools and teletherapy machine. He has been involved in development of servo manipulators, cooperative servo robot, Bhabhatron couch and laser welding system for FBTR fuel pin.

Mr. Manjit Singh graduated from BARC Training School, where he got the Homi Bhabha Award for securing first rank. He is the Associate Director of Design, Manufacturing & Automation Group and Head of the Division of Remote Handling and Robotics of BARC. Mr. Manjit Singh has developed a large number of equipment and systems related to Nuclear Reactor Control, Remote Handling, Automation and Cancer Treatment. He has developed and delivered a large number of remote handling tools and automation systems to DAE establishments, Indian Navy and Ordnance Factories. Bhabhatron, the first indigenous Teletherapy Machine was developed under the leadership of Mr. Manjit Singh.

बीएआरसी न्यूज़लेटर
BARC NEWSLETTER

RF ELECTRONICS FOR THE SUPERCONDUCTING LINEAR ACCELERATORS

Gopal Joshi, C.I. Sujo and Shyam Mohan
Electronics Division

and

J.N. Karande
Department of Nuclear and Atomic Physics
Tata Institute of Fundamental Research

Mr. Joshi is the recipient of the Scientific and Technical Excellence Award for the year 2006

ABSTRACT

The Electronics Division, BARC, has designed, developed and installed the complete RF system, for the BARC-TIFR linear accelerator. RF system provides the functionality, of independently settingup and stabilizing the amplitude and phase of RF field, in all the resonators of the linac. The control loops are implemented using RF and analog electronics. This front end RF hardware is under computer control via CAMAC interface. The linac at TIFR was commissioned in November, 2007. Excellent performance of the resonator control electronics of the BARC-TIFR linac, led to it's inclusion in two other accelerators. These are the superconducting linacs at IUAC, New Delhi and ANU, Canberra, Australia.

Introduction

The Electronics Division, BARC has been working in the area of control systems, for medium and high energy accelerators, for more than a decade. The control electronics for the superconducting linear accelerator, installed at TIFR is a recent development which includes a number of RF systems like resonator controllers at different frequencies for superconducting and normal-conducting resonators, RF power amplifiers, dynamic phase generation system etc.

To maintain the stability of the output beam energy, stabilization of the amplitude and phase of the RF fields is required. RF control system provides the functionality of independently setting-up and stabilizing the amplitude and phase of RF field in all the resonators of the linac. The linac at TIFR was commissioned in November 2007 and is now available to the users. Excellent performance of the resonator control electronics for the superconducting resonators of the BARC-TIFR linac led to it's inclusion in two other accelerators. These are the superconducting linacs at IUAC, New Delhi and ANU, Canberra, Australia. In the following sections, we present the RF system of the BARC-TIFR linac.

System Description

Fig. 1 shows the layout of the linac at TIFR, drawn with a view to highlight the RF system. The low energy bunchers, which are normal-conducting resonators operating at 16th and 8th sub-harmonic of the main linac frequency (150 MHz), are used to bunch the DC beam available from the ion source, into a range of 1-2 ns. Sweeper and corrector resonators operating at 32nd sub-harmonic of the main linac frequency are used, to remove the DC background in between the main beam pulses. The phase detector, a normal-conducting resonator has it's resonance frequency at 4th sub-harmonic of the linac frequency. It produces an RF signal in synchronism with the beam. This signal is utilized to generate suitable phase references for all the other RF systems in the linac.

The super buncher, which follows the phase detector, is a superconducting resonator. It improves the bunching, to make the beam pulses suitable for injection, into the superconducting resonators. After super buncher, the linac is modular in nature. Each module consists of one cryostat housing four quarter-wave type resonators. There are seven cryostats having twenty-eight resonators.

The complete RF system for the linac can be broadly divided into four parts.

1. Control electronics for the normal-conducting resonators at different sub-harmonics of linac frequency.
2. RF system for the overall reference phase generation.
3. Control electronics for the superconducting resonators at 150MHz.
4. RF power amplifiers.

RF Electronics for the normal-conducting resonators

Fig. 2 shows the architecture of the RF system, for the normal-conducting resonators. It is developed as

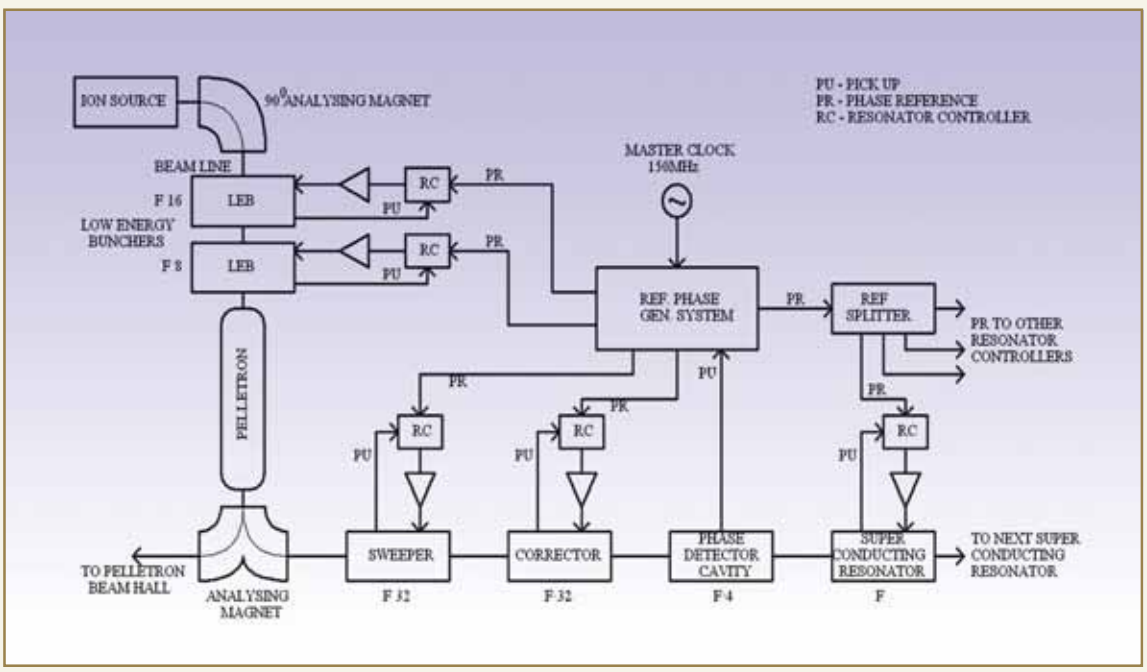

Fig. 1: RF system layout at TIFR

a generator driven scheme. The phase stabilization is achieved, by modulating the Q-port of the vector modulator. In addition to this the amplitude stabilization is achieved by controlling the drive amplitude.

Overall Reference Phase Generation System

In order to retain the timing synchronization between the beam pulses and the RF fields, the phase of RF fields in all the resonators are independently phase locked to a single master reference. To meet this requirement, a reference phase generation system has been developed. This system corrects for the travel time variation of the beam bunches through the Pelletron, which occurs due to the changes in the voltage distribution inside it. An RF signal in phase synchronism with the beam, is extracted from the phase detector resonator, which is a spiral resonator loaded with drift tubes. This phase is compared with the phase of the RF in the superconducting resonators. Any error developed is removed via a feedback loop, which corrects the reference phase of the low-energy bunchers. Feature of systematic and non-interactive setting of the phase references for all the RF systems in the linac, has been incorporated in the design.

RF control electronics for superconducting resonators

The superconducting resonators have very small intrinsic band-width, making field stabilization a challenging task. The resonant frequency deviates from the linac frequency by several band-widths due to initial tolerances, helium pressure changes in the system and mechanical vibrations. The RF system developed, retains the phase and amplitude stability of the RF field, in the presence of these effects. The two main components in the RF system are the resonator controller and the RF Power amplifier. The resonator controller performs all low level signal processing and provides the appropriate drive signal

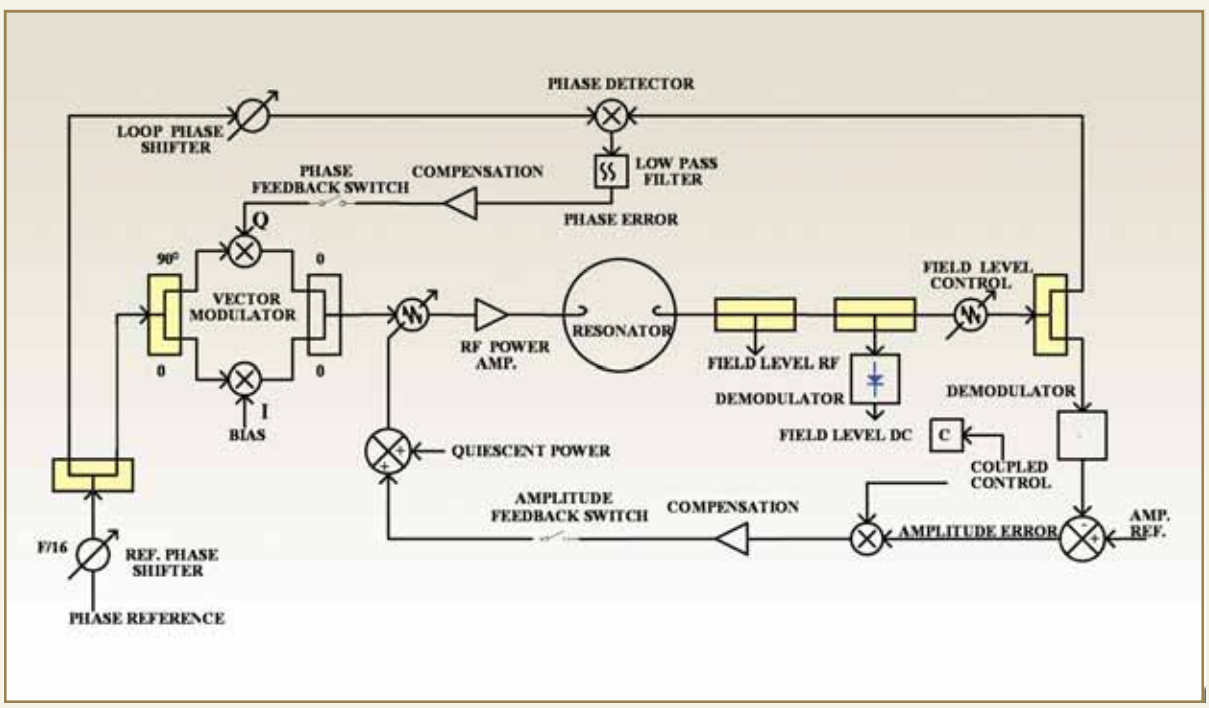

Fig. 2: Normal conducting resonator controller

for the amplifier, to retain the amplitude and phase stability, with respect to suitable references. The control strategy adopted for the BARC-TIFR linac is based on the principle of supplying the required quadrature power as the resonator centre frequency deviates from the main linac frequency. This strategy has been found very suitable for the BARC-TIFR resonators, which can be operated at field level of 3MV/m with about 100W of RF power.

A block diagram of the RF system for the superconducting resonators is shown in Fig. 3. The resonator whose amplitude and field is to be stabilized is made the frequency selective part of an oscillator, known as a Self Excited Loop (SEL). In the SEL the output of the resonator is fed back to it's input via a limiter and a phase shifter. A vector modulator has been used as the control element, to stabilize the amplitude and phase of the RF signal in the resonator. Phase and amplitude locks are achieved by modulating the quadrature and in-phase port of the vector modulator respectively. Resonator controller, is interfaced to PC via CAMAC hardware.

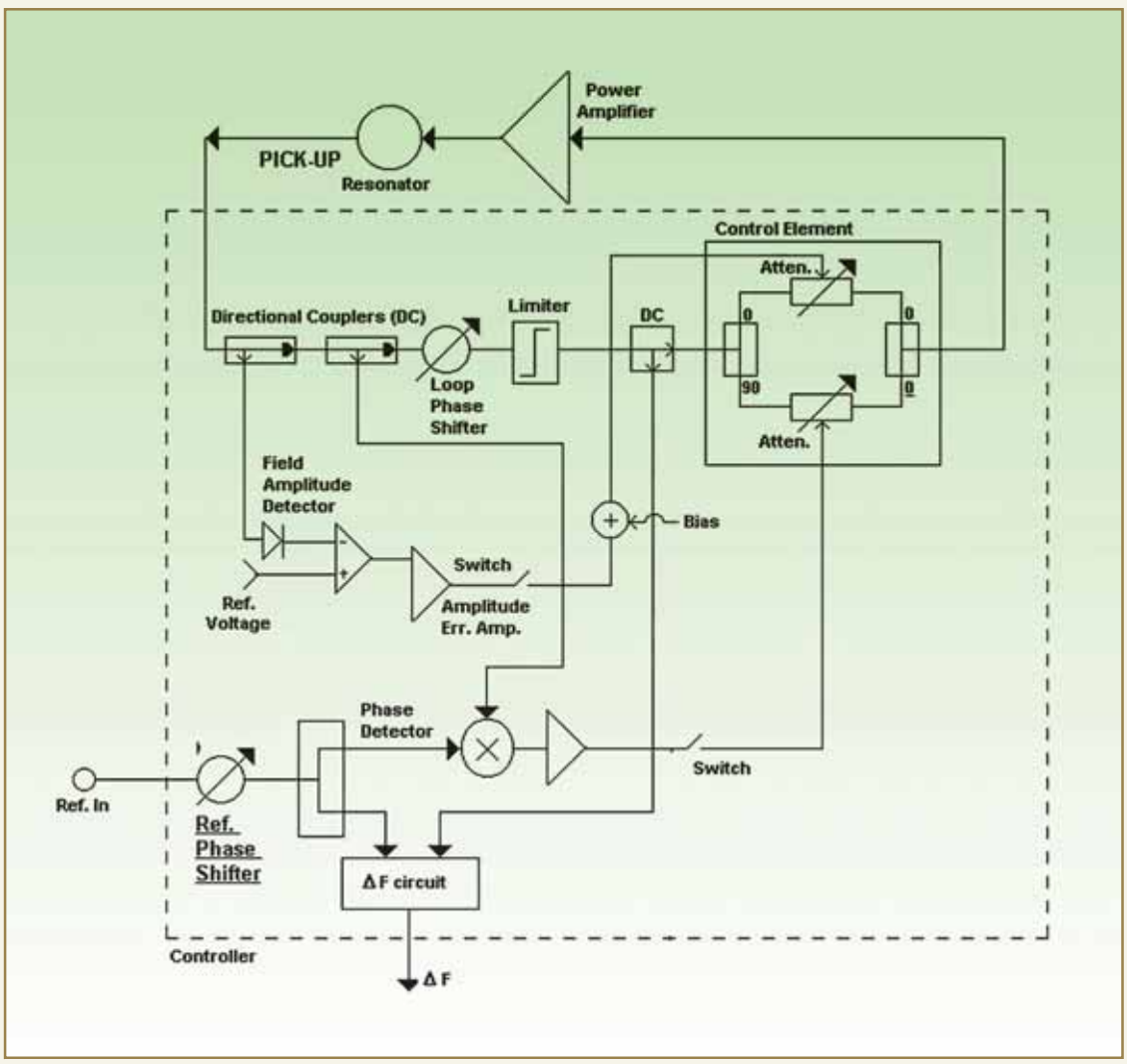

Fig. 3: RF system for the superconducting resonator

All the low frequency analog and digital input and output signals of the controller are made compatible with corresponding signals from CAMAC modules, which are developed in BARC. Through the PC placed in the control room, it is possible to control and observe the various control signals and status of resonators. A number of RF signal processing modules have been developed, to cater to the requirement of the control system, for the superconducting resonators. In order to reduce the cabling between the linac hall and the control room, a signal multiplexing system has been developed. With the help of this system, we can access six important signals pertaining to any resonator of the system.

Development of solid state RF power amplifiers

To setup and control the RF fields in the resonators, an amplifier of 150W capability with special features has been developed. This amplifier has to work under near total reflection. Good linearity and low-amplitude to phase coupling are other important requirements. The RF amplifiers for the superconducting resonators are indigenously developed. The amplifying core was developed at IUAC, New Delhi. All the control, metering, protection requirements were worked out by BARC-TIFR. Starting from these inputs, BEL, Bangalore developed and produced these units. Subsequent improvements have been carried out by BARC based on the experience gained in the field.

Fig. 4: Control electronics modules installed at TIFR for the control of 3 cryostats

RF Electronics installed at ANU, Canberra

RF control electronics developed at the Electronics Division, BARC, have been installed and commissioned successfully at the Australian National University (ANU), Australia, in April 2005. The commissioning included initial test of RF electronics, high power conditioning, tuning, phase locking and operation of each cavity and the entire linac and finally delivering 343 MeV, Ni58 beam, for the Nuclear Physics Experiments.

As per the report presented by ANU at the RF Superconductivity workshop at Cornell University in July 2005: 'The RF system supplied by BARC demonstrated very high stability, simplicity of operation and high reliability allowing sustained operation of the linac facility'. Residual amplitude and phase errors were below 0.1% and 0.1 degree during the beam run'. A total of 28 modules along with power supplies, bins and cabling was supplied to ANU in the month of January 2005, against their order.

RF control electronics supplied to IUAC, New Delhi

The superconducting bulk niobium resonators of IUAC, linac have Q values in the range of 10^9 at a center frequency of 97 MHz.This implies that the bandwidth of resonator is around 0.1 Hz. Vibration induced

Fig. 5: Control electronics supplied to Australian National University, Canberra

centre-frequency changes are of the order of a few tens of hertz in these resonators. In addition, to this the helium pressure variation can shift the resonant frequency by hundreds of hertz. Since these two disturbances occur on two very different time scales, different strategies are adopted to counteract them. Deforming the resonator using a slow tuning mechanism, minimizes the slow variations of the resonator centre frequency reducing the load on the fast tuner. This results in more appropriate utilization of the dynamic range of the fast tuner (resonator controller) and also the overall power requirement for the control comes down.

Slow tuning action is achieved, by deforming a thin plate fixed at the open circuit end of the resonator. Varying the pressure of helium gas inside a niobium bellow, controls the plate movement. The electronic control signals generated in the resonator controller operate a proportional valve regulating the pressure inside the bellow. This in turn changes the centre frequency of the resonator.

The control electronics required for 40 resonators have been developed, of which 20 resonator controllers have already been supplied and installed at IUAC, New Delhi.

ABOUT THE AUTHORS

Mr. Gopal Joshi, a graduate from the 29th Batch of BARC Training School joined the Electronics Division, in 1986. He has been working in the area of RF Control Electronics for particle accelerators and the design and the development of the complete RF electronics for the Super-conducting Linac Booster at TIFR, Mumbai, has been one of his major contributions. He has made contributions in the development of fast-pulse amplifiers for timing spectroscopy in Nuclear Physics experiments, instrumentation for nuclear power plants and electronic detection of trapped ions in Ion Traps. Currently he is involved in the development of RF control electronics for the ADSS programme.

Ms. Sujo C.I. joined the Electronics Division, BARC from 5th OCEP Batch of Training School. She has been involved in the development, installation and commissioning of Superconducting Linear Accelerator project. At present she is involved in the development of solid state RF amplifier for different applications.

Mr. Shyam Mohan joined the Electronics Division, BARC in 2002. Since then, he has been involved in the development and testing of RF control instrumentation, for the superconducting linac project. He has been involved in the design and development of signal multiplexing scheme of super-conducting linac at TIFR, Mumbai. He is also involved in the testing of RF power amplifier. His area of interest includes development of micro-controller based designs.

बीएआरसी न्यूज़लैटर
BARC NEWSLETTER

PHYSICAL METALLURGY, CHARACTERIZATION AND DEVELOPMENT OF ZIRCONIUM-BASED STRUCTURAL COMPONENTS OF PHWR

D. Srivastava, S. Neogy, K. V. Mani Krishna, M. Kiran Kumar, G. K. Dey and S. Banerjee
Materials Science Division

Dr. Srivastava is the recipient of the Scientific and Technical Excellence Award for the year 2006

ABSTRACT

Zirconium alloys are of considerable importance for fuel cladding and other structural components, such as calandria tube and pressure tube in Pressurized Heavy Water nuclear Reactors (PHWRs). Though it is true that zircaloy-2 and Zr-2.5 Nb alloy have been widely accepted for applications in heavy water reactors, there is always a demand for better and improved performance of structural components, which requires the development of new alloys of different compositions, produced through different thermo-mechanical treatments. Currently, there is lot of interest in developing alloys for structural components, for higher temperature reactor operations. There is also a need for development of cladding material with better corrosion and mechanical properties of cladding material, for higher and extended burn up applications. The performance of the cladding material is primarily influenced by the microstructural features of the material, such as constituent phases, their morphology, precipitate characteristics, nature of defects etc.. Therefore, microstructure is tailored as per the performance requirement, by suitably choosing the chemistry of the alloy through controlled additions of alloying elements, thermo-mechanical- treatments and fabrication concern of these alloys for obtaining required reliability and reproducibility of the components.

In order to understand the development of microstructure, it is important to know the phase transformation mechanism in these alloys. Dilute Zr-Nb alloys exhibit a range of diffusional, diffusionless and hybrid phase transformations which includes martensitic omega and hydride transformation.

With these points in view, detail studies on the physical metallurgy aspects of binary, ternary and quaternary Zirconium base alloys has been carried out. In this presentation, the microstructure evolution in these alloys after different heat treatments and deformations has been characterized. The resulting microstructures have been characterized using optical, scanning and transmission electron microscopy. Electron Diffraction and X-ray diffraction techniques have been used, to determine the phases, defects and their crystallographic features. Hydriding is one of the most important corrosion problems in the Zirconium cladding alloys. The mechanism of hydride phase transformation and their crystallographic and microstructural aspects has been presented in detail, in some Zirconium alloys.

Zirconium alloys being crystallographically asymmetric, it shows deformation and annealing texture. Result of the studies on bulk and micro texture in some zirconium alloys, has been included in this presentation.Texture plays an important role in the hydride formation, some micro-textural aspects on hydride formation are also presented. This paper also covers phase transformation aspects, texture aspects and hydriding aspects of some Zirconium alloys.

Introduction

Zirconium and it's alloys are extensively used as structural materials in nuclear reactors, because of their unique combination of good corrosion resistance in water near 300° C, good mechanical properties and low capture cross section for thermal neutrons. While the zircaloys, a series of alloys with tin as the primary alloying addition, are widely used in both pressurized water and boiling water reactors as fuel cladding materials, the Zr-2.5wt% Nb alloy is mainly used, as pressure tube material in Pressurized Heavy Water Reactors (PHWR), which are heavy water moderated and cooled and fuelled by natural uranium oxide.

The zircaloys which contain about 1.5 wt% Sn have two important derivatives; zircaloy-2 and zircaloy-4, differing slightly in the amounts of minor alloying elements. Russian work reported at the second Geneva Conference in 1955, strongly suggested that, an alloy of zirconium containing 1-5% niobium would have superior mechanical strength and adequate corrosion resistance. The Zr-2.5%Nb alloy as a pressure tube material and the Zr-1.0%Nb as a fuel cladding material have been found to be attractive, because of their high strengths at the operating temperature. This permits the use of thinner components, reducing the loss of neutrons by parasitic absorption with an accompanying improvement in corrosion resistance. In general, the properties of zirconium alloys can be controlled through a proper selection of thermal and mechanical treatments. In view of these, studies on phase transformations in zirconium alloys in general and on the Zr-Nb system in particular are attractive from application considerations. It has been established earlier that the Zr-Nb system is an ideal system for studying many of the basic issues in phase transformations.

The Zr-Nb equilibrium diagram provides the basis for studying the equilibrium transformations. An analysis of the phase diagrams which generates G-X plots can be utilized, in studying the metastable steps in the sequence of transformation events in this system. This system is characterized by complete solid solution in the β (bcc) phase at sufficiently high temperatures and a tendency for phase separation in the β phase, as reflected in the miscibility gap, at temperatures below about 970 °C ($\beta_{Zr} + \beta_{Nb}$ miscibility gap); the following monotectoid reaction occurring at 610 °C:

$$\beta_{Zr} \rightarrow \alpha_{Zr} + \beta_{Nb}$$

A variety of equilibrium and metastable phases can be obtained from the high temperature β phase in zirconium rich Zr-Nb alloys. The β phase in the Zr-Nb system exhibits tendencies for the $\beta \rightarrow \alpha'$ martensitic transformation, the $\beta \rightarrow \omega$ displacive transformation and the $\beta \rightarrow \beta_{Zr} + \beta_{Nb}$ phase separation reaction in different composition and temperature domains. This β phase instability is known to influence the sequence of phase transformations in zirconium (and titanium) alloys. In dilute Zr-Nb alloys, it is well established that the β phase, having the same composition as that of the alloy, cannot be retained at ambient temperatures even by very rapid quenching. In alloys containing upto 8 % Nb quenching from the β phase field rapidly through the equilibrium $\alpha+\beta$ region results in a martensitic structure. Beyond this composition and upto about 17% Nb, quenching from the β phase leads to the formation of an athermal ω phase dispersed in the β phase. The ω instability disappears beyond 20 % Nb, where the β phase is fully stabilized. Less rapid cooling of dilute Zr-Nb alloys from the β phase field, results in the formation of characteristic Widmanstatten α plates by a nucleation and growth process. The stabilized β phase in Zr-Nb alloys with higher niobium contents can decompose on ageing either by α phase formation or by isothermal ω phase formation or by both these modes, depending upon the temperature of ageing and the composition of alloy. In the niobium lean alloys where the β phase transforms martensitically to the α' phase, the β phase can reappear on tempering the martensite either on the martensite plate boundaries or within the martensite plates. In addition to the various possibilities of transformation of the β phase to athermal ω, isothermal ω, α' and α phases, it can undergo hydride

formation in alloys containing hydrogen. In the present investigation different classes of transformations associated with the β phase in Zr-Nb alloys, involving structural and compositional changes, have been examined.

The crystallographic and microstructural features associated with the bcc-hcp (e.g., in Ti, Zr and their alloys) diffusionless (displacive) martensitic transformation have been reviewed by Nishiyama. The Phenomenological Theories of the Martensitic Crystallography (PTMC) have been successfully used, in predicting the crystallographic parameters of the martensitic transformation in zirconium and few of it's alloys. The two most widely cited crystallographic theories in which the habit plane is predicted on the basis of the Invariant Plain Strain (IPS) criterion have been developed by Wechsler, Liebermann and Read (W-L-R theory) and by Bowles and Mackenzie (B-M theory).

Zirconium hydrides in zirconium alloys can form in the α phase as well as in the β phase. The formation of hydrides in α phase has been studied in considerable detail. Three types of hydrides with different compositions and crystal structures have been reported in the Zr-H binary system; these are, δ hydride (fct), ε hydride (fcc) and γ hydride (fct). The γ hydride can coexist with the α as well as with the δ hydride phases. The formation of the metastable γ hydride phase is favoured by rapid cooling from a temperature, where hydrogen is in solution in the α phase. The γ hydride phase transforms to the δ hydride phase when aged at 300 °C or above. It has been shown that the $\alpha \rightarrow \gamma$ hydride transformation involves a shear movement. The formation of a hydride phase in the β phase has been reported in Zr-Nb alloys containing high concentrations of niobium. The formation of the γ hydride phase is of particular interest, since it may form at low temperatures, where the rate of self diffusion of zirconium is not significant. It has been suggested that γ hydride formation in a β matrix occurs by a displacive or martensitic transformation. The fact that the hydride phase may form in the α phase as well as in the β phase of Zr points to some similarities in the structures of these three phases. In the present paper crsystallographic and morphological aspects of the above mentioned phase transformations in Zr-Nb alloys have been presented.

Results and Discusssion

I Phase Transformations in Zr-Nb alloys

A series of Zr-Nb alloys were chosen for investigation, in view of the potential use of these alloys as materials for fuel cladding and for pressure tubing.

a. Martensitic transformation

The heat treatment followed by tempering has been accepted as an important method of hardening for many zirconium base alloys. The following important observations pertaining to Zr-Nb alloy martensites were made.

Crystallography and Morphology

The morphology and substructure of the martensite in Zr-Nb alloys (< 8wt % Nb), were found to consist of (i) martensite lath packets composed of the same crystallographic variant stacked in a nearly parallel array; (ii) martensite lath packets composed of two twin related variants stacked alternately; (iii) internally twinned martensite plates with zig-zag habit plane; (iv) internally twinned martensite with a large twin thickness ratio; and (v) secondary martensite plates arranged in a self accommodating indentation mark morphology, composed of three mutually twin related crystallographic variants (Fig.1). The Burgers orientation relationship was found to be obeyed in all the above morphologies. The habit planes of these martensites have been found to be close to $\{334\}_{\beta}$, criterion. The experimentally observed Lattice Invariant Shear (LIS) has been identified as the $\{-1101\}_{\alpha}$ $<2\text{-}1\text{-}13>_{\alpha}$ shear system in the case of internally slipped martensite and $\{-1101\}_{\alpha}$ $<41\text{-}53>_{\alpha}$ twinning system in the case of

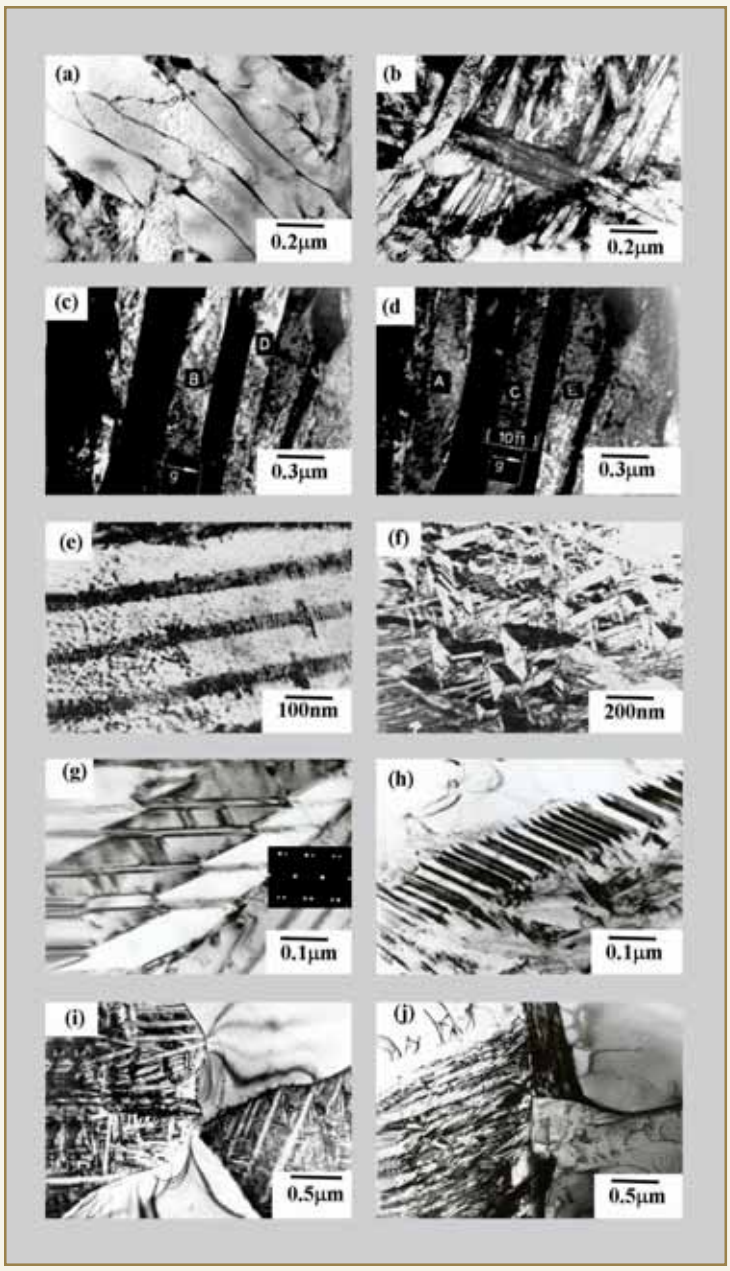

Fig. 1: **Growth Sequence of Martensitic phase in Zr-Nb**

contd.....

internally twinned martensite. These observations are consistent with the predicted results of phenomenological theory. It has been found that the arrangement of martensite plates in the martensitic microstructure of these alloys, is strongly influenced by the tendency for self accommodation. The DSA of the 3-plate $\{433\}_\beta$-$\{343\}_\beta$-$\{334\}_\beta$ and 2- plate ($\{433\}_\beta$ - $\{343\}_\beta$) variants of martensite plate morphologies were determined to be 92 %, and 68 %, which is the highest amongst all possible 3- plate and 2—plate morphologies, respectively. The frequent occurrence of these morphologies, suggested a strong tendency for self accommodation. The morphology of the martensite plate, the shear mode of the LIS and the occurrence of self accommodation, were found to be strongly related to the M_s temperature and the quenching rate.

b. Diffusional transformations

The precipitation of the α (hcp) phase from the β phase in Zr-Nb alloys was investigated in two alloy compositions, namely, Zr-2.5%Nb and Zr-20%Nb. Precipitation of the α phase in these alloys, was induced by two different heat treatment schemes. In the first, the samples were initially solutionized in the β phase field, then isothermally annealed at different reaction temperatures and quenched to room temperature (Fig. 2). The habit plane poles of the α laths in the Zr-20Nb alloy, were observed to lie between the $\{130\}_\beta\gamma$ and $\{131\}_\beta$ poles. The α/β interface of these laths was seen to be semi-coherent, consisting of a periodic array of $<2\text{-}1\text{-}13>_H$ misfit dislocations, spaced at 8-10 nm distance. On the other hand, the α/β interfaces in the Zr-2.5%Nb alloy was a semi-coherent interface consisting of $<2\text{-}1\text{-}13>_\alpha$ and $<0001>_\alpha$ misfit dislocations, spaced at ~10 nm and ~20 nm distance, respectively. The line vector of the interface dislocation and the long axis of the lath was

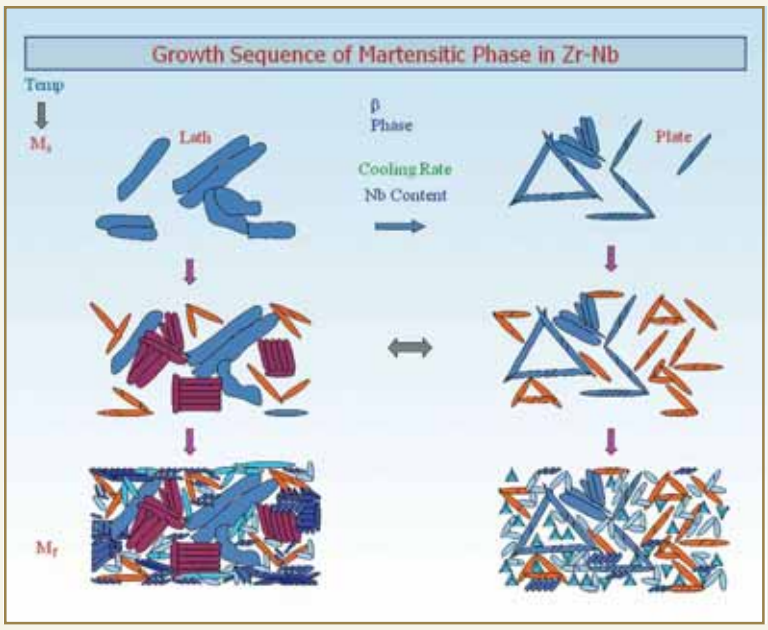

Fig.1: Bright field TEM micrographs showing different morphologies of martensites in Zr-Nb alloys (a) lath martensite in dute Zr0.5Nb alloy (b) packet of laths having similar orientation in Zr-2.5 Nb alloy. (c) and (d) alternately twinned related lath martensites (e) regularly spaced <c+a> interfacial dislocations between laths (f) self accommodating 3-plate grouping of martensites showing indentention morphology (g) internally twinned zig-zag martensite (h) internally twinned thin martensite (i) and (j) α + martensite structure in Zr-2.5Nb alloy (k) schematic representation of martensite nucleation and growth mechanism

determined to be lying along the invariant line vector of homogeneous strain of the β→α transformation. In the second scheme of heat treatment, specimens were initially solutionized in the β phase field, quenched to room temperature and then aged at different temperatures for varying durations. Specimens of the Zr-20%Nb alloy showed two distinct morphologies of the α plates. The first kind of plates generally occurs as a monolithic plate and occasionally it is seen to be internally twinned. The second kind of plates is seen to be composed of stacks of periodic twins and exhibits a serrated habit plane. The twinning plane in this case is found to be of the $\{10\text{-}11\}_\alpha$ type, which is the same as that observed in the β→α martensitic transformation. However, the observed $\{120\}_\beta$ habit plane does not match with that predicted by the Invariant Plane Strain (IPS) criterion.

C. Hydride formation

Formation of hydride in Zr alloys is shown in Fig. 3.

γ - hydride formation

The metastable γ hydride (fct) phase is found to occur as needle shaped precipitates in both α and β phases in Zr-2.5Nb and Zr-1Nb alloys (Fig.3).

The crystallographic aspects associated with the formation of the γ hydride phase (fct) from the α (hcp) phase and the β (bcc) phase in Zr–Nb alloys, have been examined in two distinct situations, viz., in the α matrix in pure Zr, Zr-1Nb and Zr–2.5Nb and in the β matrix in β stabilized Zr–20Nb alloy. The possibility of the formation of the γ hydride phase in the α phase as well as in the β phase of zirconium alloy suggests, that similarities exist in the structures of these three phases (α, β and γ hydride phase). The β-γ hydride formation can be treated primarily as a simple shear on the basal plane involving a change in the stacking sequence. In this study, the β-γ transformation has been considered in terms of the Invariant Plane Strain theory (IPS) in order to predict the crystallographic features of the γ hydride formed. The validity of the IPS criterion by employing WLR (Wechsler, Liebermann and Read) Phenomenological Theory of Martensite Crystallography (PTMC) in the α to γ hydride transformation has been examined. The lattice invariant shear (LIS) $(110)_\gamma[\text{-}110]_\beta \,||\, (111)_\beta[1\text{-}21]_\gamma$ has been considered and the crystallographic parameters associated with bcci→fct transformation, such as the habit plane and the magnitude of the LIS and the shape strain have been computed. The predi-ctions made in the present analysis have been compared with experimentally observed

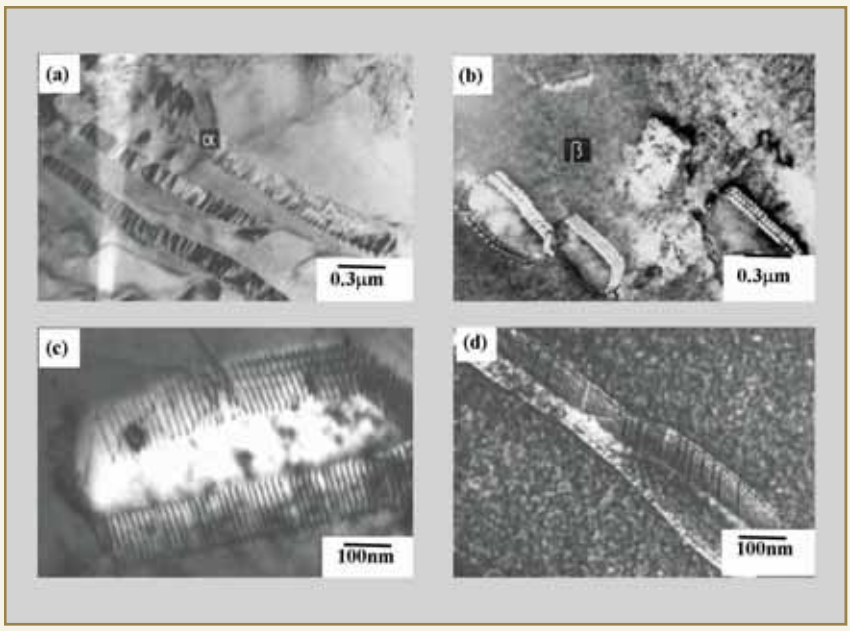

Fig. 2: Bright field TEM micrographs showing diffusional transformation microstructure in Zr-20Nb alloy (a) quenched and aged (b) stepped quenched (c) and (d) interface dislocation structure of α/β phase

habit planes. The habit plane solutions for these two shear systems were found to be of $\{1, 2.999, 0.0\}_{\beta}$ type which were close to the experimentally observed habit planes. The magnitude of shear (0.1699) corresponded to half of the lattice shear, implying a 3:1 ratio of the adjacent twin related variants in those plates, where the LIS was provided by twinning. It should be pointed out that variations in the twin thickness ratio were observed in some cases. This was possibly due to the operation of both slip and twinning for meeting the LIS requirement. The validity of the IPS criterion in predicting habit plane of γ hydride precipitates in the β matrix could be fully established from the present analysis.

δ - hydride formation

In the case of the Zircaloy-2, Zr-1Nb and Zr-2.5 Nb alloys, two different morphologies of the δ hydride phase were observed, when samples were slowly cooled from 400 ^{0}C. An acicular morphology was noticed in all the samples whereas a zigzag morphology was noticed in samples containing higher concentrations of hydrogen. It was seen that the hydride plates at many instances disregard the α / α and α / β interfaces. Hydriding studies of Zircaloy-2 were also carried out, with hydrogen charging to the level of 100, 200 and 300 ppm. Optical, EBSD and TEM observations confirmed, that hydrides were present at grain boundary predominantly. These grain boundary hydrides exhibited preference for certain type of grain boundaries. Different criteria were used to characterize such boundaries. Coincidence Site Lattice (CSL) concept was used and it could be demonstrated that low CSL boundaries were showing less preference for hydride formation owing to their lower energies and correspondingly lower nucleation rates. However, all boundaries could not be analyzed in terms of CSL. It was seen that the elastic modulus of the adjoining grains also plays an important role. The accommodation of stresses generated during formation of hydrides, is expected to be easier in elastically softer grains and thus it's formation is favoured. This study has given a possibility to engineer grain boundary which to resistant to hydride formation.

d. ω phase formation

The formation of the ω phase by thermal treatment in Zr 2.5 Nb alloy were induced, by quenching from the α+β phase field, where it was possible to get a β phase having composition which can transform to the ω phase. The metastable β_{Nb} phase present in the hot extruded pressure material, is enriched with niobium upto a level of 15-20 %, Precipitation of the ω phase in this material could be seen to occur in the β_{Nb} phase of such composition, during subsequent annealing. (Fig. 4). In

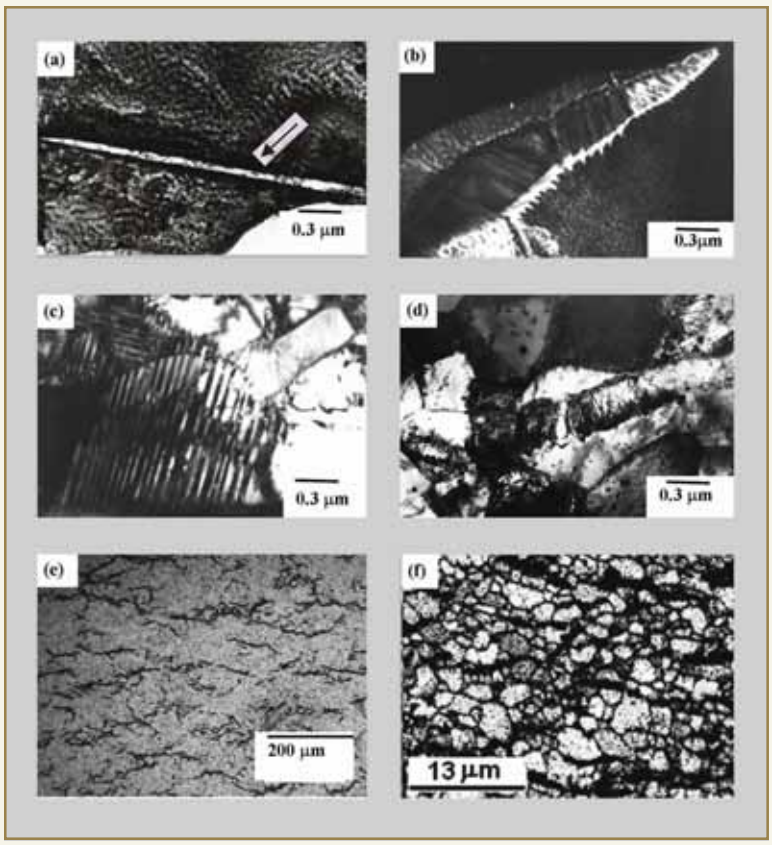

Fig. 3: Bright field TEM micrographs showing γ hydride formation in (a) needle shaped in Zr-2.5 Nb alloy (b) internally twinned γ hydride in α matrix and (c) in β matrix. δ hydride formation in (d) Zr-1Nb alloy (e) optical microstructure (f) SEM-OIM image showing grain boundary hydrides

the case of a Zr7Nb alloy ω phase was formed when quenching from the β as well as from the α+β phase fields. In some instances the ω phase was found to be ordered. The ω morphology was found to be ellipsoidal in both the alloys. In Zr-20Nb alloy, the β phase could be retained by quenching from the β phase field. No ω like fluctuation could be seen in the as quenched ß phase. The formation of the isothermal ω phase occurred on ageing, at a temperature of 300 °C. These ω particles had a cuboidal morphology and were arranged along the <100> direction.

In the Zr20Nb alloy, decomposition of the metastable β phase under electron irradiation was studied and examined. This decomposition process was found to be similar to that occurring during isothermal ageing . The ω precipitation could be induced at a significant rate even at temperatures as low as 27 °C on electron irradiation. However, the morphology of the ω phase was found to be ellipsoidal unlike the cuboidal morphology observed in the case of thermal treatment.

e. Evolution of microstructure during fabrication of Zr2.5 Nb alloy pressure tubes

The evolution of microstructure during each stage of Zr-2.5 Nb tube fabrication is shown in Fig. 5. Some specific features of the microstructure developed, are summarized below:

The β quenched structure consists of acicular martensite plates similar to those observed in conventionally processed tubes. During hot extrusion, the α and β_{Nb} phases dynamically recrystallize and β_{Nb} phase layers are sandwiched between α stringers. (Fig. 5). The aspect

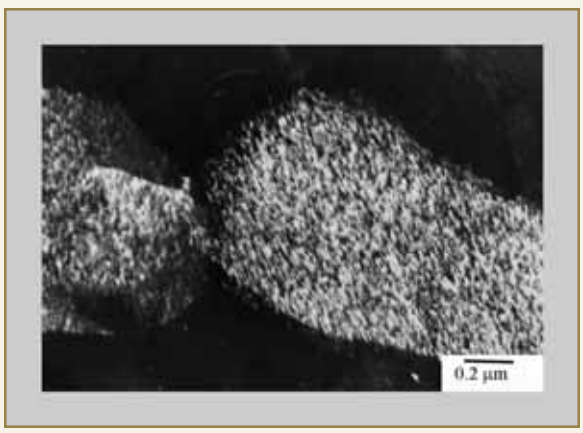

Fig. 4: Formation of ω phase in hot extruded Zr-2.5 Nb pressure tube material

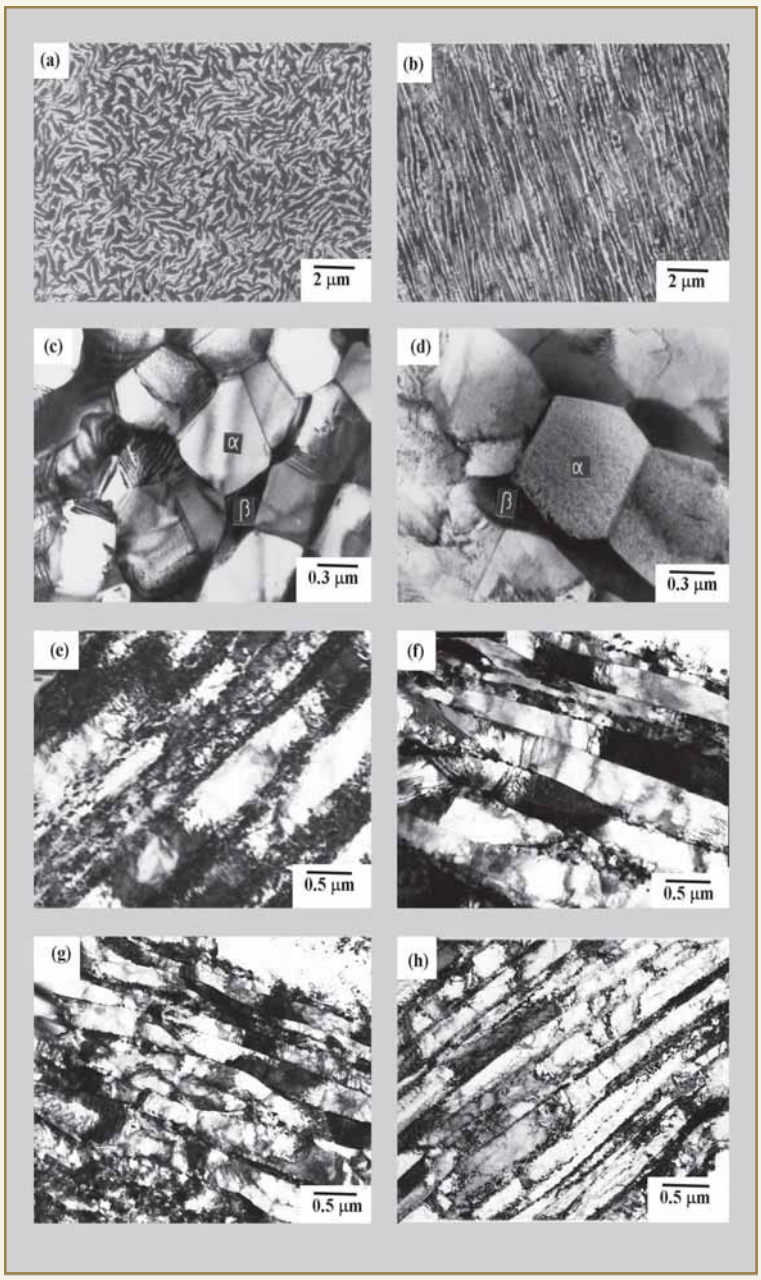

Fig. 5: Evolution of microstructure during fabrication of Zr-2.5Nb pressure tube-Scanning and transmission electron micrographs of hot extruded material in transverse and axial direction (a)-(b) and (c)-(d) respectively. Bright field TEM micrographs showing microstructure of (e) Ist pilgered, (f) Intermediate annealed 550C/3h (g) IInd pilgered and (h) final pressure tube microstructure.

ratio of both the phases is considerably lower than conventional processing, which will produce lower irradiation growth. The volume fraction of the β_{Nb} phase is higher than that obtained in conventionally processed tubes. The first pilgering operation further elongates both α and β_{Nb} microstructure and during subsequent annealing treatment, static recrystallization of the two phases occurs. The optimum annealing treatment (550 °C for 6h) retains the elongated morphology of the two phases produced in the hot extrusion step. The tensile strength at 310 °C of the annealed product also remains at the same level as that attained after hot extrusion. The improved microstructure due to the additional processing steps, provides a better control of dimensional tolerances, less variability in the finished product and tighter control of mechanical properties.

II. Texture evolution

a. *Development of texture and microtexture during different Stages of fabrication of Zr-2.5 Nb pressure tube and Zircaloy-4 cladding tube*

The evolution of texture during each stage of Zr-2.5 Nb tube fabrication is shown in Fig. 6. Significant crystallographic texture development was obtained during hot extrusion. The effectiveness of pilgering with regard to texture/microtexture development, depended on the relative presence/ continuity of the second phase β. In case of β continuity, the lattice rotations were restricted, limiting misorientation development (and also developments in bulk texture) of the α grains. The relatively more β discontinuity during the second pilgering explains a strong texture

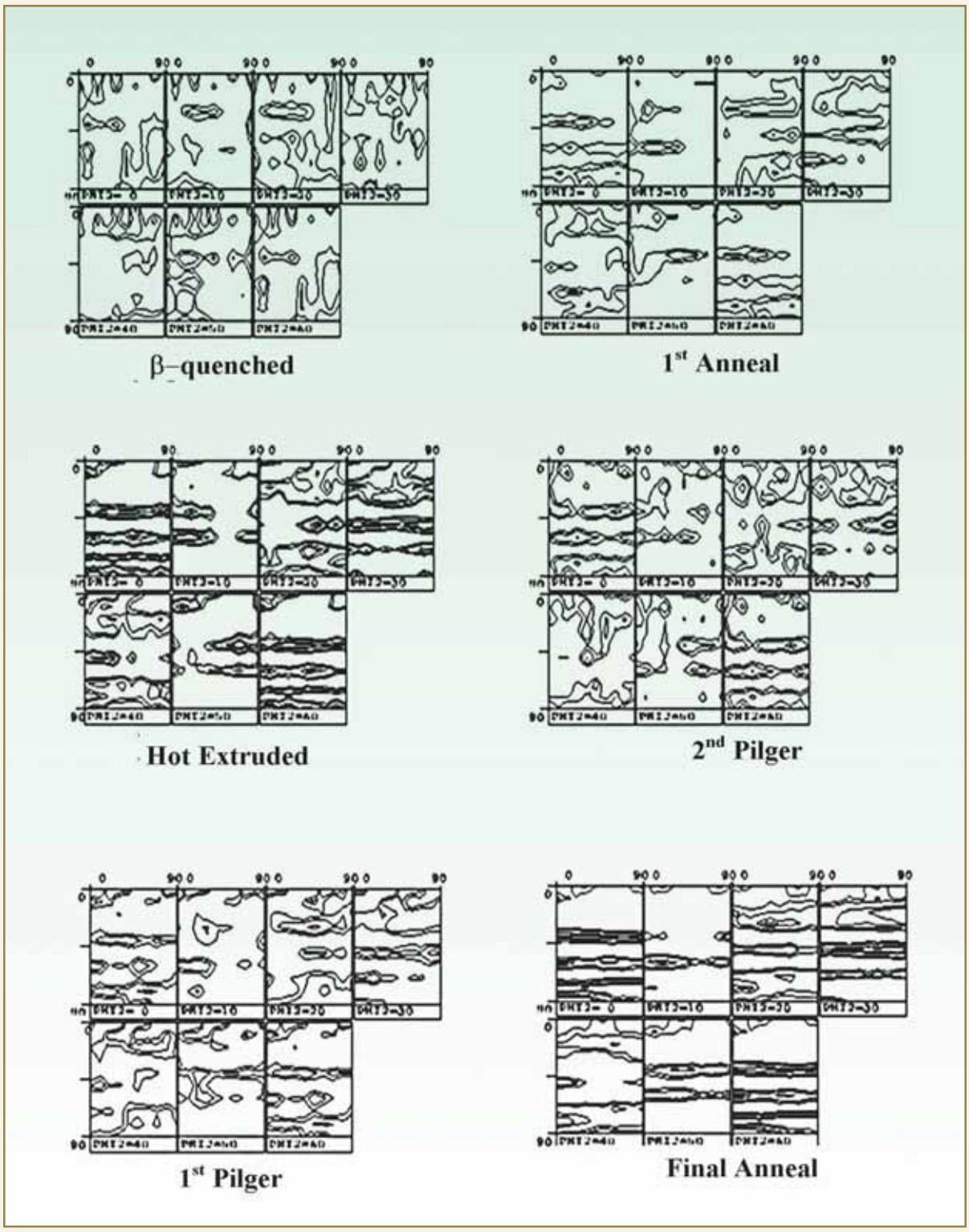

Fig. 6: Evolution of texture during fabrication of Zr-2.5Nb pressure tube.

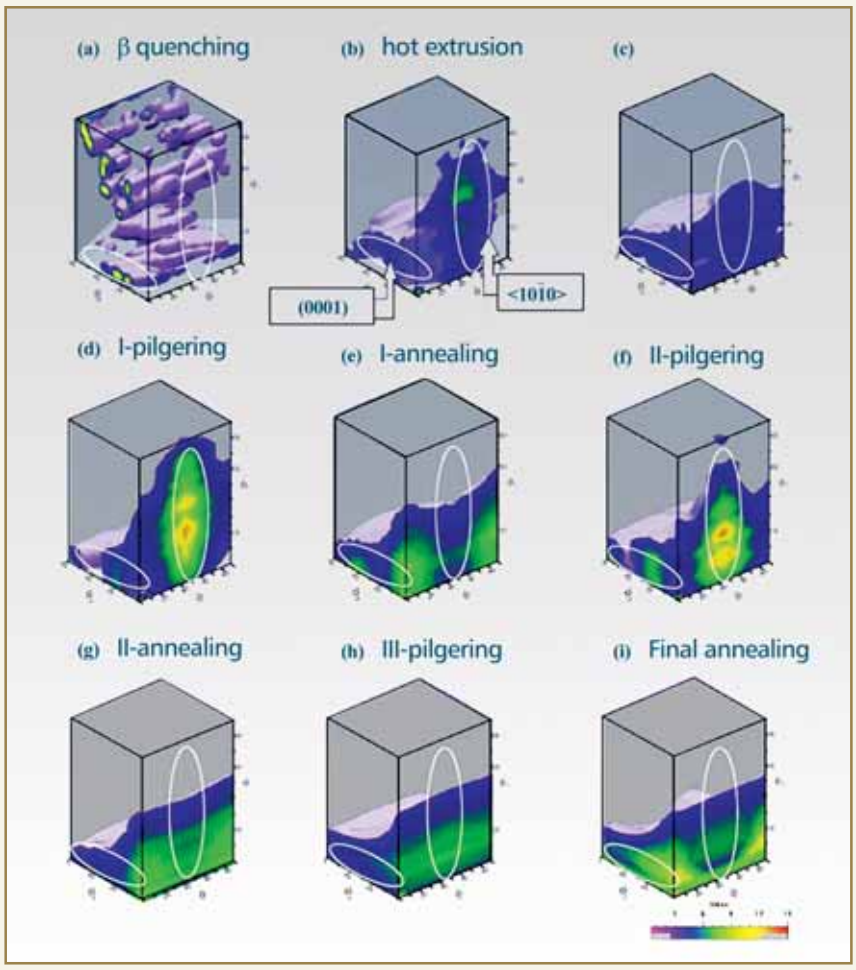

Fig. 7: Evolution of texture during fabrication of Zr-4 cladding tube.

development with only 25% reduction in thickness (as compared to 50-55% in the first pilgering). During annealing, no significant changes in texture could be observed. Relative softening during annealing, as evident from reduced X-ray peak broadening, was mainly through recovery.

The evolution of texture and microtexture during each stage of Zircaloy-4 cladding tube are shown in Fig. 7 and Fig. 8 respectively. The detail of the work is described in another publication. The basal pole texture of the cladding tube and pressure tube is shown in Fig. 9.

b. Texture development during cold deformation in Zr-2.5Nb alloy

In this study, single phase (hcp α') and two-phase (hcp α and bcc β) structures were deformed by cold rolling to different reductions. Development of deformation texture was noticeable in the single phase alloy, but insignificant in the two-phase material. Taylor type deformation texture models could predict the texture changes in the single phase microstructure, but could not explain the lack of change in the two phases. The majority of the two-phase structure consisted of Widman stätten α in a β matrix. Deformation in such regions was restricted to the softer β. Microtextural developments in two-phase regions indicated 'in-plane rigid body rotation' of α plates in an apparently continuous β matrix. Such a mechanism or model, though simplistic, explains the absence of quantitative texture development in the rolled two-phase alloy.

III. Developments of recrystallization texture in zircaloy2

Bulk texture developments during recrystallization were studied for Zircaloy 2, with both 40 and 60 % prior deformation (Fig. 10). At the initial stages of recrystallization (till 10-15 % recrystallized) the texturing increased, while above 20-24 %

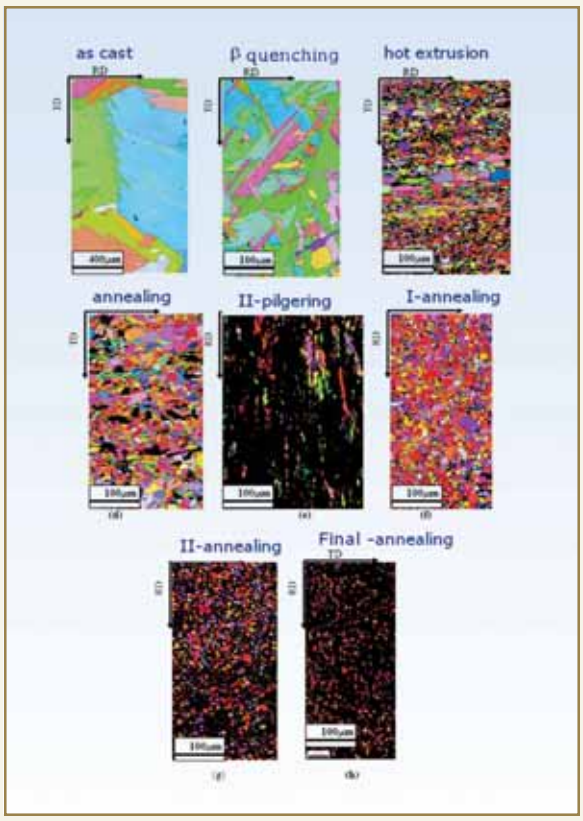

Fig. 8: Evolution of micro-texture during fabrication of Zr-4 cladding tube.

recrystallization, the texturing dropped, the drop being significant beyond 50-55 % recrystallization and in material with 40 % prior deformation. Recrystallized grains originating from strain localizations (type I) were smaller and had a relatively narrow spread of orientations. Recrystallized grains originating from 'deformed bands' (type II had strong size advantage over type I grains and also had high aspect ratios. Preferred presence or frequency advantage of the type I grains defined the increased texturing at the early recrystallization stages. Size advantage of the type II grains determined the texture randomization at the latter stages of recrystallization.

Studies on potential fuel tube alloys: Binary and quaternary alloys

Binary Zr-1Nb and it's derivative quaternary

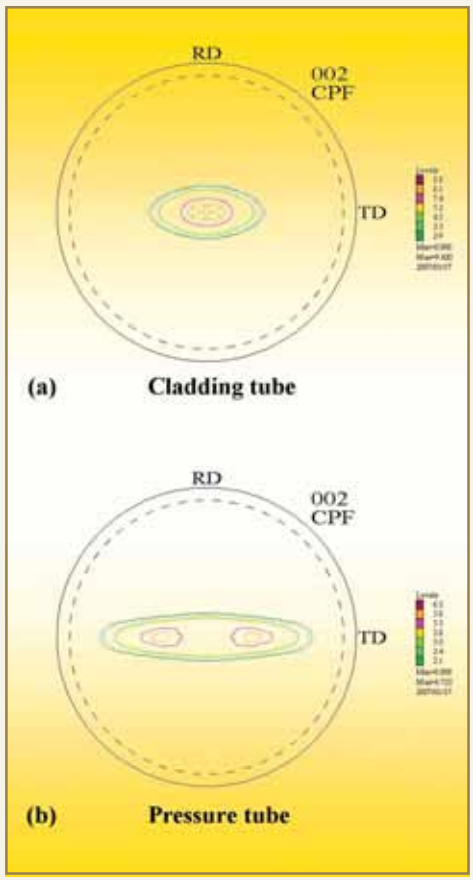

Fig. 9: (a) and (b) Direct pole figures of basal pole for cladding tube and pressure tube respectively.

Zr-1Nb-1Sn-0.1Fe alloys have shown much superior properties, mainly resistance to corrosion and irradiation creep, in comparison to zircaloys. Microstructural studies on these alloys, after different thermomechanical processing have revealed the shape, size distribution and nature of the precipitate phases, the extent of recrystallization and the texture of the matrix hcp a grains-factors which are expected to have strong effects on both short term mechanical behaviour and long term performance during service (Fig.11). The distribution of β_{Nb} particles in Zr-1Nb is of significance in the context of corrosion properties. The optimized fabrication schedule was found to generate the desired precipitate distribution in Zr-1Nb. The annealed microstructure in the case of this binary alloy showed, that the second phase

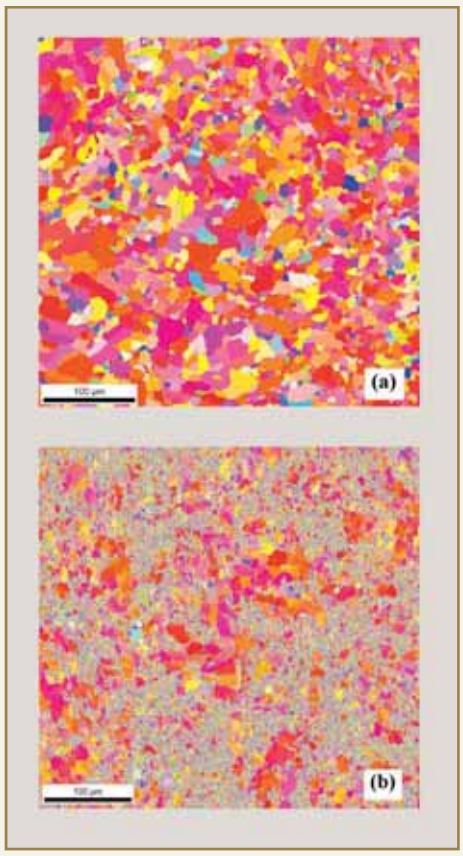

Fig. 10: (a) and (b) SEM-OIM image of Zicaloy-2 material before and after deformation

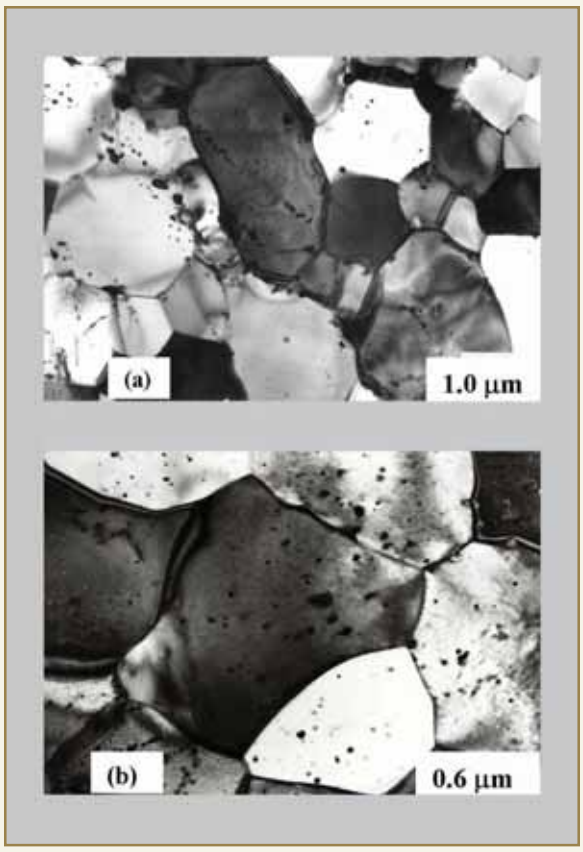

Fig. 11: (a) and (b) Bright field TEM micrographs of quaternary and binary alloy

precipitates were of β type, having compositions varying from β_{Zr} (20 wt % Nb) to β_{Nb} (85 wt % Nb), depending on the heat treatment temperature and time. The second phase precipitates in the quaternary alloy were of Zr_4Sn, Zr_5Sn3 and Zr_3Fe types. In case of the binary alloy the mechanical properties were not influenced by the second phase precipitate size, distribution and volume fraction. In contrast the second phase precipitates in the quaternary alloy significantly influenced the mechanical properties.

Conclusions

The phase transformation aspects, texture aspects and hydride aspects of dilute Zr-Nb alloys have been presented in this paper. The mechanism involved in these phenomenon have been investigated in detail. The understanding and knowledge base provided by this study, would be useful in developing new alloys and fabrication process for zirconium based component for PHWR reactors.

Acknowledgement

The authors would like to thank Dr. A. K. Suri, Director, Materials Group for their support and encouragement Mr. R.N. Jayraj, Chief Executive, Mr. N. Saibaba, Deputy Chief Executive Nuclear Fuel Complex. The authors would like to thank our collaborator Prof. I Samajdar, IIT (B), Mumbai for his contribution and for providing all the facility at his "National Facility of Texture and OIM".

ABOUT THE AUTHORS

Dr. Dinesh Srivastava joined the 28th Batch of Training School and earned his Ph.D. degree in Metallurgy. His research activities involves basic physical metallurgy studies of Zr- base alloys, alloy development, fabrication flow sheet optimization of Zr-base alloy component for PHWR reactors. His other research interests are direct laser fabrication process and synthesis, processing and characterization of nano crystalline soft magnetic material. He has published more than 65 research papers and is the recipient of the Binanai Gold Medal.

Mr. Suman Neogy joined the 44th Batch of Training School of BARC. His main research interests are Phase transformation studies in zirconium based systems, bulk metallic glasses, transmission electron microscopy. He is the recipient of the M. N. Dass Memorial Award, Jadavpur University Medal, Sankar Kumar Das Memorial Gold Medal and Homi Bhabha Prize. He has more than 20 research publications.

Mr. K. V. Mani Krishna joined the 2nd DGFS Batch of BARC Training School. His main research interests are mathematical modeling and simulation, characterization and analyses of materials for developing superior performing materials for nuclear applications, which includes alloy development, fabrication route for heat treated Zr-2.5nb pressure tubes. At present his main thrust is on hydriding phenomenon in Zirconium base alloys.

Dr. M. Kiran Kumar acquired his PhD in Metallurgy from the Indian Institute of Technology (B), Mumbai. After completing his tenure as Dr. K.S. Krishnan Research Fellowship, Dr Kiran Kumar joined the Materials Science Division, BARC. Currently he is actively involved in research on corrosion degradation related issues in nuclear power plants. He has published about 17 research papers.

ABOUT THE AUTHORS

Dr. Gautam Kumar Dey joined the 23rd Batch of Training School in BARC and was awarded the Homi Bhabha Prize. He has won several awards for his scientific contributions; of these mention can be made of the Young Scientist award, Young Metallurgist Award, MRSI Medal and Metallurgist of the Year award. He is a fellow of the Indian National Academy of Engineering (FNAE) and Indian Academy of Sciences (FAS). Areas of his research interest are Phase Transformation in Zirconium and Nickel Base Alloys, Amorphous Alloys, Rapidly Solidified Crystalline and Quasicrystalline Alloys, Electron Microscopy and defect Characterization and High Resolution Electron Microscopy. He has more than 190 scientific publications to his credit. Currently, he is the Head of the Materials Science Division, BARC.

Dr. S. Banerjee is internationally well known for his work in the field of physical metallurgy and materials science, especially in zirconium and titanium based alloys. A Distinguished Scientist, Dr. Banerjee has been the recipient of many awards and honours. These include Shanti Swarup Bhatnagar Award, G.D. Birla Gold Medal, INSA Prize for Materials Science and Indian Nuclear Society Award. Notable among the international awards received by him are Acta Metallurgica Outstanding Paper Award and Humboldt Research Award. Dr. Banerjee is a Fellow of Indian National Science Academy, Indian Academy of Sciences, Indian National Academy of Engineering and the National Academy of Sciences. Currently he is the Director of Bhabha Atomic Research Centre.

बीएआरसी न्यूज़लेटर BARC NEWSLETTER

MODULATION OF γ - RADIATION-INDUCED REDOX SIGNALLING IN SPLEEN LYMPHOCYTES BY COPPER (II)–CURCUMIN (1:1) COMPLEX

Amit Kunwar and K. Indira Priyadarsini
Radiation & Photochemistry Division

and

H. Narang and M. Krishna
Radiation Biology & Health Sciences Division

This paper received the ABB Young Investigator Award for the Best Poster Presentation at the International Conference on "Emerging Trends in Free Radical and Antioxidant Research" held at Lonavala, during January 8-11, 2007

ABSTRACT

Mononuclear 1:1 copper complex of curcumin was examined, for it's modulatory effect on radiation activated redox signal transduction in spleen lymphocytes, from Swiss albino mice and the results were compared with that of curcumin. Initial response of both curcumin and the complex on modulation of radiation-induced activation of PKC δ and NFκB was similar, however it was different at later time periods. The early responses have been attributed to mere stress responses and the activation of crucial signaling factors at later time periods, was found to be determinant of the fate of the cell. The complex was also found to be less cytotoxic than curcumin at similar concentration.

Introduction

Exposure of cells to ionizing radiation, leads to production of various Reactive Oxygen Species (ROS) and subsequent activation of signaling pathways, that may be cytotoxic or cytoprotective. Among the cytoprotective pathways that are: activated following ionizing radiation are Protein Kinase C (PKC), Mitogen Activated Protein (MAP) Kinase and the Nuclear Factor-κB (NF-B) pathways, which may also confer radioresistance to the cells. An additional mechanism related to subsequent reduction of free radical mediated cellular damage, is to upregulate the transcription of ROS scavenging enzymes. A major class of these protective enzymes belongs to the mitochondrial SuperOxide Dismutase (SOD), which is also the transcript of NF-kB.

Curcumin, an important natural phytochemical, found in the rhizomes of *Curcuma longa* or turmeric, is an efficient free radical scavenger and reacts with most of the reactive ROS, associated with oxidative stress

such as superoxide, peroxyl, hydroxyl and nitrogen oxide radicals. In addition to it's antiradical activity, curcumin has been reported to modulate the PKC and NF-κB signalling pathways. Since copper chelates of antioxidants are well known as SOD mimics, in our laboratory, we synthesized a copper (II)-curcumin complex with the stoichiometry of 1:1 and characterized by spectroscopic methods. The structures of curcumin and the copper-curcumin complex are given in Scheme 1.

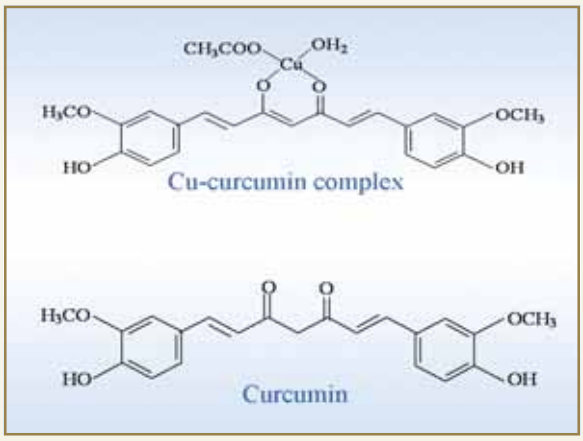

Scheme 1: Structure of Curcumin and the Copper-Curcumin complex

In the present study, we investigated the effects of the complex treatment on **γ**-radiation induced activation of PKC and NF-**κ**B signaling in spleen lymphocytes.

Material and Methods

Spleen cell suspension was prepared from the mice, reared in the animal house of BARC as described in our earlier references. The stock solution of curcumin and the complex were prepared, in nitrogen saturated aqueous solutions, with 0.2 M NaOH. Spleen lymphocytes suspended in RPMI 1640 medium were seeded at 2.5 X 10^6 cells / ml, to which stock solution of either curcumin or the complex was added to get final concentration of 10μM. Treated and untreated lymphocytes were exposed to γ-radiation using a ^{60}Co γ-source with a dose rate of 6 Gy min^{-1} as measured by standard Fricke dosimeter and incubated at 37°C in humidified incubator with 5% CO_2 in air, for different times as desired in the study.

Cells were lysed and western blotting for MnSOD and PKCd proteins were performed. To know the translocation of NF-κB into the nucleus, nuclear extracts were prepared and probed with anti-NF-κB (p65) antibody using BM chemiluminiscence western blotting kit as per manufacturer's instructions. Equivalent protein loading was demonstrated, by staining membranes in 1% Ponceau S. Fold changes were calculated after normalization to Ponceau S.

Results

(i) Effect of curcumin and the complex on protein kinase Cδ phosphorylation after irradiation

The phosphorylation at Ser 40 residue of PKCδ in lymphocytes, was assessed at 5, 15, 30 and 60 min after irradiation alone or after pre-treatment with either curcumin or the complex. Western blots and relative intensities representing the level of phosphorylated PKCδ at the above four time points are shown in Fig. 1 (A, B, C) and Fig. 1 (D). Following γ-irradiation, an increased phosphorylation of PKCδ was observed within 5 min, which reappeared at 60 min.

When irradiation was preceded by curcumin or the complex treatment, the increased phosphorylation observed at 5 min was suppressed. Here, the complex showed stronger inhibition than curcumin.

However, at 60 min, pretreatment with the complex resulted in increased phosphorylation of PKCδ, as compared to irradiation alone or pretreatment with curcumin. Treatment with curcumin or the complex alone also resulted in increased phosphorylation of PKCδ but with different kinetics of activation. The complex showed time-dependent increase, upto eight fold at 60 min, indicating that the complex promotes growth in normal cells since increased expression of PKCδ could be anti apoptotic.

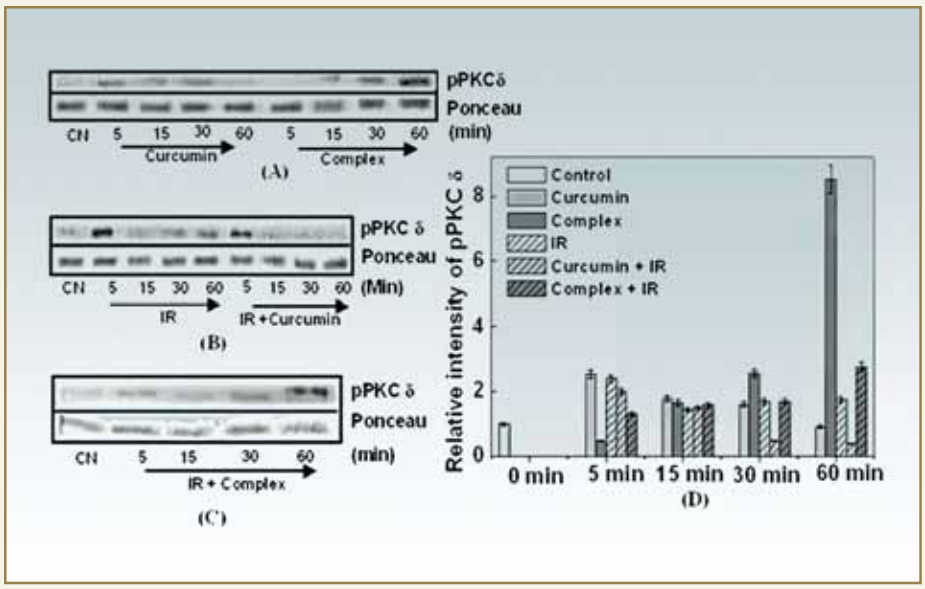

Fig.1: Western blot analysis of phospho (Ser40) PKCδ protein in spleen lymphocytes treated with curcumin or the complex in the absence (A) and presence (B & C) of γ-radiation. (D) Relative intensity representing expression levels of phospho-PKCδ at different timepoints. IR - Irradiation (2 Gy)

(ii) Effect of curcumin and the complex on nuclear transport of NF-κB and MnSOD expression

Fig. 2 shows western blots (A) and relative intensities (B) respectively of NF-κB in nuclear extract of same samples at a time point of 60 min. Following irradiation, the level of NF-κB decreased in the nuclear extract of untreated lymphocytes. However, when irradiated spleenocytes were pretreated with curcumin or the complex, the decrease in the level of NF-κB was reversed marginally by curcumin, but very efficiently by the complex. Treatment with either curcumin or the complex alone also reduced the level of NF-κB in nuclear extract. Western blot and relative intensities of MnSOD, in untreated or treated lymphocytes, are also shown in Fig. 2. A marked increase in the level of MnSOD was observed after irradiaiton, Treatment with curcumin or the complex before irradiation, inhibited this increase with the complex, showing more profound effect than curcumin. The complex or curcumin treatment alone inhibited the expression of MnSOD.

Discussion

The metal chelating ability of curcumin has been utilized by several groups to enhance it's antioxidant activity. However, there are very few reports in the literature, about the modulation of radiation induced redox disturbances, by such metal chelates of curcumin.

The present study therefore deals with the modulation of γ-radiation activated signalling pathways by a copper (II)-curcumin complex in spleen lymphocytes and the results have been compared with those of curcumin. We followed the activation of PKC δ and NF-kB after irradiation in presence or absence of these compounds over a time period of 5 to 60 min. The inhibition of irradiation-induced phosphorylation of PKCδ at 5 min was observed, by both the complex and curcumin, with complex showing stronger inhibition. Since the early response seen at 5 min could be stress responses, which occurs due to the production of ROS, the complex therefore seems to be a better scavenger of ROS *in vivo* and could prevent the initial activation of PKCδ observed with irradiation. After the initial damage response, the cell assesses the damage and activates the signaling pathways, which then determine the fate of the cell. In this study, the activation, which is observed at 5 mins, may be a stress response following which at later time periods (60 min), the signals that will protect the cells were

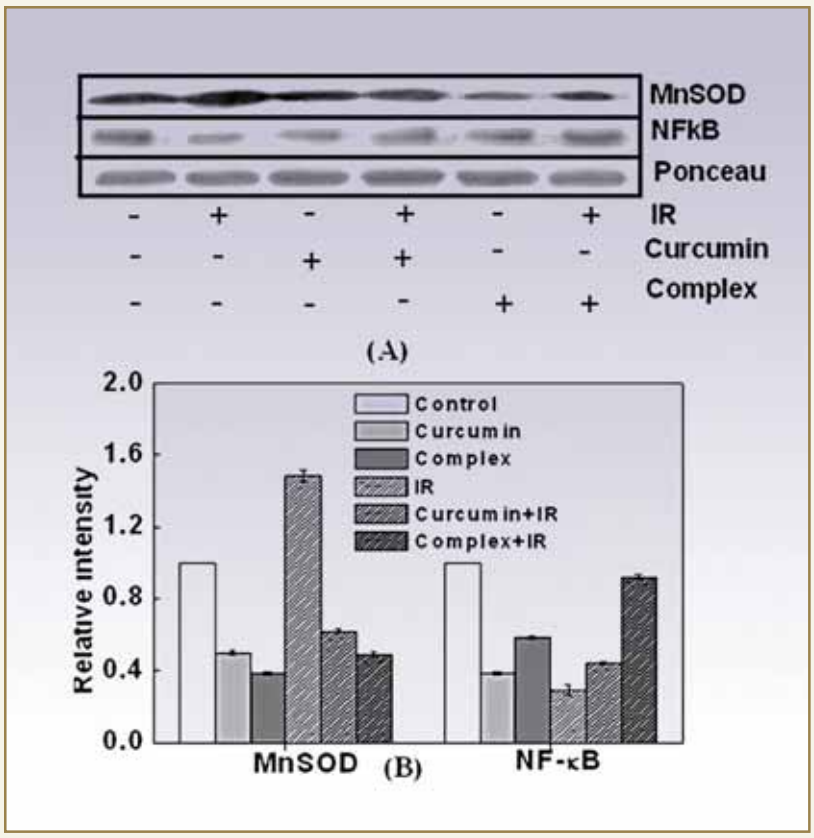

Fig. 2: (A) Western blot analysis of NF-κB and MnSOD in nuclear and cytoplasmic extract of curcumin or complex treated spllen lymphocytes in presence and absence of γ-radiation. (B) Relative intensity representing expression levels of NF-κB and MnSOD respectively. IR - Irradiation (2 Gy)

initiated. PKCδ has been shown previously to activate various cytoprotective genes. The extensive phosphorylation of PKCδ at 60 minutes in the complex pretreated and irradiated spleenocytes, indicate that, the complex is more efficient than curcumin, in activating cytoprotective pathways after the damage. These results were further supported by the content of NF-κB in the nucleus, which was found to be more in the complex pretreated irradiated spleenocytes at 60 min after irradiation (Fig. 2). The delayed phosphorylation of PKCδ, in the complex treated lymphocytes along with the delayed activation of NF-κB indicate a more prolonged action of the complex as compared to curcumin. The reason for this could be the delayed biological half-life of the complex and hence it's higher effectiveness. The expression of *MnSOD*, a cytoprotective gene and a transcript of NF-κB was next looked at, after 60 min of treatment with the compounds. ROS are known to induce the expression of *MnSOD* in the cell. This has also been observed in our results with irradiated spleenocytes (Fig. 2). Pretreatment with the complex or curcumin prevented this increase, indicating the strong scavenging capacity of the compounds, with complex again faring better than curcumin. Comparing the translocation of NF-κB and it's downstream target gene *MnSOD*, it was observed that the complex did not inhibit the translocation of NF-κB to the nucleus as much as curcumin did. Inspite of increased translocation of NF-κB to the nucleus in the complex treated spleenocytes, the expression of *MnSOD* was inhibited more by the complex. The reason for this could be the superoxide dismutating activity of the complex.

Conclusion

Our results thus show that the complex scores better than curcumin, in the activation of cytoprotective signaling pathways in temporally relevant manner i.e. PKCδ and NFκB, which would then play a crucial role in protecting the cells from radiation-induced oxidative stress.

ABOUT THE AUTHORS

Mr. A. Kunwar obtained his M. Sc. degree in Biotechnology from the Centre for Plant Molecular Biology, Tamil Nadu Agricultural University in 2003. After graduating from BARC Training School in 2005 (48th Batch, Bioscience discipline), he joined the Radiation & Photochemistry Division, BARC. Since then he is involved in free radical cellular biochemistry and evaluation of synthetic as well as natural molecules for their antioxidant and pro-oxidant activity employing spectroscopic, cell biology and biochemical techniques.

Dr. (Ms.) K. I. Priyadarsini joined BARC in 1983. She is currently working on the elucidation of mechanisms of antioxidant action involving natural products and herbal extracts with potential application as radioprotectors, employing electron pulse radiolysis and *in vitro* biochemical studies. Dr. Priyadarsini has co-authored more than 100 papers in peer reviewed international journals on radiation chemistry, photochemistry and radiation biology. She has been elected as the Fellow of the National Academy of Sciences, India and is the recipient of the Homi Bhabha Science & Technology Award.

Ms. Himanshi Narang is from the 44th Batch of Training School. Her fields of interest are radiation and nitric oxide induced signaling in mammalian cells.

Dr. (Ms.) Malini Krishna is from the 16th Batch of Training School and is currently Head of Radiation Signaling Section, RBHSD. Her fields of interest are carcinogenesis, radiation and nitric oxide induced signal transduction, identification of signaling markers of radioresistance and high LET radiation.

CORRELATING THE GPX ACTIVITY OF SELENOCYSTINE DERIVATIVES WITH ONE-ELECTRON REDOX REACTIONS

B. Mishra, A. Barik, A. Kunwar and K.I. Priyadarsini
Radiation and Photochemistry Division

and

L.B. Kumbhare and V.K. Jain
Chemistry Division

This paper was awarded the Travel Grant for an Oral Presentation at the "Tenth International Conference on the Chemistry of Selenium and Tellurium (Xth ICCST) held at Lodz, Poland during June 22-27, 2007

ABSTRACT

With an aim to develop water soluble, less toxic glutathione peroxidase (GPx) mimics, three selenocystine (SeCys) derivatives, viz., selenocystamine (SeA), diselenodipropionic acid (DSePA), and methyl ester of diselenodipropionic acid (MeSeP) have been synthesized and examined for GPx activity along with SeCys. The GPx activity of the compounds was found to be in the order SeCys $\cong$ SeA $>$ MeSeP $>$ DSePA. The relative affinity of these GPx mimics towards the substrates thiol and hydroperoxide were determined by Lineweaver-Burk (L-B) plots. Since the enzyme activity involves several steps of reduction and oxidation reactions, attempts have been made to understand the role of such processes, in deciding the efficacy of diselenides as GPx mimics. For this, one-electron redox chemistry of these compounds was studied in aqueous solutions at pH 7, using nanosecond pulse radiolysis technique. From these studies it was concluded, that SeCys and SeA, which can undergo easy one-electron reduction, exhibit high GPx activity

Introduction

Selenium is an essential micronutrient playing a crucial role in the biochemistry of redox active proteins. At least more than thirty proteins, containing selenium as active centre have been identified. One of the most studied selenoproteins is glutathione peroxidase (GPx), which is an antioxidant enzyme that neutralizes hydroperoxides at the expense of thiol. Of late, there is a growing interest in developing new organoselenium compounds having GPx-like activity. Recently, several low molecular weight organoselenium compounds have been tested, for the GPx enzyme mimicking activity. Even among the most effective GPx mimics, the therapeutic utility remained limited, due to their low water solubility and high cellular

toxicity. Recently it is reported, that certain aliphatic seleno-ethers and diselenides showed GPx activity depending on the substitution on the aliphatic chain. It is shown that the GPx activity of selenocystine depends both on one and two electron reduction potential. With this background, and with an aim to develop water-soluble, non-toxic GPx mimics, we have synthesized and tested the GPx activity of three selenocystine derivatives and compared them with those of selenocystine. Attempts have also been made to correlate their redox properties with their GPx activity. Here in this paper, all these compounds are collectively termed as diselenides (RSeSeR) and their structures are given in Scheme 1.

Materials and Methods

Selenocystine, selenocystamine dihydrochloride, NADPH, glutathione reductase, glutathione (GSH), cumene hydroperoxide (CuOOH), methyl viologen (MV^{2+}) and 2,2'-Azinobis(3-ethylbenzo-thiazoline-6-sulfonate) ion ($ABTS^{2-}$), were obtained from Sigma. DSePA and MeSeP were synthesized. All the compounds were characterized by ^{1}H, ^{13}C, ^{77}Se NMR, IR and elemental analysis. For pulse radiolysis studies, 7 MeV electrons of 500 ns pulse width from a linear accelerator were used. The transients were detected by absorption spectrometry and absorbed dose was determined by thiocyanate dosimetry.[7] The reducing formate ($CO_2^{\bullet-}$) radicals and oxidizing trichloromethyl peroxyl ($CCl_3O_2^{\bullet}$) radicals were generated as described elsewhere.

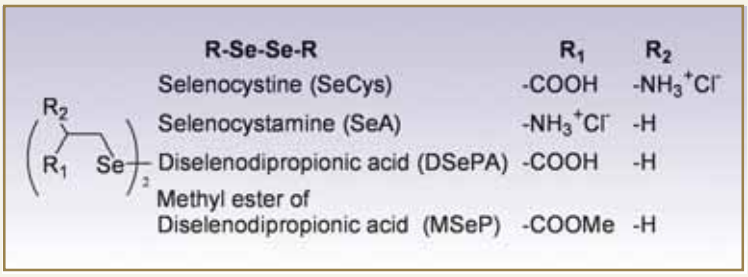

Scheme 1: Chemical structure of the diselenides (R-Se-Se-R)

Results and Discussion

Enzyme kinetic studies

To compare the GPx activity of diselenides, NADPH coupled assay was employed, using CuOOH and GSH as the oxidant and reductant respectively, by following the decay of NADPH at 340 nm, in the absence and presence of the diselenides. From the initial portion of the NADPH decay trace, the initial rate (v) is calculated and this v value is fitted to the Lineweaver-Burk (L-B) equation against varying concentrations of either GSH or CuOOH, to estimate the enzyme kinetic parameters, i.e. Michealis-Menten constant (K_m) and V_{max} according to equation (1).

$$\frac{1}{v} = \frac{K_m}{V_{max}}\frac{1}{[S]} + \frac{1}{V_{max}} \qquad (1)$$

Here S is either GSH or CuOOH. L-B plot for thiol was obtained by keeping the concentration of CuOOH fixed and varying the concentration of GSH. The linear fit of the data in accordance with equation (1) gave K_m and V_{max} values for thiol which are given in Table 1. Similarly L-B plot for CuOOH was obtained at different concentrations of CuOOH keeping the concentration of the GSH fixed and K_m and V_{max} values were calculated (Table 1).

Selenium compounds may enter the GPx cycle in two pathways i.e. either by reduction or oxidation mechanism. In the former, the diselenide is reduced by thiol to form a selenol, which in turn reduces the hydroperoxide with concominent formation of selenenic acid, that is finally regenerated back to selenol by GSH. In the latter pathway, the selenium compound reacts with the hydroperoxide directly, to form the selenenic acid. The relative importance of these two pathways

Table 1: Enzyme kinetic parameters for the diselenides derived from L-B plots

RSeSeR	Thiol			CuOOH		
	K_m (m μM^{-1})	V_{max} (μM/min)	Turn-over number (min^{-1})	K_m (μM^{-1})	V_{max} (μM/min)	Turn-over number (min^{-1})
SeCys	0.5	56.0	1.1	64	58.0	1.1
SeA	0.4	29.0	0.6	28	50.0	1.00
DSePA	10.2	4.8	5.0×10^{-2}	140	2.2	2.0×10^{-2}
MeSeP	0.9	5.6	0.1	280	25.6	0.5

depends on the relative affinity of the selenium compounds for either the thiol (GSH) or the hydroperoxide (CuOOH). This can be understood, by estimating the values of K_m and V_{max} determined from the L-B plots. K_m is inversely related to the binding of the substrate to the enzyme, i.e. higher the value of K_m, lower is the binding of the substrate to the enzyme. Comparing the K_m values (Table 1), it can be seen, that all the compounds have higher affinity for CuOOH. The SeA, SeCys and MeSeP show affinity towards thiol, also whereas DSePA shows least affinity towards the thiol. Since all these diselenides exhibit GPx activity, it is necessary to compare their relative efficiency in terms of the turn-over number, which is defined as the number of moles of substrate consumed or product formed by per mole of the catalyst. Here the substrates are GSH and CuOOH and the turn-over number is expressed as (equation 2):

$$\text{Turn - over number} = \frac{V_{max}\,(\mu M/min)}{[\,RSeSeR\,](\mu M)} \qquad (2)$$

As evident from Table 1, SeCys shows maximum turn over number which is very close to that of SeA, while DSePA shows the least activity. Comparing the above determined K_m values with the turn-over number, it can be seen that, although SeA shows higher affinity for the thiol, the enzyme activity for SeCys is the maximum. GPx is an oxidoreductase enzyme; therefore it undergoes both oxidation and reduction during it's catalytic cycle. Thus, the redox properties of organoselenium compounds must contribute to their overall GPx activity. The redox processes can be mediated either by one or two-electron transfer. In order to understand the role of one-electron transfer processes in the overall GPx activity of the diselenides, pulse radiolysis studies have been carried out. Pulse radiolysis is an excellent technique to study and follow one-electron induced redox processes directly.

Pulse radiolysis studies

Pulse radiolysis induced one-electron reduction and oxidation studies of these compounds, were carried out in aqueous solutions at pH 7. One-electron reduction was studied, by using radiolytically-produced secondary one-electron reductant $CO_2^{\bullet-}$ radical anion. The reaction of $CO_2^{\bullet-}$ with diselenides proceeds by one –electron reduction as given below.

$$(R\text{-}Se)_2 + CO_2^{\bullet-} \rightarrow (R\text{-}Se)_2^{\bullet-} + CO_2 \qquad (3)$$

$$(R\text{-}Se)_2^{\bullet-} \rightarrow R\text{-}Se^{\bullet} + R\text{-}Se^{-} \qquad (4)$$

Similarly, reactions of oxidizing radicals with these diselenides were studied. Reaction of DSePA with radicals, produced radical cation of DSePA, formed by one-electron oxidation. Other diselenides did not show any transient formation indicating that the oxidation of these diselenides is more difficult than DSePA. The reaction with radicals is represented by the equation

$$(R\text{-}Se)_2 + CCl_3O_2^{\bullet} \rightarrow (R\text{-}Se)_2^{\bullet+} \qquad (5).$$

The above studies with $CO_2^{\bullet-}$ and $CCl_3O_2^{\bullet}$ radicals indicate that while SeA is easy to reduce, DSePA is oxidized easily. The ease of a compound to undergo reduction or oxidation can be predicted, from the rate constant, for a given reaction. Therefore, the bimolecular rate constants for the reaction of $CO_2^{\bullet-}$ and

$CCl_3O_2^{\bullet}$ radicals with the diselenides were estimated, by competition kinetics employing methyl viologen (MV^{2+}) as a reference solute for reduction and $ABTS^{2-}$ as the reference for the oxidation. Table 2 shows the bimolecular rate constants for the reaction between the diselenide and radicals. The results indicate that SeA and SeCys show higher reactivity towards the reducing radical while DSePA shows the least and therefore is difficult to participate in reduction.

Similarly on comparing the bimolecular rate constant for the reaction between the diselenide and $CCl_3O_2^{\bullet}$ shows that DSePA can be oxidized easily and shows higher reactivity towards the peroxyl radical.

Table 2: Bimolecular rate constants for the reactions of reducing and oxidizing radicals with diselenides from pulse radiolysis studies

RSeSeR	k_1 $M^{-1}s^{-1}$ RSeSeR+ $CO_2^{\bullet-}$	k_1 $M^{-1}s^{-1}$ RSeSeR+$CCl_3O_2^{\bullet}$
SeCys	2.1×10^9	nd
SeA	3.4×10^9	8.3×10^6
DSePA	8.4×10^8	1.7×10^8
MeSeP	9.6×10^8	1.1×10^8

Conclusions

Four water soluble diselenides, derivatives of selenocystine, have been examined for GPx activity. All of them showed GPx activity with differences in their efficiency. SeCys and SeA having amino substitution showed highest GPx activity, while DSePA having only carboxylic acid substitution showed the least activity. Using L-B plots, the relative affinity of the diselenides towards thiol and hydroperoxide were estimated. The results indicated, that all the diselenides have higher affinity for the hydroperoxides, while SeA and SeCys showed affinity to thiol. These observations were further supported by one-electron redox reactions studied by pulse radiolysis. The studies confirmed that the diselenides having amino substitution are easy to undergo reduction, due to the presence of electron withdrawing amino groups, which exerts –I effect on the Se-Se bond. On the other hand DSePA, due to electron donating carboxylic group shows +I effect and increases the electron density on the Se-Se bond. DSePA is therefore difficult to undergo reduction but is easily oxidized. Thus the results confirm, that the diselenides that can easily undergo reduction, show efficient GPx activity and reduction pathway is important in the GPx cycle of these diselenides.

ABOUT THE AUTHORS

Dr. Beena Mishra joined the Radiation and Photochemistry Division, BARC as a DAE Research Fellow. After submitting her thesis in 2006, she joined the same division as a K. S. Krishnan Research Associate. Presently she is employed as Scientific Officer and is involved in developing organoselenium based antioxidants and radioprotectors. Her work involves elucidation of mechanism of free radical reactions with organoselenium compounds utilizing pulse radiolysis technique and enzyme kinetics.

ABOUT THE AUTHORS

Dr. Atanu Barik after graduating from BARC Training School in 2000 (43rd Batch, Chemistry discipline), joined the Radiation & Photochemistry Division, BARC. Since then he is actively involved in free radical chemistry and excited state properties of important biomolecules, employing photochemical and radiation chemical techniques. He obtained his Ph. D. degree in Chemistry, from University of Mumbai in 2006.

Mr. Amit Kunwar obtained his M. Sc. degree in Biotechnology from Centre For Plant Molecular Biology, Tamil Nadu Agricultural University in 2003. After graduating from BARC Training School in 2005 (48th Batch, Bioscience discipline), he joined the Radiation & Photochemistry Division, BARC. Since then, he is involved in free radical cellular biochemistry and evaluation of synthetic as well as natural molecules, for their anti-oxidant and pro-oxidant activity, employing spectroscopic and biochemical techniques.

Dr. K. Indira Priyadarsini joined BARC in 1983. She is currently working on the elucidation of mechanisms of antioxidant action, involving organoselenium compounds, natural products and herbal extracts with potential application as radioprotectors, employing spectroscopic methods, electron pulse radiolysis and biochemical studies. Dr Priyadarsini has co-authored more than 125 papers. She has been elected as the Fellow of the National Academy of Sciences, India and is the recipient of the Homi Bhabha Science & Technology Award.

Mr. Liladhar B. Kumbhare joined the Radiochemistry Division after graduating from the 41st Batch of BARC Training School. Subsequently he joined the Chemistry Division in 2002. He is currently involved in the design and synthesis of organo-chalcogen compounds, their complexes with Pt group metals and utilizing such metal complexes for the preparation of metal chalcogenide nanoparticles.

Dr. V. K. Jain joined the Chemistry Division in 1984 after his Post Doctoral work at the University of Guelf, Canada. He has been actively working in a broad area of organometallic chemistry and NMR spectroscopy. He has published more than 225 research papers. He has received several awards including the Homi Bhabha Science and Technology Award (1996) of DAE and is a fellow of the National Academy of Sciences.

बीएआरसी न्यूज़लेटर BARC NEWSLETTER

OPTIMIZATION OF STRESS RELIEF HEAT TREATMENT OF PHWR PRESSURE TUBES (ZR-2.5NB ALLOY)

Gargi Choudhuri, K.R. Gurumurthy and B.K. Shah
Quality Assurance Division
and

D. Srivastava
Materials Science Division

This paper won the Best Paper Award at the International Symposium on Advances in Nuclear Materials (ANM-2006), held at Mumbai, during December 12-16, 2006

ABSTRACT

The microstructure of cold-worked Zr-2.5%Nb pressure tube material consists of elongated grains of α-zirconium enclosed by a thin film of β-zirconium phase. This β-Zr phase is unstable and on heating, progressively decomposes to α-Zr phase and β phase enriched with Nb and ultimately form β_{Nb}. Meta-stable α-phase precipitates as an intermediate step during decomposition depending on the heat treatment schedule.

Morphological changes occur in the β-zirconium phase during the decomposition. The continuous ligaments of β_{Zr} phase turn into a discontinuous array of particles followed by globulization of the β-phase. The morphological changes impose a significant effect on the creep rate and on the delayed hydride cracking velocity due to reduction in the hydrogen diffusion coefficient in α_{Zr}. If the continuity of β-phase is disrupted by heat treatment, the effective diffusion coefficient decreases with a concomitant reduction in DHC velocity. The pressure tubes for the Indian PHWRs are made by a process of hot extrusion, followed by cold pilgering in two stages and intermediate annealing. Autoclaving at 400°C for 36 h ensures stress relieving of the finished tubes. In the present studies, autoclaving duration at 400°C was varied from 24 h to 96 h at 12h-steps and the micro-structural changes in the β-phase were observed by TEM. Dislocation density, hardness and the micro-structural features such as thickness of β phase, inter-particle spacing and volume fraction of the phases were measured at each stage. Autoclaving for a longer duration was found to change the morphology of β- phase and increase the interparticle spacing. Progressive changes in the aspect ratio of the β phase and their size and distribution are documented and reported. These micro-structural modifications are expected to decrease DHC velocity during reactor operation.

Introduction

The current generation of CANDU pressure tubes are manufactured from Zr-2.5 Nb alloy due to it's higher strength, lower creep rate [1], improved corrosion behaviour and lower deuterium pick up [2]. Further, the phenomena of accelerated corrosion and hydriding do not occur in Zr-2.5 Nb pressure tubes[2]. The magnitude of critical stress for hydride reorientation to radial direction is higher for Zr-2.5 Nb

(180- 220MPa) as compared to Zr-2 (80-110MPa) [2]. Fabrication flow sheet of these Zr-2.5 Nb pressure tubes, mainly consists of vacuum arc melting, forging and extrusion at 800 °C followed by 2-stage cold drawing to obtain 20-30% cold work in the final product. The finishing stage is autoclaving at 400 °C to produce a protective black lustrous oxide layer [3] and to relieve the internal stresses. The microstructure of the tube consists of flat, elongated α-$_{Zr}$ grains containing about 1 at% Nb and a high dislocation density with β phase sandwiched between α lamellae having composition ~20 at% Nb [4]. These β phase are meta-stable at reactor operating temperature (260-300 °C), below the monotectoid temperature (610 °C). The β-phase decomposes first to the ω-phase and enriched β phase and ultimately to the equilibrium α_{Zr} and β_{Nb}(85wt%Nb) [5]. Upon thermal aging or irradiation, fine β_{Nb} particles precipitate which improves corrosion resistance of the pressure tube [6]. Generally, α grain size is 0.3 - 0.5 μm keeping the aspect ratio 1:5:50 (radial: transverse:axial direction).This grain morphology gives strength and prevents formation of radial hydrides during reactor operation. These grains have a texture that has resolved basal pole components, oriented approximately one third in radial, most of the remainder in transverse and only a small fraction in the longitudinal direction [6].

In place of extrusion and cold drawing route, hot extrusion followed by a 2-stage cold - pilgering with intermediate annealing at 550 °C ± 10 °C for 6 hr has also been established [7]. This route is being followed for pressure tube fabrication for the Indian PHWRs. Stress relieving of the finished tubes takes place during autoclaving (400 °C for 36 h). In the present study, duration of autoclaving at 400 °C was varied from 24 h to 96 h at 12 h-steps and the micro-structural modifications in the β -phase were observed by TEM.

Pressure tube life is limited by hydrogen damage mechanisms, namely hydride embrittlement, Delayed Hydride Cracking (DHC) [8,9] and hydride blistering. DHC requires hydrogen (H) migration under stress gradient and is responsible for growth of flaws. Breaking the continuity of beta (β) phase at α grain boundaries is expected to reduce H diffusivity and thereby DHC velocity. The objective of the present study is to standardize the parameters to be followed, for stress relieving that brings about modification in the microstructure to reduce the DHC velocity.

Experimental

Zr-2.5 Nb pressure tubes manufactured by Nuclear Fuel Complex were used in this study. Coupons sliced from tubes just before autoclaving were used as starting material and are referred to as-received material. The -βphase morphology was analyzed in as-received and stress relieved conditions by carrying out the stress relieving at 400 °C, 10kg / cm^2 pressure for 24, 36, 48, 72 and 96 hours. 100 μm thick discs of 3 mm diameter were cut from the longitudinal-radial (L-R) section of the autoclaved pressure tube. The disks were electro-polished in a solution of 20 % perchloric acid and 80 % methanol at -50 °C using jet-thinning apparatus. These electron transparent foils were examined at 160KV using JEOL transmission electron microscope. Elemental analysis was obtained using an Energy Dispersive Spectrometer (EDS) attached with TEM.

Vickers hardness measurements using 300 g load were made on all the three principal planes for as received and stress relieved specimens. Dislocation density measurement was carried out by X-ray line profile analysis on the coupons stress, relieved in 2 different conditions, viz. (i) 400 °C / 36 hrs and (ii) 400 °C / 96 hrs. There are two basic techniques for measurement of dislocation density from X-ray line profile analysis:(i) Fourier space technique which involves Fourier analysis, (ii) real space techniques in which integral breadth analysis is most popular. In the integral breadth method, the peaks that are affected by stacking fault are also included, to give overall dislocation density including the stacking fault concentration. On

the other hand, Fourier analysis gives separate estimation of stacking fault concentration in addition to dislocation density (ρ), coherent domain size (D), micro strain (ε).The correction for instrumental broadening is the most important step in estimation of material properties from line profile analysis.

Samples were taken from the outer surface of a pressure tube (L-T section). The autoclaved specimens were ground flat, polished mechanically and then etched. The specimens were irradiated using Phillips expert pro machine with Cu-$K_{\acute{a}}$ radiation falling on this surface. Scan step size was 0.02° and scan rate 0.3° per min.

Measurement of dislocation density was also carried out by counting the number of dislocation in the defined area of the TEM microphotographs.

Results

The bright field micrographs obtained in TEM of L-R section of as received sample (25% cold pilgered) are shown in Fig.1. The α-Zr matrix is surrounded by discontinuous β-Zr phase. The β-Zr phase is 32.5 nm thick and has a volume fraction of 8-15 % and an aspect ratio of 2.6. Inter particle distance of β in the longitudinal direction is in the range of 16.7-33 nm. The alpha grain is 0.28-0.36 μm thick in radial direction and has aspect ratio greater than 25. Matrix is heavily cold-worked which restricts the measurement of dislocation density by TEM. Maximum hardness is observed in the L-R section and in the as-received specimen it is at HV 243.

The TEM micrographs of specimen that were stress relieved at 400° C for 24 hrs are shown in Fig. 2a. Matrix is still heavily cold-worked. Volume fraction of β is reduced to be in the range of 4.7-5.5 % and the aspect ratio of β has reduced to 1.67; the inter-particle spacing is increased to 36 nm. Nb content was 1wt.% in α- Zr and 11-14.6 wt% in β-phase. After 36 hours of stress relieving, matrix dislocation density is decreased and isolated dislocations could be resolved as shown in Fig. 2b. Measurement of dislocation density was carried out, by measuring number of dislocations in the defined area of the microphotographs (It is around 7.6 x 10^{14} per m^2). Volume fraction of beta is further reduced to be in the range of 2-3% and inter particle spacing is increased to 63 nm.

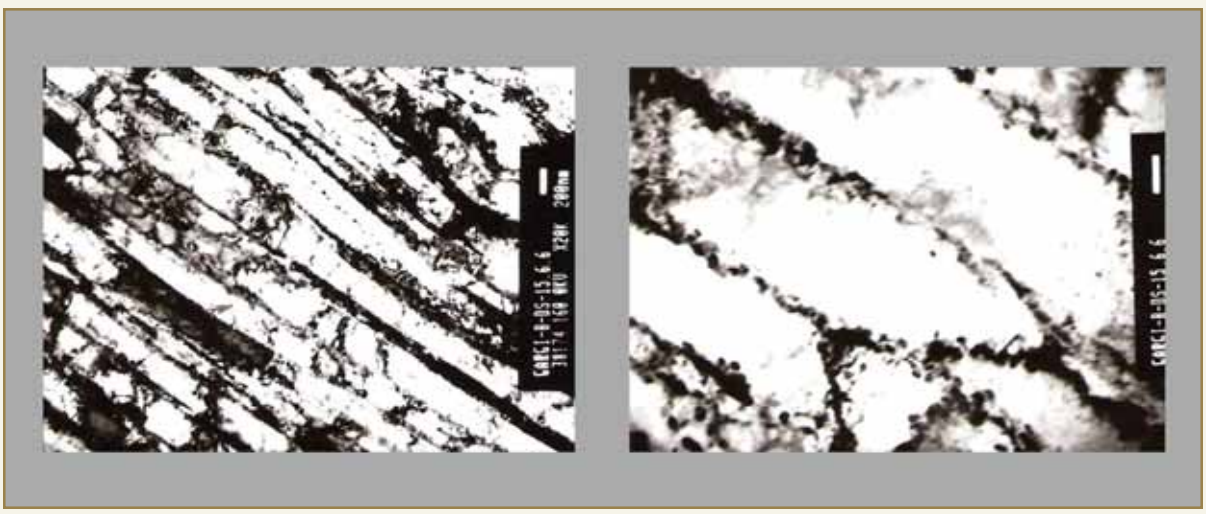

Fig.1: Transmission electron micrographs showing elongated α-zirconium grains surrounded by a network of discontinuous β-phase in as received indigenously made Zr-2.5Nb pressure tube material.

Marginal reduction in dislocation density to 5 x 10^{14} per m^2 is observed after 48 hours of stress relieving. Inter particle spacing of β is further increased to 78.8 nm. The aspect ratio of β was found to be 1.5 which confirms that the beta particles are progressively globulized and are more widely separated as shown in Fig. 3a. After 72 hours of stress relieving, no great change in microstructure was observed, but the trend of globulization continue as shown in Fig. 3b.

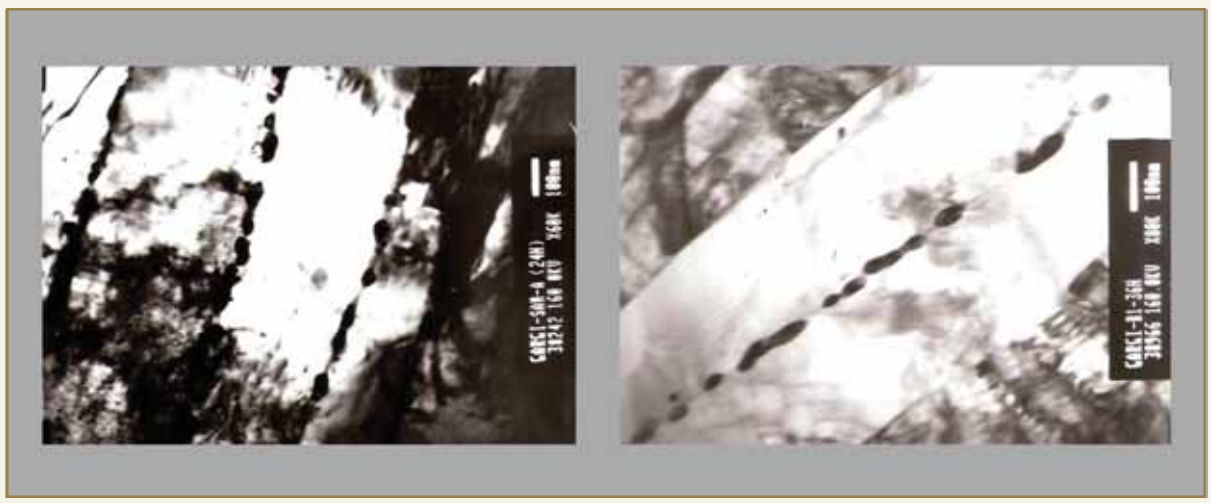

Fig. 2 TEM micrographs of pressure tube material autoclaved at 400°C
a. Stress relieved for 24 h showing a network of discontinuous β-phase in the grain boundary of α.
b. Stress relieved for 36 h showing isolated dislocation distributed in the matrix of α.

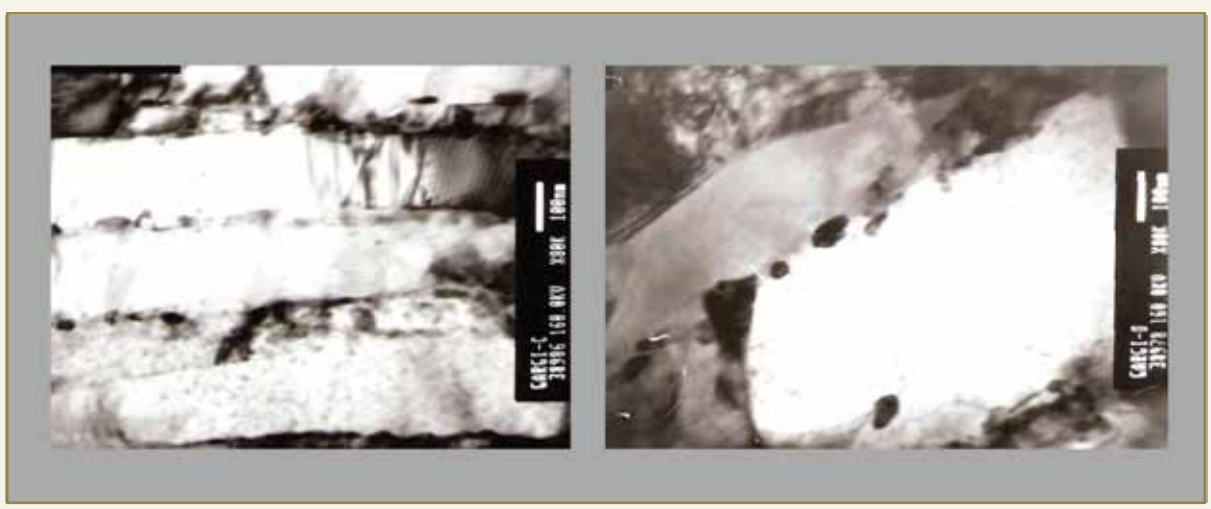

Fig. 3: TEM microphotographs of pressure tube material autoclaved at 400°C
a. Stress relieved for 48 h showing discontinuous β-particles in the α grain-boundary
b. Stress relieved for 48 h showing a widely spaced globular β-particles in the grain-boundary of α phase

After 96 hrs stress relieving, dislocation density is around 3 x 10^{14} per m^2. Volume fraction of beta is 2-3 % and thickness of beta is increased to 45 nm. Inter particle spacing of beta is further increased to 79.2 nm and they are widely separated as shown in Fig. 4., which is beneficial from hydrogen diffusion point of view. Aspect ratio of beta is 1.14:1 which confirms that particles more or less become globular.

Omega phase (ω) was not observed in the TEM micrograph of as received as well as after 96 hrs stress relieving at 400 ^{0}C, which is also confirmed by selected area diffraction pattern in TEM.

The micro hardness value is slightly increased to HV 255 after 24 hrs stress relieving and then it remains constant up to 36 hours. The micro-structural changes observed during beta phase decomposition at 400 °C are summarized in Fig. 5 and Table 1.

Specimens stress relieved at 400 °C for 36 and 96 hours were subjected to X-ray diffraction. Dislocation density was calculated by Line Profile Analysis of the XRD pattern using integral breadth technique. The results are presented in Table 2.

The dislocation densities calculated by this technique show close agreement with those estimated from TEM micrographs. It can be seen from the results, that a progressive increase in coherent domain size and decrease in dislocation density but no appreciable change in micro-strain occurs during extended stress relieving.

Discussion

The indigenously made pressure tube is produced by extrusion and two stage pilgering with intermediate annealing route .Due to this intermediate annealing at 585 °C for 6 hours, the continuous thin boundary film of β-phase is decomposed into particles having a thickness of 32.5nm, in the radial direction with aspect ratio 2.6. With further stress relieving, these broken discontinuous particles start to globulize and the inter particle spacing is increased. After 96 hours of autoclaving, the particles are globular and widely separated. The inter particle spacing is increased to 80 nm. As a result, the diffusion of hydrogen within the pressure tube is slowed down. The aim of this autoclaving step is to reduce the hydrogen diffusion velocity, resulting in reduced DHC velocity.

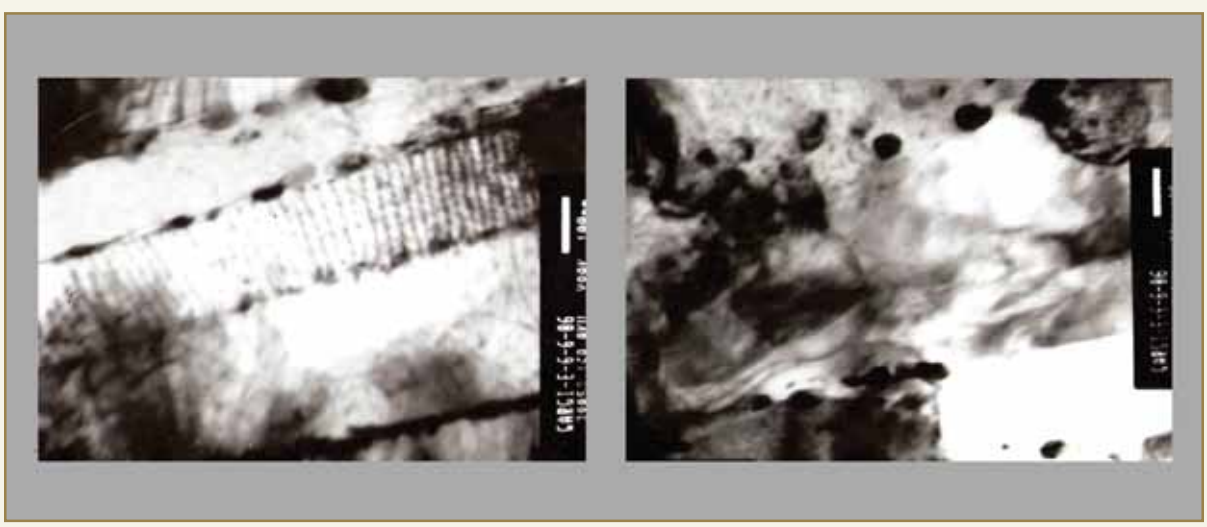

Fig. 4: Bright field transmission electron micrographs of indigenously made Zr-2.5Nb pressure tube material in 96 hours autoclaved at 400°C

CANDU pressure tubes are fabricated through extrusion followed by cold drawing route. They are stress relieved at 400 °C for 24 hours. As no intermediate annealing is involved, the microstructure of non-autoclaved tube consists of α grain, surrounded by continuous βphase having length in the range of 5500±3100 nm and thickness 300±140 nm. After 24 hr of stress relieving, their length becomes 4500±1500 nm and thickness

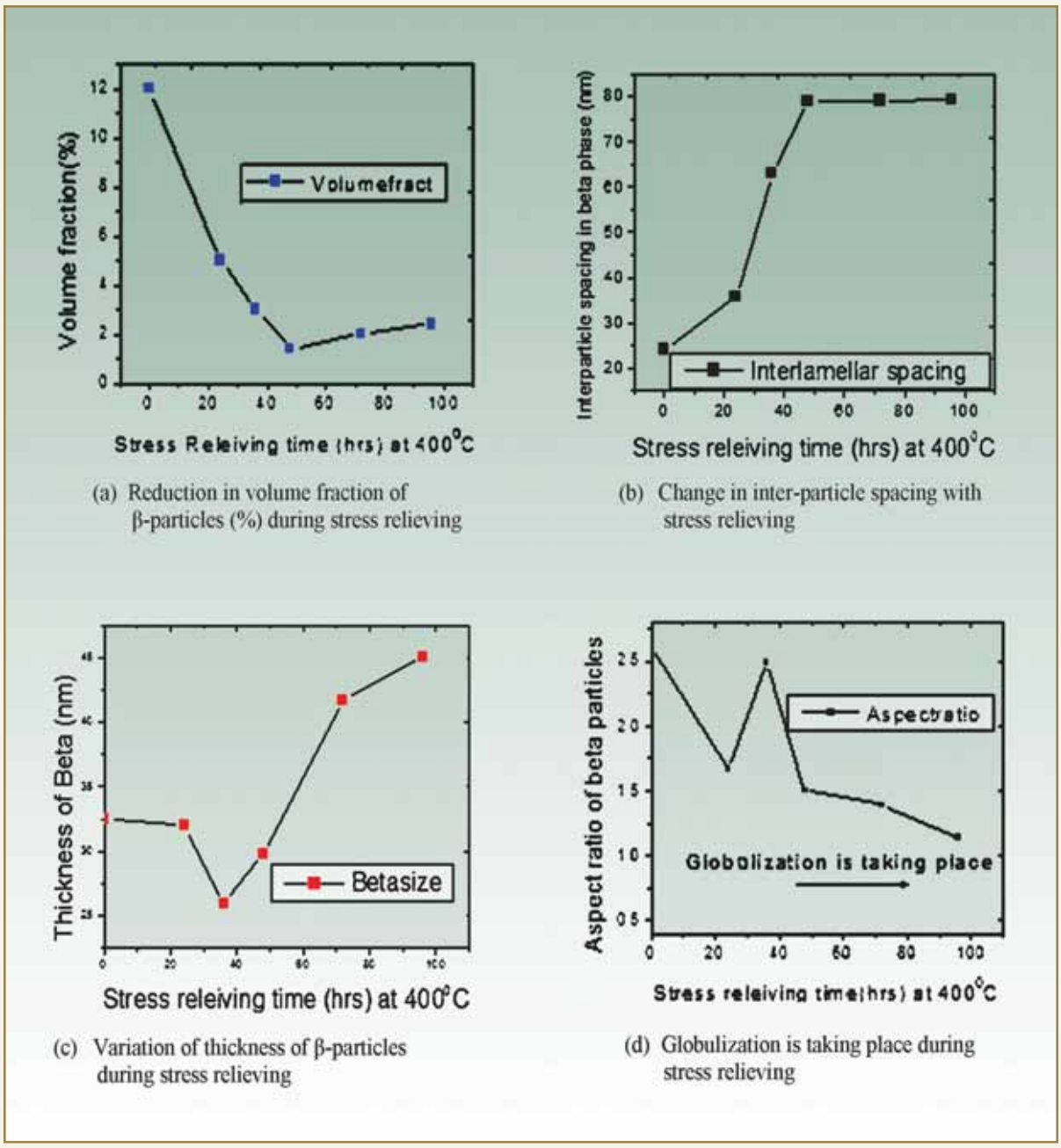

(a) Reduction in volume fraction of β-particles (%) during stress relieving

(b) Change in inter-particle spacing with stress relieving

(c) Variation of thickness of β-particles during stress relieving

(d) Globulization is taking place during stress relieving

Fig. 5: Graphical representation of the effect of stress relieving at 400°C on the dimensions of beta phase in indigenously produced Zr-2.5Nb pressure tube material

Table1: The effect of stress relieving at 400°C on the dimensions of beta phase in the L-R section of indigenously produced Zr-2.5Nb pressure tube material

Stress relieving Condition	Dislocation density (TEM) per m^2	Hardness HV*	Thickness of β particles (nm)	Aspect ratio of β	Inter particle spacing of β (nm)	β-phase Volume fraction (%)	a-aspect ratio	a Thickness (μm)
As received	Not able to measure	243.0	32.5	2.5-2.7	16.7-33	8-15	>25	0.28-0.36
24 hrs	-	255.0	32	1.67	35.7	4.66-5.30	>13	0.36
36 hrs	7.6×10^{14}	255.0	26	2.49	62.9	2.3-3.0	>9	0.28
48 hrs	5.4×10^{14}	245.7	29.76	1.5	78.8	1.4	>9	0.15
72 hrs	-	249.7	41.66	1.39	-	2.0	>12	0.16
96 hrs	2.9×10^{14}	254.6	45	1.14	79.2	2.4	>14	0.24

Table 2: Results of line profile analysis using integral breadth technique

Sample description	Dislocation density by XRD (per m^2)	Dislocation density by TEM (m/m^3)	Coherent domain size (Å)	Micro-strain
Autoclaved at 400° C / 36 hrs	11.8×10^{14}	7.6×10^{14}	201.17	0.0014025
Autoclaved at 400° C / 96 hrs	2.9×10^{14}	2.9×10^{14}	350.8	0.0017443

240±65 nm [5, 10]. Higher reduction in particle size and larger increase in interparticle spacing is achieved in the hot extrusion, followed by pilgering with intermediate annealing as compared to cold-drawing route.

Conclusions

- Indian pressure tube in as received condition has discontinuous β-phase which is expected for better performance of the tube from hydrogen intake and creep point of view.
- After 96 hrs autoclaving, beta phase becomes globular and interparticle spacing increased to 80 nm .ie they are widely separated as compared to 36 hrs autoclaving.
- Adoption of modified stress relieving heat treatment, will be based on evaluation of mechanical properties and ensuring the design requirement.

References

1. J.W. Evans, et al. Atomic Energy Canada Limited, Report No. AECL-2982(1971).
2. D.Warr, et al. Zirconium in Nuclear Industry-13th International symposium, p 313-335.
3. D.O. Northwood and W.L. Fong, Metallography vol.13:(1980), p97-115.
4. Glen M, et al. Zirconium in Nuclear Industry-13th International symposium, p 247-271.
5. M.T. Jovanovic , et al. *Journal of Nuclear Materials* vol. 244 (1997) p141-146.
6. Urbanic V. et al. ASTM STP 1354, p 641-657.
7. P. Pande, et al. Conference proceedings of "ZARC-91" p155-167, conducted by BARC during 12-13 December, 1991, Mumbai.
8. Stefan Sagat, et al. Zirconium in Nuclear Industry-10th International symposium, p 35-61.
9. M.T. Jovanovic, et al. Material Characterization Vol.40:p 15-25,1998.
10. M.T. Jovanovic, et al. *Material Characterization* vol.47(2001), p259-268.

ABOUT THE AUTHORS

Ms. Gargi Choudhuri did her B.E in Metallurgical Engineering from Jadavpur University in the year 2000 and completed graduation from the 44th Batch of BARC Training School. She is involved in Microstructural Characterization, Corrosion Studies of Stainless Steel and Zirconium base alloys used for critical components of various reactors, Metallurgical Failure Analysis and Fractography of Nuclear and Non- Nuclear components.

Mr. K.R. Gurumurthy is a Metallurgist working in the Quality Assurance Division. His field of work is fuel fabrication & welding, metallurgical evaluation of materials & failure analysis. He has about 25 technical publications to his credit.

Mr. B.K. Shah is currently Head, Quality Assurance Division, BARC. He has done M.Tech. (Corrosion Sc. & Engg.) from Indian Institute of Technology (IIT) Mumbai. He belongs to the 17th Batch of BARC Training School. His field of work includes Quality Assurance (QA) in the manufacture of Nuclear Fuels and Reactor Core Components, Metallurgical Failure Analysis, Flaw and Material Characterization by NDT, Corrosion Studies on Reactor Materials, etc. He has published more than 200 technical papers. He has received many awards which include National NDT Award (1998), NACE Award for Excellence in Corrosion Science (2005) and that Best Paper Award for 8 technical publications.

Dr. Dinesh Srivastava did his B.E. in Metallurgy from University of Roorkee and joined the 28th Batch of Training School. He earned his Ph.D. degree in Metallurgy in 1997. His research activities involves Basic Physical Metallurgy Studies of Zr- base Alloys, Alloy Development, Fabrication Flow Sheet Optimization of Zr-base alloy Component for PHWR Reactors, Direct Laser Fabrication Process and sysnthesis, processing and characterization of NanoCrystallization of Soft magnetic material. He has extensively studied Structural, morphological defects and analytical studies by Transmission electron microscopy. He is a recipient of the Binanai Gold Medal for Best Paper publication in Trans IIM and the DAE Science and Technology Excellence award.

बीएआरसी न्यूज़लेटर
BARC NEWSLETTER

NEW UNDERSTANDING OF CELLULAR TARGETS OF RADIATION: A PARADIGM SHIFT IN RADIATION BIOLOGY

Badri Narain Pandey
Radiation Biology and Health Sciences Division

This paper received the M. R. Raju Award for the Invited Lecture delivered at the International Conference on Radiation Biology and 5th LOWRAD International Conference on Effect of Low Dose Radiation Effects on Human health and Environment, held at Banaras Hindu University, Varanasi, from November 20-22, 2006

ABSTRACT

While considering DNA as primary target of radiation response, it is presumed, no radiation effect would be expected in cells that receive no direct radiation exposure through nucleus. However, recent experimental evidences generated in many laboratories reveal the fact that radiation effects also occur in cells or populations, where cells do not encounter direct DNA damage. These emerging concepts in radiation biology are in support of more than one target in a radiation hit cell and the consequent biological effects in population involve multiple effector cells which might be at close proximity or at a distance from the radiation exposed cell. Moreover, the thought developed in support of non-DNA radiation targets, radiation-induced bystander effect, adaptive response and genomic instability has challenged the validity of Linear No-Threshold (LNT) model of radiation effects. These results brought in a paradigm shift in understanding that a cell in population hit by radiation could no longer be considered in isolation while studying manifestation of radiation consequences. In fact, the biological response to radiation at tissue or organism level is a complex process of integrated response of cellular targets as well as extra-cellular factors

Introduction

Cellular targets of radiation in mechanism of acute and long term biological effects have been matter of intense investigation and discussion for radiation biologists. Radiation exposure causes damage to bio-molecules through free radical triggered mechanism(s). The major biological effect would involve ionization in aqueous compartments of cellular and sub-cellular organelles generating reactive oxygen species, which, in turn, damage the DNA and other critical bio-molecules. The health effects of ionizing radiation under different exposure conditions, i.e. under high background areas, occupational, accidental exposure, has emerged as a frontier research field in radiation science and of great interest to public. Moreover, advancement of knowledge about mechanism of radiation effects to biological systems has provided greater insight in cellular radio-sensitivity, which not only made us handle radiation / radio-isotopes more

safely, but also their exploitation for better diagnostic and therapeutic tool. It addition to this, it also provided a better understanding of short as well as long term health effects of radiation in human population. Deeper elucidation of radiation biological concepts has paved the way for the new milestone achievements in radio-sensitization of tumor cells for improved cancer radiotherapy, protection against undesired radiation exposure, safe standards/limits in radiation risk assessment and better management of radiation exposure patients (Fig. 1).

Cellular targets to radiation

The radiation damage to biological systems were explained based on target theory by Lea in the 1940s, which suggests that death of a cell after radiation exposure is caused by the inactivation of specific targets within cells. This theory was mainly used to explain the survival curve in bacteria. However, Lea's target theory was confined to existing understanding of cell biology, however, it did not consider the complex phenomenon of repair mechanism, which was not fully understood at that time. The major breakthrough in radiation biology occurred with discovery of DNA as hereditary material in 1950s and it's establishment as cellular target of radiation. The theory of DNA centered target could not only answer many un-explained questions in radiation biology but also cleared the roadblocks for smooth progress of cellular and molecular radiation biology. This left little scope to think beyond nucleus and DNA. During this period many intriguing and unresolved issues like role of DNA repair and replication in determining the fate of cells were solved and induction of apoptosis in radiation exposed cells (MacCallum et al.,1996) were established. The impact of DNA centered thoughts was so powerful, that other targets of radiation either could not get emerge or when they appeared they could not gain much attention. As a corollary, it was more or less the hardcore truth that radiation damage was limited to cells which had received direct hit to nucleus. Later these thoughts became the basis to determine radiation doses related to radiation risk assessment and cancer radiotherapy.

Evidences supporting Non-DNA targets

Even if, many radiobiological processes could get explained based on DNA as radiation target, some of the observations like radiation induced bystander effect, genomic instability, modification in cellular radio-sensitivity by protection of plasma membrane etc. could not get fully explained considering solely DNA based radiation target. The evidences generated from many laboratories using different experimental systems and major technological advancement like microbeam technology and low fluence radiation sources from high LET, further strengthened the notion of existence of non-DNA radiation targets. Based on these observations, there is shift in thinking from classical theory that a radiation hit cell get

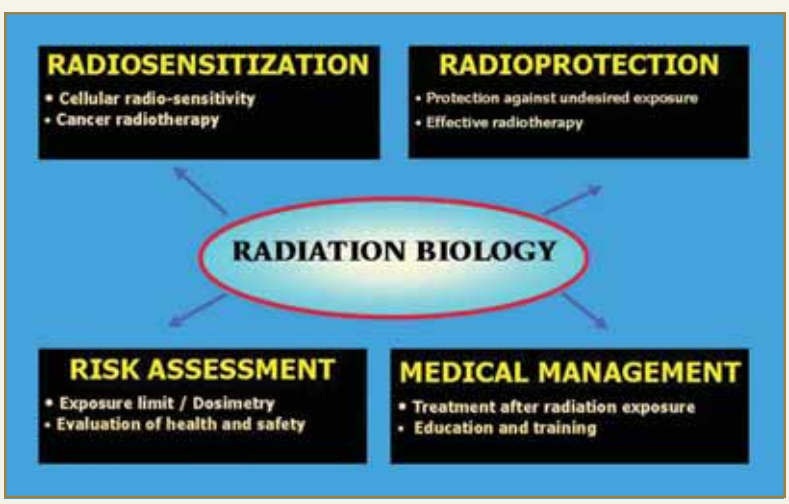

Fig. 1: Relevance of radiation biological concepts to enhance radio-sensitivity of tumour cells, protection against undesired radiation exposure, radiation risk assessment and medical management of radiation exposed patients

damaged (effector) involving DNA as only target, to the notion that a radiation hit cell involve more than one target in exhibition of biological effect, which can be the same cell and/or other cells (multiple effectors). Similarly, evaluation of damage at population level is more complex as the colony that is apparently surviving after irradiation might include mutated or genetically unstable progeny cells (Fig. 2), and may reveal consequence of radiation damage in due course of time.

Evidences gathered from following emerging areas of studies have shown that radiation-induced cellular damage involve non-DNA targets and damage consequences may arise in cells, that have not been directly irradiated.

Radiation-induced bystander effect

Deviating from classical paradigm, radiation damage has been observed in cells that have not received radiation; but are residing in close proximity to irradiated cell(s) in a population. The phenomenon, termed as 'radiation-induced bystander effect' (Fig. 3) has been observed both *in vitro* and *in vivo* experimental systems. This type of radiation effects were observed in bystander cells, in terms of chromosomal aberrations, alterations in gene expression and induction of cell lethality. The major thoughts believed to be involved underlying the bystander response are (a) diffusible extra-cellular factors; (b) communication between adjacent cells through membrane localized hemi-channels called gap-junctions; (c) induction of oxidative metabolism in bystander cells. The regulation of closure and opening of gap junction determines the magnitude and nature of intra-cellular communication from irradiated cell to neighboring cell. The crucial function of gap junctions involves phosphorylation / hyperphosphorylation of gap-junction associated proteins like connexin-43. The manifestation of bystander response in irradiated cell population is perhaps one of the strongest evidence in support of non-targeted radiation effects. Overall, the phenomenon has challenged the paradigm that radiation traversal through the nucleus of a cell is a prerequisite to produce genetic changes or a biological response.

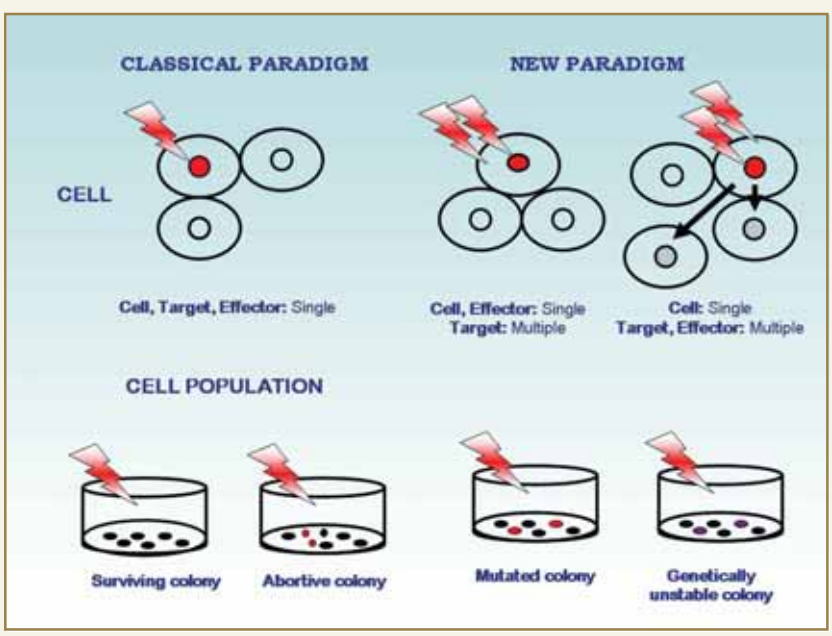

Fig. 2: Cellular targets of radiation and their consequences in cell population level according to classical and new paradigm in radiation biology. Effectors are cell(s) that showed response to radiation. Adapted from Reference.

Genomic instability

The phenomenon of genomic instability is the persistent production of genomic changes in the progeny of surviving cells after irradiation, which could be detected as delayed chromosomal aberrations, increased mutation rates and delayed reproductive cell death.

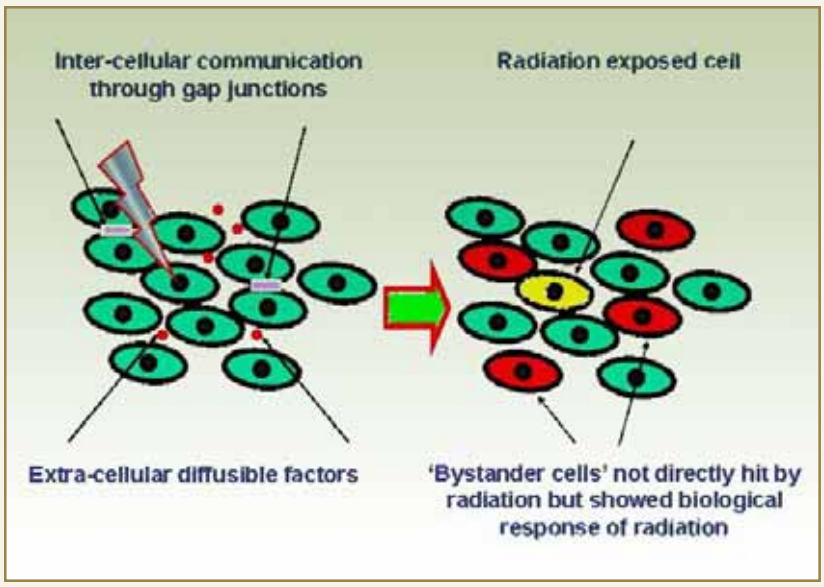

Fig. 3: Manifestation of radiation induced bystander effect at the level of cell population. When a cell in population is hit by radiation, it may transmit effects to neighbouring cell either through contact points i.e. gap junction inter-cellular communication or through release of extra-cellular diffusible factors

The process of genomic instability not only induced in progeny of directly irradiated cells but may also be induced in bystander cells. It was further interesting to observe that survivors of irradiated cells showed different genetic lesions than that initially occurred in the radiation exposed parental cells. Genomic instability further supports non-DNA targets of radiation and a clear deviation from established DNA based targets.

Membrane as a sensitive target of radiation

The biological membranes are fluid-like phospholipid bilayer (5-8 nm thick) into which freely diffusing globular proteins are embedded to varying degrees. Non-polar regions of lipids face each other at the core of bilayer, while their polar head groups face outward. In addition to cellular plasma membrane, intracellular organelles in cells are also compartmentalized with membrane-boundaries in eukaryotic system. The hypothesis of membrane as critical target of radiation was being supported by observations from many laboratories that factors affecting membrane function also modify cellular radio-sensitivity. Two major constituents of biological membranes, namely, lipids and proteins are prone to oxidative damage due to presence of unsaturated bonds in lipids resulting in lipid (also protein) peroxidation and perhaps constitute a major event in radiation induced membrane damage. Radiation induced membrane damage after cellular radiation exposure results in alterations in surface charges, membrane bound enzymatic activity and receptor function. Studies from our laboratory using liposome as model membrane, have shown that inclusion of cholesterol in membrane, which would increase in membrane rigidity, was found correlated to reduction in radiation-induced membrane oxidative damage measured in terms of lipid peroxidation and diene conjugate formation. Furthermore, it has been shown that inclusion of cholesterol in membrane of thymocytes resulted in inhibition of radiation induced apoptotic death. Moreover, during the last decade, a number of research groups contributed strongly to advocate the role of cellular membrane as a sensitive and critical target in the mechanisms of cellular radiation damage. It has been demonstrated that lipid peroxidizing agents such as t-butyl hydroperoxides and fatty acid hydroperoxides could trigger apoptotic cell death in various cell systems. In addition to this, we have also shown that protection of membrane using antioxidants such as eugenol resulted in prevention of membrane signaling as well as cellular radiation damage including induction of apoptosis. Involvement of membrane related signaling mechanism has been demonstrated through radiation-induced hydrolysis of sphingomyelin generating ceramide in plasma membrane. It has been

shown that inhibition of ceramide generation significantly prevents apoptosis in irradiated cells. In human lymphoblasts and mice deficient of acid sphingomyelinase were found to be resistant against radiation-induced apoptosis. In studies using labeling of DNA with 5-[^{125}I]-iodo-29-deoxyuridine (^{125}IdU), it has been suggested that radiation damage to DNA may be necessary to induce cell death, but DNA damage alone is not sufficient to kill cells.

Anti-cancer property of alkylphospholipid analogues, a new class of drug which do not directly target DNA, but insert in plasma membrane and subsequently induce a broad range of biological effects including synergistic enhancement of radiation toxicity in a variety of tumor cells. These drugs have been routed for clinical applications in combination with radiotherapy. Based on different available lines of supportive evidences, it may be suggested that membrane is not only a cellular barrier but also a complex signaling site to sense the external stresses including ionizing radiation that determine fate of the cell.

Mitochondria: Major determinant of cellular radio-sensitivity

Mitochondria are considered as 'power house' of cell as they play key role in respiration, ATP synthesis and thermoregulation in eukaryotic cells. However, more than that they also participate in numerous crucial metabolic pathways, homeostasis of intracellular inorganic ions and in execution of the process of apoptosis. During respiration, mitochondria consume about 90% of the body's oxygen and are the richest source of ROS, hence are major determinant of cellular redox environment. Considering the involvement of mitochondria in broad spectrum of physiological processes, they may be termed as the 'nucleus' of cellular physiology. In the field of radiation research, mitochondria have been well studied as signaling organelle in radiation-induced apoptotic death and major determinant of cellular radio-sensitivity after low or high dose of radiation. In microbeam studies, cytoplasmic irradiation has been reported to induce gene mutations suggesting extra-nuclear radiation targets in cells. The line of thinking was further supported by observation that cytosol from irradiated cells can induce apoptotic morphology onto naive nuclei. However, the role of mitochondria in other radiation-induced effects/phenomena is not well elucidated, which may be new research areas in radiation biology.

Cellular microenvironment and tissue architecture determine the radio-sensitivity

Manifestation of radiation response at tissue level is governed by complex and integrated cellular interactions through tissue microenvironment. Role of extra-cellular components in governing cellular response to external stress agents was not very evident, till the findings that tissue architecture and microenvironment determine cell division, differentiation and organ development. Interaction of cells with their microenvironment and subsequent alterations in cellular radio-/chemo-sensitivity has been reported in normal and tumor cells. The dynamic interaction and contribution of different components of extra-cellular matrix to their residing cells would determine the radiation sensitivity of cells. In further studies, effects of ionizing radiation on extra-cellular matrix modulated radiation survival, and adhesion / invasion was studied in glioblastoma cell lines, which showed a differential cellular radio-sensitivity in these tumor cells by fibronectin or matrigel. It may be pertinent to mention some of reports suggesting that the cellular response to radiation or drugs is associated with tissue architecture and hence, the sensitivity to cells grown in two-dimensional (2D) cell culture were found to be very different from cultures grown on three-dimensional (3D) matrix. Based on these observations, it may be concluded that cell culture in three dimensions is ideal to investigate radiation-induced adaptive and bystander responses (de Toledo et al., 2006). In another study, transgenic rodent

cells exposed to high LET radiation (Fe-charged particles), showed higher mutation frequency in 3D samples than in 2D. Interaction of different mammary cell types of breast tissue exposed to low dose radiation response in a three-dimensional co-culture system suggest role of tissue microenvironment in radiation-induced carcinogenesis. Better understanding of the involvement of microenvironment and tissue architecture in modification of cellular radiation response would improve the experimental protocols and the most importantly would orient thoughts based on integrated response of biological effects of radiation.

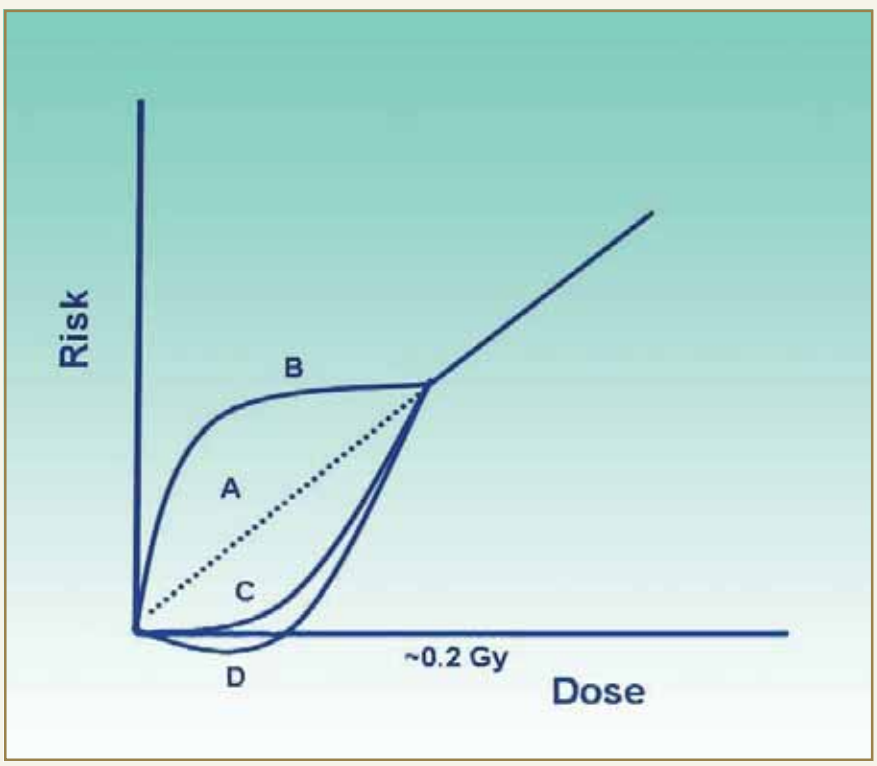

Fig. 4: Deviations from Linear No-Threshold (LNT) Model for dose and risk of radiation. The validity of classical and well considered LNT model (A: dotted) is being challenged by different groups of radiation scientists with either (B) supra-linear i.e. the risk are more predominant with increase in per unit dose of radiation; (C) up to certain dose range there is no risk, which follow linearity at subsequent doses of radiation; (D) the protective or advantageous effects by low dose / dose rate of radiation (also called 'radiation hormesis'), which may reduce in rate of mutations and neoplastic transformation below the spontaneous frequency.

Non-DNA targets of radiation and Low dose radiation response

The risk of induced stochastic biological effects in humans (e.g., mutations, neoplastic transformations, and cancers) after low doses of ionizing radiation assessed by national and international regulatory agencies are based on the Linear-No-Threshold (LNT) hypothesis. According to LNT model, risk associated with radiation exposure is presumed to increase linearly without a threshold (Fig. 4) and probability of radiation associated risk is based on traversal of radiation track(s) through nucleus. Till now, LNT hypothesis is considered as the basis for establishing radiation protection guidelines and dose limits of radiation exposure for nuclear workers and the general public. The deeper insight of non-DNA radiation targets and contribution of extra-cellular components of irradiated cell would decide the ultimate fate of radiation exposed cells and its neighbors. Establishment of these facts and relative contribution in biological effects of radiation would provide more realistic shape of dose response curve at low dose range and the validity of LNT model.

Conclusion

Evidence generated from many laboratories including ours are strong enough to support the

existence of non-DNA targets in determining cellular radio-sensitivity. It is now being considered that penumbra of biological radiation response is bigger than physical boundary of radiation exposure. There is a need to look beyond the nucleus, where key target(s) might be governing the radiation biological processes silently but significantly. Based on recent understanding, there is a conceptual change amongst radiation biologists that man- ifestation of biological consequences of radiation exposure involves much complex processes than physical interaction of radiation with living system merely as matter.

Acknowledgement

I would like to acknowledge Dr. K. P. Mishra, Former-Head, Radiation Biology and Health Sciences Division and colleagues in our laboratory for their support and encouragement, and Prof. E. I. Azzam and his colleagues at New Jersey Medical School, Newark, USA for scientific interaction. I thank Department of Atomic Energy, Government of India for providing all support during my research work.

ABOUT THE AUTHOR

Dr. B. N. Pandey joined the Radiation Biology and Health Sciences Division after graduation from the 38th Batch of Biology-Radiobiology Orientation Course (1994-95). Currently, he is working in the field of Cancer and Radiation Biology. Dr. Pandey has been elected as Member, Executive Council (2007-2009) of the Indian Society of Radiation Biology. He is the Editor, for '*Radiation Science Today*' an eNewsletter being published by the Indian Society for Radiation Biology. Dr. Pandey is also serving as Member, Podcast Committee, Radiation Research Society, USA for the Journal '*Radiation Research*'.

RADIATION AND FREE RADICAL EXPOSURE AND REGULATION OF PROTEIN SYNTHESIS BY THE HEME-REGULATED EUKARYOTIC INITIATION FACTOR 2α KINASE

Abhijeet P. Kulkarni and Jayanta K. Pal
Department of Biotechnology, University of Pune
and
T. P. A. Devasagayam
Radiation Biology and Health Sciences Division

This paper received the Best Poster Award at the International Conference on "Emerging Trends in Free Radical and Antioxidant Research" held at Lonavala, during January 8-11, 2007

ABSTRACT

The Heme Regulated Inhibitor (HRI) is a member of the eIF-2α kinase family and is a potent regulator of protein synthesis. During a variety of cytoplasmic stresses such as, heme deficiency, heat shock, drug toxicity and lead toxicity, HRI undergoes activation and inhibits protein synthesis. (Investigations from our lab have earlier demonstrated that HRI can be used as a molecular marker of drug induced anemia. Further, over expression and activation of HRI leading to regulation of protein synthesis has been reported during lead exposure and heat shock in human cells *in vitro.)* However, very little information is available about oxidative stress and HRI-mediated regulation of protein synthesis.

In the present investigation, two oxidants namely, hydrogen peroxide and 2, 2′-azobis (2-methyl propionamidine) dihydrochloride (=2.2′-Azobis (2-amidinopropane) dihydrochloride) (AAPH) were used, to induce oxidative stress in K562 (human erythroleukaemia) cell line as a model. Effect of various concentrations of these compounds on cell proliferation, antioxidant enzyme activity, lipid peroxidation, HRI activity and expression at mRNA level has been assessed. The results suggest that oxidative stress exerted by H_2O_2 and peroxyl radicals generated by thermal decomposition of AAPH, inhibits cell proliferation, affecting cell viability in K562 cells in a concentration-dependent manner. In case of H_2O_2, at a dose of 150 mM, concurrent with decreased cell proliferation, there was an induced eIF-2 kinase activity and HRI expression indicating inhibition of protein synthesis. Similarly, peroxyl radical induced lipid peroxidation and eIF-2α kinase activity, in a concentration-dependent manner.

Therefore, H_2O_2 and AAPH-induced oxidative stress, inhibits cell proliferation and protein synthesis in K562 cells by inducing activity and expression of HRI.

Introduction

Protein synthesis is regulated both at the levels of transcription and translation. However, regulation of translation appears to be a predominant mode of protein synthesis regulation, in response to environmental stimuli. Several studies have suggested, that regulation of translation in cells is exercised mostly at the initiation step, by modifications, primarily phosphorylation of components of translational

machinery. Phosphorylation of the alpha (α) subunit of eukaryotic initiation factor 2 (eIF-2) is one of the well known mechanisms, in regulating the overall rate of protein synthesis in eukaryotes. There is a family of eIF-2α specific Ser/Thr protein kinases, each member of which can phosphorylate the alpha subunit of eIF-2. Different members of this family undergo activation during different stress stimuli. Among these, contribution of the heme regulated eIF-2α kinase (which is also called as the heme regulated inhibitor, HRI) in regulating protein synthesis in erythroid precursors has been well established. During heme deficiency, heavy metal toxicity, heat shock, drug toxicity etc., HRI gets activated. Upon activation through autophosphorylation, it phosphorylates the 38 kDa α subunit of eIF-2 at Ser51 residue. Phosphorylated eIF-2 [eIF-2a(P)] sequesters eIF-2B, which is a guanine nucleotide exchange factor (also called the reversing factor), because of formation of a stable complex. Since eIF-2B is rate limiting, unavailability of free eIF-2B inhibits the GTP-GDP exchange, which is essential for reactivation of eIF-2 for recycling. Inhibition of this exchange leads to inhibition of protein synthesis.

Among all the conditions and stress stimuli that induce HRI activity and inhibit protein synthesis, oxidative stress is of interest here. Reactive oxygen species (ROS) and Reactive Nitrogen Species (RNS) are very common and of great importance in biological systems. Free radicals, such as superoxide ($O_2^{\cdot-}$), hydroxyl ($^{\cdot}OH$) and peroxyl ($ROO^{\cdot}$) radicals, besides non-radical species like hydrogen peroxide (H_2O_2), singlet oxygen ($^1O_2$) and hypochlorous acid (HOCl), are produced during

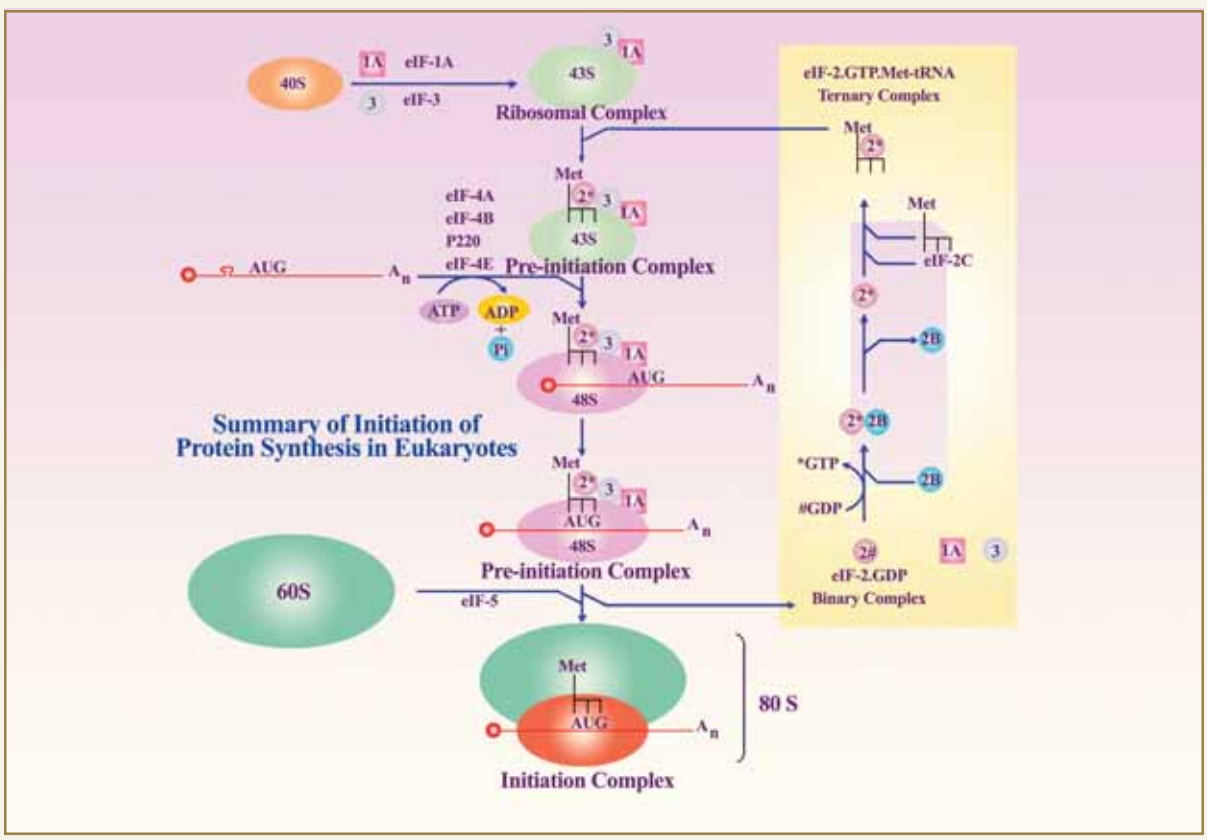

Fig. 1: Schematic diagram showing the summary of initiation of protein synthesis in eukaryotes

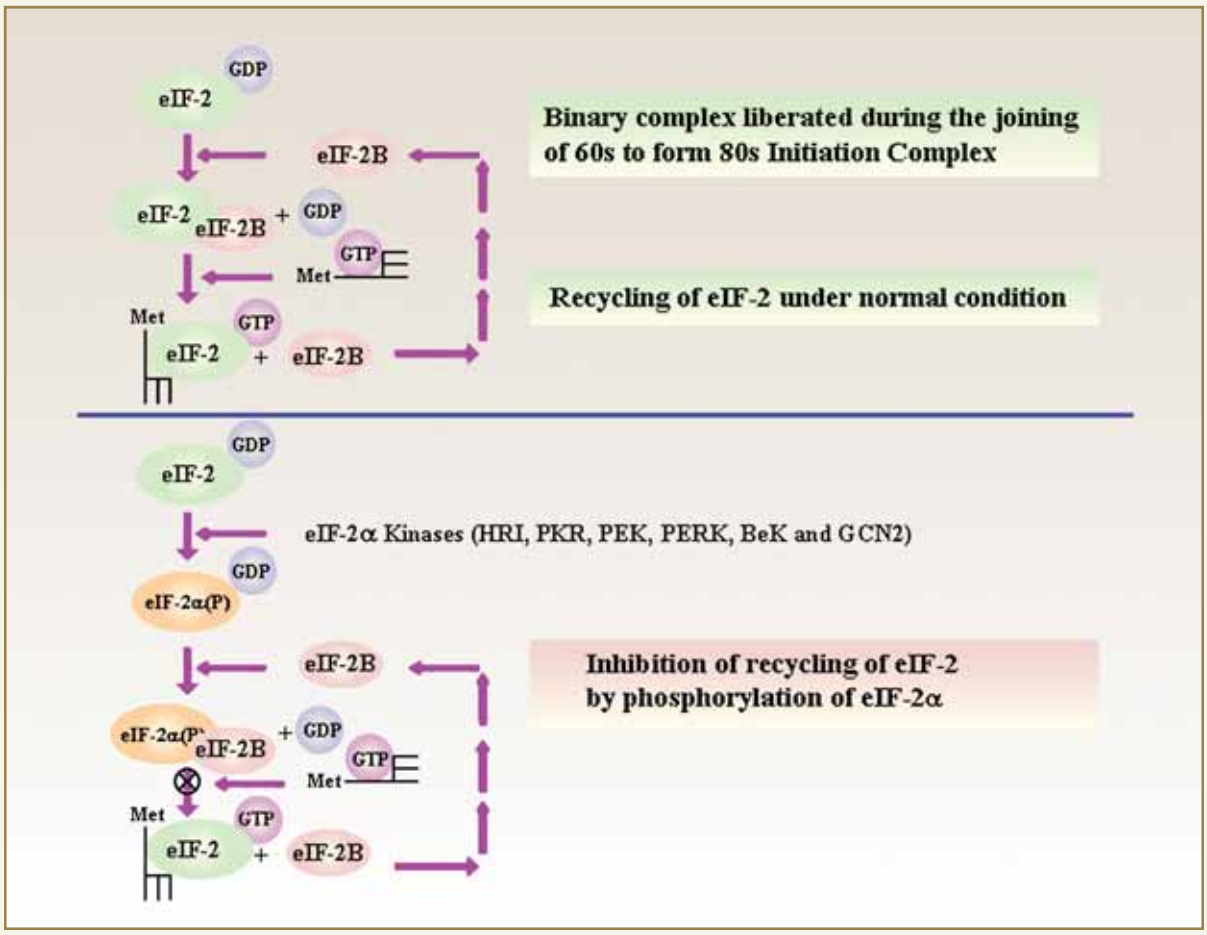

Fig. 2: Schematic diagram showing the role of eIF-2α kinases in initiation of protein synthesis in eukaryotes

normal and altered physiological processes of a cell. For example, H_2O_2 is produced in mitochondria and cytosol by the activity of intracellular oxidases and superoxide dismutases (SOD). Similarly, superoxide radicals are produced due to the auto-oxidation reactions of biologically important molecules as well as during mitochondrial electron transport. Radiation is one of the major factors, that increase the generation of reactive oxygen species in living organisms. Both H_2O_2 and peroxyl radicals are key components of radiation induced oxidative stress. Hence studying their effects on protein synthesis regulation indirectly is linked to radiation-induced modulation of such regulation.

Role of free radicals in mediating various cellular events has been studied in detail. Involvement of free radicals in the regulation of growth and differentiation, gene expression, cell signaling, proliferation and apoptosis indicate their importance in biological systems. On the other hand, their elevated levels are linked with a number of diseases and disorders, indicating their potential to cause cell injury leading to cell death. Protein synthesis also is one of the vital processes which needs to be extensively regulated, in response to oxidative stress. Therefore, it was important to investigate the role of HRI in regulation of protein synthesis during oxidative stress. We have addressed this question by designing experiments using human

K562 cells. Our results, for the first time indicate, that under conditions of oxidative stress generated by two potent oxidants, namely, H_2O_2 and peroxyl radicals generated by 2, 2'-azobis (2-amidinopropane) dihydrochloride (AAPH), there is a significant increase in the expression as well as eIF-2α kinase activity of HRI. Thus our data suggests that inhibition of protein synthesis under oxidative stress may be the combined effect of induced activity and expression of HRI.

Materials and Methods

All the cell culture reagents, namely, Dulbecco's Modified Eagle's Medium (DMEM), Fetal Bovine Serum (FBS), Antibiotic-antimycotic solution (100X) and most of the other molecular biology reagents used in the present study, were purchased from Sigma Chemical Co. (USA). Custom made HRI- and b-Actin cDNA specific primers, TRI reagent, DNase I (amplification grade), Enhanced Avian Hs RT-PCR kit were also purchased from Sigma Chemical Co. (USA). AAPH was purchased from Aldrich chemicals (USA). Anti-phospho-eIF2α (Ser51) and anti-eIF-2α polyclonal antibodies were purchased from Cell Signaling Technology (USA). BM Chemiluminescence Western Blotting kit (Mouse/Rabbit) was purchased from Roche Molecular Biochemicals (Germany). Human erythroid K562 cell lines were obtained from the cell repository at the National Centre for Cell Science, Pune, India.

Human K562 cells were maintained as continuous culture under standard conditions in DMEM. To generate oxidative stress, cells were exposed either to various concentrations of H_2O_2 or AAPH for 1 h at 37^0C. Cell viability and rate of cell proliferation in control and treated groups were determined by trypan blue staining and MTT (3-(4,5-dimethylthiazol-2-yl)-2,5-diphenyl tetrasodium bromide) assay, using standard protocols. Effect of AAPH treatment on lipid peroxidation in K562 cells was determined, by estimating total lipid hydroperoxides (LOOH) using FOX II reagent H_2O_2 was used as standard hydroperoxide for calibration.

Effect of various concentrations of H_2O_2 on catalase activity was determined by Native-PAGE activity staining of gels, using protocol described earlier. Total eIF-2α kinase activity in control and treated cells was indirectly determined by detecting the extent of eIF-2α phosphorylation using western blotting. In brief, equal amount of protein from control and treated cells was separated, using SDS-PAGE. Following SDS-PAGE, proteins were electrophoretically transferred to nitrocellulose membranes which were subsequently used for immunoblotting with anti- eIF-2α and anti- eIF-2α(P) antibodies. Blots were developed using the chemiluminescence detection method. The results were analyzed using quantity one software on gel documentation system.

Level of HRI expression in control and treated cells was determined by RT-PCR. In brief, RNA extraction from control K562 cells and cells exposed to oxidative stress was done, using TRI reagent as per the manufacturer's protocol. RNA quantification was done spectrophotometrically. Prior to cDNA synthesis, RNA samples were treated with DNase I (amplification grade) to remove genomic DNA contaminations. 1 μg of RNA was reverse transcribed to cDNA using eAMV-reverse transcriptase provided with Enhanced Avian Hs RT-PCR kit. Equal amount of cDNA was PCR amplified, using HRI- and β-Actin specific primers as described earlier. PCR products were analyzed on a 1.2% agarose gel followed by ethidium bromide staining. The results were analyzed using quantity one software on gel documentation system.

Results

Loss of cell viability and inhibition of cell proliferation in K562 cells exposed to oxidative stress

In order to determine the effect of oxidative stress on K562 cell viability and proliferation, a series of preliminary experiments using increasing concentrations of H_2O_2 and AAPH were carried out. Results obtained from these experiments indicate that,

both the oxidants caused loss of cell viability in K562 cells, as a function of increasing concentrations (Figs. 3A and 3B). Results of experiments with MTT assay done after AAPH treatment revealed, that peroxyl radicals were inhibiting K562 cell proliferation. This inhibition was gradual up to 5 mM. However, at higher concentrations (10 mM to 100 mM) there was a further increase in inhibition of cell proliferation (Fig. 3C). All these experiments were performed three times and the results are presented as mean ± standard deviation.

AAPH-induced lipid peroxidation in K562 cells

Our results on lipid peroxidation, as measured by total lipid hydroperoxides produced after AAPH treatment to K562 cells, indicated that peroxyl radicals generated due to thermal decomposition of AAPH were inducing lipid peroxidation in a concentration-dependent manner (Fig. 4). In lower concentrations of AAPH (0.1 mM to 5 mM) there was practically no increase in lipid peroxidation. However, at higher concentrations (10 mM to 100 mM), a significantly high level of lipid peroxidation was observed.

Regulation of eIF-2a kinase activity during oxidative stress

We determined modulation of total eIF-2α kinase activity during H_2O_2 and AAPH-induced oxidative stress, by measuring the eIF-2α phosphorylation by western blot, using a specific antibody that recognizes Ser51 phosphorylated form of eIF-2α. After H_2O_2 exposure, there was approximately a two-fold increase in eIF-2α phosphorylation with 150 μM H_2O_2 as compared to

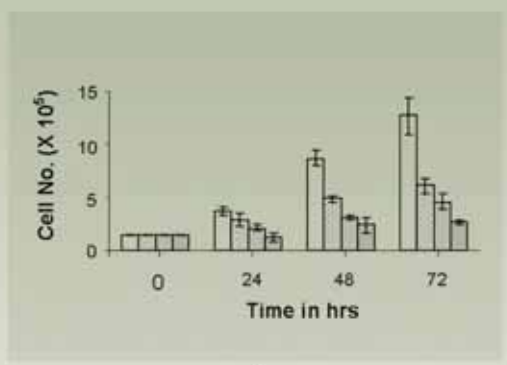

a

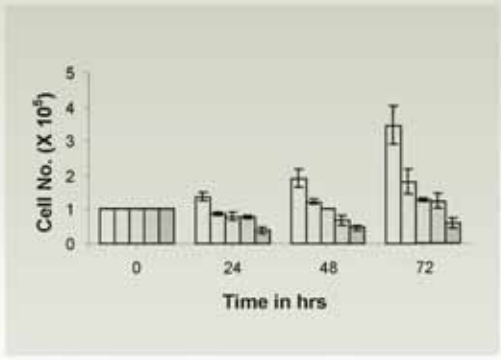

b

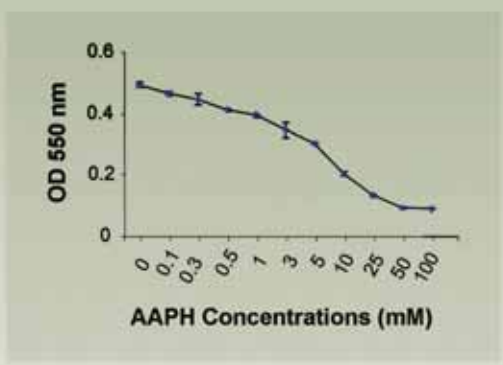

c

Fig. 3: Effect of H_2O_2 and AAPH-induced oxidative stress on K562 cell viability and cell proliferation. K562 cells were grown in DMEM with 10 % FBS for 24 h and were then treated with various concentrations of H_2O_2 (A) or AAPH (B) for 1 h. Viable cell counts were taken by trypan blue staining at every 24 h for 72 h and the data were analyzed. (a) Bar1-Control; 2, 3 and 4- 100, 150 and 200 μM H_2O_2 treated K562 cells, respectively. (b) Bar1-Control; 2, 3, 4 and 5- 1, 5, 10 and 100 mM AAPH treated K562 cells, respectively. (c) Inhibition of cell proliferation in K562 cells treated with different concentrations of AAPH as determined by MTT assay.

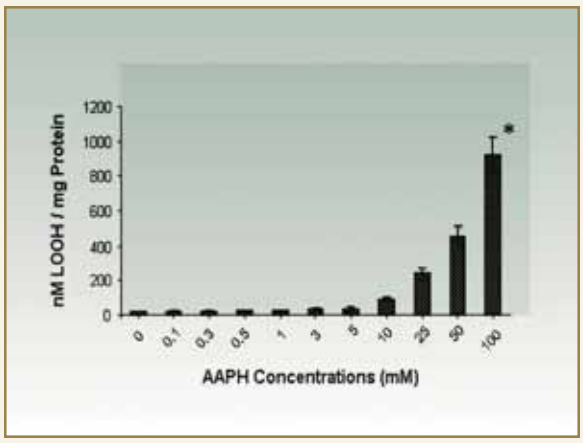

Fig. 4: AAPH-induced lipid peroxidation in K562 cells. K562 cells grown in culture were treated with different concentrations of AAPH. The effect of AAPH treatment on lipid peroxidation in these cells was determined by estimating total lipid hydroperoxides using LOOH assay. The results are expressed as nM LOOH/mg Protein. The asterisk indicates statistically significant difference in lipid peroxidation between control and 100 mM AAPH treated K562 cells (Student's *t* test $p < 0.05$)

the control (Fig. 5A; lane 3 vs lane 1). However, after AAPH treatment (Fig. 6), phosphorylated eIF-2α amount was increased in a concentration dependent manner. Maximum phosphorylation, about 2-fold over control, was observed with 3 mM AAPH (Fig. 6A lane 6 vs lane 1). There was a reduction in eIF-2α phosphorylation in concentrations beyond 3 mM, indicating the toxic effects of higher concentrations. The total amount of eIF-2α was determined by another antibody which recognizes total eIF-2α irrespective of any modification (Figs. 5B, 6B). These results indicated that due to the increased eIF-2α kinase activity during oxidative stress, global protein synthesis was getting inhibited.

Effect of H_2O_2-induced oxidative stress on HRI expression in K562 cells

To determine the effect of oxidative stress on HRI expression, K562 cells were exposed to different concentrations of H_2O_2 (100, 150 and 200 μM) for a duration of 1 h. Total RNA from control and treated cells were extracted and used for RT-PCR experiments.

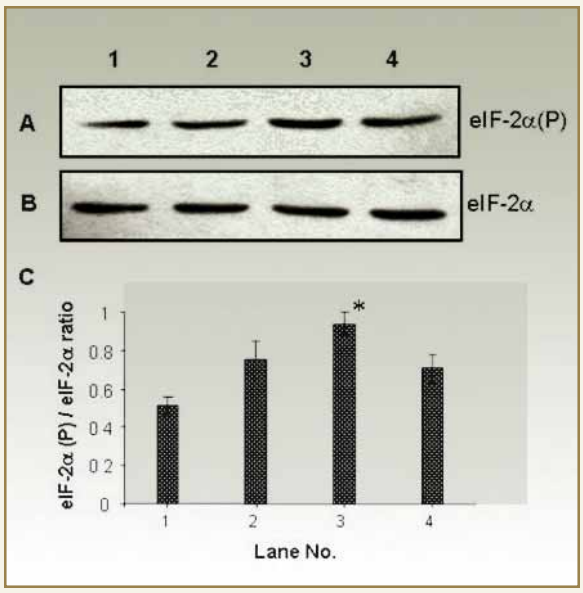

Fig. 5: H_2O_2 induces eIF2-α kinase activity in K562 cells. (A) and (B) are western blots of soluble extracts of cell sample reacted with anti-eIF-2a (P) and anti-eIF-2a antibodies, respectively. Samples loaded in various lanes are Control (lane1), 100, 150 and 200 μM H_2O_2 treated (lanes 2 to 4, respectively). (C) is quantification profile of (A) and (B) expressed as eIF-2α (P) / eIF-2α optical density ratio. The asterisk indicates statistically significant difference in eIF-2a phosphorylation between sample 1 and 3 (Student's *t* test $p < 0.05$)

Results obtained from these experiments indicated, that H_2O_2 could induce HRI expression. At 150 μM concentration, there was maximum HRI expression and it was almost 1.5 fold over control (Fig. 7A, lane 3 vs lane 1). These experiments were carried out keeping levels of β-Actin expression as internal control. Thus these results indicate, that induced HRI activity as well as expression is instrumental, in regulating protein synthesis during oxidative stress in K562 cells.

Effect of H_2O_2 on catalase activity

Catalase activity is a marker of H_2O_2-induced oxidative stress. So to make sure that H_2O_2 concentrations selected for this work are able to exert the oxidative stress and protein synthesis, related parameters can be analyzed at these concentrations, in gel catalase

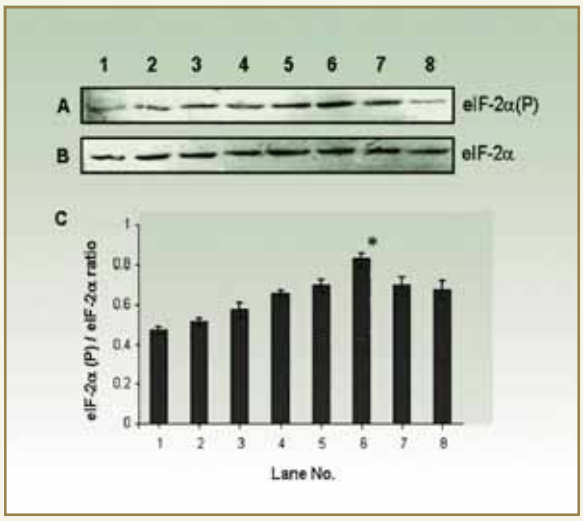

Fig. 6: Effect of AAPH on total eIF-2α kinase activity in K562 cells. (A) and (B) are western blots of soluble extracts of cell sample reacted with anti-eIF-2α (P) and anti-eIF-2α antibodies, respectively. Samples loaded in various lanes are control (lane1), 0.1, 0.3, 0.5, 1, 3, 5 and 10 mM AAPH treated (Lanes 2 to 8, respectively). (C) is quantification profile of (A) and (B) expressed as eIF-2α (P) / eIF-2α optical density ratio. The asterisk indicates statistically significant difference in eIF-2α phosphorylation between sample 1 and 6 (Student's *t* test $p < 0.05$)

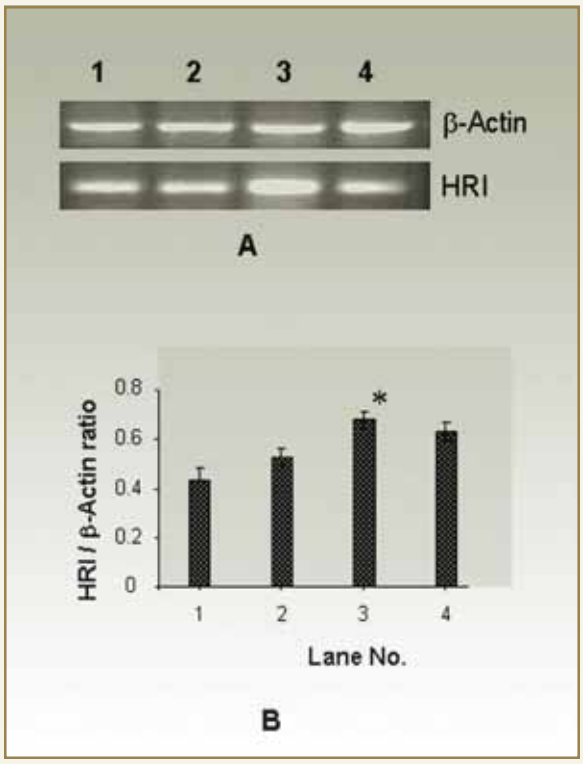

Fig. 7: Oxidative stress upregulates HRI expression in K562 cells. (A) and (B). RT-PCR was carried out using 1 μg RNA. PCR products were analyzed on a 1.2 % agarose gels. In (A), samples loaded in various lanes are, control (lane 1), 100, 150 and 200 μM H_2O_2 treated (lanes 2, 3 and 4, respectively). (B) Quantification profiles of (A) expressed as HRI / b-Actin optical density ratio. The asterisk indicates statistically significant difference in HRI expression between samples. (Student's *t* test $p < 0.05$)

activity. There was increased catalase activity and the highest activity was observed at 150 μM of H_2O_2. (Fig. 8)

Discussion and Conclusion

In the present study, for the first time, we demonstrate the contribution of HRI in the regulation of protein synthesis during H_2O_2- and AAPH-induced oxidative stress, in cultured human K562 cells. Although, there are a few reports indicating oxidative stress-induced eIF-2α phosphorylation and inhibition of protein synthesis, there are no reports on the effect of oxidative stress on HRI expression, it's eIF-2α kinase activity, and regulation of protein synthesis *in vivo*. Our results indicate that during oxidative stress, inhibition of protein synthesis in K562 cells is caused because of induced activity as well as expression of HRI.

Experiments carried out to determine the effect of H_2O_2 and AAPH on K562 cell viability and proliferation indicated that, oxidative stress induces loss of cell viability and inhibits cell proliferation in a concentration dependent manner. There are reports available stating that, AAPH and H_2O_2 induce apoptosis, which also can be true in case of K562 cells. However, further studies will be required to verify this possibility. Increased lipid peroxidation leading to loss of membrane integrity, induced apoptosis and inhibition of protein synthesis due to induced activity and expression of HRI, might be responsible for loss of viability in K562 cells.

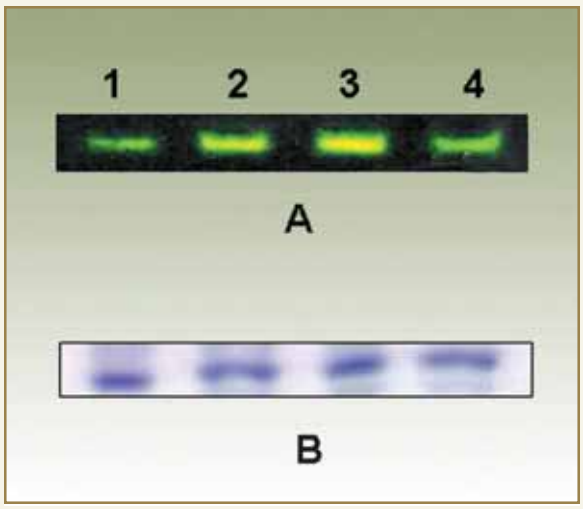

Fig. 8: Oxidative stress induces catalase activity in K562 cells. (A) Catalase activity (Native-PAGE activity staining *in situ* on gel) in the extracts of K562 cells treated with various concentrations of H_2O_2. Samples loaded in various lanes are, control (lane 1), 100 μM H_2O_2 (lane 2), 150 μM H_2O_2 (lane 3) and 200 M H_2O_2 (B)- CBB stained gel profile of the samples as in (A).

Our data indicates that AAPH and H_2O_2 in the exposure time of 1 h, induce eIF-2α kinase activity in a dose dependent manner. The transduction of an oxidant signal into a biological response can be mediated in several ways, but one principal mechanism involves the oxidation of thiols (–SH), present on side chain of amino acids. Lipid peroxides are known to induce HRI activity by oxidation of thiol (–SH) groups of this protein. Therefore, in the present study, AAPH-induced lipid hydroperoxides might be responsible for HRI activation, through thiol oxidation in K562 cells.

RT-PCR analysis indicated that oxidative stress caused by H_2O_2 induces HRI expression in K562 cells, indicating the possibility of activation of some redox sensitive transcription factor during H_2O_2 exposure.

Considering these results together, we conclude that

1) induced lipid peroxidation and HRI-mediated inhibition of protein synthesis, are responsible for inhibition of cell proliferation in human K562 cells,

2) oxidative stress-induced inhibition of protein synthesis in K562 cells is a combined effect of induced activity and expression of HRI and

3) lipid peroxides produced during oxidative stress might be playing a role in HRI activation, by altering the oxidation status of –SH groups of this protein.

ABOUT THE AUTHOR

Dr. T. P. A. Devasagayam joined BARC in 1975, after completing the BARC Training School programme in Biology and Radiobiology subsequent to his Masters in Zoology from the American College, Madurai. At present he is Scientific Officer (H) and Head, Radiation Biochemistry Section in the Radiation Biology and Health Sciences Division of BARC. His major area of research relates to role of free radicals in human health and radiation biology and potential uses of natural antioxidants. He has done his Post-Doctoral research in Germany and USA and has over 130 publications.

PROTECTION AGAINST γ -RADIATION INDUCED CELLULAR DAMAGE BY DENDRODOINE ANALOGUE

Strayo De and T.P.A. Devasagayam
Radiation Biology and Health Sciences Division
and
Mandakini Soni
BIMR, College of Life Sciences, Jiwaji University, Gwalior
and
V.P. Menon
Department of Biochemistry, Annamalai University, Annamalai Nagar, Tamilnadu

This paper received the Best Poster Award at the International Conference on "Emerging Trends in Free Radical and Antioxidant Research" held at Lonavala, during January 8-11, 2007

ABSTRACT

Ionizing radiations such as γ-rays exert their biological effects through generation of free radicals and by damaging biological macromolecules. Several natural compounds, especially with antioxidant abilities are known to be radioprotective. Our earlier experiments have already established the antioxidant activity of a novel, chemically-synthesized compound, DA (dendrodoine analogue). The aim of our present study is to examine the radioprotective ability of DA. We have studied the radioprotective effect of DA against DNA damage using plasmid pBR322 DNA. Among the cellular components, sub-cellular membranes form important targets of radiation damage. The assays used for DNA studies are strand-break estimation and DNA binding, while protein carbonyl, protein sulphydryl and lipid peroxidation assays were performed for membrane damage, using rat liver mitochondria and mouse liver homogenate as model systems. Significant membrane damage was observed with 450 Gy and strand break formation with 8 Gy. In all the assays, DA showed a concentration-dependent radioprotection. Inhibition of lipid peroxidation and protein oxidation was observed with low concentrations of DA (1-10 μg/ml). In case of DNA damage, a concentration of 100 mg / ml gave maximum protection. Preliminary studies also indicate protection against loss of reduced glutathione levels and different antioxidant enzymes. Our results indicate that DA, apart from being an effective antioxidant, is also a potent radioprotector, against free radical damage in plasmid DNA and cellular membranes.

Introduction

Ionizing radiation has attracted a lot of attention in recent years due to it's beneficial as well as possible harmful effects to human populations. When a biological system is exposed to ionizing radiation, the energy is absorbed by the system which triggers a number of successive events and the end result of

these could be cell death. When cells are exposed to radiation, the water molecules undergo dissociation (radiolysis) producing free radicals. These, in turn, may act on DNA, mitochondria, membrane lipids and cellular proteins. Proteins and nucleic acids are the building blocks of living matter and for the understanding of radiation damage; their behavior under the action of radiation is of primary importance. DNA is the primary target of radiation-induced damage. Damage to DNA can lead to cell cycle arrest and the recruitment of DNA repair enzymes to the damaged site. The residual damage or the misrepair can cause genetic instability, higher frequency of mutations and cytogenetic damage, resulting in disease and lethality.

People subjected to accidental or intentional exposures such as those involved in nuclear power generation and people using radiation sources for medical, industrial and scientific purposes, undergo radiation exposure, for short and long-term periods. All these categories of people need to be protected against radiation damage. Radiotherapy is one of the most common therapies for treating human cancers. To obtain optimum results, a cautious balance between the total dose of radiotherapy delivered and the threshold limit of the surrounding normal critical tissues is required. To obtain better tumour control with a higher dose, the normal tissues should be protected against radiation injury. Thus, the role of radioprotective compounds is very important in clinical radiotherapy also. Hence, compounds capable of radiation protection have potential applications in the above situations. Several novel approaches are on, to locate a potent radioprotector.

Ionizing radiations cause their biological effects mainly through the generation of free radicals and other reactive species. The radioprotectors can elicit their action by various mechanisms such as: (1) suppressing the formation of free radicals, (2) detoxifying the radiation-induced reactive species, (3) inducing the cellular defenses such as superoxide dismutase (SOD), glutathione, prostaglandins and interleukin-1, (4) enhancing the DNA repair by triggering one or more cellular DNA repair pathways and (5) delaying cell division and inducing hypoxia in the tissues. Various models corresponding to different levels of organization have been used, to examine the radioprotective abilities. These include Plasmid DNA, subcellular organelles, cell-cultures and whole animal models. Besides this, mechanistic studies and clinical trials, representing the opposite ends of the spectrum, are also being carried out and at different stages, these models provide useful information. Detailed mechanisms pertaining to radiation damage to various biomolecules and it's modulation by natural compounds will pave the way for developing efficient radioprotectors. Many natural and synthetic chemicals have been investigated in the recent past, for their efficacy to protect against radiation-induced damage in biological systems. These include mimics of antioxidant enzymes, nitroxides, melatonin, growth factors, gene therapy, hyperthermia apart from natural products. However, the inherent toxicity of some of the synthetic agents at the effective radio-protective concentration warranted further search for safer and more effective radio-protectors. Amifostine is the only one that is currently in use having good radioprotection to normal tissues, during radiotherapy, even though there are reports about contra-indications in some cases.

Several marine compounds have shown pharmacological activities for many diseases like cancer, AIDS, diabetes, arthritis, etc. Dendrodoine analogue (DA) has chemically synthesized and is similar to dendrodoine, an alkaloid extracted from *Dendrodoa grossularia*, a marine tunicate (Fig.1). Our earlier experiments already indicated the antioxidant activity of the compound DA. Several natural compounds, especially with antioxidant abilities are known to be radioprotective. Thus we also tried to examine the radioprotective ability of DA, using *in vitro* and *ex vivo* model systems and possible mechanisms involved.

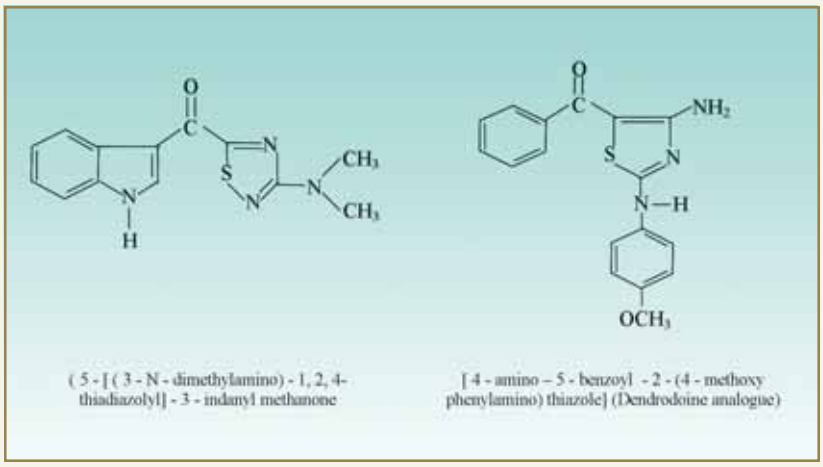

Fig. 1: Structure of Dendrodoine and it's analogue

Materials and methods

Chemicals

Ascorbic acid, dinitrophenyl dydrazine (DNPH), 5,5'-dithio-bis(2-nitrobenzoic acid) (DTNB), glutathione, guanidine hydrochloride, phosphoric acid, superoxide dismutase, 1,1,3,3-tetraethoxypropane, 2-thiobarbituric acid (TBA) xylenol orange, pBR322 plasmid DNA were purchased commercially. The other chemicals used in our study were of highest quality, commercially available from reputed suppliers. DA was synthesized in the lab of Dr. V. P. Menon.

Animals

Three to four months old female Wistar rats weighing 250-300 g were housed in standard temperature and humidity controlled room (25 ± 2°C) with a 12/12 hour light/dark cycle and were given a standard laboratory diet and water *ad libitum*. The guidelines issued by the Institutional Animal Ethics Committee of Bhabha Atomic Research Centre, Government of India, regarding the maintenance and dissections of small animals in scientific research were strictly followed.

Methods

Mitochondria from rat liver treated with or without test compound *in vitro* were exposed to 450 Gy -radiation at a dose rate of 7 Gy/min g-rays from a ^{60}Co source. The products of lipid peroxidation such as pink coloured ThiobarBituric Acid Reactive Substances (TBARS) formed, were estimated at 532 nm spectrophotometrically . Lipid hydroperoxides were detected using the Fox II method. Protein carbonyl was measured using the method based on the reaction of carbonyl groups with 2,4-dinitrophenylhydrazine (DNPH) to form a 2,4- dinitrophenylhydrazone, which can be measured at 366 nm. Superoxide dismutase activity was estimated using epinephrine. The difference between O.D. of standard and O.D. of enzyme was used, for calculation of activity. SOD activity was expressed as units/mg protein. To measure GSH levels, *O*-phthaldehyde was used. To study the effect of DA on single strand breaks in DNA, pBR322 plasmid DNA was irradiated (8 Gy g-radiation at a dose rate of 4.6 Gy/min) in the presence and absence of different concentrations of DA and was then subjected to agarose gel electrophoresis. DNA bands were stained with ethidium bromide and quantified by Advanced American Biotechnology (AAB) programme (software).

Statistical analysis

Statistical analyses were performed with the Student's paired t-test and P values <0.05 were considered to be significant. The values presented are means ± SEM (standard error of the mean) of four different experiments.

Results

Most of the natural radioprotectors are believed to exert radioprotective effect by scavenging the radiation-induced ROS. Our earlier experiments already established the antioxidant activity of the

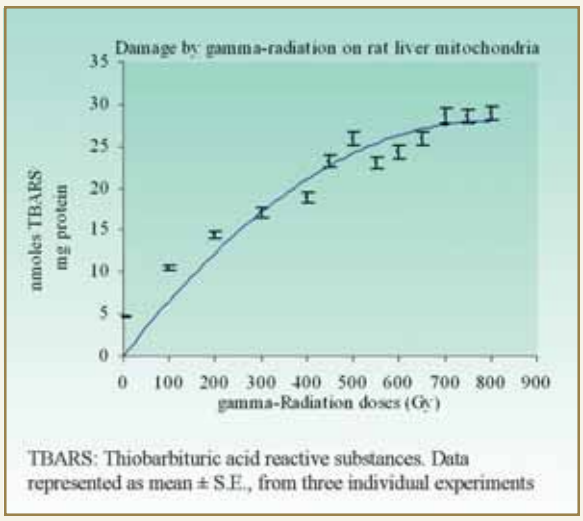

Fig. 2: Evaluation of the optimum oxidative damage (in terms of lipid peroxidation) to Rat Liver Mitochondria over a gamma-radiation dose range of 0-800 Gy.

compound DA. In the present study, we tried to examine the radioprotective ability of DA. The radioprotective effect of DA was studied, using assays corresponding to their ability to inhibit the damage caused to biomolecules. All experiments were carried out with different concentrations of DA, in order to investigate whether an increase in the concentration

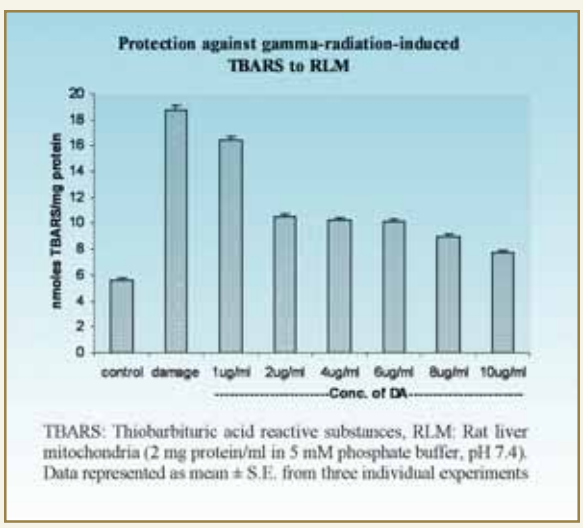

Fig. 3: Protection against γ-radiation-induced lipid peroxidation in terms of TBARS

influences the radioprotective activity. DA gave protection against radiation-induced oxidative damage in all our experiments. The capacity of DA to prevent mitochondrial damage induced by radiation was examined, in terms of lipid peroxidation and protein oxidation. Lipid peroxidation was assessed as formation of lipid hydroperoxides (LOOH) and thiobarbituric acid reactive substances (TBARS). Significant membrane damage was observed with 450 Gy (Fig. 2). Figs. 3 and 4 reveal that DA inhibits γ-radiation-induced lipid peroxidation significantly (more than 70% protection) even at a low concentration of 10 μg/ml.

Free radicals can oxidize proteins increasing their hydrophobicity and sensitivity to proteolysis. Oxidation of proteins by radiation-derived reactive oxygen/ nitrogen species (ROS/RNS) can generate a range of stable as well as reactive products such as protein hydroperoxides, that can generate additional radicals particularly upon interaction with transition metal ions. Protection against protein oxidation was assessed as formation of protein carbonyls and depletion of protein sulphydryls. Concentration range of 1-100 μg/ml of DA was used (Table 1). DA inhibits γ-radiation-induced protein oxidation significantly even at a low concentration of 10 μg/ml (more than 75% protection).

Fig. 5 (a) shows the agarose gel electrophoresis pattern of pBR322 DNA exposed to different doses of γ-radiation (dose = 4 - 15 Gy). Maximum damage was obtained from 8 Gy onwards. Thus using γ-radiation dose of 8 Gy, the agarose gel electrophoresis pattern of pBR322 DNA in the presence and absence of DA at different concentrations was obtained (Fig. 5(b)). On exposure of plasmid DNA to γ-radiation, the intensity of the band corresponding to Form II (open circular) was increased. Addition of DA (10, 100 and 200 μg/ml in lane 3, 4 and 5 respectively), reduced the extent of increase in Form II. DA thus protected against γ-radiation-induced single strand breaks in pBR322 DNA. 10, 100 and 200 μg/ml DA gave 58, 71, and 75 % protection, respectively.

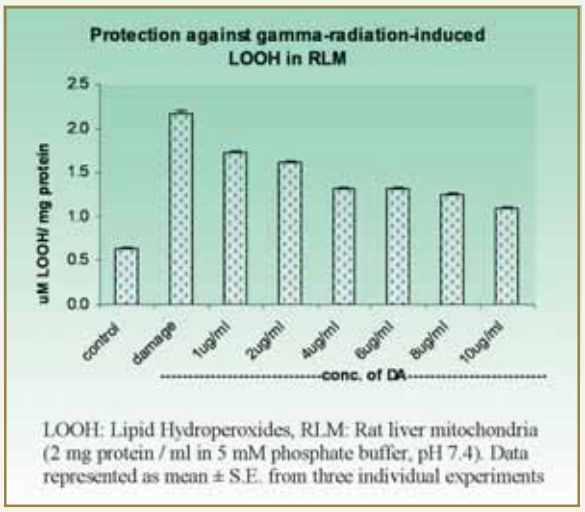

Fig. 4:. Protection against γ-radiation-induced lipid peroxidation in terms of LOOH

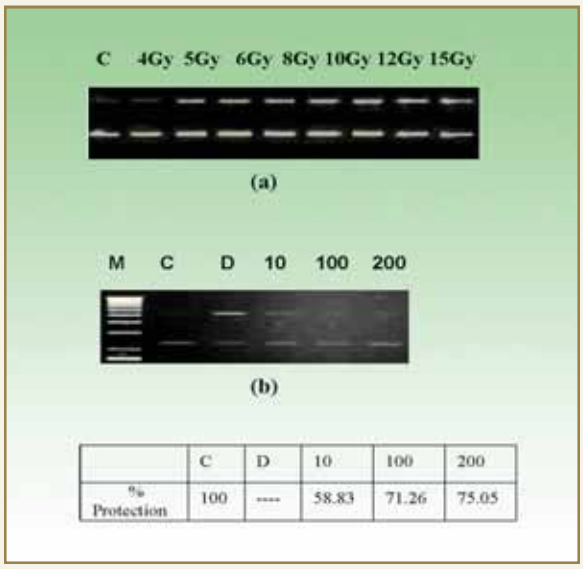

	C	D	10	100	200
% Protection	100	----	58.83	71.26	75.05

Fig. 5: (a) Radiation–induced damage to plasmid pBR322 DNA as a function of dose. Maximum damage obtained from 8Gy onwards.(b) Protection against 8 Gy-radiation–induced damage to plasmid pBR322 DNA by different concentrations of DA. Maximum protection was obtained at 200 µg/ml, C: Control, D: Damage, M: Marker (Experiments in duplicate)

Apart from enhancing lipid, protein and DNA damage, radiation treatment leads to inactivation of antioxidant enzymes. Hence we have also studied the effect of DA on reduced glutathione (GSH) levels and the antioxidant enzyme SOD in rat liver homogenates on exposure to radiation. DA protected both GSH and SOD (Table 2).

Discussion and Conclusion

Ionizing radiations such as γ-rays exert their biological effects through generation of reactive oxygen species and by damaging biological macromolecules such as lipids, proteins, carbohydrates and DNA. Antioxidants are capable of preventing damage caused by free radicals. Presently the focus is on developing natural compounds as radioprotectors, especially antioxidants that would scavenge radiation-induced ROS when present during irradiation. Natural compounds are generally preferred due to their lower toxicity and easier availability. Thus we tried to examine the radioprotective ability of DA in this study. The radioprotective effect of DA was studied, using assays corresponding to their ability to inhibit the damage, caused to biomolecules. All experiments were carried out with different concentrations of DA in order to investigate whether

Table. 1: Protection against radiation-induced protein oxidation in rat liver mitochondria by different concentrations of DA

Concentration of DA	nmoles of Protein Carbonyls (nmoles/mg protein*)	Protein Sulphydryl (nmoles/mg protein*)
Control	2.5 ± 0.05	26.69 ± 0.85
Damage	8.81 ± 0.1	15.25 ± 0.12
1 µg /ml	5.24 ± 0.2 (56.60%)	16.05 ± 0.92 (60.15%)
5 µg /ml	4.99 ± 0.2 (60.38%)	19.02 ± 0.39 (76.77%)
10 µg /ml	3.80 ± 0.02 (79.25%)	20.32 ± 2.03 (76.40%)
50 µg /ml	2.38 ± 0.05 (>100%)	23.50 ± 2.84 (88.07%)

Data represented as mean ± S.E., from three individual experiments. *Rat liver mitochondria (2 mg protein/ml in 5 mM phosphate buffer, pH 7.4) % Protection values are given in brackets

Table 2: Protection of mitochondrial glutathione (GSH) and superoxide dismutase (SOD) by different concentrations of DA from radiation-induced oxidative damage

Groups	GSH (nmoles/mg protein)	SOD (Units/mg protein)
Control	70.73 ± 0.02	5.69 ± 0.02
Damage	66.6 ± 0.07	4.66 ± 0.01
10 µg/ml	68.16 ± 0.56	4.93 ± 0.65
50 µg/ml	69.3 ± 0.08	5.35 ± 0.09
100 µg/ml	70.18 ± 0.04	5.48 ± 0.45

Data represented as mean ± S.E., from three individual experiments. *Rat liver mitochondria (2 mg protein/ml in 5 mM phosphate buffer, pH 7.4) % Protection values are given in brackets

an increase in the concentration influences the radioprotective activity. DA gave protection against radiation-induced oxidative damage in all our experiments. Mitochondria are crucial targets for γ-radiation and free radical-mediated damage. One of the major forms of cellular damage induced by ionizing radiation is lipid peroxidation. As is evident by the formation of TBARS exposure to γ-radiation, as a function of dose, ranging from a dose of 0 to 800 Gy, resulted in enhanced lipid peroxidation. There was a significant increase in TBARS formation with increasing radiation dose. Exposure to 200–500 Gy showed sharp increase, while higher doses were only slightly effective in enhancing peroxidation. Hence the optimum dose of 450 Gy was selected for the experiments, as this dose caused optimum damage in terms of lipid peroxidation in rat liver mitochondria. This dose is much higher than those used in radiotherapy (1–6 Gy) or for radioprotection pertinent to mammals (LD50 in the range of 5–7 Gy). Since mitochondria are devoid of cytosolic antioxidants, as in a whole cell, they are fairly resistant to γ-radiation. Hence, a dose of 450 Gy is needed to achieve optimum concentration of free radicals, capable of inducing significant damage measurable by simple spectrophotometric means. Date presented in the Figures and Tables reveal that DA inhibits γ-radiation-induced lipid peroxidation and protein oxidation significantly (more than 70% protection) even at a low concentration of 10 µg/ml.

Ionizing radiation-induced damages to cellular DNA are of prime biological significance. DNA damage is mainly induced by abstraction of the H atom from the C′-4 position of the deoxyribose or by attack of the bases via the hydroxyl radicals. Lipid peroxidation products such as malondialdehyde can also form adducts with cellular DNA. The types of damages suffered by DNA due to ionizing radiation include single-strand breaks (SSBs), double-strand breaks (DSBs), DNA-DNA as well as DNA-protein crosslinks and damage to bases. Protecting cellular DNA from radiation damage might result in prevention of the cancers/mutations induced by radiation. The present study shows that DNA is protected from deleterious effects of γ-radiation by DA. The figure reveals that the recovery of DNA damage, in groups containing DA was concentration-dependent.

The antioxidant enzymes such as superoxide dismutase (SOD), glutathione peroxidase (GPx), glutathione reductase (GR), and catalase (CAT) can block the initiation of free radical chain reactions MnSOD may play a central role in protecting cells against reactive oxygen species injury during ionizing radiation exposure. GSH is an important cellular antioxidant. Role of GSH in reductive processes are important for the synthesis and degradation of proteins, regulation of enzymes, formation of the deoxyribonucleotid precursors of DNA and protection of the cells against ROS and free radicals, produced even in normal metabolism. GSH is a versatile protector. Several distinct mechanisms of radioprotection by GSH have been recognized, including radical scavenging, restoration of damaged molecules by hydrogen donation, reduction of peroxides and maintenance of protein thiols in the reduced slate. Of these mechanisms, the most important one is probably hydrogen donation to DNA radicals and this mechanism requires a high

concentration of GSH. It is postulated that ionizing radiation would rapidly oxidize the thiol groups of cells. In accordance with this hypothesis, radiation decreases the cellular concentration of GSH and leads to formation of glutathione disulfide. Radiosensitivity of cells depends on the intracellular thiol level. Administration of various thiols can protect the cells and animals against the effects of radiation. Some investigators measured GSH levels in animals exposed to radiation and noted that the GSH levels were significantly lower in the groups exposed to radiation as compared to the control groups. We have thus also studied the effect of DA on reduced glutathione levels and the antioxidant enzyme SOD in rat liver homogenates on exposure to radiation. Our studies show that DA protects both GSH and SOD.

In conclusion, the present study suggests that DA can prevent damage to lipids, proteins and DNA from gamma radiation-induced oxidative stress. The possible reason for the observed radioprotective effect of DA can be due to it's antioxidant property, which can be because of radical scavenging. Our studies, therefore, reveal that DA, an analogue of a compound from a marine tunicate can be a valuable radioprotector with potential applications in health.

ABOUT THE AUTHORS

Ms. Strayo D. De received her B.Sc. degree in Microbiology and Biophysics in 2004 from Mumbai University. During her Post Graduation, she was a topper in her subject and overall fifth in the University. At present, she is a DAE fellow attached to Radiation Biology and Health Sciences Division, BARC, pursuing her Ph.D. on "Studies pertaining to potential applications of some novel materials in human health and radioprotection."

Dr. T.P.A. Devasagayam joined BARC in 1975, after completing the BARC Training School programme in Biology and Radiobiology, subsequent to his Masters in Zoology from the American College, Madurai. At present he is Scientific Officer (H) and Head, Radiation Biochemistry Section in the Radiation Biology and Health Division of BARC. His major area of research relates to role of free radicals in human health and radiation biology and potential uses of natural antioxidants. He has done his post-doctoral research in Germany and USA and has over 130 publications.

बीएआरसी न्यूज़लेटर BARC NEWSLETTER

ANTIBACTERIAL COTTON FABRIC PREPARED BY RADIATION GRAFTING TECHNIQUE

N.K. Goel, Virendra Kumar, Y. K. Bhardwaj, K.A. Dubey, C.V. Chaudhari and S. Sabharwal
Radiation Technology Development Section

This paper won the Best Poster Award at the International Conference on Frontiers of Radiation and Photochemistry (PhotoRadChem-2007) held at M.G. University, Kottayam, during February 8-11, 2007

ABSTRACT

Radiation-induced grafting of a quaternary ammonium type monomer, MAETC, onto cotton fabric has been carried out by mutual radiation grafting technique using ^{60}Co gamma radiation. Effect of different experimental parameters like dose, dose rate, ambience and monomer concentration, on grafting yields was investigated to optimize the grafting process. The grafted cotton samples were characterized by various techniques like grafting yield, water uptake, Elemental analysis, Fourier Transformed Infrared Spectroscopy (FTIR) and Scanning Electron Microscopy (SEM). Aqueous solution of radiation synthesized Poly(MAETC) showed very good antibacterial activity, against both the strains, however, the (MAETC-*g*-Cotton) samples showed better antibacterial activity against *S. aureus* as compared to *E. coli*.

Introduction

Radiation grafting is an easy and highly efficient procedure, for modifying the properties of polymeric substrates of synthetic as well as natural origin. Cotton is the most abundant natural polymer and used in many applications in our day-to-day life. But it is found to be vulnerable to attack by various kinds of microorganisms. Quaternary ammonium compounds are well known for their germicidal activities. MAETC is a monomer containing quaternary ammonium group and was expected to show antibacterial activity. Therefore, in this work, radiation synthesized Poly(MAETC) was first tested for antibacterial activity, against both gram-positive and gram-negative bacteria. After getting positive results from those studied, PMAETC was grafted on to cotton, in order to add antibacterial property of MAETC.

Experimental

Radiation grafting

Mutual irradiation grafting method was used, to graft MAETC (75% solution from Aldrich) onto cotton pieces (from local supplier) using ^{60}Co gamma radiation source (GC-5000). The grafting yield was estimated gravimetrically using the following relation.

$$\text{Grafting yield (GY)} = \frac{\text{Weight after grafting - Initial weight}}{\text{Initial weight}} \times 100$$

Antibacterial test

The Radiation synthesized linear Poly(MAETC) and (*MAETC-g*-Cotton) samples were tested for antibacterial properties, against two types of bacterial strains namely, *S. aureus* and *E.coli,* using agar well method and colony count method.

Results and Discussion

Effects of various parameters on grafting yields were investigated.

Effect of Dose and dose rate

The results of effect of radiation dose and dose rate on GY are shown in Fig. 1. It was found that the GY increased with radiation dose and finally saturated above total dose of 1.25 kGy. However, the GY decreased with increase in dose rate.

Effect of ambience conditions

It was found that in aerated condition, the extent of grafting was much lower than that obtained in N_2 purged condition (Fig. 2.). This indicates that the grafting yield is suppressed due to the presence of O_2, a well-known efficient radical scavenger, that inhibits radical initiated reactions.

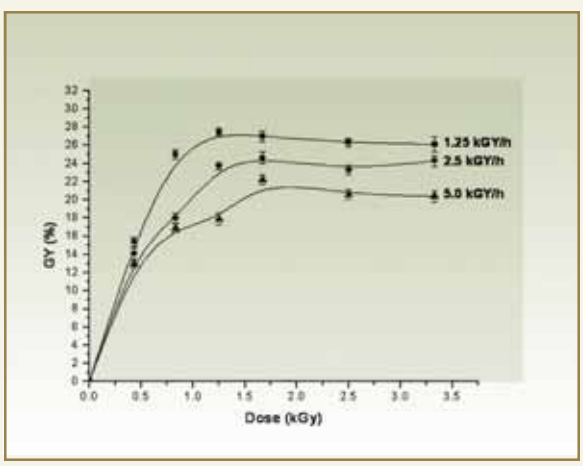

Fig. 1: Results of effect of radiation dose and dose rate of GY

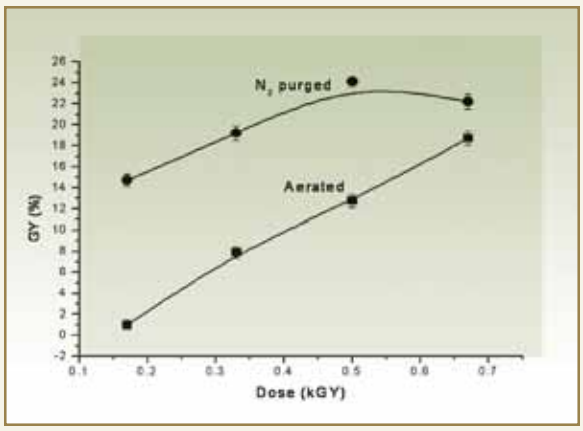

Fig. 2: Effect of grafting in purged and aerated conditions

Effect of monomer concentration

The grafting yield was found to be almost linear in function of monomer concentration, in the concentration range studied (Fig. 3), but the homo-polymerization of monomer also increased simultaneously.

Characterizations

Prepared samples were characterized by various techniques like gravimetric, elemental analysis, FTIR

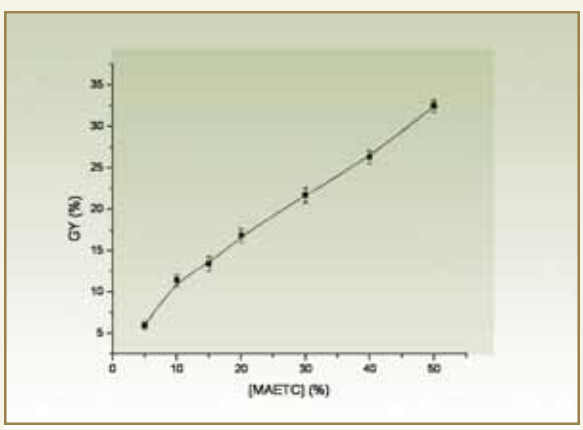

Fig. 3: Grafting yield

and SEM. Fig. 4 showed the FTIR spectra of virgin cotton, poly-MAETC and grafted cotton. Figs. 5 and 6 are the SEM images of grafted and ungrafted cotton and it is very much clear that there is remarkable change in the thickness and roughness of surfaces of grafted and ungrafted sample.

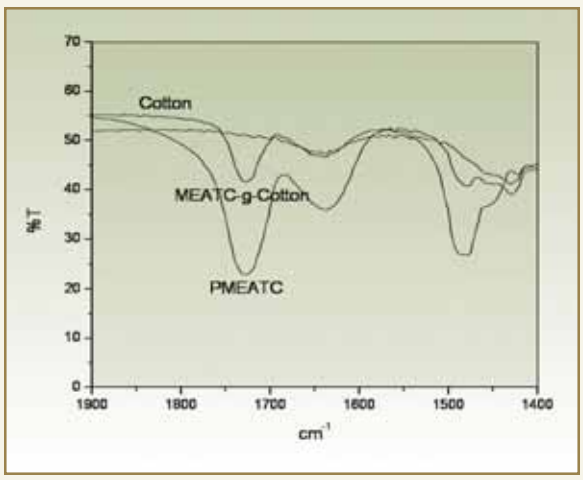

Fig. 4: FTIR spectra of virgin cotton, MEATC and grafted cotton.

Fig. 5: Ungrafted Cotton : SEM Image

Fig. 6: Grafted Cotton : SEM image

Antibacterial study

The qualitative test for anti-bacterial activity of various concentrations of radiation synthesized PMAETC by agar well method, showed significant zone of inhibition against test organisms (Table 1). It was found, that the antibacterial efficacy of PMAETC increased with it's concentration and it started showing toxicity against the test organism at even 5 % concentration.

Table 1: Results of antibacterial test by agar well method

MAETC conc. (%)	Zone of inhibition dia. (mm)	
	E. coli	*S. aureus*
0 %	8.0	8.0
5 %	9.0	9.0
20 %	10.0	11.0
25 %	12.0	14.0
35 %	15.0	17.0

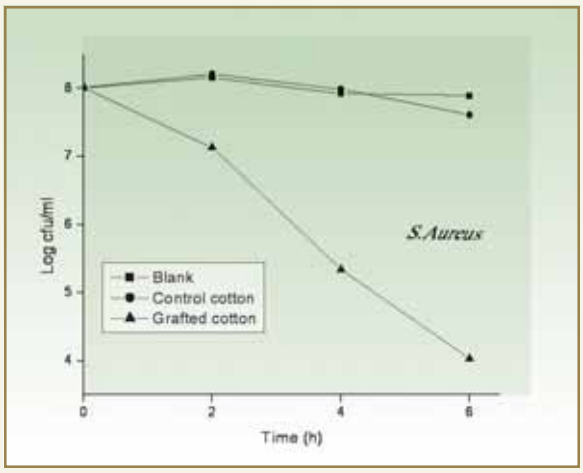

Fig. 7: Reduction in bacterial counts; *S. Aureus*

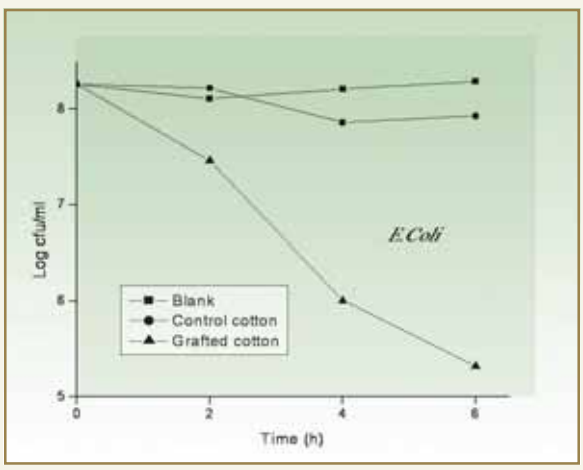

Fig. 8: Reduction in bacterial counts ; *E. coli*

PMAETC polymer exhibited more toxicity against S. *aureus* as compared to *E. coli*. Quantitative analysis of the grafted samples grafted to an extent of ~35 % showed approximately 3-log cycle reduction in bacterial counts of *E. coli* and ~4-log cycle reduction for *S. aureus* within 6 hours of exposure (Figs. 7 and 8).

Conclusion

Grafting extent increased with increase in radiation dose. However, grafting yield was found to inverse function of dose rate. Presence of O_2 and salts of Fe^{+2}, Ce^{+4} and Cu^{2+} suppresses the grafting yield. Presence of organic solvents like methanol, ethanol and n-propanol suppress grafting yield significantly. The grafted sample shows significantly higher water uptake and water retention properties. Various concentrations of radiation polymerized PMAETC in aqueous solutions were tested for their antibacterial efficacy, against a gram-positive bacteria i.e. *Staphylococcus aureus* and a gram-negative bacteria i.e. *Escherichia coli*. The MAETC g-cotton was found to show better antibacterial activity against *S. aureus* as compared to *E.coli.* Grafted samples (with 35 % G.Y.) decreased the colony counts by more than 4 log cycle for *S. aureus* and about 3 log cycle for *E. coli* within six hours of exposure.

ABOUT THE AUTHORS

Mr. N.K. Goel completed his Post graduation in Chemistry from M.D. University, Rohtak with Gold medal in 2001 and joined the Radiation Technology Development Section, BARC in 2003. He is from the 46th Batch. Since then, he has been involved in modification of polymers with Gamma radiation for various biomedical and environmental applications.

ABOUT THE AUTHORS

Dr. Virendra Kumar completed his Post graduation in Chemistry from IIT Roorkee, in 1998 and joined the Radiation Technology Development Section; BARC in 1999 after successful completion of one year of orientation programme at BARC. He is from the 42nd Batch. Since then, he has been involved in modification of surface of woods by radiation curing method. He has a number of publications in international journals and symposia / conferences to his credit.

Dr. Y. K. Bhardwaj is engaged in the research work including development of grafted polymer matrices for various applications, elastomer blends and high performance coatings. He has been actively involved in the studies on radiation polymerization / crosslinking of monomers / polymers, development of radiation processed hydrogels for medical and pharmaceutical applications, synthesis of fast stimuli-responsive hydrogels and radiation crosslinking behaviour of water soluble polymers.

Mr. K.A. Dubey completed his Post graduation in Chemistry from IIT Roorkee, in 2000 and joined the Radiation Technology Development Section; BARC in 2001 after successful completion of one year of orientation programme at BARC. He is from the 44th Batch. Since then, he has been involved in modification of polymers with Gamma radiation for various high-performance applications.

Mr. C.V. Chaudhari joined BARC in 1988 and is presently working in the Radiation Technology Development Section. He did his M.Sc. in Chemistry, in March 1999 from University of Mumbai. He is involved in the area of radiation processing of polymers, radiation vulcanization of natural rubber latex and modification of polymers by using radiation grafting.

Dr. S. Sabharwal after graduating from the 22nd Batch of BARC Training School, joined the Chemistry Division of BARC in 1979. Presently he is Head, Radiation Technology Development Section. His focus has been on studying radiation effects on polymeric materials and radiation chemistry studies of polymers with a view to develop industrial applications. Dr. Sabharwal has published 80 scientific papers.

MORPHOTROPIC PHASE BOUNDARY LIKE CHARACTERISTIC IN A LEAD-FREE AND NON-FERROELECTRIC (1-X)$NANBO_3$-X$CATIO_3$ SYSTEM

Saurabh Tripathi and Dhananjai Pandey
School of Materials Science and Technology,
Institute of Technology, Banaras Hindu University, Varanasi

and

Sanjay Kumar Mishra and P.S.R. Krishna
Solid State Physics Division

This paper won the Best Poster Award at the 10th International Conference on Advanced Materials (IUMRS-ICAM 2007) held at Bengaluru, during October 8-13, 2007

ABSTRACT

We report here an anomalous peak in the composition dependence of the dielectric permittivity of non-ferroelectric (1-x)$NaNbO_3$-x$CaTiO_3$ ceramics, for the composition range $0.10 < x < 0.20$. This is reminiscent of a similar phenomenon in the ferroelectric Morphotropic Phase Boundary (MPB) ceramics. Rietveld analysis of the powder X-ray diffraction data for various compositions reveals that this peak is linked with a change of crystal structure from one orthorhombic phase in the Pbma space group for $0 \leq x \leq 0.10$ to another orthorhombic phase in the Pbnm space group for $x \geq 0.20$ through an intermediate long period modulated orthorhombic phase whose lattice parameter is ~14 times the lattice parameter of the Pbnm phase of $CaTiO_3$ in the [010] direction (q~[0,1/14,0]).

The phase diagrams of several mixed solid solutions of the ABO_3 type perovskites contain a Morphotropic Phase Boundary (MPB). The MPB compositions have been found to be of special technological significance for numerous sensor and actuator devices as several physical properties like dielectric permittivity, electromechanical coupling coefficients and piezoelectric strain coefficients are maximized around this composition. In the well known commercial MPB systems, like $Pb(Zr_xTi_{(1-x)})O_3$(PZT), (1-x)$Pb(Mg_{(1/-3)}Nb_{(2/3)})O_3$-x$PbTiO_3$(PMN-xPT) and (1-x)$Pb(Zn_{(1/3)}Nb_{(2/3)}O_3$-x$PbTiO_3$(PZN-xPT), this peak in the composition dependence of dielectric and piezoelectric properties around the MPB, has been linked with the change of crystal structure from tetragonal to a pseudo rhombohedral phase, through a narrow range of stability of monoclinic phases observed experimentally and predicted theoretically. Amongst the environmentally friendly Pb free systems, solid solutions of $NaNbO_3$ with $KNbO_3$ and $LiNbO_3$, both of which are ferroelectric at room temperature, also exhibit MPB near 50 mol % and 12 mol % of the ferroelectric phases, respectively.

The MPB systems, discovered so far, have at least one component, that is ferroelectric in nature (e.g. $PbTiO_3$, $KNbO_3$, $LiNbO_3$). We present here the results of combined dielectric and powder diffraction studies on Pb free (1-x) $NaNbO_3$-x$CaTiO_3$ (NN-xCT) ceramics, revealing MPB like characteristic in a non-ferroelectric system. One of the end members of this system, $NaNbO_3$, is an antiferroelectric at room temperature but becomes ferroelectric at low temperatures. The other end member, $CaTiO_3$, is a quantum paraelectric showing a saturation of dielectric permittivity below ~ 30K. We find that the dielectric permittivity of this mixed system at room temperature exhibits a sharp rise in the composition range $0.10 < x < 0.20$ with a peak at $x \approx 0.16$. This anomalous rise in the dielectric permittivity is shown to be linked with a change of crystal structure, from an orthorhombic structure in the Pbma space group for $x \leq 0.10$ to another orthorhombic structure but in the Pbnm space group for $x \geq 0.20$, reminiscent of a similar rise in the dielectric permittivity near the MPB composition of the technologically important PZT and PMN-xPT ceramics due to a change of crystal structure from tetragonal to pseudo-rhombohedral. We also show that in the intermediate composition range ($0.10 < x < 0.20$), the structure corresponds to a long period modulated phase. To the best of our knowledge, the NN-xCT ceramics are the first example of a non-ferroelectric and non-piezoelectric MPB system, in contrast to the well known MPB systems which are all ferroelectric and piezoelectric.

NN-xCT powders were prepared by the solid state reaction method, using 99% pure powders of $NaCO_3$, $CaCO_3$, Nb_2O_5 and TiO_2 at 1150 ^{0}C for 6 hours in open alumina crucible. The calcined powder was pressed into circular pellets of 13 mm diameter, using an uniaxial hydraulic press at an optimized load of 70 kN. Sintering of the green pellets was carried out in the temperature range 1250 ^{0}C - 1300 ^{0}C, depending upon the composition, for 6 hours in open alumina crucibles. For capacitance measurements, fired-on silver paste (curing temperature: 500 ^{o}C) was used. Capacitance was measured using HP4192 impedance analyzer. For powder diffraction experiments, the sintered pellets were crushed to fine powder and subsequently annealed at 800 °C to remove strains introduced, if any, during crushing. Powder X-ray diffraction data was collected using a 18kW based Rigaku Powder Diffractometer (RINT 2000/ PC series) operating in Bragg-Brentano geometry and fitted with curved crystal monochromator in the diffraction beam. Rietveld and *Le Bail* analysis of the powder diffraction data was carried out using the crystal structure refinement programme "Fullprof." Pseudo-Voigt function was used, to define the peak profiles in the refinements. Background was described in terms of a sixth coefficients polynomial. Except for the occupancy parameters of the atoms, which were kept at their nominal composition, all other parameters i.e., scale factor, zero correction, background, half width parameters along with mixing parameters, lattice parameters, positional coordinates and thermal parameters were refined.

Fig.1 shows the composition dependence of the room temperature dielectric permittivity of (1-x)$NaNbO_3$-x$CaTiO_3$. The value of the dielectric permittivity of NN-xCT is ~300 for $x<0.10$ and $x>0.20$. In the composition range $0.10 < x < 0.20$, the dielectric permittivity increases sharply, peaking to a value of ~1250 at $x \approx 0.16$. In order to explore if there is any structural change as a function of composition across $x \approx 0.16$, we analyzed the powder x-ray diffraction data for NN-xCT compositions. Fig. 2 depicts the evolution of the powder x-ray diffraction data for NN-xCT in the composition range $0 \leq x \leq 1$ for a limited 2θ range of 26-56 degrees. These patterns contain two types of reflections: the main perovskite reflections and the superlattice reflections. Both types of reflections can be indexed with respect to a doubled perovskite cell (i.e. $2a_p$, $2b_p$, $2c_p$, where a_p, b_p and c_p are the cell parameters of the elementary perovskite cell). The superlattice reflections assume Miller indices, represented by one or more odd integers while the

main Bragg reflections are represented by all even integered indices. Superlattice reflections with all-odd integered indices (i.e., 'ooo' type) and two-odd and one even integered indices, result from anti-phase (- tilt) and in-phase (+ tilt) tilting of the adjacent oxygen octahedra, due to structural phase transitions driven by softening and freezing of the phonons at R (q= ½, ½, ½) and M (q = ½, ½, 0) points of the cubic Brillouin zone, respectively. The superlattice reflections with two-even and one odd integered indices (i.e., 'oee' type) are due to antiparallel cationic shifts in the structure and are linked with lattice instabilities corresponding to q = 0, 0, ½ and ½,½,½ points of cubic Brillouin zone, respectively. As can be seen from Fig. 2, superlattice reflections with: (i) odd-odd-odd (e.g. 311), (ii) odd-odd-even (e.g. 310 and 312) and (iii) even-even-odd (e.g. 203, 421) indices are present in the diffraction pattern of pure $CaTiO_3$ (x=1.00), in agreement with the literature for the $a^-a^-c^+$ tilt system in the Pbnm space group. For the other end member, pure $NaNbO_3$ (x=0), one observes superlattice reflections with all odd (e.g. 311) indices and also with fractional indices (e.g. 3 1 7/2, near $2\theta = 55$ degrees). The fractional indices indicate the quadrupling of the elementary perovskite cell, along one of it's axes. This has been attributed to softening and freezing of the Δ point (q=0,0,$^1/_4$) phonon. A compound tilt system, $[(a^-b^+a^-)_1(a^-b^-a^-)_2(a^-b^+a^-)_3]$, along with a complex anti-parallel displacement pattern of the ions, in the orthorhombic space group Pbma, which is equivalent to Pbcm in the bca setting, has been found to be consistent with all the features of the diffraction patterns for pure $NaNbO_3$.

It is evident from Fig. 2 that the peaks with fractional indices, such as the one near $2\theta = 55$ degrees, which are characteristic of the $NaNbO_3$ structure, disappear for x > 0.10. For 0.20 ≤ " x ≤ " 1.0, new superlattice reflections, like that near 2θ=44 degree, appear indicating a change of crystal structure to $CaTiO_3$ type. For the composition x=0.16, additional weak reflections (marked with arrows in Fig. 2), not present in the patterns of NN-xCT for x ≥ 0.20 and x ≤ 0.10, are also observed. This suggests that the structure of NN-xCT for x=0.16 may be different from those for x ≥ 0.20 and x ≤ 0.10. It is interesting to note, that this composition corresponds to the peak value of the dielectric permittivity shown in Fig. 1.

The change of crystal structure of NN-xCT from $CaTiO_3$ like for x ≥ 0.20 to $NaNbO_3$ like for x ≤ 0.10 was confirmed by Rietveld refinement of NN-xCT using the orthorhombic structures of $CaTiO_3$ and $NaNbO_3$ in the Pbnm and Pbma space groups, respectively. We did not find any signature of monoclinic distortion, proposed for $NaNbO_3$, in the refinements for x ≤ 0.10. The asymmetric unit of the orthorhombic structure with Pbnm space group contains one Na/Ca atom at the 4c Wyckoff site (0± u, ½ ± v, ¼) and Nb/Ti at the 4a Wyckoff site (0, 0, 0). There are two types of oxygen atoms: O(1) at 4c Wyckoff site (0± u, 0± v, ¼), O(2) at 8d Wyckoff site (¼ ± u , ¼ ± v, 0 ± w). For the Pbma space group, the asymmetric unit of the structure of the antiferroelectric phase consists of two Na/Ca [Na/Ca(1) and Na/Ca(2)], one Nb/Ti, and four O atoms [O(1), O(2), O(3), and O(4)]. Na/Ca(1) occupies the 4c Wyckoff site (¾, 0, ¼ ± w,) and Na/Ca (2) occupies the 4d Wyckoff site (¾±u, ¼, ¼ ± w). Nb/Ti occupies 8e Wyckoff site (¼ ± u, $^1/_8$ ± v, ¼ ± w). The oxygen atom O(1) occupies the 4c Wyckoff site (¼, 0, ¼ ± w), O(2) occupies the 4d Wyckoff site (¼ ± u , ¼ , ¼ ± w), O(3) occupies the 8e Wyckoff site (0±u, $^1/_8$± v , ½ ± w) and O(4) occupies the 8e Wyckoff site (½ ± u, $^1/_8$ ± v, 0 ± w). For the Pbnm space group of $CaTiO_3$, use of isotropic thermal parameter gave satisfactory results. However for the Pbma space group, the isotropic thermal parameters for Na(1)/Ca(1) site was found to be very large (~3.80Å^2), similar to that reported for pure $NaNbO_3$. It was found necessary to use anisotropic thermal parameters for Na1/Ca1 site, which led to the reduction of R_{wp} and R_B with respect to isotropic thermal parameters. The refined structural parameters, along with the R-factors, for these two compositions

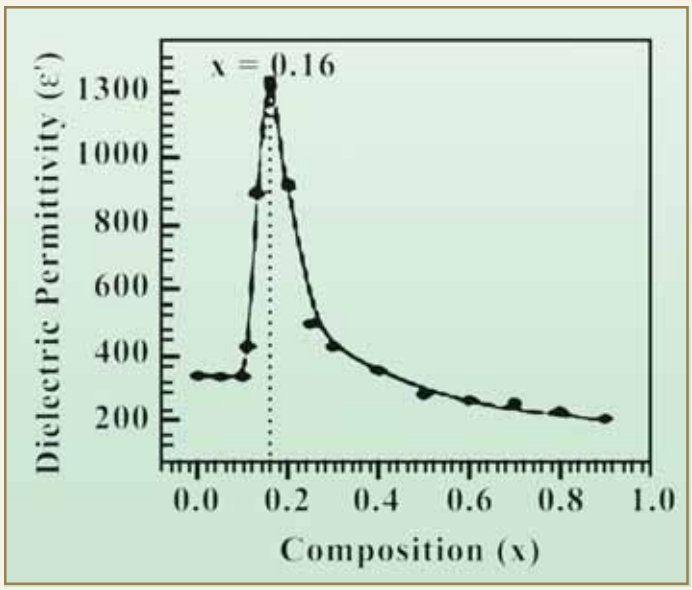

Fig. 1: Variation of the real part of the dielectric permittivity (ε') with composition (x) at ambient temperature for NN-xCT ceramics

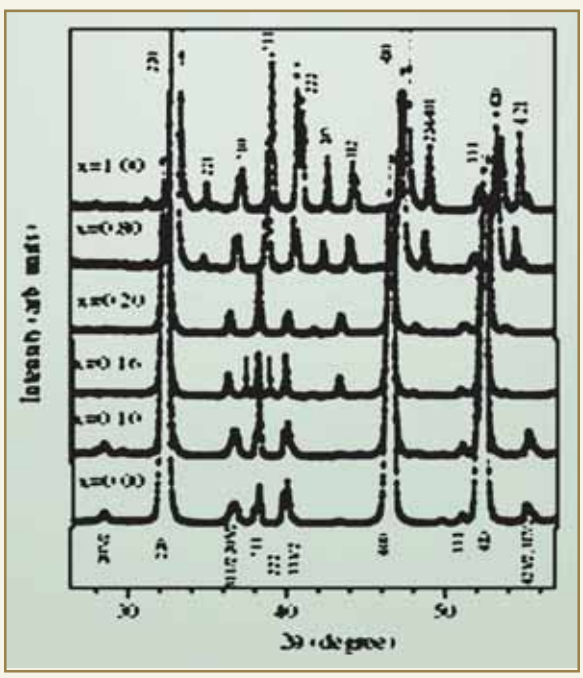

Fig. 2: Evolution of powder x-ray diffraction patterns of NN-xCT ceramics with composition (x) at room temperature. The additional peaks for x=0.16 are marked with arrows. The Miller indices are with respect to a doubled pseudo-perovskite cell

are given in Tables 1 and 2. Similar refinements were carried out for the other NN-xCT compositions, for the entire $0 \leq x \leq 1$ composition range, except for $0.10 < x < 0.20$. The variation of the pseudocubic lattice parameters (a_p, b_p, c_p), as obtained from the Reitveld refined orthorhombic lattice parameters using the relationships $A_o = \sqrt{2}a_p$, $B_o = \sqrt{2}b_p$ and $C_o = 2c_p$ for the Pbnm space group, and $A_o = \sqrt{2}a_p$, $B_o = 4b_p$ and $C_o = \sqrt{2}c_p$ for the Pbma space group, and pseudocubic cell volume is shown in Fig. 3. The lattice parameters as well as the unit cell volume, decrease with increasing $CaTiO_3$ content (x) as expected, on the basis of the smaller ionic radii of Ca and Ti as compared to Na and Nb, respectively.

Table 3 lists the bond lengths for NN-xCT with x=0.10 and 0.20. The isotropic thermal parameter of Na1/Ca1 is larger than that for Na2/Ca2 and other atoms. This is similar to pure $NaNbO_3$ where it has been argued that the long average bond length for Na1-O as compared to Na2-O (counting neighbours within 2.9 Å) is responsible for larger amplitude of vibration. In 10% Ca^{2+} substituted $NaNbO_3$ also, we find that the average of the nine Na1/Ca1-O bond lengths within ~2.9 Å (i.e. 2.68 Å), is larger than the average of Na2/Ca2-O bonds (i.e. 2.579 Å). Further we find that the thermal ellipsoid for Na1/Ca1 is elongated along the [100] direction and flattened in the two perpendicular directions. The smallest bond length of 2.364(9)Å along [001] direction seems to correlate well with the small value of β_{33} in the same direction, as has been noted for pure $NaNbO_3$ also. The high isotropic $B_{equivalent}$ of Na1/Ca1 for the composition x=0.1 decreases for the composition x=0.2 due to the fact, that the average of bond lengths Na/Ca-O in the Pbnm phase is 2.587Å (counting neighbours within 2.9 Å) which is smaller than the average of the Na1/Ca1-O bond lengths for pure $NaNbO_3$. It is also

Table 1: Refined structural parameters of NN-0.10CT using orthorhombic space group Pbma

Atoms	Positional coordinates			Thermal Parameters B (Å^2)
	X	Y	Z	
Na1 / Ca1	0.750	0.000	0.244 (3)	β_{11}= 0.019 (4), β_{22}= 0.008 (8), β_{33}= 0.007 (4), β_{12}= -0.013 (2) $B_{equivalent}$= 3.80
Na2 / Ca2	0.777 (2)	0.2500	0.254 (3)	B= 1.47 (20)
Nb/Ti	0.2620 (4)	0.1252 (2)	0.252 (1)	B= 1.43 (20)
O1	0.250	0.000	0.329 (3)	B= 0.0 (3)
O2	0.227 (3)	0.250	0.229 (4)	B= 0.9 (4)
O3	0.039 (2)	0.1481 (7)	0.533 (2)	B= 0.6 (3)
O4	0.449 (2)	0.1135 (8)	0.955 (2)	B= 1.5 (3)
A_o=5.5430 (2)Å, B_o= 15.5385 (6) Å, C_o=5.4888 (2)Å, Volume=472.76 (3) Å^3				
R_p=10.4, R_{wp}=13.0, R_{exp}=8.75, R_B=8.51, χ^2= 2.22				

Table 2: Refined structural parameters of NN-0.20CT using orthorhombic space group Pbnm

Atoms	Positional coordinates			Isotropic Thermal Parameters B (Å^2)
	X	Y	Z	
Na/Ca	0.003 (1)	0.521 (1)	0.25	1.08 (4)
Nb/Ti	0.00	0.00	0.00	0.24 (1)
O1	-0.072 (1)	0.012 (2)	0.25	0.78 (2)
O2	0.217 (1)	0.286 (1)	0.031 (1)	0.01 (1)
A_o= 5.4695(1)Å , B_o=5.5133(1)Å, C_o= 7.7719(1)Å, Volume=234.362(7)Å^3				
R_p=8.45, R_{wp}=11.2, R_{exp}=9.50, R_B=3.88, χ^2= 1.40				

interesting to note that significantly larger mean-square displacements in one direction suggests disorder of this site in NN-xCT with x=0.10 which probably leads to destabilization in the orthorhombic Pbma phase.

The structural results presented above clearly show, that the increase in the dielectric permittivity in the composition range $0.10 < x < 0.20$ with a peak at $x \approx 0.16$ is linked with the change of crystal structure from orthorhombic Pbma space group for $x \leq 0.10$ to the Pbnm space group for $x \geq 0.20$. A similar peak in the composition dependence of the dielectric permittivity, is known to be linked with a change of crystal structure, from tetragonal to

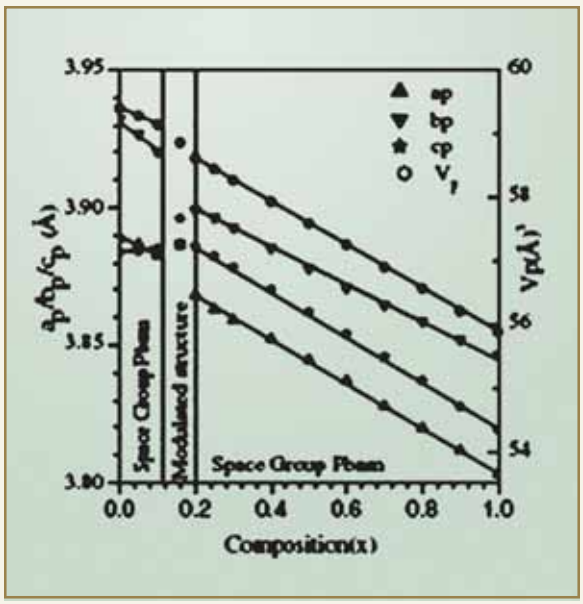

Fig. 3: Variation of the (a) equivalent elementary perovskite cell parameters (a_p, b_p, c_p) and (b) volume (V_p) with composition(x) for NN-xCT at room temperature. Dotted region corresponds to MPB.

pseudorhombohedral, in the MPB ceramics like PZT and PMN-PT. In these MPB ceramics, new monoclinic phases have been discovered in the MPB region. The fact that new superlattice reflections appear in NN-xCT ceramics for $0.10 < x < 0.20$ suggests, that there is an intermediate phase in this system also, whose structure is different from those for $x \leq 0.10$ and $x \geq 0.20$. The new superlattice reflections, shown with arrows in Fig. 2, could be indexed using an orthorhombic cell of $\sqrt{2}a_p$, $14\sqrt{2}b_p$, $2c_p$, as confirmed by *Le-Bail* profile fitting technique. This unit cell indicates that the structure of MPB phase of NN-xCT is a modulated structure, in which the lattice parameter along [010], is ~14 times the B_o lattice parameter of the Pbnm phase. Modulation periods less or more than $14B_o$ could not account for the observed peak positions. Fig. 4 depicts the *Le Bail* fits for $13B_o$, $14B_o$ and $15B_o$ modulations for NN-0.16CT. It is evident from this figure, that an orthorhombic cell size of A_o, $14B_o$, C_o, where A_o, B_o,C_o are the cell parameters of the Pbnm phase (for $x > 0.16$), accounts extremely well for the new reflections.

Notwithstanding the striking similarity of the NN-xCT system, with the well known MPB systems like PZT and PMN-xPT, there is a very significant difference between the two systems. The NN-xCT ceramics are all non-ferroelectric at room temperature and therefore are also non-piezoelectric in the sintered ceramic form. No polarization hysteresis loop was observed even for the intermediate composition range $0.10 < x < 0.20$, in which the dielectric permittivity shows a peak and powder x-ray diffraction data exhibits new reflections. The well known PZT and PMN ceramics with MPB characteristics are, on the otherhand, ferroelectric and strongly piezoelectric at room temperature. In all the ferroelectric MPB ceramics, it is now known

Table 3: Na/Ca-O Bond lengths for NN-xCT with x=0.10 and x=0.20 for Na/Ca-O bonds

NN-0.10CT (Pbma)	NN-0.10CT(Pbnm)
(NA1/Ca1)-(O1) X 2: 2.810(4)	(Ca/Na)-(O1): 2.973(9)
(NA1/Ca1)-(O1): 3.15(2)	(Ca/Na)-(O1): 2.602(9)
(NA1/Ca1)-(O1): 2.34(2)	(Ca/Na)-(O1): 2.364(9)
(NA1/Ca1)-(O3) X 2: 3.223(14)	(Ca/Na)-(O1): 3.118(9)
(NA1/Ca1)-(O3) X 2: 2.853(14)	(Ca/Na)-(O2) X 2: 2.443(6)
(NA1/Ca1)-(O4) X 2: 2.904(15)	(Ca/Na)-(O2) X 2: 3.174(6)
(NA1/Ca1)-(O4)X 2: 2.351(14)	(Ca/Na)-(O2) X 2: 2.715(6)
(NA2/Ca2)-(O2): 3.05(2)	(Ca/Na)-(O2) X 2: 2.708(6)
(NA2/Ca2)-(O2): 2.50(2)	
(NA2/Ca2)-(O2): 2.67(3)	
(NA2/Ca2)-(O2): 2.85(3)	
(NA2/Ca2)-(O3) X 2: 2.641(16)	
(NA2/Ca2)-(O3) X 2: 2.365(15)	
(NA2/Ca2)-(O4) X 2: 3.241(16)	
(NA2/Ca2)-(O4) X 2: 2.592(15)	

that one or more monoclinic phases are present in the MPB composition range. In the non-ferroelectric NN-xCT system also, we find the presence of a new orthorhombic phase with a long modulation period (14 times) along the B_o direction of Pbnm phase.

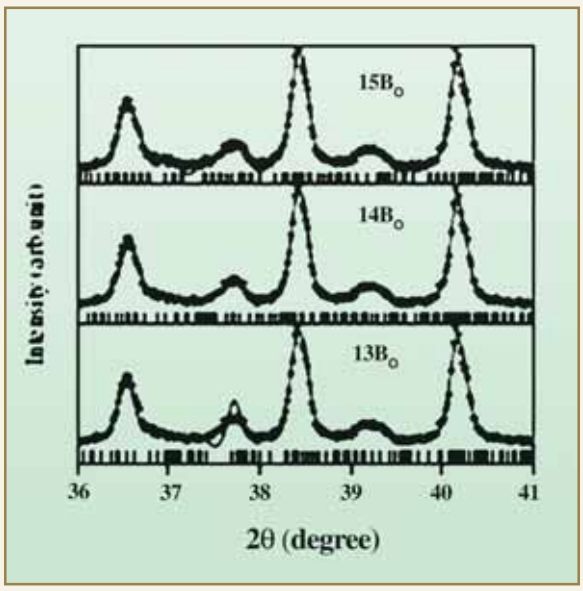

Fig. 4: *Le Bail* fits of NN–xCT with x=0.16 in the 2θ range 36-41 degrees for $13B_o$, $14B_o$ and $15B_o$ modulations

In conclusion, we have shown that in the mixed system $(1-x)NaNbO_3$-$xCaTiO_3$, the dielectric permittivity shows a peak at x~0.16 in the composition range $0.10 < x < 0.20$, similar to that observed in the well known morphotropic phase boundary ceramics. The peak in the dielectric permittivity of NN-xCT at $x \approx 0.16$ is linked with a change of space group from Pbma for $x \leq 0.10$ to Pbnm for $x \geq 0.20$, through an intermediate long period modulated orthorhombic phase, whose lattice parameter is ~14 times the lattice parameter of the Pbnm ($CaTiO_3$) phase in the [010] direction, corresponding to a modulation wavevector q~[0,1/14,0]. Unlike the well known MPB systems, this MPB system is non-ferroelectric and non-piezoelectric at room temperature.

ABOUT THE AUTHORS

Dr. S. K. Mishra completed his post graduation and Doctoral degree from Banaras Hindu University and joined the Solid State Physics Division, BARC as a K. S. Krishnan Research associate in 2005. Subsequently he was absorbed in the same division in 2006. He is a recipient of BHU prize for standing first in B. Sc. (Physics) examination. He is currently working on neutron scattering studies, Lattice dynamical calculations and impedance spectroscopy studies of ferroic/multifunctional materials.

Mr. P.S.R. Krishna received M.Sc.(Physics) degree from the University of Hyderabad and joined the Solid State Physics Division in 1988 from the 31st Batch of BARC Training school. His main interest is neutron diffraction from materials. He has designed and installed the present versions of High-Q diffractometer and Powder diffractometer in the Dhruva reactor, which are national facilities. He has used powder diffractometer for studying structures of many Ferroic materials, CMR materials and magnetic materials. Using High-Q diffractometer he has studied structures of many types of oxides and chalcogenide glasses along with H-bonded simple alcohols.

बीएआरसी न्यूजलैटर
BARC NEWSLETTER

SYNTHESIS AND CHARACTERIZATION OF COPPER NANOSTRUCTURES ON SILICON SUBSTRATES

Prajakta Kanitkar and R. C. Aiyer
Department of Physics, University of Pune

and

Shashwati Sen, K.P. Muthe and S.K. Gupta
Technical Physics and Prototype Engineering Division

This paper was awarded the Best Poster Award at the International Symposium on Vacuum Science and Technology, held at TIFR, Mumbai, from Nov. 28-30, 2007

ABSTRACT

Vacuum deposition technique was utilized, for the synthesis of copper nanostructures on (111), (100) and (110) oriented silicon substrates, at an optimized substrate temperature of 750°C. The samples were characterized by SEM, AFM and XPS. Morphology of copper structures was found to be governed by orientation of the substrate. It was possible to realize the growth of triangular, square-like and rod-shaped geometries, by choosing an appropriate substrate orientation. This variation of Cu structures is attributed to the surface reconstruction on silicon, that occurs at high temperature.

Introduction

Nanostructured materials are of great interest, because of their spectrum of applications in nanodevices and nanoelectronics. Nanostructures have unique physical, chemical and optical properties as their size is intermediate between the bulk and atomic scales. As the bulk is reduced to the nano scale, the electronic motions get confined i.e. fewer energy states are available for the electrons, which result in a modified band gap in the nanomaterials. Further, nanomaterials have increased surface-to-volume ratio, that helps enhancement of chemical interactions. These properties of nanoparticles may be useful in biological, optoelectronics and gas sensing applications and semiconductors. In futuristic alternative metallization schemes for ultra large-scale integrated technology, Cu is being considered as a potential replacement for Al interconnects. Therefore, preparation of it's nanostructures has immediate relevance to the semiconductor technology. In this respect, the studies addressing the synthesis of it's dense arrays, especially on Si and the interaction of Cu film with Si surface, assume particular importance. Synthesis of copper nanoparticles has been extensively reported by various techniques which include chemical routes, electrochemical method and template- assisted synthesis. The yields achieved by these processes are low and involve multiple steps. Further, it is difficult to assemble them on Si substrates for use in nano-devices.

Experimental

Cu thin films were deposited on Si substrates of various orientations, by a simple vacuum deposition technique, in a turbo-molecular pump-based vacuum system (Make:Hind High Vaccum Pvt. Ltd. model No.15 F6). The depositions were carried out at a vacuum of 5×10^{-6} m bar. Prior to deposition, the substrates were cleaned by ultrasonication technique in organic solvents. The substrates were mounted on a heater whose temperature was measured through a thermocouple and maintained, using a temperature controller to an accuracy of $\pm$ 5°C. The substrate temperature was varied between 550-850°C and was maintained at constant value for two hours, prior to each deposition. The depositions were carried out using copper wire of 99.99 % purity, loaded in a Molybdenum boat. The film thickness was varied from 10 to 750 Å using a quartz crystal thickness monitor, placed near the substrate holder at normal angle to the incoming Cu flux. The rate of deposition was maintained at 1Å/ sec. After deposition, the substrates were cooled to room temperature for 30 mins.

The samples were characterized by a Scanning Electron Microscope (SEM) VEGA MV2300T/40 (TS 5130 MM TESCAN) to study their morphology and shape. Atomic Force Microscope (AFM) model JEOL JSPM 5200, with a rectangular cantilever of Si_3N_4 (length 200 mm and width 40 mm), having a force constant of 3 N/m was also employed, to study the morphology. EDX spectra were recorded, to analyze the purity of deposited films. X-ray Photoeletron Spectra were recorded using Al K_a source (CX-700), incorporated with MBE system EVA 32 R&D (Make: RIBER) and a MAC-2 electron energy analyzer. The binding energy scale was calibrated using Au $4f_{7/2}$ line of 83.9 eV. For XPS, measurements were performed immediately after depositions, in order to minimize oxidation of the surface of the sample.

Results and Discussion

At substrate temperatures of 550-650°C , we observed continuous films with spherical grains on all the substrates. As the substrate temperature was increased, islands of definite shapes for different orientations of Si substrates were obtained. Fig. 1 shows an SEM image of 60 Å thick Cu film, deposited at 750°C on Si(111) substrate. SEM images of similar films on Si(100) and Si(110) substrates are shown in Figs. 2 and 3 respectively. It is observed that nanostructures of triangular, square and rod-shaped patterns are distributed uniformly on (111), (100) and (110) oriented substrates respectively. The structures are found to be dispersed uniformly over the substrates and are oriented in a particular direction, with respect to each other. The length of the edge of the triangular islands on Si(111), is of the order of 300-400 nm. The sides of square islands on Si (100) is around 350 nm while the nanorods on Si(110) are of nearly 50 nm width and 2-3 μm in length. On varying the thickness of deposited Cu film, the size of the nanostructures was found to remain almost constant, in the thickness range of 10-100 Å. However, in case of Si(100) substrate, with increase in thickness of the Cu film, few of the square-like patterns were found to get elongated, forming rod-like structures. The EDX spectra confirmed the structures to be that of pure copper.

The AFM images of 10 Å Cu films, deposited on different substrates are shown in Figs. 4 - 6. It is

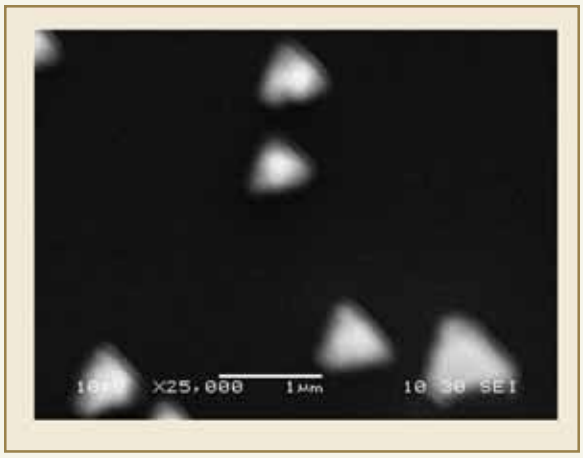

Fig.1: SEM micrograph of 60 Å Cu film deposited on Si(111) at 750°C

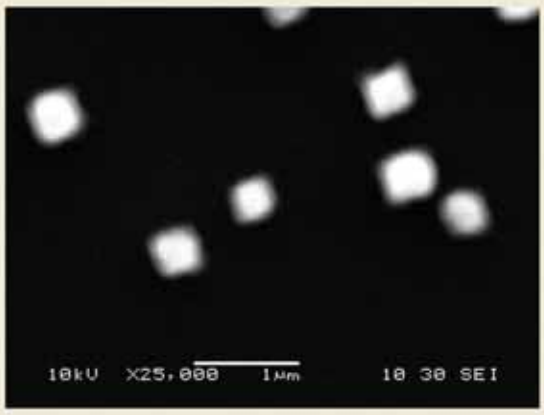

Fig. 2: SEM micrograph of 60 Å Cu film deposited on Si(100) at 750°C

Fig. 3: SEM micrograph of 60 Å Cu film deposited on Si(110) at 750°C

observed that the nano-structures are tapered with larger thickness at the centre of the islands. The height of these nanostructures for a 10 Å thick film on all the substrates, was found to be in the range of 200 nm. With increase in film thickness, the height of the nano structures was found to increase. The height for a film thickness of 100 Å was observed to be around 450 nm. AFM images also showed layered structures.

X-ray photoelectron spectroscopy (XPS) was carried out on 100 Å thick Cu films, deposited on Si(111) substrate at 750°C. Fig. 7 shows XPS spectra in Cu 2p region. The two peaks corresponding to Cu 2p1/2

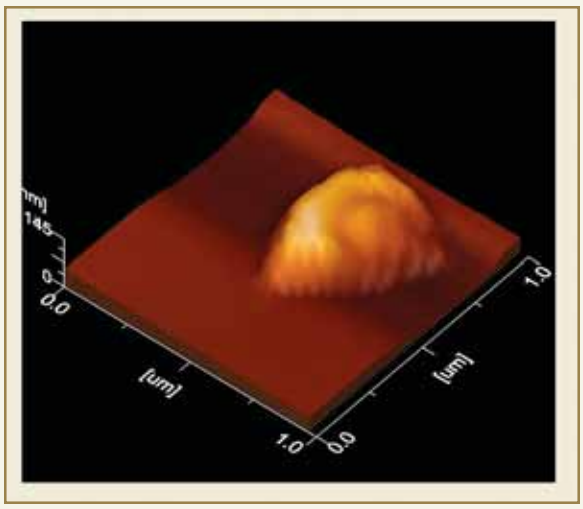

Fig. 4: 10 Å Cu deposition on Si(111) at 750°C

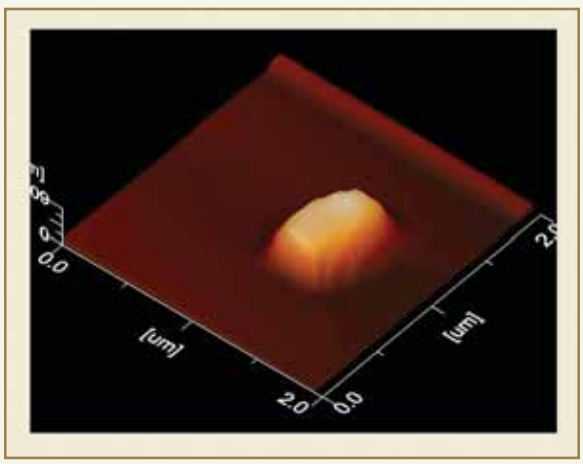

Fig. 5: 10 Å Cu deposition on Si(100) at 750°C

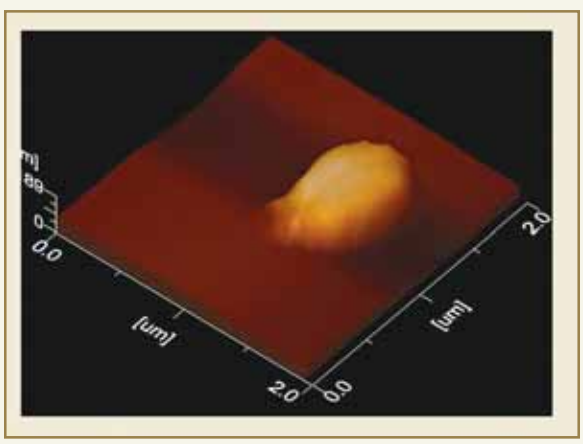

Fig. 6: 10 Å Cu deposition on Si(110) at 750°C

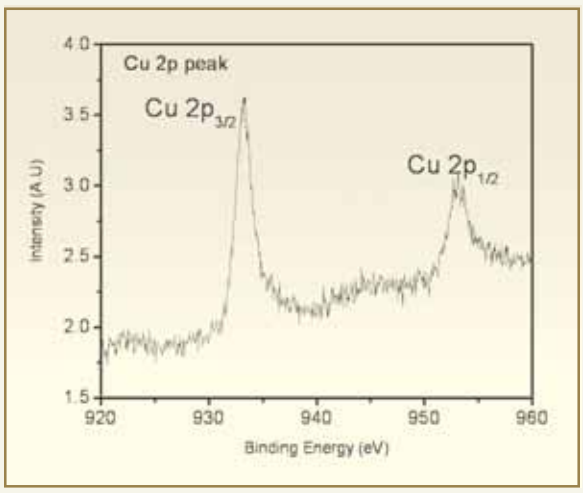

Fig. 7: XPS spectra of Cu nanostructure deposited on Si(111) substrate for Cu 2*p* peak

and Cu 2p3/2 are observed. The absence of any satellite peaks, indicates that there is no oxide formation on the surface. The Auger parameter calculated for the copper peak, was also found to correspond to metallic copper. The O 1S spectra are shown in Fig. 8. This peak can be deconvoluted into two peaks the one which corresponds to the adsorbed oxygen and the presence of SiO2 on the surface of the substrate, further confirms, that the observed nanostructures are of pure copper.

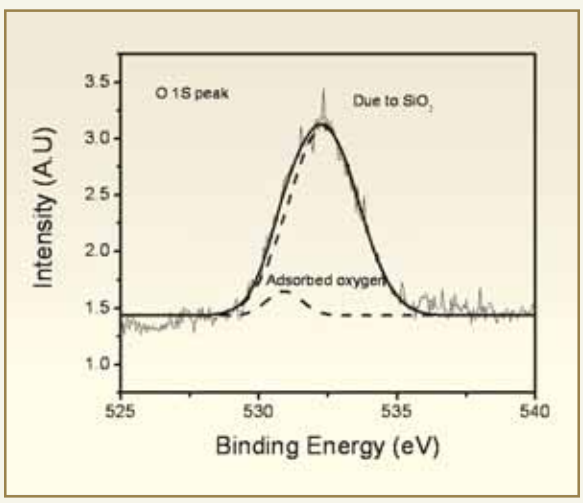

Fig. 8: XPS spectra of Cu nanostructure deposited on Si(111) substrate for oxygen 1*s* peak

We have observed the formation of self assembled nanostructures of copper on silicon substrates, with the orientation of the substrate playing an important role on the shape of the nanostructure. In some studies, very thin films (few monolayers) of different metals have been deposited, on atomically clean and reconstructed Si substrates the mechanism for the growth of different shapes has not been extensively investigated.

The nanopatterns formation on the silicon substrates has been attributed to the reconstruction of silicon surface occuring at high temperatures. The reconstruction takes place at solid vacuum interface, in order to minimize the dangling bonds and attain minimum energy configuration. The dangling bonds get rearranged to minimize the surface energy. When adatoms approach these substrates, they get attached to the sites of minimum energy on reconstructed surface and attain their shape.

In case of Si(111) substrate, the most commonly reported surface reconstruction is the Si(111)-(7 x 7). The driving force for the formation of the (7 x 7) reconstruction, is the reduction of the number of dangling bonds by the formation of *dimers*, *adatoms* and a *stacking fault*. The unit cell of (7 x 7) reconstruction of the Si(111) surface is of rhombic shape which consists of two different triangular Half Unit Cells (HUC), one with a *stacking fault* (faulted half) and one without a *stacking fault* (unfaulted half) with respect to the bulk. The nucleation of adatoms on this surface, takes place at these triangular half unit cells and thus we obtain triangular nanostructures on reconstructed Si(111) susbtrate.

The most generally reported reconstruction of the Si(100) surface, is the Si(100)-(2x1). Prior to the reconstruction, each Si atom on the surface has two dangling bonds. During the reconstruction, the Si atoms of the surface layer form covalent bonds with adjacent surface atoms and form dimers. These dimers arrange themselves in a row, perpendicular to

the dimer axis. In the initial stages of growth, the adatoms nucleate on the dangling bonds of the dimer row and form a square-like nano-structure. Since the mobility of atoms is high along the dimer rows and low across them, with increase in number of adatoms on the Si(100)-(2x1) surface, the atoms arriving on the sides of the square islands are transported to ends along one direction, resulting in 1-D growth. Thus the square islands get elongated resulting in the formation of Cu nanowires on Si(100) surface at few places at higher thickness. The wires are oriented along two perpendicular directions because of the stacking sequence in the Si(100) substrate, the dimers are rotated through 90° on two adjacent terraces, separated by a monoatomic step.

Si(110) surface exhibits a 16 x 2 reconstruction. The Adatom-Tetramer-Interstitial (ATI) reconstruction in this case, yields the lowest surface energy for models of the Si(110) 16 x 2 surface with terraces. Similar to the above two cases, the arriving adatoms nucleate on these trenches and grow along the direction of the unit cell of the reconstructed surface. This yields nanorods with their long axis parallel to each other.

Thus, the surface reconstruction of Si substrate surface at 750°C explains the formation of the self assembled nanostructures of Copper. The nanopatterns of Cu on Si may have technological applications in various nanodevices.

Conclusion

We have fabricated a self-assembled array of copper nanostructures on silicon substrates of different orientations. The islands formed are distributed uniformly on the substrate and are aligned along specific directions. The substrate temperature is found to play a key role in the island formation as pattern formation is found to occur only at a temperature of 750°C. The reconstruction of Si surfaces at higher temperatures is believed to be responsible for the shape of these nanostructures.

ABOUT THE AUTHORS

Dr. (Ms.) Shashwati Sen joined BARC in 1996 through the 40th Batch of Training School. She obtained her Ph.D. degree from Mumbai University in 2003 for her work on "Dissipation mechanism in high temperature superconductors."Currently she is working on gas sensors based on elemental and metal oxide semiconductors, thin films and nanostructures.

ABOUT THE AUTHORS

Mr. K.P. Muthe is working in the field of thin film growth and characterization. He has studied the growth behaviour of HTSC films using MBE. He has extensively used X-Ray Photoelectron spectroscopy to solve several material related problems like corrosion and mechanisms of gas detection and contributed to around 50 publications.

Dr. S.K. Gupta joined BARC in 1975 and is presently Head of Thin Films Devices Section in TPPED. Over the years, he has worked on space quality silicon solar cells, high temperature superconductor thin films and single crystals, gas sensors and thermoelectric materials. He has carried out extensive studies on vortex dynamics in superconductors. He is a member of the National Academy of Sciences, India.

बीएआरसी न्यूजलैटर
BARC NEWSLETTER

BIOREGULATORY ROLE OF *"THIOUREA"* IN MULTISTRESS TOLERANCE OF THE INDIAN MUSTARD (*BRASSICA JUNCEA*)

A.K. Srivastava, N.K. Ramaswamy and S.F. D'Souza
Nuclear Agriculture and Biotechnology Division

This paper was selected for the "New Phytologist Trust Award" during the 18th New Phytologist symposium on "Calcium Based Signaling Systems in Plants" held at Dublin, Ireland, during December 5-7, 2007

ABSTRACT

Thiourea (TU) application has been identified as a novel bioregulator technology, for imparting stress tolerance in crop plants. TU application has shown normal growth of *Brassica juncea* seedlings under salinity stress. In order to study the molecular mechanism underlying TU mediated response, genome wide transcriptome profiling of *Brassica juncea* seeds was undertaken. In one hour soaking time, the expression level of 111 genes was altered in response to NaCl treatment. Of these, 33 genes were regulated towards the level of distilled water control if thiourea was added along with NaCl treatment. These genes were classified as *'Thiourea responsive genes'* including particularly those associated with calcium signaling, oxidative stress and hormonal regulation. The effectiveness of thiourea under the combined effect of salt, drought and cold stress was also established, by validating the expression level of important thiourea responsive genes through real-time PCR. Thiourea mediated modulation in the gene expression varied and depended upon the magnitude of stress present in the system. The time kinetics studies showed that one hour incubation time was sufficient for the maximal effect of thiourea action. In conclusion, the result suggested that thiourea mediated changes in the expression profile of various stress responsive genes, can impart stress tolerance in *Brassica juncea*. The results imply that, thiourea can be considered as an important bioregulatory molecule, for increasing stress tolerance of crops under field conditions.

Introduction

In the current scenario of increasing demand for sustainable agriculture, understanding and improving crop plants for environmental stress tolerance, has become necessary. Abiotic stress factors cause extensive losses to agricultural production worldwide. Globally, there has been extensive research concern to achieve stress tolerance in crop plants without compromising their yield. The technique of developing stress tolerant plants, began with the transfer of individual functional genes either through plant breeding or genetic engineering. Both the approaches have so far generated wealth of information resource and germplasm base, but could not give much impact as far as consistency, reliability and visible effect at the field level are concerned. An alternative approach in this direction has been the application of some external effector molecules, which can induce the expression of critical signaling molecules involved in stress tolerance.

Presently, there is a greater research interest in identifying and employing bioregulatory molecules, which can be used to achieve the stress tolerance in crops under field conditions. In this direction, we have identified certain thiol molecules whose application not only enhances crop productivity, but also does not generate any kind of metabolic imbalances. Thiols were selected as they are well-known to maintain the redox state (–SH/-S-S- ratio) of the cell and its proper functioning under stress conditions. Three different thiol compounds [Thiourea (TU), Dithiothreitol (DTT) and Thioglycollic acid (TGA)] were selected and their effect on the performance of wheat and mustard crops was monitored in drought and salinity affected fields of Rajasthan (India). The results indicated that the pre-treatment of seeds with these compounds, enhanced stress tolerance and also increased the crop productivity. Among the three types of thiols tested at the field-level, TU was selected for further experimental investigations because of it's cost effective and eco-friendly nature.

To gain insight into the molecular mechanisms of TU induced stress tolerance, genome wide expression profiling of *Brassica juncea* seeds, soaked under different treatment conditions was sought. The time kinetics study was done to find out the optimum time required for the action of TU. All this experimental data supports the view that TU has the capability to serve as a potential bioregulatory molecule, to impart multistress tolerance in plants under field conditions.

Methodology

Plant Material; Stress Induction and Thiol Treatment

The entire study was performed on Indian mustard (*Brassica juncea*) var. TM-4. The differential phenotype of seedlings in response to TU was assessed, by observing their growth pattern under different conditions. For this purpose, four sets of genetically homogeneous seeds were surface sterilized with 30% ethanol for 3 min and then spread independently on the petriplates. The seeds were germinated under control condition for four days on a 12-h light-12-h dark cycle at 25 ^{O}C and 70% humidity. After four days of germination, 0.7 M NaCl; 0.7 M NaCl+500 ppm TU and 500 ppm TU treatments were given independently to the three sets and the remaining set was maintained as a control. Comparative growth patterns as well as relative electrolyte leakage in all the four sets were monitored after four days of treatment.

Genome wide expression analysis

For expression analysis, surface sterilized seeds were subjected to different treatments (DW; 1 M NaCl; 1 M NaCl + 500 ppm TU and 500 ppm TU) for 1 hour and then used for RNA isolation. Microarray analysis was performed as per the standard protocols of Agilent technology.

Real-time PCR

DNA-free intact RNA (10 μg) was taken from each sample separately and then subjected to cDNA synthesis using Stratagene High fidelity 1st-strand cDNA synthesis kit, as per the manufacturer's instruction. Two-step RT-PCR was chosen to avoid the problem of primer dimer formation. Real-time quantitative RT-PCR was carried out using a Corbett rotor gene 3000. Detection of real-time RT-PCR product was done using the SyBr green.

Results and Discussion

Differential phenotype of seedlings

The differences in the phenotype of *Brassica juncea* seedlings under different treatments were observed. Control seedlings showed proper germination with

normal shoot length and opened cotyledons (Fig.1-A) while the stressed phenotype was characterized by diminutive growth and unopened cotyledons (Fig. 1-B). Under similar conditions if TU was provided along with NaCl treatment, the phenotype of seedlings showed resemblance to that of the control (Fig. 1-C). Apart from this, an increase in the root length was also observed in NaCl+TU treatment, which clearly indicated that TU treatment helps in the normal growth of seedlings under NaCl treatment and also it did not have any negative impact on the growth pattern (Fig. 1-D). These observations were also reconfirmed by measuring the relative electrolyte leakage of seedlings under similar treatments. As expected, we found that the presence of TU along for with NaCl treatment resulted in ~50% reduction in the effective stress. Similarly, there was no indication of any kind of stress in the presence of TU alone (Fig. 2). In the current experiment relatively higher concentration of NaCl was employed to achieve the required signaling effect. Moreover, use of such a higher concentration was intended to establish the protective nature of TU under any field condition.

Microarray analysis

To study the differentially induced genes, genome wide expression profiling of *Brassica juncea* seeds soaked under different treatments for 1h was conducted. The sequence information of *Arabidopsis thaliana* was used,

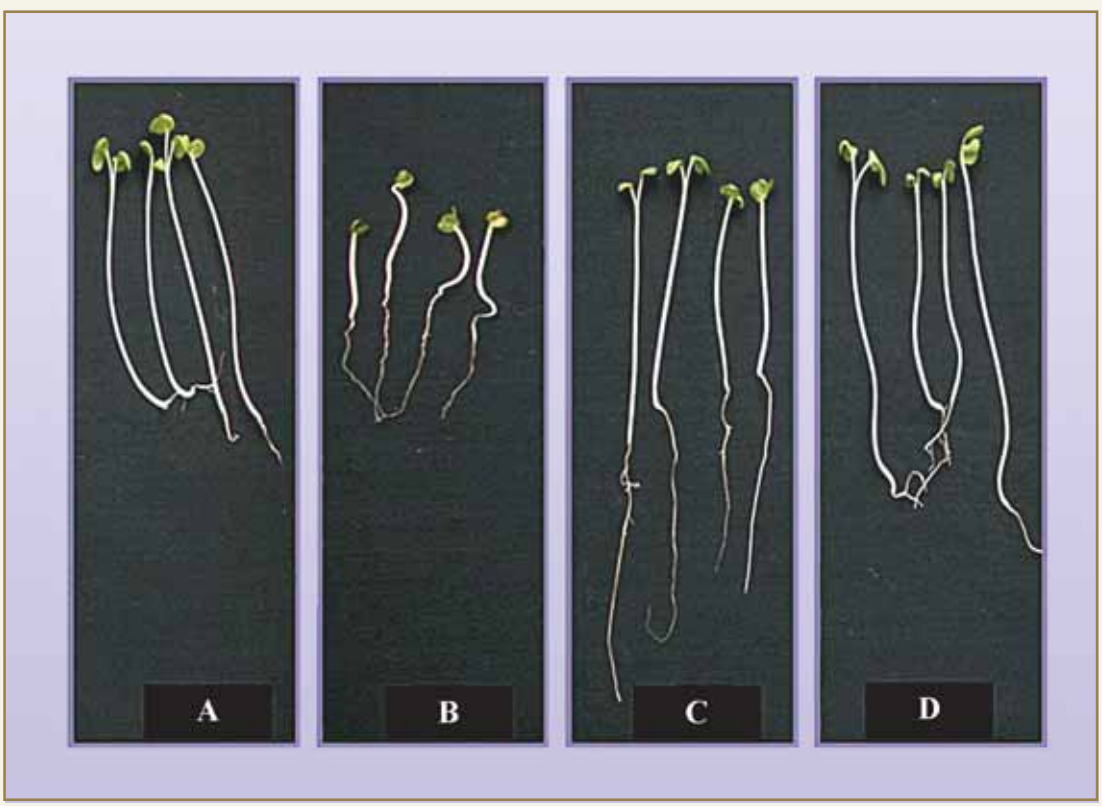

Fig. 1: Differential Phenotype of seedlings under different treatments. Panels A, B, C and D represent the differential growth pattern of 8-day old seedlings that were given different treatments of distilled water control, 0.7 M NaCl, 0.7 M NaCl+500 ppm TU and 500 ppm TU respectively on their 4th day of germination.

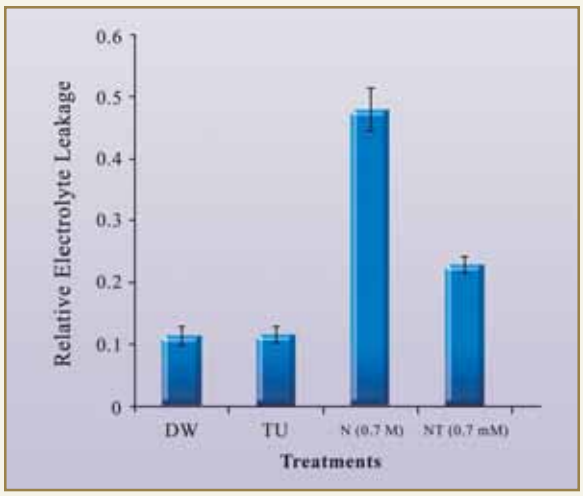

Fig. 2: Relative electrolyte leakage of 8-day old seedlings under different treatments. Seedlings were given different treatments on their 4th day of germination and then relative electrolyte leakage was measured on 8th day. The values represent the mean±S.D. of six technical and two biological replicates. The difference in mean value was found to be statistically significant in one-way anova ($p<0.01$).

the transcriptome analysis of *Brassica juncea*. The *Arabidopsis* array is an established tool for gene expression analysis of *Brassica* species, because of their close phylogenetic relationship. Thus, even with the heterologous probes used in our experiment, we obtained sufficient signal intensity after hybridization Three sets of microarray hybridizations were performed, in which the expression profile of NaCl, NaCl+TU and TU was compared with that of control. Overall, 83 down regulated and 28 up regulated ESTs were identified, in response to NaCl treatment. Clustering analysis was done on these 111 differentially expressed ESTs. This resulted into cluster 2 and 3 that corresponded to 19 down regulated and 14 up regulated genes, in response to TU treatment (Fig. 3). These 33 genes were classified as 'Thiourea Responsive Genes' and considered to be responsible for the ameliorative effects seen under NaCl+TU treatment.

The thiourea responsive genes were broadly classified in two groups according to their expression level under NaCl treatment. The set of genes which were down regulated in NaCl treatment but maintained towards the level of control in NaCl+TU treatment (Cluster-2), contained proportionally more transcription factors/post transcriptional regulatory genes, (ethylene responsive transcription factors, F-box and auxin responsive family proteins); oxidative stress related genes (Catalase and Cytochrome P450) and calcium signaling related genes (calcium transporting ATPase, calcium exchanger and calmodulin like proteins). Hence, TU mediated increase in the expression of these genes will activate the stress response mechanisms which leads to the reduction in the effective stress under NaCl+TU treatment.

Another group of thiourea responsive genes which were upregulated in NaCl but maintained towards the level of control in NaCl+TU treatment (Cluster-3) included heat shock proteins, lipid transfer proteins and few transcriptional regulators like zinc finger protein. All these genes which are well-known markers for stress induced damage and hence are over expressed in NaCl treatment. On the contrary, in NaCl+TU treatment, their levels were at par with that of control which signifies that presence of TU decreases the extent of stress induced by NaCl.

Expression profiling of thiourea responsive genes under salinity and multistress conditions

It is known that salinity results in the change of calcium signature which is more or less responsible for all kinds of damages. The extent of damage depends on the capability of the plant to revert back to the changes in calcium signature as swiftly as possible In this process, calcium transporting ATPase is one of the important genes which helps in the reversal of calcium signature. The level of this gene was found to be 0.67 and 3.97 fold downregulated in NaCl (Fig. 4A) and multistress (Fig. 5A), respectively as compared to control. However, the presence of TU in these two treatments, resulted in the reversal of expression profile. The sequential 0.4 and 4.3 fold increase in the expression

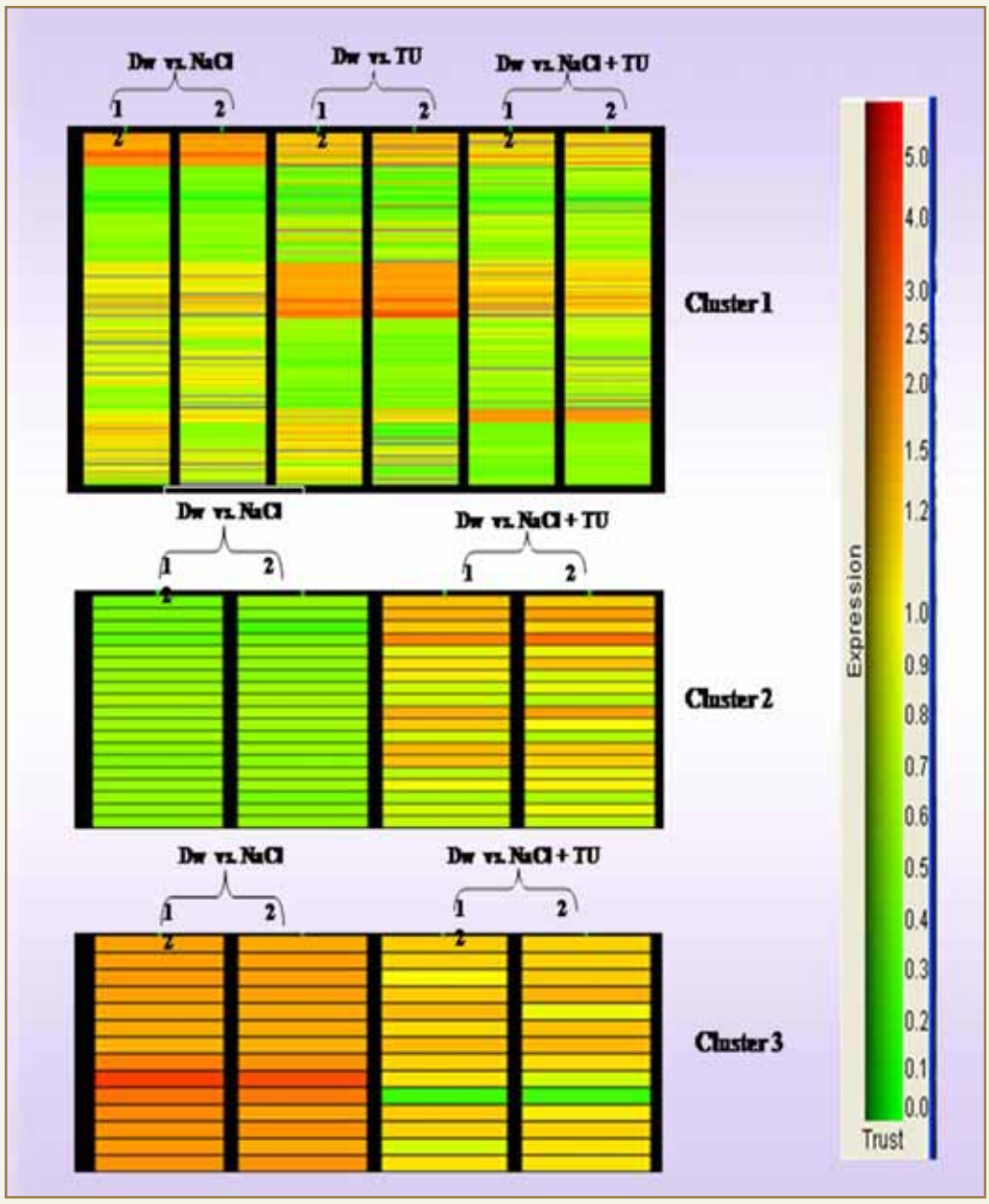

Fig. 3: Cluster analysis. All the differentially expressed genes associated with the three sets of Microarray are represented in cluster 1. Overall, 28 up regulated and 83 down regulated ESTs were identified in response to NaCl. Clustering analysis was done on these 111 differentially expressed ESTs to produce cluster 2 and 3 that corresponds to 20 (down regulated) and 15 (up regulated) genes respectively whose expression is influenced by thiourea

was observed in NaCl+TU and multistress+TU as compared to NaCl and multistress respectively. Thus, it was clear that TU treatment helps in the quick reversal of calcium signature. Another interesting feature was that, TU mediated change in the expression of calcium transporting ATPase was dependent upon the magnitude of stress. For instance, the difference in the expression level of calcium transporting ATPase

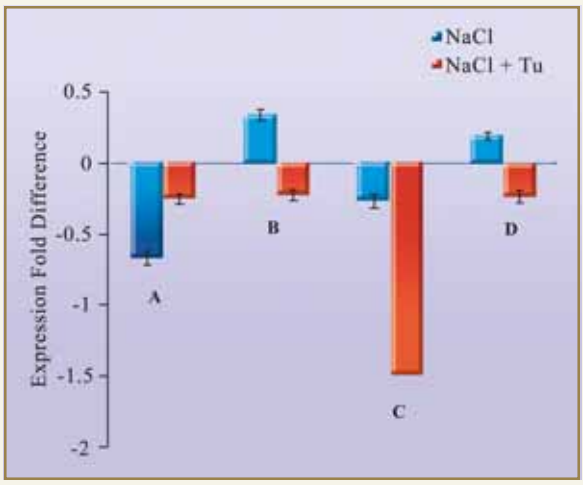

Fig. 4: Real-time expression profiling of thiol responsive genes in seeds soaked for 1 h under different treatments. Panels A, B, C and D represent the expression level of Ca-transporting ATPase, Catalase, Auxin Responsive and Ethylene responsive element binding gene respectively in seeds soaked for 1 hour in NaCl and NaCl+TU. The base line expression (0 Value on y-axis) represents the expression level of distilled water control. The values represent the mean of three technical and two biological replicates. The difference in the mean was found to be statistically significant at $p<0.01$, in one way anova test.

between multistress and multistress +TU was more prominent than that in the NaCl and NaCl+TU treatment.

The level of antioxidant enzymes is an important parameter of stress tolerance and therefore the involvement of catalase in TU functioning was evaluated. The increased expression of catalase observed under NaCl treatment can be explained, as an in built response mechanism of plant (Fig. 4B). On the contrary, in the NaCl+TU treatment it was 0.22 fold downregulated which indicated that TU reduces the extent of oxidative stress and hence the upregulation of catalase was not required. Unlike NaCl alone, under multistress treatment, catalase was 2.13 fold downregulated as compared to control (Fig. 5B), which showed the inability of plants to respond towards multistress. However, in multistress+TU treatment, the expression of catalase was upregulated by 0.3 fold (Fig. 5B). This again signifies that TU mediated change in gene expression is dependent upon the requirement of the system.

In stress management, auxin and ethylene mediated responses play an important role. Therefore, the possible involvement of these elements in TU mediated stress tolerance was investigated. Auxin regulates a myriad of processes in plants where auxin responsive gene (Aux/IAA) plays a key role. We found that the level of auxin responsive gene was 1.23 times lower in NaCl+TU, as compared to NaCl (Fig. 4C). Hence it is clear, that TU enhanced the auxin mediated response under salinity stress. As is evident from Fig. 5C, the expression of auxin responsive gene remained downregulated both in multistress and multistress+TU treatments as compared to the control. This indicates the complex regulation of auxin-mediated signaling under multistress environment. Ethylene Responsive Element Binding gene (EREB) is another unique group of plant transcription factor, but it's biological significance is not fully understood. In case of NaCl+TU, it's level was 0.42 times lower as compared to NaCl (Fig. 4D). This logically suggests that in the presence of TU, the enhanced expression of this transcription factor for combating stress is not required. On the contrary, under multistress+TU it was 3.3 times upregulated as compared to multistress (Fig. 5D). This further confirms the ability of TU, to modulate the gene expression as per the demand of the system. In NaCl+TU, the level of auxin responsive gene was 1.23 times lower (Fig. 4C) as compared to NaCl. However, repression was observed both in multistress and multistress+TU treatments as compared to the control (Fig. 5C). In case of NaCl+TU, the expression level of EREB was 0.42 times lower as compared to NaCl (Fig. 3D). On the contrary, under multistress+TU, it was 3.3 times higher as compared to multistress treatment (Fig. 4D).

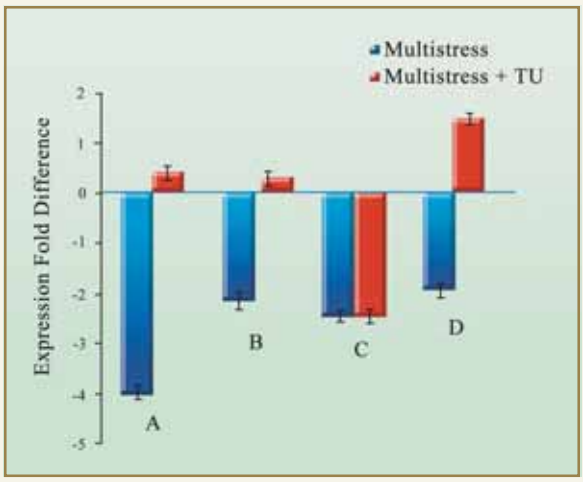

Fig. 5: Real-time expression profiling of thiol responsive genes in seeds soaked for 1 h under different treatments. Panels A, B, C and D represent the expression level of Ca-transporting ATPase, Catalase, Auxin Responsive and Ethylene responsive element binding gene respectively in seeds soaked for 1 hour in multistress and multistress+TU. The base line expression (0 Value on y-axis) represents the expression level of distilled water control. The values represent the mean of three technical and two biological replicates. The difference in the mean was found to be statistically significant at $p<0.01$, in one way anova test.

Temporal regulation of calcium transporting ATPase

The temporal regulation of calcium transporting AT Pase was checked in the roots of 8-day old seedlings (Fig. 6). Roots were chosen as they remain in direct contact with stress treatment. The time kinetic studies revealed that the expression was downregulated at 15 min in all the three treatments of NaCl, NaCl+TU and TU as compared to control. However, the maximum downregulation was observed in case of NaCl treatment. After 15 min, in TU alone the expression continued to increase until 30 min and then stabilized, while in case of NaCl and NaCl+TU treatments, the expression decreased till 30 min and then increased significantly up to 60 min. The expression of Calcium transporting ATPase at 60 min was two times higher in NaCl+TU than NaCl alone. This showed that 60 min was sufficient time for TU to reverse the expression profile observed in case of NaCl treatment.

Summary

In summary, it is demonstrated that TU reduces the extent of stress induced damage and the entire process can be summarized as the modulated expression profile of a set of genes under stress condition. Further investigations are required in this direction, to elucidate the exact mechanism of TU action. The application of TU is cost effective and eco-friendly, which permits it's simple usage. Thus, the application of thiourea as a bioregulatory molecule can augment new avenues for basic as well as for applied research in the area of stress management.

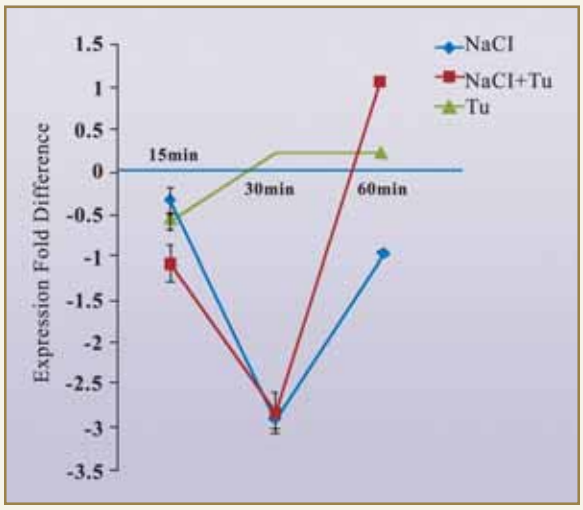

Fig. 6: Temporal regulation of Calcium transporting ATPase in roots of 8-day old seedlings. Expression level of Ca-transporting ATPase was monitored at different time intervals of 15, 30 and 60 min in roots of 8-day old seedlings given NaCl, NaCl+TU and TU treatments and represented in comparison with the distilled water control (0 Value on y-axis). After 60 min. incubation time, Ca-transporting ATPase is upregulated in NaCl+TU while in NaCl it was still downregulated as compared to control. The values represent the mean of three technical and two biological replicates. The difference in the mean was found to be statistically significant at $p<0.01$, in one way anova test.

ABOUT THE AUTHORS

Mr. Ashish Kumar Srivastava graduated from the 48th Batch of Bioscience BARC Training School in 2005 and joined the Nuclear Agriculture and Biotechnology Division, BARC. He did his M.Sc. Biotechnology from Guru Nanak Dev University, Amritsar. He has been actively engaged in understanding the molecular mechanism underlying the thiol mediated stress tolerance in the Indian mustard (*Brassica juncea*)

Dr. N. K. Ramaswamy's areas of research interest include stress physiology and biochemistry of crop plants with an emphasis on photosynthesis and crop productivity. He has developed a process for production of banana juice from ripe banana and this technology has been transferred to ITE Matrix Co., Thailand. He has three enzymes listed / classified in the International Union of Biochemistry and has more than 100 publications.

Dr. S. F. D'Souza joined BARC after graduating from the 15th Batch of Training School. He is currently the Associate Director-A, Biomedical Group and Head, Nuclear Agriculture and Biotechnology Division, BARC Mumbai. His major research interests are in the field of Enzyme and Microbial Biotechnology with special reference to immobilized biomaterials for use in bioprocessing, biosensors and bioremediation. He has authored about 150 scientific papers.

बीएआरसी न्यूज़लेटर
BARC NEWSLETTER

SMALL ANGLE SCATTERING FOR CHARACTERIZING SOFT MATTER

V.K. Aswal
Solid State Physics Division

Dr. Aswal received the SCOPUS Young Scientist Award in Physics for the year 2007

ABSTRACT

Small-angle scattering is a powerful technique to study soft matter. This technique covers a length scale (1 -100 nm), where most of the structures of soft matter are found. Small angle scattering can be used, to obtain information about the structure (shape and size), composition and interactions in soft matter. The possibility to vary the contrast by different ways, makes this technique very special. This helps to enhance the weak scattering signals and study of different components of the systems. We have extensively used small angle scattering for characterizing a variety of materials in soft matter such as micelles, ferrofluids and proteins.

Introduction

Soft matter deals with materials, which are easily deformable by external stresses, electric or magnetic fields or even by thermal fluctuations. These materials typically possess structures at mesoscopic length scales, which are much larger than atomic or molecular scales. Interestingly, the structure and dynamics at the mesoscopic scales, determine the macroscopic physical properties. The goal of research in this field has been to probe and understand this relationship.

Examples of materials in soft matter include polymers, colloids, surfactants, biopolymers, gels, liquid crystals, foams and emulsions. Fluid interfaces also, often play an essential role. Moreover, avalanches in granular materials and the non-equilibrium dynamics of disordered systems are also studied. Soft matter research often provides an important underpinning of biophysics, while other important research areas include biomaterials and biopolymers.

Soft matter research addresses questions concerning the microstructure, kinetics, dynamics and rheology of complex and nanostructured materials. The materials used for studies are both synthetic and biological materials and interests vary from fundamental science to technological applications. This involves *in-situ* processing, site-selective chemistry and tailoring of molecular assemblies as well as structure determination of thin organic films and membranes or diffraction from fibres, small unit-cell systems and biological entities. Small angle scattering of x-rays and neutrons are well studied tools, to study structure and interaction of soft matter. These methods cover a size range from a few nanometers up to hundreds of nanometers.

Herein, we present the usefulness of small-angle scattering as applied to soft matter and some of our results, where in these techniques have been used.

Small Angle Scattering

The small-angle scattering intensity $I(Q)$ as a function of scattering vector Q ($=4\pi\sin\theta/\lambda$,, where 2θ is the scattering angle and l is the wavelength of the incident radiation) for a soft matter system consisting of particles dispersed in a solution can be expressed as

$$I(Q) = nP(Q)S(Q) \quad (1)$$

where n is the number density of the particles. $P(Q)$ is the intraparticle structure factor and depends on the shape and size of the particles. $S(Q)$ is the interparticle structure factor and is decided by the spatial distribution of the particles. $P(Q)$ is given by the integral

$$P(Q) = \left| \int (\rho(\mathbf{r}) - \rho_s) \exp(i\mathbf{Q}.\mathbf{r}) d\mathbf{r} \right|^2 \quad (2)$$

In the simplest case of a monodispersed system of homogeneous particles with a radius R, $P(Q)$ is given by

$$P(Q) = (\rho - \rho_s)^2 V^2 \left[\frac{3J_1(QR)}{QR} \right]^2 \quad (3)$$

where $V=(4/3)\pi R^3$, ρ_s is the scattering length density of the solvent and ρ is the mean scattering length density of the particle.

The expression for $S(Q)$ depends on the relative positions of the particles. In case of isotropic system, $S(Q)$ can be written as

$$S(Q) = 1 + 4\pi n \int (g(r) - 1) \frac{\sin Qr}{Qr} r^2 dr \quad (4)$$

where g(r) is the radial distribution function. g(r) is the probability of finding another particle at a distance r from a reference particle centered at the origin. The details of g(r) depend on the interaction potential U(r) between the particles.

The term $(\rho - \rho_s)^2$ is referred to as a contrast factor. The above equations are valid both for the SAXS and the SANS experiments. The contrast factor, however, depends on the radiation used. The values of ρ and ρ_s depend on the chemical composition of the particle and the solvent and are different for neutrons and x-rays. The differences in ρ values for neutrons and x-rays arise from the fact, that while neutrons are scattered by the nucleus of an atom, the x-rays are scattered by the electron clouds around the nucleus. It is seen that as one goes across the periodic table, the neutron scattering lengths vary in a random way and the x-ray scattering lengths increase with the atomic number of the atom. For example, unlike x-rays where ρ_s (H_2O) = ρ_s (D_2O), the values of ρ_s change significantly for neutrons when solvent is changed from H_2O to D_2O. X-rays are scattered more strongly from heavy elements (e.g. Cl^-, Br^- etc.) as compared to light elements such as C, H etc.

Some Results

The type of sample that can be studied by the scattering techniques, the sample environment that can be applied, the actual length scales that can be probed and the information that can ultimately be obtained, all depend on the nature of the radiation employed. For example, light scattering cannot be used to study optically opaque samples and SAXS cannot easily be employed to study thick samples, also different techniques probe to different length scales. Thus, to a large extent, these techniques are complementary. However, they also share several similarities. Perhaps the most important of these is the fact that, with minor adjustments to account for different types of radiation, the same basic equations and laws can be used, to analyze data from any of these techniques. Herein, we show the versatility of the SANS and SAXS as applied to some of our selected studies.

Counterion Condensation in Charged Micelles

Micellar solutions are the suspension of the colloidal aggregates of the surfactant molecules in aqueous solutions. Surfactant molecules such as cetyltrimethylammonium bromide (CTABr), ionize in aqueous solution and the corresponding micelles are aggregates of CTA^+ ions. The micelle is charged and the Br^- ions, known as counterions, tend to stay near the CTA^+ micellar surface. In charged micellar solutions, the counterion condensation plays a very important role in deciding the effective charge on the micelle and consequently the formation, structure and interaction of the micelles. Small Angle Neutron Scattering (SANS) and Small Angle X-ray Scattering (SAXS) in combination, provide a direct method to study the counterion condensation on ionic micelles. While neutron scattering in micellar solutions is from the core of the micelle, x-rays are largely scattered by counterions, especially when the counterion has a large atomic number (e.g. Br-). The neutron scattering intensity from the counterion distribution is negligible in comparison to that from the core. Thus neutrons see the core of the micelle and x-rays give information relating to the counterion condensation around the micelle.

Fig. 1 shows the SANS data on 100 mM CTABr micellar solution and in the presence of varying concentrations of KCl. The inset shows the variation of neutron scattering length densities for different components of the micelles in 100 mM CTABr micellar solution. The contrast for any component depends on the square of the difference of scattering length densities of that component and solvent. It is clear from the variation of scattering length density for neutrons, that there exists a very strong contrast for the micelles in D_2O, with respect to that for the counterions. This makes the scattering from counterions negligible and neutrons only see the core of the micelles. All the SANS data show a correlation peak, which is due to peak from the interparticle structure factor S(Q). The peak usually occurs at $Q_m \sim 2\pi/d$, where d is the average distance

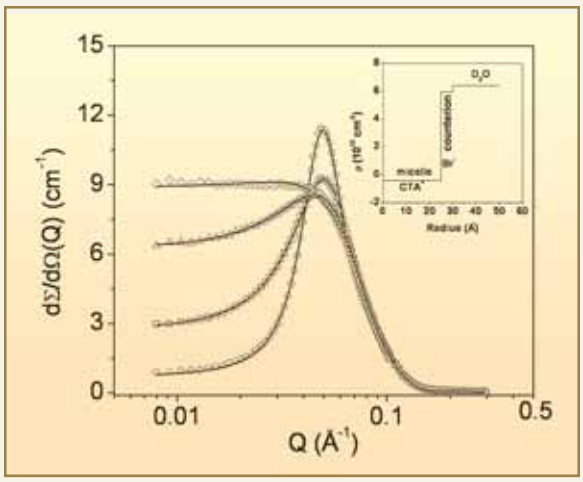

Fig. 1: SANS data from a micellar solution of 100 mM CTABr in the presence of varying KCl concentrations. The data from bottom to top in the low Q region corresponds to KCl concentrations of 0, 20, 60 and 100 mM, respectively. The inset shows the variation of neutron scattering length density for different components of the micelle in 100 mM CTABr micellar solution.

between the micelles and Q_m is the value of Q at the peak position. The correlation peak broadens without any significant shift in the peak position. The screening in the presence of salt, reduces the extent of short-range order between the charged micelles, which, in turn, broadens the peak. The micellar size and interaction parameters in these systems are given in Table 1. It is seen that fractional charge α on the micelle decreases and the aggregation number increases when the electrolyte concentration in the micellar solution is increased. This suggests the increase in counterion condensation ($1-\alpha$) on the micelle as the electrolyte is added. The charge neutralization at the surface of the micelle by the increase in the counterion condensation decreases the effective head group area for the surfactant monomer to occupy in the micelle and hence the increase in the aggregation number of the micelle.

Fig. 2 shows the SAXS data corresponding to the same samples for which the SANS data are shown in Fig. 1. The inset shows the variation of x-ray scattering length

densities for different components of the micelles in 100 mM CTABr micellar solution. Unlike in the case of neutrons, it is seen that for x-rays there exists a similar contrast for counterions as well as for the core of the micelles. SAXS data similar to SANS data show a correlation peak at the same Q values. The fact that the average distance between the micelles mainly decides the position of the correlation peak, and is independent of the radiation used. The second peak in the SAXS data at higher Q values arises from scattering of shell-like structure of the condensed counterions around the micelles.

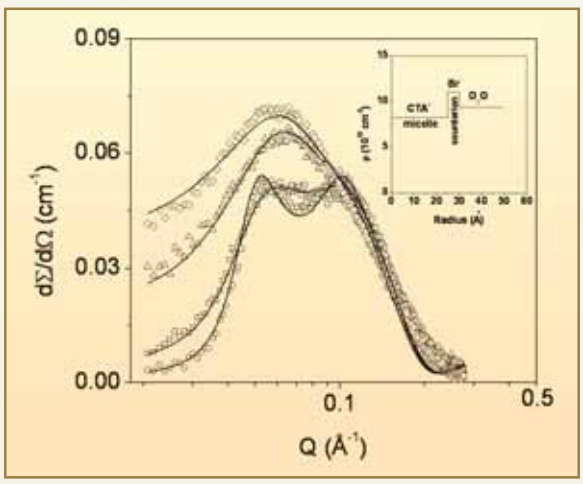

Fig. 2: SAXS data from a micellar solution of 100 mM CTABr in the presence of the varying KCl concentrations. The data from bottom to top in the low Q region corresponds to KCl concentrations of 0, 20, 60 and 100 mM, respectively. The inset shows the variation of x-ray scattering length density for different components of the micelle in 100 mM CTABr micellar solution

The changes in features of SAXS data (Fig. 2) with the addition of KCl in CTABr micellar solution, are significantly different than those of SANS data (Fig. 1). The two peak characteristics of SAXS data in pure CTABr micellar solution, gradually change to one peak data, with the addition of electrolyte. It is an indication of the scattering from the condensed counterions that decreases with the addition of electrolyte. This is possible if some of the Br^- (higher atomic number) counterions are exchanged by the added Cl^- (lower atomic number) counterions. Table 2 shows the fitted number fraction of the condensed Br^- and Cl^- counterions around the micelle, along with the thickness of shell over which they are condensed. The distribution of condensed counterions is treated as a step function and it fits the data reasonably well as perhaps due to the large condensation of the counterion on the charged micelles (Table 1). It is found that the number fraction of condensed Cl^- counterions increases and Br counterions decreases with increase in the concentration of KCl.

Table 1: Micellar parameters as obtained by SANS on 100 mM CTABr in the presence of varying concentrations of KCl

Micellar system	Aggregation number N	Semiminor axis b=c (Å)	Semimajor axis a (Å)	Fractional charge α	Counterion condensation 1-α (%)
100 mM CTABr	174±9	24.0±0.5	40.2±1.2	0.23±0.01	77
100 mM CTABr + 20 mM KCl	189±9	24.6±0.5	41.8±1.2	0.19±0.01	81
100 mM CTABr + 60 mM KCl	202±10	24.6±0.5	44.7±1.2	0.16±0.01	84
100 mM CTABr + 100 mM KCl	208±11	24.6±0.5	46.0±1.2	0.11±0.01	89

The thickness of the condensed shell shows a trend of small increase with the addition of KCl as expected because of exchange of Br^- counterions by Cl^- counterions. Usually, small ions are hydrated more and need larger thickness to condense on the micelles.

Core-Shell Structure of Ferrofluids

Ferrofluids are the suspension of the nanosized magnetic particles in appropriate carrier liquid. One of the ways to prepare the stable ferrofluids is by the surfactant coating on the magnetic fine particles, which prevent them from agglomeration even when the strong magnetic field gradient is applied to the ferrofluids. Different scattering techniques can be used, to get different types of information on the magnetic particles. We have used SANS and SAXS together to show the usefulness of these techniques to characterize a ferrofluid.

The SAXS data from a ferrofluid having ferrite (Fe_3O_4) particles coated with oleic acid and prepared in water are shown in Fig. 3. Due to low contrast of surfactant for x-rays (inset of Fig. 3), there is negligible scattering from the surfactant shell. The scattering is therefore mainly from the ferrite particles. The analysis gives mean radius of particle R_m = 4.8 nm and polydispersity σ = 50 % as accounted by the Schultz distribution.

Fig. 4 shows the SANS data on ferrofluid with variation in D_2O composition, in a mixture of D_2O and H_2O solvent. It is observed that the scattering intensity first decreases and then increases as the D_2O composition in the mixed D_2O / H_2O solvent is increased. This behavior of scattering intensity can be explained, in terms of the variation of scattering length density of solvent (ρ_s) with the change in the composition of the solvent. The scattering at low D_2Ocompositions is dominated by decrease in the contrast for magnetic particles and hence the intensity decreases [Fig. 4 (a)]. On the other hand, at high D_2O compositions, the scattering intensity is dominated by the contrast of the surfactant shell and hence scattering intensity increases, with increase in the contrast for shell as the D_2O concentration is increased [Fig. 4 (b)].

Fig. 5 shows the fitted scattering data from ferrofluid prepared in D_2O to H_2O ratios of 10:90 and 90:10. The data of ferrofluid in D_2O to H_2O ratio of 10:90 has been used, to get the size of the ferrite particle as

Table 2: Micellar parameters as obtained by SAXS on 100 mM CTABr in the presence of varying concentrations of KCl.

Micellar system	Number fraction of condensed Br^- counterions	Number fraction of condensed Cl^- counterions	Condensed counterions thickness t (Å)
100 mM CTABr	1.0	0.0	4.2±0.2
100 mM CTABr + 20 mM KCl	0.83	0.17	4.3±0.2
100 mM CTABr + 60 mM KCl	0.63	0.37	4.4±0.2
100 mM CTABr + 100 mM KCl	0.5	0.5	4.5±0.2

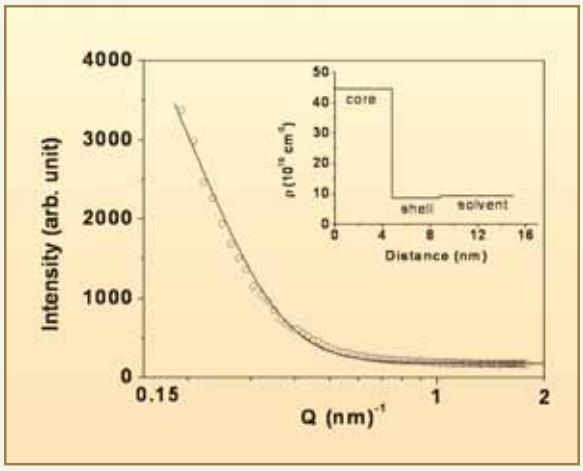

Fig. 3: SAXS data from a ferrofluid. Inset shows the variation of x-ray scattering length density for different components of the ferrofluid

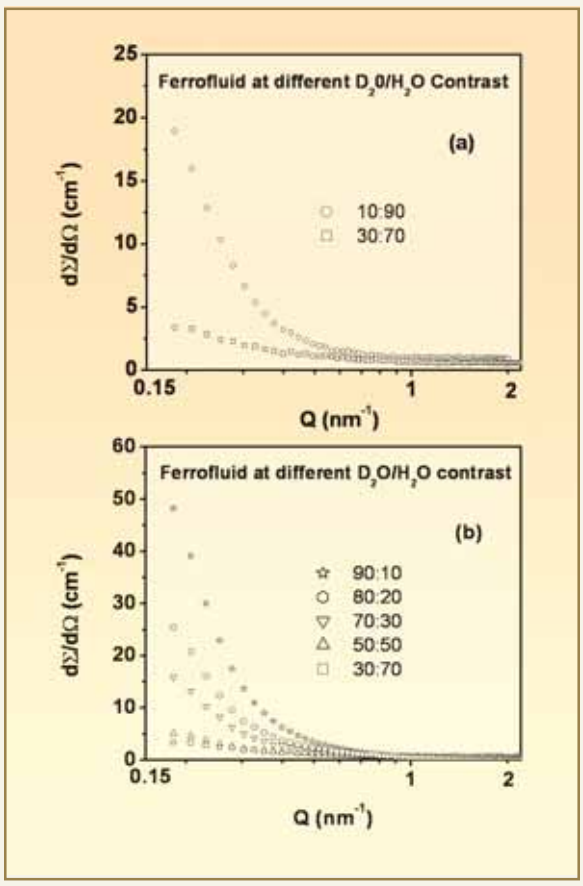

Fig. 4: SANS data from a ferrofluid as the fraction of D_2O in the solvent of mixture of D_2O and H_2O is varied

for this sample there is no contrast for the shell. The analysis gives similar values of mean radius and polydispersity as obtained using SAXS. The size distribution of the particles is given in the inset of Fig. 5. In case of ferrofluid prepared in solvent of higher fraction of D_2O, there exists strong contrast for the shell of surfactant layer around the ferrite particle. The core-shell structure of the particle has been used, to fit the data. It is found that double coating of oleic acid has a thickness t = 4.0 nm around the magnetic particles.

Table 3 summarizes the results of SANS and SAXS with Dynamic Light Scattering (DLS) technique as obtained from the ferrofluid samples. DLS gives the overall size of the magnetic particle with surfactant coating. The value obtained (R_h = 10.5 nm) is larger than the combined value of radius of the particle and thickness of the surfactant coating as obtained using SANS. The arger value obtained using DLS is expected, because of the particle diffusion with water of hydration. The value thus obtained in DLS is the hydrodynamic size and is larger than the bare size of the total particle. SAXS only gives the information on the size of the

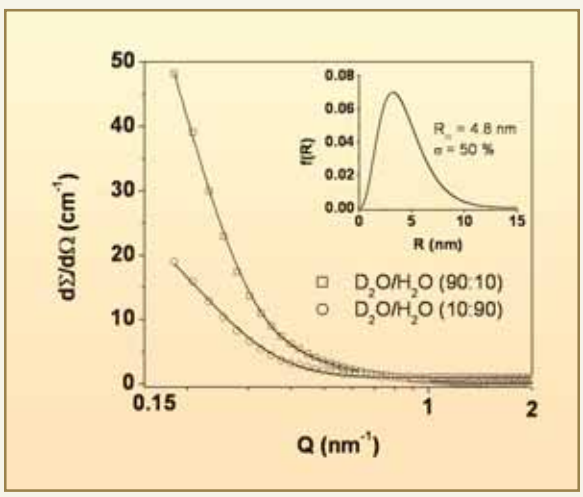

Fig. 5: Fitted SANS data from a ferrofluid when the surfactant is contrast-matched for D_2O to H_2O ratio of 10:90 and the core-shell structure of the ferrofluid as determined for D_2O to H_2O ratio of 90:10.

lferrite particles, as scattering from the surfactant is negligible for the x-rays. SANS with the possibility of contrast variation provides the core-shell structure of the ferrofluid. It may be further added that SANS with polarized neutrons can be used, to separate the nuclear and magnetic nanostructures of the ferrofluid.

Surfactant-Induced Protein Unfolding

The function of a protein depends absolutely on it's three-dimensional folded structure. Protein unfolding process involves the disruption of H-bonds, disulphide bonds, salt bridges and hydrophobic interactions, leading to it's successive alteration of quaternary, tertiary and secondary structure. However, peptide bonds are not broken leaving the primary structure unaltered. Protein unfolding is one of the most widely studied topics in molecular biology due to its wide spread application in the industrial and scientific world. The unfolding process can be brought about by various means and conditions. Each different route of unfolding has it's own application and advantage in material processing and basic sciences. Protein unfolding in the case of amphiphilic molecules such as surfactant is caused, due to binding of these molecules to the hydrophobic patches of the protein. The surfactant induced unfolding is known to play an important role in the pharmaceutical and cosmetic industry.

Table 3: The various structural parameters of the ferrofluid as obtained by combining different scattering techniques

Technique	Information obtained	Ferrofluid parameters
DLS	Overall size along with hydration	R_h = 10.5 nm
SAXS	Only size of the ferrite particle.	$R_m(Core)$ = 4.8 nm σ = 50 %
SANS	Particle size and thickness of surfactant coating	$R_m(Core)$ = 4.8 nm, σ = 50 % $t(Shell)$ = 4.0 nm

Fig. 6 shows SANS data for 1 wt% BSA in the presence of varying SDS concentrations. Based on the features of the scattering profiles, the data can be grouped into two different sets as the surfactant concentration is increased. The first data set corresponds to proteins at low surfactant concentrations (0 to 10mM), where the scattering data shows similar behaviour to that of pure protein solution. In this data set, the overall scattering cross-section increases with increase in surfactant concentration. It can be explained if the individual surfactant molecules bind to protein and the volume of the scattering particle increases. The features of the scattering data in the second data set at higher surfactant concentrations (>10 mM) are very different to those of the first data set. One of the interesting features, is the linearity of the scattering profiles on log-log scale in the intermediate Q range, with a Q range of linearity increasing with surfactant concentration. This is an indication of formation of fractal structure by the protein-surfactant complex. The build up of scattering cross-section in the higher cut-off of the linearity of scattering data, suggests the formation of surfactant aggregates and the lower cut-off corresponds to the overall size of the protein-surfactant complex. It is observed that the position of high Q cut-off remains almost the same while the position of low Q cut-off shifts to smaller Q values with increasing surfactant concentration. The calculated structural parameters in this system are given in Table 4.

At low surfactant concentrations, the data in Table 4 shows changes in the dimensions of the protein on increasing binding of surfactant molecules, as a function of surfactant concentration. The semiminor axis remains almost the same while the semimajor axis increases with increasing surfactant concentration. It is believed that the six protein sub-domains forming BSA remain intact, but separate from each other,

leading to an elongation of the protein on addition of the surfactant. The fractal structure of the

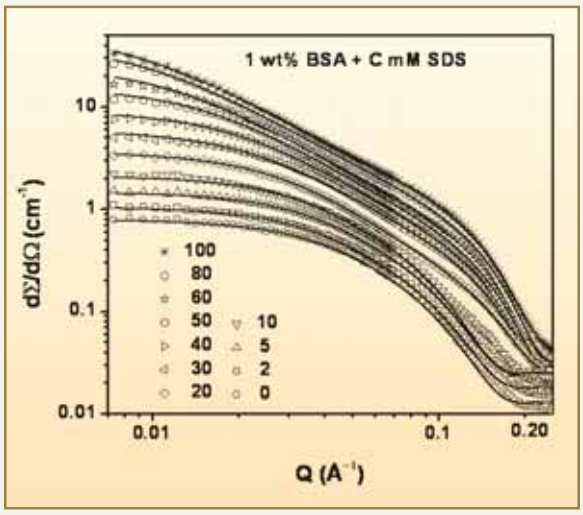

Fig. 6: SANS data for 1 wt% BSA in the presence of varying concentrations of surfactant

protein-surfactant complex at higher surfactant concentrations, is modeled on the basis of the necklace model, which considers micelle-like clusters of the surfactant, formed along the unfolded polypeptide chain of the protein. It is found that the fractal dimension decreases and the overall size of the complex increases on increasing surfactant concentration. The size of micelle-like clusters (R) does not change while the number of such micelle-like clusters (N) in protein-surfactant complex increases with surfactant concentration. The calculated aggregation number of micelle-like clusters in the complex decreases from 51 to 42 on increasing surfactant concentration from 20 to 100 mM. It is interesting to note, that these values of aggregation numbers are much smaller than one would have found (about 70) in pure surfactant solution, for similar size of micelles.

This indicates the participation of the hydrophobic portions of the unfolded protein chain in the micellar formation. The participation of the unfolded protein in the formation of micelle-like clusters is enhanced with increase in unfolding and this results in decreasing aggregation number of micelle-like clusters. Also all the surfactant molecules probably participate in the micelle-like clusters to avoid exposure of hydrophobic portions of the protein on it's unfolding with increase in surfactant concentration.

Table 4: Fitted parameters of SANS analysis of protein-surfactant complex for:

(a) 1 wt% BSA with low SDS concentrations 0 to 10 mM

[SDS] (mM)	Semi-major axis a (Å)	Semi-minor axis $b = c$ (Å)
0	70.2 ± 5.1	22.2 ± 0.8
2	77.3 ± 5.8	22.2 ± 0.8
5	80.0 ± 6.1	22.2 ± 0.8
10	88.0 ± 6.4	23.0 ± 0.9

(b) 1 wt% BSA with high SDS concentration 20 to 100 mM

[SDS] (mM)	Fractal dimension D	Correlation length ξ (Å)	Micelle radius R (Å)	No. of micelles N
20	2.27 ± 0.15	38.0 ± 1.9	18.0	2
30	2.15 ± 0.14	43.0 ± 2.7	18.0	3
40	2.05 ± 0.13	54.0 ± 3.8	18.0	4
50	1.95 ± 0.10	67.8 ± 4.9	18.0	6
60	1.88 ± 0.09	87.9 ± 5.4	18.0	8
80	1.79 ± 0.06	117.9 ± 6.9	18.0	10
100	1.71 ± 0.04	144.3 ± 7.5	18.0	13

in summary, small-angle scattering is an ideal method to the study of structure and interactions in soft matter. The use of SANS and SAXS provide complementary information. At BARC, these techniques have been extensively used to study a variety of systems in soft matter. Some of these results have been presented.

Acknowledgement

The author would like to acknowledge Dr. P.S. Goyal, Dr. A.G. Wagh and all other collaborators for their support.

ABOUT THE AUTHOR

Dr. V.K. Aswal, after obtaining his M.Sc. in Physics from IIT Mumbai, joined the BARC Training School in 1992 (36th Batch). Subsequently, he joined the Solid State Physics Division and has been working in the field of Small-Angle Scattering for instrument development and it's applications to Soft Condensed Matter. He obtained his Ph.D. degree in 1999 from University of Mumbai for his work on Small-Angle Neutron scattering from Micellar Solutions. He did his Post-doctoral studies at the Swiss Spallation Neutron Source, Paul Scherrer Institute, Switzerland. Dr. Aswal was awarded the Homi Bhabha Prize, the Best Ph.D. Thesis Presentation Award and the N. S. Sathya Murthy award for young scientist.

FLAW CHARACTERIZATION IN PHWR PRESSURE TUBES BY ULTRASONICS: INDIA'S EXPERIENCE DURING IAEA-CRP

P.P. Nanekar, M.D. Mangsulikar and B.K. Shah
Quality Assurance Division

and

J. Cleveland
Division of Nuclear Power
International Atomic Energy Agency, Vienna, Austria

This paper received the Best Technical Paper Award and was published in the Journal of Non-Destructive Testing and Evaluation, during the year 2007

ABSTRACT

The pressure tubes of Pressurized Heavy Water Reactor (PHWR) operate under high temperature, high pressure aqueous environment and are subjected to fast neutron irradiation. In order to assure the structural integrity of pressure tube during service, it is periodically examined by Non-Destructive Examination (NDE) techniques. The International Atomic Energy Agency (IAEA) conducted a Coordinated Research Programme (CRP) involving several countries operating heavy water reactors. The CRP involved round-robin transfer of pressure tube samples containing artificial flaws, resembling closely with real defects of concern. The paper gives details of ultrasonic testing techniques employed by India during this CRP and India's performance on flaw detection and sizing in pressure tube samples. Based on the analysis of inspection results, the most effective NDE techniques were identified for flaw characterization in PHWR pressure tubes.

Introduction

A typical Indian Pressurized Heavy Water Reactor (PHWR) consists of few hundred horizontally placed coolant channels. The coolant channel comprises of a Zr-2.5% Nb pressure tube, encircled by a Zircaloy-4 calandria tube and four garter spring spacers (Zr-2.5 Nb-0.5 Cu), which prevent these two tubes to come in contact during their service life (Fig. 1). The pressure tube carries the nuclear fuel, high temperature, high pressure, heavy water coolant and is subjected to fast neutron irradiation. The integrity of pressure tube is central to the safety of PHWRs. To ensure this, they are periodically subjected to in-service inspection by Non-Destructive Examination (NDE) techniques. The International Atomic Energy Agency (IAEA) conducted a Coordinated Research Programme (CRP) titled 'Intercomparison of Techniques for Pressure Tube Inspection and Diagnostics' involving countries that operate heavy water reactors. The first phase of this CRP dealt with flaw characterization in pressure tubes by *in-situ* NDE techniques. This paper deals with India's

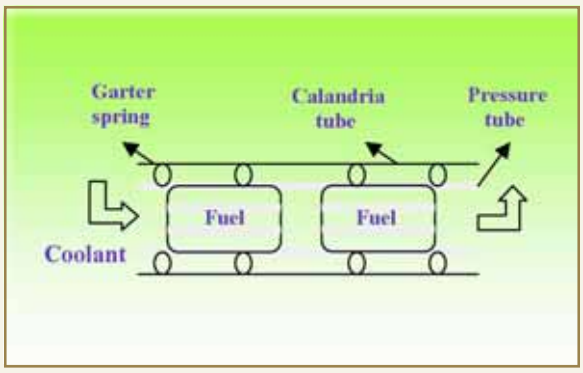

Fig. 1: Simplified sketch of coolant channel

experience during NDE of pressure tube samples, which were circulated as part of this CRP. The results of these investigations and the analysis of test results are discussed.

Pressure Tube Degradation and it's Life Management

The 540 MWe Indian PHWR consists of 392 coolant channels. The pressure tube, 103.4 mm ID, 4.3 mm wall thickness, is approximately 6.3 meter long. It operates at 300 °C, 11 MPa internal pressure and is subjected to neutron flux of the order of 10^{13} n/cm^2/s. These conditions lead to degradations in the pressure tube with respect to i) dimensional changes as a result of irradiation creep and growth, which result in increase in it's diameter and length, ii) deterioration in mechanical properties due to irradiation embrittlement, thereby reducing it's flaw tolerance, iii) the growth of existing flaws, which were too small or 'insignificant' at the time of installation and iv) initiation and growth of new flaws like fretting damage due to debris and fuel element bearing pads. The pressure tube material also undergoes corrosion in heavy water aqueous environment during service. This reaction releases hydrogen, a part of which gets absorbed in the pressure tube. The absorbed hydrogen can limit the life of a pressure tube due to the degradation mechanisms such as Delayed Hydride Cracking (DHC), hydride blister formation and cracking and hydride embrittlement. It is a regulatory requirement to periodically subject pressure tubes to in-service inspection by employing non-destructive examination techniques. In India, these inspections are carried out by an automated tool called BARCIS (BARC Channel Inspection System). The BARCIS inspection head includes ultrasonic and eddy current sensors and involves four specific tasks: detection of flaw, if any, in the pressure tube, measurement of pressure tube wall thickness, measurement of gap between pressure tube and the calandria tube and location of garter spring spacers. In addition to BARCIS, there are several other indigenously developed diagnostics tools and analytical models, to assess and predict the health of coolant channels in Indian PHWRs. These life management tools provide valuable inputs to designers, plant operators and the regulatory authorities, on fitness-for service assessment of pressure tubes.

Objective of IAEA-CRP

To foster international collaboration in the efficient and safe use of nuclear power, the IAEA conducted a Coordinated Research Programme (CRP) on Inter-comparison of techniques for Heavy Water Reactor (HWR) pressure tube inspection and diagnostics. This CRP was carried out within the frame of the IAEA Department of Nuclear Energy's Technical Working Group on Advanced Technologies for HWRs (the TWG-HWR). The TWG-HWR is a group of experts nominated by their respective governments and designated by the Agency, to provide advice and to support implementation of IAEA's project on advanced technologies for HWRs.

The primary objective of this CRP was to arrive at the most effective NDE techniques, for pressure tube inspection. It is crucial that the NDE techniques that are employed for this purpose are very reliable, in the detection of all significant flaws and very accurate to characterize them in terms of their geometry and

nature. In order to assess the effectiveness of these techniques for their intended purpose, it is important that they are periodically subjected to 'blind tests' on pressure tube samples containing known flaws. This CRP gave the opportunity for the participating laboratories, to prepare their own pressure tube samples containing flaws and to carry out blind tests on pressure tube samples prepared by others. Because these were blind tests, the results of examination on pressure tube samples can be directly correlated with the effectiveness of NDE techniques for detection and characterization of flaws. A good detectability and accurate characterization would strengthen the confidence in the technique(s) employed, while poor detectability and inaccurate characterization would give a feedback to the laboratory, that the existing technique needs improvements or new techniques should be developed. The inter-comparison of NDE techniques based on the results of investigation of pressure tube samples, highlights the most reliable and accurate NDE method (ultrasonic, eddy-current or a combination of both) and also a specific technique for that NDE method (time-of-flight monitoring, amplitude monitoring, C-scan image, etc.) for detection and characterization of various kinds of flaws encountered in pressure tubes. This information is useful for the heavy water reactor community, to improve the tools being used for pressure tube inspection and diagnostics, by modifying the existing techniques or adapting new ones, so that the inspection is carried out in the most effective manner. The inter-comparison of NDE techniques also helps in identifying those areas, where none of the existing techniques are reliable or effective to the desired level. It identifies areas of research for future collaboration in this field.

Conduct of IAEA-CRP on Pressure Tube Inspection and Diagnostics

A total of seven laboratories from six countries, including India participated in this CRP. The participating laboratories prepared pressure tube samples containing artificial flaws resembling real defects of concern. Details on these laboratories and their samples can be found in IAEA TECDOC 1499 [5]. The flaws on the outside surface were hidden by a cover, to facilitate blind testing. The CRP was conducted in a round-robin manner during which the pressure tube sample moved from one laboratory to other. All samples had to be inspected from the inside surface, as in real conditions during in-service inspection. The samples, after examination by participating laboratories, were returned to the originating laboratory, which determined 'flaw truth' in it's sample by destructive means or non-destructively by using either measuring microscope or profilometry of replica. The originating laboratory analyzed the sample inspection reports from investigating laboratories on it's pressure tube sample and assessed their performance on flaw detection and sizing. The intercomparison of NDE techniques employed by investigating laboratories, provided a very good platform to arrive at the most effective NDE technique(s) for detection and sizing of flaws in pressure tube. These findings are reported in IAEA TECDOC 1499.

Indian Pressure Tube Sample

The Indian pressure tube sample IND1 is 103.4 mm ID, 4.3 mm wall thickness and 500 mm long. It contains a total of 17 flaws, including the reference flaws required for calibration of ultrasonic and eddy current examination. The reference flaws are made as per Canadian standard [6] and included axial and circumferential notches and flat bottom reflectors at different depths. In addition to these, the Indian pressure tube sample contains OD notches resembling axial, circumferential and oblique Delayed Hydride Cracking (DHC) and ID grooves, resembling fretting damage, due to debris and bearing pad. Table 1 gives the details of all the flaws in IND 1 sample:

Table 1: Flaws in IND1 pressure tube sample

Sr. No.	Location and Orientation	Flaw Size*			Flaw type
		Length (mm)	Width (mm)	Depth (mm)	
1	OD, Oblique at 45°	5.84	0.21	0.16	DHC
2	ID, equiaxed	2.50	2.3	1.15	smooth debris fret
3	OD, equiaxed	1.46	0.80	0.63	laminar flaw near OD
4	ID, axial	11.50	2.3	1.00	bearing pad fret
5	ID, axial	6.00	0.4	0.22	reference flaw
6	ID, circ.	6.00	0.3	0.21	reference flaw
7	OD, oblique at 20°	5.81	0.24	0.16	DHC
8	OD, equiaxed	1.92	1.27	3.67	laminar flaw near ID
9	ID, axial	2.00	1.0	1.10	sharp debris fret
10	OD, circ.	5.88	0.32	0.11	shallow DHC
11	OD, axial	5.85	0.28	0.13	reference flaw
12	OD, circ.	5.76	0.27	0.14	reference flaw
13	OD, circ.	11.96	0.39	0.23	DHC
14	OD, oblique at 20°	5.84	0.17	0.13	DHC
15	OD, equiaxed	1.62	1.15	2.14	Laminar flaw at mid-wall
16	OD, axial	5.80	0.24	0.068	shallow DHC
17	OD, axial	11.88	0.35	0.17	DHC

** In the above Table, the flaw dimensions for OD flaws are found out by measuring microscope and for ID flaws by profilometry of replica.*

Ultrasonic Testing Techniques for Pressure Tube Examination

The selection of NDE techniques for pressure tube examination was left open to the participating laboratory. The underlying condition was that, the applied techniques should be useful during in-service inspection. The CRP witnessed two NDE methods for examination of pressure tube samples: ultrasonic and eddy current. India used only ultrasonic testing for examination of pressure tube samples.

The inspection head carries six ultrasonic transducers: four for angle beam examination and the remaining two for normal beam examination. Fig. 2 shows the inspection head employed during pressure tube examination.

The angle beam transducers were arranged in two pairs (axial and circumferential) in which one transducer acted as transmitter and the other as receiver. They are placed on an inspection head such that the ultrasonic beam from transmitter (T) reaches the receiver (R) after travelling two skip distance in the pressure tube. One of the normal beam transducers was focused on OD, while the other on ID of the pressure tube. The ultrasonic beam from four angle beam and one normal beam converged at one point in the pressure tube. The schematic arrangement of transducers for different scans is shown in Fig. 3.

The ultrasonic transducers for angle beam are 10 MHz frequency, 10 mm dia. and 30 mm focal length. The normal beam OD focused transducer is 10 MHz frequency, 6 mm diameter and 25 mm focal length, while the one focused on ID is 20 MHz frequency, 6 mm diameter and 12 mm focal length. All the transducers are point focused. The ultrasonic technique for flaw detection included pulse-echo and pitch-catch scan, using angle beam and pulse-echo scan using normal beam. The angle beam pitch-catch scan is very effective for detection of flaws not favorably oriented, like oblique and tilted flaws. With such an arrangement of transducers, any flaw in the pressure tube, irrespective of it's orientation and location is detected in more than one scan. This ensures high

Fig. 2: Inspection head for pressure tube examination

degree of reliability in flaw detection. The length and width sizing of flaws was based on 6 dB drop technique, while the depth sizing was based on time-of-flight. Tip diffraction technique was used, to get the diffracted signals from flaw tip in angle beam and normal beam scan. Depth of ID flaws was found by ID focused normal beam transducer, which monitors the shift in ID signal (surface profiling). The time-of-flight is measured with a resolution of 10 nanosecond (100 MHz digitizer) to get good accuracy in depth sizing. The data record included time-of-flight and amplitude plots and the B-scan images.

Pressure Tube Examination Set-up

The pressure tube samples are examined in a semi-automated set-up. The tube is held in fixtures and then filled with water from inside surface. The inspection head carrying ultrasonic transducers is driven by two stepper motors, one for axial and other for rotary motion. During examination, the data is collected by: angle beam pulse-echo axial and circumferential scan, angle beam pitch-catch axial and circumferential scan and normal beam pulse-echo scan. Any indication having amplitude of 6 dB over noise in angle beam pulse-echo scan and/or resulting in amplitude drop of 5% or more in reference signal in normal beam pulse-echo and angle beam pitch-catch scan, is evaluated. If the indication is suspected to be from a genuine flaw, then it is evaluated for length, width and depth. The depth is found out by both, angle beam pitch-catch and normal beam. Signals from scratches and dents created in the tube due to handling, are only recorded and not evaluated in details.

India's Performance during CRP

The Indian inspection team examined a total of seven pressure tube samples from different participating laboratories. These samples contained a total of 170 flaws. All the flaws, which are likely to be present in PHWR pressure tubes, were a part of these samples. India detected all the 170 flaws in these pressure tube samples.

With respect to the sizing, the accuracy of length sizing was very good for all the flaws, except the oblique ones. These flaws are required to be imaged in C-scan mode to get the true estimate of their length. The width of fretting damage and the lap type/laminar

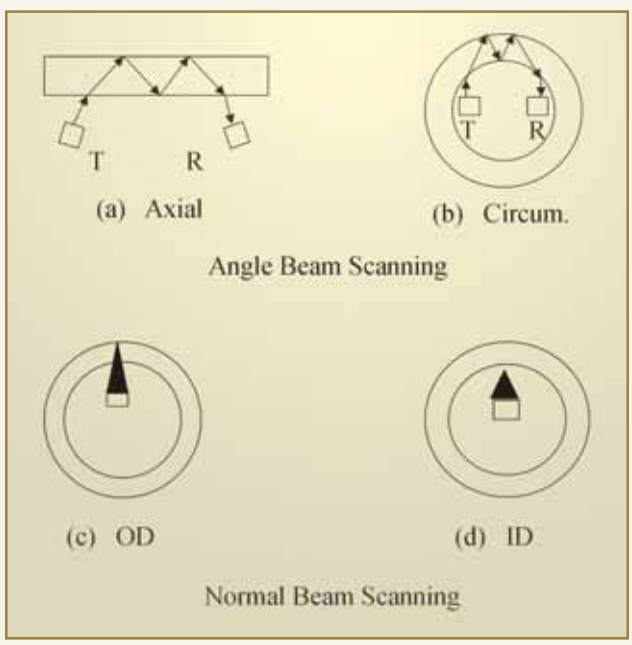

Fig. 3: Angle and normal beam

flaws was sized very accurately. For crack-like flaws simulated by very fine notches, the width was not reported. None of the NDE techniques employed during this CRP by various participating laboratories, could give satisfactory results on width of fine notches. The accuracy of depth sizing for majority of flaws was very good.

Table 2 gives India's result on depth sizing of flaws in one of the pressure tube samples.

Table 2 indicates that the NDE estimate on depth is very accurate, except for three flaws. It is observed that other investigating laboratories also encountered error of this order for these flaws. This indicates that the true depth reported by the originating laboratory for these flaws may not be correct.

Table 3 consolidates India's performance on flaw sizing accuracy for all the flaws, in all the pressure tube samples examined during this CRP. The flaws in these samples are grouped in to six categories: (i) OD shallow DHC, (ii) OD deep DHC, (iii) ID shallow DHC, (iv) OD oblique DHC, (v) shallow fretting damage and (vi) deep fretting damage. Not included in this Table are: (i) reference notches and flat bottom reflectors as per the Canadian Standard, (ii) lap type or laminar flaws, as their depth sizing is not of interest during in-service inspection, (iii) flaws, for which it is quite likely that the true value reported by the originating laboratory isincorrect and (iv) very deep DHC. The depth sizing accuracy for the above flaw types is expressed in terms of Root Mean Square (RMS) error. It is calculated as follows:

RMS Error $= [\Sigma(x_{it} - x_{im})^2 / (n-2)]^{0.5}$, $i = 1$ to n

x_{it} is the true flaw depth,

x_{im} is NDE estimate on flaw depth,

n is the number of flaws

Table 3 indicates that the accuracy of depth sizing for all the types of flaws in pressure tube samples was very good. For shallow ID and OD DHC, considering the difficulty associated with locating the flaw-tip, the accuracy achieved in their depth sizing is extremely good. The depth of oblique flaws was also sized very well, considering their unfavourable orientation. The debris fret, shallow and deep, were sized most accurately, when seen in relation to the RMS error encountered in terms of percentage of true depth.

Fig. 4 shows the B-scan images for some of the flaws in pressure tube samples.

Table 2: Inspection results on a pressure tube sample

Flaw Type	Flaw Depth (mm)		
	True value	NDE estimate	Error (mm)
OD, DHC (Semi-elliptical)	2.40 (max.)	2.26	0.14
OD, DHC (Semi-elliptical)	1.56 (max.)	1.38	0.18
OD, DHC (Semi-elliptical)	2.95 (max.)	2.78	0.17
OD, DHC (Semi-elliptical)	0.81 (max.)	0.74	0.07
OD, DHC (Semi-elliptical)	2.05 (max.)	1.65	0.40
OD, DHC (Semi-elliptical)	1.45 (max.)	0.97	0.48
Equiaxed OD Dent	1.52	1.48	0.04
Equiaxed OD Dent	0.53	0.48	0.05
Equiaxed OD Dent	2.03	1.96	0.07
Equiaxed OD Dent	1.04	1.04	0.0
Bearing Pad Fret	1.94	2.26	0.32
Bearing Pad Fret	0.94	0.99	0.05
OD long shallow notch	0.15	0.12	0.03

Table 3: India's performance on flaw depth sizing

Flaw Type	Depth Range (mm)	Average Depth (mm)	RMS Error (mm)
OD shallow DHC	0.07 - 0.18	0.14	0.027
	0.23 - 0.31	0.27	0.041
OD deep DHC	0.38 - 0.81	0.65	0.113
ID shallow DHC	0.14 - 0.29	0.21	0.026
Oblique DHC	0.11 - 0.17	0.14	0.038
Shallow fretting damage on ID	0.21 - 0.25	0.24	0.045
Deep fretting damage on ID	0.78 - 1.51	1.10	0.075

Fig. 4a shows the B-scan image for the DHC on OD (simulated by a fine notch). The corresponding A-scan at the flaw location is also shown. The image is collected by circumferential movement of a normal beam OD transducer. X-axis represents the time-of-flight and the Y-axis represents the transducer travel. The signal on the left is from pressure tube ID and the one on the right is from pressure tube OD. The semi-elliptical profile of the notch, which is typical of DHC, is clearly seen in the image. The time of-flight plot for this flaw is shown in Fig. 5a. From this plot, one can find the maximum shift in time-of-flight ("TOF) of the flaw tip signal, with respect to the reference signal (OD) and get the depth estimate. In the present case it this shift is 0.408 microsecond and the calculated depth is 0.97 mm. Fig. 4b shows the B-scan image for a bearing pad fret (simulated by ID groove). The image shows the change in surface profile of the ID signal at the flaw location. This image is collected by moving the ID focused normal beam transducer along the width of the flaw. The time of-flight plot for this flaw is shown in Fig. 5b. From this plot, one can find the maximum shift in time-of-flight of the reference signal (ID) at the flaw location and get the depth estimate. In the present case this shift is 0.354 microsecond and the calculated depth is 0.27mm.

Fig. 4c shows the B-scan image for a laminar flaw, which is simulated by a flat bottom reflector. The flaw is at the mid-wall of the pressure tube. The image shows the signals from pressure tube ID and OD and an additional signal from the laminar flaw close to the centre of the pressure tube thickness. For these types of flaws, sizing of their through-thickness dimension is not of concern. They only need to be

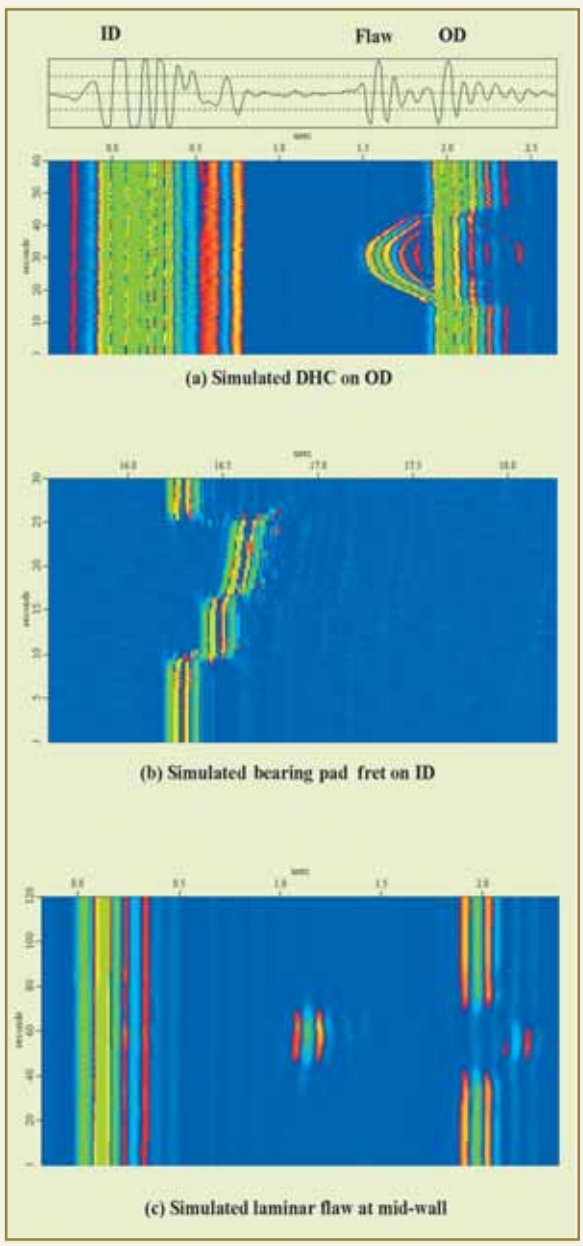

Fig. 4: B-scan images of simulated flaws in pressure tube samples

reliably detected and reported in terms of length, width and depth from scanning surface.

Analysis of Inspection Results

The Sample Inspection Reports submitted by investigating laboratories on Indian pressure tube sample were analyzed. The objective of this analysis, was to assess the performance of investigating laboratories, but more importantly on the effectiveness of various NDE techniques for flaw detection and sizing. For flaw detection, this analysis was based on comparing the relative response that was observed from a particular flaw, using various techniques.

For example, in case of ultrasonic testing, the angle beam pulse-echo technique is based on the reflected signal, while the angle beam pitch-catch and normal beam is based on the drop in the amplitude of the transmitted and backwall signal respectively. If the flaw gives higher amplitude of reflected signal in pulse-echo mode and a lesser amplitude drop of transmitted signal in pitch-catch mode, then pulse-echo technique is adjudged the 'Best'. Contrary to this, if the pulse-echo shows lesser response in terms of amplitude of the reflected signal and a pitch-catch or normal beam shows better response in terms of drop in the amplitude of the transmitted or backw all signal, then they are adjudged as the 'Best' technique(s).

For flaw sizing, the analysis was based on comparing the true flaw dimensions with the ones estimated by NDE. The first step in this analysis is to find out the error encountered by individual laboratory during NDE sizing of length, width and depth for each flaw in pressure tube sample. The next step was to find out the laboratory, which encountered least error for these dimensions. Finally, the NDE technique employed by this laboratory for that particular dimension is identified. This analysis was carried out for all the flaws in Indian pressure tube sample. This analysis helped in identifying techniques, which worked consistently well for sizing flaw dimensions for different types of flaws in pressure tube sample.

The analysis of inspection results revealed, that for axial and circumferential flaws, the conventional pulse-echo technique in circumferential and axial direction is good enough. However, for the oblique flaws, the angle beam pitch-catch works much better. The lap-type or laminar flaws are best detected by normal beam scan. The same is also true for ID fretting damage. With respect to flaw sizing, it is observed that for the length, 6 dB or 20 dB drop technique using ultrasonic normal beam is the most suitable technique. The same is applicable for width of the flaw, if it is greater than the size of the ultrasonic beam. For fine crack-like flaws, none of the existing NDE techniques could give desired results. For depth sizing, time-of-flight measurement using normal beam

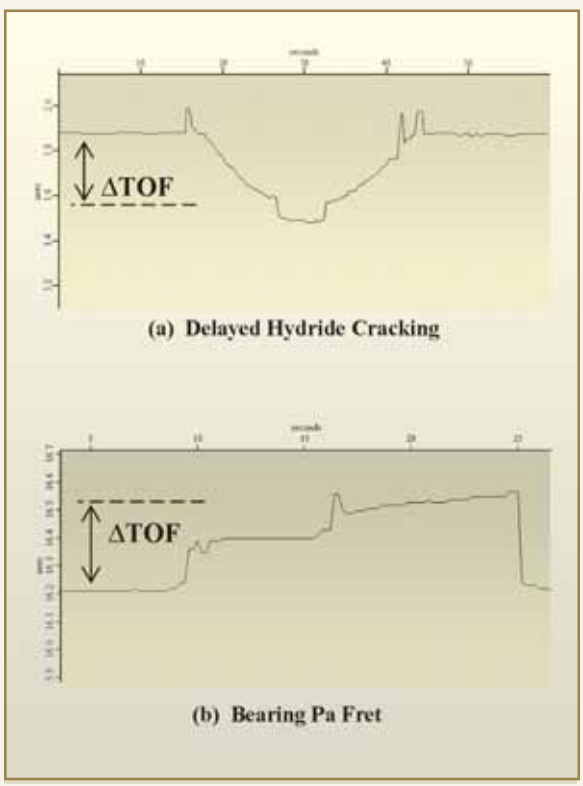

Fig. 5: Time-of-flight plots for simulated flaws in pressure tube

and/or angle beam pitch-catch gave accurate results for OD flaws. ID flaws are best sized by time-of-flight measurement using high frequency normal beam ID focused transducer.

Conclusion

The structural integrity of pressure tube is of prime importance for the safe operation of heavy water reactors. Non-destructive examination during in-service inspection plays a crucial role in this regard by providing inputs in the form of flaw characteristics. It is of utmost importance that the inspection techniques employed for *in-situ* pressure tube examination, reliably detect all the harmful flaws and characterize them very accurately. The IAEA-CRP on pressure tube inspection gave a very good opportunity to the participating laboratories, to assess the effectiveness of various NDE techniques (both established and under development) by carrying out blind test on the pressure tube samples. The intercomparison of these techniques based on the results of examination helped in identifying technique(s) most suited for detection and sizing of various types of flaws, encountered in heavy water reactor pressure tubes.

ABOUT THE AUTHORS

Mr. Paritosh Nanekar of Quality Assurance Division is working in the field of Non-Destructive Evaluation (NDE) for the past 15 years. His area of expertise includes: development of NDE techniques for in-service inspection of components in nuclear facilities, advanced NDE techniques for flaw and material characterization, quality assurance during manufacturing of reactor components and quality control during nuclear fuel fabrication.

Mr. M.D. Mangsulikar of Quality Assurance Division is working in the field of Non-Destructive Evaluation (NDE) for the past 23 years. His area of expertise includes: quality control during fabrication of nuclear fuel, in-service inspection of components in nuclear plants and quality assurance during manufacturing of nuclear components.

Mr. B.K. Shah is currently Head, Quality Assurance Division, BARC. He belongs to the 17th Batch of BARC Training School. His field of work includes Quality Assurance (QA) in the manufacture of Nuclear Fuels and Reactor Core Components, Metallurgical Failure Analysis, Flaw and Material Characterization by NDT, Corrosion Studies on Reactor Materials, etc. He has published more than 200 technical papers. He has received National NDT Award, NACE Award.

बीएआरसी न्यूज़लेटर
BARC NEWSLETTER

INDIRECT ELECTRO-OXIDATION PROCESS FOR LEACHING OF MOLYBDENITE CONCENTRATE BY HYPOCHLORITE: A MODIFIED APPROACH

V.S. Bhave, Pamela Alex and R.C. Hubli
Materials Processing Division

and

A.K. Suri
Materials Group

This paper won the "Misra Award " for Best Paper at the IIME Seminar on "Mineral Processing Technology – 2007 held at IIT, Mumbai during Feb. 22-24, 2007

ABSTRACT

The leaching of low-grade molybdenite concentrate by hypochlorite, generated *in situ* by the modified approach has been investigated. The electrolysis of the pulp is conducted in the presence of calcium chloride, in order that quantitative precipitation of calcium sulfate and calcium molybdate is facilitated, as dissolution progresses. Therefore, at all times during electro-oxidation, the brine composition remains unaltered. The brine solution does not leave the electrolysis circuit and is recirculated without any purification. The solids, after filtration, containing calcium molybdate, calcium sulfate and unreacted gangue are leached with recycled Mo solution at ambient temperature to build molybdenum concentration, leaving behind calcium sulfate and gangue.

Introduction

Low grade molybdenite concentrates recovered from porphyry copper ores, contain copper suphides in various amounts. Selective dissolution of molybdenum values has been achieved by sodium hypochlorite generated externally or electrolytically generated *in situ* The pilot plant was operated at an optimum pH between 5.5 and 7.0, in order to minimize copper dissolution, so that, formation of insoluble copper molybdate leading to molybdenum loss, could be lowered. Warren and Mounsey (1983) found an optimum pH of 9.0 in solutions containing carbonate. At higher pH, as against 5.5 and 7, copper molybdate is unstable and copper forms oxide or hydroxide.

The salient features of the USBM process are as follows: at the start of the electro-oxidation process, the brine solution essentially consists of Na^+, Cl^-, and $CO_3^=$ besides OH^- as the major species. As dissolution progresses, the solution chemistry becomes increasingly complex with the entry of chlorites, chlorates, molybdate, sulfate and copper ions, when pH of the slurry is maintained between 5.5 and 7.0. Build up of some of the species, is known to lead to the catalytic decomposition of hypochlorite to chlorate, that does not participate in the dissolution process. The leach liquor, containing low molybdenum values and a host of ionic species, is subjected to purification wherein molybdenum is transferred to a recovery stage.

Chemistry of the Electro-Oxidation Process

The electrolysis of brine, in alkaline media, followed by the oxidation of molybdenite can be represented as Electrode reactions:

$$2\ Cl^- \rightarrow Cl_{2(g)} + 2\ e^- \quad \text{(anode)} \qquad (1)$$

$$2\ H_2O + 2\ e^- \rightarrow 2\ OH^- + H_2 \text{(cathode)} \qquad (2)$$

Solution reactions:

$$Cl_{2(g)} \leftrightarrows Cl_{2(aq)} \qquad (3)$$

$$Cl_{2(aq)} + 2OH^- \leftrightarrows ClO^- + Cl^- + H_2O \qquad (4)$$

Hypochlorite consumption reaction:

$$MoS_2 + 9\ ClO^- + 6\ OH^- \rightarrow MoO_4^{2-} + 9\ Cl^- + 2\ SO_4^{2-} + 3\ H_2O \qquad (5)$$

Chlorate formation reaction:

$$3\ ClO^- \leftrightarrows ClO_3^- + 2\ Cl^- \qquad (6)$$

chlorate is also formed electrochemically by the reaction at anode [Barr et al, 1979]:

$$6\ OCl^- + 3H_2O \leftrightarrows 2ClO_3^- + 4Cl^- + 6\ H^+ + 3/2\ O_2 + 6\ e^- \qquad (7)$$

The total chlorate production is the sum of reactions (6) and (7). The stability domain of ClO_3^-, in the presence of chloride, covers the domains of HClO and ClO^-. The transformation of ClO^- to chlorate is catalyzed by the presence of transition metal compounds, such as nickel and copper hydroxides.Solution pH is maintained at an optimum value of 6 to 8 by periodic additions of Na_2CO_3. During prolonged electro-oxidation, the chlorate concentration continues to build up, as do Cu^{2+}, $CO_3^=$ and $SO_4^=$, reducing the availability of free chloride. At pulp densities of around 2-3% solids, reported in the literature, the molybdenum concentration in the electrolyte is expected to be low, even after extended duration of electro-oxidation. Circulating large volume of lean solutions through the purification stage, for recovery of molybdenum values, reduces throughput.

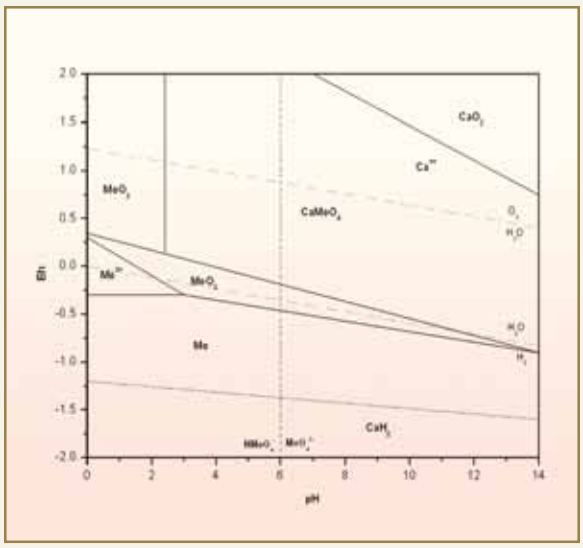

Fig.1: Eh-pH diagram of Ca -Mo-H_2O system[7]

In an effort to minimize chlorate build up, along with $CO_3^=$, $SO_4^=$ and Cu^{++}, maintain uniform reaction rate as well as solution chemistry, addition of calcium chloride in place of sodium carbonate has been attempted. The addition of controlled amounts of calcium chloride to the brine, at the start of electrolysis, ensures the formation of calcium molybdate, calcium sulfate and copper carbonate and at all times the concentration of molybdate ions in solution is maintained around 10^{-2}M. At pH values 9-10, calcium molybdate is the stable species as indicated by the Eh-pH diagram in Fig. 1.

As a result, the temperature of the brine can be maintained at 303-308 K, in order to improve the dissolution kinetics with reduced conversion, both electrochemical as well as chemical, to chlorate. Higher temperatures affect the dissolution of chlorine gas evolved at the anode as well as the stability of hypochlorite. The schematic flowsheet of the modified electro-oxidation process is indicated in Fig. 2.

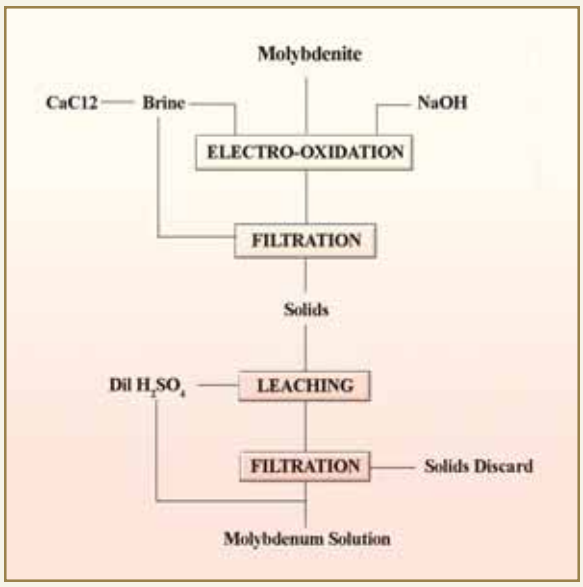

Fig. 2: Modified electro-oxidation process

Experimental

Low-grade molybdenite concentrate from UCIL, Jaduguda, Bihar, India was used, for the electro-oxidation experiments. Analysis of the concentrate is shown in Table 1.

Experiments were conducted using two types of electrode assemblies viz., monopolar and bipolar. A schematic of the bipolar assembly is indicated in Fig. 3. The assembly consisted of four graphite electrodes, separated by perspex frames to maintain uniform gap and prevent charge jumping at the edges, with the end electrodes connected to the graphite busbars. The assembly was suspended in a 10 L glass beaker fitted with a Nylon® lid, to restrict the evolved chlorine from escaping. The lid, was provided with openings for graphite busbars, pH sensor, inlet for sodium hydroxide as well as for drawing of samples for analysis. The brine solution volume was maintained at 4.0 L, 1.2 L for monopolar cell, with 10 wt% NaCl. The slurry containing 2 wt% solids was stirred using a PTFE® coated magnetic stirrer. Known amount of $CaCl_2$ was added to the slurry at the beginning of each electro-oxidation experiment, with anode current density varying between 450 – 775 A/m^2. At all times, the pH of the slurry was maintained between 9.0 and 10.0 by frequent additions of NaOH. The solids, containing $CaMoO_4$ and $CaSO_4$, were leached with recycled Mo solution.

Table 1: Analysis of low grade molybdenite concentrate

Particle Size		Wt% (Bal. SiO_2)				
µm	#	Mo	Cu	Ni	Fe	S
150	100	30.56	0.6	0.3	5.1	22.6

Results and Discussion

The results of the monopolar electrode arrangement are shown in Fig. 4. The monopolar electrode assembly consisted of concentric graphite cylinders suspended in the slurry. The dissolution was rapid, resulting in

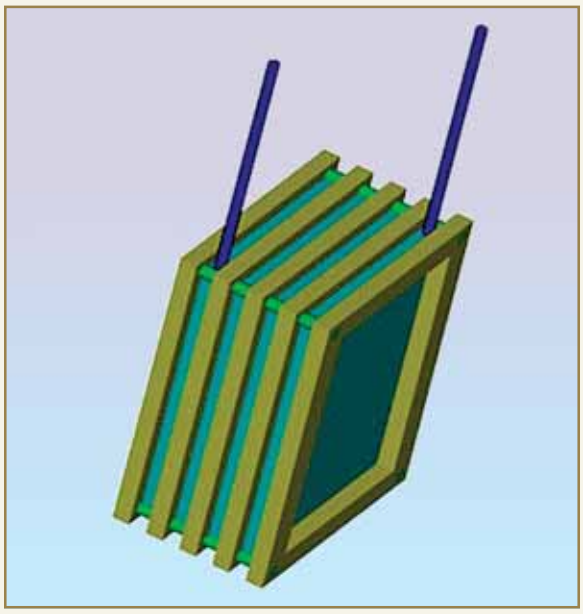

Fig. 3: Bipolar electrode assembly: a schematic representation

proportional changes in pH of the slurry. It has been reported that the rate of molybdenite oxidation was directly proportional, to the square root of the concentrations of hydroxyl and hypochlorite ions. In the present study, under reasonably constant [OH^-] and current density of 775 A/m^2, the rate of molybdenum dissolution was linear for the duration of study.

The experiments were carried out under similar experimental conditions and the results of various electrode configurations, have been depicted in a single plot shown in Fig. 5. As the pulp density, as well as the anode current density were maintained

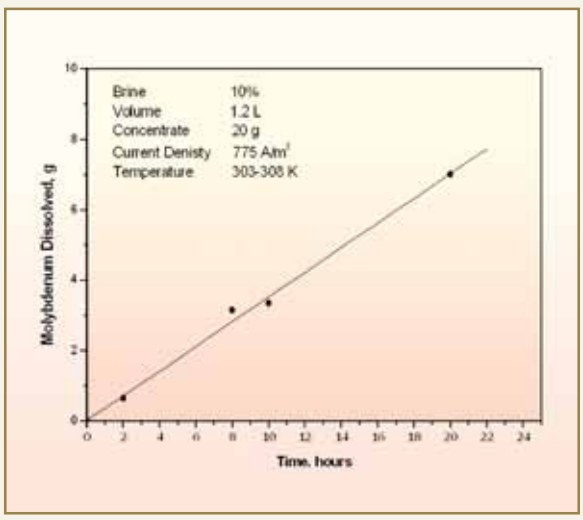

Fig. 4: Results for monopolar electrode assembly

constant for all investigations, the rate of dissolution was found to be consistent, indicating that, the formation as well as the precipitation of molybdate, sulfate and degradation of hypochlorite, if any, had little effect. The solution, after electro-oxidation, contained low amounts of sulfate and chlorate and could be recycled repeatedly without any intermediate purification. The solids were leached with recycled molybdenum solution, in order to maintain low solution volume for further purification.

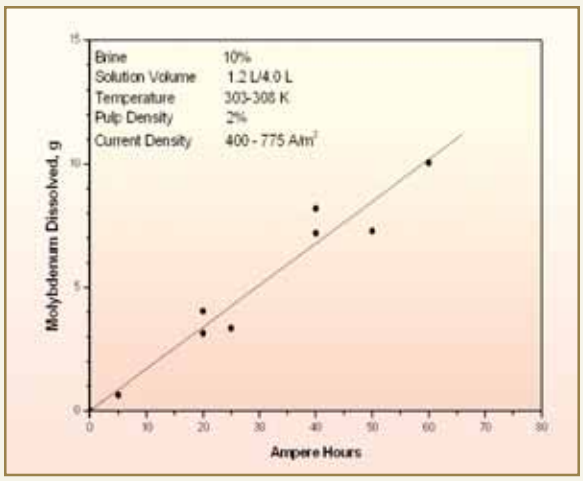

Fig. 5: Molybdenum dissolution with monopolar and bipolar assembly

The same brine solution was used for all the investigations, without the need for any purification and recycled directly from a reservoir. The objective of the exercise was to detect changes in leaching behaviour, owing to the build-up of significant amounts of chlorate and other ions, if any. The amounts of molybdenum and sulfate ions in the solution were found to be below 0.1 gpl, while the amount of chlorate was not analyzed.

Conclusion

Initial investigations in the use of controlled amounts of calcium chloride during leaching, proved encouraging, as the rate of molybdenite oxidation remained relatively unaffected, owing to the low build-up of molybdate and sulfate ions. Electro-oxidation was carried out at pH between 9.0 and 10.0, in order to maintain a high hydroxyl ion concentration, as the rate is reported to be directly proportional to the square root of hydroxyl and hypochlorite concentrations. Brine solution could be successfully recycled for all investigations without any purification.

ABOUT THE AUTHORS

Mr. V.S. Bhave joined BARC in 1988 with B.Sc. (Chemistry) from Karnatak University. His research areas include secondary resources processing for metal recovery and preparation of high purity reactive metals.

Dr. Pamela Alex joined BARC in 1979. Dr. Alex obtained her Ph.D in Chemistry from the University of Mumbai in 1991. Her research areas include secondary resources processing for metal recovery and development of electrochemical processes for deposition, bulk as well as powder form and electro winning of metals. She has successfully transferred knowhow for recovery of metal values from hard metal scrap with special reference to cobalt.

Dr. R.C. Hubli joined BARC as a Scientific Officer in the year 1978 after completing the one year BARC Training School orientation course in Metallurgy. He obtained his Ph.D. in Metallurgical Engineering from IIT Mumbai for his work on Modeling of Metallurgical Process for sulfides. His research areas include secondary resources processing for metal recovery, surface treatment of nuclear materials, preparation of high purity reactive metals and advanced ceramics.

Dr. A.K. Suri, Director, Materials Group has made significant contributions in the areas of Chemical Process Metallurgy, Materials Synthesis and Advanced Materials & Processes. Dr. Suri has been instrumental in the development of processes leading to the setting up of production scale facilities for strategic materials critical to the nuclear programme. Besides being conferred with several prestigious awards for his contributions during his illustrious career, he received the G.D. Birla award (2007) for the development of a new route for the processing of an indigenous uranium resource.

A NOVEL ELECTROSTATIC ION TRAP AND FOURIER TRANSFORM MEASUREMENTS FOR HIGH-RESOLUTION MASS SPECTROMETRY

K. G. Bhushan, S. C. Gadkari, J. V. Yakhmi and V. C. Sahni
Technical Physics and Prototype Engineering Division

This paper received the Best Innovative Research Presentation Award at the 12th ISMAS Symposium-cum-Workshop on Mass Spectrometry held at Goa, during March 25-30, 2007

ABSTRACT

We report on the development of a novel electrostatic ion trap, for high-resolution mass spectrometry. The ion trap works on purely electrostatic fields, thereby allowing simultaneous trapping and studying of multiple mass species, over a large mass range. Ions are trapped and stored as a bunch between two collinearly placed electrostatic ion mirrors and oscillate continuously. The oscillatory signals are fourier transformed to produce the frequency spectrum, wherein each frequency corresponds to a particular mass of the trapped ions. From the initial experiments, a mass resolving power (m/Äm) of about 20,000 and a storage lifetime of about 100 ms is observed. This unique feature and several other important characteristics of this ion trap are presented, along with it's application as a high resolution mass spectrometer.

Introduction

Since the invention of Ion trapping techniques about 50 years ago, ion traps have been utilized for mass spectrometric purposes. These ion traps range from small tabletop size to large ion storage rings. In general, in most of the small ion traps, ions are trapped and confined to a small region of space using a combination of magnetostatic or time-dependent (RF) fields. The motion of the ions under the influence of such fields, is usually a complex function of these fields and in general, has been well understood. Another method of trapping and storing ions is the storage-ring technique, where ions with high kinetic energy are kept circulating with the help of magnetic steering and focusing systems. These are large systems and are particularly advantageous when used with electron-cooler, inside which, the circulating ion beam can be merged with the electron beam, in nearly zero relative velocity conditions. Storage rings require external injection followed by acceleration either externally with a linac or within the ring itself using synchrotron-type acceleration capabilities.

Several techniques have been developed for time-of-flight mass spectrometry such as time-lag focusing and compensating mirrors.

Design of the Ion Trap

'Photon-storage' devices such as 'optical resonators' have long been used in optical devices such as lasers, and their properties have been well studied. In such devices, photons can be trapped between two focusing mirrors and the stability condition is given by [14]:

$$0 \le \left(1-\frac{D}{\rho_1}\right)\left(1-\frac{D}{\rho_2}\right) \le 1 \qquad (1)$$

where D is the distance between the mirrors and ñ$_1$ and ñ$_2$ are the radii of curvature of the mirrors. In the case of a symmetric resonator $(\rho_1 = \rho_2)$ and using the relationship for focal length $f = \frac{\rho}{2}$ the above equation can be simplified to:

$$\frac{D}{4} \le f \le \infty \qquad (2)$$

The ion trap presented here works on a similar principle, in which, the photon mirrors are replaced by 'electrostatic ion-mirrors' and the photon beam is replaced by a well-defined ion-beam. The main advantage with electrostatic ion mirrors is that, they are not mass limited unlike 'magnetic mirrors', which means, very massive ions can also be trapped and stored along with lighter ions provided, they have the same kinetic energy.

A photograph of the actual ion trap is shown in Fig. 1. The ion trap consists of two collinearly placed electrostatic ion mirrors, each consisting of five electrodes. The mirrors are arranged on an optical bench with suitable tie-rods that ensure that they are collinear. In order to have lateral confinement, an einzel lens is added before each mirror. Together with the einzel lens, the ion mirrors have both reflecting and focusing properties that obey Eqn.(2). The inner most electrodes on each mirror are grounded thereby keeping the region between the two mirrors field-free.

In order to have reflecting properties, the ion mirrors need to have a potential which is high enough to stop the ions i.e. $V_\phi > \frac{E_\mu}{q}$ where E_μ is the kinetic energy of the ion beam and q is the charge of the ions. The performance of the ion trap was simulated with SIMION v7.0 software. The initial set of voltages on the ion mirrors and the einzel lenses could be obtained from the simulation, in order to determine stable conditions of trapping. However, in order to perform mass spectrometry with the ion trap, it is important

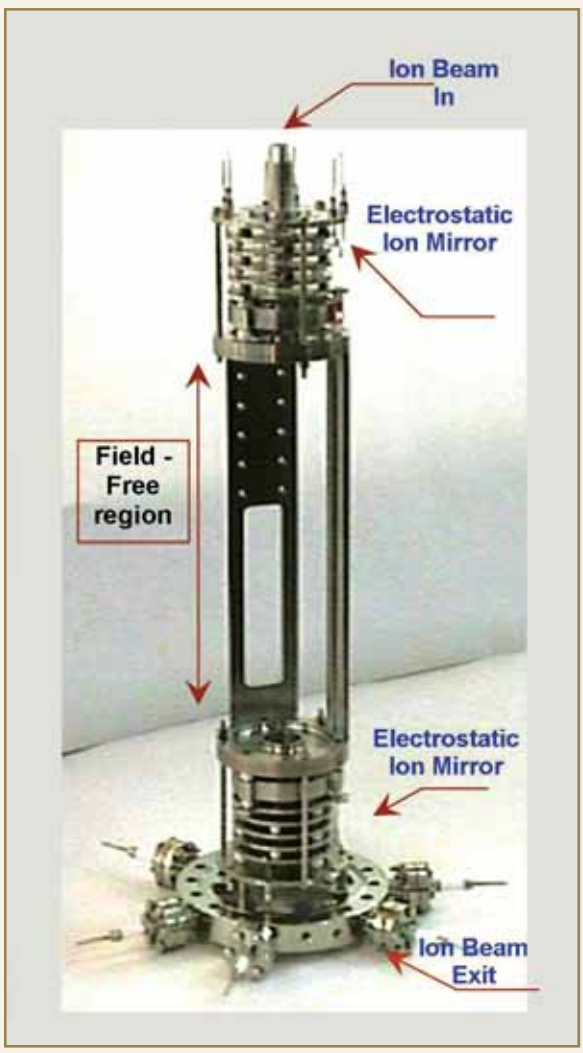

Fig. 1: Photograph of the ion trap

that the trapped ions remain bunched for a long period of time. In order to achieve this, the voltages on the ion mirrors and the einzel lenses were adjusted such that, the energy spread in the ion beam which translates into velocity spread could be compensated by determining the turnaround points inside the ion mirror. It should be noted that this procedure only reduces the time-spread in the arrival of the ion bunch, due to the energy spread in the ion beam, at the centre of the ion trap, where the image charge detector is located.

Experimental Setup and Results

A. Storage lifetime measurement

A schematic of the experimental setup is shown in Fig. 2. The setup consists of an electron impact ion source followed by suitable acceleration and focusing elements. An electrostatic chopper is utilized to pulse the DC beam with pulse widths ranging from 0.5 to 5 microseconds.In order to remove the energetic neutrals that are produced along the beamline, a zeman type 90° electrostatic deflector is employed. The pulsed ion beam is allowed to enter the ion trap, through a 1mm aperture, with the help of suitable XY deflectors and einzel lenses. The entire beamline is kept at very low base pressure of about 5 x 10^{-9} mbar with the help of triode sputter ion pumps, while the ion trap is pumped with the help of a 1000 l/s cryopump and a base pressure of about 7 x 10^{-10} mbar could be achieved, which rises to about 1 x 10^{-9} mbar with the ion source operating. DC ion beam currents of about 50 nA could be injected into the ion trap with every injection, or about 80,000 ions equivalent per microsecond pulse.

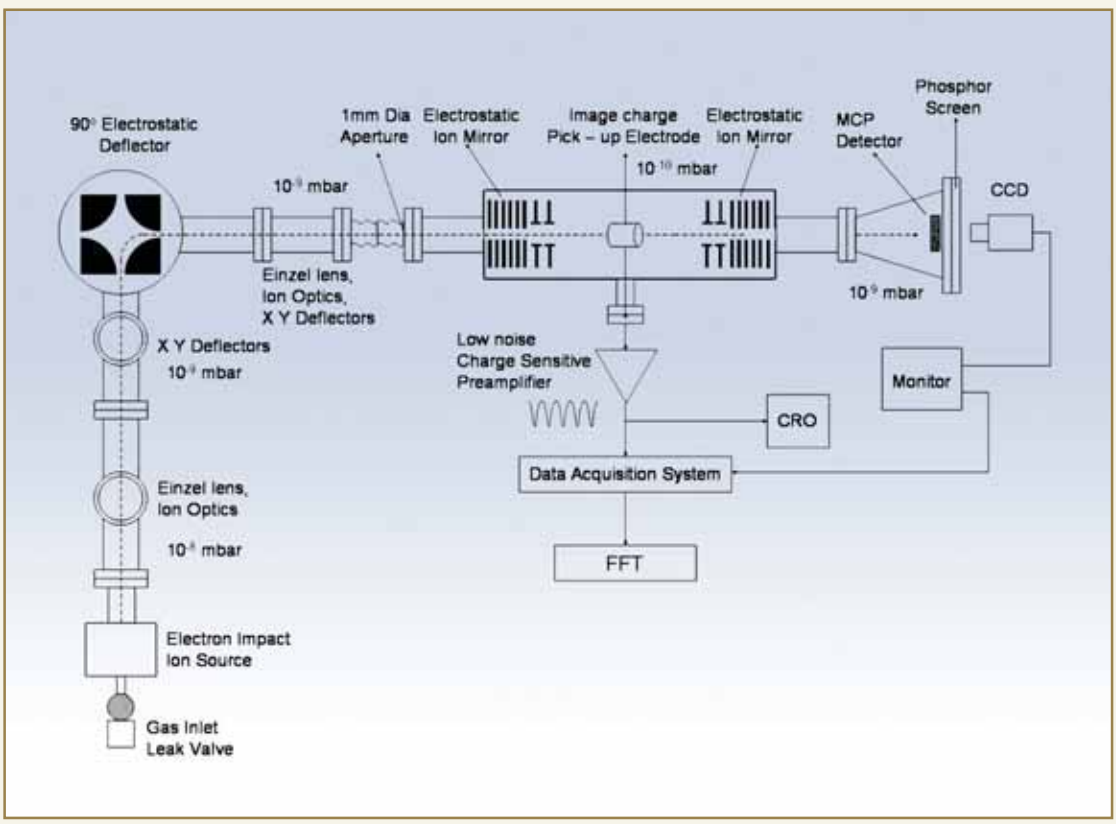

Fig. 2: Schematic of the experimental setup

The voltages on the entrance mirrors are lowered to zero while injecting the ion bunch into the ion trap and the voltages on the exit mirror are kept high, all the time. The voltages on the entrance mirror are switched ON (identical to the exit mirror) as the bunch enters the image charge pickup tube, located at the center of the ion trap. This reduces any interference due to the high voltage switching. Fast high voltage switches with rise times of less than 100ns are utilized, to effect the high voltage switching. The ion bunch is now trapped between the two mirrors and oscillates with a frequency that is inversely proportional to the square root of the mass of the ions. Once the ion bunch is trapped, the ions can decay either by a charge transfer type of reaction (the ions are neutralized by colliding with a residual gas molecule and are no longer trapped) or by elastically scattering off a residual gas molecule and no longer within the realm of stability condition of the trap.

The storage lifetime of the ions is given by : $\tau = \frac{1}{\eta\sigma\upsilon}$ where η is the number density of residual gas molecules in the ion trap, σ is the charge transfer cross section and υ is the velocity of the ions. The storage lifetime is measured by monitoring the energetic neutrals that leave the trap (roughly about a quarter of the stored particles at any given time) are detected by a Microchannel plate detector and counted by a PC based Multichannel scaler (FAST ComTec, Germany. Model P7887), which histograms the data given the bin sizes. The start of the multichannel scaler is slightly delayed with respect to the start of the trapping cycle. The entire timing cycle is controlled by a specially designed 6-channel, <5ns jitter, timer whose pulse widths and delay could be adjusted for individual channels in 100 ns steps. Storage lifetimes measured for different ions are shown in Fig. 3. Storage lifetimes of about 100 ms or greater could be achieved routinely, which was only limited by the base pressure in the ion trap. Under these conditions, an argon ion bunch oscillates with a frequency of about 332 KHz, which when measured for 50 ms turns out to be 16,500 oscillations or the equivalent of a 6 Km long time-of-flight tube, when unfolded.

B. Mass Spectrometry

The oscillation of the ions is detected with the help of an image charge detector (a small metallic tube of 18mm length and 12mm diameter) located at the center of the ion trap. A proportional image charge is induced on the detector, every time the ion bunch passes through it. This charge is then amplified with a suitable low noise charge sensitive preamplifier and the output signal of the preamplifier is digitized by a PC based high speed digitizer card. A fourier transform operation is performed on the digitized signal, to obtain the frequency spectrum.

Two types of ion trapping modes were employed, to optimize the oscillation signals of the ions. In the first case, the dispersive case, the potentials on the ion mirrors were chosen to be linear which made the mirror a 'hard' mirror. In the second case, the self-bunching case, a velocity compensated approach was applied to the potentials on the ion mirrors which made the ion mirror function as a 'soft' mirror.

Fig. 4 shows an FFT spectrum obtained in the 'dispersive mode' from the oscillations of a $^{40}Ar^{+}$ ion bunch, which was used to calibrate the mass

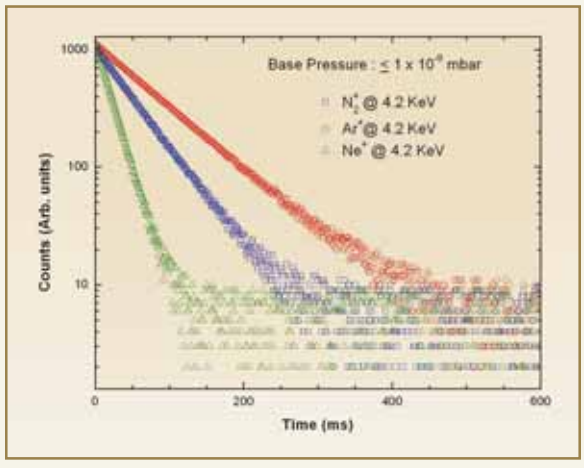

Fig. 3: Storage lifetimes of various ions

spectrometer. The sensitivity of the ion trap was limited by the capacitance of the image charge detector, the capacitance of the ultrahigh vacuum electrical feedthrough, used to transfer the signal out of the vacuum chamber and the input capacitance and the noise levels of the pre-amplifier. Thus, in the present setup, we could not observe $^{36}Ar^{+}$ due to its very low natural abundance.The FWHM (Δf) of the fundamental harmonic is 50Hz and using $R = m/\Delta m = f/2\Delta f$, we obtain a mass resolution of about $\sim$ 3320. The FFT spectrum was averaged for about 100 injection cycles.

Fig. 5 shows an FFT spectrum obtained from the same $^{40}Ar^{+}$ ion bunches trapped in the self bunching mode. In this case, the oscillatory signals decayed much slower than in the dispersive mode, which contributed to a better FFT spectrum. The FWHM (Δf) of the fundamental harmonic is now 20Hz and using $R = m/\Delta m = f/2\Delta f$, we obtain a mass resolution of about $\sim$ 8300. The FFT spectrum was averaged for about 100 injection cycles.

Fig. 6a shows an 'as recorded' Xe^{+} frequency domain spectrum obtained in the 'self-bunching' mode averaged for about 100 injection cycles. The peak amplitudes closely match the known natural abundances of the various isotopes. Further, even higher harmonics could be detected for longer observation times in the self-bunching mode, indicating that a very high mass resolution is possible with this type of mass spectrometer.

Fig. 6b shows a 5th harmonic from which the mass resolution is calculated as $R = m/\Delta m \sim 21{,}000$. This is mainly because the oscillations of the ion bunches in the ion trap are not affected by the usual factors that affect normal TOF instruments such as trigger jitter, time response of the MCP detector, etc. These and other interesting features such as its ability to be

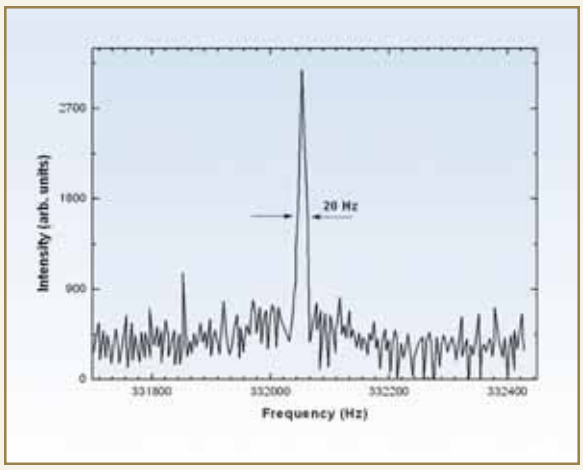

Fig. 4: Frequency domain spectrum showing the first harmonic of trapped Ar^{+} ions in the dispersive mode

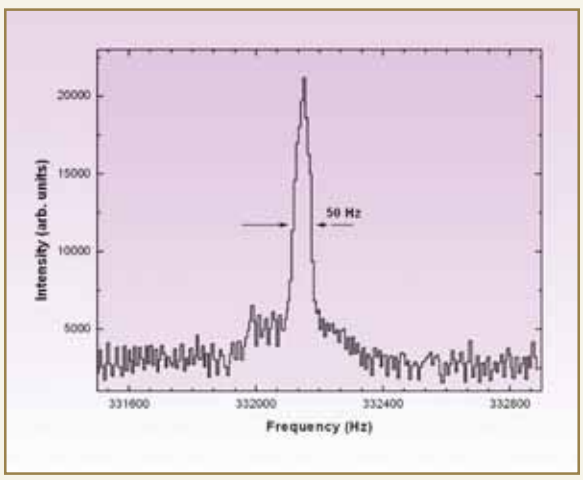

Fig. 5: Frequency domain spectrum showing the first harmonic of trapped Ar^{+} ions in the 'Self-bunching' mode

coupled with multiple ion sources such as MALDI ion source, Electrospray ion sources, etc., make this ion trap a versatile instrument for mass spectrometry.

Conclusion

We have demonstrated a novel electrostatic ion trap, which traps and stores ions as a well defined beam,

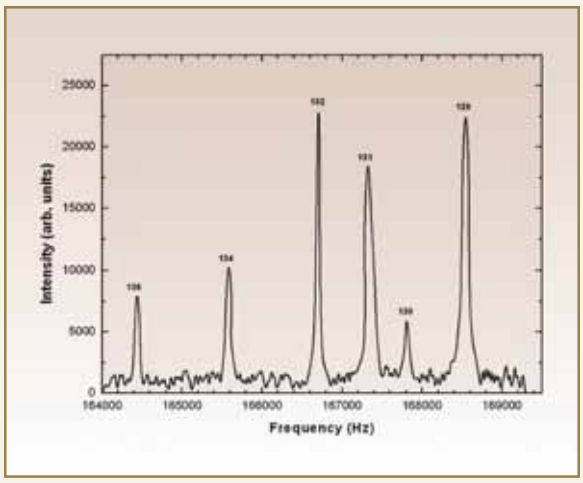

Fig. 6a: Frequency domain spectrum showing the first harmonic of trapped Xe^+ ions in the 'Self – bunching' mode

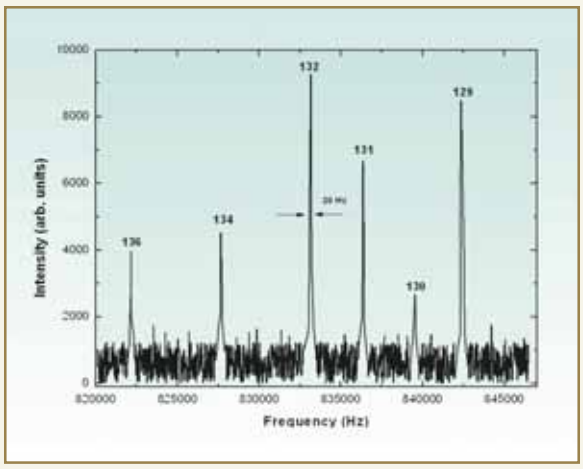

Fig. 6b: Frequency domain spectrum showing the fifth harmonic of trapped Xe^+ ions in the 'Self – bunching' mode

that works on the principle of an optical resonator. Storage lifetimes of about >100 ms for various ions could be achieved. We have also demonstrated the capabilities of the ion trap as a high resolution mass spectrometer, with mass resolutions over 20,000. Further improvements are presently underway, to enhance the mass resolution, by utilizing extremely low ripple high voltage power supplies, very low-noise, charge-sensitive pre-amplifiers and to improve the base pressure in the ion trap. With these developments, we expect this ion trap to be capable of studying large bio-molecules, with particularly interesting functional properties.

ABOUT THE AUTHORS

Dr. K. G. Bhushan completed his Ph.D. in Experimental Atomic/Molecular Physics, from Indian Institute of Technology, Mumbai, in 1997. Soon after, he was awarded a prestigious 'Postdoctoral Fellowship' by the "Feinberg Graduate School' of Weizmann Institute of Science, Israel. where he developed and tested an electrostatic ion-trap for dissociative-recombination studies on 'cooled' molecular ions. He has implemented a novel version of the electrostatic ion-trap as part of the X-plan project. Currently, he is involved in basic research on experimental electron-molecule collisions, high-resolution mass spectrometry and ultrahigh vacuum technology.

ABOUT THE AUTHORS

Dr. Sanjay C. Gadkari joined BARC through 24th Batch of training school. He has been working on the development of technologies for material synthesis, single crystals, thin/thick films based gas sensors and electronic instruments. Areas of his current interest include development of beamlines on synchrotron radiation sources INDUS-I and INDUS-II at RRCAT, Indore and development of ultra-high vacuum based analytical instruments.

Dr. J.V. Yakhmi, Associate Director (S) Physics Group and Head, Technical Physics and Prototype Engineering Division, has worked in BARC for the past 39 years on diverse areas of research in materials science, such as, high-Tc superconductors, magnetic alloys, molecular materials etc. His contributions to the field of molecular electronics and bio-sensors are internationally recognized.

Dr. V.C. Sahni is a well-known Physicist, who has been working in DAE in various capacities for over four decades. At present, he is the Director of the Raja Ramanna Centre for Advanced Technology, Indore and Director of Physics Group, BARC.

बीएआरसी न्यूज़लेटर
BARC NEWSLETTER

ELECTROCHEMICAL STUDIES OF PRUSSIAN BLUE (PB) FILMS IN THE PRESENCE OF DIFFERENT CATIONS

M. K. Sharma and S. K. Aggarwal
Fuel Chemistry Division

This paper was awarded the First Prize for Poster Presentation at the Third International Conference on Electro-analytical Chemistry and Allied Topics (ELAC-2007) held at Shimla, during March 10-15, 2007

Introduction

The modification of an electrode surface has received considerable attention recently. The details of electrochemical studies of Prussian Blue (PB) film modified electrode are discussed. The electrochemistry of PB modified electrode is examined in solutions of various supporting electrolytes, including cationic surfactant. Cations e.g. K^+ can be expected to transport through the crystal of PB films, because of its zeolitic nature. Two proposed formulae of PB are – water insoluble PB $Fe_4[Fe(CN)_6]_3$ and water soluble PB $KFe_2(CN)_6$. The chemical reduction and oxidation of PB give Prussian white (Everitt's salt) and Prussian green (Berlin green), respectively. PB is a mixed valence species with high spin iron (3+) ligated by six N atoms and low spin iron (2+) ligated by six carbon atoms of cyanide and formulated as ferric ferrocyanide. *In situ* Mossbauer measurements have shown, that the reduction of Prussian blue to Prussian white (Everitt's salt) proceeds via the reduction of high spin iron (3+) to iron (2+). Prussian blue has been manufactured as an important pigment for paints, lacquers, printing inks and other colour uses, but recent interest in PB and related surface modified electrodes is due to their potential application as electrochromic devices, electrocatalyst and cathode materials for batteries, in chemical analysis and in ion exchange. We have studied the effect of electrolyte cation size, on the electrochemistry of electrode surface bound PB. Attempts have been made to investigate the possible formation of Self-Assembled Monolayer (SAM) of cationic surfactant on PB-modified surface, by electrostatic attraction between positively charged surfactant and cation deficient Prussian white. This SAM can act as a template for nanostructure synthesis and molecular recognition. SAM can be formed by simply switching to PB reduction potential. Electrochemical synthesis of PB film on Au and Pt electrode was carried out and charge transfer through PB film and across the interface, was studied by Cyclic Voltammetry (CV), Chrono Amperometry (CA) and Electrochemical Quartz Crystal Microbalance (EQCM).

Experimental

Potassium ferricyanide, ferric chloride, potassium chloride, dodecyl trimethyl ammonium chloride and hydrochloric acid used, were of analytical grade. Water was purified with a milli Q (18.2 M&!cm^{-1}) system.

CV, CA and EQCM experiments were performed on CHI 440 electrochemical workstation. Gold coated quartz crystals were used for EQCM experiments. The synthesis of Prussian blue (PB) film on Au and Pt electrode was carried out by cycling potential between 0.6 V and -0.2 V (vs. SCE) in mixture of 2 mM $FeCl_3$ and 2 mM $K_3Fe(CN)_6$ prepared in 0.01 M HCl solution. The solution of 1 M KCl and 10 mM surfactant (dodecyl trimethyl ammonium chloride) was prepared in Millipore water. Chronoamperometry experiments were performed at -0.2 V and 0.6 V (vs/SCE) for different time periods in 1 M KCl as well as in 10 mM surfactant solution.

Result and Discussion

Fig. 1 and Fig. 2 show the CV and EQCM data, respectively, for the synthesis of Prussian blue film on Au electrode. The increasing peak current and decreasing frequency (i.e. increasing mass) with increasing numbers of CV cycles show the synthesis and growth of PB film on electrode. In Fig. 2, decrease in frequency in the region between 0.22 V and -0.2 V shows, formation of PB film and insertion of K^+ ions into PB film and increase in frequency between 0.22 and 0.3 V shows exclusion of K^+ ions from PB film.

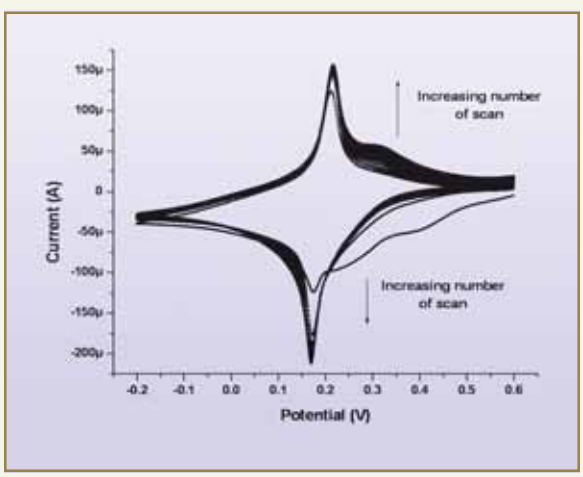

Fig. 1: Synthesis of Prussian blue film on Au electrode. Scan rate 50 mV s^{-1}.

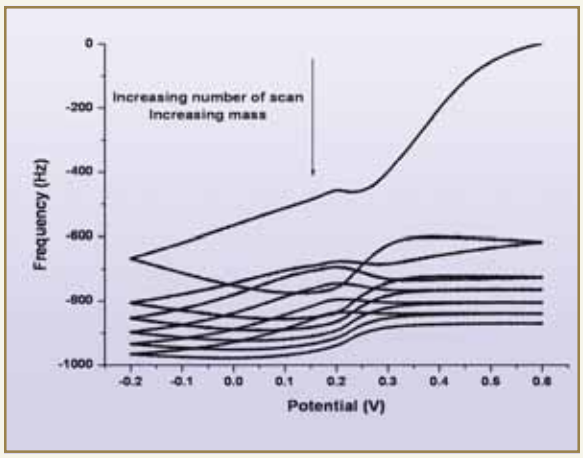

Fig. 2: EQCM data for Prussian blue film synthesis on Au electrode

Fig. 3 and Fig. 4 show the CV and EQCM data of PB film coated Au electrode in 1 M KCl, respectively. In Fig. 4, rapid change in slope between 0.25 V and 0.1 V during cathodic scan indicates the entering of K^+ into the reduced and negatively charged PB film to maintain electrical neutrality and rapid change in slopebetween 0.2 V and 0.35 V during anodic cycle indicates exclusion of K^+ from the reoxidized and neutral film.

Fig. 5 shows that electron transfer between PB film and electrode is highly irreversible in surfactant solution. Since surfactant cations are much bulkier and larger

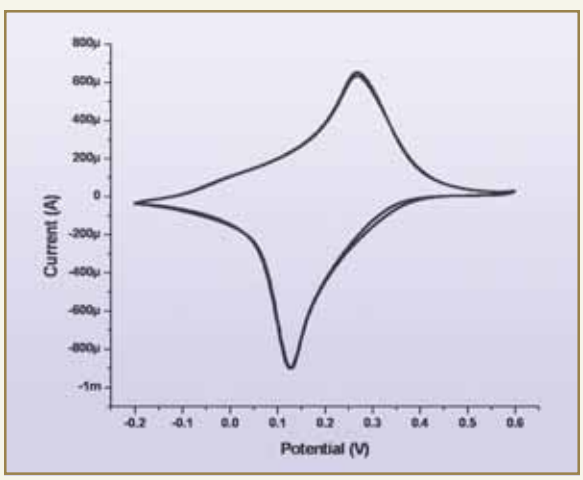

Fig. 3: CV of PB film coated Au electrode in 1 M KCl.

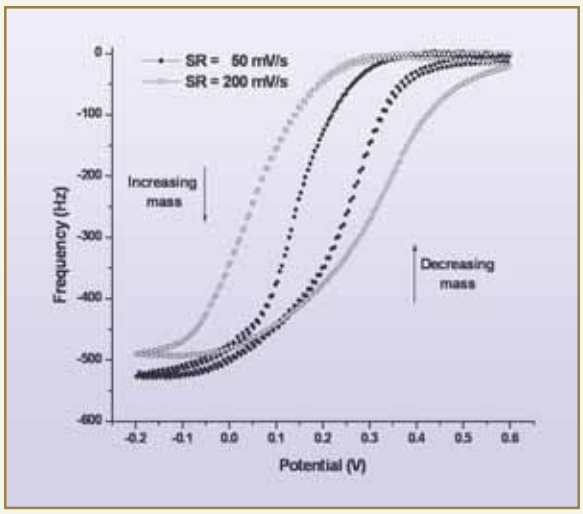

Fig. 4: EQCM data during CV of PB film coated Au electrode in 1 M KCl at different scan rates

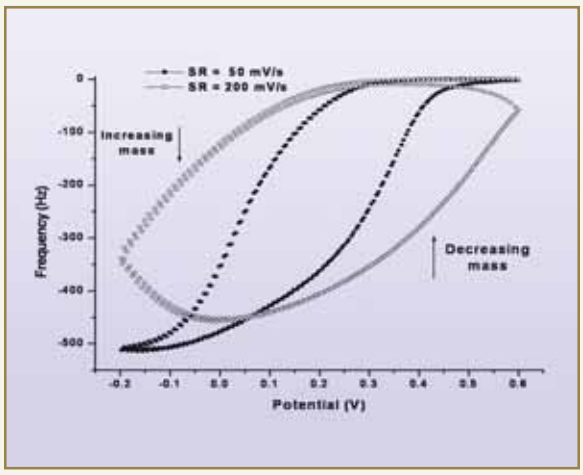

Fig. 6: EQCM data during CV of PB film coated Au electrode in 10 mM surfactant at different scan rates

than K^+ ions, they may not be able to enter into the PB film, but increase in mass during cathodic scan and decrease in mass during anodic scan indicate, that surfactant cations bind electrostatically to reduced PB film surface during cathodic scan and release from the PB surface during anodic scan.

In Fig. 7 EQCM data during CA experiment in 1 M KCl also supports the insertion of K^+ into the reduced PB film and exclusion of K^+ from the reoxidized neutral PB film.

In Fig. 8, CA and EQCM data for 5 s shows that PB film is not completely reduced at -0.2 V and there is no mass saturation in 5 seconds as observed in the case of KCl, but in Fig. 9, CA and EQCM data for 20 s shows that reduction of PB film is almost complete and mass saturation occurs. The diffusion of bulkier surfactant cations is much slower than that of K^+ ions and they may not enter into the PB films. Instead, they bind electrostatically to PB surface.

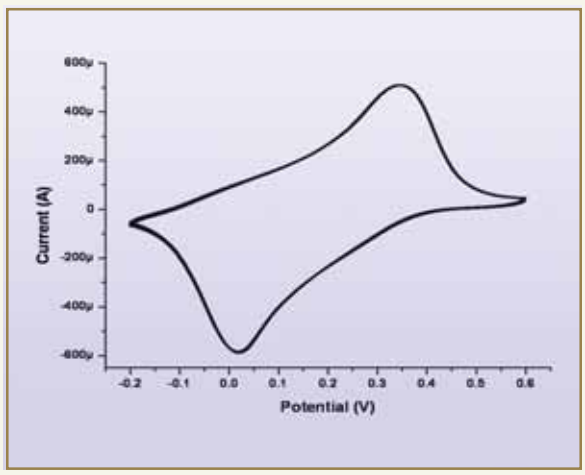

Fig. 5: CV of PB film coated Au electrode in 10 mM surfactant. Scan rate 50 mVs^{-1}

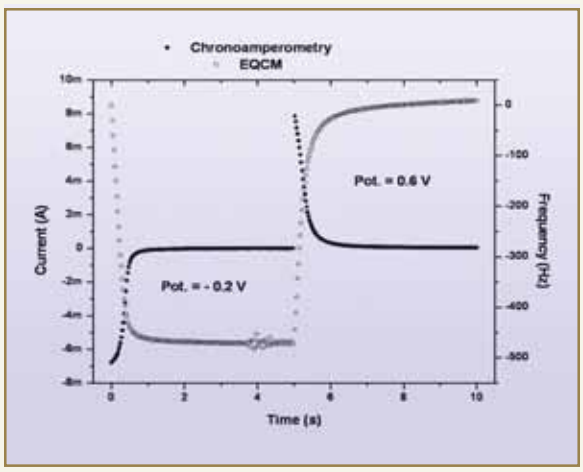

Fig. 7: CA and EQCM data of PB coated Au electrode in 1 M KCl at -0.2 V and 0.6 V for 5 seconds

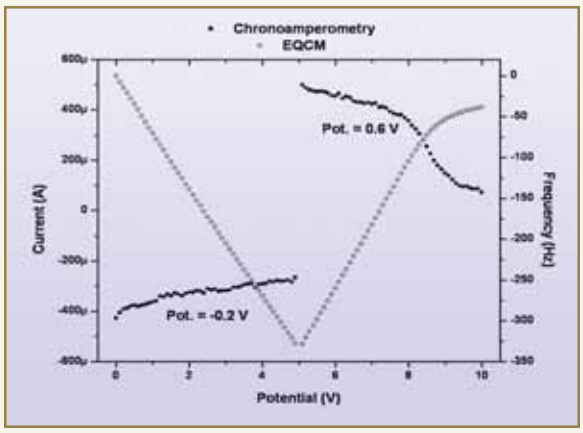

Fig. 8: CA and EQCM data of PB coated Au electrode in 10 mM surfactant at -0.2 and 0.6 for 5 s

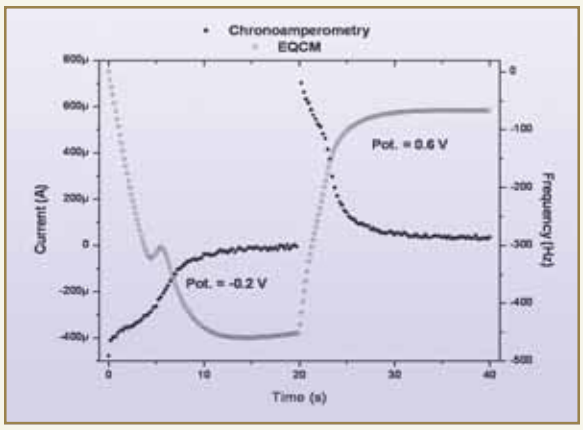

Fig. 9: CA and EQCM data of PB coated Au electrode in 10 mM surfactant at -0.2 and 0.6 V for 20 s

Conclusion

The rate of electron transfer between electrode and PB film is dependent on electrolyte. Since surfactant cations are bulkier than K^+ ions, they diffuse slowly toward the electrode surface and may not able to enter into the PB films. Instead, they bind electrostatically to PB surface. Attempts have been made to investigate the possible formation of Self-Assembled Monolayer (SAM) of cationic surfactant on PB modified surface by electrostatic attraction between positively charged surfactant and cation deficient Prussian white. This SAM can act as a template for nanostructure synthesis and molecular recognition. It can be formed by simply switching to PB reduction potential. Further surface probe microscopic investigations are required to confirm our interpretation.

ABOUT THE AUTHORS

Mr. Manoj Kumar Sharma obtained his M.Sc. degree in Chemistry from IIT Delhi. He joined the Fuel Chemistry Division of BARC, after graduating from the 46th Batch of Training School in 2003. He is working on various electroanalytical techniques and his area of interest includes nanomaterials, development of modified electrodes for sensor applications and ion-selective electrodes.

Dr. S.K. Aggarwal is currently Head, Fuel Chemistry Division, BARC, Trombay. He joined the 16th Batch of BARC Training School in 1972 and received the Homi Bhabha Award. He is a specialist in the field of atomic mass spectrometry and alpha spectrometry and is interested in various mass spectrometric techniques. His other areas of interest include electrochemistry, X-ray spectroscopy and solvent extraction. He is a recognized Ph.D. guide of the Mumbai University and of HBNI.

बीएआरसी न्यूज़लेटर BARC NEWSLETTER

A NOVEL DOXORUBICIN-ENCAPSULATED PH-SENSITIVE LIPOSOME FOR TARGETED CANCER THERAPY

Shailesh Sonar and Sandra E. D'Souza
Radiation Biology and Health Sciences Division
and
K. P. Mishra
Research Institute for Radiation Biology and Medicine, Hiroshima University, Japan

This paper received the " K.S. Kongaonkar Award" at the Indian Biophysical Society's (IBS-2007) National Symposium on Biophysics: Trends in Biomedical Research, held at the Indian National Science Academy (INSA), New Delhi, during Feb.13-15, 2007

ABSTRACT

Liposomes represent unique biomaterial, with potential to encapsulate and deliver a variety of therapeutic drugs, to target organs. The acidic pH of tumour interstitial fluid, a characteristic of many solid tumours, has prompted the development of pH-sensitive liposomes, with the prospect of selective delivery of anti-cancer drugs to the tumour. To achieve this goal, initial efforts were devoted to design liposomes with pH sensitivity, by incorporating the cone-shaped dioleoylphosphatidylethanolamine (DOPE) (40-60 % of total lipid). The present report describes the design of a novel doxorubicin (DXR)- loaded pH-sensitive liposome using DSPC, cholesterol and oleic acid (molar ratio, 40:40:20), with significantly reduced fraction of DOPE (2-8 % of total lipid). A novel feature of the present formulation consists of a single-step preparation protocol, based on ethanol injection method, avoiding extrusion or sonication but achieving significant amount of DXR entrapment (~ 98 %, for DXR: PL molar ratio 0.2:1). Despite small fraction of DOPE in the formulation, the designed liposomes showed marked release of entrapped DXR in the pH range of 6 to 4, which compared well with the DOPE-based liposomes. The pH-dependent DXR release in this formulation, was found independent of DOPE fraction, but a small fraction of DOPE along with DSPC and cholesterol (1:1), imparted greater stability to the serum. It was interesting to note that the designed liposomal formulation, DSPC: DOPE: CHOL:OA (molar ratio, 36:4:40:20) displayed a remarkable pH-sensitivity in the acidic range. Typically, the optimized formulation showed ~ 60 % DXR release at pH < 6.0 within 2 minutes and exhibited significant stability in the 50 % serum, indicating possible practical application.

Introduction

Chemotherapy and Drug Delivery for the Treatment of Solid Tumours

The clinical use of most conventional chemotherapeutics is often restricted, due to inadequate delivery of therapeutic drug concentrations, to the tumour target tissue or due to serious toxic effects on normal organs. In attempts to improve therapy with these anticancer agents and lessen the coupled side effects, Drug Delivery Systems

(DDS) have been introduced, with the objective of meeting four key requirements for tumour-targeted drug delivery. These requirements are "Retain (drug while in circulation), Evade (the body's defenses), Target (tumour tissue and vasculature) and Release (drug specifically in tumours)". Several DDSs have been introduced: namely, liposomes, microparticles, polymeric conjugates, micelles and nanoparticles, to facilitate effective chemotherapy with anticancer agents. The present studies describe doxorubicin-loaded liposomes Fig. 1, which are designed to respond to changes in pH, in order to target acidic milieu of solid tumours for targeted drug delivery.

Promising Strategies

Several strategies have been proposed, to accomplish site-specific triggered release in tumour tissue. New liposome strategies consist of constructs capable of stimuli-sensitive release: such liposomes are designed to go through structural changes in response to physicochemical stimuli, thus allowing more controlled release of encapsulated drug. These approaches include the use of pH-sensitive liposomes triggered by the characteristic acidic milieu of solid tumours, temperature-sensitive liposomes triggered by exogenous application of heat (hyperthermia), light and more recently the enzymatically-triggered approach. All these approaches have been shown to be valuable concepts, for releasing encapsulated drugs.

pH-sensitive liposome

Release of drug triggered by environment-sensitive lipids or polymers, that respond to changes in pH, such as at pH ~6.0 in the tumour interstitium or at pH ~5.0 in endosomes, if successfully accessed by specific targeting (eg. Folate receptor targeted).

Present work

Single-step liposome preparation

- A novel feature of the present formulation consists of a single-step preparation protocol, based on the ethanol injection method.
- Avoids extrusion orsonication.
- Entrapment of remarkably high amount of DXR without any additional drug-loading step.
- Simple, fast, cost-effective and scalable.

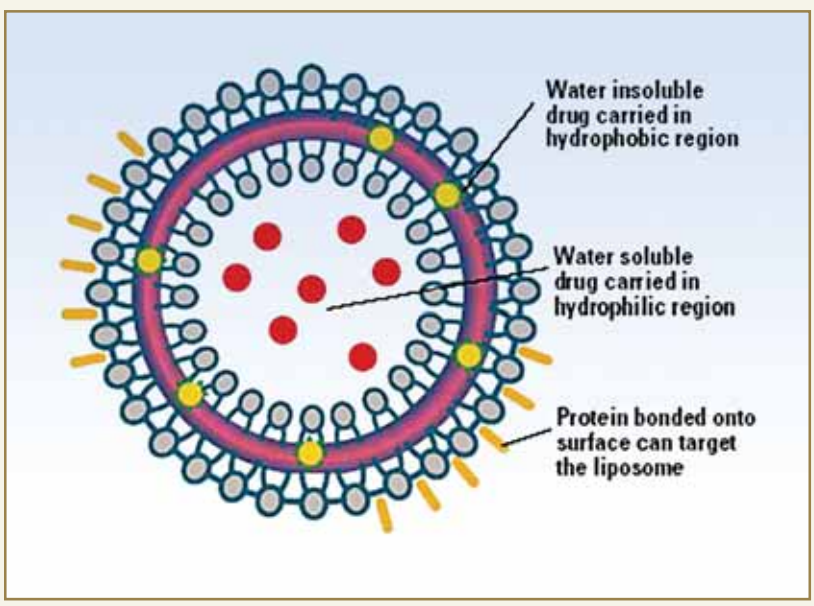

Fig. 1: Schematic diagram of liposome

Liposomes were prepared by injecting 1ml ethanolic solution of a given composition of lipids [PL (50 µmoles)/ CHOL (50 µmoles) / OA (25 µmoles) dissolved in 1ml ethanol] into 9 ml sterile distilled water, containing 10 µmoles doxorubicin (as shown in Fig. 2).

Table 1: Liposomal formulations prepared by single-step protocol

Formulation	Composition (Molar ratio)	Liposome Size (nm)	% DXR Encapsulation	DXR to PL molar ratio
MCOL-2-DXR	DMPC/CHOL/OA (40/40/20)	123 ± 8	95 ± 5	0.19
PCOL-2-DXR	DPPC/CHOL/OA (40/40/20)	126 ± 5	95 ± 6	0.19
SCOL-2-DXR	DSPC/CHOL/OA (40/40/20)	135 ± 2	96 ± 3	0.192
SECOL-1-DXR	DSPC/DOPE/CHOL/OA (36/4/40/20)	135 ± 9	92 ± 2	0.184
SECOL-2-DXR	DSPC/DOPE/CHOL/OA (36/8/40/20)	136 ± 11	91 ± 2	0.182
SECOL-3-DXR	DSPC/DOPE/CHOL/OA (38/2/40/20)	139 ± 4	94 ± 3	0.188

DMPC: Dimyristoylphospatidylcholine
DSPC: Distearoylphospatidylcholine
CHOL: Cholesterol
DPPC: Dipalimitoylphospatidylcholine
DOPE: Dioleoylphosphatidylethanolamine
OA: Oleic acids

Experimental Protocol

pH-sensitivity of liposomes

Liposome solutions incubated with buffer (20 mM HEPES, 150 mM NaCl, pH 7.5, 7.0; 20 mM Citrate, 150 mM NaCl, pH 6.0, 5.0, 4.0) at 37°C for the duration of the experiment.

Fluorescence intensity was measured at each time point (λex = 470 nm, ex. slit= 2.5 nm and λem = 590 nm, em. slit=10 nm).

% DXR Release = (FpH – F0)*100/ (F100 – F0)

F_0 : fluorescence at pH 7.5 at time = 0,

FpH: fluorescence following incubation at respective P^H, F_{100}: fluorescence after the addition of 0.3 M HCl-50% ethanol (Total fluorescence intensity).

Serum-stability of liposome

Serum stability of liposome was determined as changes in size when incubated in 50% serum at 37°C as a function of time.

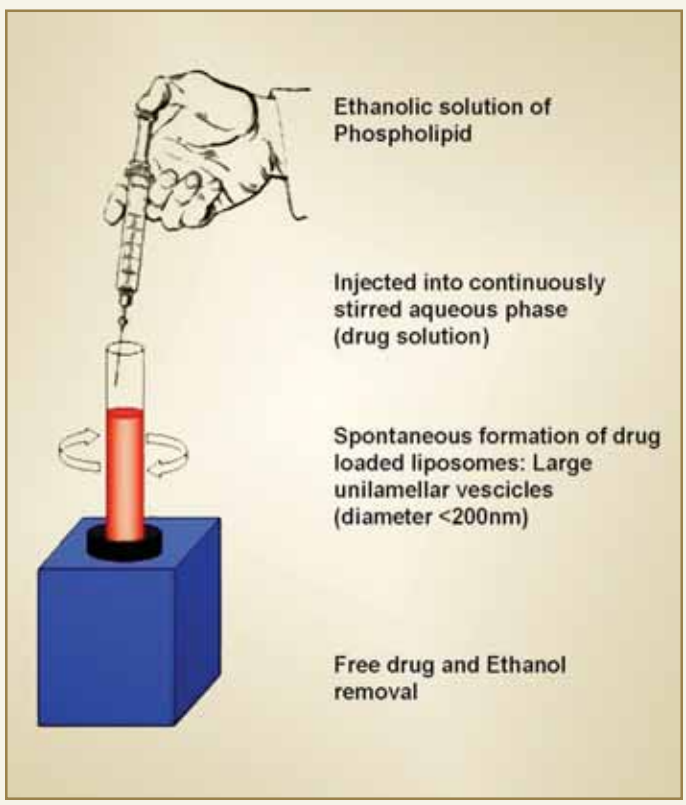

Fig. 2: Process flow chart for single-step liposome preparation by ethanol injection method

Results

pH-sensitive properties of liposomes are detailed in Fig. 3 and the serum stability of liposomes is shown in Fig. 4.

Salient Features

Incorporation of oleic acid during liposome preparation:

- Loaded Doxorubicin (~ 98 %, DXR: PL molar ratio 0.2:1).

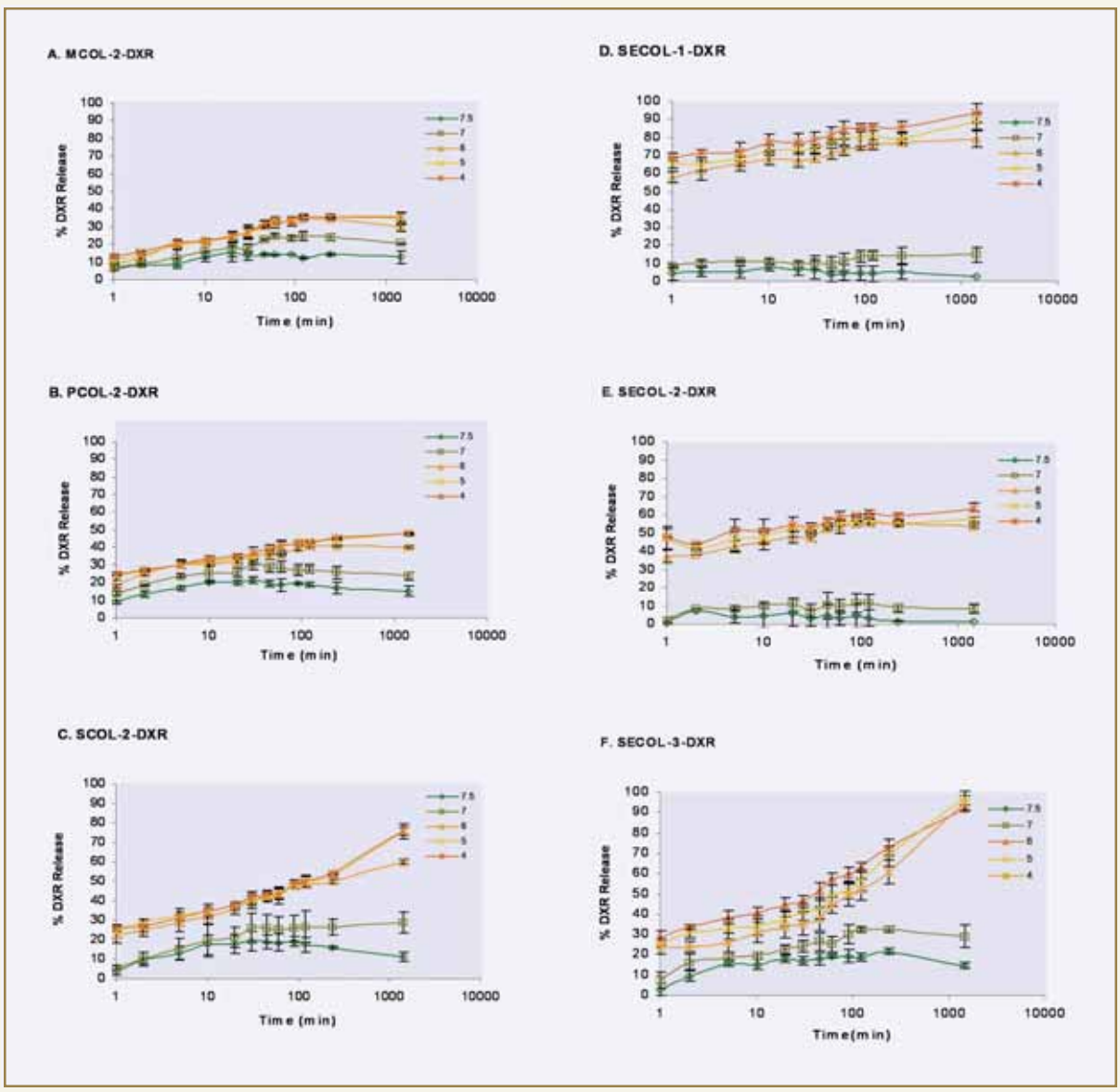

Fig. 3: pH-dependent DXR release kinetics from (A) MCOL-2-DXR, (B) PCOL-2-DXR, (C) SCOL-2-DXR (D) SECOL-1-DXR, (E) SECOL-2-DXR and (F) SECOL-3-DXR at various pHs as indicated by legends. Bars represent standard deviation of the mean.

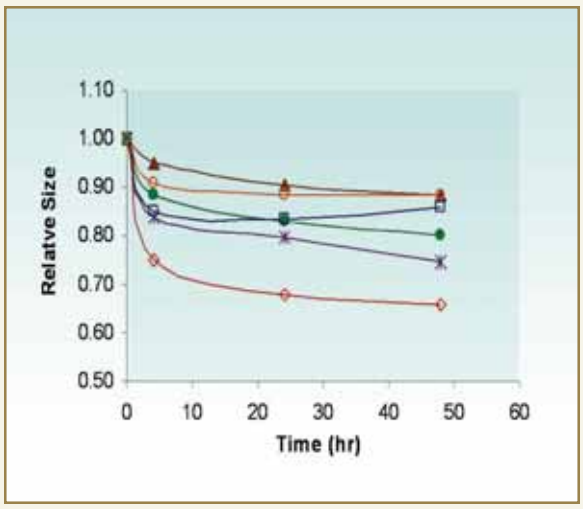

Fig. 4: Serum-stability of liposomes determined as changes in the liposome size after incubation at 37°C in 50% serum

- Conferred pH-sensitive increased drug release from liposomes at acidic pH (δ" 6.0) from SCOL-2-DXR.

The special feature of the designed liposome (mainly SECOL-1-DXR) consists in small fraction of DOPE in the formulation but capable to yield marked release of loaded DXR at acidic pH.

DSPC and cholesterol (1:1) imparted greater stability in the serum.

Results indicate the possibility of applicability in achieving targeted drug delivery for improving cancer therapy.

ABOUT THE AUTHORS

Mr. Shailesh Sonar joined the Radiation Biology and Health Sciences Division, BARC in January 2004 as a Ph.D. student under the BARC-University of Mumbai collaboration scheme. His area of research is design and development of liposomes for drug delivery and diagnostic imaging.

Dr. Sandra E. D'Souza (Retd.) was a senior scientist at the Radiation Biology and Health Sciences Division, BARC.

INERT MATRIX FUELS: MATERIALS FOR FUTURISTIC NUCLEAR REACTORS

V. Grover and A.K.Tyagi
Chemistry Division

Dr. (Ms.) V. Grover is the recipient of the IUPAC Young Chemist Programme Award – 2007
Dr. A.K.Tyagi is the recipient of IANCAS - Dr. Tarun Datta Memorial Award - 2007

ABSTRACT

The development of uranium-free Inert Matrix Fuel (IMF) is of worldwide interest, as by using this approach, it is possible to annihilate the large stock of plutonium. In these fuels, an inert matrix serves as a support for the actinide phases, as does the non-fissile $^{238}UO_2$ matrix for PuO_2 in a typical fast breeder MOX fuel. Inert matrix, as suggested by it's name, does not lead to the formation of any fissile material, after irradiation. This concept is also being contemplated to prepare targets for minor actinides transmutation. Suitable system should include an inert matrix component, a burnable poison, a suitable stabilizer and a fissile material. Considerable work carried out in our group, in establishing phase relations in CeO_2-ThO_2-ZrO_2, CeO_2-Gd_2O_3-ZrO_2, CeO_2-Gd_2O_3-ThO_2 and CeO_2-Dy_2O_3-ZrO_2 systems, with relevance to Inert Matrix Fuels, has been discussed. Ceria is used as a surrogate for plutonia. Certain silicates have also been explored with reference to the same. Almost 500 compositions have been synthesized in these systems and characterized using various techniques like X-Ray Diffraction, High temperature X-Ray Diffraction and EPMA (Electron Probe for Micro-Analysis). Phase relations showed the presence of various monophasic and biphasic phase fields. Several interesting results like stabilization of cubic gadolinia and metastable form of $ThSiO_4$ could be observed.

Introduction

Inert matrix fuel is an innovative concept, for developing materials that could be utilized to annihilate plutonium and also minor actinides transmutation. An inert matrix consists of the inert matrix components, fissile component (Pu), suitable burnable poison, a stabilizer or a fertile additive to improve the neutronic characteristics of the fuel. The choice of inert matrix depends on many criteria such as: Compatibility with cladding and coolant, high thermal conductivity, low thermal expansion, high melting temperature, good heat capacity, good mechanical properties, high irradiation stability. Also, in case of heterogeneous diluents, fuel and diluent have to be compatible and must have similar total vapor pressure at any given temperature to prevent redistribution and demixing because of the radial temperature gradient along the fuel pin during irradiation. Hence, to design an inert matrix, we have to consider Choice of element (low neutron absorption cross section), suitable compound form of these elements (Oxides, carbides, nitrides), right kind of crystalline structure (fluorite, perovskites, spinels, silicates, YAG etc.), Forms of inert matrices viz. CERCER (ceramic-ceramic), CERMET (ceramic – metal), Solid solution Pellet (SSP).

Our work on Inert Matrix Fuels

While proposing an inert matrix for plutonium utilization, it is important to determine the phase distribution and compatibility of PuO_2 with the suggested components of inert matrices. For this purpose, various ternary phase relations have been studied by our group, on systems like CeO_2-ThO_2-ZrO_2, CeO_2-Gd_2O_3-ThO_2, CeO_2-Gd_2O_3-ZrO_2, CeO_2-Dy_2O_3-ZrO_2, with components having relevance to inert matrix fuels. CeO_2 was used as surrogate for PuO_2. ZrO_2 was included to act as the host material for holding the actinide phase because it has got high mechanical strength, chemically inert and a very low absorption cross-section for neutrons and it can be stabilized by rare earth oxides (like Er, Ho, Eu, Gd, Dy ... Y), which are potential burnable poisons, in a single phase cubic structure. Thoria being a very stable oxide (chemically inert), is also a potential host. The inclusion of thoria is likely to improve the neutron economy and *in situ* produced U-233 would increase the burn up of the inert matrix based fuel. Higher melting point and higher thermal conductivity of ThO_2 will also enhance the safety margin of the core. The other motivations for using thorium are enhancement of cycle proliferation-resistance due to reduced plutonium production and economic benefits from reducing the initial enrichment needs. About 500 compositions were prepared by mixing the reactants and firing them at 1200°C, 1300°C and 1400°C with intermittent grindings under slow cooled conditions. The samples were characterized by various techniques like XRD (X-Ray diffraction), HTXRD (High Temperature X-Ray diffraction) and EPMA (Electron Probe for Micro analysis).

CeO_2-ThO_2-ZrO_2 system

This was an interesting phase relation, wherein ThO_2 and CeO_2 formed complete solid solution whereas only 5 mol% of ZrO_2 was taken up by ThO_2. Also, in the $Ce_{1-x}Zr_xO_2$ series ($0.0 \leq x \leq 1.0$), about 20 mol % ZrO_2 is soluble in ceria and then a nearly single-phasic t-ZrO_2 was obtained at the nominal composition $Ce_{0.20}Zr_{0.80}O_2$. An important observation is the absence of the cubic zirconia phase. Thus suitable aliovalent substitution is needed to stabilize the cubic zirconia. In pseudo-ternary systems, ZrO_2-$Th_{0.5}Ce_{0.5}O_2$, CeO_2-$Th_{0.5}Zr_{0.5}O_2$ and ThO_2-$Zr_{0.5}Ce_{0.5}O_2$ and the corresponding opposite apex were chosen as the end members. Only 10 mol % zirconia in the ZrO_2-$Th_{0.5}Ce_{0.5}O_2$ system was found to get incorporated in the lattice of $Th_{0.5}Ce_{0.5}O_2$. The CeO_2-$Th_{0.5}Zr_{0.5}O_2$ system has a two-phase region, consisting of the cubic solid solution of ceria in thoria and m-ZrO_2 upto the $x = 0.30$. Beyond that, small amount of t-ZrO_2 also appears resulting in the triphasic field. The lattice parameter surprisingly increases in the compositions with $x = 0.70$ which can be attributed to the opposite effects of the incorporation of Th^{4+} and Zr^{4+} into CeO_2 lattice. In ThO_2-$Zr_{0.5}Ce_{0.5}O_2$ system, the end member $Ce_{0.5}Zr_{0.5}O_2$, consists of a cubic solid solution and t-ZrO_2. The m-ZrO_2 phase appears from $Ce_{0.40}Zr_{0.40}Th_{0.20}O_2$, to $Ce_{0.15}Zr_{0.15}Th_{0.70}O_2$ giving a triphasic field. The pseudo-ternary phase relation is shown in the Fig. 1a wherein a cubic solid solution phase field and a biphasic field could be delineated unequivocally. Several specimens of CeO_2-ThO_2-ZrO_2 systems were subjected to detailed electron probe microanalysis (EPMA) after quenching. Based on the volume fraction of both the phases and microstructural evidences in these bulk compositions and phase relations at 1400°C, Fig. 1(b) gives the isotherm of the CeO_2-ThO_2ZrO_2 system at 1400°C. Also, a number of single phasic compositions with fluorite-type structure were identified and their lattice thermal expansion was investigated in the temperature range 293 to 1473 K by HTXRD.

CeO_2-RE_2O_3-ZrO_2 system (RE: Gd, Dy)

The ternary phase relation established in CeO_2-Gd_2O_3-ZrO_2 and CeO_2-Dy_2O_3-ZrO_2 systems are shown respectively in Fig. 2 and Fig. 3. In case of $Ce_{1-x}RE_xO_{2x/2}$ system, for both the rare earths, the phase relations are characterized by presence of a single-

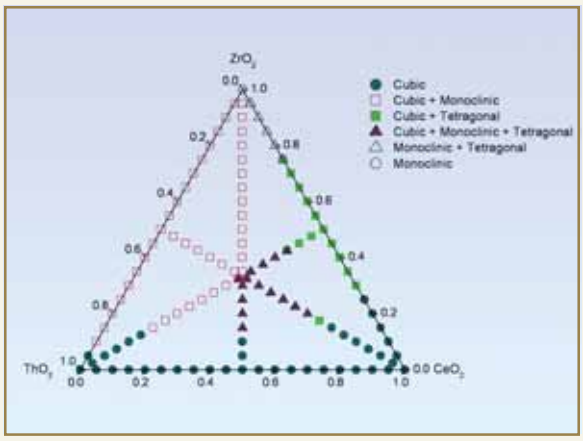

Fig. 1(a): Ternary phase relations in CeO_2-ThO_2-ZrO_2 system

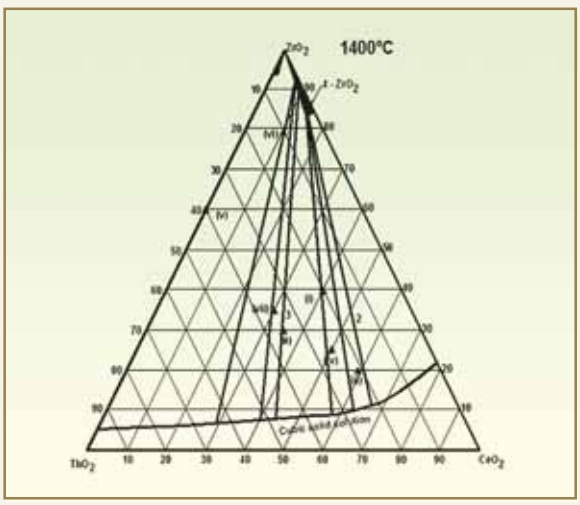

Fig. 1(b): Isotherm of CeO_2-ThO_2-ZrO_2 at 1400°C

phasic fluorite-type phase field and a single-phasic C-type cubic phase field. The lattice parameter of F-type solid solutions increases on incorporation of RE^{3+} whereas the lattice parameter of C-type phase shows an increase on incorporation of Ce^{4+}. Also, since the ionic size difference between Dy^{3+}(0.94 Å) and Ce^{4+}(0.91 Å) is less than as compared to that between Gd^{3+} (0.98 Å) and Ce^{4+} (0.91 Å), there is a steeper increase in lattice parameter of F-type solid solution in CeO_2–Gd_2O_3 as compared to the CeO_2–Dy_2O_3 series whereas the lattice parameter of the C-type solid solution in the latter shows greater variation than in former. Another interesting observation was the stabilization of C-type gadolinia upto much higher temperatures. The structural analysis was done on anion-rich Gd_2O_3 i.e., $Gd_{1-x}Ce_xO_{1.5+x/2}$ (x = 0.20 and 0.40). These are isostructural with C-type rare earth oxides, with excess anions required for charge balance. The $Zr_{1-x}RE_xO_{2-x/2}$ series was characterized by a very wide homogeneity range of rare earth-stabilized-zirconia from 15 mol% $GdO_{1.5}$ to 40 mol% in case of Gd^{3+} and upto 60 mol% in case of Dy^{3+}. In case of Gd^{3+}, x = 0.5 and 0.6 compositions were pyrochlores. Coming to $(Zr_{0.5}RE_{0.5})_{1-x}Ce_xO_{1.75+x/4}$ system, $(Zr_{0.5}Gd_{0.5})_{1-x}Ce_xO_{1.75+x/4}$; (x=0.1 to 0.6) were found to have broad peaks in their XRD patterns, due to the presence of a F-type lattice with another unidentified (presumably F-type) lattice. In case of Dy^{3+}, the compositions with x= 0.1 and 0.15 are single phasic F-type solid solution and beyond that till x=0.5 broad peaks like Gd^{3+} were observed. The lattice parameters increase with increase in ceria content due to increase in average cationic radius. The conversion of pyrochlore to fluorite type phase for Gd^{3+} can be attributed to the fact that Ce^{4+} prefers 8-fold coordination in oxides rather than octahedral coordination. In $(Ce_{0.8}Zr_{0.2})_xRE_{1-x}O_{1.5+x/2}$ series, in case of Gd^{3+}, this series shows a two phase region viz. an F-type phase field till 50 mol% $GdO_{1.5}$ and C-type phase field beyond that. In case of Dy^{3+} though, a biphasic phase field containing two fluorite type solid solutions is observed till 30 mol% doping of $(Ce_{0.8}Zr_{0.2})O_2$ into $DyO_{1.5}$. In $(Zr_{0.5}Ce_{0.5})_{1-x}Gd_xO_{2-x/2}$ series, on doping $GdO_{1.5}$ in $(Zr_{0.5}Ce_{0.5})O_2$, a monophasic fluorite-type phase is stabilized which could be explained by stabilization of zirconia which then forms a solid solution with ceria. Also, broad peaks for compositions containing 30 to 60 mol% $GdO_{1.5}$ indicate a biphasic region comprising of an anion deficient F-type and anion-excess C-type lattice. Now, in the next series $(Ce_{0.5}Gd_{0.5})_{1-x}Zr_xO_{1.75+x/4}$, when ZrO_2 was doped into $Ce_{0.5}Gd_{0.5}O_{1.75}$ (C-type), it got converted to a F-type lattice which is probably due to incorporation of excess anions accompanied by Zr^{4+} substitution which disrupts the ordering of 0.5

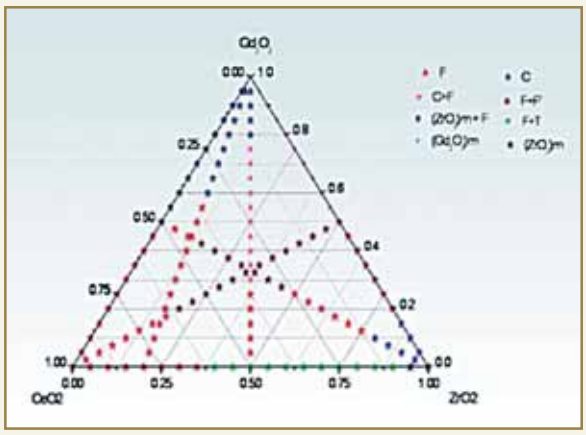

Fig. 2: Ternary phase relations in CeO_2-Gd_2O_3-ZrO_2 system

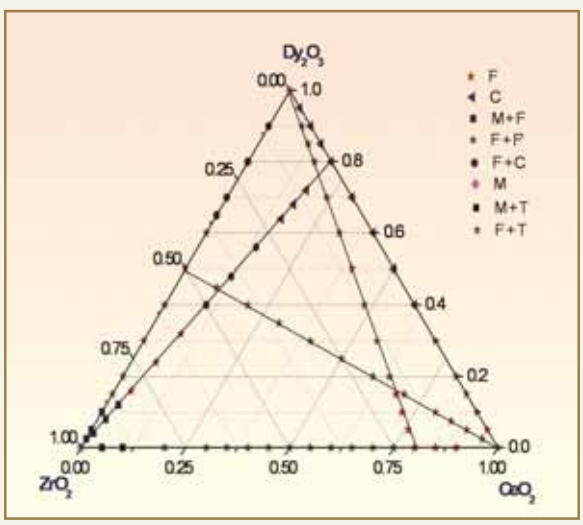

Fig. 3: Ternary phase relations in CeO_2-Dy_2O_3-ZrO_2 system

vacancies in fluorite-type basis cell of $GdO_{1.5}$ and hence converts it into a defect fluorite structure in which all the three cations, Gd^{3+}, Zr^{4+} and Ce^{4+}, are statistically distributed.

CeO_2-Gd_2O_3-ThO_2 system

In this system XRD data revealed the presence of different phase regions namely, cubic fluorite-type solid solution, C-type solid solution and the biphasic regions containing C and F-type solid solutions and two F-type solid solutions. In $Th_{1-x}Gd_xO_{2-x/2}$ system, ThO_2 takes upto 30 mol% $GdO_{1.5}$. In $(Gd_{0.5}Th_{0.5})_{1-x}Ce_xO_{1.75+x/4}$ system, $(Gd_{0.5}Th_{0.5})O_{1.75}$ and CeO_2 are soluble throughout the entire range. In $(Ce_{0.5}Th_{0.5})_{1-x}Gd_xO_{2-x/2}$ system, $GdO_{1.5}$ dissolves upto 40 mol% in $(Ce_{0.5}Th_{0.5})O_2$ lattice giving an F-type lattice and beyond that splits into an F-type phase and a C-type phase with decrease in amount of F-type phase with increasing $GdO_{1.5}$. Lattice parameters trends are a compromise between contraction of the lattice due to oxygen ion vacancies and the expansion due to ionic size. In $(Ce_{0.5}Gd_{0.5})_{1-x}Th_xO_{2-x/2}$, substitution of ThO_2 in $(Ce_{0.5}Gd_{0.5})O_{1.75}$ leads to filling up of oxygen vacancies and the loss of ordering and hence F-type lattice is observed for $x = 0.2$ to 0.5. Beyond that, further nominal compositions are biphasic which can be explained on the basis of partial immiscibility of ThO_2 and Gd_2O_3. This ternary phase relation is depicted in Fig. 4. EPMA studies were done on some of the representative biphasic nominal compositions which could clearly delineate the compositions of two phases corresponding to each of these nominal compositions.

Silicates with zircon structure have a high-potential from the point of view of inert matrix fuel because of their high melting point and the highly stable structure. Two series of compositions with the general formula $M_{1-x}Ce_xSiO_4$ (M = Th, Zr; x = 0.0–0.5; 1.0) were studied by powder XRD. A striking observation was the stabilization of tetragonal modification of $ThSiO_4$, which is metastable, by 10 mol% ceria substitution. There was no solubility of ceria in zircon ($ZrSiO_4$) lattice. The average linear thermal expansion coefficient (293–1123 K) of $ZrSiO_4$, $ThSiO_4$ and $Th_{0.9}Ce_{0.1}SiO_4$ are 4.65×10^{-6}, 4.97×10^{-6} and 5.14×10^{-6} K^{-1}, respectively.

Conclusions

Tremendous R & D work has been devoted to the transmutation of Pu and minor actinides by applying

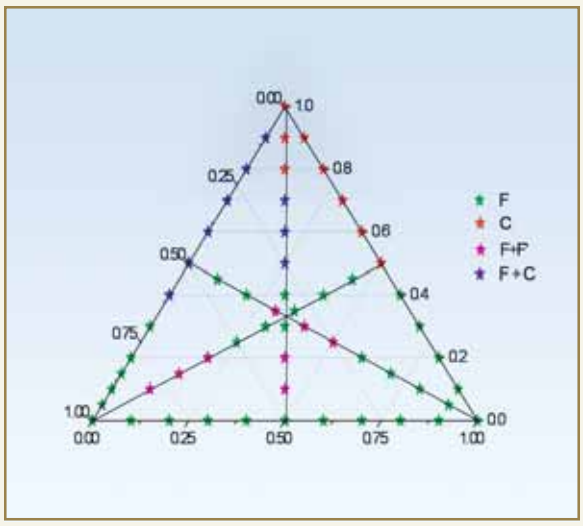

Fig. 4: Ternary phase relations in CeO_2-Gd_2O_3-ThO_2 system

inert matrix fuel (IMF) concept. Our group has been engaged in developing phase relations in systems pertaining to inert matrix fuels. The systems showed the presence of various monophasic and biphasic phase fields comprising of Fluorite-type, C-type, tetragonal and monoclinic phases. Suitable single-phasic compositions were chosen and their thermal expansion properties have been studies. Thermal expansion behavior of these single-phasic ceria bearing compositions can be used to simulate the corresponding compositions containing plutonia.

ABOUT THE AUTHORS

Dr. Vinita Grover Gupta was awarded Ph.D. in 2006 by Mumbai University. Her Ph.D. work has been dedicated to establishing phase relations in the materials to be used as inert matrix fuels in futuristic nuclear reactors. This work resulted in developing ternary phase relations in some of the rare earth oxides for the first time. In addition to nuclear materials her research interests include phase relations and structural studies in rare-earth oxides and alkaline earth fluorides. She is currently working on synthesis and optical properties of rare earth nanofluorides. She has co-authored about 30 scientific articles in international journals.

Dr. A. K. Tyagi joined Chemistry Division,BARC in 1986. He has made important contribution in Thoria based Fuels for AHWR, Glasses for AHWR waste, Inert Matrix Fuels and radiation resistant materials. His other research interests are in the field of Nanomaterials and Functional materials. He is a recipient of Tarun Datta Memorial Award, Dr. Laxmi Award, Rheometric Scientific-ITAS Award, Gold Medal of the Indian Nuclear Society, MRSI Medal, CRSI Medal and Homi Bhabha Science and Technology Award. and National Academy of Sciences, India.

बीएआरसी न्यूज़लेटर
BARC NEWSLETTER

CHLORINE DETERMINATION IN (U,PU)C FUEL BY TOTAL REFLECTION X-RAY FLUORESCENCE SPECTROMETRY

Nand Lal Misra, Sangita Dhara, Khush Dev Singh Mudher and Suresh K. Aggarwal
Fuel Chemistry Division

and

Uday Kumar Thakur, Dipti Shah, R.M. Sawant and K.L. Ramakumar
Radio Analytical Chemistry Section, Radiochemistry & Isotope Group

This paper was adjudged as the Best among the Poster Presentations at the Symposium on Nuclear and Radiochemistry (NUCAR 2007) held at M.S. University of Baroda, Vadodara from Feb. 14 -17, 2007

ABSTRACT

A Total Reflection X-ray Fluorescence (TXRF) method, for the determination of chlorine in (U,Pu)C has been developed. The method involves calibration of the instrument with standard solutions and validation of TXRF determination of chlorine, using synthetic standard solutions. Cl K_a line excited with W L_a source was used, for TXRF determinations of chlorine. Chlorine present in trace amounts in (U,Pu)C samples was first separated by pyrohydrolysis. The evolved chlorine, in the form of HCl, was collected in 5 μM NaOH solution. This solution was analyzed for chlorine by Total Reflection X-ray Fluorescence Spectrometry, using cobalt as an internal standard. The TXRF detection limit of chlorine was found to be 3.6 pg with sample size of 30 μL. In order to assess the applicability of TXRF method for chlorine determinations in other nuclear materials, one U_3O_8 trace element standard was also analyzed for chlorine, in a similar way. The precision of the method was found to be 25% (1s) at ng level in most of the cases.

Introduction

Quality control of nuclear materials such as nuclear fuels, structural materials, cladding etc. for the presence of trace elements, is an important step from the point of view of efficient and safe operation of a nuclear reactor [1,2]. The amount of chorine which can be tolerated in nuclear fuels and structural materials is quite low, because of it's corrosive nature and separation of phases. Presently chlorine in these materials is determined by Ion Chromatography (IC) and Spectrophotometry [1-2] after it's separation from the main matrix by pyrohydrolysis, involving heating of the sample at 900°C in flow of moist argon and

absorbing the liberated chlorine, in the form of HCl in acetate buffer. TXRF is being increasingly used as a trace elemental analytical technique, for metals as well as non-metals alike, in different scientific areas [3]. This technique was previously standardized for trace determination of metals in uranium and thorium oxides [4-5]. In this paper, we report studies carried out to assess the applicability of TXRF for the determination of chlorine in (U,Pu)C fuel.

Experimental

For TXRF measurements, an ITAL Structures Total Reflection X-ray fluorescence Spectrometer TX-2000 was used. Cl K_α line excited by W L_α characteristic X-rays obtained from a W-Mo dual target tube operated at 40 kV and 30 mA was used, for chlorine determination. The W L_α line was monochromatized using a W-C multilayer. A Si(Li) detector with a resolution of 139 eV (FWHM) for Mn K_α(5.39 keV) was used, for detection and measurement of X-ray intensities. For IC measurements, a Dionex DX-500 ion chromatography system consisting of an IP-20 isocratic pump, a self regenerator suppressor in external recycle mode and an ED-40 conductivity detector with a conductivity cell and DS-3 stabilizer was used, for obtaining the chromatograms. Separation of the anions was achieved with an analytical column (Dionex, Ion Pac, AS 18, 250x4 mm) coupled with a guard column (AGIX8, 50 x4 mm).

The TXRF spectrometer was calibrated using a Merck ICP multielement standard solution IV and synthetic standard solution of chlorine, prepared by dissolving NaCl in 5 mM NaOH solution. Similarly the method was validated by analyzing NaCl solutions, having chlorine concentrations in 125 to 4000 ng/mL range, using a cobalt single element internal standard solution. For TXRF determinations of chlorine in (U,Pu)C samples, different amounts of these samples, as shown in Table 1, were pyrohydrolyzed at 900°C. An all quartz pyrohydrolysis set up consisting of two concentric tubes was used. The outer tube has an inlet and serves as a preheater for (Ar/O_2) + H_2O gas used for pyrohydrolysis. The inner tube houses the sample boat and is attached to the gas outlet which is cooled by a condenser. The condensates consisting of liberated chlorine were collected in 5 mM aqueous solution of NaOH in polypropylene bottles and were made up to 25 mL. 200 µL of cobalt internal standard (990 ng/mL) was mixed with one mL of this solution. Two aliquots of 30 µ L (10 µL x 3) of such solutions were deposited on quartz sample supports, by drying under an IR lamp. These sample supports were loaded in TXRF spectrometer sample chamber and the TXRF spectra were recorded in duplicate, for each sample, for a live time of 2000 s. These samples were also analyzed for chlorine content by ion chromatography. In order to assess the applicability of TXRF for chlorine determination in other nuclear materials, one U_3O_8 trace element standard was also analyzed in a similar way.

Results and Discussion

Determination of chlorine by normal XRF technique is difficult, due to it's comparatively low fluorescence yield and matrix effects. Total Reflection X-ray Fluorescence spectrometry has a good potential for it's determination, due to negligible matrix effects and better detection efficiency. However, TXRF determinations require drying of the sample on a sample support and in similar studies made earlier, we observed that even slight acidic nature of the solution drives out chlorine in the form of HCl while drying the sample on quartz carrier and the TXRF spectrum did not show the presence of chlorine. In order to avoid such losses of chlorine, we prepared the chlorine samples in slightly alkaline medium, instead of using Milli-Q water. The TXRF determined concentrations of synthetic chlorine standards were found to be within 15% of the expected concentrations, in most of the cases, with a precision of 15 % (1σ for n=4). A comparison of the expected and TXRF determined concentrations of such synthetic

standards is shown in Fig. 1. The TXRF spectrum of the NaOH solution containing liberated chlorine from a (U,Pu)C-3 sample using cobalt internal standard is shown in Fig. 2. It can be seen that the Cl K_α, peak is quite strong and well separated from Ar K_α peak from the atmosphere. The TXRF and IC results are shown in Table 1 and have a good agreement. From these results, it can be concluded that TXRF spectrometry has good potential for determination of chlorine in nuclear samples. Also it can be seen that S K_α peak is also clearly visible in the spectrum, indicating that this technique can be used for sulfur determination also after similar studies.

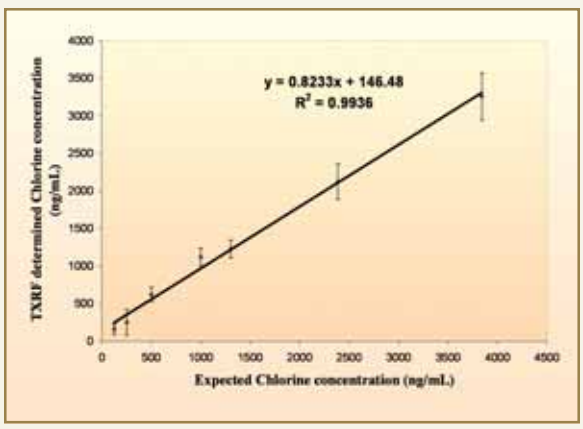

Fig. 1: Comparison of TXRF determined and expected chlorine concentrations in synthetic standards

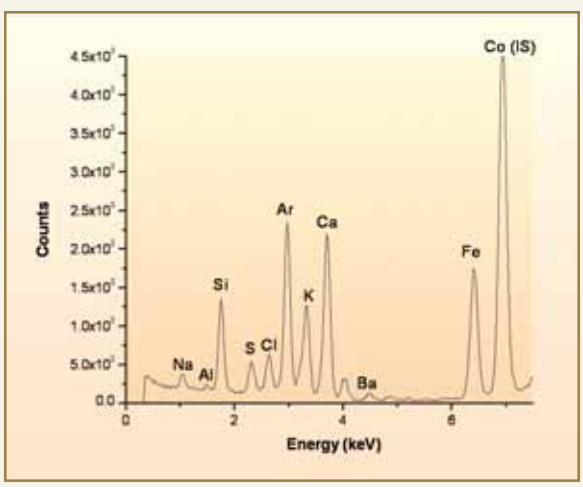

Fig. 2: TXRF spectrum of processed (U,Pu)C-3 sample

Table 1: Comparison of TXRF and IC determinations of chlorine

Sample	Sample mass taken for pyrohydrolysis$ (g)	TXRF*	IC#
U_3O_8	0.9969	890 ± 232	1232
(U,Pu)C-1	0.5173	323 ± 69	278
(U,Pu)C-2	0.5299	208 ± 52	257
(U,Pu)C-3	0.5233	411 ± 148	333

$: The evolved Cl was collected in 5 mM NaOH made up to 25 mL
*: TXRF determined Conc. of chlorine in solution (ng/mL)
: IC determined Conc. of chlorine in solution (ng/mL).

Conclusion

Total reflection X-ray Fluorescence Spectrometry can be used for the determination of chlorine at ultratrace levels in (U,Pu)C and other nuclear materials. However, before using this technique for such trace determination on a routine basis, more studies are required for better sample preparation to avoid loss of chlorine.

Acknowledgements

The authors express their sincere thanks to Dr. V. Venugopal, Director RC & I Group for his keen interest in the work.

References

1. R. B. Yadav and B. Gopalan, Characterization and Quality Control of Nuclear Fuels, ed. C. Ganguli and R. N. Jayaraj, Allied Publishers, New Delhi, (2002) 455-471.
2. S. Jeyakumar and K. L. Ramakumar, Characterization and Quality Control of Nuclear Fuels, ed. C. Ganguli and R. N. Jayaraj, Allied Publishers, New Delhi, (2002) 546-559.

3. R. Klockenkaemper, A. von Bohlen, *Spectrochim. Acta Part B*, 56 (2001) 2005-2018.

4. N. L. Misra, K. D. Singh Mudher, V. C. Adya, B. Rajeshwari and V. Venugopal, *Spectrochim. Acta Part B*, 60 (2005) 834-840.

5. N. L. Misra, S. Dhara, V. C. Adya, S. V. Godbole and K. D. Singh Mudher, in Proceedings of Nuclear and Radiochemistry Symposium (NUCAR) held at Guru Nanak Dev University, Amritsar, India, 2005, 381-382.

ABOUT THE AUTHORS

Dr. Nand Lal Misra joined the Fuel Chemistry Division in the year 1983 and is working in the area of application of Total reflection X-ray Fluorescence (TXRF) for trace element determination in different matrices and solid state chemistry of uranates, molybdates, their solid solutions and uranyl molybdates. During his stay at the Paul Scherrer Institute, Switzerland he studied the applicability of TXRF for trace element determination in Ice Core samples. He has developed TXRF analytical methods for the trace determination of metals and non metals in nuclear, environmental and forensic matrices.

Ms. Sangita Dhara joined the Fuel Chemistry Division, BARC in 2004 from the 47th Batch of BARC Training School and is currently working in the area of TXRF applications for trace element determination in different matrices and solid state chemistry of alkali metal uranates and their solid solutions. She is involved in the development of TXRF methods for trace and bulk determination of different elements in nuclear, environmental and forensic matrices.

Dr. K.D. Singh Mudher joined BARC in the year 1971 after completing his Ph.D. from the Indian Institute of Technology, Mumbai. He has been working in different areas of solid state chemistry of nuclear materials and has expertise in x-ray diffraction, x-ray spectrometry and thermal methods of characterization of solid materials.

Dr. S.K. Aggarwal is currently, Head, Fuel Chemistry Division, BARC, Trombay. He joined the 16th Batch of BARC Training School in 1972 and received the Homi Bhabha Award. He did his Ph.D. from Mumbai University in 1980 and completed his Post-doctoral training during 1987-89 at University of Virginia, USA. He is a specialist in the field of atomic mass spectrometry and alpha spectrometry and is interested in various mass spectrometric techniques. His other areas of interest include electrochemistry, X-ray spectroscopy and solvent extraction. He is a recognized Ph.D. guide of the Mumbai University and of HBNI.

ABOUT THE AUTHORS

Mr. U. K. Thakur joined BARC in 2002 and is working with a group analyzing non-metallic trace elements in various nuclear fuels. He is working in the field of aqueous fluoride complexation of transition metal and actinides in different oxidation states. He has over 20 publications in international journals and various symposia/conferences to his credit.

Ms. D. J. Shah joined BARC Tarapur, in 1990. She worked in the field of destructive and non-destructive analysis of uranium and plutonium in nuclear fuel samples. She joined BARC. Mumbai in 2003 and is now working with a group analyzing non-metallic trace elements in various matrices relevant to nuclear industry. She worked in the field of aqueous fluoride complexing of transition metal and actinides in different oxidation states. She has over 15 publications in international journals and various symposia/conferences to her credit.

Dr. R. M. Sawant joined BARC in 1980. He was awarded Ph.D. by Mumbai University in 1990. Dr. Sawant has contributed significantly in developing methodologies for the analysis of non-metallic trace elements in various matrices relevant to nuclear industry. He worked extensively in the field of aqueous fluoride complexing of actinides and lanthanides in different oxidation states. Presently, Dr R. M. Sawant is the Head, Complex Chemistry Section, RACS, RC&IG; BARC. He has to his credit two review articles and over 50 publications.

Dr. K. L. Ramakumar is from 18th Batch of BARC Training School Orientation Course in Nuclear Science and Engineering. He is currently the Head, Radio Analytical Chemistry Section , BARC. He is a specialist in the field of chemical quality control of nuclear materials, trace elemental analysis by Mass Spectrometry and Ion – chromatography, Thermal analysis by differential scanning calorimetry as well as in post - irradiation examination of nuclear fuels by chemical analysis. He was also on an expert assignment to IAEA's Safeguards Analytical Laboratory (SAL) at Seibersdorf, Austria to check and establish calibration procedure for precise and accurate mass spectrometric analysis. He is a recognized guide of Mumbai University. He has more than 200 publications to his credit.

UPTAKE OF RHODAMINE 6G DYE BY BOROSILICATE GLASSES

Jayshree Ramkumar, S. Chandramouleeswaran and P.V. Ravindran
Analytical Chemistry Division

and

V. Sudarsan and R.K.Vatsa
Chemistry Division

and

V.K. Shrikhande and G.P. Kothiyal
Technical Physics & Prototype Engineering Division

and

T. Mukherjee
Chemistry Group

This paper received the Best Poster Award at the DAE Solid State Physics Symposium, held at Mysore, from Dec. 27-31, 2007

ABSTRACT

Sodium boroaluminosilicate glass samples with different B_2O_3 to Na_2O mole ratio (0.23 and 9.8) were prepared, by the conventional melt-quench method and their uptake of Rhodamine 6G dye from aqueous solution was investigated. The experimental conditions were optimized to get maximum uptake and was found to be 2.5 mmol of dye, per gram of the glass sample. Based on ^{29}Si and ^{11}B MAS NMR studies, it has been confirmed that the increased concentration of $Si\text{-}O^- Na^+$ and $BO_4^- Na^+$ linkages in the glass with B_2O_3 to Na_2O mole ratio 0.23, is responsible for the increase in it's uptake of the dye.

Introduction

Effluents from industries like dye manufacturing, textile, paper and pulp are highly coloured and considerable research has been done, for the removal of these coloured products. Adsorption process is an attractive treatment, especially if the adsorbent is inexpensive and readily available like wood, coir pith etc [1]. Borosilicate glasses behave as ion exchangers and this property is made use of, extensively, in various applications, including nuclear industries. Synthetic dyes are major industrial pollutants and water contaminants. Due to their complex structure, most of the dyes are resistant to biodegradation. Therefore, the release of these chemicals into the aqueous stream should be avoided. So the uptake or removal from the aqueous streams becomes important.

In this paper, the use of boroaluminosilicate glass for removal of dye from aqueous solution has been tried. The uptake of dye by two borosilicate glasses with different concentrations of Na_2O and B_2O_3 has been studied, as a function of various experimental parameters such as contact time, pH and amount of adsorbent.

Experimental

Two glass samples BS1 $[(Na_2O)_{0.22}\ (B_2O_3)_{0.05}\ (SiO_2)_{0.69}\ (Al_2O_3)_{0.011}\ (K_2O)_{0.029}]$ (B_2O_3/Na_2O = 0.23) and BS2 $[(Na_2O)_{0.025}\ (B_2O_3)_{0.245}\ (SiO_2)_{0.69}\ (Al_2O_3)_{0.011}\ (K_2O)_{0.029}]$ (B_2O_3/Na_2O=9.8) were prepared, by the conventional melt-quench method from reagent grade SiO_2, H_3BO_3, Al_2O_3, $NaNO_3$ and KNO_3 at 1400-1500°C. ^{29}Si and ^{11}B MAS NMR spectra were recorded using Bruker Avance DPX 300 machine with a spinning speed of 5kHz.

The uptake studies were carried out in batch mode. 10 ml of aqueous dye solution of known concentration at a particular pH was equilibrated, with a weighed amount of glass sample for different periods of time. The concentration of dye left behind in solution after equilibration was determined.

Results and Discussion

The effect of contact time on the uptake of dye is shown in Fig. 1. It is seen that a period of 6h is optimum and this was used for further studies. It is seen from the figure, that the uptake of the dye by BS1 is much higher than that of BS2.

Since this is an ion exchange of the dye, which is cationic in nature, it was expected that the pH of the external solution would have an effect on the uptake. The variation in the uptake with pH is shown in Fig. 2.

It is seen that at lower and much higher pH, the uptake is low and the optimum was around pH of 6. Hence

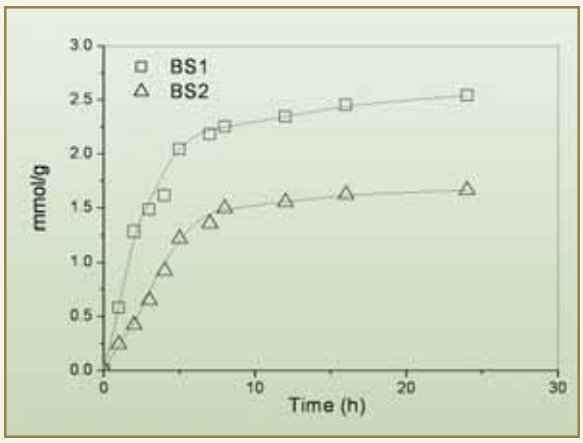

Fig. 1: Effect of contact time

pH was maintained at 6 for all further studies. At lower pH, the dye undergoes chemical degradation to a lactone structure and at higher pH the dye exists in it's neutral or anionic form. Both these changes result in low uptake at the two extreme ends of the pH.

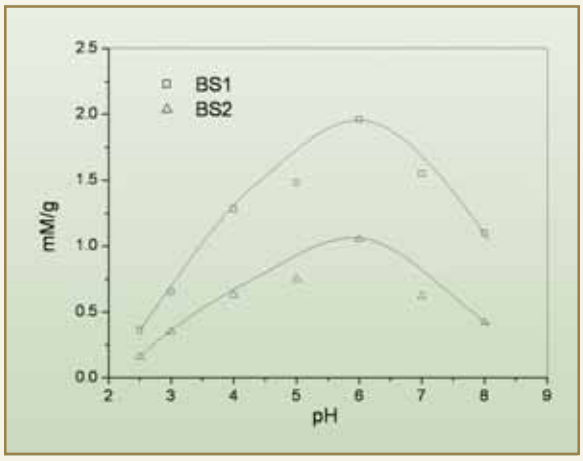

Fig. 2: Effect of pH
* represent spinning side bands

The effect of the amount of adsorbent on the uptake was studied, by varying the mass of glass, in the range of 0.02 to 0.2 g. The results are shown in Fig. 3. It is observed that about 0.1 g of glass was sufficient to bring about maximum uptake.

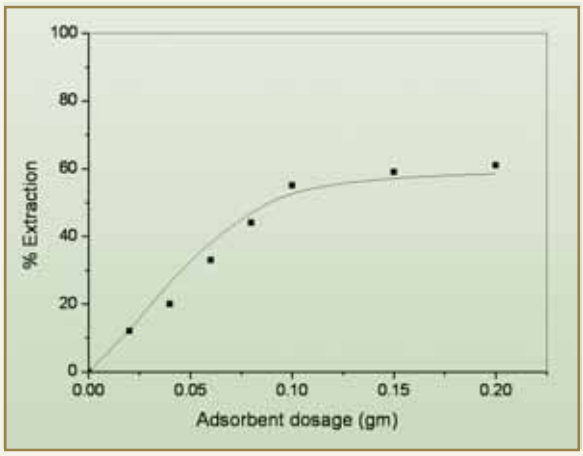

Fig. 3: Effect of amount of adsorbent

The difference in ion exchange behaviour of BS1 and BS2 samples could be due to the difference in structure of the two glasses. The ion exchange behaviour of glasses is attributed to the presence of nonbridging oxygen atoms present in the silicon network. The difference in the number of non-bridging oxygen atoms present is revealed by structural elucidation by ^{11}B and ^{29}Si MAS NMR studies.

From ^{29}Si MAS NMR patterns (Fig. 4a), it is seen that for BS1, the ratio of Q^3 ($Si\text{-}O^-$) and Q^4 (SiO_4) units of silicon is 60:40, whereas in BS2, it is 25:75. From ^{11}B MAS NMR patterns (Fig. 4b), it is seen that BS1 contains only one sharp peak, around –22 ppm, characteristic of the tetrahedral $(BO_4)^-$ units, whereas, for BS2 in addition to the sharp peak at –22ppm, a broad peak characteristic of trigonally coordinated (BO_3) units is observed [2]. From ^{11}B and ^{29}Si MAS NMR studies, it is established that $Si\text{-}O^-\text{-}Na^+$ and $B\text{-}O^-$ Na^+ are more in BS1 as compared to BS2. This explains the higher exchange capacity of BS1 as compared to BS2.

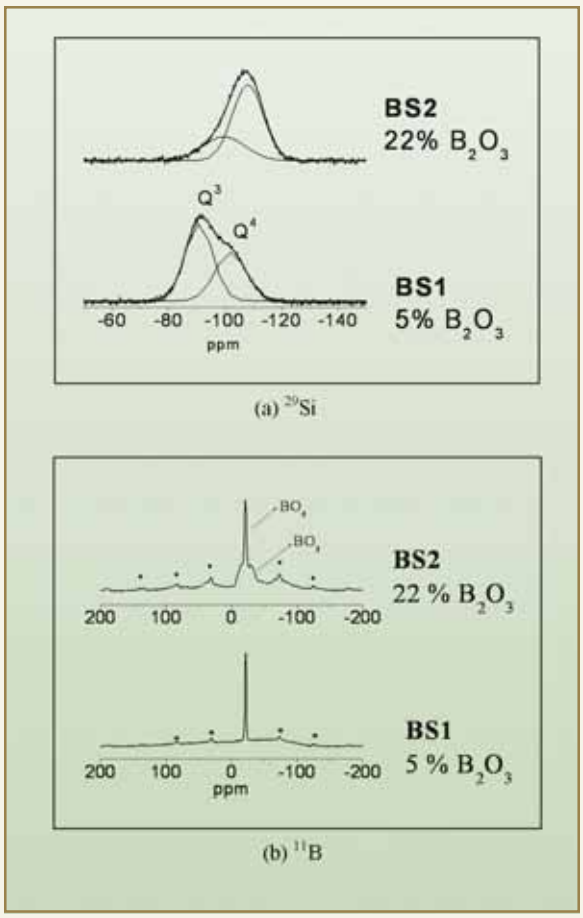

Fig. 4: MAS NMR patterns of BS1 and BS2.
* represent spinning side bands

Conclusions

It is seen that BS1 has good affinity for the dye and the uptake is high at a pH of 6 using 0.1g of glass and equilibrating for 6h. Increase in concentration of $Si\text{-}O^-$ Na^+ and BO_4^- Na^+ linkages in the glass is responsible for the improved uptake of dye for the glass with B_2O_3 /Na_2O ratio 0.23.

References

1. C. Namasivayam, et. al., *Waste Management* 21 (2001) 381.
2. V. Sudarsan et al. *J. Phys.: Condens. Matter* 14 (2002) 6553.

ABOUT THE AUTHORS

Dr. Jayshree Ramkumar joined Analytical Chemistry Division, BARC from the 37th batch of Training School after completion of M.Sc. from University of Madras, Chennai. Since then, she is involved in the development of new separation procedures for different metal ions and toxic substances using membranes and various conventional and unconventional adsorbents. She was awarded Ph.D. in 2005 on her work on ion exchange and related studies using Nafion membrane. She has more than 25 international journal publications to her credit in the field of membrane separation.

Mr. S. Chandramouleeswaran joined the Analytical Chemistry Division after completing B.Sc. Chemistry from Madurai Kamaraj University. Since then, he has been involved in the development of various methodologies for analytical applications.

Dr. P.V. Ravindran, Head Thermal & Electrochemical Methods Section of ACD, has been involved in research work in the field of thermal analysis studies. He was awarded Ph.D. in 1987 for his work on non-isothermal kinetics of solid state reactions. He has more than 70 publications including international journals and contribution to chapters in books. His fields of interest are high temperature synthesis, solid state reaction mechanisms, computer applications in analytical chemistry. He is also involved in the development of chromatographic and electroanalytical methods of analysis.

Dr. V. Sudarsan joined the Chemistry Division of BARC in the year 1994 after graduating from the 37th batch of the Training School. He received his Ph.D. from Mumbai University in the year 2002 for his work on the structural aspects of inorganic glasses. Currently he is working on the optical properties and structural aspects of nanoparticles and glassy materials.

ABOUT THE AUTHORS

Dr. R.K. Vatsa is currently heading the Structural Chemistry Section of Chemistry Division, BARC. He passed M. Sc. from Delhi University in 1986 and graduated from the 30th batch of BARC Training School. He has been involved with the gas phase photodissociation/ionization of atoms, molecules radicals and clusters. He obtained his Ph.D. in 1994 from Bombay University. He along with other coworkers indigenously developed the Time-of-Flight Mass Spectrometer (TOFMS) system. His group has recently discovered a simple and cheaper way of generating highly energetic, multiply charged atomic ions. He has more than 65 publications to his credit and is a recognized Ph.D. guide of the University of Mumbai and the Homi Bhabha National Institute.

Mr. V.K. Shrikhande joined BARC from Chemistry discipline of the 13th batch of Training School in 1970, after completing his B.Sc. from Shivaji University is involved in the development and fabrication of glass-based electron devices like hot ionization BA gauges for UHV measurements; various types of glass-to-metal and ceramics-to-metal seals and in the development of hollow cathode lamps used in Atomic Absorption Spectrophotometers as import substitute. His current research interest is in the development of special glasses and glass-ceramics with designed/tailored properties for hermetic sealing applications in ultra high vacuum (UHV) related devices / systems and process chambers with corrosive ambients at high pressures.

Dr. G. P. Kothiyal is Head, Glass and Ceramics Technology Section of Technical Physics and Prototype Engineering Division (TPPED), BARC . He is spearheading the programme on special glasses and glass-ceramics and produced them with designed/tailored properties for applications in high voltage and ultra high vacuum (UHV) related devices/systems. Such materials/devices have also been delivered for use in nuclear, laser, defence and space applications as level sensors, multipin feedthroughs, spacers/isolators, sealants etc. He is a Ph.D. guide in Physics at the Mumbai University and the Homi Bhabha National Institute (HBNI) Mumbai. He has published more than 230 papers in International/National journals/proceedings. He is a recipient of the Materials Research Society of India (MRSI) Medal Lecture award for the year 2003 and has been recently selected Chairman for MRSI Subject Group (Ceramics & Glass).

Dr. T. Mukherjee, director, Chemistry Group, BARC, is well-known for his research contribution in various areas of radiation and photochemistry and analytical sciences including forensic science. He has been deeply involved in establishing various sophisticated techniques in BARC. He is currently the President, Indian Society for Radiation and Photochemical Sciences. He is also the Chairman of the Chemistry Committee for HRDC, BARC. Recipient of many prestigious awards, he is a well-known personality in Chemistry Discipline with more than 275 journal publications.

बीएआरसी न्यूज़लेटर
BARC NEWSLETTER

DEVELOPMENT OF AUTOMATED REMOTE OPERATED INSIDE DIAMETER MEASUREMENT SYSTEM FOR PRESSURE TUBE OF INDIAN PRESSURIZED HEAVY WATER REACTOR

Sanjay Panwar, Nirupam Das, B.S.V.G. Sharma and B.B. Rupani
Reactor Engineering Division

This paper won the Best Poster Presentation Award and the Dr. N.G. Patel Prize at the 12th National Seminar on Physics and Technology of Sensors (NSPTS-12), held at Mumbai, during March 7-9, 2007.

ABSTRACT

Pressure tubes of Indian Pressurized Heavy Water Reactors (PHWRs) are made from zirconium alloy. The service life of a pressure tube is affected, due to various degrading mechanisms such as corrosion and hydriding, dimensional deformations, changes in mechanical properties and service-induced flaws. Hence, these degrading mechanisms are to be monitored as a part of in-service inspection, to estimate the service life of pressure tubes.

Introduction

Precise measurement of the diametrical creep of a pressure tube is necessary. The pressure tubes in operating PHWRs are highly radioactive components. Conventional two or three point micrometers are not suitable for measurement of the inside diameters of these saggy pressure tubes, due to unavailability of straight-line access, to the bore of a pressure tube and excessive exposure of the operating personnel, to radiation environment. Therefore, design and development of remote-operated, pressure tube Inside Diameter (ID) measurement system, was felt necessary, to precisely measure the bore size of saggy, highly radioactive pressure tubes, located in coolant channels of operating PHWRs. The system designed and developed indigenously, uses a hydraulically actuated micrometer, which is controlled through a PC-based control system, to measure the inside diameter of a pressure tube, remotely, from a distance of 100 meters. The system is designed for accuracy of 50 microns in the range of inside diameter variation between 82 mm to 86 mm. The system has been successfully tested in full-scale mock-up at reactor site.

The paper describes details of design of the software and hardware modules of the system, assembly and integration of system modules, testing and it's performance evaluation.

Working Principle

The system is based on the principle of conventional 3-point micrometer with a tapered piston rod, instead of tapered screw for ease in remotization. The tapered piston rod, as shown in Fig. 1, is operated with the

help of a stepper motor driven pressurizing unit. Displacement and pressure feedbacks are obtained with incremental encoder and pressure transmitter respectively.

As the lead screw nut of pressurizing unit is rotated by the stepper motor, the pressurizing piston moves forward, resulting in same movement of inspection head piston. The angle of tapered piston is arranged such that, one rotation of the inspection head piston creates a change of 0.5 mm in probe leg diameter.

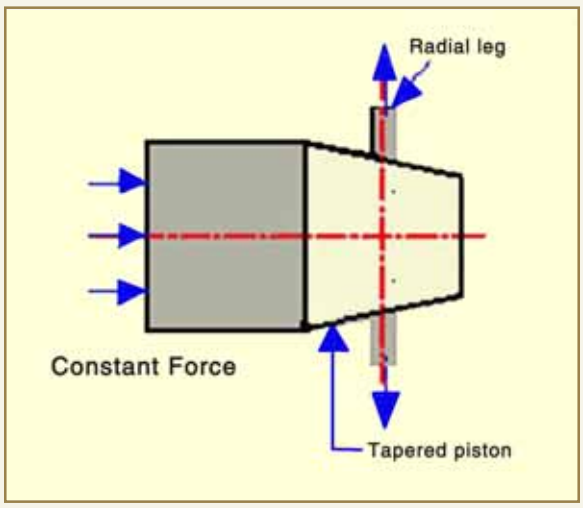

Fig. 1: Inspection head

Incompressible fluid displacement principle has been used, to generate movement of radial legs of inspection head.

Displaced volume = $A_1 * d_1 = A_2 * d_2$
So, $d_2 = (A_1 * d_1) / A_2$

Where,
A_1 and A_2 are areas of the pressurizer and inspection head cylinders respectively.
d_1 = Movement created in the pressurizer piston by stepper motor
d_2 = Movement generated in the inspection head piston.

Hence,
Change in diameter of radial leg = $2 * d_2 * \tan\theta$, where "$\tan\theta$" is slope of the conical portion of inspection head.

System Description

A computerized system has been developed, to acquire, control and process various parameters of all the sub-modules of this system. This system mainly consists of an inspection head and a pressurizing unit connected by a hydraulic hose as shown in Fig. 2. The inspection head, as shown in Fig. 3, is to be loaded in the tube for measurement of it's inside diameter. The pressurizing unit actuates the inspection head during measurement, through the connecting hose. Thus, the inspection head acts as a slave to the pressurizing unit.

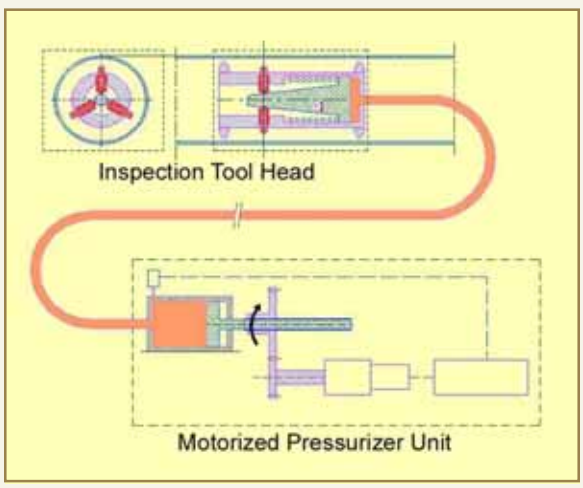

Fig. 2: Schematic arrangement of RIM system

Fig. 3: Inspection head for ID measurement system

The raw data of the system pressure and displacement of the tool-tip is generated, from output of the pressure transmitter and incremental encoder mounted on motor shaft. A PC-based data acquisition system, as shown in Fig. 4, has been developed, to process this data on internal diameter estimation. The pressure is measured using a precise pressure transmitter and transmitter data is acquired in analogue format (4 to 20 mA), by an industrial PC port. In addition to this, pressure data is also available on local display unit. The system software controls motion of the lead screw in pre-defined sequence, using a geared stepper motor coupled with a quadrature encoder. PC add-on-cards are used, to interface all the feedback and control signals to the computer. Manual control panels are also used, for controlling motor operation in manual mode. Over travel limit switch and over-pressure switches are hard-wired in manual control panel circuit for safe operation of the system. Digital lines from PC add-on-cards are connected to manual panel, via solid-state relay board, for controlled motor operation. The components of the control unit are shown in Fig. 4 and the on-line graph of pressure vs tool-tip diameter is shown in Fig. 6.

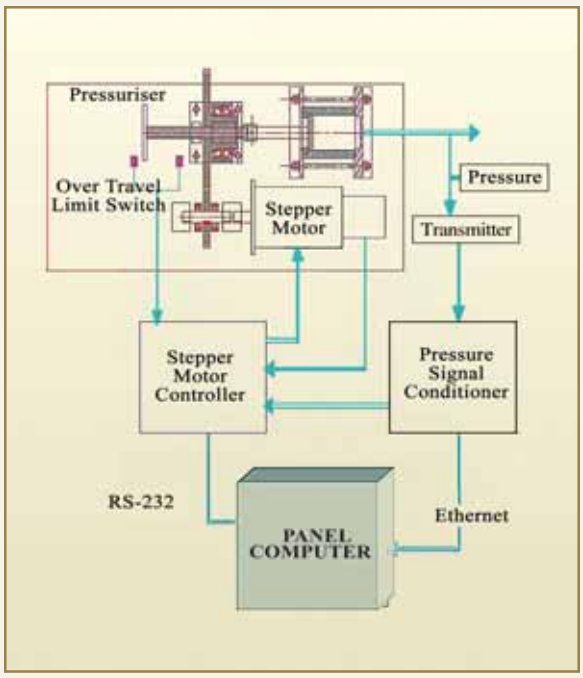

Fig. 4: Schematic arrangement of control system

The lead screw nut is rotated in step incremental mode, until a slightly higher torque is felt. The torque is monitored in terms of pressure reading, which is noted continuously for movement of radial legs. Change in slope of pressure rise gives the point of contact as shown in Fig. 5. Radial movement as measured with the help of encoder is converted into diameter by appropriate calibration.

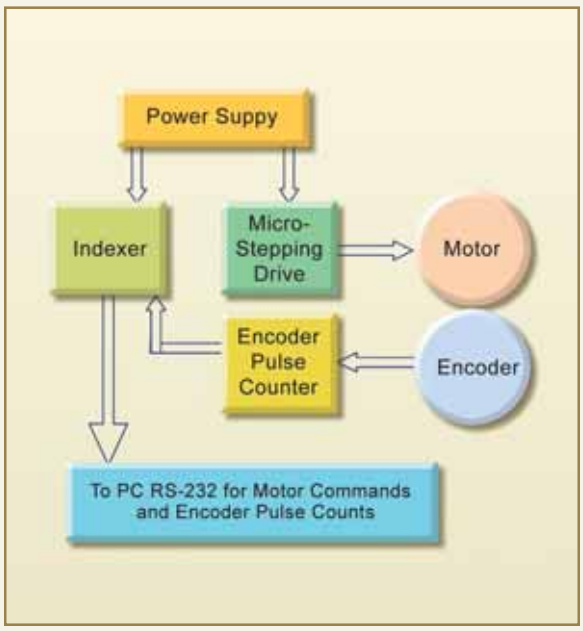

Fig. 5: Schematic of stepper motor arrangement

A computer controlled lead-screw drive has also been developed, for positioning of the inspection head in the coolant channel. This drive is mounted on an X-drive, for alignment of the inspection head, to various coolant channels.

A two-tier mechanism is provided, for withdrawal of the radial legs. Withdrawal is normally actuated by the springs at the radial legs. In case of failure of these springs, another spring (axial spring) with higher spring force ensures the withdrawal of radial legs, through an axial guide.

Hardware Description

The system is designed around a computer as a central control element. It mainly consists of stepper motor control arrangement, for creating a piston motion in the pressurizer system and pressure signal conditioner for conditioning the pressure signal i.e. 4 to 20 mA and to generate an Ethernet interface with the computer. Stepper motor has been used for simple and accurate control of angle of rotation and rotation speed. Stepper motor control arrangement consists of geared stepper motor for higher torque, quadrature encoder to keep track of motor motion and a controller to control various process sequences. Further, the stepper motor is pulsed at lower pps(pulse per sec) to keep motor in high torque region. The controller box, as shown in Fig. 5, houses an indexer for outputting the pulse and direction commands to the drive, motor power supply to power the motors and optically-isolated digital input and output lines and a micro-stepping drive, which translates the pulse and direction commands from the indexer to actual motor movement. The motor steps resolution has been increased to 2000 steps/rev from 200 steps/rev by this

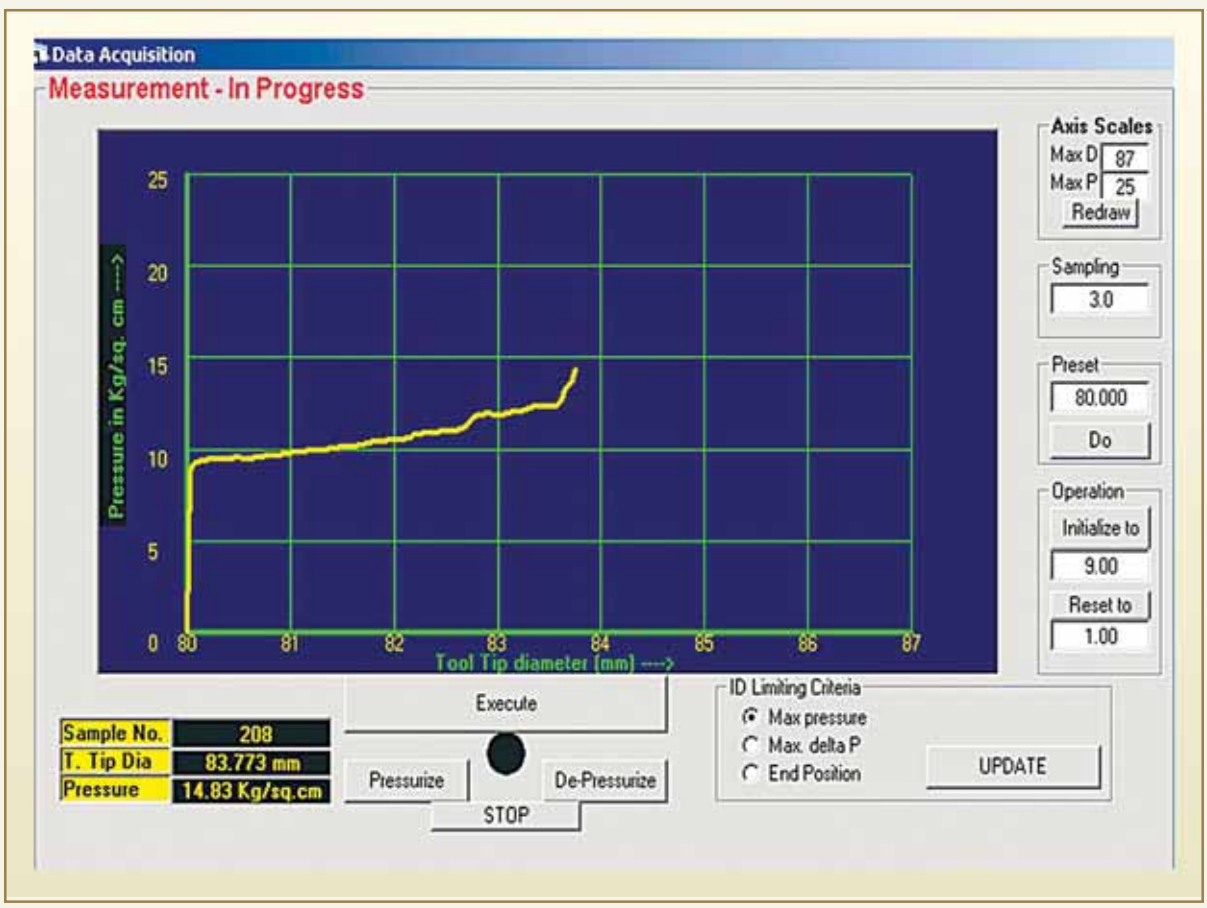

Fig. 6a: On-line graph of pressure vs tool-tip diameter

micro-stepping unit for fine control. Pressure conditioning unit converts current signal to voltage and then to standard unit of pressure. It generates software alarms when pressure is out of range and cut-off motor motion in case pressure shoots up above safe limit. It is connected to computer by a crossover twisted pair 10BaseT cable. The computer communicates with pressure conditioner unit with client-server methodology (IEEE802.3 10Base T) in which pressure conditioner is server. Once the server is connected, pressure and alarm information are updated at client at a sufficiently fast rate.

Software Description

The user programmes of computer control, for probe motion with all the safety interlocks and data acquisition, are written in Microsoft Visual Basic Ver. 6.0.

The pressure data acquired through the computer is processed, using a software differentiator as shown in Fig. 6a and Fig. 6b. First and second derivative of system pressure, with respect to the tool-tip displacement, will help to fine tune the contact point.

Double differentiation with error correction gives the internal diameter of tube at location of measurement. Measured ID at different axial locations is used, to generate ID profile of tube. This software is compatible with all Windows-based operating systems. The data received from sensors is conditioned and preserved in Excel file format, for future reference and is coupled with a computational code, for on-line internal diameter measurement.

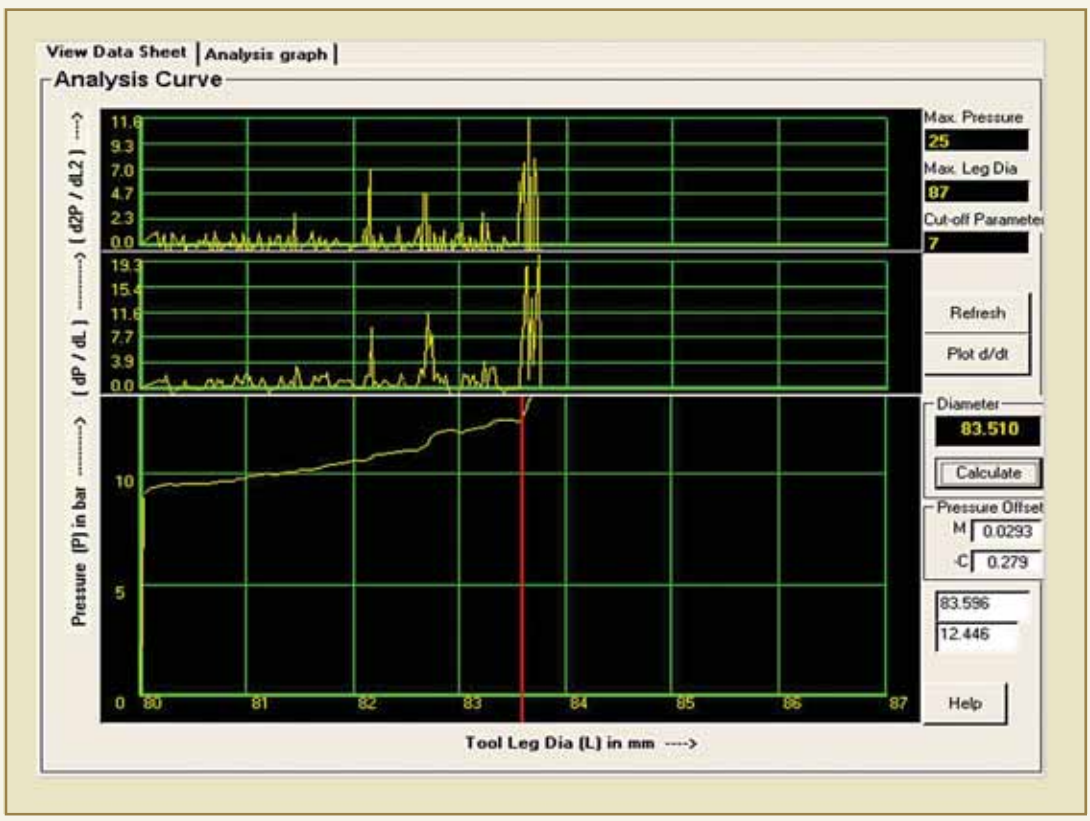

Fig. 6b: Software processing steps of pressure signal

Safety Features

This system has a number of built-in designed safety features, against any malfunction and for safe withdrawal of inspection head from the channel, in case of component failure. The important safety features are listed below:

A two-tier mechanism is provided for withdrawal of the radial legs. Withdrawal is normally actuated by the springs at the radial legs. In case of failure of these springs, another spring (axial spring) with higher spring force ensures the withdrawal of radial legs, through the axial guide. Also, before every operation, as part of normal operational procedure, full withdrawal of the radial legs is checked and confirmed, by actuating the inspection head.

The over-pressure safety interlocks are provided in the software and in pressure conditioner alarm, which automatically stops the stepper motor in case of any alarm. In addition to that, an over-pressure relief valve is also installed, to protect the system components against accidental over-pressurization.

A torque-limiting coupling is installed between the lead-screw drive shaft and the motor shaft. This coupling will protect the inspection head and pressure tube, from any damage in case of jamming inside the channel.

Results and Conclusion

The internal diameter measurement system for the pressure tube of Indian Pressurized Heavy Water Reactor has been designed and developed as shown in Fig. 7.

A large number of mockup trials have been carried out, to confirm accuracy of measurement and to check for the compatibility of the system with the handling system. The trials were carried out at coolant channel mockup facility at Hall-7, BARC and at the mock-up facility at KAPS, Kakrapara (Guj.) under wet channel conditions. The total control system with all it's feedback elements, inspection head and pressurizing unit, performed satisfactorily during the trials. The required accuracy of measurement of inside diameter of pressure tube was verified. The inside diameter of the mockup pressure tube was earlier measured in dry condition, with the help of three-point micrometer for verification. Necessary changes are being made in the system, so that, it can be deployed in the reactor for measurement of internal diameter of tubes.

Fig. 7: Control station for ID measurement system

Acknowledgement

The authors are grateful to Mr. R.K. Sinha, Director, Reactor Design and Development Group and Mr. D. Saha, Head, Reactor Engineering Division for their constant encouragement during the course of the work.

References

1. Press W.H. et. al.," Numerical Recipes in C", Cambridge University Press.
2. Microsoft VB help file, source "www.microsoft.com."
3. Bajpai, Calus, Fairley, Loughborough University of Technology "Numerical methods for engineers and scientists" 1978.

ABOUT THE AUTHORS

Mr. Sanjay Panwar, B. Tech. in Electronics & Communication Engineering from R.E.C. Kurukshetra, graduated from the 37th Batch of Orientation Course of BARC Training School and joined RED in 1994. He was actively involved in development of "Integrated garter spring repositioning system" and "Coolant Channel Replacement Machine" for pressure tubes of Indian PHWRs. He has also developed controls for a number of inspection systems. He played a key role in development of *In-situ* Property measurement system for estimation of mechanical property of pressure tube of Indian PHWRs. Presently he is working on the development of tool delivery system for coolant channels and other life assessment tools for Zr-2.5%Nb pressure tubes of Indian PHWRs.

Mr. Nirupam Das, B.E. in Mechanical Engineering, graduated from the 33rd Batch of Orientation Course of BARC Training School and joined RED in 1990. He was involved in the development of various inspection and rehabilitation tools and techniques, for life management of coolant channels of Indian Pressurized Heavy Water Reactors (PHWRs) such as Wet scraping technology and coolant channel replacement machine.

Mr. B.S.V.G. Sharma, graduated from the 25th Batch of BARC Training School (Electrical) and joined the Reactor Engineering Division in the year 1982. Subsequently he obtained his M. Tech. in Control and Instrumentation from IIT, Mumbai in the year 1988. He is currently the Head of the Instrumentation Section of Reactor Engineering Division of BARC. The main thrust area of his work is design and development of special purpose transducer systems required for In-service-Inspection tools for inspection of coolant channels of Pressurised Heavy Water Reactors (PHWR). He has played a lead role in the design and development of Unconventional Tubular Linear Induction Motors, Instrumentation and control systems for innovative tools, systems and techniques required for in service inspection, repair, life extension and replacement of PHWR coolant channels. He is currently associated with various projects related to two-phase flow measurement and Passive Valve development for the Advanced Heavy Water Reactor.

Mr. B.B. Rupani, M.E. (Machine Design), graduated from the 17th Batch of BARC Training School and joined the Dhruva project in 1974. After successful completion of the Dhruva project, he was transferred to the Reactor Engineering Division (RED) in 1985. Presently he is heading the Reactor Coolant Channel Section of RED. He has developed various innovative inspection and rehabilitation tools and techniques for life management of coolant channels of Indian Pressurized Heavy Water Reactors (PHWRs). Presently he is responsible for development of coolant channels and reactor block components of the Advanced Heavy Water Reactor (AHWR) and development of inspection technologies required for Zr-2.5%Nb pressure tubes of Indian PHWRs. He is the recipient of VASVIK award in "Mechanical & Structural Sciences & Technology-2000."

DEPTH PROFILE STUDY OF ION-IRRADIATED AND ETCHED POLYMER USING MONOENERGETIC POSITRON BEAM

S.K. Sharma, D. Dutta, K. Sudarshan, P.K. Pujari and A.V.R. Reddy
Radiochemistry Division

and

S. K. Gupta
Nuclear Physics Division

This paper received the Best Paper Award at the DAE-BRNS Solid State Physics Symposium 2007 (SSP07), held at M.S. University, Vadodara, from Dec. 27-31, 2007

ABSTRACT

Polyethyleneterephthalate (Mylar) polymer of density 1.39g / cm^2 was irradiated by ^{35}Cl beam (7 ´ x 10^7 ions/ cm^2) and etched with 6N NaOH for 45 minutes. The S-parameter and 3γ/ 2γ ratio vs implanted positron energy in the positron energy range of 200 eV to 10 keV were measured in unirradiated, ion-irradiated and etched polymer, from Doppler broadening spectroscopy, using slow positron beam. VEPFIT was used to extract the diffusion length of positrons / Positronium, by fitting the S- parameter profile. The diffusion length of positron / positronium was 34.2 ± 9.3 nm, 3.4 ± .5 nm, 4.3 ± .5 nm in unirradiated, ion-irradiated and etched polymer respectively. The observed changes in S-parameter and 3γ/ 2γ ratio after ion irradiation and etching are discussed.

Introduction

Long chain molecules are spatially arranged in a particular fashion, to provide the specific properties to the polymers e.g. mechanical stability, conductivity, optical properties, transport properties and porosity etc. Ion irradiation of polymer is used, to modify the porosity or transport properties of polymers, which are further modified by etching the polymers in acidic or alkaline medium.

Slow positron beam in addition to Doppler Broadening Spectroscopy (DBS), is a useful technique to evaluate the porosity of polymers as a function of depth.[2,3] The positrons implanted into polymers after thermalization, directly annihilate with the available electron, in two (511kev) or three (0-511kev) gamma photons according to spin of annihilating electron. In polymers, in addition to direct annihilation, thermalized positron can form positronium (Ps) (a quasi-stable atom) by picking one electron. In case of polymers, positrons / Ps are trapped in available free volumes, due to their negative work function. Ps exits in two states, *singlet*, para-positronium (p-Ps) and *triplet*,

ortho-positronium (o-Ps). Intrinsically, o-Ps and p-Ps annihilate into three and two photons respectively with life-times of 142 ns and 125 ps but life-time of o-Ps is lowered, due to a process called pick-off annihilation, in which the intrinsic electron of o-Ps is exchanged with opposite spin electron and it annihilates through two gamma photons mode. When positrons / Ps annihilate through two photons mode, the 511 keV peak is broadened due to only electron momentum with which positron annihilates, because positron gets thermalized before annihilation. The broadening of the 511 keV peak is examined in terms of sharpness parameter (S) and wing parameter (W) as a function of implantation depth of positrons in polymers. In Doppler broadening spectroscopy, 3γ / 2γ ratio measurement as a function of implantation depth of positron has been evolved as a good technique, because the fraction of implanted positrons annihilating in two or three gamma photons, depends upon the size and distribution of free volumes, electron density and inter connectivity of the free volumes.[4]

In this study, we present DBS using slow positron beam in unirradiated, ^{35}Cl ion-irradiated and 6N NaOH etched Polyethyleneterephthalate (Mylar) polymer film.

Slow Positron Beam

Slow positron beam used for the present study is shown in Fig. 1. Ultra high vacuum compatible sealed ^{22}Na radioisotope is the positron source. Positrons emitted from the source are thermalized by W single crystal floated at 200 V (moderator), which has negative work function for the positrons. The thermalized positrons diffuse to the surface of moderator, which are extracted by an einzel lens to the solenoid. Positrons travel in spiral motion under the magnetic field in the solenoid, which act as a velocity filter to enhance the monochromatic nature of the positron beam. Positrons in the form of beam, fall on the sample in the target chamber, where the magnetic field is maintained by two Helmholtz coils. The sample holder can be floated from 0 V to 50 kV which can accelerate positrons to the required energy.

Fig.1: Front view of the Slow Positron Beam at the Radiochemistry Division, BARC

Experimental

Mylar polymer film of 25m thickness and 1.39g/cm^2 density was irradiated by 100 MeV ^{35}Cl beam (7´x10^7 ions/cm^2) at BARC-TIFR pelletron accelerator facility. The ion-irradiated film was etched with 6N NaOH solution for 45 minutes. DBS was carried out in unirradiated, ion-irradiated and etched Mylar using slow positron beam in positron energy range of 200 eV to 10 keV. From 511 keV photo peak, S-parameter was calculated by taking ratio of integrated counts in the region of 511 ± .75 keV to the counts in the region of 511 ±7.67 keV. The S-E curve were fitted to VEPFIT to evaluate the diffusion length of positrons/Ps.[5] 3γ/ 2γ ratio was also calculated from the spectra.

Results and Discussion

The S-E and 3γ/ 2γ ratio curve obtained from DBS of unirradiated, ion-irradiated and etched Mylar films are shown in Fig.1 and Fig. 2 respectively. In Fig.1, S-parameter increases as a function of positron energy upto 1.5 keV in all three samples and then remains the same throughout the bulk.[6] The increase in S parameter indicates the enhancement in trapping of positrons, p-Ps annihilation and pickoff annihilation fraction as a function of positron implantation depth. The diffusion length of positrons / Ps in unirradiated, ion-irradiated and etched Mylar was found to be 34.2 ± 9.3 nm, 3.4 ± .5 nm and 4.3 ± .5 nm. In case of ion-irradiated Mylar, S remains higher as compared to unirradiated Mylar, which may be due to formation of free volumes and free radicals, responsible for more Ps formation and trapping of positrons/Ps. Due to more trapping of positrons / Ps in ion-irradiated polymer, diffusion length of positrons / Ps reduces and reemission of positrons / Ps to the surface decreases, where they annihilate in three photons and 3γ/ 2γ value at low positron energies for ion-irradiated Mylar is lower as compared to unirradiated, as shown in Fig. 3. The higher S-parameter of ion-irradiated Mylar having similar 3γ/ 2γ ratio to unirradiated Mylar can be explained due to formation of free volumes and free radicals where most of the o-Ps undergo pick-off annihilation, through two photon annihilation mode.

The ion-irradiated Mylar was etched with 6N NaOH, for enlargement of the free volumes, as it dissolves the broken chains and removes the free radicals also. At lower energies of positrons, S-parameter of etched Mylar is lower as compared to unirradiated and ion-irradiated Mylar, but 3γ/ 2γ ratio for etched Mylar is

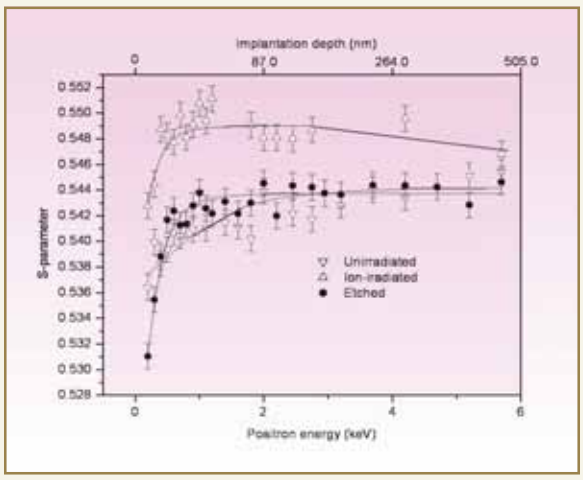

Fig. 2: S-parameter vs positron energy (shown upto 6 keV); Solid line shows fitting using VEPFIT

higher as compared to two other cases. In this case the diffusion length of positrons / Ps is longer than that of ion-irradiated ones as discussed before. These observations can be explained as a result of reemission of positrons/Ps after trapping which indicates that, the etching of ion-irradiated Mylar has increased the interconnectivity of the free volumes. In Fig. 3, a cross over in 3γ/ 2γ ratio occurs around 90 nm, below the surface after that ion-irradiated and etched Mylar has the similar decreasing trend having lower 3 / 2γ ratio, than unirradiated Mylar. This can be an implication of change in microstructure from larger free volume to smaller free volumes[7] and etching for 45 minutes has not enlarged the free volumes at this depth.

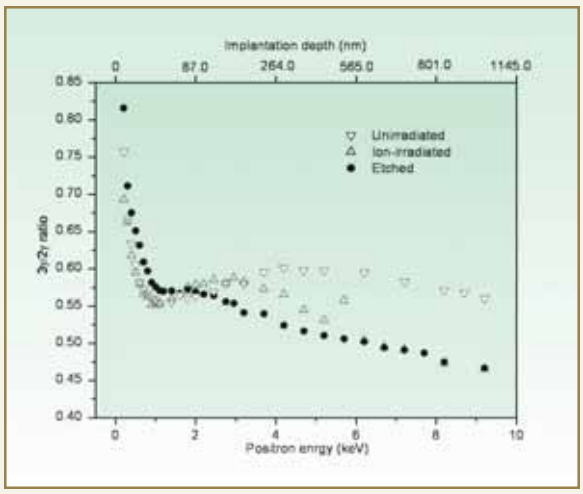

Fig. 3: 3γ / 2γ ratio vs Positron energy

Conclusions

DBS of Mylar irradiated by ^{35}Cl and etched with 6N NaOH were carried out, using slow positron beam. The changes in microstructure of Mylar were predicted, in terms of change in electron density and free volumes on irradiation. The enlargement of free volume and enhancement in inter connectivity of free volumes were observed, from surface to .5m below the surface of Mylar.

References

1. N. Itoh and K. Tanimura Special issue of the Seventh International Conference on Radiation effects in Insulators (REI-7), Nogoya, Japan, 1993, *Nucl. Instrum. Methods Phys. Res. Sect. B* 91, 1-700 1994.
2. P. J. Schultz and K. G. Lynn, *Rev. Mod. Phys*. 60, 701 (1988).
3. Positron Spectroscopy of solids, Eds. A. Dupasquier and A. P. Mills Jr. (IOS, Amsterdam, 1995).
4. D. W. Gidely, K. G. Lynn, M. P. Petkov, M. H. weber, J. N. Sun, and A. F. Yee, in New Direction in Antimatter Chemistry and Physics, Eds. C. M. Surko and F. A. Gianturo (Kluwer Academic, Dordrechet), 2001, p.151.
5. A.Van.Veen, H. Schut, J. de. Vries, R. A. Hakvoort and M. R. Ijpma, AIP Conf. Proc. 218 (1990) 171.
6. P. K. Pujari, D. Sen, G. Amarendra, S. Abhya, A. K. Pandey, D. Dutta and S. Mazumder, *Nucl. Instruments and Methods in Phys. Res. B*. 254 (2007) 278.
7. U. Myler, X. L. Xu, M.R. Coleman and P. J. Simpson. *J. Polym. Sci*.: part B, 36 (1998) 2413.

ABOUT THE AUTHORS

Mr. Sandeep K. Sharma obtained his M.Sc. (Chemistry) from the Indian Institute of Technology, Delhi in 2005. He joined the Radiochemistry Division of BARC in 2006 from the 49th Batch of Training School. His research areas include positron annihilation spectroscopy. He has 2 publications in international journals.

ABOUT THE AUTHORS

Dr. D. Dutta obtained his M.Sc. in Physics from Visva-Bharati University in 1999 and Ph.D from Jadavpur University, Kolkata in 2006. He was a KSKRA Fellow before joining the Radiochemistry Division of BARC in 2006. His research areas include Positron Annihilation Spectroscopy in porous materials. He has 15 publications in international journals and 6 conference publications.

Mr. Kathi Sudarshan is a gold medalist from the University of Hyderabad in M.Sc. (Chemistry) in 1998. He joined the Radiochemistry Division of BARC in 1999 from the 42nd Batch of Training School. His research areas include positron annihilation spectroscopy, radio analytical techniques and heavy ion induced reactions. He has published about 30 papers in peer-reviewed journals.

Dr. P.K. Pujari did M. Sc. in Chemistry from IIT Delhi in 1984. He is a Homi Bhabha Award winner from the 28th Batch of Training School. After one year of training, he joined the Radiochemistry Division of BARC in 1985. He specializes in positron annihilation spectroscopy and it's applications.

Dr. A.V.R. Reddy joined the Nuclear Chemistry Section, Radiochemistry Division in 1977. At present he is the Head of Nuclear Chemistry Section. His areas of research are nuclear fission, nuclear reactions, neutron activation analysis, radiochemical separations, heavy element chemistry and non destructive assay methods. He has about 250 publications in journals and symposia and has authored 3 books and edited 5 compilations.

Mr. S. K. Gupta, an Electrical Engineer from the 28th Batch of Training School, joined the Nuclear Physics Division in 1985. He has been associated with commissioning and operation of 14 MV Pelletron Accelerator Facility at TIFR and involved with development and operation of FOTIA facility. His areas of expertise are design and development of SF_6 Gas Handling, Ultra High Vacuum and High Voltage systems.

बीएआरसी न्यूज़लेटर
BARC NEWSLETTER

CASTING AND CHARACTERIZATION OF AEROGEL OBJECTS IN METALLIC MOULDS

P.B. Wagh, S.V. Ingale and Satish C. Gupta
Applied Physics Division

Dr. Wagh was honoured with the First Prize for Best Oral Presentation at the National Conference on Current Trends in Materials Research for Advanced Technology (NCMRAT), held at Aurangabad, during Jan. 29-31, 2007

ABSTRACT

Potential applications of silica aerogels such as super-insulating fillers in windows, solar energy devices and ICF targets, require aerogel objects in prescribed shapes and sizes and there is a need for encasing them for safe handling, due to their fragile nature. Conventional method of casting of aerogels is time-consuming and it requires pre-volume shrinkage of alcogels, which is not reproducible and it suffers from difficulties in handling of delicate alcogels. We have developed a method for casting of aerogel objects directly into metallic moulds, which results in zero volume shrinkage, good optical transparency and reproducibility in terms of density and monolithy. Detailed studies have been conducted to understand the effect of additives like dimethylformamide (DMF) and silica powder on volume shrinkage, optical transparency and surface area of retrieved aerogels. DMF/TEOS molar ratio was varied from 0 to 0.8 in steps of 0.2 and silica powder/TEOS molar ratio was varied from 0.04 to 0.12 in steps of 0.04. With precursors TEOS: EtOH: water (0.001M citric acid): DMF: silica powder (added at sol state) at optimal molar ratio of 1: 5: 7:0.6:0.04, respectively, we have obtained aerogel objects with zero volume shrinkage, good optical transparency (90%) and of 50 mm diameter and 10 mm thick size, encased in aluminium ring.

Introduction

Silica aerogels are extremely porous and transparent materials, consisting of > 95% air and < 5% silicon dioxide. Due to their high porosity and large surface area (1600 m^2/g) [1] they are used as catalyst supports [2] and containers for liquid rocket propellants [3]. Because of their low refractive indices (1.01 to 1.1) aerogels are suitable for detection of Cerenkov radiations [4]. They are being tested in double-walled window applications and solar energy systems, for super thermal insulation. Recently, silica aerogels have found application as inertial confinement fusion targets [5]. For these potential technological applications, silica aerogels are required in prescribed shapes and sizes and there is also a need for encasing them for safe handling, due to their fragile nature.

Silica aerogel are conventionally produced, by using tetramethoxysilane (TMOS) precursor. One of the authors, P.B. Wagh has demonstrated that, silica aerogels can be obtained from tetraethoxysilnae (TEOS), which is less toxic as well as cheaper precursor but observed 15 % volume shrinkage and low optical transparency of 60% [6]. Because of large shrinkage, these materials are casted in approximate shapes and then dried separately.

Experimental Method

Silica alcogels were prepared by hydrolysis and polycondensation of EtOH-diluted TEOS, in the presence of catalyst. The preparation of alcosol was started with molar ratios of precursors; TEOS precursor: ethanol (EtOH) solvent: water (0.001M catalyst) as 1:5:7, respectively, which was found to give minimum shrinkage of 15% in TEOS aerogels [6]. This molar ratio resulted in monolithic but volume-shrinked and semi-transparent (60%) aerogels. To achieve zero volume shrinkage and transparent TEOS aerogels, we examined the effect of addition of DMF as Drying Control Chemical Additive (DCCA) and silica powder in the sol state. The DMF/TEOS molar ratio (A) was varied from 0 to 0.8 in steps of 0.2 and silica powder/ TEOS molar ratio (B) was varied from 0.04 to 0.12 in steps of 0.04. Precursors chemicals were stirred in a 100 ml beaker and resulting sols were transferred to moulds. After gelation, the mould was placed in a 3-liter volume capacity pressure vessel and an additional 300 ml of ethanol was poured in the pressure vessel. After 3 hours of aging, alcogels were supercritically dried in an autoclave to obtain aerogels.

Densities of aerogel samples were measured, by known dimensions and weights. The percentage of porosity (P%) was obtained from the values of bulk (ρ_b) and skeletal (ρ_s) densities (2.2 g / cm^3) using the relation, $P\% = (1 - \rho_b/\rho_s) \times 100$. Optical transparency of aerogel samples (1cm thick) was measured, at a wavelength of 900 nm, using a Perkin-Elmer spectrophotometer. Surface area of aerogel samples was measured, using multiple point nitrogen gas adsorption BET surface analyzer (Model ASAP 2000).

Results and Discussion

Effect of DMF/TEOS molar ratio (A)

The pore sizes in the aerogels can be controlled by adding an organic solvent, called a Drying Control Chemical Additive (DCCA) to the sol. Formamide, Dimethylformamide, Glycerol and Acetonitrile are some of the DCCAs that have been used, for making xerogels [7]. DMF is known to decrease the hydrolysis rate and enhance polymerization [8] that helps in maintaining uniformity of the pores. Controlling the uniformity of pore size, optical transparency of the aerogels can be improved. We have examined the effect of DMF/TEOS molar ratio, on the optical transparency and volume shrinkage. The molar ratio of DMF/TEOS (A) was varied from 0 to 0.8 within step of 0.2. The effect of DMF/TEOS molar ratio (A) on physical properties of aerogels is tabulated in Table 1. It has been found that 'A' values between 0 and 0.6 resulted in lowering of density of aerogels from 0.23 to 0.20 g/cm^3 and reduced volume shrinkage from 15% to 5%. It may be due to increase in porosity because of enhancement of polymerization but as it controls the formation of smaller particles, ultimately the surface area was also found to be decreased (for A=0.6, surface area = 795 m^2/g). For 'A' values from 0 to 0.6, the optical transmission- increases up to 92 % and for A= 0.8, optical transparency decreases to 85 %. Increase of optical transparency up to 92 % may be due to uniformity of both pore and particle size, on the other hand decrease in optical transparency for higher A values (≥ 0.8) may be due to formation of larger size SiO_2 particles and irregular pores, as a result of enhanced polymerization reaction.

Effect of silica powder/TEOS molar ratio (B)

To strengthen the silica network and prevent volume shrinkage, we added nanosized silica powder directly

Table 1: Effect of DMF / TEOS Molar ratio and additives (silica powder as binder) on the physical properties of aerogels

Sr. No.	DMF/TEOS Molar ratio and silica powder/ TEOS molar ratio	Bulk density (g/cm^3)	Specific surface area by BET method (m^2/g)	% of porosity	% of volume shrinkage	% of optical transmittance at wavelength of 900nm
1.	DMF/TEOS (A)= 0	0.23	875	89%	15%	60%
2.	DMF/TEOS (A)= 0.2	0.22	850	90%	12%	80%
3.	DMF/TEOS (A)= 0.6	0.20	795	92%	5%	92%
4.	DMF/TEOS (A)= 0.8	0.21	785	91%	8%	85%
5.	DMF/TEOS (A)=0.6 silica powder/TEOS (B) =0.04	0.12	741	95%	0	90%
6.	DMF/TEOS (A =0.6 silica powder/TEOS (B) =0.08	0.14	703	93%	0	75%
7.	DMF/TEOS (A =0.6 silica powder/TEOS (B)=0.12	0.17	676	92%	0	50%

in a sol. Silica powder/TEOS molar ratio (B) was varied from 0.04 to 0.12, for fixed value of A= 0.6. The externally added silica powder acts as binder for SiO_2 particles formed due to hydrolysis and condensation reaction and helps to prevent volume shrinkage of resulted aerogels. Table 1 indicates the effect of silica powder/TEOS molar ratios, on the physical properties of resulted aerogel. For B=0.04 resulted in low density (ρ =0.12 g/cm^3) of aerogels, where added silica powder is counterbalanced, by reduction in volume shrinkage as compared to aerogels obtained without addition of silica powder (ρ=0.20 g/cm^3). For increase in B values from 0.04 to 0.12 resulted in an increase in the density of aerogels from 0.12 to 0.17 g/cm^3. This is because, physical addition of excess silica powder, resulted in an increase in mass of resulted aerogels, but does not contribute towards lowering of the shrinkage. Transparency was found to be drastically decreased from 90 % to 50 % with increase in B values from 0.04 to 0.12, which might be due to non-uniform size of SiO_2 particles and non-uniform pore size distribution, due to agglomeration of added silica powder. On the other hand, for B = 0.04 resulted in optically transparent (~ 90 %) aerogels which might be due to uniform pore size distribution.

Casting of aerogel objects

Conventional casting process needs pre-volume shrinkage as well as handling of delicate alcogels, which results in damage of samples at alcogel stage only. Hence, to overcome this problem, alcogels were casted directly in the mould and placed in an autoclave for supercritical drying. As the mould has to be put in an autoclave and subjected to critical temperature and pressure condition of solvent, it should withstand such high temperature and pressure. For ethanol, critical temperature and pressure are 240°C and 63 bars, respectively. Hence, aluminium ring was chosen to cast aerogels for demonstration. Top and bottom SS plates and sandwiched aluminium ring were highly polished (surface finish ≤ 16 microns) to prevent leakage of sol as well as to prevent sticking of aerogels to metal surfaces. The aerogels with zero volume shrinkage and confined in the metal rings are shown in Fig. 1.

Conclusions

Zero volume shrinkage of retrieved aerogels is achieved, by making use of DMF (as DCCA) and silica powder additives. In a pressure vessel of 100 mm diameter and 3-liter volume capacity and at optimal molar ratio of the precursors TEOS: EtOH: H_2O (0.001 M citric acid): DMF: silica powder = 1:5:7:0.6:0.04, respectively, we have obtained silica aerogel objects of large size, up to 10 mm thick and of 50 mm diameter and encased in a metallic ring. The resulting aerogels are monolithic with zero volume shrinkage, high optical transparency ~ 90 % (at λ = 900 nm) and low density of 0.12 g / cm^3.

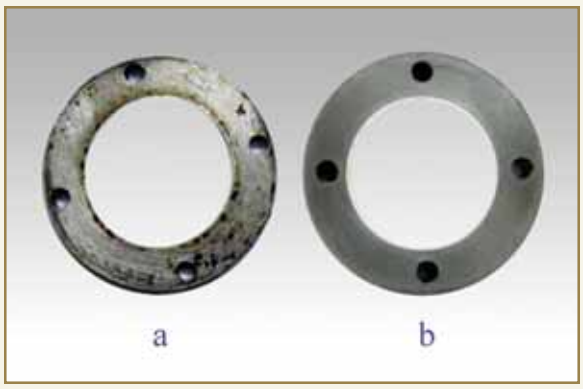

Fig. 1: Aerogels with zero volume shrinkage confined in metallic rings: a) 5 mm thick and b) 10 mm thick aerogel samples

References

1. C. A. M. Mulder, et al., in J. Fricke (Ed), Aerogels, Springer, Berlin, 1986, 68.
2. G. M. Pajonk, *Appl. Catal*. 72 (1991) 217.
3. G. M. Pajonk, et al. in J. Fricke (Ed), Springer, 1986, 193.
4. M. Bourdinaud et al. *Nucl. Instrum. Methods* 136 (1976) 99.
5. K. Y. Jang et al., *J. Vac. Sci. Technol*. A8 (1990) 1732.
6. P. B. Wagh et al., *Materials Chemistry and Physics* 53 (1998) 41 – 47.
7. J. B. Chan, et al. *J. Non-Cryst. Solids* 126 (1990) 79.
8. Adachi, et al. *J. Non-Cryst. Solids* 99 (1998) 118.

ABOUT THE AUTHORS

Dr. P. B. Wagh joined BARC in 2002. He obtained his Ph. D. degree in Physics from Shivaji University, Kolhapur in 1999. He has published about 25 research papers in National and International journals. His current areas of interest include research in the field of Aerogel materials and high energy density materials. Since 2003 he is a life member of the High Energy Materials Society (HEMS) of India.

Mr. Sanjay V. Ingale completed his M.Sc. in Physics with specialization in Materials Science from Shivaji University, Kolhapur. Since 2002, he is working in the Applied Physics Division, BARC. He is involved in development and processing of nanostructured materials and high energy density materials.

Dr. Satish C. Gupta joined BARC in 1972 through the 15th Batch of BARC Training School. He has to his credit a large number of publications in internationally reputed journals. He is a recipient of the prestigious DAE Special Contribution Award. His research interests are in the field of behaviour of high energy density matter and response of material to dynamic compression at high strain rate using shock wave. Presently he is leading the activities of the Applied Physics Division.

बीएआरसी न्यूज़लेटर BARC NEWSLETTER

MATRIX EFFECT IN PROMPT GAMMA-RAY NEUTRON ACTIVATION ANALYSIS

R. Tripathi, K. Sudarshan, A. Goswami, A.G.C. Nair and A.V.R. Reddy
Radiochemistry Division

and

S. K. Kataria
Electronics Division

This paper won one of the Best Papers Award at the DAE-BRNS Nuclear and Radiochemistry Symposium (NUCAR 07), held at M.S. University, Vadodara, during Feb. 14-17, 2007

ABSTRACT

Sensitivities of hydrogen and chlorine in aqueous samples, with varying hydrogen concentration have been measured. Sensitivities were found to vary with hydrogen concentration, indicating the effect of neutron scattering in PGNAA. With increasing hydrogen concentration, sensitivities were observed to increase for samples with small path length (0.5 cm) and decrease for the samples with large path length (2 cm). However, ratio of the sensitivity of Cl to that of H was observed to be independent of H concentration

Introduction

Prompt Gamma ray Neutron Activation Analysis (PGNAA) is a powerful on-line analytical technique, for elemental analysis. It is suitable for elements with large neutron absorption cross section and is commonly used for the analysis of low Z elements which are not amenable to conventional Neutron Activation Analysis (NAA). The lower flux of thermal neutron beams as compared to that in the reactor irradiation positions, necessitates the use of larger sample quantities, resulting in the large path length for the neutrons in the sample. This results in significant perturbation of the neutron flux inside the sample. For example, the presence of elements with large neutron absorption cross section such as Boron and Cadmium, results in attenuation of the neutron flux. A correction method has been suggested and is in use for the PGNAA of the samples containing these elements [1] in significant concentrations. Another matrix effect which can perturb neutron flux and requires corrective measures, is neutron scattering. This effect is more important for the samples containing low Z elements, particularly hydrogen. Hydrogenous matrix of the sample significantly changes neutron flux and may result in variation of the sensitivity of an element, in samples

of different dimensions and hydrogen content [2-4]. Analysis of aqueous samples which contain hydrogen as the bulk matrix element, is such an example. In order to investigate the effect of neutron scattering in the analysis of aqueous samples, sensitivities of hydrogen and chlorine were measured, with varying hydrogen content in the sample. The hydrogen content of the aqueous solution has been varied by adding D_2O in the aqueous solution, keeping the total volume constant.

Experimental

Experiments were carried out at DHRUVA reactor, BARC, Mumbai using diffracted neutron beam of energy 0.018 eV. Fig. 1 shows a schematic of PGNAA set up at the DHRUVA reactor. The neutron flux at the position of irradiation was about 10^6 $n.cm^{-2}.s^{-1}$. Aqueous samples were suspended in the path of neutron beam and prompt gamma-rays were measured, using an HPGe detector kept at 90^0 with respect to the beam. The detector was connected to an 8k-channel analyzer, to acquire the gamma-ray spectrum. The detector was surrounded by lead to shield from the emanating gamma-rays, from the capture of scattered neutrons. The detector was covered with boron carbide, to minimize the exposure of the detector to the scattered neutrons.

Sensitivity of hydrogen in H_2O-D_2O mixture was determined, from the count rate of 2223 keV prompt gamma-ray of hydrogen. In order to correct for the contribution from the hydrogen present in D_2O, pure D_2O was irradiated. In H_2O-D-$_2O$ mixture, concentration of D_2O was in the range of 0-85%. The diameter of the container was 2 cm. The sensitivity of chlorine in H_2O-D_2O mixture was determined from the count rate of the 786 keV gamma-ray. A constant volume of NaCl solution was added to H_2O-D_2O mixture, for the measurement of the sensitivity of chlorine. In order to investigate the effect of path length on neutron scattering, the sensitivities of hydrogen and chlorine were also measured, in a small container with path length 0.5 cm.

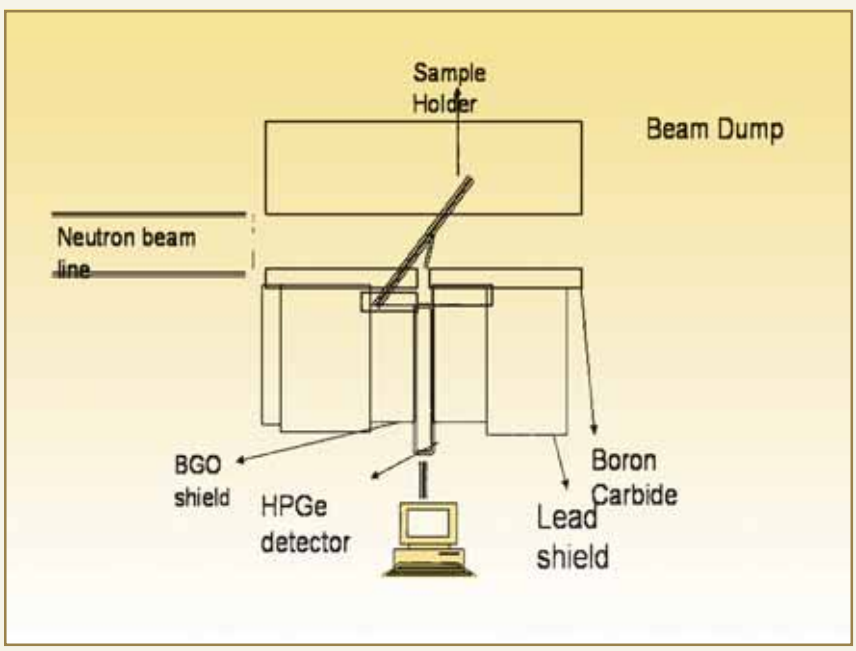

Fig. 1: Schematic representation of the PGNAA set up

Results and Discussion

As the samples (containing D_2O) were irradiated in air, there was a possibility of exchange of D_2O from the sample, with the moisture in air. To account for this, 2223 keV prompt gamma-ray count rates of hydrogen were measured, as a function of time taking a fresh D_2O sample. Fig. 2 shows a plot of the count rate of 2223 keV gamma-ray of hydrogen as a function of time. It can be seen from the figure, that the count rate of hydrogen

systematically increases with time, due to the exchange of deuterium with atmospheric hydrogen. In the case of H_2O-D_2O mixture, the measured count rates of 2223 keV gamma-ray were corrected, for the time-dependent increase due to H-D exchange.

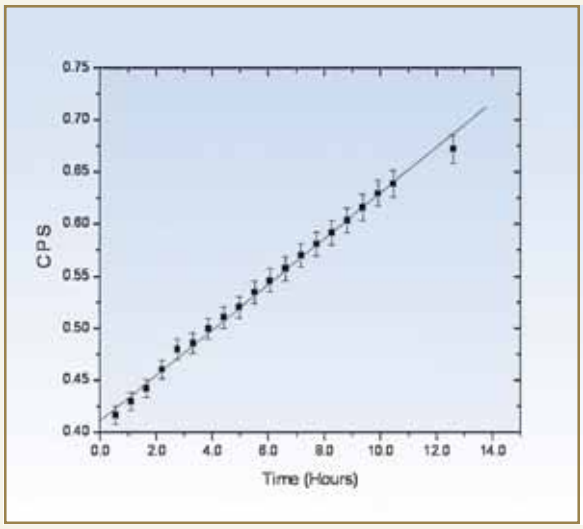

Fig. 2: Count rate of 2223 keV gamma ray of H as a function of time

Sensitivity of hydrogen in H_2O-D_2O mixture with varying concentration of D_2O is shown in Fig. 3. Filled and hollow symbols represent the sensitivities of hydrogen, in large and small containers respectively. It can be seen from Fig. 3 that the change in D_2O concentration has a different effect on the sensitivity of hydrogen, in the case of small and large containers. Sensitivity of hydrogen increases in the case of small container and decreases in the case of large container, with decreasing concentration of D_2O. The change in sensitivity is mainly due to the difference in the neutron scattering cross sections of hydrogen and deuterium. In the case of small container, neutron scattering increases with decreasing concentration of D_2O and in turn, path length of the neutron inside the sample increases. This results in an increase in the sensitivity of hydrogen. In the case of a large container, neutron scattering results in the attenuation of the neutron flux inside the sample. Further, in the present experiment, neutron beam is slightly colder as compared to the thermal neutron beam. The large amount of scattering may result in thermalization of the neuron beam and thereby result in a decrease in neutron absorption probability.

In Fig. 4, ratio of sensitivities of hydrogen and chlorine are plotted as a function of D_2O concentration in the H_2O-D_2O mixture. It can be seen from the figure, that the ratio of sensitivities is independent of the hydrogen content of the sample. Thus, in the analysis of aqueous samples, concentration of analytes should be determined with respect to hydrogen. Conversion of relative concentrations into absolute concentration, requires knowledge about hydrogen amount.

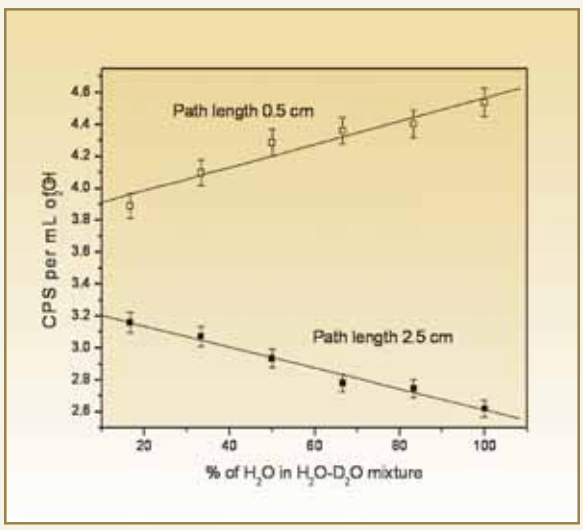

Fig. 3: Sensitivity of hydrogen vs H concentration

Measurement of H and Cl sensitivities in the aqueous solution of varying concentrations indicated that, the sensitivity increases or decreases with increasing H concentration, depending on the size of the sample. It was observed, that the sensitivity of H and Cl varies with varying H content of the aqueous solution, for a given sample size. However, ratio of the sensitivity of Cl and H, remains independent of the H concentration. Thus, in PGNAA of aqueous samples containing 1/v-nuclei, scattering effects can be taken care of, by

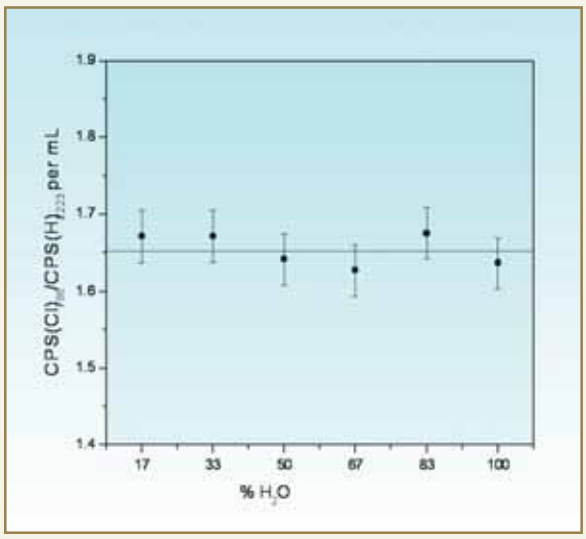

Fig. 4: Ratio of sensitivity of chlorine to hydrogen vs H concentration

determining the concentration of analyte elements, relative to H.

References

1. K. Sudarshan, R. Tripathi, A. G. C. Nair, R. Acharya, A. V. R. Reddy, A. Goswami, *Anal. Chim. Acta* 549, 205 (2005).
2. K. Sudarshan, R. Tripathi, A. G. C. Nair, R. Acharya, A. V. R. Reddy, A. Goswami, *Anal. Chim. Acta* 535, 309 (2005).
3. Elizabeth A. Mackey, Glen E. Gordon, Richard M. Lindstrom, David L. Anderson, *Anal. Chem*. 63, 288 (1991).
4. Elizabeth A. Mackey, Glen E. Gordon, Richard M. Lindstrom, David L. Anderson, *Anal. Chem*. 64, 2366 (1992).

ABOUT THE AUTHORS

Mr. Rahul Tripathi completed his M. Sc. (Chemistry) from Dr. Ram Manohar Lohia (Avadh) University in 1997. He is a Homi Bhabha Award winner from the 43rd Batch of Training School. After one year training, he joined the Radiochemistry Division of BARC in 2000. His research areas include heavy ion induced reactions and radio analytical techniques. He has about 20 publications in peer-reviewed journals.

Mr. Kathi Sudarshan is a gold medalist from the University of Hyderabad in M.Sc. (Chemistry). He joined the Radiochemistry Division of BARC in 1999 from the 42nd Batch of Training School. His research areas include positron annihilation spectroscopy, radio analytical techniques and heavy ion induced reactions. He has published about 30 papers in peer-reviewed journals.

ABOUT THE AUTHORS

Dr. A. Goswami did his M. Sc. in Chemistry from Burdwan University in 1978. After completion of one year training, he joined the Radiochemistry Division of BARC in 1980. His areas of research interest are nuclear fission / reactions, PGNAA and nondestructive assay methods. He has about 80 publications in international journals.

Dr. A.G.C. Nair joined the Radiochemistry Division of BARC in 1969. His fields of interest include development of radiochemical separation procedures of fission products and trace element analysis by Neutron Activation Analysis (NAA) and Prompt Gamma ray NAA (PGNAA). He has about 130 publications (journals and symposia) to his credit.

Dr. A.V.R. Reddy joined the Nuclear Chemistry Section, Radiochemistry Division in 1977. At present he is the Head of Nuclear Chemistry Section. His areas of research are nuclear fission, nuclear reactions, neutron activation analysis, radiochemical separations, heavy element chemistry and non destructive assay methods. He has about 250 publications in journals and symposia and has authored 3 books and edited 5 compilations.

(Late) Dr. S.K. Kataria was a Homi Bhabha Award winner from the 7th Batch (Physics) of Training School. He retired as Associate Director, Electronics Group (E), Electronics & Instrumentation Group and was closely associated with development of Radiation Detectors & Instrumentation, Data Acquisition Systems, Micro-Electronics and Software, Biomedical Instrumentaion, XRF and X-Ray Spectroscopy Systems. He contributed to Medium Energy Nuclear Reaction Theory and Experiments, Nuclear Models and Statistical Properties of Nuclei, Relativistic Heavy Ion Reaction Experiments.

ANOMALOUS FISSION FRAGMENT ANGULAR DISTRIBUTION IN $^{11}B+^{243}AM$ REACTION AT NEAR BARRIER ENERGIES

R. Tripathi, K. Sudarshan, S. Sodaye, S.K. Sharma and A.V.R. Reddy
Radiochemistry Division

This paper received one of the Best Papers Award at the DAE-BRNS Nuclear and Radiochemistry symposium 2007 (NUCAR07), held at M.S. University, Vadodara, from Feb.14-17, 2007

ABSTRACT

Fission fragment angular distributions were measured in $^{11}B+^{243}Am$ reaction, at E_{lab}=60, 66 and 72 MeV, to understand the role of target deformation and entrance channel mass asymmetry, in the contribution from non-compound nucleus fission. From the fission fragment angular distribution, angular anisotropies were deduced, which were found to be higher than those calculated using statistical theory. From the present study it appears that, target deformation is responsible for the contribution from non-compound nucleus fission in $^{11}B+^{243}Am$ reaction

Introduction

Fission fragment angular distribution is a sensitive probe to investigate the mechanism of fusion-fission. Fission fragment angular distribution is reproduced by statistical theory [1] for compound nucleus fission. In the case of contribution from non-compound nucleus fission, angular distribution deviates from the prediction of statistical theory. Pre-equilibrium fission model Ramamurthy and Kapoor [2,3] and entrance channel dependent (ECD) K-state model, Vorkapic and Ivanisevic [4] were proposed, to explain the fission fragment angular distribution for systems, having contribution from non-compound nucleus fission. Both the models could explain the anomalous fission fragment angular distribution, although, basic assumptions are significantly different. In the pre-equilibrium fission model, entrance channel mass asymmetry (α) is crucial, in deciding the contribution from non-compound nucleus fission. According to this model, if the entrance channel mass asymmetry (α) of the reaction system is lower than the Bussenaro-Gallone critical mass asymmetry (α_{BG}) [5], there will be contribution from non-compound nucleus fission. In the ECD K-state model, target deformation plays an important role. At near and sub barrier energies, fusion

predominantly takes place by the collision of the projectile, with the tip of the deformed target. If the composite system formed after collision is more elongated as compared to the saddle point, it may escape into the exit channel without being captured within the saddle point, to form the compound nucleus, resulting in non-compound nucleus fission. It has been shown by Vorkapic and Ivanisevic [4] that the anomalous fission fragment angular distribution in $^{16}O+^{232}Th$ ($\alpha<\alpha_{BG}$) and $^{12}C+^{236}U$ ($\alpha>\alpha_{BG}$) reactions can be explained, by ECD K-state model. The fact that both $^{16}O+^{232}Th$ and $^{12}C+^{236}U$ reactions show anomalous fission fragment angular distribution indicates, that fission entrance channel mass asymmetry, is not dictating the contribution from non-compound nucleus fission, in this reaction system. In this study, the compound nucleus is ^{248}Cf. It would be interesting to study the other fissioning systems through reaction routes with $\alpha<\alpha_{BG}$ as well as $\alpha>\alpha_{BG}$. Hinde et al [6] have studied the fission fragment angular distribution in $^{16}O+^{238}U$ ($\alpha<\alpha_{BG}$) at near and sub-barrier energies. This study has shown significant contribution from non-compound nucleus fission. However, recent measurement of cross section of evaporation residues (ERs) by Nishio et al [7] in $^{16}O+^{238}U$ reaction at near and sub-barrier energies, are consistent with the statistical theory indicating that, the contribution from non-compound nucleus fission is not significant. In the present work, fission fragment angular distribution has been measured in $^{11}B+^{243}Am$ reaction producing the same compound nucleus ^{254}Fm at near barrier energies. For this system $\alpha>\alpha_{BG}$, therefore, deviation of the fission fragment angular distribution from statistical theory is not expected, on the basis of pre-equilibrium fission model [2,3]. However, since ^{243}Am is a deformed target, deviation of fission fragment angular distribution from statistical theory is expected, on the basis of ECD K-state model [4]. Measurements have been carried out at E_{lab}=60, 66 and 72 MeV corresponding to E_{cm}/V_b of 1.00, 1.10 and 1.20 respectively. The results have been analyzed in the light of statistical theory.

Experimental

Experiments were carried out BARC-TIFR pelletron accelerator, Mumbai, India. An electrodeposited target of ^{243}Am (thickness ~100 μg/cm^2) on Ni-Cu backing was mounted, at the centre of a 1 m diameter scattering chamber, with ^{243}Am layer facing the beam. The target was bombarded with ^{11}B beam E_{lab}=60, 66 and 72 MeV and fission fragments were measured in the backward hemisphere, using two E-DE silicon telescopes. The thickness values of the two DE detectors were 10 and 12 mm. A monitor detector was kept at 35^0 with respect to beam direction to detect the elastically scattered ^{11}B ions. The data of the monitor detector was used, to normalize the count rates of the telescopes, to obtain absolute fission cross section.

Results and Discussion

The kinetic energy spectra of fission fragments were integrated, to obtain fission fragment angular distribution in laboratory frame of reference. The lab angular distributions were transformed from laboratory to center of mass frame of reference, assuming fission following complete fusion at all the beam energies. In the transformation from laboratory to center of mass frame of reference, the kinematics relevant to symmetric fission were considered, with kinetic energies calculated from the prescription of Rossner et al [8]. The fission differential cross sections were obtained, after normalizing for the target thickness and beam current, using the data of the monitor

detector. In order to deduce the angular anisotropies, fission fragment angular distributions were fitted, using the statistical theory expression [1]. According to statistical theory, fission fragment angular distribution for a spin zero projectile target combination is given by the following expression

$$W(\theta) \alpha C \sum_{I=0}^{\infty} \frac{(2I+1)^2 T_I \exp\left[-(I+1/2)^2 \sin^2\theta / 4K_0^2\right] J_0\left[i(I+1/2)^2 \sin^2\theta / 4K_0^2\right]}{(2K_0^2)^{1/2} \operatorname{erf}\left[(I+1/2)/(2K_0^2)^{1/2}\right]} \quad [1]$$

where, T_l is the transmission coefficient for the l^{th} partial wave. K_0^2 is the variance of the K distribution. J_0 is the zeroth order Bessel function. The constant C has been introduced in equation (1), to normalize the calculated angular distribution to the experimental angular distribution. The experimental angular distributions were fitted using equation (1) with C and K_0^2 as free parameters. The l distribution of the compound nucleus was calculated using the code CCFUS [10]. The experimental fission fragment angular distributions and fitted curves are shown in Fig. 1. The fitted curves were extrapolated to 180^0 and 90^0 to obtain angular anisotropies (*W(180) / W(90)*). Fig. 1 shows the center of mass angular distributions of fission fragments in the $^{11}B+^{243}Am$ reaction. The solid curves represent the best fits to the data obtained, using the statistical theory expression [1]. The fitting procedure is given in detail Tripathi et al [9]. The fission cross sections at different beam energies, obtained by integrating the fitted curves, were in good agreement with the fusion cross sections, calculated using the coupled channel code CCFUS [10]. From the fitted curves angular anisotropies (W(0) / W(90)) were determined. In order to calculate the angular anisotropies, l-distribution of the compound nucleus was approximated as the l-distribution of the fissioning nucleus. Experimental and calculated anisotropies are shown in Fig. 2. The experimental anisotropies are shown as filled symbols and the calculated values are shown as solid and dotted lines which correspond to the values calculated using the coupled and uncoupled l-distributions respectively. It can be seen from the figure, that the experimental

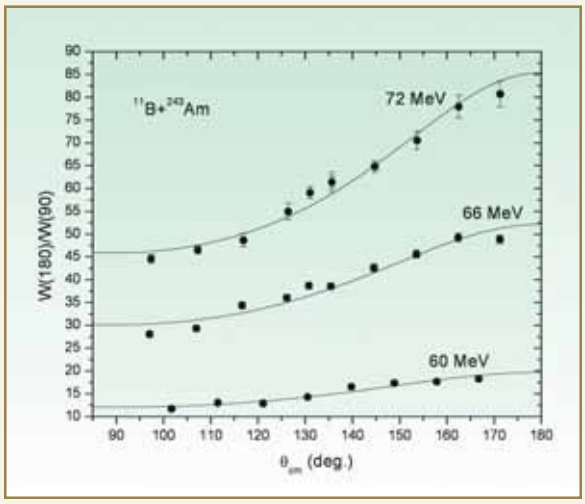

Fig. 1: Fission fragment angular distribution in $^{11}B + ^{243}Am$ reaction

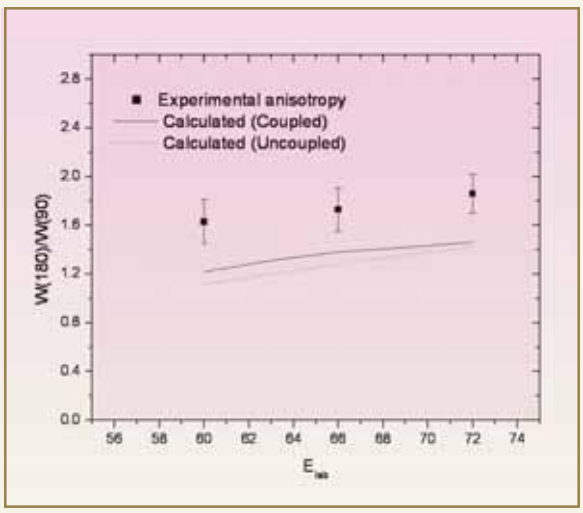

Fig. 2: Experimental and calculated anisotropies in $^{11}B+^{243}Am$ reaction

anisotropies are higher than the calculated values at all the beam energies of the present study, indicating the contribution from non-compound nucleus fission. For the present reaction system, entrance channel mass asymmetry $\alpha > \alpha_{BG}$, therefore observation of anomalous angular distribution cannot be attributed to the entrance channel mass asymmetry. Thus, the present study indicates the role of target deformation in deciding the contribution from non-compound nucleus fission in the fission of ^{254}Fm. The study also indicates that contribution from non-compound nucleus fission is significant at the above barrier energies.

References

1. R. Vandenbosch and J. R. Huizenga, *Nuclear Fission* (Academic Press, 1973) London.
2. V. S. Ramamurthy and S. S. Kapoor, *Phys. Rev. Lett*. 54, 178 (1985).
3. V. S. Ramamurthy and S. S. Kapoor, *Phys. Rev. C* 32, 2182 (1985).
4. D. Vorkapic and B. Ivanisevic, *Phys. Rev. C* 52, 1980 (1995).
5. K U. L. Businaro and S. Gallone, Nuovo Cimento 5, 315 (1957); K. T. R. Davies and A. J. Sierk, *Phys. Rev. C* 31, 915 (1985).
6. D. J. Hinde *et al.*, *Phys. Rev. Lett.* 74, 1295 (1995).
7. K. Nishio *et al.*, *Phys. Rev. Lett*. 93, 162701 (2004).
8. H. H. Rossner, J. R. Huizenga, and W. U. Schröder, *Phys. Rev. Lett*. 53, 38 (1984).
9. R. Tripathi et al., *Phys. Rev. C* 74, 014610 (2006).
10. C. H. Dasso and S. Landowne, *Comput. Phys. Commun*. 46, 187 (1987).

ABOUT THE AUTHORS

Mr. Rahul Tripathi completed his M.Sc. (Chemistry) from Dr. Ram Manohar Lohia (Avadh) University in 1997. He is a Homi Bhabha Award winner from the 43rd Batch of Training School. After one year training, he joined the Radiochemistry Division of BARC in 2000. His research areas include heavy ion induced reactions and radio analytical techniques. He has about 20 publications in peer-reviewed journals.

ABOUT THE AUTHORS

Mr. Kathi Sudarshan is a gold medalist from the University of Hyderabad in M.Sc. (Chemistry). He joined the Radiochemistry Division of BARC in 1999 from the 42nd Batch of Training School. His research areas include positron annihilation spectroscopy, radioanalytical techniques and heavy ion induced reactions. He has published about 30 papers in peer-reviewed journals.

Ms. Suparna Sodaye completed her M.Sc. in Chemistry from Delhi University and graduated from the 39th Batch of BARC Training School. After one year training, she joined the Radiochemistry Division in 1996. Her research areas include heavy ion induced reactions, radiochemical separations and tracer applications. She has about 25 publications in peer-reviewed journals.

Mr. Sandeep K. Sharma obtained his M.Sc. (Chemistry) from the Indian Institute of Technology, Delhi in 2005. He joined the Radiochemistry Division of BARC in 2006 from the 49th Batch of Training School. His research areas include positron annihilation spectroscopy. He has 2 publications in international journals.

Dr. A.V.R. Reddy joined the Nuclear Chemistry Section, Radiochemistry Division in 1977. At present he is the Head of Nuclear Chemistry Section. His areas of research are nuclear fission, nuclear reactions, neutron activation analysis, radiochemical separations, heavy element chemistry and non destructive assay methods. He has about 250 publications in journals and symposia and has authored 3 books and edited 5 compilations.

बीएआरसी न्यूज़लैटर
BARC NEWSLETTER

DETERMINATION OF IODINE IN FOOD PRODUCTS BY EPITHERMAL NEUTRON ACTIVATION ANALYSIS

R. Acharya, A.G.C. Nair and A.V. R. Reddy
Radiochemistry Division

and

P.R. Bhagat and N.S. Rajurkar
Department of Chemistry University of Pune, Pune

and

D. Partha Sarathi
College of Science GITAM, Visakhapatnam

This paper won one of the Best Papers Award at the DAE-BRNS Nuclear and Radiochemistry Symposium 2007 (NUCAR 07), held at M.S. University, Vadodara, from Feb. 14-17, 2007

ABSTRACT

An Epithermal Neutron Activation Analysis (ENAA) method using boron carbide shielding was standardized, for the determination of concentrations of low levels of iodine, in food materials namely milk, milk powder and baby foods. Advantage of iodine determination by ENAA has been evaluated, by determining boron ratios of iodine and its interfering elements like Na, K, Mn and Br. The concentrations of iodine determined in these samples were in the range of 0.2-5.5 $mg.kg^{-1}$. For method validation, iodine concentration was determined in NIST SRM 1549, a low fat milk powder.

Introduction

Iodine is an important essential trace element and is required for proper growth and thyroid hormone functioning of human beings. The daily dietary intake of iodine as recommended by WHO is 50-200 µg for infants to adults. However, deficiency or excess intake of iodine can lead to disorders called iodine disorders. The accurate determination of iodine in food products, is therefore, of considerable scientific interest. The analytical techniques most commonly employed for measuring iodine concentrations are colorimetry, ion selective electrode, isotope exchange, gas chromatography and Neutron Activation Analysis (NAA). Out of these techniques, NAA is one of the best techniques for iodine determination due to it's favorable nuclear properties leading to high sensitivity, isotope specificity and it's applicability for trace

elements. However, determination of low levels of iodine in biological samples is often difficult, by Instrumental NAA (INAA) due to high Compton background, by the presence of activation products of interfering elements like Na, K, Mn, Br and Cl [1]. In order to overcome this problem, Epithermal NAA (ENAA) using thermal neutron absorbers like B and Cd are used. The ENAA method is based on the fact that the resonance integral (I_0) to thermal neutron (n,γ) cross-section (σ_0) ratio (Q_0) for ^{127}I is 24.8 which is much larger than that for some of the interfering nuclides such as ^{23}Na, ^{37}Cl, ^{27}Al, ^{41}K, and ^{55}Mn (0.59, 0.69, 0.71, 0.97, and 1.053, respectively). Usually, any nuclide having Q_0 value >10 is a very good candidate for it's determination via ENAA. Boron or boron carbide is the better shielding material as compared to Cd in the case of iodine, since cadmium produces more residual activity. Since half-life of ^{128}I is short (25 min), ENAA with boron carbide filter is used for short irradiation and quick counting. In the present work, milk, milk powder and baby foods were analyzed by ENAA using B_4C for the determination of low level concentrations of iodine. Detection limits of iodine were also determined.

Experimental

Elemental standard for iodine was prepared by drying a known volume of standard solution of potassium iodate on a filter paper. Samples of mass about 100 mg along with elemental standard were sealed in polythene. SRM 1549 was also prepared in a similar way. Sealed samples along with the standards were wrapped with 3 mm thick boron carbide rubber (B_4C containing 30% B) and then wrapped in Teflon tape and finally sealed with polythene. Elemental standards of I, Na, K, Mn and Br were prepared on filter papers for determining boron ratios. They were packed with and without B_4C cover. Samples along with elemental standard for iodine were irradiated in D 8 position of APSARA reactor, BARC for one hour. Neutron flux in this position is ~5×10^{11} n.cm^{-2}.s^{-1}. After appropriate cooling, samples and standards were mounted on the Perspex plates and the radioactivity was assayed using a high-resolution gamma ray spectrometer consisting of 40 % HPGe detector connected to a Multi Channel Analyzer (MCA). The gamma ray spectrum was analyzed by using PHAST software, developed at BARC [2]. Boron ratios of elements of interest were calculated, using the ratios of activities produced by direct INAA and ENAA. The concentrations of elements were calculated using relative method of INAA.

Results and Discussion

The nuclear reaction, Q_0 values, half-life of activation products and the principal gamma ray energies are listed in Table 1. The boron ratios of elements are given in Table 2. The advantage factors for iodine in the presence of Na, K, Mn and Br are 10.9, 8.7, 8.3 and 1.2 respectively. It was calculated by dividing boron ratios of interfering element to element of interest (iodine). This indicates that iodine can be determined with better detection limits in the presence of the interfering elements such as Na, K, Mn and Br by using ENAA.

Table 1: Relevant nuclear data

Nuclear reaction	Q_0 (I_0/σ_0)	Radio-nuclides	Half-life	Eγ (keV) (aγ %)
$^{127}I(n,\gamma)^{128}I$	24.8	^{128}I	25 min	442.9 (16.9)
$^{37}Cl(n,\gamma)^{38}Cl$	0.69	^{38}Cl	37.2 min	1642 (31)
$^{81}Br(n,\gamma)^{82}Br$	19.3	^{82}Br	35.7 h	776 (100)
$^{55}Mn(n,\gamma)^{56}Mn$	1.053	^{56}Mn	2.58 h	847 (98.9)
$^{23}Na(n,\gamma)^{24}Na$	0.59	^{24}Na	15 h	1368.5 (100)
$^{41}K(n,\gamma)^{42}K$	0.87	^{42}K	12.8 h	1525 (1.8)

Table 2: Boron ratio for elements

Element	Activity by INAA	Activity by ENAA	Boron ratio
I	517542	106392	4.9
Na	17106	323	52.9
K	10419	245	42.5
Mn	1057484	26208	40.3
Br	311	51	6.1

Table 3: Total iodine concentrations in food samples obtained by ENAA

Food Material	Iodine Estimated/mg.kg^{-1}	Detection Limit/ mg.kg^{-1}
NIST SRM 1549 (Milk powder)	3.40 ± 0.03 (3.38 ± 0.03)	0.8
IAEA RM 153 (Milk powder)	1.59 ± 0.11 (NA)	NA
Infant milk powder	3.60 ± 0.15	1.3
Milk Powder (Amul)	5.50 ± 0.16	NA
Low fat Milk	0.16 ± 0.01	0.1
Cerelac wheat baby food	0.79 ± 0.08	NA
Farex baby food	2.79 ± 0.10	0.23

( ) - Certified values, NA - Not available

Fig. 1 shows a gamma ray spectrum of iodine of irradiated NIST 1549 (milk powder) using ENAA and INAA. It can be seen from the spectrum, that the peak due to ^{128}I at 443 keV is seen in the spectrum of ENAA, whereas this peak cannot be seen in the spectrum of INAA. The results of iodine concentrations determined in different food and food products are given in Table 3. The iodine concentration in NIST 1549 was obtained 3.40 ± 0.03 mg.kg^{-1} with respect to certified value of 3.38 ± 0.03 mg.kg^{-1}. The concentration of iodine as discussed in IAEA-RM-153, was found to be 1.59±0.11 mg.kg^{-1} and the certified value of which is not reported. Results of concentrations of iodine of 5 other samples are in the range of 0.16-5.5mg.kg^{-1}. The detection limit (L_D) was calculated using Currie's formula [3], $L_D = 2.71 + 3.29\ \sigma_b$, where σ_b is the square root of background counts under the characteristic photo-peak of interest. The L_D (counts) is converted to L_D(µg) and L_D(mg.kg^{-1}) by dividing sensitivity of iodine (S) and sample mass respectively. The L_D values are in the range of 0.1 – 1.3 mg.kg^{-1}, which depend on the salt content i.e., concentrations of Na, K and Cl. It was observed that the L_D for low fat milk was lowest (0.1 mg.kg^{-1}) since it is expected to have lower salt content.

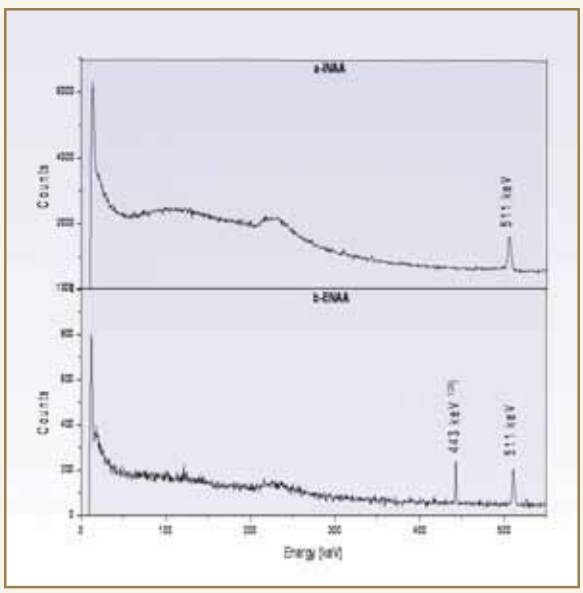

Fig. 1: Comparison of neutron activated spectra

References

1. R.R Rao and A. Chatt, Fres. *J. Anal. Chem*., 352 (1995) 53.
2. P.K. Mukhopadhyay, Proc. of the symposium on Intelligent Nuclear Instrumentation (INIT-2001), BARC, Mumbai, 2001.
3. L.A. Currie, *Anal. Chem*., 40 (1968) 586.

ABOUT THE AUTHORS

Dr. R. Acharya obtained M.Sc. from Utkal University and joined the 37th Batch of BARC Training School in Chemistry discipline. He joined the Radiochemistry Division in 1994 and since then he has been engaged in R&D work on conventional and k_0 based Neutron Activation Analysis (NAA), Prompt Gamma-ray NAA (PGNAA) and trace element speciation. Recently, he was selected for the Young Scientist Award 2008 instituted by the International Committee on Activation Analysis. He has about 135 publications (journals and symposia) to his credit.

Dr. A.G.C. Nair joined the Radiochemistry Division of BARC in 1969. His fields of interest include development of radiochemical separation procedures of fission products and trace element analysis by Neutron Activation Analysis (NAA) and Prompt Gamma ray NAA (PGNAA). He has about 130 publications (journals and symposia) to his credit.

Dr. A.V.R. Reddy joined the Nuclear Chemistry Section, Radiochemistry Division in 1977. At present he is the Head of Nuclear Chemistry Section. His areas of research are nuclear fission, nuclear reactions, neutron activation analysis, radiochemical separations, heavy element chemistry and non destructive assay methods. He has about 250 publications in journals and symposia and has authored 3 books and edited 5 compilations.

बीएआरसी न्यूज़लैटर
BARC NEWSLETTER

TRANSPORT OF CS(I) ACROSS LIQUID MEMBRANES USING CALIX [4]–BIS-2,3-NAPTHOCROWN-6 AS CARRIER LIGAND

D.R. Raut, S.A. Ansari, P.K. Mohapatra and V.K. Manchanda
Radiochemistry Division

This paper received one of the Best Papers Award at the DAE-BRNS Nuclear and Radiochemistry symposium 2007 (NUCAR 07), held at M.S. University, Vadodara, from Feb 14-17, 2007

ABSTRACT

Selective separation of ^{137}Cs from high level waste is quite challenging, in view of the presence of a large number of metal ions in varying oxidation states. Substituted calix [4]bis-crown-6 ligands have been found to be promising extractants for selective Cs recovery from complex matrices. Liquid membranes containing calix [4]bis-crown-6 ligands were used, in the investigations involving the transport behaviour of ^{137}Cs. Selectivity studies were carried out employing the gamma spectrometric analyses.

Introduction

The global inventory of ^{137}Cs is estimated to be around 3.7 x 10^{14} kBq by the year 2010. Due to it's long half-life and reasonable gamma energy (661 keV), it has potential application as a radiation source in gamma irradiators in the environmental pollution control, food preservation and sterilization of medical accessories. ^{137}Cs ($t_{1/2}$=31.2 year) in HLW, is one of the major radionuclides responsible for MANREM problem encountered during the processing of radioactive waste. Removal of ^{137}Cs from HLW, facilitates it's safe disposal in deep geological repository as vitrified mass [1]. It is, therefore, required to develop efficient separation methods for it's recovery from HLW.

Calixcrowns have been used as complexing agents for the alkali / alkaline earth metal cations, due to the presence of a glycol chain in their framework [2,3]. The selectivities of the complexation for metal ions, depend on the conformation adopted by the rigidified calix [4]arenes. For example, the partial cone isomer of 1,3-dimethoxy-p-tertbutylcalix [4] crown-5 was found to be selective for potassium cation [4]. Calix [4]-bis-2,3-Naphtho-Crown-6 (CNC, Fig. 1) possesses a cavity (1.5Å) that is highly selective for Cs(I) cation over other alkali metal ions, making it possible to separate cesium from a solution containing 10^4 to 10^6 - fold higher concentration of Na(I) [5]. Though calixcrown ligands exhibit high selectivity towards the alkali cations, their high cost has prohibited their use

on a large scale. Membrane-based methods have drawn the attention of separation chemists in view of low inventory of ligand. In the present paper, membrane-based separation of radio-cesium has been reported, using Calix[4]-bis-2,3-Naphtho-Crown-6 as a carrier dissolved in a mixture of 80% NPOE in n-dodecane as the diluent.

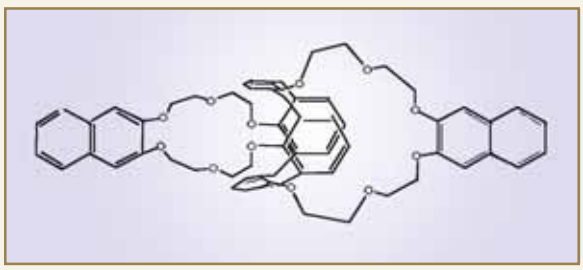

Fig.1: Calix [1, 3]-bis-2, 3-napthocrown-6(CNC)

Experimental

Calix [4] -bis-2,3-naphtho-crown-6 was purchased from Acros Organics, Belgium. PTFE membranes (47mm diameter) of pore size 0.45 μm having a nominal thickness of 85 μm and 72% porosity (Sartorius, Germany) were used as the solid support. The effective membrane area (Q), computed by multiplying the geometrical area and membrane porosity, was equal to 3.14 cm^2.Transport studies were performed in 20 mL glass transport cells, with feed / strip solutions stirred at 200 rpm. The PTFE membrane was soaked in the carrier solution for about 30 minutes prior to use. Membrane permeabilities were determined, by assaying the samples from the feed as well as the strip sides at different time intervals. The permeability coefficient (p) for the metal ions transport was calculated, by using the following formula:

$$\ln (C_{f,t} / C_{f,0}) = -(Q / V)Pt \qquad (1)$$

where $C_{f,t}$ and $C_{f,0}$ are the concentrations of metal ions in the feed side at a given time and at the start of the experiment, respectively, Q is the effective membrane area, V is the volume of the feed solution in cm^3 and t is the permeation time (seconds). For the distribution studies, 1mL of aqueous phase containing the ^{137}Cs radiotracer was equilibrated, with an equal volume of organic phase at constant temperature, in a thermostated water bath. The two phases were then centrifuged and assayed radiometrically. The distribution ratio (D_{Cs}) was calculated as the ratio of metal ion concentration in organic phase to that in the aqueous phase.

Results and Discussion

Supported Liquid Membrane (SLM) studies

The suitable diluent for SLM studies was evaluated by determining the distribution ratio of Cs(I) by 5.0 x 10^{-4} M Calix[4]-bis-2,3-Naphtho-Crown-6 in a mixture of NPOE and dodecane in different proportions (i.e. 20, 40, 60, 80 and 100% NPOE). The NPOE was selected due to the solubility of CNC, whereas dodecane was utilized for its soaking properties of PTFE membrane. The D_{Cs} values observed at 3M HNO_3 for different proportions of the solvent are listed in Table 1. Though maximum D_{Cs} value was observed with 100% NPOE, further studies were carried out with 80% NPOE and 20% *n*-dodecane since 10%

Table 1: Distribution ratio of Cs(I) by 5 x 10^{-4} M CNC in different diluents; Aqueous phase: 3M HNO_3

Obs. Nos.	% NPOE	% Dodecane	D_{Cs} at 3M HNO_3
1	20	80	0.05
2	40	60	0.27
3	60	40	0.95
4	80	20	2.53
5	100	0	4.01

NPOE could not wet the PTFE membrane. The stripping of Cs(I) from the loaded organic phase (80% NPOE) was carried out with distilled water where the backward D_{Cs} value obtained was 0.08, suggesting satisfactory stripping of the monovalent cation. With the optimized parameters from the solvent extraction studies, SLM studies were carried out, using CNC dissolved in a mixture of 80% NPOE and 20% *n*-dodecane as the carrier supported in PTFE membrane. Distilled water was employed as the strippant in all the studies.

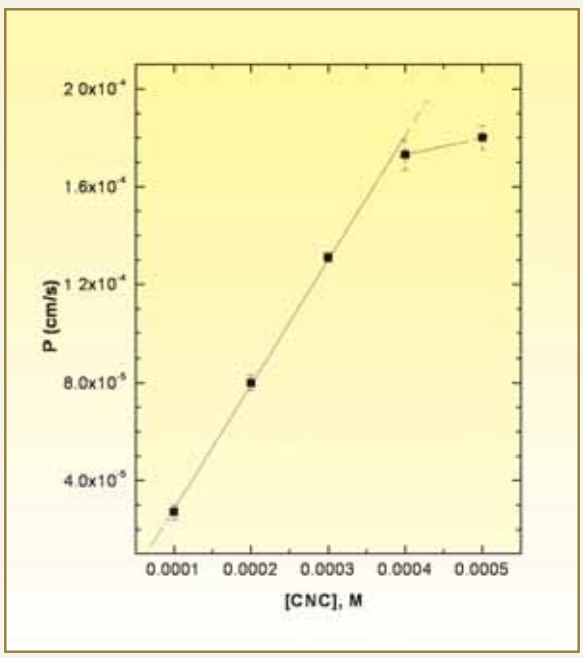

Fig. 2: Variation of permeability coefficient with ligand concentration. Feed: 2 M HNO_3

Ligand variation studies, carried out at feed acidity of 3M HNO_3, suggested increase in the permeability coefficient (P) with the ligand concentration (Fig. 2). Further studies were, therefore, carried out at the ligand concentration of 5 x 10^{-4}M CNC, due to limited solubility of the ligand beyond this concentration. The permeability coefficient of Cs(I) as a function of HNO_3 concentration is represented in Fig. 3. The permeability coefficient of Cs(I) increased with the acid concentration up to 3 M HNO_3 and then decreased

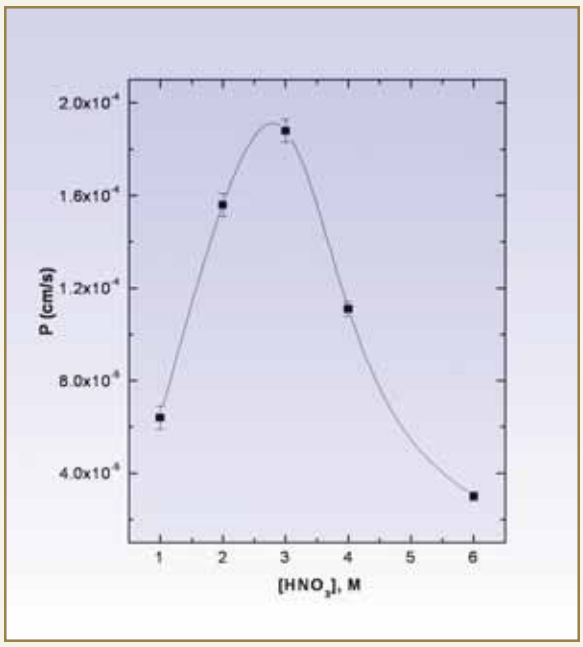

Fig. 3: Variation of P with HNO_3 concentration; Org. phase: 5x10^{-4} M CNC in 80% NPOE + 20% n - dodecane

thereafter. SLM transport studies were carried out at 3M HNO_3 as the feed and distilled water as the strippant. The permeability coefficient (P, cm/s) observed for Cs (I) at 3M HNO_3 was 1.9 x 10^{-4} employing 5.0 x 10^{-4}M CNC dissolved in 80% NPOE + 20% dodecane corresponding to about 90% transport of Cs(I) in 24hrs.

As shown in Fig. 3, the permeability coefficient (P, cm/sec) value increased with nitric acid concentration to a maximum at 3M HNO_3. This was attributed to the increased Cs(I) extraction as per the following equation.

$$Cs^{+}_{(aq.)} + CNC_{(org.)} + NO_3^{-}{}_{(aq.)} \rightleftharpoons [CsCNC]^{+}\ NO_3^{-}{}_{(org.)}$$

On the other hand, decrease in the transport rate at higher acidity, was due to acid transport as hydronium ion [5]. A typical PHWR fuel with a burn up of 7000 MWd/t has about 0.543 g/L of Cs in the HLW. The role of Cs concentration on the transport rates was also investigated, using a maximum concentration of

0.5 g/L of Cs. The transport data reported in Table 2 indicated a significant decrease in the % Cs transport with increasing Cs concentration, which is understandable from the flux equations. It is possible to increase the transport rate by increasing the membrane surface area, using a hollow fiber supported liquid membrane.

Selective transport studies of Cs(I) was carried out with irradiated uranium metal at 3M HNO_3. As depicted from the gamma spectrum in Fig. 4, the selective transport of Cs(I) was observed from the feed solution containing different fission products, where ~85% transport of pure Cs(I) was observed in 24hrs.

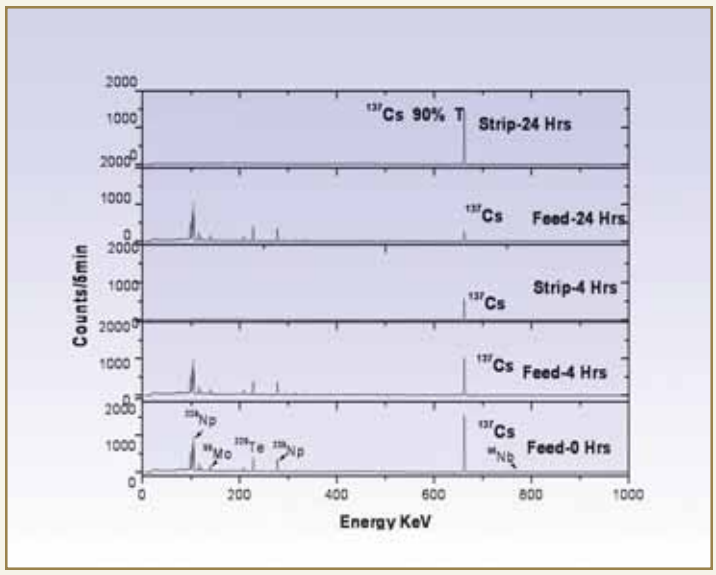

Fig. 4: Gamma spectra of the feed and strip phases which indicated selective transport of Cs-137.

Table 2: Effect of varying feed Cs concentration on permeability coefficients (P). Carrier: 5.0 x 10^{-4} M CNC in 80% NPOE + 20% dodecane; Solid support: PTFE; Receiver: Distilled water

Concentration of Cesium (M)	% Cs transport (24 h)	R^2	P x10^4 (cm/s)
Tracer	88.9	0.998	1.88±0.05
0.1	49.9	0.979	0.39±0.03
0.3	18.8	0.917	0.17±0.03
0.5	14.7	0.978	0.12±0.05

This observation clearly demonstrated that radio cesium can be selectively separated from acidic high level waste solution, employing CNC -supported liquid membrane. The stability of SLM was also studied by using the same support in several runs of 24hrs duration over a period of 20 days. The results suggested excellent stability of the liquid membrane.

Polymer Inclusion Membrane (PIM) studies

PIMs have the distinct advantage of higher stability as compared to the SLMs. Though the SLM studies indicated reasonably good stability of the membrane, PIM studies were also carried out for comparison purpose. PIM studies involved Cellulose TriAcetate (CTA) membranes containing 80 mg CTA,150 ìL NPOE, 4 mg CNC for Cs transport from feed solutions of 1M HNO_3. The permeability coefficient (P) in such case was found to be 5.5 x 10^{-5} cm/s corresponding to about 54% transport of Cs(I) in 24hrs. An increase in the transport rate was observed when CNC concentration was increased from 2 mg (P = 3.3 x 10^{-5} cm/s) to 10 mg (P= 8.5 x 10^{-5} cm/s). Though HLW usually contains 3 M HNO_3, the PIM was not stable at such acidity. The transport studies were,

therefore, carried out at varying concentration of $NaNO_3$ and HNO_3. When the feed contained 1M HNO_3 + 2 M $NaNO_3$ the P value was 7.2 x 10^{-5} cm/s which decreased to 5.7 x 10^{-5} cm/s 2M HNO_3 + 1M $NaNO_3$ indicating competition due to hydrogen ion.

Conclusions

From the transport studies involving supported liquid membrane (SLM) and Polymer Inclusion Membrane (PIM) containing Calix[4]-bis-2,3-Naphtho-Crown-6 (CNC), the following conclusions can be made:

- SLM studies appear promising when a diluent mixture of 80% NPOE + 20% *n*-dodecane was used.
- Though selectivity was excellent, a decrease in permeability coefficient was observed with increasing Cs loading. This can be improved by increasing the membrane surface area, i.e., hollow fiber supported liquid membrane appear promising.
- SLM system has shown excellent stability over a period of 20 days.
- PIM studies have indicated much lower permeability coefficient as compared to the SLM studies. However, the PIM showed much lower stability at 3 M feed acidity.

References

1. IAEA Technical Data Series No. 356, IAEA, 1993.
2. J. Vicens and V. Bhomer, Calixarenes, a versatile class of macrocyclic compounds; Kluwer Academic Publishers, Dordrecht, Holland, 1991.
3. Z. Asfari, C. Bressot, J. Vicens, C. Hill, J.F. Dozol, H. Rouquette, S. Eymard, V. Lamare and B. Toumois, *Anal. Chem*., 67 (1995) 3133.
4. E. Ghidhini, F. Ugozzoli, R. Ungaro, S. Harkema, A. El-Fadl and D.N. Reinhoudt, *J. Am. Chem. Soc*., 113 (1990) 6979.
5. P.K. Mohapatra, S.A. Ansari, A. Sarkar, A. Bhattacharyya and V.K. Manchanda, *Anal. Chim. Acta*, 571 (2006) 308.

ABOUT THE AUTHORS

Mr. D.R. Raut is working as a Junior Research Fellow in Radiochemistry Division, BARC since January 2006 under the collaboration scheme between University of Mumbai and Department of Atomic Energy. His area of specialization is separation of radiocesium using calix-crown ligands.

ABOUT THE AUTHORS

Mr. S.A. Ansari is working as a Senior Research Fellow in the Radiochemistry Division, BARC since January 2003 under the collaboration scheme between University of Mumbai and Department of Atomic Energy. His area of specialization is separation of actinides and fission products using novel extractants. He has 20 publications in reputed international Journals.

Dr. P. K. Mohapatra joined the Radiochemistry Division, BARC in 1987. His research interests include separation of actinides and fission products using solvent extraction, ion-exchange, extraction chromatography and liquid membranes. A recognized guide of HBNI, Dr. Mohapatra has to his credit over 90 publications in reputed international journals.

Dr. V.K. Manchanda is currently the Head, Radiochemistry Division, BARC. His research interests include CQC of Pu based fuels, Separation of actinides using novel extractants, Macrocyclic complexes and Speciation of long lived radionuclides in aquatic environment. A recognized guide of University of Mumbai and HBNI, he has more than 170 publications in reputed international journals to his credit. He is the President of professional organizations such as IANCAS and INASAT. He is on the Editorial Board of International Journals, *Radiochimica Acta* and *Solvent Extraction & Ion Exchange*.

बीएआरसी न्यूज़लेटर
BARC NEWSLETTER

ELECTROCHEMICAL STUDIES OF UO_2^{2+} IN 1-OCTYL 3-METHYLIMIDAZOLIUM HEXAFLUOROPHOSPHATE ($OMIMPF_6$) ROOM TEMPERATURE IONIC LIQUID

J. V. Kamat, N. Gopinath, K.V. Lohithakshan and S. K. Aggarwal
Fuel Chemistry Division

This paper was awarded the Second Prize for Poster Presentation at the Third International Conference on Electroanalytical Chemistry and Allied Topics (ELAC-2007) held at Shimla, during March 10-15, 2007

Introduction

Room Temperature Ionic Liquids (RTILs) are composed of large organic cations and weakly coordinating inorganic anions [1]. A series of hydrophobic and hydrophilic RTILs are known [2]. Hydrophobic RTILs are of particular interest due to their water stability, relatively low viscosity and good electrochemical stability [3-5]. However, it has been reported that PF^-_6 based RTIL undergoes degradation, when used in liquid / liquid separation from higher acidic aqueous phases [5].

Therefore, it was thought worthwhile to study the effect of the degraded products, on the Electrochemical Window (EW) of ($OmimPF_6$). Studies were also carried out to optimize conditions for extraction of UO_2^{2+} to investigate it's redox behaviour in $OmimPF_6$ and to determine the number of electrons involved in the redox chemistry. The Chronoamperometric technique of evaluating n without knowing the diffusion coefficient, D, was devised by Kakihana et al [6] and has been used in the present work [7]. The number of electrons involved was determined from the values of the slope and intercept of the Cottrell plot. The results of these studies are presented in this paper.

Experimental

All voltammetric experiments were performed with CH-instrument-model 400A. All chemicals used were of high purity. All reagents were prepared in Millipore water. An electrochemical mini cell (capacity ~1mL) with three electrodes was used. A platinum rod (1.5 mm dia) and a graphite rod (1.5mm dia) immersed in the solution as a quasi reference electrode and as auxiliary electrode respectively were used. The working electrode was Glassy carbon microelectrode (10 mm dia). Uranium solution was prepared by dissolving nuclear grade uranium oxide powder in dilute HNO_3. The ionic liquid procured from Acros organics (USA) was used without purification. CMPO was supplied by the Bio-Organic Division, BARC in pure

form (98%). Cyclic voltammetry (CV) was performed in the quiescent solution. Dissolved oxygen was removed by bubbling high pure nitrogen gas into the solution.

Electrochemical window of $OmimPF_6$

The test solution (0.2 mL) of $OmimPF_6$ was transferred into the cell. Cyclic Voltammetry (CV) was performed by scanning the potential of working electrode from +3 V to –3 V at a scan rate of 20 mV s^{-1}.

Electrochemical window of $OmimPF_6$ in the presence of CMPO

CV for 0.2M CMPO in $OmimPF_6$ was performed, by scanning the potential of working electrode from +3V to –3V at a scan rate of 20 mV s^{-1}.

Stability of $OmimPF_6$ in contact with HNO_3

$OmimPF_6$ was equilibrated in varying concentrations of nitric acid (0.5, 1, 2 and 5 M) and 0.2 mL of it was subjected to CV studies.

Electrochemistry of UO_2^{2+} in $OmimPF_6$

U (VI) [1.4mM] was quantitatively extracted from 0.5M HNO_3 in $OmimPF_6$ phase by employing CMPO as complexing agent. 0.2 mL was subjected to CV, by scanning the potential of electrode from +2 V to -2 V at a scan rate of 20 mVs^{-1}.

Evaluation of 'n' number of electrons involved in the redox reaction

Chronoamperometry was performed for UO_2^{2+} extracted from 0.5 M nitric acid by 0.2 M CMPO/ $OmimPF_6$, by applying an initial potential –0.4 V at which no faradaic reaction is occurring, then stepping the potential to a value of –1.4 V at which the electrochemical reaction takes place, current was measured throughout the experiment.

Results and Discussion

The results of studies of EW carried out are shown in Fig.1. The cyclic voltammogram of $OmimPF_6$ demonstrates, that electrochemical window of the $OmimPF_6$ spans the potential range from –2.5 V to +1.8 V, indicating an electrochemical window of 4.3 V.

Voltammogram in the presence of CMPO is shown in Fig. 2. From the figure it can be concluded that the presence of CMPO did not have any effect on the electrochemical window of $OmimPF_6$.

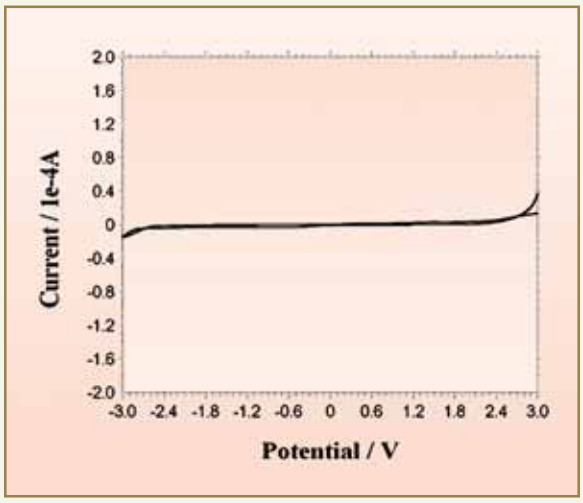

Fig.1: C V of 0.2 mL of $OmimPF_6$: Scan rate : 20 mVs^{-1}

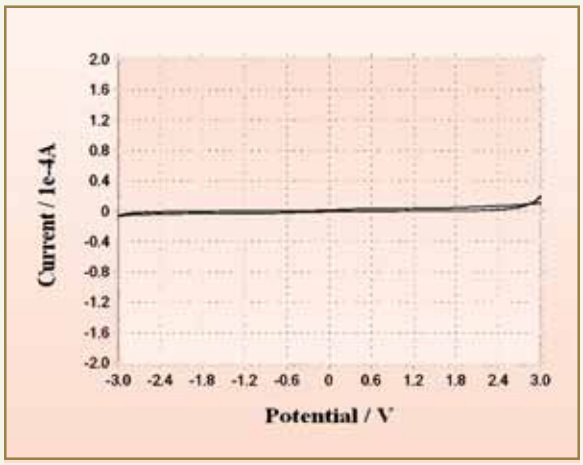

Fig. 2: C V of 0.2mL of $OmimPF_6$ / 0.2 M CMPO Scan rate : 20 mVs^{-1}

The result of effect of HNO_3 on the stability of $OmimPF_6$ is shown in Fig. 3. It can be seen that the cathodic peak at –0.55 V in contact with (1, 2 & 5 M) HNO_3 appeared. This peak corresponds to degraded product of $OmimPF_6$, which limits the EW of RTIL. Further it can be seen that the peak disappears with 0.5M HNO_3.This suggests 0.5M HNO_3 is ideally suited for liquid/liquid extraction studies.

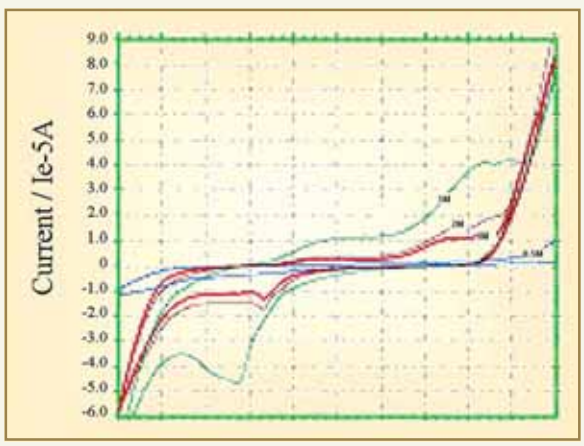

Fig. 3: CV of equilibrated 0.2 M CMPO/ of $OmimPF_6$ with (0.5, 1, 2, 5 $MHNO_3$) Scan rate : 20 mVs^{-1}

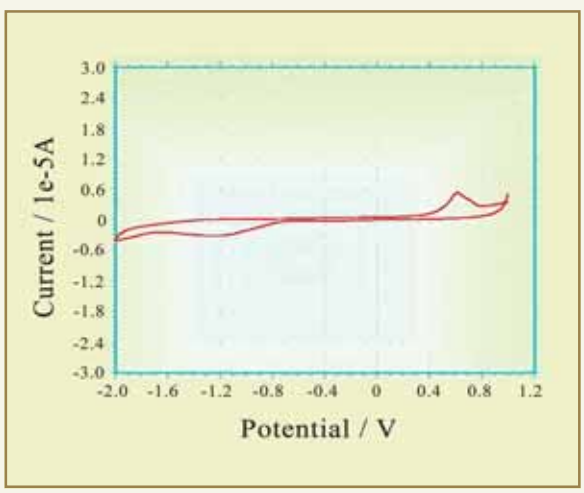

Fig. 4: CV of 1.4 mM uranium extracted from 0.2M CMPO / of $OmimPF_6$ 0.5 M nitric acid scan rate: 20 mVs^{-1}

Cyclic voltammogram of UO_2^{2+} extracted from 0.5M HNO_3 in OmimPF6 phase by employing CMPO as complexing agent shows (Fig. 3) a cathodic peak at -1.1V, which can be attributed to reduction of UO_2^{2+} and corresponding oxidation peak at +0.68 V.

The result of Chronoamperometry studies for evaluation of number of electrons involved in the redox reaction is shown in Fig. 4. Cottrell plot, i vs $t^{-1/2}$ exhibited

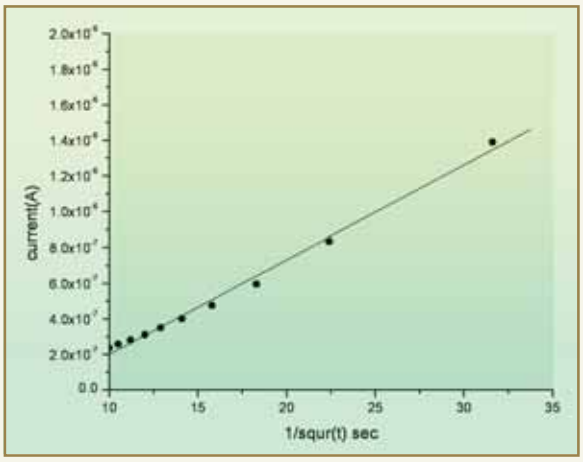

Fig. 5: Cottrell plot of the current for 1.4 mM uranium extracted from 0.5 M nitric acid by 0.2 M CMPO/ of $OmimPF_6$

linearity. Inserting the value of slope (s) and intercept (p) in eq., $n(1-e^t) = s^2/pFa^3c$ where, a = electrode radius C= concentration of electroactive species F= Faraday constant, we obtain number of electrons n for redox reaction. A value of 1.96 for n was obtained. This value confirms that UO_2^{2+} undergoes a single step, two-electron reduction to UO_2.

Conclusion

The degraded product of $OmimPF_6$ formed when equilibrated with acids, is electroactive and decreased the cathodic limit of $OmimPF_6$ from -2.5V to –0.55V. However equilibration with 0.5M, HNO_3 did not yield any degraded RTIL product and hence, suitable for liquid-liquid extraction studies. The value of 1.96 for n, confirms that UO_2^{2+} is reduced to UO_2.

References

1. P. Wasserscheild, T. Welton, Ionic liquids in Synthesis. Eds:Wiley: Weinheim Germany 2003.
2. S. I. Nikitenko and P. Moisy, *Inorg. Chem*., 45 (2006) 1235.
3. T. Welton, *Chem. Rev*., 99 (1999) 2071.
4. J. D. Holbrey, K. R.Seddon, *Clean. Prod. Processes,* 1 (1999) 223.
5. J. G. Huddleston, A.E. Visser, R .D. Rogers. *Green Chemistry*, 3 (2001) 156.
6. M.Kakihana, H. Ikenchi, G. P. Sato, K. Tokuda, *J.Electranal. Chem*., 117 (1981) 201.
7. A.S. Baranski, W.R.Faweett, C.M. Gilbert, *Anal.Chem.,* 57 (1985) 166.

ABOUT THE AUTHORS

Dr. (Ms.) J. V. Kamat obtained her M.Sc. degree from Mumbai University in the year 1980. She joined the Fuel Chemistry Division in 1982. She obtained her Ph.D. in Chemistry from Mumbai University in 2004. She is involved in the applications of various Electroanalytical Techniques for elements of interest in the nuclear fuel cycle. She is the Treasurer at the Indian Society of Electro Analytical Chemistry (ISEAC).

Mr. N. Gopinath obtained his M.Sc. degree in Physical Chemistry from Sri Venkateswara University, Tirupati in 1973. He joined the department in 1977. He has been actively involved for the last 30 years in developing and employing various Electroanalytical Techniques for different applications in the nuclear fuel cycle. He is the Secretary for the Indian Society for Electro Analytical Chemistry (ISEAC).

Dr. K.V. Lohithakshan obtained his M.Sc. in 1989 and Ph.D. in 2000 from Mumbai University after joining BARC in the year 1981. He is actively involved in the chemical quality control work of nuclear fuels as well as separation studies of actinides by solvent extraction method.

Dr. S.K. Aggarwal is currently Head, Fuel Chemistry Division, BARC, Trombay. He joined the 16th Batch of BARC Training School in 1972 and received the Homi Bhabha Award. He did his Ph.D. from Mumbai University in 1980 and completed his Post-doctoral training during 1987-89 at the University of Virginia, USA. He is a specialist in the field of atomic mass spectrometry and alpha spectrometry and is interested in various mass spectrometric techniques. His other areas of interest include electrochemistry, X-ray spectroscopy and solvent extraction. He is a recognized Ph.D. guide of the Mumbai University and of HBNI.

बीएआरसी न्यूज़लेटर
BARC NEWSLETTER

EVALUATION OF PHASE MODIFIER FOR THE EXTRACTION OF ND(III) BY N,N,N',N'-TETRAOCTYL DIGLYCOLAMIDE

S.A. Ansari, P.K. Mohapatra and V.K. Manchanda
Radiochemistry Division

This paper received the Second Prize at the National Seminar on Emerging Trends in Supramolecular Research, held at Gujarat University, Ahmedabad, between March 30-31, 2007

ABSTRACT

In order to eliminate the third phase formed during the extraction of macro concentration of Nd(III) by 0.1 M TODGA (N,N,N',N'-tetra octyl diglycolamides) in n-dodecane, several phase modifiers viz. TBP (tri-n-buty phosphate), 1-decanol and DHOA (di-n-hexyl octanamide) were evaluated. Out of these modifiers, DHOA was found to be superior. Based on the present work, 0.1M TODGA and 0.5M DHOA are proposed to be the solvents for the partitioning of lanthanides / actinides from acidic high-level waste solutions.

Introduction

The N,N,N',N'-tetra alkyl diglycolamides are a class of emerging extractants for the separation of lanthanides / actinides from nitric acid solutions of different origin. Amongst several diglycolamide derivatives, tetraoctyl diglycolamide (TODGA) shows promise for the actinide partitioning in the reprocessing of spent nuclear fuel or treatment of nuclear wastes [1,2]. In general, paraffinic hydrocarbon solvents, such as dodecane, kerosene, NPH are preferred, for fuel reprocessing / actinide partitioning, because of their chemical / radiolytic stability and favourable physico-chemical characteristics, as compared to aromatic and chlorinated solvents [3]. However, a major challenge with TODGA in paraffinic solvent (n-dodecane) is the third phase formation that occurs, when contacted with high concentration of nitric acid solution (>5 M HNO_3).

The third phase formation is the splitting of organic phase into two parts, resulting in a light organic phase rich in diluent and lean in extractant; and a dense organic phase rich in ligand-metal/ligand-nitric acid complexes. The third phase is often eliminated by addition of diluent modifiers such as long chain alcohols, monoamides, trialkyl phosphates, etc. which are capable of specific solvation of ligand-metal complexes / ligand-nitric acid salt through either dipole-dipole interaction or hydrogen bonding. The present

paper deals with the development of a suitable phase modifier for the loading of Nd from nitric acid solution. Limiting Organic Concentration (LOC) of Nd, was determined under different experimental conditions.

Experimental

The syntheses of TODGA as well as DHOA were carried out in our laboratory, employing established procedure described elsewhere [2,4]. Other chemicals used were of analytical reagent grade. Solvent extraction experiments were performed, by equilibrating equal volumes of organic and aqueous phases in stoppered glass tubes. All the experiments were carried out at room temperature (25°±1°C). Analysis of Nd was carried out by complexometric titrations employing standard EDTA solution as well as by radiometry employing ^{147}Nd tracer.

Results and Discussion

Our earlier studies on TODGA revealed third phase formation at very low metal ion concentration in the organic phase. The formation of third phase during counter-current extraction, may severely affect the hydrodynamics of the contactor. The third phase is often eliminated by addition of polar diluents such as long chain alcohols, monoamides and organic phosphates, often referred to as phase modifiers. The phase modifiers are capable of specific solvation of metal-ligand complexes / acid-ligand salts either through dipole-dipole interaction or through hydrogen bonding. Earlier, a series of long chain monoamides, viz. dibutyl decanamide (DBDA), di(2-ethylhexyl) acetamide (D2EHAA), di(2-ethylhexyl) propionamide (D2EHPRA), di(2-ethylhexyl) isobutyramide (D2EHIBA), dihexyl octanamide (DHOA) and dihexyl decanamide (DHDA) were investigated in our laboratory, as phase modifiers. Amongst these amides, DHOA was found to be promising. However, the present studies were extended to long chain alcohol (1-decanol) and an organic phosphate (TBP) as the phase modifiers and the results were compared with those of DHOA.

The Limiting Organic Concentration (LOC) of Nd was evaluated, by determining loading of Nd at different aqueous metal ion concentrations. Fig. 1 represents the Nd loading by 0.1M TODGA and 0.5M phase modifiers, viz. DHOA, TBP and 1-decanol, dissolved in n-dodecane from feed solutions containing 3 M HNO_3. As is evident from the figure, the loading of Nd increased with increase of the aqueous metal concentrations. Though no third phase was observed with any of the phase modifiers, Nd concentration in the organic phase reached a maximum organic loading value. The LOC of Nd was found to follow the order: TBP (6.19g/L) > DHOA (4.90g/L) > decanol (3.74g/L). However, at lower aqueous Nd concentration, DHOA system shows higher loading due to higher distribution values of Nd.

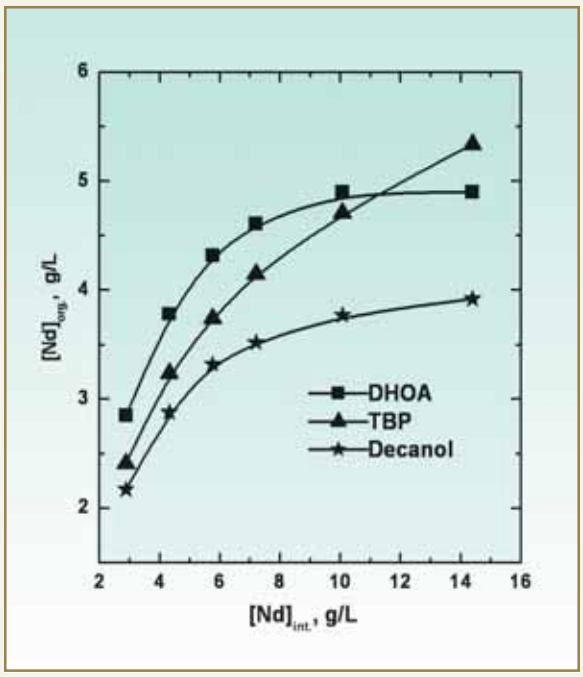

Fig. 1: Loading of Nd as a function of aqueous Nd concentration; Org. phase: 0.1M TODGA + 0.5M phase modifier; Aq. phase: 3M HNO_3

Though LOC with TBP was the highest, better loading (Fig. 1) as well as larger D_{Nd} was observed for DHOA, at lower metal ion aqueous concentration (Fig. 2). It

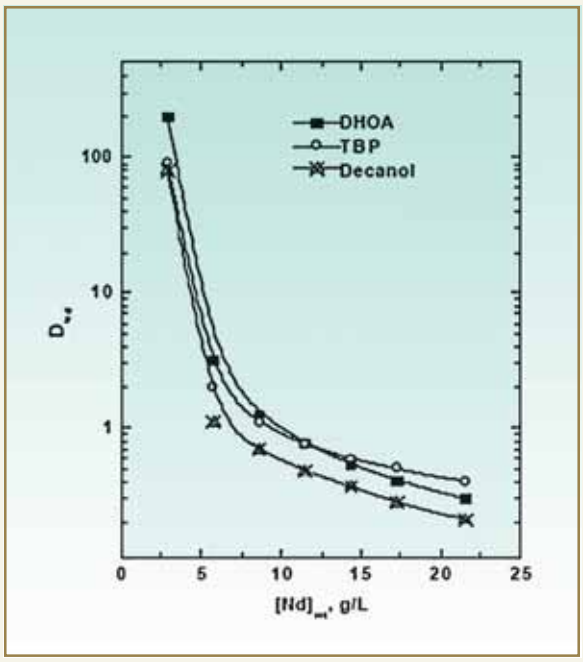

Fig. 2: D_{Nd} as a function of aqueous Nd(III) concentration; Org. phase: 0.1M TODGA + 0.5M phase modifiers; Aq. phase: 3M HNO_3

should be noted, that the concentration of lanthanides in high level waste is in the range 1-4 g/L. Therefore, data referring to the lower aqueous Nd concentration is relevant to the partitioning of actinides / lanthanides from nuclear waste solutions. It is evident from Figs. 1 and 2, that DHOA was found to be a better phase modifier as compared to TBP and decanol under the conditions of high level waste solutions. Use of DHOA was also preferred over TBP as the latter is a phosphorus based molecule, which creates problems in disposal of secondary waste.

The effect of phase modifier concentration on the LOC of Nd was also studied and is presented in Table 1. It is evident from the table that no significant increase in the LOC of Nd was observed, beyond 0.5 M concentration of phase modifiers. Therefore, 0.5 M concentration of phase modifier was employed in subsequent studies. Loading of Nd in the organic phase was studied employing 0.1M TODGA and 0.5 M phase

Table 1: LOC of Nd by 0.1M TODGA + phase modifiers; Diluent: *n*-dodecane; Aq. phase: 20g/L Nd at 3M HNO_3; Temperature: 25°C

Concentration of phase modifiers	LOC of Nd, g/L		
	DHOA	TBP	Decanol
0.00	1.15	1.15	1.15
0.5	4.90	6.19	3.74
0.8	4.90	6.91	3.89
1.0	4.75	7.05	4.03
1.2	4.90	7.05	3.89

modifiers from a solution containing 2.85 g / L Nd at 3 M HNO_3. As is presented in Table 2, >99% metal ion was loaded in a single contact for all the three systems. Similarly, stripping of Nd from loaded organic phase was carried out, with 0.01M HNO_3. In case of DHOA, ~85% stripping was observed in the first contact. On the other hand, only ~50% stripping was observed for TBP which was attributed to the higher acid uptake in the forward extraction. However, quantitative stripping was observed in the third stage for all the three systems.

Table 2: Loading and stripping of Nd by 0.1M TODGA + 0.5M phase modifiers; Aq. phase: 2.85g/L Nd at 3M HNO_3; Strip solution: 0.01M HNO_3

No. of Steps	% Loading		
	DHOA	TBP	Decanol
Load-I	99.75	99.28	99.46
Strip-I	83.95	51.32	70.89
Strip-II	99.89	99.51	99.49
Strip-III	99.99	99.99	99.99

Conclusions

Quantitative extraction of Nd(III) was observed by 0.1M TODGA and 0.5M phase modifiers from a solution containing 2.85 g/L Nd at 3M HNO_3 which was relevant to HLW solution. DHOA was found to be a better phase modifier as compared to TBP and decanol. It is proposed that 0.1M TODGA and 0.5M DHOA may be used, for the partitioning of lanthanides / actinides from acidic high level waste solutions.

References

1. S. A. Ansari, P. N. Pathak, M. Husain, A. K. Prasad, V. S. Parmar and Manchanda; *Solv. Extr. Ion Exch*., 23, 643 (2005).
2. S. A. Ansari, P. K. Mohapatra, D. R. Prabhu and V.K. Manchanda; *J. Membr. Sci*., 282, 133 (2006).
3. E. P. Horwitz, D. G. Kalina and H. Diamond; *Solv. Extr. Ion Exch*., 3, 75 (1985).
4. G. Thiollet and C. Musikas; *Solv. Extr. Ion Exch.,* 7, 813 (1989).

ABOUT THE AUTHORS

Mr. S.A. Ansari is working as a Senior Research Fellow in the Radiochemistry Division, BARC since January 2003, under the collaboration scheme between University of Mumbai and Department of Atomic Energy. His area of specialization is separation of actinides and fission products using novel extractants. He has 20 publications in reputed international journals.

Dr. P. K. Mohapatra joined the Radiochemistry Division, BARC in 1987. His research interests include separation of actinides and fission products using solvent extraction, ion-exchange, extraction chromatography and liquid membranes. A recognized guide of HBNI, Dr. Mohapatra has to his credit over 90 publications in reputed international journals.

Dr. V.K. Manchanda is currently the Head, Radiochemistry Division, BARC. His research interests include CQC of Pu based fuels, Separation of actinides using novel extractants, Macrocyclic complexes and Speciation of long lived radionuclides in aquatic environment. A recognized guide of the University of Mumbai and HBNI, he has more than 170 publications in reputed international journals to his credit. He is the President of professional organizations such as IANCAS and INASAT. He is on the Editorial Board of International Journals, *Radiochimica Acta* and *Solvent Extraction & Ion Exchange*.

बीएआरसी न्यूज़लेटर
BARC NEWSLETTER

SIMULTANEOUS DETERMINATION OF URANIUM AND PLUTONIUM IN DISSOLVER SOLUTION OF IRRADIATED FUEL, USING ID-TIMS

Raju Shah, K. Sasi Bhushan. R. Govindan, D. Alamelu,
P.S. Khodade and S.K. Aggarwal
Mass Spectrometry Section, Fuel Chemistry Division

This paper secured the 2nd Place in the Innovative Research Presentation Session at the 12th ISMAS Symposium-cum-Workshop on Mass Spectrometry, held at Goa, during March 25-30, 2007.

ABSTRACT

A simple sample preparation and simultaneous analysis method, to determine uranium and plutonium from dissolver solution, employing the technique of Isotope Dilution Mass spectrometry has been demonstrated. The method used co-elusion of Uranium and Plutonium from anion exchanger column, after initial elution of major part of uranium in 1:5 HNO_3, in order to reduce the initial U/Pu ratio from 1000 to about 100-200 in the co-eluted fraction. Due to the availability of variable multi-collector system, different Faraday cups were adjusted, to collect the different ion intensities corresponding to the different masses, during the simultaneous analysis of Uranium and Plutonium, loaded on Re double filament assembly. ^{233}U and PR grade Plutonium were used as spikes, to determine Uranium and Plutonium from dissolver solution of irradiated fuel, from a research reactor. The possibility of getting the isotopic composition of uranium from the simultaneous analysis of co-eluted purified fraction of U and Pu from spiked aliquots is also explained.

Introduction

The determination of isotopic composition and concentration of uranium and plutonium from the dissolver solution of spent fuel, requires their chemical separation and purification from fission products and from each other, using anion exchange purification procedure. Conventionally, U and Pu purified fractions from unspiked and spiked aliquots, are analyzed separately for the same. Due to the more or less similar evaporation and ionization characteristics of U and Pu in the ionization source and the availability of variable multi-collector detector systems, it was decided to analyze U and Pu simultaneously from the same filament loading. ^{233}U and power grade Pu are used as spikes for IDMS. Absence of ^{233}U in the dissolver solution, made it possible even to calculate the isotopic composition of U, from different atom ratios obtained

by collecting all intensities, due to different masses of U at different collectors, during the simultaneous analysis of U and Pu from purified fraction of their spiked aliquot. Simultaneous analysis of uranium and plutonium from a same filament loading is reported in literature (2). Mass spectrometric analysis of uranium and plutonium after directly loading the dissolver solution having high burn up (U/Pu=300) on the filament, has also been reported (1). But in dissolver solution where U/Pu ratio is very high, (about 1000), it is not possible to analyze uranium and plutonium simultaneously, due to the presence of large amounts of uranium. Further, the direct loading of the dissolver solution on the filament, may pose the problem of contamination of the ion source, due to the presence of the large amounts of fission products associated with it. In this work, we have demonstrated an efficient technique for the simultaneous analysis of uranium and plutonium from low as well as high burn up dissolver solution samples. For this, the conventional ion-exchange procedure for purifying U and Pu has been modified, to elute them together from spiked aliquots, with reduction in U/Pu ratio. Also the possibility of obtaining uranium isotopic composition from the analysis of these purified fractions of U and Pu has been explained, with reference to the determination of ^{235}U / ^{238}U atom ratio due to adjustment problems particularly of cup no. 9 due to tear and wear problems.

Experimental

Three real dissolver solutions from research reactor fuel were taken for the present work. From each dissolver solution sample, three aliquot, one for isotopic composition and two for IDMS were taken. In aliquots for IDMS, appropriate amounts of ^{233}Pu and ^{233}U were added as spikes. Samples were treated twice with conc. HNO_3 and dried, to assure complete homogenization of sample and spike. Plutonium is converted to tetravalent state by treating with H_2O_2 in 1:5 HNO_3. After drying, residue was taken in 1:1 HNO_3 and loaded onto Dowex 1X8 (200-400 mesh), nitrate form resin using 1:1HNO_3 as the loading solution. The Column was washed twice with two column volumes of 1:1 HNO_3 to elute the Am and fission products. After that, two column volume of 1:5M HNO_3 was added to elute the major fraction of uranium which reduced the uranium-to-plutonium ratio on the column. The remaining uranium, retained on the column, was eluted along with plutonium in 10 column volumes of 1:50 HNO_3. This eluted solution was dried and re-dissolved in about 1M HNO_3 (about100-200 λ). From this, about 5λ solution was loaded on rhenium double filament assembly for mass spectrometric analysis

Table 1: Arrangement of Faraday Cups w. r. to various isotopes of U and Pu.

Cup Configuration Used	Cup No.	9	8	7	6	5	4	3
	m/z	233	235	237	238	239	240	241
Other Probable Cup Configuration	m/z	233	234	235	236	238	239	240

employing Thermal Ionization Mass Spectrometer, model MAT-261. Arrangement of Faraday cups used in the present work for different isotopes is given in Table 1. For determining U/Pu ratio in eluted solution, after washing with 1:5 M HNO_3, two unspiked aliquots of sample 1 and 2 were treated in the same way as real samples and in them U and Pu conc. was determined using ID-TIMS.

Results and Discussion

It was found that if the U/Pu ratio in the dissolver solution was reduced to about 100-200, by using modified anion exchange, procedure demonstrated in the present work, it is possible to analyze uranium and plutonium simultaneously with expected precision and accuracy. The data from three dissolver solution samples from irradiated research reactor fuel is presented in Table 2. This saves the time required to sample preparation, mass spectrometric analysis and reduces the cost of analysis as compared to their separate analysis. It also enhances each other's ionization efficiency with added ion current stability during simultaneous analysis, predicting the possibility of analyzing still lower amounts of plutonium to be loaded on the filament. In addition to this, isotopic composition of U can be calculated, from the different isotopic ratios from the analysis of the purified fraction of U and Pu from the spiked aliquot and knowing the isotopic composition of ^{233}U spike. ^{235}U / ^{238}U atom ratios for these samples obtained from spiked samples and that obtained by analyzing U from purified fractions of uranium from unspiked aliquots is presented in Table 3 and there exists good agreement between the two. The overall precision and accuracy of better than 0.3% can be achieved, for the determination of uranium and plutonium concentrations in irradiated fuel samples, if sufficient care is taken.

Sample No.	Aliquot No.	$^{233}U/^{238}U$ Atom Ratio	$^{240}Pu/^{239}$ Pu Atom Ratio	Uranium Conc. (mg/g of D.S.)	Mean U Conc. (mg/g of D.S.)	Plutonium Conc. (µg/g of D.S.)	*Mean Pu Conc. (µg/g of D.S.)
D.S.-1	D.S.-1A	0.01421 ± 0.03%	0.18593 ± 0.03%	14.220	14.21 ± 0.2%	14.44	14.43 ± 0.2%
	D.S.-1B	0.01349 ± 0.04%	0.18475 ± 0.04%	14.197		14.41	
D.S.- 2	D.S.-2A	0.01051 ± 0.06%	0.17541 ± 0.07%	15.317	15.32 ± 0.01%	15.24	15.22 ± 0.3%
	D.S.-2B	0.00918 ± 0.05%	0.17065 ± 0.04%	15.316		15.19	
D.S.-3	D.S.-3A	0.01067 ± 0.05%	0.18155 ± 0.20%	15.290	15.30 ± 0.2%	14.42	14.40 ± 0.3%
	D.S.-3B	0.01268 ± 0.09%	0.18629 ± 0.03%	15.314		14.38	

Table 2: Concentration data for U and Pu from simultaneous analysis of U and Pu

Table 3: Comparison of $^{235}U/^{238}U$ atom ratio calculated from spiked sample data and that obtained by analyzing purified fractions of pure Uranium

Sample No.	Aliquot No	Observed $^{235}U/^{233}U$ Atom Ratio $(^{5/3}R_{ob})Sa$	Observed $^{238}U/^{233}U$ Atom Ratio $(^{8/3}R_{ob})Sa$	Calculated $^{235}U/^{238}U$ Atom Ratio $(^{5/8}R_{Cal})Sa$	* Mean $^{5/8}R_{Cal}$	$^{235}U/^{238}U$ from Purified fraction of U
D.S.-1	D.S.-1A	0.4218 ± 0.06%	70.3581 ± 0.03	0.00599	0.00600	0.00601
	D.S.-1B	0.4453 ±0.06%	74.1564 ±0.04	0.00600		
D.S.-2	D.S.-2A	0.5734 ± 0.06%	95.1475 ±0.06	0.00603	0.00601	0.00603
	D.S.-2B	0.6566 ± 0.06%	108.9681 ±0.05	0.00602		
D.S.-3	D.S.-3A	0.5632 ±0.04%	93.7119 ±0.05	0.00601	0.00601	0.00601
	D.S.-3B	0.4738 ± 0.09%	78.8768 ±0.09	0.00601		

** in 250λ original dissolver solution, 5 ml HNO_3 was added and sent for mass spectrometric analysis*

* $(^{5/3}R_{Corr})_{Sa} = (^{5/3}R_{ob})_{Sa} - (^{5/3}R)_{Sp}$ and $*(^{8/3}R_{Corr})_{Sa} = (^{8/3}R_{ob})_{Sa} - (^{8/3}R)_{Sp}$

* $(^{5/8}R_{Cal})_{Sa} = (^{5/3}R_{Corr})_{Sa} / (^{8/3}R_{Corr})_{Sa}$

* $(^{5/3}R)_{Sp}$ = $^{235}U/^{233}U$ atom ratio in spike i.e 0.00008

* $(^{8/3}R)_{Sp}$ = $^{238}U/^{233}U$ atom ratio in spike i.e 0.00134

References

1. F.L. Moore and J.E. Hudgens *Jr., Anal Chem*. 29 1767(1957).
2. S.A.Chitambar, et. al. Preprint vol. of DAE International Symp. on Radiochem. and Radiation Chem. (Plutonium 50 years), Feb. 4-7, 1991, BARC, Bombay, Paper No. AC-16.

ABOUT THE AUTHORS

Mr. Raju Shah obtained his B.Sc. degree in Chemistry from Mumbai University. After completing one year training (2005), he joined the Mass Spectrometry Section of the Fuel Chemistry Division, B.A.R.C., Mumbai. He is currently working with Thermal Ionization Mass Spectrometer for isotopic analysis and concentration determination.

ABOUT THE AUTHORS

Mr. K. Sasi Bhushan obtained his B.Sc. degree in Chemistry from Andhra University. After completing one year training (2005) he joined the Mass Spectrometry Section of the Fuel Chemistry Division, B.A.R.C., Mumbai. He is currently working with Thermal Ionization Mass Spectrometer for isotopic analysis and concentration determination.

Mr. R. Govindan obtained his M.Sc. Degree in Chemistry from Annamalai University. He is currently working in the field of inorganic Mass Spectrometry for precise isotopic analysis and concentration determination of elements which are important in nuclear technology. He actively participated in the chemical characterization of mixed oxide fuel for BWR, Tarapur. His other areas of interest include Potentiometry and Electro-analytical chemistry involving ion selective electrodes.

Ms. D. Alamelu obtained her M.Sc. Degree in Physics from Annamalai University. After graduating from 38th Batch of Training School, BARC, she joined the Mass Spectrometry Section of the Fuel Chemistry Division in 1995. Her areas of interest include thermal ionization mass spectrometry alpha spectrometry, radiometric techniques and Laser Induced Breakdown Spectrometry. She has submitted her Ph.D.thesis to the Mumbai University.

Mr. P.S. Khodade is working as a scientific officer in the Mass Spectrometry Section of the Fuel Chemistry Division, BARC, Trombay, Mumbai. Since 1975, he has been working in the field of inorganic Mass Spectrometry and Alpha Spectrometry for precise isotopic analysis and concentration determination of elements which are important in nuclear technology. He coauthored 50 scientific publications in various journals and symposia.

Dr. S.K. Aggarwal is currently Head, Fuel Chemistry Division, BARC, Trombay. He joined the 16th Batch of BARC Training School in 1972 and received the Homi Bhabha Award. He did his Ph.D. from Mumbai University in 1980. He is a specialist in the field of atomic mass spectrometry and alpha spectrometry and is interested in various mass spectrometric techniques. His other areas of interest include electrochemistry, X-ray spectroscopy and Solvent extraction. He is a recognised Ph.D. guid of the Mumbai University and 0f HBNI.

FISSION FRAGMENT ANGULAR DISTRIBUTION IN $^{16}O+^{188}OS$ REACTION

R. Tripathi, K. Sudarshan, S. K. Sharma,
S. Sodaye, A. V. R. Reddy and A. Goswami
Radiochemistry Division

This paper received the Third Prize at the DAE-BRNS Nuclear Physics Symposium 2007 (NP07), held at Sambhalpur University, Sambhalpur, from Dec.11-15, 2007

ABSTRACT

Fission fragment angular distributions were measured in $^{16}O+^{188}Os$ reaction, at E_{lab}=80, 84, 89, 94 and 99 MeV, to investigate the contradicting results of the measurement of fission angular distribution and evaporation residue cross section. From the fission fragment angular distributions, angular anisotropies were deduced. Angular anisotropies were found to be consistent with those calculated using statistical theory. This observation is consistent with that of our earlier measurement in $^{19}F+^{197}Au$ reaction.

Introduction

Fusion hindrance in heavy ion induced reactions, is currently an active area of investigation. Suppression in the formation of evaporation residues, anomalous fission fragment angular distribution and broadening in the fission fragment mass distribution are taken as signatures of Fusion hindrance. Results of a few recent measurements on the fission fragment angular distributions and evaporation residue cross sections, are not consistent. Berriman et al [1] reported fusion hindrance in $^{19}F+^{197}Au$ and $^{30}Si+^{186}W$ reactions based on the measurement of the evaporation residue cross section. Observation of fusion hindrance in these reactions, was attributed to the lower entrance channel mass asymmetry α of these systems compared to the Businaro-Gallone critical mass asymmetry α_{BG} [2]. However, fusion hindrance in these reaction systems was observed to be much higher than that expected on the basis of preequilibrium fission model [2]. According to the preequilibrium fission model [2], angular distribution is expected to deviate from statistical theory, for reaction systems with $\alpha < \alpha_{BG}$. Measurement of fission fragment angular distribution in $^{19}F+^{197}Au$ and $^{24}Mg+^{188}Os$ reactions, forming same compound nucleus [3,4], showed that experimental anisotropies are consistent with the statistical theory and significantly lower than those calculated using the fusion suppression data from evaporation residue measurement [1]. Disagreement between the results of the measurement of evaporation residue cross section and fission fragment angular distribution was also observed in $^{16}O+^{238}U$ reaction [5,6]. These observations indicate, that results of the measurement

of fission fragment angular distribution and evaporation residue cross sections, do not corroborate for reaction systems with small Z_PZ_T ~700 (Z_P and Z_T are the atomic numbers of the projectile and target respectively). Investigation of this aspect, requires measurement of fission fragment angular distribution and evaporation residue cross section, in systems with varying entrance channel mass asymmetry. As part of these studies, fission fragment angular distribution and evaporation residue cross sections have been measured, in $^{16}O+^{188}Os$ reaction at E_{lab}=80, 84, 89, 94 and 99 MeV using ^{16}O beam from BARC-TIFR pelletron accelerator. In this paper, we report results on the fission fragment angular distribution in $^{16}O+^{188}Os$ reaction.

Experimental

Experiments were carried out at BARC-TIFR pelletron accelerator, Mumbai, India. Electrodeposited target of ^{188}Os on ^{nat}Cu backing, was mounted at the center of a 1 m diameter scattering chamber, with ^{188}Os layer facing the beam. The target was bombarded with ^{16}O beam and the fission fragments were detected using two E-ΔE Si telescopes in the backward hemisphere. The thickness values of the two ΔE detectors were 10 and 12 mm. Angular distribution was measured in the angular range of θ_{lab}=85^0-165^0. A monitor detector was kept at 30^0 at E_{lab}=99, 94 and 89 MeV and at 35^0 at E_{lab}=84 and 80 MeV, with respect to the beam direction, to detect the elastically scattered ^{16}O ions. The data of the monitor detector was used, to normalize the count rates of the telescopes, to obtain absolute fission cross section.

Results and Discussion

The kinetic energy spectra of fission fragments were integrated, to obtain fission fragment angular distribution, in laboratory frame of reference. The lab angular distributions were transformed into Centre of Mass (CM) frame of reference. In the transformation of angular distributions from laboratory to center of mass frame, the kinematics relevant to symmetric fission were considered, with kinetic energies calculated from the prescription of Rossner et al [7]. In order to deduce the angular anisotropies, fission fragment angular distributions were fitted, using the statistical theory expression [8]. According to statistical theory, fission fragment angular distribution for a spin zero projectile target combination, is given by the following expression

$$W(\theta) \alpha C \sum_{I=0}^{\infty} \frac{(2I+1)^2 T_I \exp\left[-(I+1/2)^2 \sin^2\theta/4K_0^2\right] J_0\left[i(I+1/2)^2 \sin^2\theta/4K_0^2\right]}{(2K_0^2)^{1/2} \operatorname{erf}\left[(I+1/2)/(2K_0^2)^{1/2}\right]} \quad (1)$$

where, T_l is the transmission coefficient for the l^{th} partial wave. K_0^2 is the variance of the K distribution. J_0 is the zeroth order Bessel function. The constant C has been introduced in equation (1) to normalize the calculated angular distribution to the experimental angular distribution. The experimental angular distributions were fitted using equation (1) with C and K_0^2 as free parameters. The I distribution of the compound nucleus was calculated using the code CCFUS [9]. The experimental fission fragment angular distributions and fitted curves are shown in Fig. 1. The fitted curves were extrapolated to 180^0 and 90^0 to obtain angular anisotropies ($W(180)/W(90)$). Experimental anisotropies, determined from the fitted curves, are shown in Fig. 2. In order to calculate angular anisotropies using the statistical theory expression (1), K_0^2 was calculated using the following expression

$$K_0^2 = I_{eff}T/h^2 \quad (2)$$

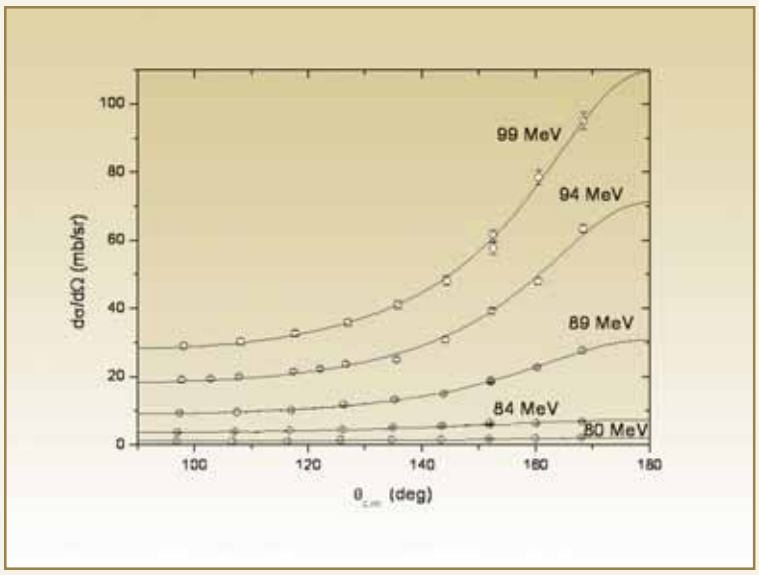

Fig. 1: Fission fragment angular distribution

mass asymmetry α_{BG}. Due to the large fission barrier, the expected contribution from preequilibrium fission is less than 3% even at the highest beam energy of the present study and therefore, any significant deviation from the statistical theory is not expected.

Thus, the observation of the present study is consistent with that of our earlier measurement in the $^{19}F+^{197}Au$ reaction [3]. Comparison of the results of the present measurement with those of the evaporation residue

where I_{eff} and T are the effective moments of inertia and temperature of the fissioning nucleus at the saddle point. I_{eff} was calculated using the rotating finite range model of Sierk [10]. Saddle point temperature was corrected for the evaporation of pre-fission neutrons. The prescription of Kozuline et al [11] was used to calculate the number of pre-fission neutrons (n_{pre}). The compound nucleus l-distribution was supplied as input to the code CASCADE [12] to calculate spin distribution of residues, which was used to correct the compound nucleus l-distribution to determine l-distribution for fission. This l-distribution was used in equation (1) to calculate angular anisotropies. As seen in Fig. 2, the calculated (solid line) and experimental anisotropies (filled circles) were found to be in reasonably good agreement. The entrance channel mass asymmetry α for $^{16}O+^{188}Os$ reaction is slightly less than the Businaro-Gallone critical

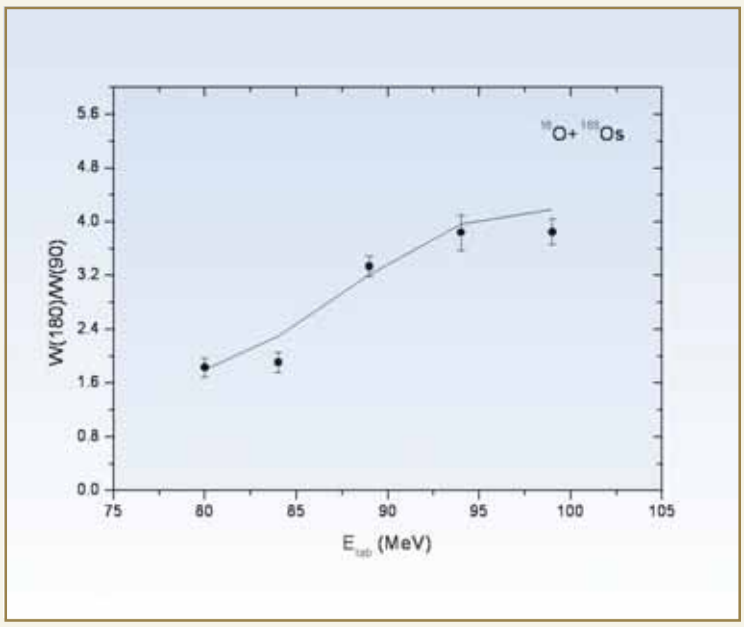

Fig. 2: Angular anisotropy vs beam energy

cross section measurement in $^{16}O+^{188}Os$ reaction and evaporation residue cross section and angular distribution measurement in systems with larger Z_PZ_T, will provide better understanding of fusion hindrance in pre-actinide region, particularly in reactions with low Z_PZ_T.

Acknowledgements

Authors are thankful to Dr. D. Dutta for his help during the experiment.

References

1. A. C. Berriman *et al*, *Nature* 413 (2001) 144.
2. V. S. Ramamurthy et al, *Phys. Rev. Lett.* 65 (1990) 25.
3. R. Tripathi et al, *Phys. Rev. C* 71 (2005) 044616.
4. R. Tripathi et al, *Int. J. Mod. Phys. E* (*In press*).
5. D. J. Hinde et al, *Phys. Rev. Lett*. 74 (1995) 1295.
6. K. Nishio et al, *Phys. Rev. Lett*. 93 (2004) 162701.
7. H. H. Rossner et al, *Phys. Rev. Lett*. 53 (1984) 38.
8. R. Vandenbosch and J. R. Huizenga, *Nuclear Fission* (Academic Press, 1973) London.
9. C. H. Dasso and S. Landowne, *Comput. Phys. Commun*. 46, 187 (1987).
10. Arnold J. Sierk, *Phys. Rev. C* 33, 2039 (1986).
11. E. M. Kozuline et al,*Phys. At. Nucl*. 56, 166 (1993).
12. F. Puhlhofer, *Nucl. Phys. A* 280, 267 (1977).

ABOUT THE AUTHORS

Mr. Rahul Tripathi completed his M.Sc. (Chemistry) from Dr. Ram Manohar Lohia (Avadh) University in 1997. He is a Homi Bhabha Award winner from the 43rd Batch of Training School. After one year training, he joined the Radiochemistry Division of BARC in 2000. His research areas include heavy ion induced reactions and radio analytical techniques. He has about 20 publications in peer-reviewed journals.

Mr. Kathi Sudarshan is a gold medalist from the University of Hyderabad in M.Sc. (Chemistry). He joined the Radiochemistry Division of BARC in 1999 from the 42nd Batch of Training School. His research areas include positron annihilation spectroscopy, radio analytical techniques and heavy ion induced reactions. He has published about 30 papers in peer-reviewed journals.

ABOUT THE AUTHORS

Mr. Sandeep K. Sharma obtained his M.Sc. (Chemistry) from the Indian Institute of Technology Delhi, in 2005. He joined the Radiochemistry Division of BARC in 2006 from the 49th Batch of Training School. His research areas include positron annihilation spectroscopy. He has 2 publications in international journals.

Ms. Suparna Sodaye completed her M.Sc. in (Chemistry) from Delhi University and graduated from the 39th Batch of BARC Training School. After one year training, she joined the Radiochemistry Division in 1996. Her research areas include heavy ion induced reactions, radiochemical separations and tracer applications. She has about 25 publications in peer - reviewed journals.

Dr. A.V.R. Reddy after completing one year orientation course in Chemistry during 1976-77, joined the Nuclear Chemistry Section, Radiochemistry Division in 1977. Since then he has been working in the Nuclear Chemistry section and at present, he is the Head of Nuclear Chemistry Section. His areas of research are nuclear fission, nuclear reactions, neutron activation analysis, radiochemical separations, heavy element chemistry and non destructive assay methods. He has about 250 publications in journals and symposia and has authored 3 books and edited 5 compilations.

Dr. A. Goswami did his M. Sc. in Chemistry from Burdwan University in 1978. After completion of one year training, he joined the Radiochemistry Division of BARC in 1980. His areas of research interest are nuclear fission / reactions, PGNAA and nondestructive assay methods. He has about 80 publications in international journals.

बीएआरसी न्यूज़लेटर
BARC NEWSLETTER

COMPARATIVE ANALYSIS OF DIFFERENT METHODS OF FIXATION OF UNICELLULAR CYANOBACTERIA FOR TRANSMISSION ELECTRON MICROSCOPY

Rachna Agarwal and Jayashree Krishna Sainis
Molecular Biology Division

and

Michael Melzer
Institute of Plant Genetics and Crop Plant Research
Gatersleben, Germany.

This paper was awarded the Best Poster Award at the National Conference for Microscopy and Allied Sciences-2007 organized by the Electron Microscopy Society of India and held at New Delhi, between Nov. 26-28, 2007

ABSTRACT

Cells of cyanobacteria were fixed using chemical fixative, with progressive lowering of temperature and cryo fixation, with high pressure and progressive increase in temperature. The high pressure freezing employed yeast cells as the cryoprotectant. No chemical fixatives were used. Although the inherent contrast of the cells fixed with high pressure was low as compared to chemically fixed cells, the samples retained intracellular organization and good immuno-reactivity.

Introduction

Sample fixation represents a critical step in the preparation of biological specimens, for Transmission Electron Microscopy (TEM). An ideal method should preserve the structure closest to *in vivo*. Traditional TEM techniques employ chemical cross linkers like gluteraldehyde and paraformaldehyde as fixatives. These methods apparently result in preservation of intracellular structures but also result in some fixation artifacts due to extensive protein cross linking. The serial dehydration and infiltration is also carried out at room temperatures, which further aggravates the artifacts. The advent of cryo-techniques such as cryo-fixation and cryo substitution have solved these problems to some extent. Currently cryo-fixation techniques like High Pressure Freezing and Metal Mirror Freezing are being used, in combination with chemical cross linkers, to achieve maximum preservation of the internal structure. Cryo fixation alone without the use of chemical crosslinkers has been rarely described. We report here the use of yeast cells and hexadecene as cryo- protectant during high pressure freezing of unicellular cyanobacteria. This method resulted in the effective preservation of internal structure as well as chemical reactivity of the epitopes as shown by immuno-electron microscopy.

Materials and Methods

Chemical fixation

Log Phase cells of both the Cyanobacteria viz. *Synechococcus* (7942) and *Synechocystis* (6803) were harvested and fixed with 0.5% gluteraldehyde and 2 % paraformaldehyde in 0.05M cacodylate buffer pH 7.2 for 1h followed by 0.5% OsO_4 for 1 h at RT. The samples were serially dehydrated in graded ethanol, followed by propylene oxide at RT, infiltrated with and embedded in low viscosity resin for 48h at 60°C.

Automatic freeze substitution

Cells were fixed as described above and serially dehydrated with progressive lowering of temperature form 4°C to -35°C, infilterated with HM20 resin at low temperature and UV polymerized for 48h at -35°C.

High pressure freezing

Log phase cells were taken in micro capillary tubes, coated with yeast cell paste or hexadecene or both and put between aluminium planchets. The cells were quickly frozen in a Leica high pressure freezer 2100 psi and freeze substituted with 100% acetone at low temperature from -90°C to +20°C over 7 days.

The samples were infiltrated with LR-white resin and embedded in the same resin.

Sectioning and staining

70 nm thin sections were cut with Leica ultamicrotome, stained using 2% Uranyl acetate for 30 min. and viewed

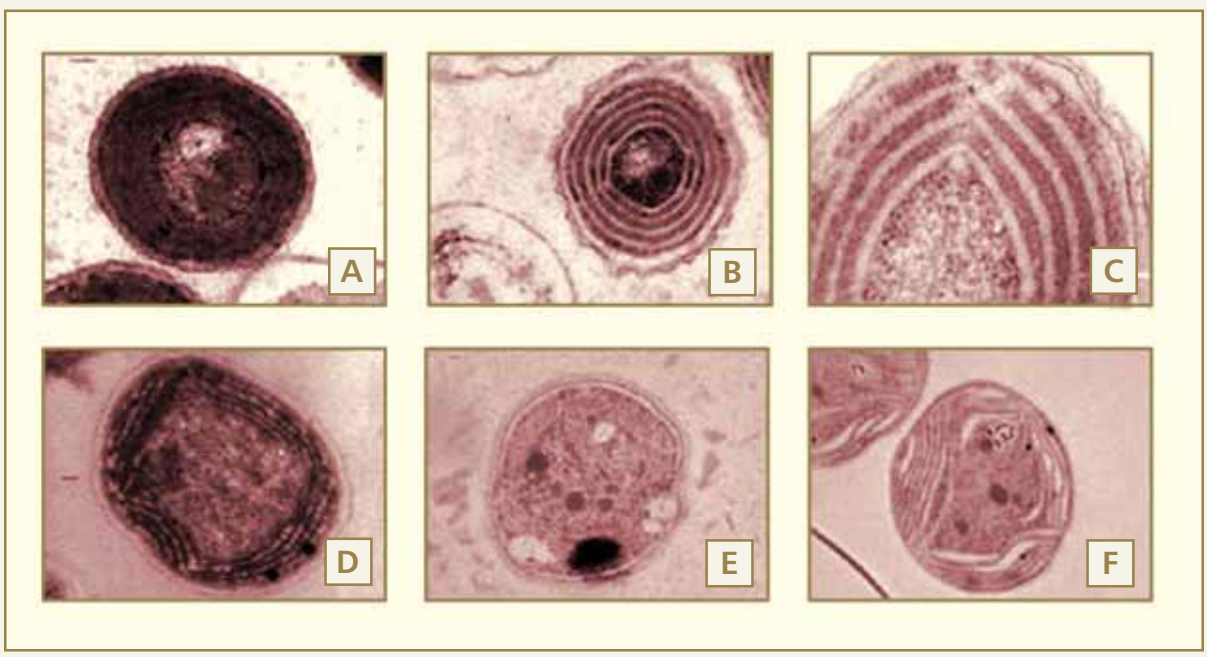

Fig.1: Transmission electron micrographs of unicellular Cyanobacteria
A) Chemically fixed *Synechococcus* 7942 in low viscosity resin
B) Chemically fixed and PLT dehydrated *Synechococcus* 7942 in HM20 resin
C) HPF fixed *Synechococcus* 7942 in LR white resin
D) Chemically fixed *Synechocystis* 6803 in low viscosity resin
E) Chemically fixed and PLT dehydrated *Synechocystis* 6803 in HM20 resin and
F) HPF fixed *Synechocystis* 6803 in LR white resin

under Tecnai G^2 Sphera Transmission Electron Microscope at 120 KeV.

Results and Discussion

Fig. 1 shows the ultrastructure of cells fixed by chemical preservatives and by high pressure fixation. As seen in Fig. 1 (A, B, D and E), chemically fixed cells showed the typical ultra structure. The thylakoids had even diameter throughout and thylakoid lumen was visible. However, plasma membrane was seen to be receded from the outer envelope and the contrast was comparatively high probably due to extensive protein cross linking. This leads to formation of large complexes that take up large quantities of stain leading to higher contrast. Extensive linking resulted in loss of reactivity of the epitopes as seen by immunolabeling. In contrast, in cryo fixed cells, the thylakoid membranes appeared uneven in diameter and the luminal space was barely visible. The contrast was weaker probably due to non availability of protein aggregates. The plasma membrane and outer envelope were preserved and looked pressed against each other, which may be closer to the situation *in vivo*. Antibody reactivity data showed that epitopes were available in HPF fixed cells.

Recently transmission electron microscopy of cyanobacteria (cryo fixed in conjunction with chemical fixatives) was used for 3-D tomography (1, 2). The use of yeast as cryo-protectant not only preserves the structure in a better way, but also retains the immuno reactivity of the antigenic sites in our studies . 3-D tomography of these samples may reveal more accurate intracellular details.

References

1) Michelle Liberton, et al *Protoplasma* (2006) 227: 129–138.
2) Reinat Nevo, et al, *The EMBO Journal* (2007) 26, 1467–1473.

ABOUT THE AUTHORS

Ms. Rachna Agarwal joined the Molecular Biology Division of BARC from the 47th Batch of OCES, BARC Training School and is currently working under Plant Biochemistry Section. Her area of research includes studies on molecular architecture and biogenesis of photosynthetic apparatus and effects of ionizing radiation on photosynthesis in unicellular cyanobacteria.

Dr. Ms. Jayashree Krishna Sainis is Head, Plant Biochemistry Section, Molecular Biology Division, BARC. Her areas of research are Enzyme superstructures of photosynthesis, DNA repair and recombination processes, Chromatin remodeling, Computer vision technologies in Biology, Artificial photosynthesis and Stress responses of photosynthesis in unicellular organisms etc.

ISOLATION AND FUNCTIONAL CHARACTERIZATION OF OSRAD51, A RECOMBINASE FROM RICE

C. Rajani Kant and Jayashree K. Sainis
Molecular Biology Division

This paper was awarded the Best Poster Award
at the DAE-BRNS Life Science Symposium-2007 (LSS-2007)
held at during December 5-7, 2007

Double Strand Breaks (DSBs) in DNA are introduced by errors in replication, action of endonucleases, programmed DNA breaks during development, exposure to chemicals, ionizing radiation and reactive oxygen species. These DSBs are repaired by two main pathways viz; Homologous Recombination (HR) and Non-Homologous End Joining (NHEJ).

In Homologous Recombination (HR) pathway, nucleolytic processing at double strand breaks generate the single strand overhangs, which in turn invade the duplex partner in a process called strand exchange. In the subsequent step, branch migration followed by resolution of Holliday junction takes place, to generate the repaired DNA molecules. In this process no genetic information is lost. Hence, the process is conservative. In Non Homologous End Joining (NHEJ) pathway, after processing the double strand breaks, direct joining of ends generates the repaired DNA molecule with the loss of genetic information. Several proteins encoded by genes in the RAD52 epistasis group, are important for Homologous Recombination dependent repair. These include RAD51, RAD52, RAD54, RAD55, RAD57 and RAD59. The RAD51, a homologue of *E. coli* RecA is an important member of the group of proteins, required for HR pathway.

OsRad51 over-expression, purification and MALDI-TOF analysis

cDNA corresponding to OsRad51 protein was isolated from cDNA library of rice flowers (*Oryza sativa*, Indica cultivar group) and cloned into pET28a expression vector. The protein, over expressed in *E. coli* BL21 (DE3), was present in the inclusion bodies. The hexa-histidine tagged OsRad51 protein was purified under denaturing conditions and refolded by stepwise dialysis as described previously (Kant et al, 2005). Purified protein could be detected by an anti-histidine antibody on western blotting. MALDI-TOF analysis of purified protein confirmed it's identity as a member of Rad51 group of proteins. OsRad51 could bind single and double stranded DNA, however it showed higher affinity for single stranded DNA. Transmission Electron Microscopy (TEM) studies of OsRad51-DNA complexes showed, that this protein forms ring-like structures and binds DNA to form helical filaments.

Renaturation activity of OsRad51 by FRET

Renaturation of OsRad51 was done by fluorescence resonance energy transfer assays, according to the procedure mentioned in Rajanikant *et al* (2006) and as depicted in Fig. 2.

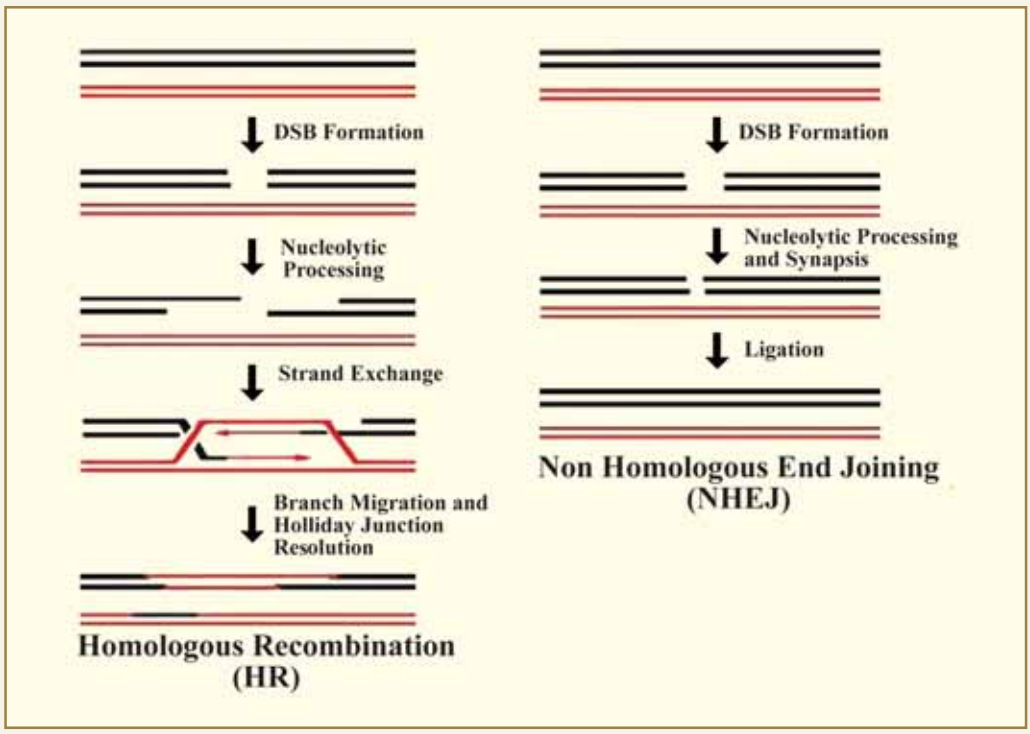

Fig. 1: A graphical representation depicting the different steps of homologous recombination and non-homologous end joining pathways of DSB repair

Briefly the assay involved the two complementary single strands Phi-C and Phi-W (55 nucleotide length) labeled with rhodamine and fluorescein at 3'and 5' end respectively. 27.5 μM of fluorescein labeled Phi-W was presynapsed with OsRad51 in assay buffer. After 5.0 min incubation at 37 ^{0}C, 27.5 μM of Phi-C labeled with rhodamine was added to the reaction mixture. Decrease in the fluorescein emission intensity was measured at 522nm, after excitation at 490 nm due to FRET, as a result of renaturation mediated pairing of complementary single strands, to form duplex DNA. Duplex formation led to decrease in the distance between fluorescein and rhodamine dyes and resulted in FRET, which in turn decreased the fluorescein emission intensity at 522 nm.

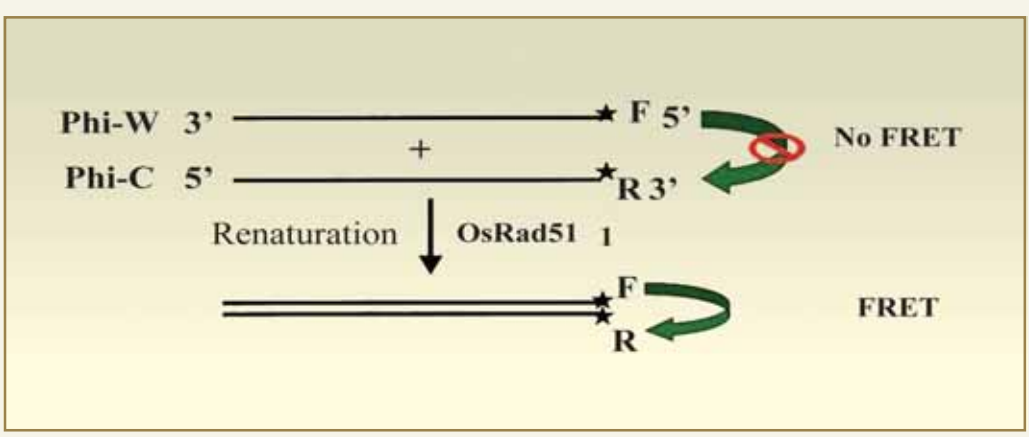

Fig. 2: Schematic representation of OsRad51 mediated renaturation assay by FRET

Fig. 3 shows the renaturation of complementary single strands promoted by OsRad51, monitored using FRET promoted the strand exchange activity even in the absence of ATP.

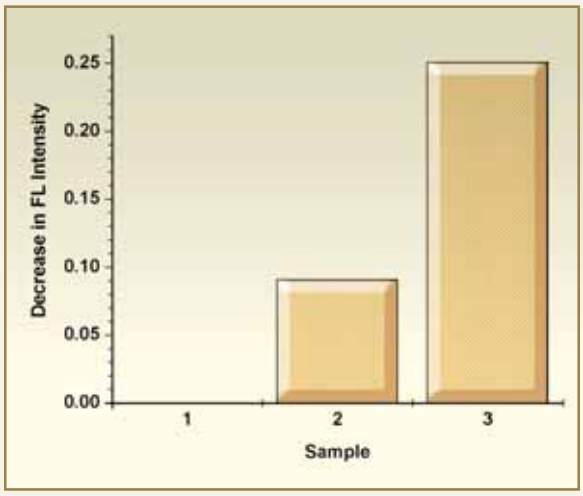

Fig. 3: OsRad51 mediated renaturation assay by FRET. 1: OsRad51 with Fluorescein carrying strand, 2: Fluorescein and Rhodamine carrying strands without OsRad51, 3: Fluorescein and Rhodamine carrying strands with OsRad51

assays in real time. Renaturation activity was promoted by OsRad51 in the presence of ATP.

Strand exchange assay of OsRad51 by FRET

Strand exchange assay of OsRad51 was done according to the procedure mentioned by Rajanikant *et al* (2006) and as shown in Fig. 4.

Briefly 27.5 µM of unlabeled Phi-C was incubated with OsRad51 protein in the assay buffer at 37 ^{0}C for 15 min. Reaction was started by adding 27.5 µM of FRET paired duplex. Increase in fluorescein emission intensity due to the strand exchange mediated loss of FRET, was monitored at 522nm. FRET assays revealed OsRad51 mediated strand exchange reaction, in a protein concentration dependent manner (Fig. 5). Renaturation and strand exchange reactions were homology sequence dependent. Interestingly OsRad51 promoted the strand exchange activity even

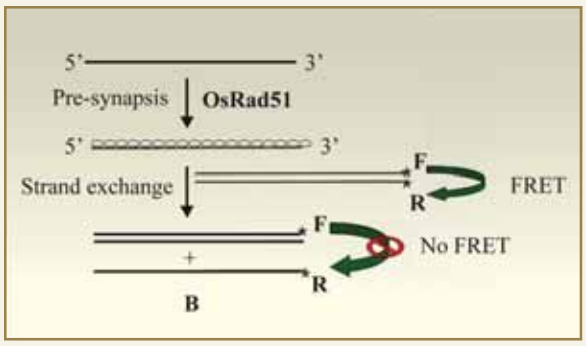

Fig. 4: Schematic representation of OsRad51 mediated strand exchange assay by FRET

in the absence of ATP. Thus purified OsRad51 protein was found to promote renaturation of complementary ssDNA molecules by FRET assays. This activity is a prerequisite for recombination function during homologous recombination. The formation of duplex DNA molecules was found to increase with increase in protein concentration. Renaturation activity of OsRad51 is well in consensus with hRad51 and

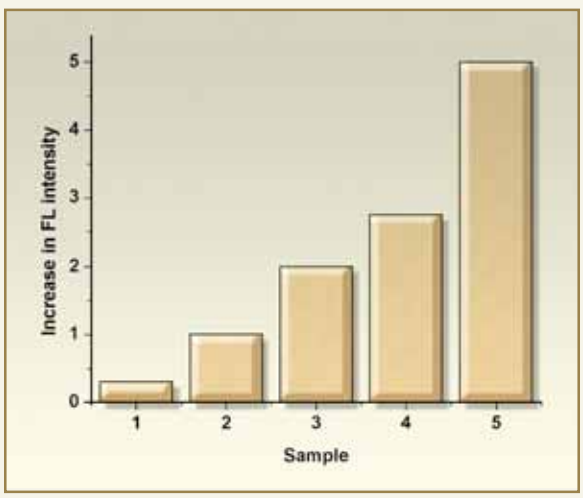

Fig. 5: OsRad51 concentration dependent strand exchange reaction mediated by OsRad51. Excitation:490nm,Emission: 522 mm. 1) No protein, 2) 1.0 µM , 3) 2.0 µM, 4) 3.0 µM, and 5) 6.0 µM of OsRad51 protein

OsDmc1 proteins. FRET assays also revealed that in the presence of ATP. OsRad51 mediated strand exchange reaction. Renaturation and strand exchange reactions were homology dependent.

This is the first report on *in vitro* biochemical properties of a crop plant recombinase, OsRad51. Genetic improvement of crop plants has been executed for many centuries using classical breeding procedures and selecting the offspring for desired trait. Hyper homologous recombination mutants over-expressing the homologous recombination proteins may improve the gene targeting frequency. Recently, efficient gene targeting strategy involving homologous recombination was demonstrated for rice. Understanding the biochemistry of homologous recombination in rice will further improve the knowledge of gene targeting.

References

1. Kant, C. R., et al *Plant Molecular Biology* 57: 1-11.
2. Rajanikant, et al *FEBS J* 273: 1497-1506.

ABOUT THE AUTHORS

Mr. C. Rajani Kant did his M.Sc in Biochemistry from Department of Biochemistry, Osmania University, Hyderabad. He joined the Molecular Biology Division after his graduation in Biology and Radiobiology from BARC Training School. Since then, he has been working on the isolation, cloning and biochemical characterization of DNA recombinases from *Oryza sativa* (rice).

Dr. Ms. Jayashree Krishna Sainis, is Head, Plant Biochemistry Section, Molecular Biology Division, BARC. Her areas of research are Enzyme superstructures of photosynthesis, DNA repair and recombination processes, Chromatin remodeling, Computer vision technologies in Biology, Artificial photosynthesis and Effect of stress responses on photosynthesis in unicellular organisms.

GAS SENSING PROPERTIES OF POLYPYRROLE THIN FILMS

Aditee Joshi and S.A. Gangal
University of Pune

and

N. Padma, D.K. Aswal and S.K. Gupta
Technical Physics and Prototype Engineering Division

This paper was awarded the Best Poster Award at the DAE Solid State Physics Symposium held at Mysore University, Mysore, during Dec. 26-31, 2007.

ABSTRACT

Polypyrrole thin films were *in-situ* synthesized by chemical polymerization. The morphological studies showed formation of uniform granular structure with average grain size of 0.6 μm. Fourier transform infrared spectroscopy revealed formation of polypyrrole. The polypyrrole films were investigated for the sensing behaviour of NH_3, H_2S and NO. It has been observed that these films are selective for ammonia gas and the sensitivity exhibited a linear response in the range of 4-25 ppm. These studies show that polypyrrole films can be used as room temperature ammonia sensors.

Introduction

In recent years conducting polymers, such as, polypyrrole, polyaniline and polythiophene have been studied as gas sensing materials, essentially, due to their operation at room temperature and easy sensor element processing [1-4]. Among various conducting polymers, polypyrrole has an edge due to it's chemical stability against atmospheric conditions and ease of synthesis by electrochemical and chemical methods. In addition to this, the morphology of polypyrrole can be easily tailored to nanowires, nanotubes and coral like structures by optimizing the synthesis parameters [2-4]. Polypyrrole has been reported for ammonia gas sensing applications, however the sensed concentrations are very high (>100 ppm) [7]. It is known that the toxic limit of ammonia is 25 ppm in air and therefore the polypyrrole based sensors should sense the gas concentrations well below this limit.

Experimental

In the present experiments, pyrrole monomer was distilled prior to use. Analytical grade ammonium per-sulphate APS, (Loba Chemie) was used as oxidizing agent. The chemical polymerization was conducted in a beaker by mixing 0.1M aqueous solution of pyrrole and 0.1 M APS in 1:1 ratio by volume. The films of polypyrrole were *in-situ* deposited simply by keeping a glass substrate (size 5 mm x 5 mm) at the

bottom of the beaker. The polymerization was conducted for a period of three hours. After removal of the films, they were washed with distilled water and dried at room temperature. The morphology of the polypyrrole films was examined using Scanning Electron Microscope (SEM) (Vega, MV 2300/T40, Tescan). Chemical structure was examined by FTIR measurement (FT-8400 spectrophotometer, Shimadzu) using KBr cell. In order to measure the gas response, the resistance of the films was measured with and without gases. For resistance measurement, two gold electrodes, separated by 1mm, were deposited on polypyrrole film and copper wires were attached using silver paint. In order to record the response of the films to various gases, the film was mounted in 250cc container and the known gas (NH_3, H_2S or NO) of particular concentration was injected through a syringe. These measurements were carried out at room temperature.

Results and Discussion

A typical SEM image of a polypyrrole thin film is shown in Fig. 1. The film has a uniform granular morphology and the average grain size is ~0.6 μm. The uniform granular morphology is considered good for gas sensing applications.

The FTIR spectrum, as shown in Fig. 2, corresponds to the polypyrrole. The characteristic peaks at 1558.4 cm^{-1} and 1487 cm^{-1} correspond to the fundamental vibration of pyrrole ring, whereas peaks at 1685.7 cm^{-1} and 1315.4 cm^{-1} represent to respectively, C=N and C-N bonds [6]. The peaks observed in the present work match well with the ones available in the literature confirming the formation of polypyrrole.

Typical gas response curves of polypyrrole films for 40 ppm concentrations of NH_3, H_2S and NO are shown in Fig. 3. The sensitivity is defined as

$$\text{Sensitivity (\%)} = \left| (R_{gas} - R_{air}) / R_{air} \right| \times 100.$$

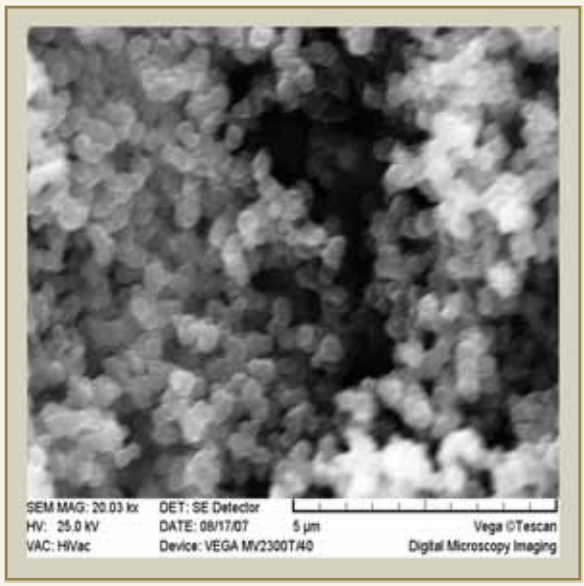

Fig. 1: SEM image of polypyrrole film

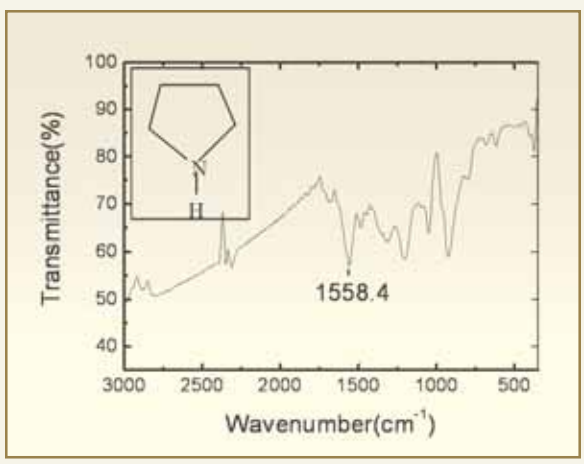

Fig. 2: FTIR spectrum of polypyrrole. The inset shows the structure of the pyrrole monomer

It is seen that the sensitivity of NH_3 (40 ppm), H_2S (40 ppm) and NO (40 ppm) are respectively 20%, 6% and 2.5%. A high sensitivity for ammonia indicates that the polypyrrole films are selective for this gas. Moreover, the response (2min) and recovery (30 min) times are very small for ammonia. The higher sensitivity towards NH_3 than NO, H_2S, can be explained, on the basis of different interactions between sensing film and adsorbed gas. Polypyrrole is a p-type material and

when it interacts with NH_3, there is reduction in charge carrier density. This results in decreasing the conductivity of material and film resistance increases. In comparison with this, interaction between polypyrrole film and other gases is less than NH_3, thereby, showing less sensitivity and response/recovery rate.

We have further investigated the NH_3 response of the polypyrrole films in the 4-25 ppm. (Fig. 4) It is seen that the sensitivity increases linearly (0.4% / ppm) with the NH_3 concentration, suggesting their suitability to be used as ammonia sensor.

Conclusion

We have *in-situ* synthesized polypyrrole thin films during the polymerization process. The films had a uniform granular morphology. These films were found to be selective for ammonia gas and the sensitivity exhibited a linear response in the range of 4-25 ppm. These studies show that polypyrrole films can be used as room temperature ammonia sensors.

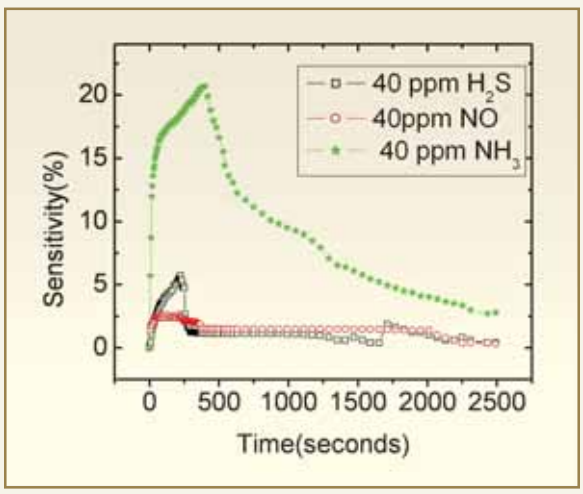

Fig. 3: Gas response curves of Polypyrrole

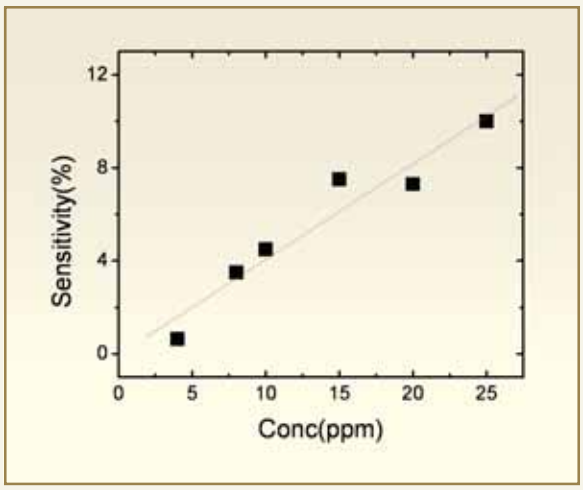

Fig. 4: Sensitivity as a function of ammonia gas

References

1. Qaisar Ameer and Samuel B. Adeloju, *Sens.& Actu. B*106 (2005) 541-552.
2. Kumaran Ramanathan , et. al., *J. Am. Chem. Soc.* **127** (2005) 496-497.
3. H.Yan, et. al., *Nanotechnology*. **17**(2006) 3446-3450.
4. M.Penza,et. al., *Sens.& Actu. B* 40 (1997) 205-209.
5. H.K. Jun, et.al., *Sens. & Actu. B*, 96(2003) 576-581.
6. Kavita Arora, et. al., *Biosens. Bioelectro*. 21(2006)1777-1783.
7. Huiling Tai,et. al., *Int..J.Environ.Anal.Chem* 87(2007)539-551.

ABOUT THE AUTHORS

Ms. N. Padma joined the Technical Physics and Prototype Engineering Division, BARC, in 1989 after graduating from the 32nd Batch of Training School. She obtained her M.Sc. in Physics from the University of Madras. Over the years she has worked on Mass Spectrometry and related instrumentation. Her present interest is preparation and studies of junction devices using organic materials.

Dr. D.K. Aswal joined the Technical Physics and Prototype Engineering Division through 30th Batch of Training School. He has made several contributions in the field of thin/thick films and single crystals of various high temperature superconductors and colossal magnetoresistive materials. He has investigated various properties of magnesium-di-boride

Dr. S.K. Gupta joined BARC in 1975 and is presently Head of the Thin Films Devices Section in TPPED. Over the years, he has worked on space quality silicon solar cells, high temperature superconductor thin films and single crystals, gas sensors and thermoelectric materials. He has carried out extensive studies on vortex dynamics in superconductors. He is a member of the National Academy of Sciences, India.

TELLURIUM THIN FILMS BASED GAS SENSOR

Shashwati Sen, V. Bhandarkar, K. P. Muthe,
S. K. Gupta and J. V. Yakhmi
Technical Physics and Prototype Engineering Division

This paper was awarded the Best Poster Award at the 12th National Seminar on Physics and Technology of Sensors (NSPTS-12) held at BARC, Mumbai during March 5-7, 2007

ABSTRACT

The use of Tellurium thin films as toxic gas sensors is investigated. The resistance of these films was found to increase reversibly on exposure to reducing gases, while the opposite effect was observed on exposure to oxidizing gases. The sensitivity as well as the selectivity of these films, with respect to different gases has been studied. The effect of various deposition parameters, film substrates on the film microstructure and their response towards gases has been discussed. The effect of operating temperature, gas concentration on the sensitivity, response and recovery has been reported.

Introduction

In recent years, efforts have been made to develop of sensors operable at lower temperatures, as this ensures the operation of low cost, low-power, reliable and small-size devices. Recently it has been reported that Tellurium (Te) can be used as a room temperature gas senor, for detection of NO_2 [1], CO and propylamine [2]. Tellurium is an elemental semiconductor with an energy gap of 0.34 eV. It's thin films show p-type conduction due to lattice defects acting as acceptors. We have studied the gas sensing properties of Te thin films, deposited by thermal evaporation. Sensitivity towards different gases has been studied, as well as the effect of different deposition parameters on the sensitivity of these films, has been investigated.

Experimental Details

Thin films have been typically deposited by thermal evaporation technique, using molybdenum or tantalum boat at a vacuum of better than 10^{-5} Torr. Deposition is carried out at the rate of ~ 0.5 to 10 nm/s to yield films of thickness 200 nm, by using quartz crystal thickness monitor. The films have been deposited at different substrate temperatures between 77-373 K and on different substrates like sapphire, polycrystalline Al_2O_3 (alumina) and glass. Metal contacts to the films are prepared, by vacuum deposition of thin Au films and attaching thin metal wires by soldering or use of silver paint. For sensitivity measurements, the film was loaded in an airtight housing having a volume of 250 cc as shown in Fig. 1. A measured quantity of the gas was taken from a canister, containing gas at 1000 ppm concentration, using a syringe and introduced in the housing so as to yield the desired gas concentration. A Keithley 2700 multimeter (Integra series) was used, to monitor the resistance of the films. The response and recovery of the films, exposed to different gas concentrations were obtained, by plotting

their resistance as a function of time. The gas response (ρ) is defined as $r = 100.|R_g - R_a|/R_a$, where R_α and R_γ are resistances of the film in air and test gas respectively. Sensitivity S is defined by S = r/C, where C is the gas concentration. Surface morphology of the films was studied, using a Scanning Electron Microscope (SEM) VEGA MV2300T/40, while their structural information was obtained using an X-ray diffractometer employing a Cu K_α radiation source.

Results and Discussion

The morphology of Tellurium films deposited on alumina substrate at various substrate temperatures, between 77-373 K, are shown in Fig. 2. We can observe a change in microstructure, from amorphous to polycrystalline, accompanied by grain growth with increasing temperatures. Films deposited at 77 K are smooth and do not show presence of any grains indicating their amorphous nature, where as, films deposited at 373 K show grain growth in the form of dendrites, with an average size of ~ 800 x 155 nm^2. Results of SEM study are supported by corresponding XRD patterns of these films shown in Fig. 3(d). Films deposited at 77 K show very small Te peaks, indicating their predominantly amorphous nature. As the deposition temperature is increased, structural

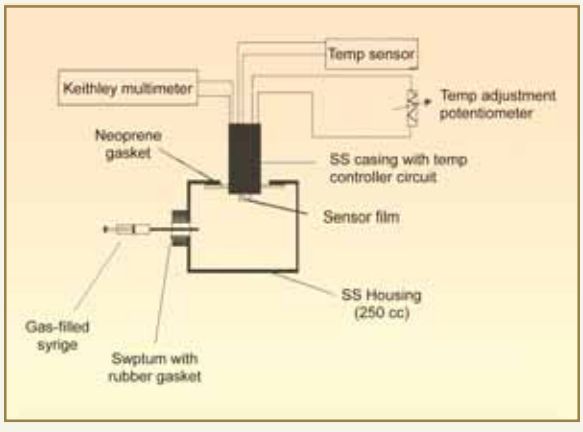

Fig. 1: Stainless steel chamber for testing response of gases with coupling for sensor housing and rubber gasket for injection of gas using syringe

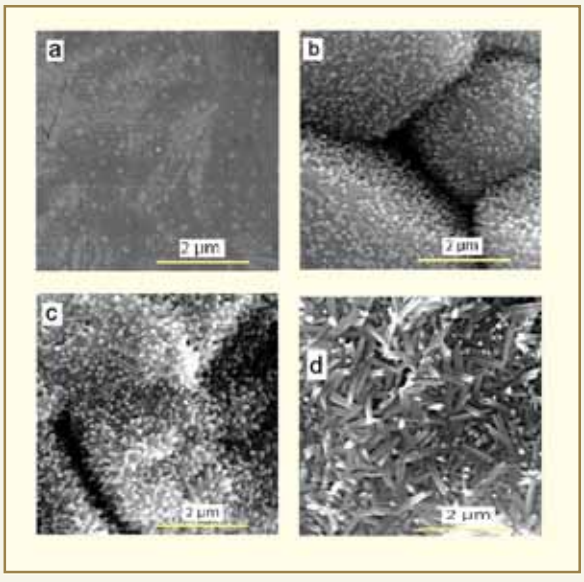

Fig. 2: SEM micrographs of Te film deposited on polycrystalline alumina substrates at temperatures of (a) 77, (b) 300, (c) 323 and (d) 373K.

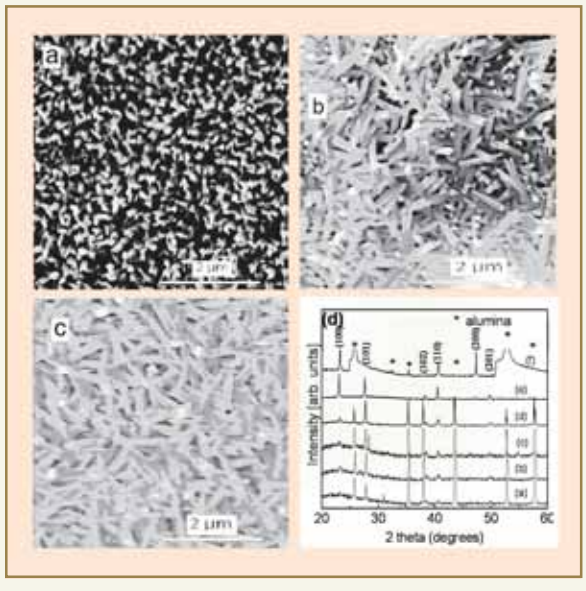

Fig. 3: SEM images of Te films deposited at 373K on (a) glass, (b) polycrystalline alumina (c) sapphire substrates and (d) X-ray diffraction (XRD) patterns of Te films deposited on alumina substrates at temperatures of (a) 77, (b) 300, (c) 323 and (d) 373 K and films deposited at 373 K on (e) glass and (f) sapphire substrates. The peaks marked (*) are attributed to alumina

evolution is found to occur yielding polycrystalline films, characterized by an increase in intensity of Te peaks. The effect of substrate crystallinity on microstructure of films has been investigated, by *in-situ* deposition of films on amorphous (glass), polycrystalline (alumina) and single crystal (sapphire) substrates, held at 373 K. SEM micrographs of films prepared on the three substrates are shown in Figs. 3 (a - c). All these films showed dendritic growth with smallest grain size on glass substrates. While the grain size is similar for films on sapphire and alumina substrates, coalescence of grains on sapphire has reduced sharp grain boundaries.

The gas sensitivity of these films was measured at various temperatures for various gases like NH_3, H_2S, NO_2 etc. Response of Te films is found to reduce with increase in temperature for both oxidizing and reducing gases and at T~ 373 K the sensitivity drops to negligibly low values (< 10 %) for all the gases as shown in Fig. 4. Thus all further studies have been done at room temperature.

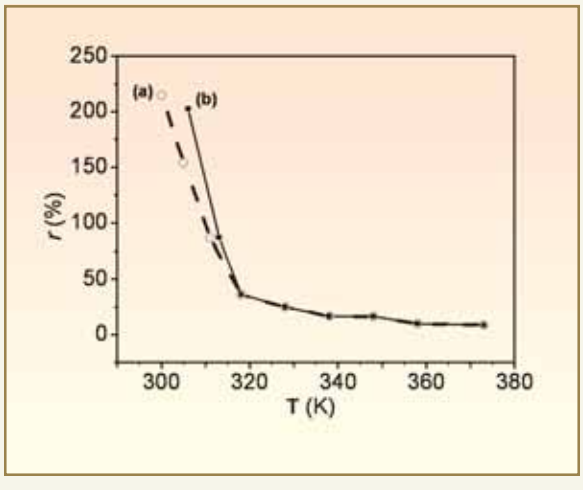

Fig. 4: Temperature (*T*) depedence of response (*r*) of tellurium films deposited at 373 K on polycrystalline alumina substrates measured on exposure to (a) 5 ppm of H_2S and (b) 100 ppm of NH_3.

The response of films on exposure to H_2S gas, as function of concentration is shown in Fig. 5. It is seen that the film is able to detect less than 0.1 ppm of H_2S. The sensitivity has been found to decrease with increase in gas concentration. Similar results have been reported for other gases [3].

Sensitivity of Te sensors at 10 ppm concentration of different gases is compared in Fig. 6. It is seen that films are most sensitive to H_2S and have a good response to NO_2, while they have no response to CO and hydrogen gases.

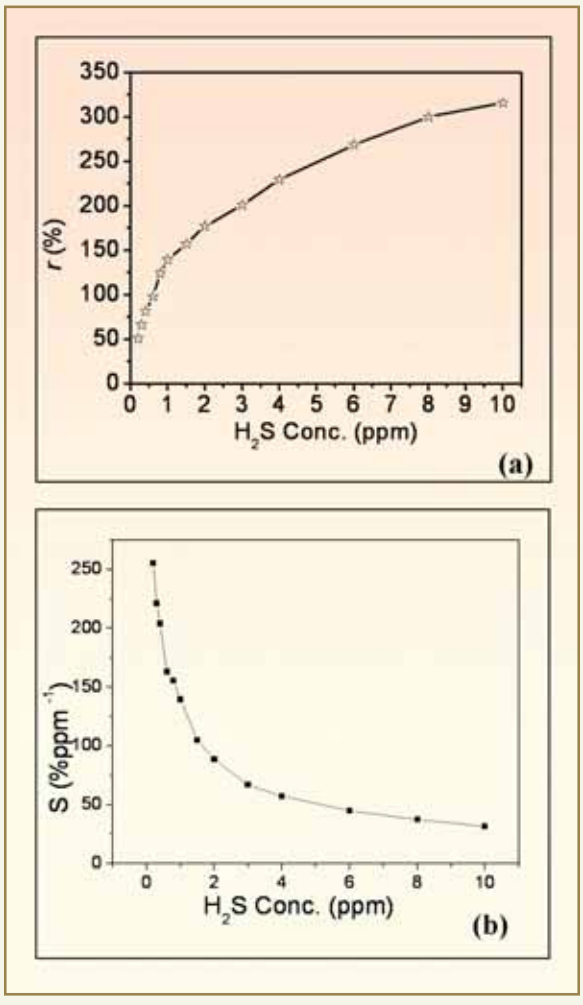

Fig. 5: Response (a) and sensitivity (b) of tellurium films deposited on alumina substrates at 373 K as a function of H_2S gas concentration

Response of the films deposited at different temperatures on exposure to H_2S is shown in Fig. 7 as

function of a concentration. It is seen that the film sensitivity increases with deposition temperature. Similar results are also obtained on exposure to other gases. Response and recovery characteristics of the films, deposited at different temperatures on exposure to 1 ppm H_2S, are shown in the inset of Fig. 7. The response time is seen to increase by a factor of 7 (from 2 mins to 14 mins), while the recovery times were found to be much less affected, as the deposition temperature of the films was decreased from 373 to 77 K.

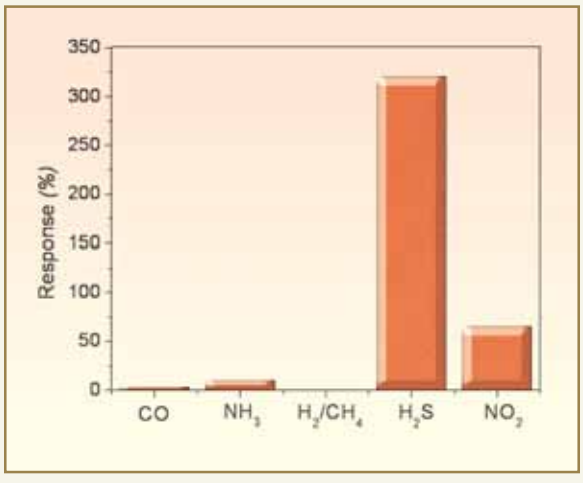

Fig. 6: Bar graph representing the response of typical Te films towards 10 ppm of different gases

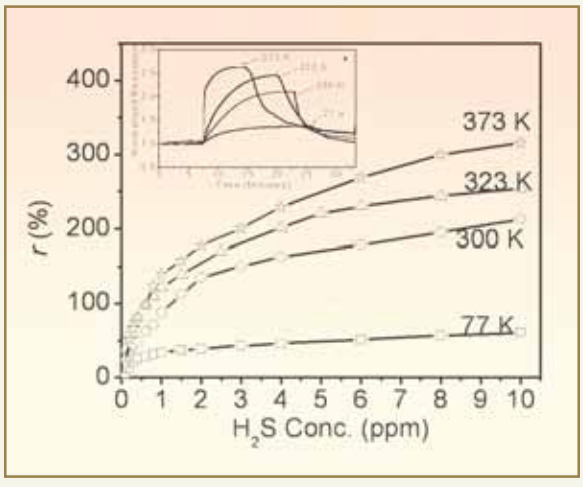

Fig. 7: Sensitivity of films deposited on polycrystalline alumina substrates at substrate temperatures of 77, 300, 323 and 373 K as a function of H_2S gas concentration. Inset shows response-recovery characteristics of above films on exposure to 1 ppm H_2S gas

Increase in sensitivity at higher deposition temperatures, is attributed to low defect density in the films at higher temperatures [4]. In the presence of defects (which increase at low deposition temperatures), excess charges (holes) generated on interaction with gases are trapped on defect centres, leading to a reduced change in conductivity (hence, sensitivity). This also leads to slower response time for films, deposited at lower substrate temperature.

Response of Te films deposited at 373K on glass, sapphire and polycrystalline alumina to H_2S, as function of concentration, are shown in Fig. 8. It is observed that the films deposited on glass substrate show maximum sensitivity while those on sapphire show minimum sensitivity. It is observed that time required for response and recovery times for a given gas, for films deposited on different substrates, are relatively similar despite large differences in their sensitivities. This is understandable, as smaller grain size for films on glass substrates provides large effective surface area for gas-film interaction, thereby improving it's gas sensitivity. Coalescence of Te grains on sapphire, reduces grain boundary area that reduces gas sensitivity.

Thus we observe that the best response is shown by Te films, deposited at 373 K on glass substrates. This is because they have smaller grain size and less defect density.

Mechanism of detection of gases with Te films is not fully understood and we discuss here proposed models. The p-type conductance in Te, arises from the presence of crystallographic defects, resulting in the formation of additional acceptor centers [5]. XPS and Raman

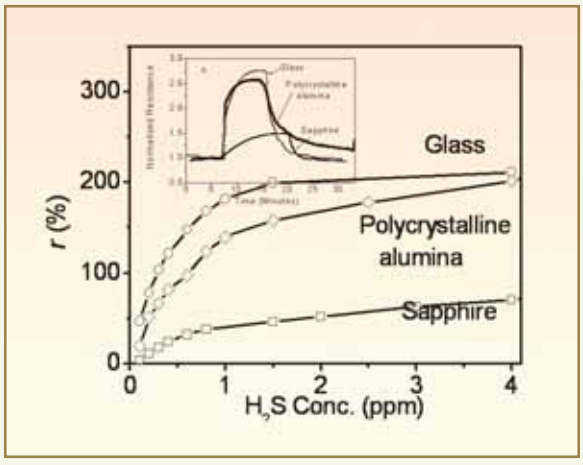

Fig. 8: Response of films deposited at 373 K on glass

spectroscopy data show, that on exposure to atmosphere, physisorption and chemical interaction of oxygen with the surface, takes place [6]. Adsorbed oxygen easily traps electrons leading to an increase in hole concentration. The film may be considered as a polycrystalline structure, consisting of p-type Te grains with significant fraction of chemisorbed (TeO_2) and physisorbed oxygen over the film surface and in the intergrain region. This induces a surface charge and a corresponding energy band, bending in the semiconductor Te film, resulting in increased hole density in intergrain as well as intragrain region. On exposure to a reducing gas such as H_2S or NH_3, bending of bands at the surface is reduced, leading to reduced hole density and increased resistivity. Exposure to an oxidizing gas such as NO_2, results in enhanced oxidation of the film surface, leading to a further increase in the hole concentration, accompanied by a decrease in it's resistivity.

Conclusions

Te thin films were investigated, for their sensitivity towards different gases. These films were found to show maximum sensitivity at room temperature and the response was maximum for H_2S. Effect of deposition temperature, substrate microstructure on the gas sensitivity of Te films has also been investigated. Films deposited at 373 K on glass substrates showed maximum sensitivity towards gases such as H_2S and NO_2. It is seen that improvement in gas sensitivity arises from (a) reduction in defect density within Te grains as seen from films deposited at higher deposition temperatures and (b) from decrease in the grain size as observed for films deposited on amorphous (glass) substrates.

References

1. D. Tsiulyanu, S. Marian, V. Miron, H. –D. Liess, *Sens. & Actuators B* 73 (2001) 35.
2. D. Tsiulyanu, S. Marian, H. –D. Liess, *Sens. & Actuators B* 85 (2002) 232.
3. Shashwati Sen, K. P. Muthe, Niraj Joshi, S. C. Gadkari, S. K. Gupta, Jagannath, M. Roy, S. K. Deshpande, and J. V. Yakhmi, *Sens. & Actuators B* 98 (2004) 154.
4. A. V. Kolobov, *J. Non-Cryst. Solids* 198-200 (1996) 728.
5. M. J. Capers and M. White, *Thin Solid Films* 15 (1973) 5.
6. Shahswati Sen, V. Bhandarkar, K. P. Muthe, M. Roy, S. K. Deshpande, S. K. Gupta, J. V. Yakhmi,V. C. Sahni, *Sensors & Actuators B*, 115 (2006) 270-275.

ABOUT THE AUTHORS

Dr. Shashwati Sen joined BARC in 1996 through the 40th batch of training school. She obtained her Ph.D. degree from Mumbai University in 2003 for her work on "Dissipation mechanism in high temperature superconductors". Currently she is working on gas sensors based on elemental and metal oxide semiconductor thin films and nano structures.

Mr. K.P. Muthe is working in the field of thin film growth and characterization. He has studied the growth behavior of HTSC films using MBE. The reference value of this work has fetched him a place in Marquis Who's Who of the world (1997) and Dictionary of International Biography (1999). He has extensively used X-Ray photoelectron spectroscopy to solve several material related problems like corrosion and mechanisms of gas detection and contributed to around 50 publications. His interests also include toxic gas detection and synthesis of Alumina based radiation sensors for personnel dosimetry. He belongs to the 30th batch of Training School.

Dr. S. K. Gupta joined Bhabha Atomic Research centre in the year 1975 after completing one year orientation course in Physics. Presently he is Head of Thin Film Devices Section and Applied Superconductivity & Cryogenics Section in Technical Physics & Prototype Engineering Division of BARC. Over the years he has been involved in the development of Space quality silicon solar cells, preparation of epitaxial thin films of high Tc superconductors, studies on vortex dynamics in superconductors and development of semiconductor thin film based H_2S and H_2 gas sensors etc. Presently he is involved in studies on Colossal MagnetoResistance (CMR) thin films, CMR/superconductor junctions and development of semiconductor and polymer based gas sensors. He Shared "Shri Hari Om Ashram Prerit SS Bhatnagar Award" for solar energy in the year 1980 and was awarded "Indo-US fellowship in Science and Technology" during the year 1992-93. He has published 80 papers in international journals and is a Member of The National Academy of Sciences, India.

Dr. J.V. Yakhmi, Associate Director (S), Physics Group and Head, Technical Physics and Prototype Engineering Division of BARC, has worked for the past 40 years on diverse areas of research in materials science, such as high Tc systems, magnetic alloys, molecular materials etc. He is a reciepent of several nantional and international awards/fellowships, such as Fellow of the National Academy of Sciences, India; Maharashtra Academy of Sciences; Elected Member of the Asia Pacific Academy of Materials; MRSI-ICSC Superconductivity and Materials Science Prize 1995 by the Materials Res. Soc. of India; Distinguished Alumni Award from Kurukshetra University (India) 1996; IIS Gold Medal awarded by the Institute of Industrial Science, University of Tokyo, 1996; "UDCT Golden Jubilee Visiting Fellow", University of Bombay, 1997; Award of 'Excellence' by the CEFIPRA Scientific Council to the Indo-French Project 1308-4 "Chemistry and Physics of Molecular-based Materials" carried out during 1996-99. He has coedited a book entitled *"Thallium-Based High Temperature Superconductors"*, and authored more than 300 scientific publications.

ELECTROMAGNETIC DESIGN OF DTL CAVITY FOR LEHIPA

Shweta Roy, Rajni Pande, S.V.L.S. Rao and P. Singh
Nuclear Physics Division

This paper was awarded the Best Poster Paper Prize at the DAE-BRNS-PSI Symposium on Ion Beam Technology and Applications (SIBTA-2007) held at BARC, Mumbai during September 19-21, 2007

ABSTRACT

This paper describes the electromagnetic design of the Drift Tube Linac (DTL). The 2D design of DTL cavities has been done, using SUPERFISH in order to tune them to the operating frequency of 352.21 MHz with maximum shunt impedance. In order to incorporate the features that break the 2D symmetry, the 3D electromagnetic field simulations have been done using CST Microwave Studio code. The tuner and vacuum port have been modeled and their effect on the resonant frequency has been studied.

Introduction

A 20 MeV, 30 mA proton linac, LEHIPA [1,2] is being built at BARC as part of our ADS programme. This system will consist of a 3 MeV RFQ, followed by an Alvarez Drift Tube Linac to accelerate the beam from 3-20 MeV. The operating frequency of the linac is 352.21 MHz. The electromagnetic design of the DTL has been done, using SUPERFISH [3] and CST Microwave Studio [4] codes. In the following sections, details of these studies are given.

Cavity Design

The DTL cavity was designed using SUPERFISH code with the aim to maximize the shunt impedance and to avoid voltage breakdown by keeping the peak surface electric field below 0.8 Kilpatrick. In addition to this, quadrupoles are housed inside the drift tubes in the DTL for focusing the beam. Hence the drift tubes must be large enough to have space for placing the quadrupoles inside. To design the DTL cavity first, the cavity diameter was optimized. The idea was to use the same tank diameter for all the DTL tanks i.e. in the entire energy range from 3-20 MeV for ease of fabrication. The effect of varying tank diameter on the various figure of merits of the cavity viz. effective shunt impedance, the peak surface electric field, power dissipation etc. at different energies was studied. As can be seen from Fig.1, the effective shunt impedance is maximum for a tank diameter of 52 cm for energies of 3-20 MeV. Hence, the optimum diameter is chosen to be 52 cm for the entire energy range. The other DTL parameters were also optimized using SUPERFISH.

The structure parameters of the DTL are listed in Table 1. The total length of the DTL is 12.5 m and it is planned to make it in four tanks. The focusing lattice is FFDD in all the four tanks as the quadrupole gradients required for focusing with FFDD is much smaller as compared to that with FD lattice [5]. The RF power dissipation is ~1.1 MW and the beam power is 0.51 MW.

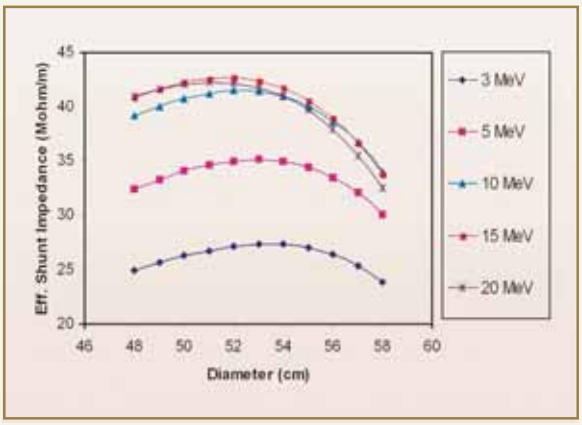

Fig. 1: Effective shunt impedance vs cavity diameter

Table 1: Cavity parameters of DTL

Parameter	Value
Frequency	352.21 MHz
Tank Diameter (D)	52 cm
Drift Tube Diameter (d)	12 cm
Bore Radius (R_b)	1.2 cm
Face Angle (α_f)	0°
Corner Radius (R_c)	1.5 cm
Inner Nose Radius (R_i)	0.5 cm
Outer Nose Radius (R_o)	0.5 cm

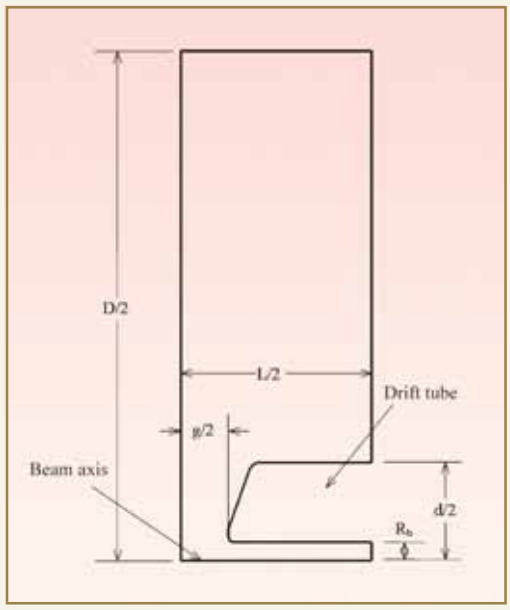

Fig. 2. DTL half cell

Three-Dimensional (3-D) Cavity Design

In order to include features that break the 2D symmetry (tuners, vacuum ports, post couplers etc.) a 3D design of the DTL tank was done, using CST Microwave Studio. The first DTL tank consists of 36 cells and accelerates the beam from 3 MeV to 6.85 MeV. In order to simplify the simulation model, the geometry of the centre cell together with drift tube no. 18 was used. Three cells of this geometry have been modeled in CST Microwave Studio and the frequency of the accelerating mode (TM_{010}) is 352.12 MHz. Fig. 3 shows the electric and magnetic fields in a DTL tank with 3 cells.

The peak surface electric fields were also calculated and are shown in Fig. 4. It is found, that the maximum surface electric fields were on the outer surface of the drift tubes.

Tuner

Slug tuners are used, to provide frequency adjustment to the RF cavity. The tuners are cylindrical rods which when pushed inside the DTL cavity decrease the

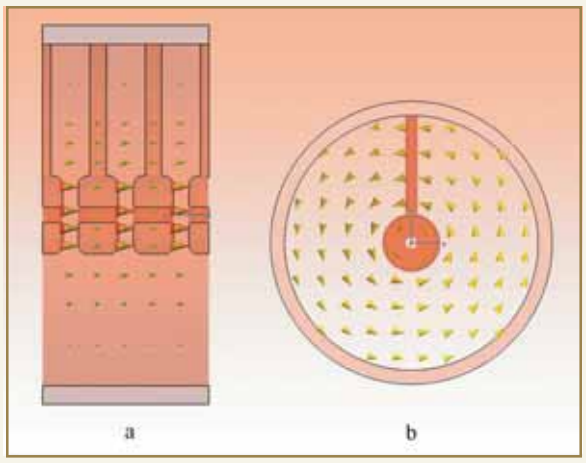

Fig. 3: (a) Electric field in the DTL
(b) Magnetic field in the DTL

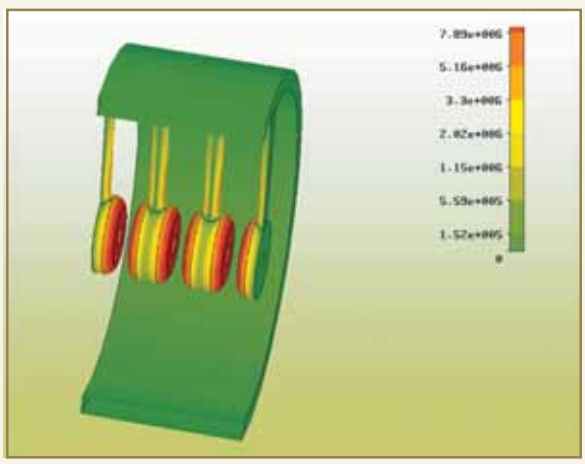

Fig. 4: Peak surface electric fields in the DTL

magnetic volume of the cavity. This leads to a decrease in the inductance and hence an increase in the resonant frequency. According to Slater's perturbation theorem [6] the frequency shift is given by,

$$\frac{\Delta f}{f} = \frac{\mu_0 \iint_{\Delta V} |\vec{H}|^2 dv - \varepsilon_0 \iint_{\Delta V} |\vec{E}|^2 dv}{\mu_0 \iint_{V} |\vec{H}|^2 dv - \varepsilon_0 \iint_{V} |\vec{E}|^2 dv}$$

where, dV is the change in cavity volume, V is the volume of the cavity without perturbation, E and H are the unperturbed electric and magnetic field amplitudes.

It is planned to put 6 slug tuners in each tank. In the simulation, one tuner is modeled and the frequency shift due to all the tuners is obtained, by multiplying the shift due to one tuner with the number of tuners. The CST MWS model of a tuner is shown in Fig. 5.

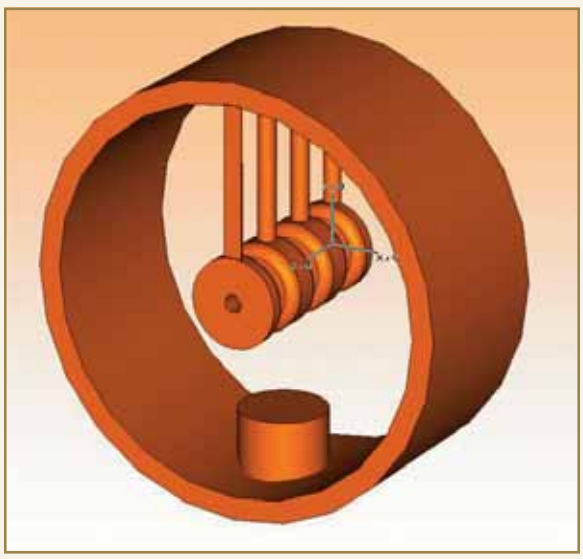

Fig. 5: A 3-cell model of a DTL cavity with tuner

The effects of tuner depth and tuner diameter on the resonant frequency have been studied and are shown in Figs. 6 and 7 respectively. As the tuner is penetrated deeper into the cavity, the resonant frequency rises linearly, because the magnetic field is large at the location where the tuners are pushed in [7]. The rise becomes slow as the tuner is penetrated deeper, since they now start reducing the electric volume as well. If the tuner is pushed further down, the electric field starts dominating over the magnetic field and the net result is a drop in the resonant frequency. The tuning range using all the 6 tuners is estimated to be 2.28 MHz for a tuner diameter of 12 cm and a depth of 11 cm.

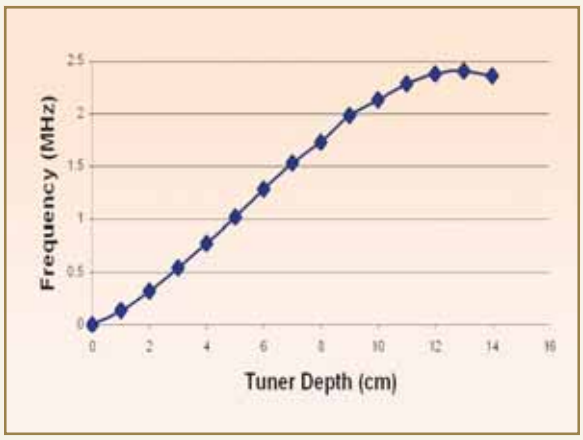

Fig. 6: Variation of frequency with tuner depth

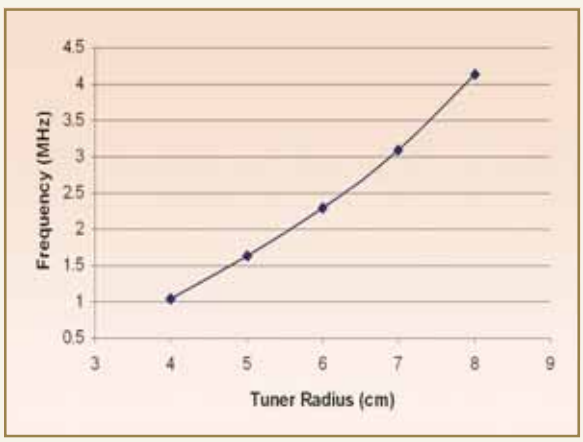

Fig. 7: Variation of frequency with tuner radius

Vacuum Port

The operating pressure for the DTL will be in the range of 10^{-7} Torr. The primary requirement of DTL vacuum systems, is to provide sufficient pumping, to overcome the surface out gassing and maintain the operating pressure. In order to achieve this vacuum, pumping ports are provided on the tank walls. The apertures of the vacuum pumping ports are slotted [8] in order to attenuate the RF power leaking out of the port and also to reduce the surface currents at the port corners, thus reducing the heat dissipation at these locations. The slot orientation is in the same direction as the RF currents. Two pumping ports will be provided in one tank. A 5 slot configuration will be used for each port, with a slot dimension of 14 cm x 1.8 cm and the spacing between two slots will be 1 cm. The conductance of each port is about 1400 l/s. A vacuum port modeled in CST Microwave Studio is shown in Fig. 8. The frequency shift due to the port openings is found to be 13.39 kHz, which is negligible. This is expected because the ports provide very small openings on the tank, as compared to the tank volume.

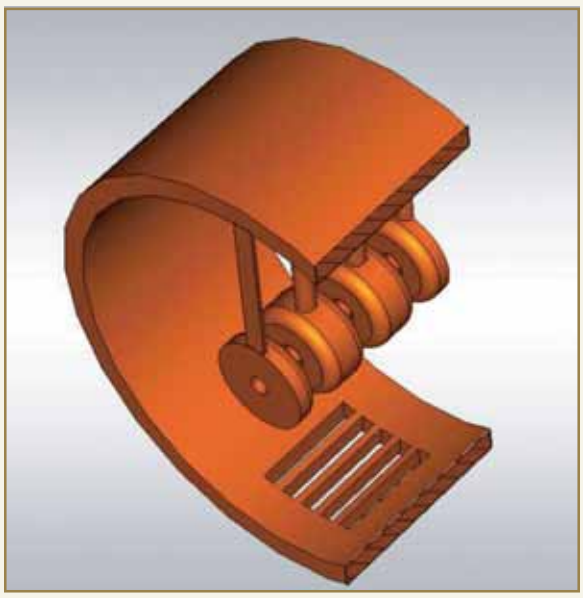

Fig. 8: DTL model showing a vacuum port

Post Coupler

The DTL operates in the zero mode in which the electric field direction is the same in all the accelerating gaps. In this mode the electric field distribution is very sensitive to even small frequency perturbations in the cells. The p/2 mode on the other hand, is the most stable mode of operation for any cell-coupled accelerating structure. However as the $\pi/2$ mode is very inefficient for acceleration, we can try to change the slope of dispersion curve at the location of the zero mode, by introducing a 2nd resonator band which is then coupled to the TM01 band of the DTL. This can be done, by inserting short cylinders called post couplers in the horizontal plane, corresponding

to the drift tube centres. The post couplers were modeled in CST Microwave Studio as shown in Fig. 9. In order to simplify the simulation model, the geometry of the centre cell along with drift tube 18 was used. Since it is too time consuming to simulate the entire tank, the model was limited to nine identical DTL cells with 4 post couplers representing almost one-fourth of the first tank.

Fig. 9: DTL model showing the post couplers

To find the post coupler (TE) mode, the boundary condition at the left and right wall was set to ideal magnetic, in simulation. For optimum stabilization, the highest post coupler mode frequency should be as close to the resonant frequency of the DTL as possible. The post coupler stem represents an inductance while the gap between the post and the drift tube represents a capacitance. Both elements represent a resonant circuit whose frequency depends on the length and the radius of the post coupler. In order to achieve stabilization, the post coupler length and radius have to be chosen such that, the highest post coupler mode frequency is close to DTL resonant frequency of 352.21 MHz. The post coupler mode frequency as a function of post coupler length and radius is shown in Fig.10. From this figure, we can interpolate the post coupler length for different radii as summarized in Table 2.

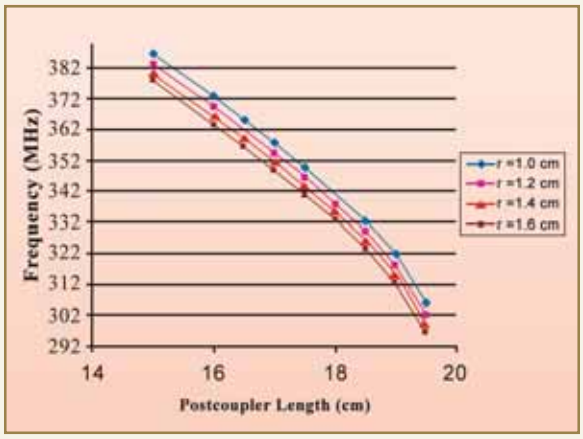

Fig. 10: TE mode frequency as a function of post coupler length and radius

Table 2: Post coupler length for different radii

PC radius (cm)	PC length (cm)
1.0	17.35
1.2	17.1
1.4	16.95
1.6	16.8

Another technique will be used, to find the optimum radius for the posts, which gives the best stabilization against frequency errors in the cells. For this purpose, the tilt sensitivity technique is used, which is usually employed to study post coupler stabilization with mechanical models. These studies are in progress.

Summary and Conclusions

The cavity design for the DTL has been accomplished. The length of the DTL (3-20 MeV) is 12.5 m and it will be made in four tanks. There will be 6 tuners and 2 vacuum ports in each tank. One post coupler will

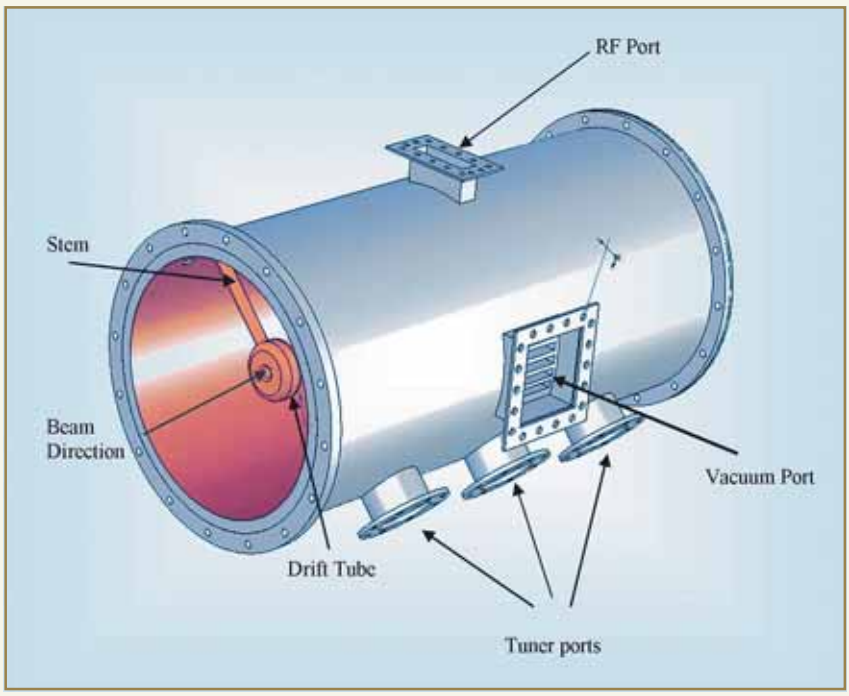

Fig.11: CAD model of 1 m long DTL

be provided at every third cell of the DTL tank for field stability. Based on these studies, a 3-D CAD model of a 1 m long DTL tank has been made (Fig.11). The fabrication of prototype DTL tank has been initiated, to validate these simulations.

Acknowledgement

We thank Dr. V.C. Sahni, Dr. S. Kailas and Dr. R.K. Choudhury for their keen interest in this work. We also thank Piyush Jain and S.C.L. Srivastava for useful discussions.

References

1. P. Singh et al, Accelerator development in India for ADS programme, *Ramana - J. Phys.*, 68, 331 (2007).

2. T. Basak et al, Physics Design of a Low Energy High Intensity Proton Accelerator, BARC/2004/I/007.

3. J.H.Billen & L.M.Young, *POISSON SUPERFISH,* LA-UR-96-1834, L.A.N.L.

4. CST Microwave Studio software.

5. T. Basak et al, Comparison of FD and FFDD lattices for DTL, roc. Ind. Particle Accelerator Conf., Mar. 1-4, 2005, VECC, Kolkata, page174.

6. J.C. Slater, Microwave Electronics, D. Van Nostrand, Princeton, N.J., 1950, pp. 80-81.

7. Thomas P. Wangler, Principles of RF Linear Accelerators, John Wiley and sons, Inc., 1998, pp. 162-163.

8. J. D. Bernardin et al, Spallation Neutron Source, Drift Tube Linac Vacuum System Final Design Report, (SNS-104020400-DE0001-R00).

ABOUT THE AUTHORS

Ms. Shweta Roy is working in the Nuclear Physics Division, BARC since 2003. She is from the 46th Batch of BARC Training School. She did her Masters in Physics from IIT, Delhi. Ms. Shweta Roy is involved in Physics Studies of the 20 MeV High Intensity Proton Accelerator being developed for ADS Programme.

Ms. Rajni Pande is from the second batch of RRCAT Training School and is working in the Nuclear Physics Division since 2002. She did her M.Sc. in Physics from Lucknow University. Ms. Rajni Pande is involved in Physics Studies of the 20 MeV High Intensity Proton Accelerator being developed for ADS Programme.

Mr. S.V.L.S. Rao did his Masters in Physics from University of Hyderabad in 2000 and joined the Nuclear Physics Division in 2001 after a one year Orientation programme at BARC. Mr. Rao is presently involved in development of High Current Accelerator for ADS.

Dr. Pitamber Singh, a graduate of the 19th Batch of BARC Training School, joined the Nuclear Physics Division, BARC in 1976. He received his Ph.D. degree in Physics from Mumbai University in 1983. In addition to participating in design and building the first 2 MV Tandem Accelerator in India and a Recoil Mass Separator for detection of heavy recoiled ions, he has made an outstanding contribution in setting up the 6 MV Folded Tandem Ion Accelerator (FOTIA) facility at BARC. He was conferred the DAE Technical Excellence Award for the year 2000, for his excellent contributions towards indigenous development of accelerator technology in the country. He is a life member of "The National Academy of Sciences, India". Dr. Singh is working on the development of High Intensity Proton Accelerators for the ADS programme of DAE. He has more than 250 publications to his credit. Presently, he is Head, FOTIA Section of the Nuclear Physics Division, BARC and Professor at the Homi Bhabha National Institute, Mumbai.

बीएआरसी न्यूज़लैटर
BARC NEWSLETTER

FEASIBILITY OF ANN-BASED ALGORITHMS FOR IMPROVING THE SENSITIVITY OF TACTIC IMAGING TELESCOPE

V.K. Dhar, A.K. Tickoo, M.K. Koul and R. Koul
Astrophysical Sciences Division

and

B.P. Dubey
Electronics & Instrumentation Services Division

This paper was given the Best Poster Award at the 25th meeting of the Astronomical Society of India, held at Osmania University, Hyderabad, during February 7-9, 2007.

ABSTRACT

The sensitivity of a Cherenkov imaging telescope, is strongly dependent on the rejection of the cosmic-ray background events. Some of the methods which have been used to achieve this segregation include methods like Supercuts, Maximum likelihood classifier, Kernel methods, Fractals Wavelets, Factorial Moments, Random Forest etc. While the segregation potential of neural network classifier has been investigated in the past with modest results, a detailed study using some recently incorporated popular algorithms in ANN (e.g. Conjugate Gradient methods, Radial Basis function algorithm, Simulated Annealing technique, Levenberg-Marquardt algorithm etc.) has not been done so far. The main purpose of this paper is to study the gamma / hadron segregation potential of these algorithms, by applying them to the Monte Carlo simulated data for the TACTIC imaging telescope. The results suggest that the algorithms based on Higer order neurons and Levenberg-Marquardt method are superior to the widely used Dynamic Supercuts procedure, for rejecting the unwanted hadronic background

Introduction

Gamma-ray photons in the TeV energy range (0.1-50 TeV), to which we shall confine our attention here, are expected to come from a wide variety of cosmic objects from both, within and outside the Milky Way Galaxy. Studying this radiation in detail can yield valuable and quite often, unique information about the unusual astrophysical environment characterizing these sources, as also on the intervening intergalactic space [1]. While this promise of the cosmic TeV γ-ray probe has been appreciated for quite long, it was the landmark development of the imaging technique and the principle of stereoscopic imaging, proposed by Whipple [2] and the HEGRA groups,[3] respectively, that revolutionized the field of ground-based very high-energy γ-ray astronomy. In this technique, the spatial distribution of the photons in the image plane (called the Cherenkov image) is recorded by using a closed-packed array of fast

photomultiplier tubes (also called the Imaging Camera with individual PMT's as it's pixels). Detailed Monte-Carlo simulation studies have shown, that the Cherenkov images resulting from γ-ray showers from a point source are compact and roughly elliptical in shape, with their major axis pointing towards the source position in the focal plane camera. On the contrary, Cherenkov images resulting from cosmic ray showers are broader in size, irregular in their shape and are randomly oriented in the focal plane due to their isotropic nature. By examining these subtle details of simulated γ-ray and cosmic - ray generated Cherenkov images using moment analysis techniques and applying them to the actual data, it becomes possible to effectively segregate the two event types, with a high degree of efficiency. Modern atmospheric Cherenkov telescopes, utilizing the imaging technique, allow the removal of more than 99.5 % of the cosmic-ray background, yielding an unprecedented sensitivity in the TeV energy range.

Simulation work, pioneered by Hillas [4], has led to the development and successful usage of several image parameters and the so called Supercuts method. Although the efficiency of this gamma/hadron event classification methodology, has been confirmed by the detection of several gamma-ray sources by various independent groups including us, this technique is still considered to be one dimensional. While the idea of applying ANN to imaging telescope data was attempted for the first time by Reynolds and Fegan [5] with moderate success, primarily because of the inherent limitations in the Backpropagation algorithm, the main aim of the present work is to investigate the potential of using some recently developed ANN algorithms, for rejecting the unwanted hadronic background.

Brief description of the ANN algorithms used in the preset work

An Artificial Neural Network (ANN) is an interconnected group of artificial neurons, that uses a mathematical model for information processing to accomplish a variety of tasks. In more practical terms, an ANN is a non-linear data modeling tool, which can be used to model complex relationships between inputs and outputs or to find patterns in the data.

The feed-forward ANN is the simplest configuration and is constructed using layers where all nodes in a given layer are connected to all nodes in a subsequent layer. The network requires at least two layers, an input layer and an output layer. In addition to this, the network can include any number of hidden layers with any number of hidden nodes in each layer. The signal from the input vector propagates through the network layer by layer till the output layer is reached. The output vector represents the predicted output of the ANN and has a node for each variable that is being predicted.

Depending upon the architecture in which the individual neurons are connected, there can be several possible ANN configurations. While algorithms like Standard backpropagation and Resilient backpropation come under the category of Local search algorithms, Conjugate Gradient methods, Levenberg-Marquardt algorithm, Radial basis function and Simulated Annealing Technique belong to the category of Global search algorithm. Hybrid algorithm category constitutes models like Higher order neurons and Neuro-fuzzy systems. A brief description of these ANN algorithms is presented below.

The Standard Backpropagation network [6], schematically shown in Fig. 1, is the most thoroughly investigated ANN algorithm. Backpropagation using gradient descent often converges very slowly. The success of this algorithm in solving large-scale problems, critically depends on user-specified learning rate and momentum parameters and there are no standard guidelines for choosing these parameters. The Resilient backpropagation(RProp) algorithm was proposed by Reidmiller [7], to expedite the learning of a backpropagation algorithm. Unlike the standard

Backpropagation algorithm, RProp uses only partial derivative signs to adjust weight coefficients.

In gradient-based algorithms, it is difficult to obtain a unique set of optimal parameters, due to the existence of multiple local optima. The presence of these local minima, hampers the search for global minimum because these algorithms frequently get trapped in local minima regions and hence, incorrectly identify local minimum as the global minimum. The conjugate gradient algorithm uses the gradient to compute a search direction and then a line search algorithm is used, to find the optimal step size along a line in the search direction. The Levenberg algorithm [8] involves the use of "blending" between the steepest descent method employed by the backpropagation algorithm and the quadratic rule employed in conjugate algorithms. The original Levenberg algorithm was improved further by Marquardt, resulting in the Lavenberg-Marquardt algorthm, by incorporating the information about the local curvature, hence forcing to move further in the direction, in which the gradient is smaller in order to get around the classic "error valley". Radial Basis Functions are powerful techniques for interpolation in multidimensional space and in artificial neural networks they are utilized as activation functions. Simulated annealing is a generic probabilistic algorithm for the global optimization problem, namely locating a good approximation to the global optimum of a given function in a large search space.

Higher order neuron model is the one which includes the quadratic and higher order basis functions in addition to the linear basis functions to reduce the learning complexity. Neuro-fuzzy systems refer to hybrids of artificial neural networks and fuzzy logic which result in a hybrid intelligent system which synergizes these two techniques, by combining the human-like reasoning style of fuzzy systems with the learning and connectionist structure of neural networks.

TACTIC Telescope and Simulation Methodology for data generation

The TACTIC (TeV Atmospheric Cherenkov Telescope with Imaging Camera) γ -ray telescope has been in operation at Mt. Abu (24.6^0 N, 72.7 ^{0}E, 1300 m asl), India, for the last several years, to study TeV gamma ray emission from celestial sources. The telescope uses a tessellated light-collector of area ~9.5 m^2 which is capable of tracking a celestial source across the sky. The telescope deploys a 349-pixe imaging camera, with a uniform pixel resolution of ~0.3^0 and a ~ 6 ^{0} x 6^0 field-of-view, to take a fast snapshot of the atmospheric Cherenkov events produced by an incoming cosmic ray particle or a γ-ray photon with an energy above ~1TeV. The photograph of the TACTIC imaging telescope is shown in Fig. 2.

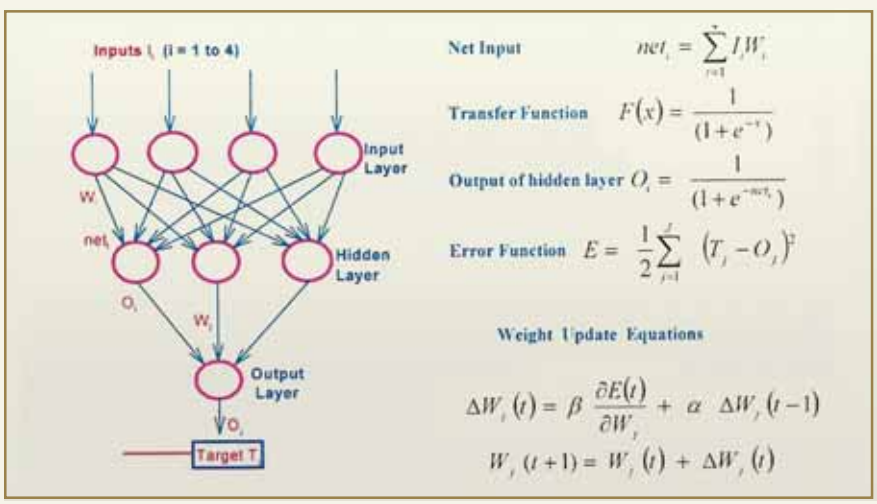

Fig.1: A schematic representation of backpropagation network

The back-end signal processing hardware of the telescope is based on medium channel density NIM and CAMAC modules, developed inhouse. The data acquisition and control system of the telescope has been designed around a network of PCs running the QNX (version 4.25) real-time operating system. The triggered events are digitized by CAMAC- based 12-bit Charge to Digital Converters (CDC) which have a full scale range of 600 pC. The telescope has a pointing and tracking accuracy of better than ~3 arc-minutes. Operating at a gamma-ray threshold energy of ~1.2 TeV, the telescope records a cosmic ray event rate of ~2.0 Hz at a typical zenith angle of 15 ^{0}. The telescope has a 5ó sensitivity of detecting the standard gamma-ray candle Crab Nebula in ~25 hours of observation time and has so far detected γ-ray emission from the Crab Nebula, Mrk 421 and Mrk 501. Other details regarding the description of the telescope subsystems and the results obtained on various candidate ã-ray sources are discussed [9-14].

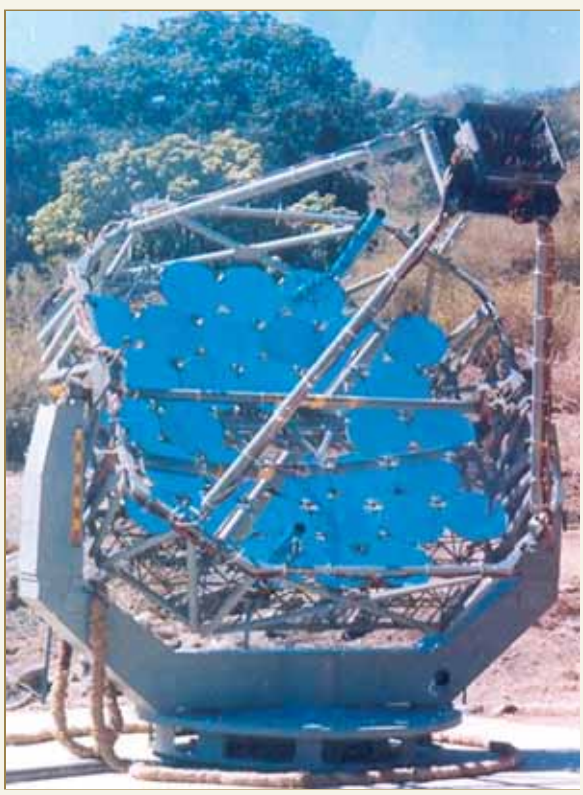

Fig. 2: Photograph of the 349-pixel TACTIC imaging telescope, Mt. Abu

We have used the CORSIKA (version 5.6211) air shower simulation code [15], for studying the gamma / hadron discrimination efficiency of various ANN algorithms. The first part of simulation work comprised generating the air showers induced by different primaries and recording the relevant raw Cherenkov data (data base generation). Folding in the light collector characteristics and PMT detector response was performed in the second part. The simulated data-base for γ-ray showers used about 34000 showers in the energy range 0.2 - 20 TeV with an impact parameter of 5-250 m. These showers have been generated at 5 different zenith angles ($\theta = 5^0$, 15 ^{0}, 25 ^{0}, 35 ^{0} and 45 ^{0}). A data-base of about 39000 proton initiated showers, in the energy range 0.4-40 TeV, in a field of view of $6^0 \times 6^0$ around the pointing direction of the telescope, were used for studying the gamma / hadron separation capability of the telescope. The Cherenkov photon data-base, consisting of number of photoelectrons registered by each pixel after folding in the relevant optical characteristics of the mirrors and the spectral response of the photomultiplier tube, is then subjected to noise injection, trigger condition check and image cleaning. Finally, the clean Cherenkov images are characterized by calculating their standard image parameters like LENGTH, WIDTH, DISTANCE, ALPHA (α), SIZE and FRAC2 [5]. Geometrical interpretation and physical significance of these image parameters is depicted in Fig. 3.

Fig. 4 shows the distributions of the image parameters LENGTH, WIDTH, DISTANCE and α for simulated protons and gamma-rays recorded by the telescope.

Training the ANN algorithms

Training the ANN means iteratively minimizing the error between the desired output and the ANN generated

value, with respect to the network weights. Clearly, in order for the network to yield appropriate outputs for given inputs, the weights must be set to suitable values. This is done by 'training' the network on a set of input vectors, for which the ideal outputs (targets) are already known.

Using the simulated data generated above, we have chosen 6 image parameters, for training the ANN to distinguish between the gamma-ray and the proton showers. These 6 parameters are : SIZE (S), LENGTH (L), WIDTH (W), DISTANCE (D), CONCENTRATION (F2) and the Zenith angle (θ). The simulated data-base was divided into 2 parts so that one part can be used for training and the other for testing the ANN configuration. The training file contains about 14000 gamma-ray and 12000 proton events. The remaining 30000 gamma-ray and proton events comprise the test data file. Each of the ANN algorithms is trained on a similar configuration viz 6:20:1 i.e. 6 nodes in the input layer with each node corresponding to one image parameter, one node in the hidden layer with 20 neurons and one node in the output layer, which is designated as 0.1 or 0.9 depending upon whether the event is a gamma-ray or a proton event. The BIKAS (BARC - IIT Kanpur ANN Simulator) ANN package and MATLAB neural net packages have been used, to study the various ANN algorithms.

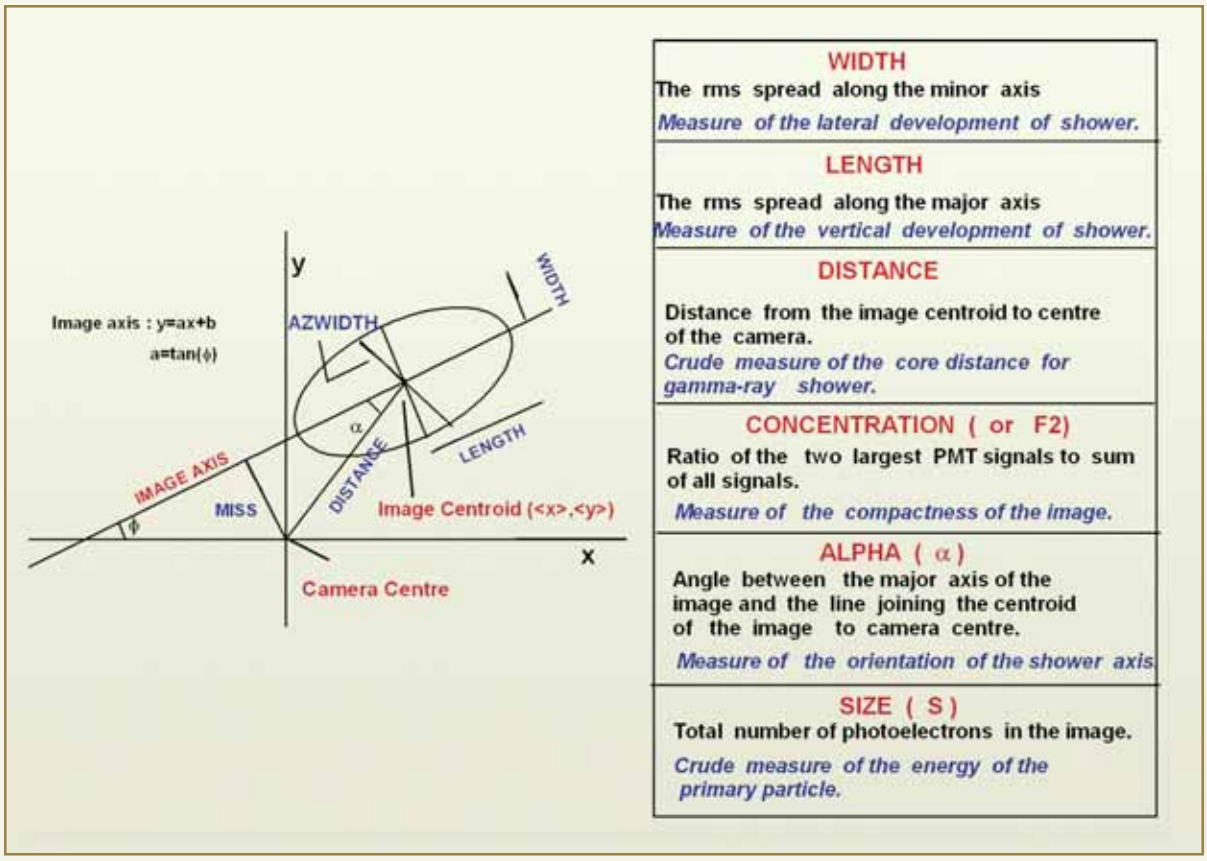

Fig. 3: Definitions of Cherenkov image parameters L,W,D,M and Alpha used for discriminating between the gamma-ray and the hadron showers

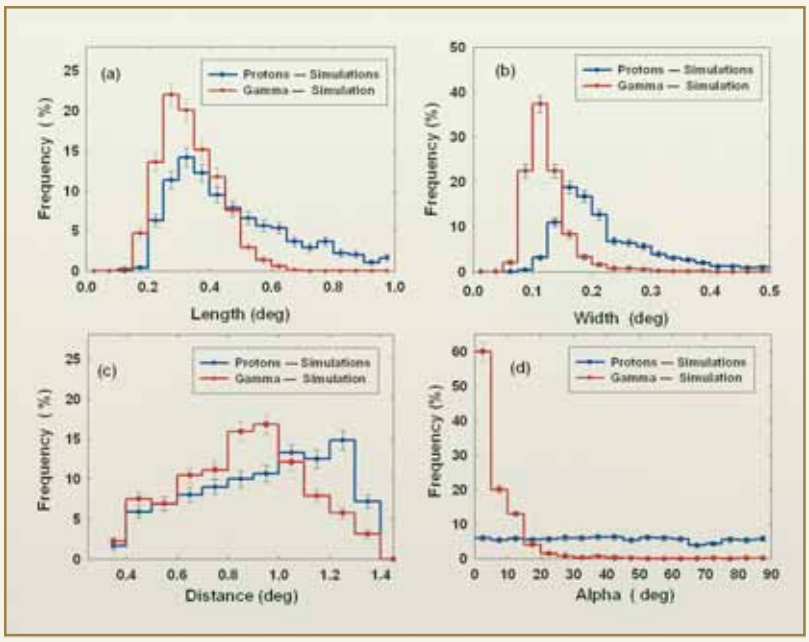

Fig. 4: Comparison of image parameter distributions from the Monte Carlo simulated data for proton and γ-ray events

In all the ANN algorithms discussed above, the training is continued till the RMS error between the expected and the ANN generated value reaches a plateau and does not decrease further. About ~15000 iterations were generally sufficient to train the ANN on various algorithms, however in certain cases, training had to be "early-stopped" to avoid overfitting. The minimum RMS error obtained for Backpropagation and Levenberg, at the end of the training session, turned out to be ~0.037 and ~0.021 respectively.

Results and Discussion

A test data base, consisting of a mixture of about 30000 gamma-ray and cosmic ray events is used, to study the event classification capability of the ANN algorithms. When presented with the test data, instead of ANN yielding the desired output as either 0.1or 0.9, the ANN output is found to lie in the range 0.1 to 0.9. This behaviour is quite expected on account of differences in the training and test data set, which arise because of the inherent fluctuations in the shower development process on event to event basis. The gamma/hadron event selection is done, by classifying an event as a gamma-ray if the corresponding ANN output (η) is less than a predefined cut-off value (η_{cut}). If the ANN output (η) is greater than η_{cut}, the event is classified as a proton initiated shower. representative example of the frequency distributions of the gamma-ray and proton retention factors, denoted by f_γ and f_p respectively is shown in Fig. 5.

Once the event is classified as gamma or proton on the basis of its 'η' parameter, the event is then subjected to α-cut. The event is finally accepted to be gamma-ray like if and only if the event satisfies the conditions of $\eta \leq \eta_{cut}$ and $\alpha \leq 15^0$. In order to find the optimum value of η_{cut} for each algorithm separately we have varied η_{cut} from 0.10 to 0.85 in steps of 0.05 and evaluated f_γ, f_p, Quality Factor ($QF = f_\gamma/\sqrt{f_p}$) and $QF\sqrt{f_\gamma}$. The optimized η_{cut} is then found out by selecting f_γ and f_p in a manner for which $QF\sqrt{f_a}$ is maximum. The significance of maximizing the quantity $QF\sqrt{f_\gamma}$ is that the signal recovery time (T_{min}) is related to it by T_{min} $\alpha 1/(QF^2 f_\gamma)$.

Table 1 summarizes the performance of various ANN algorithms and their comparison with the Supercuts event selection methodology. The optimized Supercuts selection criteria for accepting an event as a gamma-ray like are the following : $0.11^0 \leq$ LENGTH $\leq 0.35^0$; $0.06^0 \leq$ WIDTH $\leq 0.17^0$; $0.31^0 \leq$ DISTANCE $\leq 1.33^0$; SIZE $\geq$ 50 pe; $\alpha \leq 15^0$ and F2 $\geq$ 0.35. It is quite evident from the table that out of a total of 8 different ANN algorithms

studied here, 5 ANN algorithms yield superior performance as compared to the Supercuts procedure. Amongst the 5 ANN algorithms, it is found that Levenberg-Marquardt method ($f_\gamma \sim$ 70.85 % , $f_p \sim$ 0.88 %, QF$\sim$ 7.5) and Higher order neurons ($f_\gamma \sim$ 58.21 % , $f_p \sim$ 0.63 %, QF$\sim$7.2) and are the best and hence need to be seriously considered for improving the performance of the TACTIC imaging telescope.

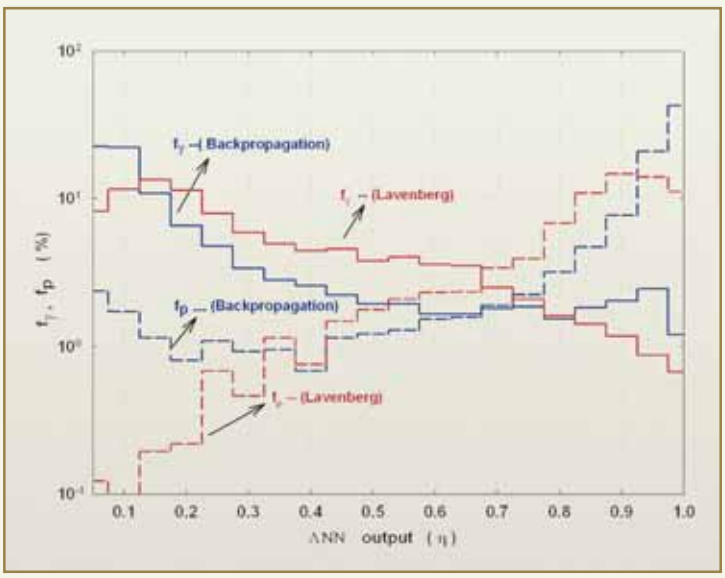

Fig. 6: Frequency distribution of gamma-acceptance (f_γ) and proton acceptance factors (f_p) for Backpropagation and Levenberg ANN algorithms

Conclusions

The main objective of the present work is to investigate the potential of using some recently developed ANN algorithms, for improving the sensitivity of TACTIC imaging telescope. The results of our simulation study suggest, that the ANN algorithms based on Levenberg-Marquardt method and Higher Order Neurons are superior to the widely used Supercuts procedure, for rejecting the unwanted cosmic ray background. These algorithms yield the best combination of f_γ and QF $\sqrt{f_\gamma}$ as compared to that of the Supercuts method. The effectiveness of these algorithms, by applying them to the actual data collected by the TACTIC telescope, is however still in progress.

Table 1: Performance of Supercuts event selection methodology and it's comparison with the ANN algorithms

Gamma / Hadron separation method	η_{cut}	f_γ (%)	f_p(%)	QF	QF $\sqrt{f_\gamma}$
Supercuts Method	------	46.02	0.78	5.2	35.3
Resilient Backpropagation	0.20	58.92	0.93	6.1	46.9
Backpropagation	0.40	71.14	1.76	5.3	45.2
Conjugate Gradient	0.60	74.42	3.27	4.0	34.0
Radial Basis Function	0.70	81.13	5.79	3.3	30.3
Simulated Annealing	0.45	62.13	0.97	6.2	49.5
Higher Order Neurons	0.35	58.21	0.63	7.2	55.7
Neuro Fuzzy systems	0.75	66.03	2.71	4.0	32.5
Lavenberg Marquardt	0.45	70.85	0.88	7.5	63.5

References

1. R.A. Ong, *Phy. Reports*, 305 (1998) 93.
2. T.C.Weekes et al, *Astrophys. J.,* 342 (1989) 379.
3. A.Daum et al, *Astropart. Part Phys.*, 8 (1997) 1.
4. A. M. Hillas, Proc. 19th ICRC , La Jolla, 3 (1985) 445.
5. P.T. Reynolds and D.J.Fegan, *Astropart. Phys*, 3 (1995) 137.
6. D.E. Rumelhart et al., *Nature*, 323 (1986) 533.
7. M. Reidmiller et al, Proc. Int. Conf. Neural Networks ICNN, (1993) 586.
8. W.H. Press et al, Numerical Recipes in C++, (2002) 668.
9. R. Koul et al, *NIM A* 578 (2007) 548.
10. A.K.Tickoo et al, *NIM A* 539 (2005) 177.
11. K.K.Yadav et al, *NIM A* 527 (2004) 411.
12. S.V.Godambe et al, *J. Phys. G: Nucl. Part. Phys.*, 35 (2008) 0065202.
13. S.V.Godambe et al, *J. Phys. G: Nucl. Part. Phys.*, 34 (2007) 1683.
14. K.K.Yadav et al, *Astropart. Phys.*, 27 (2007) 447.
15. D.Heck et al, Report FZKA, 6019, Forshungszentrum, Karlshrue (1998).

ABOUT THE AUTHORS

Mr. V.K. Dhar has been associated with the implementation of several important segments of the TACTIC gamma-ray imaging telescope set up at Mt. Abu, Rajasthan. During the last few years he has investigated several potential application areas of Artificial Neural Networks (ANN) in the field of Gamma-Ray Astronomy. He has also been an active member of the BARC –IIT (Kanpur) collaboration for validation of 'BIKAS' neural network software.

Dr. A.K.Tickoo is from the 30th Batch of the BARC Training School and has been associated with the Gamma-Ray Astronomy programme of the centre for the last 20 years. He has contributed significantly to the design, operation and data analysis aspects of the TACTIC telescope. His current areas of interest include optimizing the design features of the 21m diameter MACE telescope and application of Artificial Neural Networks and other multivariate analysis tools to Cerenkov Imaging data.

ABOUT THE AUTHORS

Mr. M.K. Koul has been working on the Monte Carlo Simulation studies related to the detection of very high energy gamma-ray events by the TACTIC telescope. He has also been an active member of the team which developed software for these studies. He has contributed significantly in developing the zenith angle dependent Dynamic Supercuts-based event selection methodology for improving the performance of the TACTIC telescope.

Mr. R. Koul is from the 21st Batch of the BARC Training School. He has been working on various aspects of instrumentation required for ground based Gamma-Ray Astronomy for more than 2 decades and has published about 50 scientific papers in national and international journals. Presently, he is leading the efforts for setting up the large area gamma-ray telescope at the high altitude astronomical site at Hanle in the Himalayas.

Dr. B.P. Dubey is from the 21st Batch of the BARC Training School and is working with EISD. He has contributed significantly to the development of Gamma-ray spectrometers, Data-Logger software of MHD Pilot plant, operator Information system of KAMINI reactor, PDCS of KAPS-1 and KAPS-2. Dr. Dubey is also involved in the development of ANN package BIKAS (BARC-IIT Kanpur ANN simulator) and an ANN-based system called Vibration Signal Analyser using Fourier Transformation and ANN (VISFoTA). He also delivers lectures on ANN and Fuzzy logic at the BARC Training School.

^{238}PU SPIKE FOR THE DETERMINATION OF CONCENTRATION OF PU BY ISOTOPE DILUTION TECHNIQUES – FEASIBILITY ANALYSIS

D. Alamelu and S.K. Aggarwal
Mass Spectrometry Section, Fuel Chemistry Division

This paper was awarded the Second Place in the Poster Session at the 12th Symposium-cum-Workshop on Mass spectrometry, held at Goa during March 25-30, 2007

EXTENDED ABSTRACT

Determination of concentration of Plutonium is required, due to its strategic importance as well as for nuclear material accounting. Since Pu is highly radiotoxic, it's determination in a variety of environmental matrices is extremely necessary. Isotope dilution techniques are usually preferred, since the quantitative separation of the element of interest is not warranted for and hence can be employed for complex matrices such as those encountered in environmental samples. Two isotopic dilution techniques employed for the determination of Pu concentration are: Isotope Dilution Mass Spectrometry (IDMS) and Isotope Dilution Alpha Spectrometry (IDAS).

For IDMS, spike solutions which are highly enriched in ^{244}Pu or ^{242}Pu and which are minor isotopes in the samples, are used. Due to the non-availability of ^{244}Pu or ^{242}Pu spikes, one can also use ^{240}Pu as a spike for the determination of Pu concentration. Since the energy of the alpha particles emitted by ^{240}Pu, is close to that emitted by ^{239}Pu, it cannot be used as a spike for IDAS experiments.

In IDAS, ^{238}Pu is used as a spike and the change in the ^{238}Pu/(^{239}Pu + ^{240}Pu) alpha activity ratio is used, for the determination of the concentration of Pu in the sample. Due to ubiquitous isobaric interference of ^{238}U in Pu samples, one cannot use ^{238}Pu as a spike in IDMS, unless a suitable methodology is employed for accounting for this isobaric interference.

Due to the utilization of different spikes used in IDAS and IDMS experiments, which are also calibrated by different physico-chemical techniques, it is not possible to directly correlate the precision and accuracy of the values obtained by the two techniques. It will always be worthwhile to develop a methodology and use the same spike for comparing the results obtained by different laboratories and operating personnel.

In this paper, feasibility considerations are studied for the possibility of using a single spike for the determination of Pu concentration in the Pu sample. It is shown here that ^{238}Pu spike with activity ratio around 20 (atom ratio 2 to 3) is useful as a spike, for both IDAS as well as IDMS experiments simultaneously. The results of this study are presented in this paper.

Acknowledgements

The authors are thankful to Dr. V. Venugopal, Director, Radiochemistry and Isotope Group, for his constant support and encouragement.

ABOUT THE AUTHORS

Ms. D. Alamelu obtained her M.Sc. Degree in Physics from Annamalai University. After graduating from the 38th Batch of Training School, BARC, she joined the Mass Spectrometry Section of the Fuel Chemistry Division in 1995. Since then, she has been actively involved in the indigenous development of Time-of-Flight Mass Spectrometer. Her other areas of interest include thermal ionization mass spectrometry and alpha spectrometry.

Dr. S.K. Aggarwal is currently Head, Fuel Chemistry Division, BARC, Trombay. He joined the 16th Batch of BARC Training School in 1972 and received the Homi Bhabha Award. He did his Ph.D. from Mumbai University in 1980 and completed his Post-doctoral training during 1987-89 at the University of Virginia, USA. He is a specialist in the field of atomic mass spectrometry and alpha spectrometry and is interested in various mass spectrometric techniques. His other areas of interest include electrochemistry, X-ray spectroscopy and solvent extraction. He is a recognized Ph.D. guide of the Mumbai University and of HBNI.

BEAM DYNAMICS OF THE HEAVY ION RFQ WITH PREBUNCHER FOR THE ALTERNATE INJECTOR AT PAF

N. Mehrotra, P.V. Bhagwat, A.K. Gupta, P. Surendran, J.A. Gore, R.K. Choudhury and S. Kailas
Nuclear Physics Division
and
M.B. Kurup
Tata Institute of Fundamental Research, Mumbai

This paper was awarded the Best Oral Presentation Prize at the BARC Golden Jubilee DAE-BRNS Indian Particle Accelerator Conference (InPAC-2006), held at BARC and TIFR from Nov. 1-4, 2006

ABSTRACT

As part of the Pelletron Accelerator Facility augmentation programme, it is planned to have an alternate injector system to the Superconducting LINAC booster. The LINAC booster has been commissioned and is now operational to provide beams up to A~60 region with E~5 MeV/A. The development of an alternate injector, will further enhance the utilization capability of booster LINAC, by covering heavier mass range ($1/7 \leq q/m \leq 1/2$) with higher intensity up to Uranium. This injector system comprises of an Electron Cyclotron Resonance (ECR) ion source, Radio Frequency Quadrupole (RFQ) Linac and superconducting low-beta cavities. The physics design of the heavy ion RFQ with prebuncher for the alternate injector is presented.

Introduction

The 14 UD Pelletron Accelerator Facility (PAF), set up as a collaborative project between Bhabha Atomic Research Centre and Tata Institute of Fundamental Research, has been a major facility of DAE for both basic and applied research in India. The accelerator utilization for basic sciences constitutes about 70% of the total beam time.

Prior to injection into the Superconducting LINAC (S-LINAC), the ion beam needs to be accelerated to 12-14 MV/q. The ion beam extracted from ECR ion source and pre-accelerated to required energy (10 keV/u), will be transported by Low Energy Beam Transport (LEBT) line (consisting of focusing bending and diagnostic elements) to the entrance of the heavy ion RFQ (see Fig. 1).

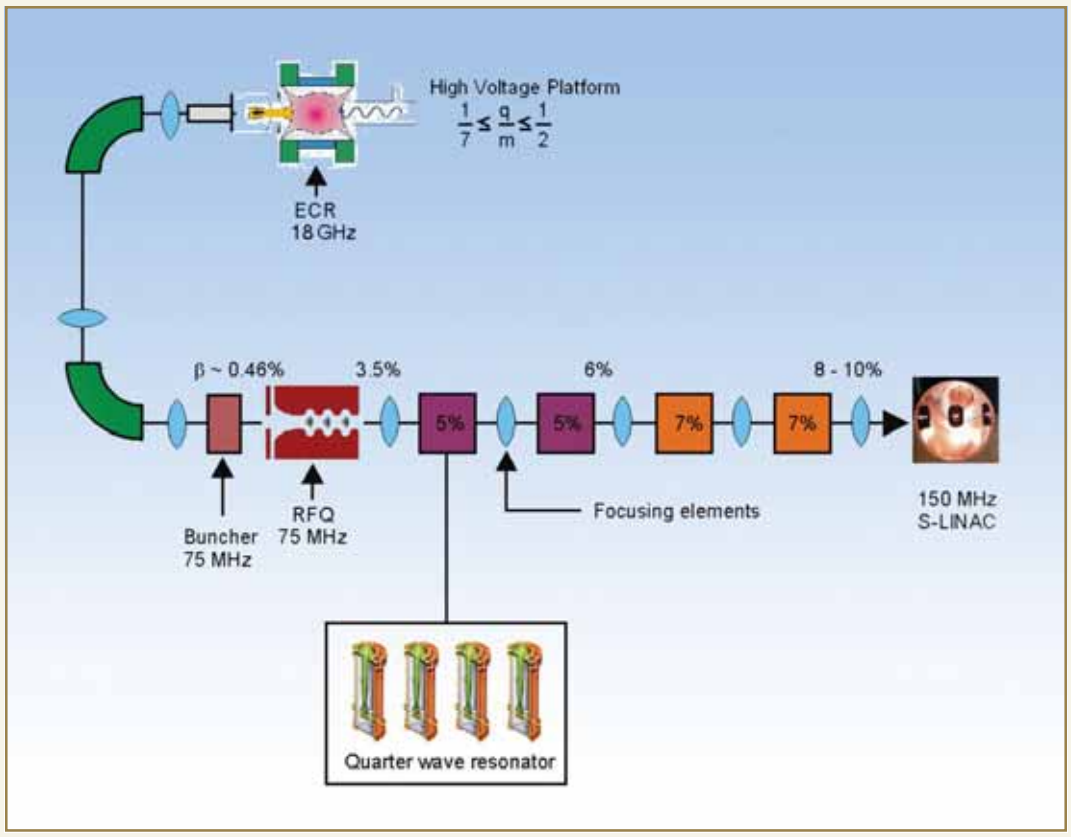

Fig. 1: Alternate injector layout

To reduce the RFQ length, a prebuncher operating at the same frequency as RFQ, was also finalized. The RFQ operating at f/2 (75 MHz) of the S-LINAC frequency, will accept beams with $\beta = 0.46\%$ and accelerate it up to $\beta = 3.5\%$. These beams would then go through two sets of superconducting cavities with $\beta = 5.0\%$ and $\beta = 7.0\%$ respectively. This acceleration is expected to bring all ion beams from carbon to uranium, in the velocity range $\beta = 8\text{-}10\%$, which is suitable for S-LINAC acceptance. After further acceleration through S-LINAC, light ions of about 12 MeV/u and uranium ions of about 7 MeV/u would be available on target (see Fig. 2).

The final energies available from this alternate injector system would vastly enhance the capability of S-LINAC as a research tool for Nuclear Physics.

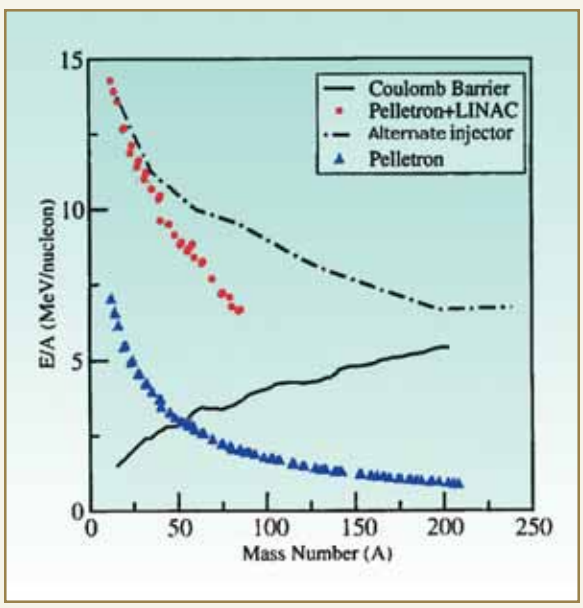

Fig. 2: Available and expected beam energies

ECR ion source

The alternate injector and S-LINAC combination aims to accelerate U^{34+} (q/m~1/7) ions with 100 pna yield on the target. To realize this, 18 GHz superconducting ECR ion source is the appropriate choice, which requires only 20 kW of power and 200 l/hr of cooling when compared to Hypernanogun [1] requiring 200 kW of power and 6800 l/hr of cooling. An advanced version of this state-of-the-art superconducting ECR ion source using HTS wire technology, to be procured from M/s Pantechnik, France, is currently under development at their site. This source will be equipped with a mass selection feature on a high voltage platform of 300 kV, making it readily available as a stand-alone facility, till the development of the downstream elements is completed. This facility will be capable of generating highly charged positive ion beams with 0.3*q MeV for a wide range of elements across the periodic table. However, for injecting into RFQ it will operate at 70 kV for U^{34+} producing about 3eμA of U^{34+}. Beside high yields of Group I, II elements like Na, K, Ca, Ba, the ECR ion source also produces beams of group VIII elements i.e. Ne, Ar, Kr etc. which cannot be produced in the present SNICS negative ion source of pelletron accelerator.

Prebuncher

Although the internal shaper and buncher of RFQ have almost 100% capture and bunching efficiencies, it is at the cost of increased length and power consumption. Hence, it was decided to have a 75 MHz prebuncher with three of it's harmonics 40 cm upstream RFQ. The phase capture for the third harmonic buncher is 75%. The buncher to RFQ distance (s) was optimized using an analytical formula (see Eq. 1) derived by Fourier series analysis of saw-tooth waveform

$$s = \beta\lambda \frac{\varphi}{2F(\varphi)} \frac{E(keV/u)}{(Z/\zeta)U(kV)}, F(\varphi) = \sum_{n=1}^{n=3} (-1)^{n+1} \frac{\sin(n\varphi)}{n} \quad (1)$$

where $\beta = v/c$, v being the velocity of incoming ions, φ is the phase at which $F(\varphi)$ is maximum, Z/ζ is the ratio of atomic number to mass number for the respective ions. All heavy ions with different Z/ζ can be bunched in the same drift length by keeping $ZU(kV)/\zeta$ constant, as all ions will have same β (see Fig. 3). The maximum bunching voltage was determined from maximum energy spread accepted by the first cell of RFQ (see Eq. 2).

$$\Delta W/u = [(qU_0/m)\, \beta_s^2 c^2 A_{10} (\varphi_s \cos\varphi_s - \sin\varphi_s)]^{1/2} \quad (2).$$

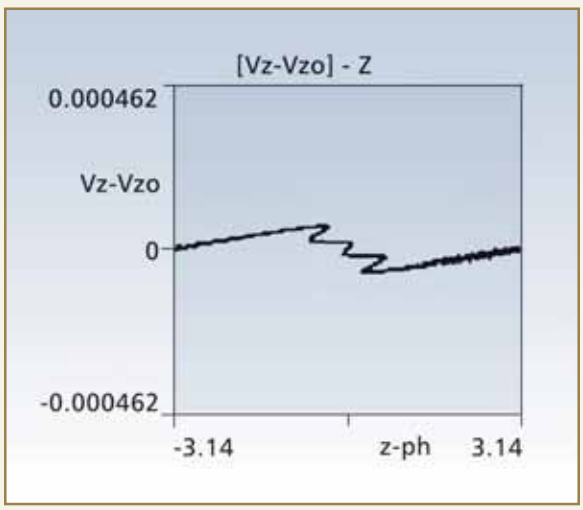

Fig. 3: Bunched beam at RFQ entry

For our case, $\varphi_s = -90^0$, m = 1.001, ΔW = 0.285 keV/u. This corresponds to bunching voltage of 2.1 kV. The prebuncher will focus the beam at the exit of RMS, to minimize longitudinal defocusing of the beam, howsoever small, in the RMS.

RFQ Linac

Among the ultra low velocity accelerating structures for heavy ions, RFQ holds merit in terms of beam quality and efficient acceleration. The choice of operating frequency of 75 MHz was driven by S-LINAC frequency and power dissipation in the RFQ. The pre-acceleration voltage (V) was then decided, by the

capability to machine the first RFQ cell i.e. the cutting tool should be able to cut cells of length βλ and depth m*(a-1). Hence, V= 10*m/q was selected so that the first period has a length of 1.8 cm.

Radial Matching Section (RMS)

The RMS consisting of 8 cells, of which the first two cells form the flange and gap to vane, matches the spatially focussed beam to the transient focussing and acceptance of the RFQ. It was optimized using our analysis [2] as outlined below. Starting with the potential function

$$U(r,\theta,z) = \frac{U_0}{2}\sum_{m}^{\infty}\sum_{n}^{\infty} A_{mn} I_n\,(mkr)\cos(n\theta)\sin(mkz)$$

where, $m=2s+1$, $n=2(2p+1)$, $s, p= 0,1,2\ldots$ and taking the first two terms for quadrupolar symmetry, the analytical results for vane profile in RMS is given by

$$(a/r_0)^2 = 2/[Sinkz\,(3 - Sin^2kz)] \qquad (3)$$

The vanes cannot be extended to the cavity end walls. Hence, this ideal vane profile becomes inadequate. It is then scaled up according to

$$a_{new}/r_0 = s(a/r_0 - 1) + 1 \qquad (4)$$

s being the scaling parameter.

The choice of scaling factor was then optimized (see Fig. 4) using LIDOS.RFQ.DESIGNER [3]. Eqs. 3 and 4 were then used, to generate the longitudinal vane profile in RMS (see Fig. 5). With this vane profile, mismatching of 1.04 and 95% overlap of particle ellipses with the acceptance ellipse (Emitt.cross./Emitt.) was achieved. This optimization leads to low amplitude envelope oscillations, caused by the mismatched input beam (see Fig. 6).

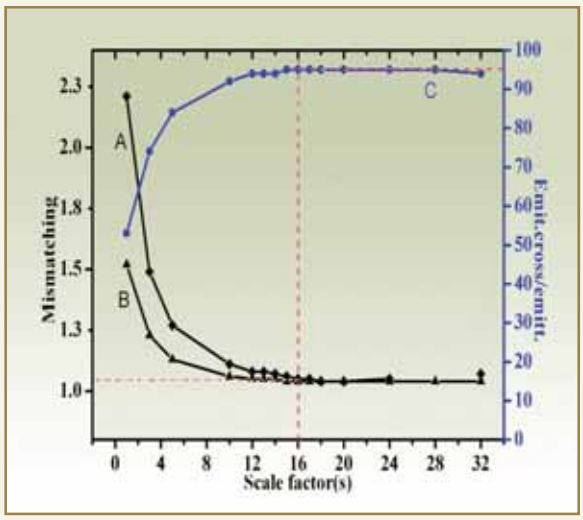

Fig. 4: Scale factor optimization. 'A' represents mismatching for non-optimum beam parameters. 'B' represents mismatching for optimal beam parameters. 'C' represents emitt.cross./emitt. for both

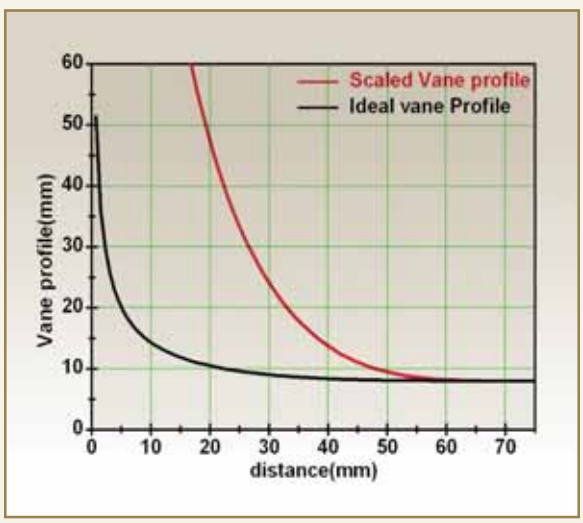

Fig. 5: Vane profile in the RMS

Cell Parameters

Using our earlier experience [4], this heavy ion RFQ was also designed with constant mean aperture radius (r_0) in order to keep the intervane capacitance per unit

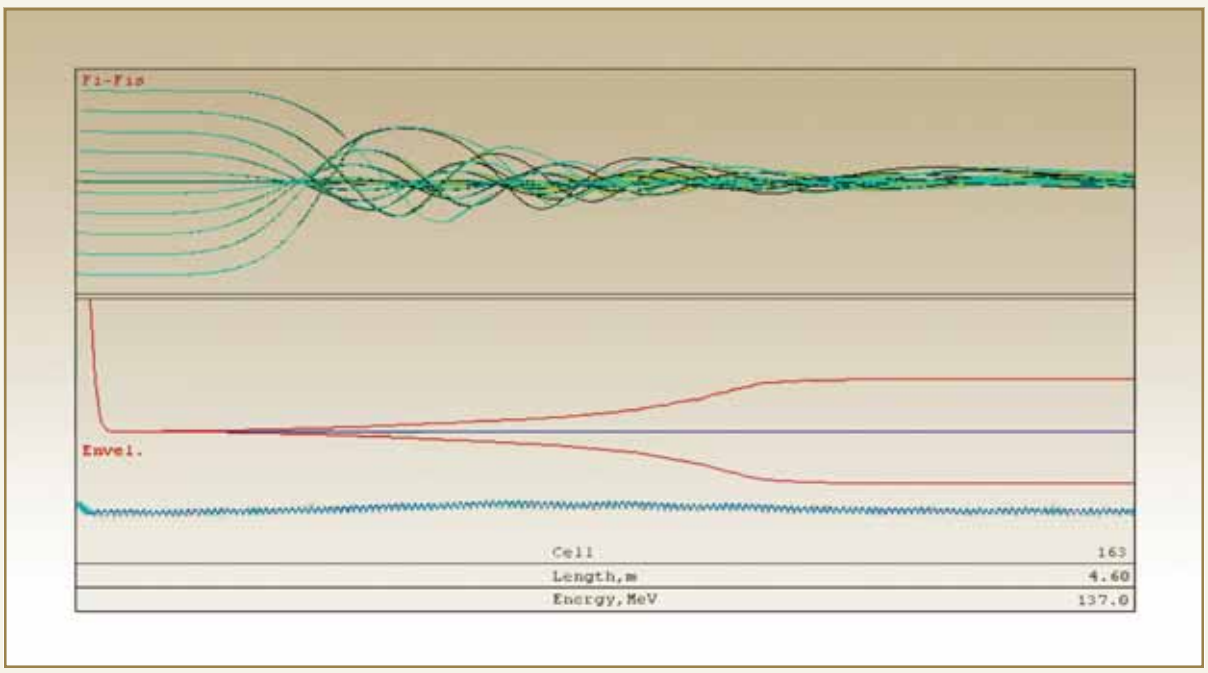

Fig. 6: Phase and envelope oscillations in RFQ

length, constant. The smooth variation approach [5] was utilized for optimizing modulation and phase in the design (see Fig. 7).

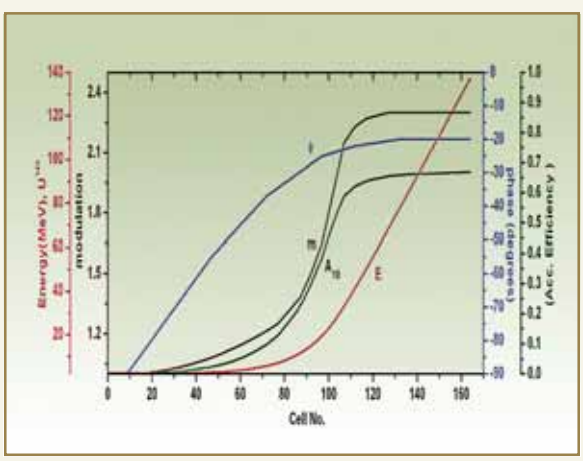

Fig. 7: Cell parameters along RFQ

The smooth variation in modulation and phase, results in gradual variation in minimum aperture, until it becomes constant (see Fig. 8). The matched beam radius was calculated using the formula:

Match beam radius $= (\varepsilon_n \lambda/\sigma)^{1/2} = 3.3$ mm

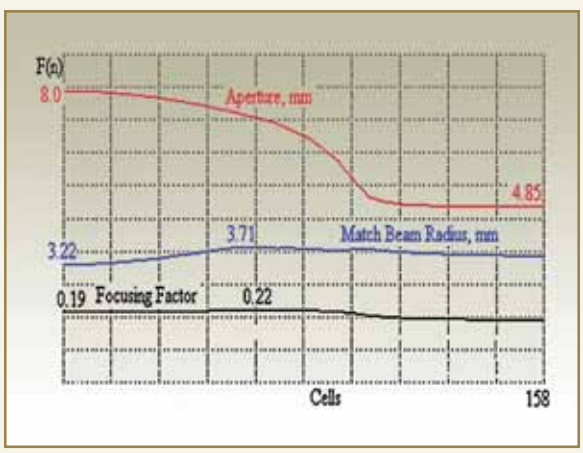

Fig. 8: Focusing channel parameters along RFQ

It is crucial to avoid parametric resonances in the RFQ. Hence, ratio of longitudinal-to-transverse oscillation frequency, should be less than 0.5. For this RFQ, the maximum ratio of longitudinal-to-transverse oscilation frequency is 0.38 (see Fig. 9).

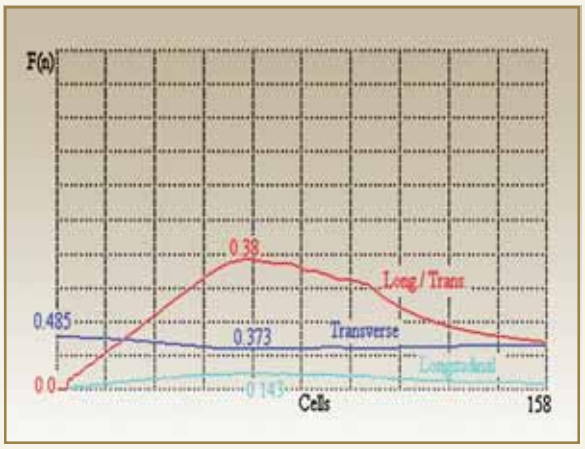

Fig. 9: Frequencies of transverse and longitudinal oscillations

A short bunching section was introduced, to capture some part of the 25% unbunched beam. This explains the slow variation of phase along the RFQ. The defocusing factor was increased faster to take advantage of the already bunched beam (see Fig. 10). Due to this, the longitudinal and transverse phase advances cross over (see Fig. 11). The salient feature of this design is the final phase of -20^0.

Vane Design

Extensive simulations were done, to optimize vane

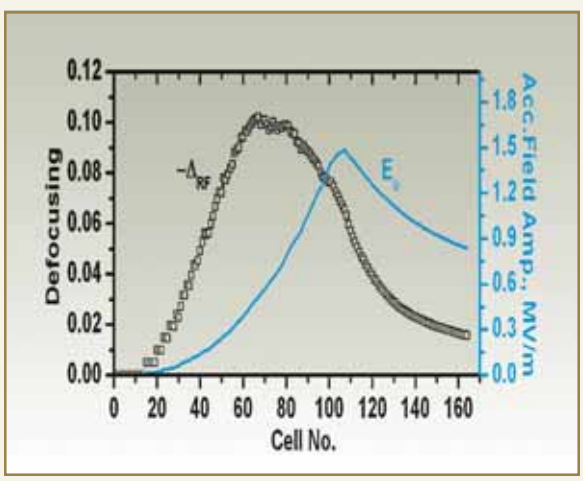

Fig. 10: Defocusing and accelerating field amplitude along RFQ

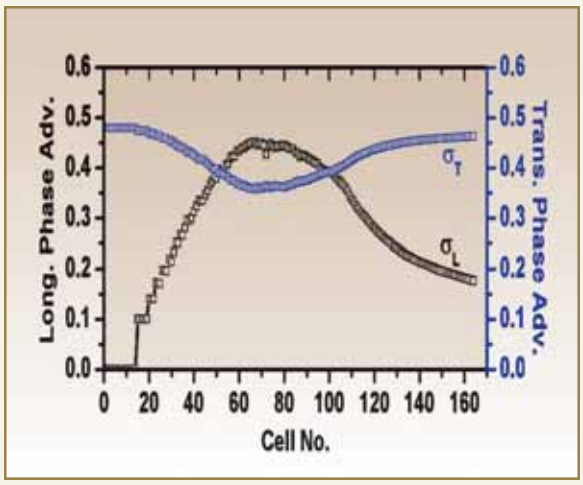

Fig. 11: Phase advance along RFQ

related parameters [6]. Near the beam axis, the vane geometry is approximated by circular arcs instead of hyperbolae in the transverse plane. Based on simulations (see Fig. 12), the following parameters were zeroed on.

Table 1: Vane parameters

ρ/r_0	0.875
Incl. Angle of Vane-Tip, deg	21.0
Semi-Width of Vane Tip, mm	12.5

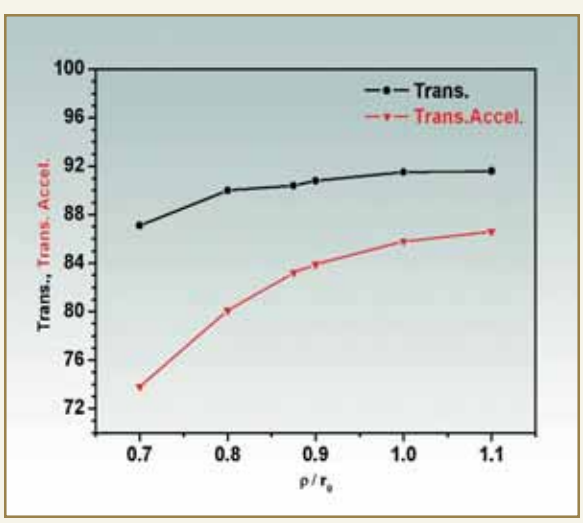

Fig. 12: ρ/r_0 optimization

A ρ/r_0 value of 0.875 was chosen, to lower the peak surface electric fields, while maintaining good transmission. Inclination angle of 21 degrees was chosen, to bring the vane profile close to the ideal two-term vane profile (see Fig. 13). The choice of semi-width of vane tip has more to do with the droop of vanes and cooling requirement, than controlling the intervene capacitance.

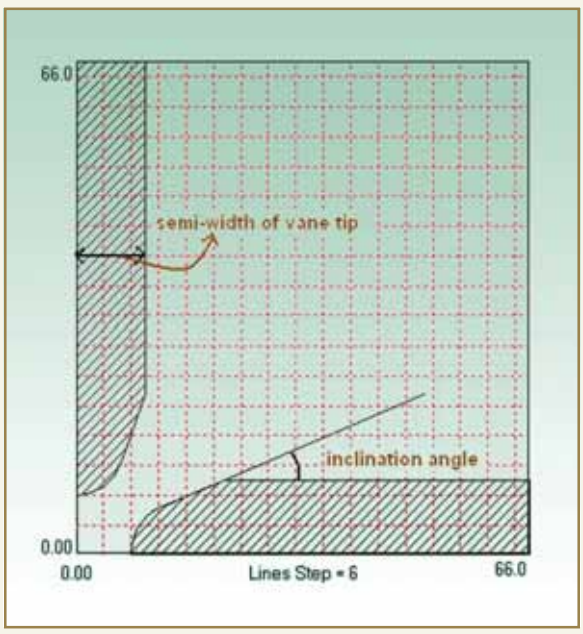

Fig. 13: Vane shape in the transverse plane

PIC Simulation

Particle In Cell (PIC) simulations were performed, using LIDOS for gaussian distribution with 50,000 particles and real vane shape. A simulated transmission of 92.5% and 87% of Trans. Accel. was obtained, for the prebunched beam. Trans. Accel. is a measure of transmission of longitudinally accelerated particles. A phase width of $\pm 9^0$ and momentum spread of $\pm 0.35\%$ was obtained at the exit of RFQ (see Fig. 14). The 90% longitudinal emittance portrait is shown in Fig. 15. The final RFQ parameters are summarized in Table 2. There is no emittance growth for 65% particles, inside the ellipse for the Gaussian distribution (see Fig. 16).

Table 2: RFQ specifications

q/m	1/7, U 34+
Ein / Eout, keV/u	10 / 575
Frequency, MHz	75
Kilpatrick Factor	1.4
Focussing Parameter (B)	4.26
Intervane Voltage, kV	16*m/q
Mean Aperture Radius (r_0)	8.0 mm
Minimum Aperture (a), mm	8.0-4.51
Current (I), mA	0.1
ε (input, norm.) π mm mrad	1.0
Modulation (m)	1.0 - 2.3
Synchronous Phase (ϕ_s)	-90^0 to -20^0
Number of cells (n)	167
Length, m	4.62
RMS Long. Emitt., keV/u*ns	0.3
Maximum Surface Field	17.1 MV/m

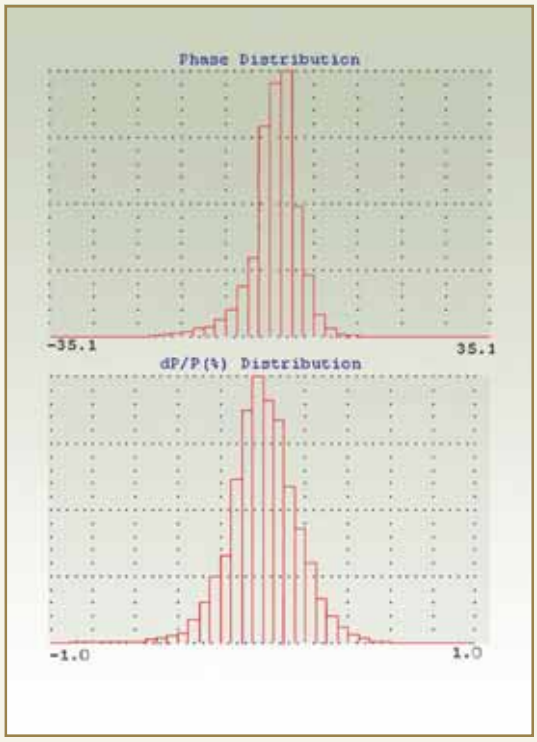

Fig. 14: Phase and momentum distribution at RFQ exit

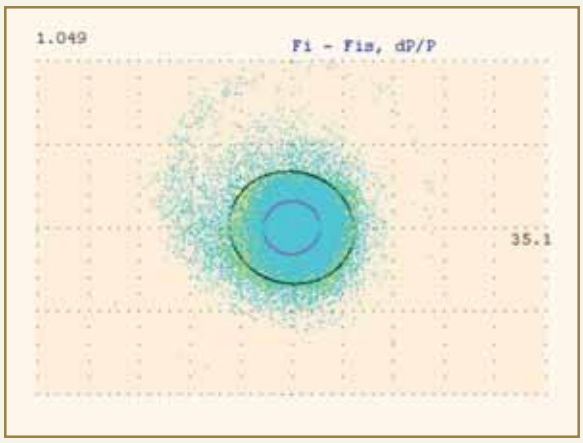

Fig. 15: Longitudinal phase space at RFQ exit

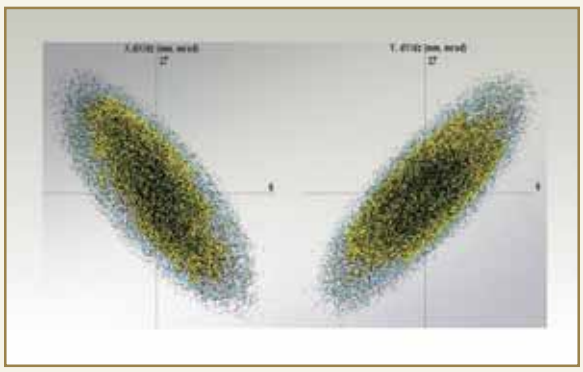

Fig. 16: Output characteristics of beam at RFQ exit

Sensitivity (or Error) Study

The effect of errors arising due to improper vane machining and misalignment, on the performance of RFQ was studied, using the statistics module of LIDOS. Perturbations in vane voltage (dU/U), modulation (dm) and average cell radius (dR) were simulated separately and simultaneously as well. At the beginning of each cell, the code adds uniformly distributed random deviations on the specified cell parameter over ± tolerance level. Cell radius (dR) varies as cubic spline while voltage and modulation vary as linear spline along the accelerator length. The cell-to-cell random deviations are statistically independent. Based on simulations with 10,000 particles and 9 statistical

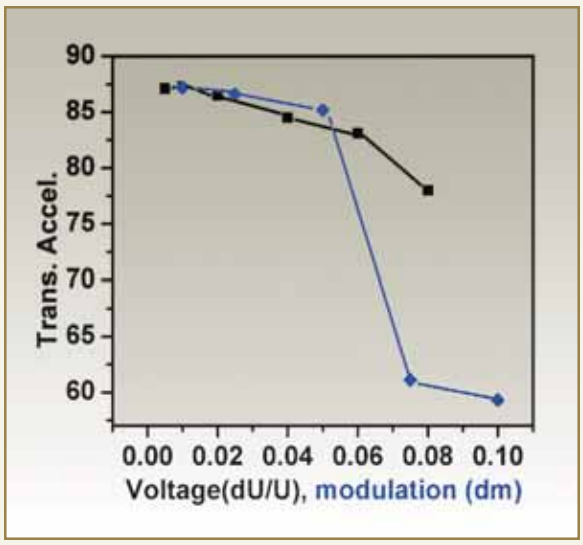

Fig. 17(a): Tolerance study for voltage and modulation errors

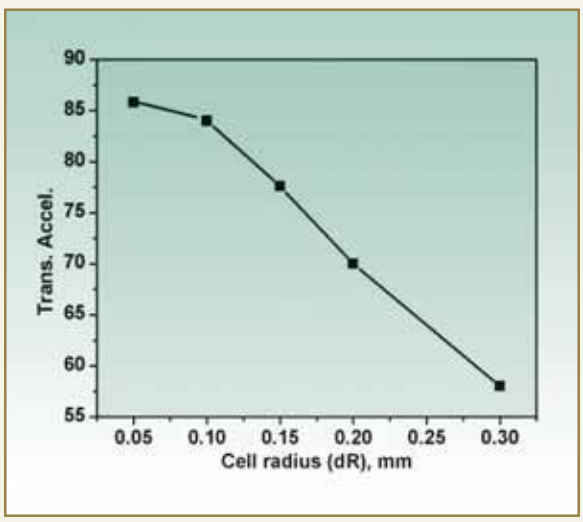

Fig. 17(b): Tolerance study for cell radius errors

realizations, dU / U = 0.04, dm = 0.05 and dR = 0.1mm was acceptable for Trans. Accel. greater than 84% (see Fig. 17 (a), 17 (b)). When these errors were simulated simultaneously, Trans. Accel. dropped to 72.6%.

Alignment errors were also simulated with a linear symmetric taper separately. From positive taper (away

from axis) of 200 μm to negative taper of 200 μm (towards axis) along the RFQ length, Trans. Accel. was within 1% of zero taper value. A negative taper was preferred, even at the cost of increasing surface field, to keep Long./Trans. frequency in check and to maintain adequate transverse focusing.

Electromagnetic Design

The detailed electromagnetic structure design of RFQ is in progress. The 3-D electromagnetic simulation of the heavy ion RFQ is performed, using SOPRANO module of OPERA-3D software [7]. The resonant structure of the RFQ consists of four electrodes called vanes, assembled in quadrupolar symmetry on support posts called stems, arranged on a base plate. Each stem holds two vanes, which are at the same potential. The vanes act as capacitors and the stems act as inductors. Two adjacent opposite stems holding the four vanes, make one RF cell. The RFQ assembly is schematically shown in Fig. 18. The resonant structure consisting of vanes, stems and base plate is enclosed in a rectangular cavity. The inter-stem distance, height and width of the stem was varied, to get the desired resonant frequency of 75 MHz. The quadrupole nature of electric field is evident near the vane-tip in Fig. 19. An extended vane type structure has been chosen, for the RFQ electrodes, for better mechanical strength and stability.

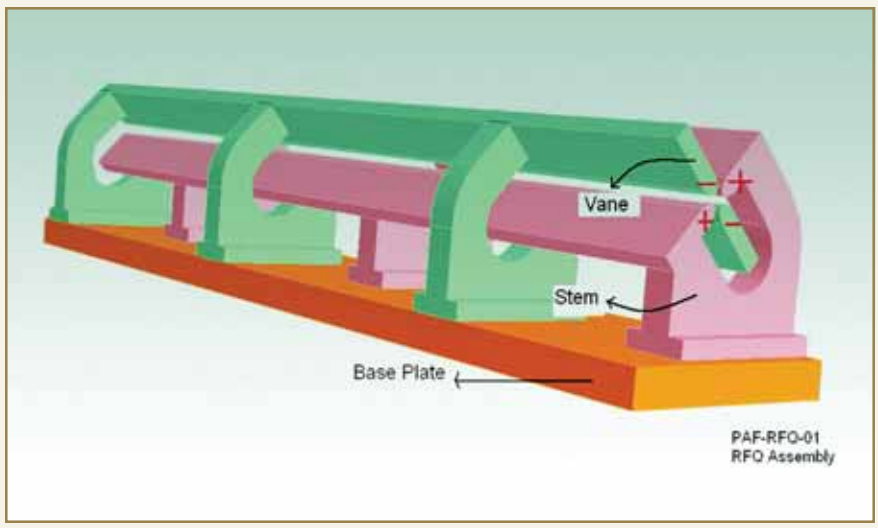

Fig. 18: Model of heavy ion RFQ

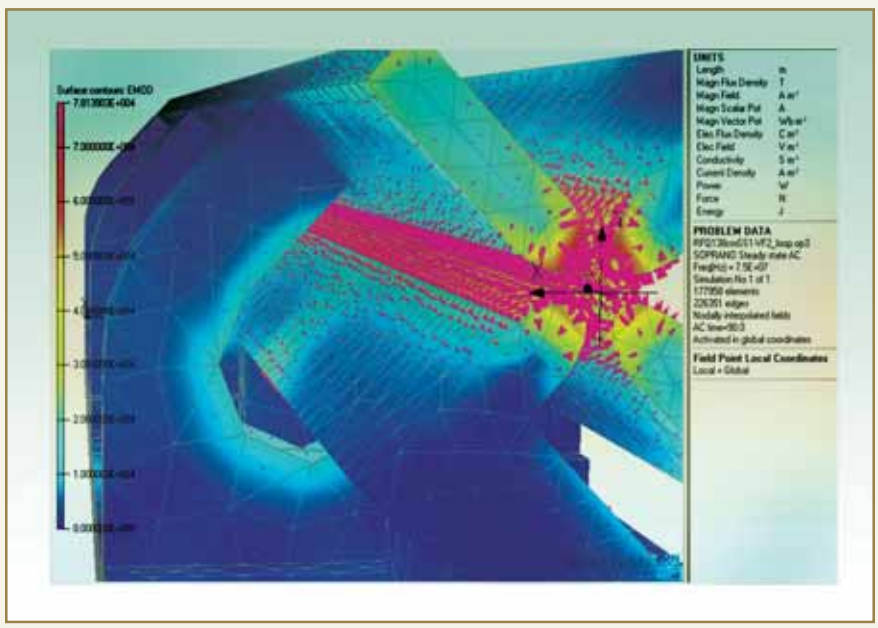

Fig. 19: Electric field on the vane surface

Results and Discussion

Having a same frequency prebuncher before RFQ, has manifold advantages. When compared to the without prebuncher case, this RFQ has a length shorter by 2m. This means that it will require about 80 KW less power than it's counterpart. Moreover, the phase width is ±9 degrees and momentum spread is ±0.35%, both of which are half of what they were, without prebuncher. This implies, that better beam quality is achieved at RFQ exit, for matching it into the next accelerating structure. Added to this is the increased transmission and accelerated particles, in contrast to the without prebuncher case.

Acknowledgement

We acknowledge the guidance and support of Dr. V. C. Sahni and Dr. S. S. Kapoor for this project.

References

1. http://www.pantechnik.fr
2. N. Mehrotra, et al., *NIM A* 545 (2005) 57-62.
3. LIDOS.RFQ.DESIGNERÔ Version 1.3, http://www.ghga.com/accelsoft/.
4. N. Mehrotra, et al., Indian Particle Accelerator Conference (InPAC-2005), March 1 - 5, VECC, Kolkata, pp.162-163.
5. N. Mehrotra, et al., DAE Symposium on Nuclear Physics, Vol 51(2006), pp. 668-669.
6. N. Mehrotra, et al., Indian Particle Accelerator Conference (InPAC-2005), March 1 - 5, VECC, Kolkata, pp.166-167.
7. OPERA-3D/SOPRANO v11.0 ©Vector Fields Limited, Oxford OX51JE, U.K. http://www.vectorfields.com/.

ABOUT THE AUTHORS

Mr. N. Mehrotra is from the 45th Batch of BARC Training School and joined the Nuclear Physics Division in 2002. He does beam dynamics design, electromagnetic design of accelerating structures and is also involved in ion source activities at Pelletron. His current field of interest is design and development of heavy ion RFQ Linac for the injector system to superconducting Linac at Pelletron Accelerator Facility.

Mr. P. V. Bhagwat, Head, Pelletron Accelerator Facility, is an accelerator technologist. He has participated in many accelerator activities of the department. His current fields of interest are room temperature RFQ Linac, accelerator based applications like AMS and Production of track etched membranes. He is heading the team working on the design and development of the alternate injector, for superconducting linear accelerator.

ABOUT THE AUTHORS

Dr. A. K. Gupta is an accelerator physicist specializing in ion sources and ion beam technology. His current fields of interest are atomic cluster physics, isotopic ratio measurements, alternate ECR injector system and radioactive ion beam development at BARC-TIFR Pelletron Accelerator Facility.

Mr. J. A. Gore is associated with the electronics group at BARC-TIFR Pelletron Accelerator Facility. He was on deputation at CERN, Geneva for magnetic measurements of superconducting magnets for LHC, under the Indo-CERN collaboration.He is presently involved in the development of beam diagnostic devices for high current proton accelerator and computer-based control systems for accelerator.

Mr. P. Surendran is an accelerator physicist working at BARC-TIFR Pelletron Accelerator Facility. He was on deputation at CERN, Geneva for magnetic measurements of superconducting magnets for LHC, under the Indo-CERN collaboration.He is actively involved in AMS and beam dynamics for the new injector system.

Dr. R. K. Choudhury is currently Head, Nuclear Physics Division. His research work is in the frontier areas of Nuclear Physics and accelerator-based applications. He has also contributed to accelerator technology developments. During his tenure as Director, IOP, Bhubaneshwar, he successfully completed the commissioning of the AMS programme for radiocarbon dating with the 3MV tandem accelerator.

Dr. S. Kailas is currently Associate Director (N), Physics Group. He is a fellow of Indian Academy of Science. His current areas of interest are basic research in the frontier areas of Nuclear Physics and accelerator-based applications such as accelerator driven sub-critical system, accelerator mass spectrometry, track etch membrane etc. He is also leading a team for heavy ion based alternate injector for the Pelletron Accelerator.

बीएआरसी न्यूज़लैटर
BARC NEWSLETTER

ACCELERATOR MASS SPECTROMETRY PROGRAMME AT BARC-TIFR PELLETRON ACCELERATOR

P. Surendran, A. Shrivastava, A.K. Gupta, J.P. Nair, M.L.Yadav, J.A. Gore, H. Sparrow, P.V. Bhagwat and S. Kailas
Nuclear Physics Division

This paper was awarded the Best Poster Presentation Prize at the BARC Golden Jubilee DAE-BRNS Indian Particle Accelerator Conference (InPAC-2006), held at BARC and TIFR from Nov. 1-4, 2006

Introduction

Accelerator-based Mass Spectrometry (AMS), is an ultra sensitive means of counting individual atoms, having sufficiently long half life and available in small amount. The 14 UD Pelletron Accelerator is an ideal machine to carry out AMS studies with heavy isotopes like ^{36}Cl and ^{129}I. Cosmogenic radioisotope ^{36}Cl is being widely detected using AMS, as it has applications in ground water research, radioactive waste management, atmospheric ^{36}Cl transport mechanism studies of Arctic Alpine ice core etc. [1]. As part of the ongoing AMS programme at 14 UD Pelletron Accelerator Facility at Mumbai [2], a segmented gas detector developed for identification of ^{36}Cl was tested for performance [3]. Recently, a beam chopper required for this measurement has been developed. Further progress made in this programme, is discussed in this paper.

Beam Optimization

^{35}Cl and ^{37}Cl beams from a natural sample (AgCl), were transported through the machine up to the Faraday Cup, just before the detector system and their ratios were matched to their natural abundance values. This was done, by operating the machine in GVM mode and alternately injecting the two isotopes, ^{35}Cl and ^{37}Cl, into the accelerator and changing the terminal voltage while keeping magnetic rigidity (ME / q2) of analyzing magnet, quadrupole and steerers the same. The magnetic field of the analyzing magnet was set at 4623.149 Gauss and the terminal voltage at ~7MV to get 56 MeV of ^{36}Cl and ^{36}S beams of charge state 7^+.

Detector Details

As the interfering isobar in the ^{36}Cl detection is ^{36}S, the most suited detector is a split anode ionization chamber, which was developed indigenously [3]. This detector has three anodes followed by one Silicon surface barrier detector. The detector window is made from 3.5 micron thick Mylar foil.

A schematic diagram and photograph of the detector are given in Fig.1a and Fig.1b repectively.

Energy loss curves for ^{36}Cl and ^{36}S in P10-gas at pressure of 58 mbar is shown in Fig. 2.

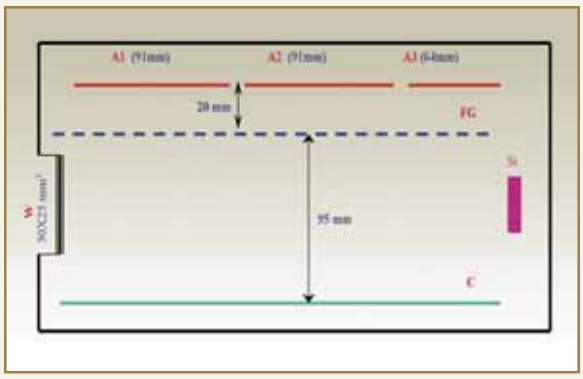

Fig. 1(a): Gas detector schematic

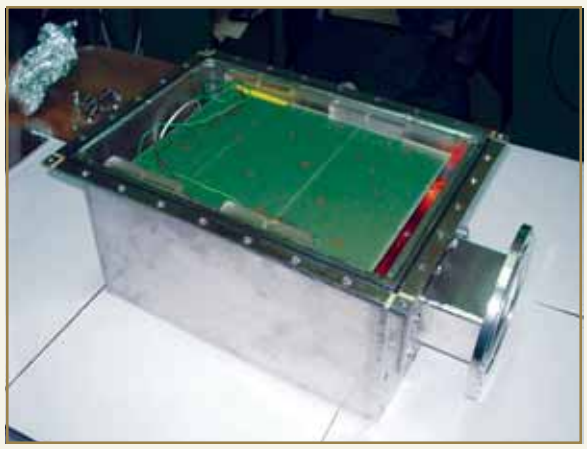

Fig. 1(b): Gas detector

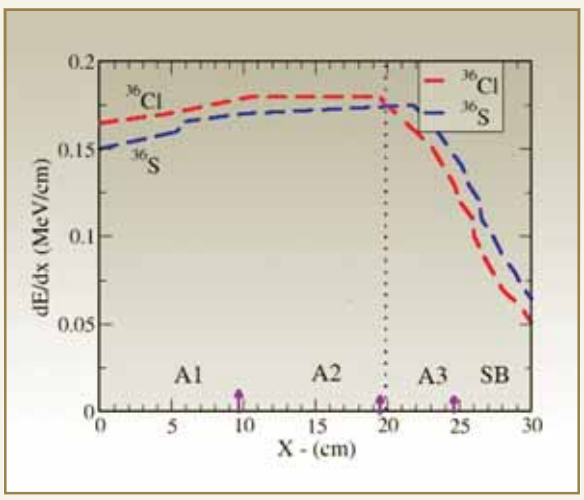

Fig. 2: Energy loss curves for ^{36}Cl & ^{36}S

Sample Preparation

About one gram of Sodium Chloride (NaCl) crystals was irradiated with thermal neutrons at the Apsara reactor, BARC, to produce ^{36}Cl through the nuclear reaction ^{35}Cl(n,λ)^{36}Cl. The irradiated sample was dissolved in de-ionized water and mixed with silver nitrate solution, to get silver chloride precipitated. The precipitate was filtered, washed with de-ionised water and heated in an oven for more than twenty four hours to make it anhydrous. It was then pressed in the ion source sample holder.

Measurements and Results

The detector was calibrated using very low currents of ^{35}Cl and ^{37}Cl (keeping ion source filament current very low) from the natural sample. Filament current was increased and Mass 36 was selected by injector magnet and transported through the machine up to the detector. Background ^{36}S (coming from the ion source as an impurity or memory effect) was identified in the detector. At this point, ion source sample was changed to the enriched one, containing ^{36}Cl and the same procedure was repeated. The distinct peaks of ^{36}Cl and ^{36}S could be seen in the signals from anode A2 and Silicon detector (Figs. 3a, b). By measuring the yield of ^{36}Cl in the detector and the ^{35}Cl beam intensity in the Faraday cup located in front of the detector, ratio ^{36}Cl / ^{35}Cl in the sample was found to be approximately $1.5*10^{-10}$. However, this value is two orders of magnitude less than the calculated one, based on irradiation conditions. This discrepancy needs to be understood.

Conclusion

We have successfully, demonstrated the detection and identification of ^{36}Cl in the presence of rather intense ^{36}S-background. We are planning to carry out another measurement with dated sample in the next available beam time, to precisely determine the ^{36}Cl / ^{35}Cl ratio. It is proposed to use the chopper for optimum performance.

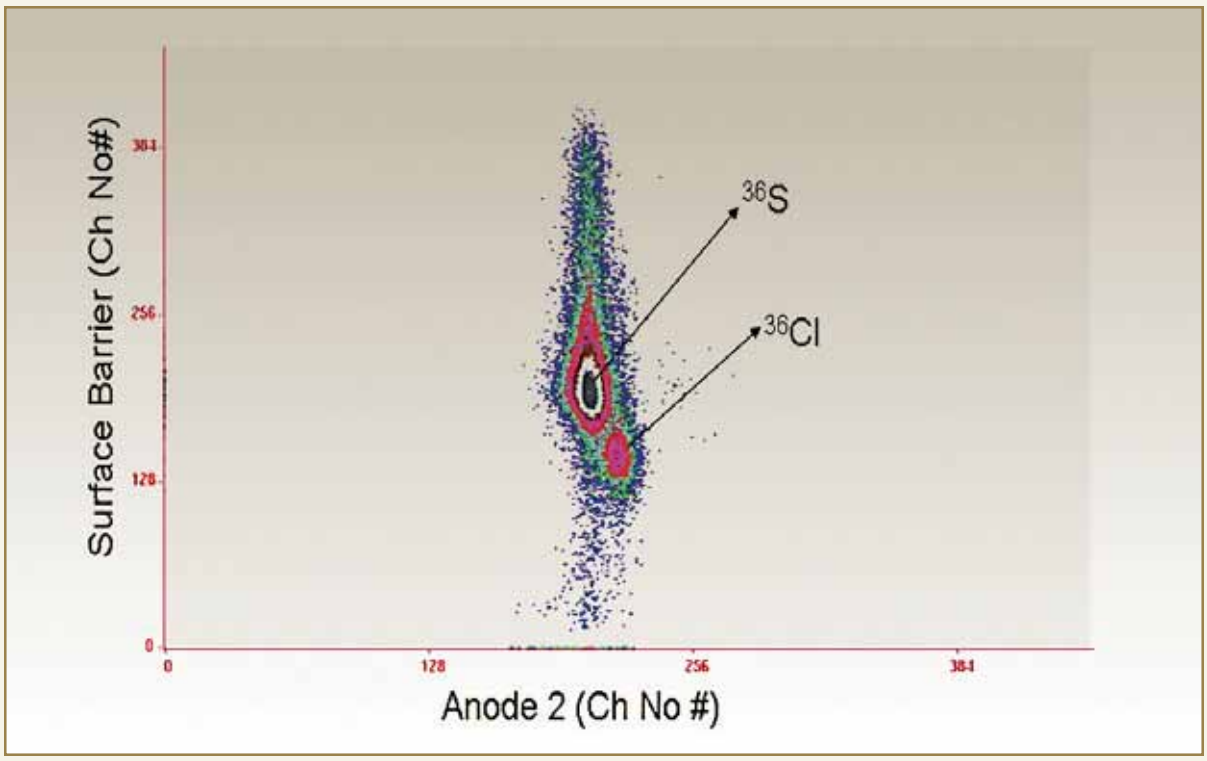

Fig. 3(a): Detector spectra

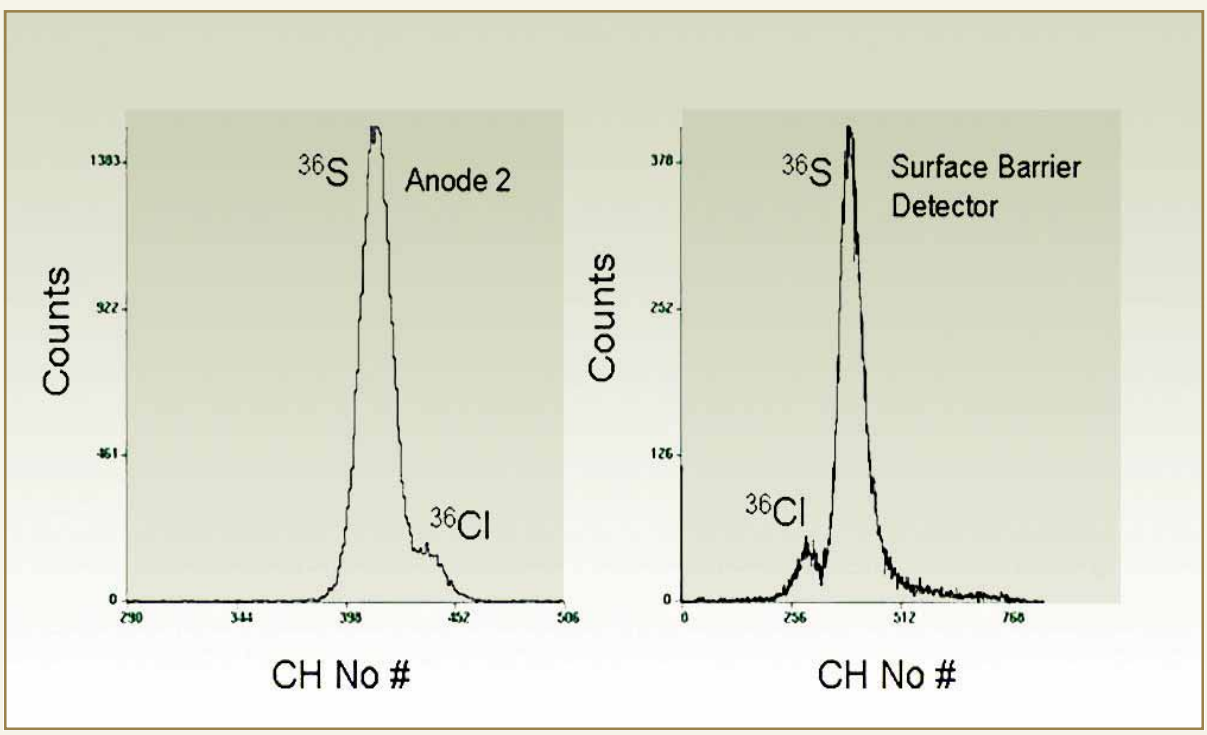

Fig. 3(b): Detector spectra

We acknowledge the support of the staff of Apsara reactor for providing irradiated sample. The efforts put in by Ms. Deepa Thapa and Mr. Mahadkar for sample preparation, are sincerely acknowledged.

References

1. L.K.Fifield. *Rep. Prog. Phys*. 62, 1223 (1999).
2. S.Kailas et al. Indian Particle Accelerator Conference-2003, p. 692.
3. A.Shrivastava et al. Xth ISMAS Symposium-2006, p.158.

ABOUT THE AUTHORS

Mr. P. Surendran is an accelerator physicist working at BARC-TIFR Pelletron Accelerator Facility. He was on deputation at CERN, Geneva for magnetic measurements of superconducting magnets for LHC, under Indo-CERN collaboration.He is actively involved in AMS and beam dynamics for new injector system.

Dr. (Ms.) A. Shrivastava is a nuclear physicist working in the Nuclear Physics Division. Presently she is working on Nuclear Reaction studies with weakly bound and Radio Active Ion beams and AMS. She has worked in the area of Radio Active Ion beams at Orsay, France and GSI, Germany.

Dr. A. K. Gupta is an accelerator physicist specializing in ion sources and ion beam technology. His current fields of interest are atomic cluster physics, isotopic ratio measurements, alternate ECR injector system and Radioactive Ion Beam development at BARC-TIFR Pelletron Accelerator Facility.

Mr. J. P. Nair is working at BARC-TIFR Pelletron Accelerator Facility and his field of activity is Track Etch membrane filters and other accelerator-based applications.

ABOUT THE AUTHORS

Mr. M. L. Yadav is associated with the Electronics group at BARC-TIFR Pelletron Accelerator Facility. His current field of interest is accelerator-based electronics and instrumentation.

Mr. J. A. Gore is associated with the Electronics group at BARC-TIFR Pelletron Accelerator Facility. He was on deputation at CERN, Geneva for magnetic measurements of superconducting magnets for LHC, under Indo-CERN collaboration.He is presently involved in the development of beam diagnostic devices, for high current proton accelerator and computer-based control system for accelerator.

Mr. Hillary Sparrow is associated with BARC-TIFR Pelletron Accelerator Facility and is instrumental in accelerator maintenance and accelerator-based applications.

Mr. P. V. Bhagwat, Head, Pelletron Accelerator Facility, is an accelerator technologist. His current fields of interest are accelerator-based applications like AMS and Production of track etched Membranes. He is heading the team working on design and development of the alternate injector for superconducting linear accelerator.

Dr. S. Kailas is currently Associate Director (N), Physics Group. He is a fellow of Indian Academy of Sciences. His current areas of interest are basic research in the frontier area of Nuclear Physics and accelerator-based applications such as accelerator driven sub-critical system, accelerator mass spectrometry, track etch membrane etc. He is also leading a research team for heavy ion based alternate injector for the Pelletron Accelerator.

PULSE RADIOLYSIS STUDIES OF 3-HYDROXYBENZYL ALCOHOL

S.B. Dhiman and D.B. Naik
Radiation and Photochemistry Division

This paper was awarded the Best Poster Presentation Award at the National Symposium on Radiation and Photochemistry (NSRP-2007) held at the National Centre for Ultrafast Processes, University of Madras, Chennai, during January 29-31, 2007

ABSTRACT

Pulse radiolysis studies of 3-hydroxybenzyl alcohol (3-HBA) were carried out at various pHs. At pH 6.8 OH-radicals were found to react with 3-HBA ($k = 2 \times 10^9$ dm^3 mol^{-1} s^{-1}) giving an species having absorption maximum at 340 nm, which decayed by unimolecular process ($k_1 = 1.5 \times 10^5$ s^{-1}) to another transient species having absorption maxima at 290 and two closely lying peaks at 390 and 410 nm. Latter time window spectrum is assigned to phenoxyl radicals by comparing spectrum of the species formed in reaction of $N_3^{\cdot}$ radicals with 3-HBA. At pH 6.8, decay of OH adduct as well as formation rate of phenoxyl radicals were found to increase with buffer ion concentrations. At pH 6.8, in addition to adduct species, OH radicals were found to abstract H-atoms from $-CH_2OH$ group giving reducing radicals. At pH 1, reaction of OH radicals ($k = 4 \times 10^9$ dm^3 mol^{-1} s^{-1}) with 3-HBA, exclusively gives phenoxyl radical as confirmed by the formation of identical species in the reaction with $Cl_2^{\cdot -}$ radicals. At pH 13.3, where 3-HBA exists in anionic form, reaction of $O^{\cdot -}$ radicals was found to give a mixture of phenoxyl radicals and reducing radicals by H-abstraction from $-CH_2OH$ group. H-atoms also reacted with 3-HBA ($k = 3 \times 10^9$ dm^3 mol^{-1} s^{-1} giving the transient species ($\lambda_{max} = 330$ nm) which were capable of reducing methylviolgen quantitatively, suggesting that H-atoms also abstract H-atom from $-CH_2OH$ group 3-HBA.

Introduction

There have been reports that hydroxybenzyl alcohols (HBA) that are biologically important molecules, are very good free radical scavengers.[1,2] However there are no studies on kinetic and mechanism of their free radical induced oxidation activities. Reactions of OH radicals give adduct species, which in turn decay to phenoxyl radicals depending on the nature of substitution.[3] Due to the presence of phenolic OH group and–CH2OH group in HBA, reactions of hydroxyl radical with HBA, can take place either by addition pathway, one electron oxidation as well as H-atom abstraction. In connection with earlier studies carried out on radiolytic reactions of 2-hydroxybenzyl alcohol and 4-hydroxybenzyl alcohol, studies on their isomer viz. 3-hydroxybenzyl alcohol (3-HBA) were carried out, to have structure-reactivity relationships. We have characterized the transient species formed at various pHs in the reactions with of .OH/O.- radicals with

3-HBA-based on spectral characteristics and comparison with phenoxyl radicals generated exclusively with specific oxidants such as N3. and a suitable reaction mechanism is given in this paper.

Experimental

3-hydroxybenzyl alcohol (3-HBA) was obtained from Fluka Co and was used as such. Solutions were prepared using water from Millipore A-10 system having conductivity less than 0.1 μS/cm. Gases such as N_2, O_2 and N_2O used for saturating the solutions were of IOLAR/Instrument grade from Indian Oxygen Ltd. pH of the solutions were adjusted using NaOH, $HClO_4$, KH_2PO_4 and Na_2HPO_4 at appropriate concentrations. Details of the pulse radiolysis set up are described elsewhere. [4,5] 50 ns pulses of 7-MeV electrons from linear electron accelerator were used for irradiation and the pulse dose was about 15 Gy. Pulse dosimetry was performed by using 0.01 mol dm^{-3} potassium thiocyanate solution, using a value of 21520 for (G.e) for $(SCN)_2^{\cdot-}$ per 100 eV at 500 nm.[6]

Results and Discussion

Reactions of OH radicals with 3-HBA were studied at pH 6.8. Time resolved absorption spectra of the transient species formed on pulse radiolysis of N_2O saturated 1 x 10^{-3} mol dm^{-3} 3-HBA solution at pH 6.8 is given in Fig. 1. As can be seen from Fig. 1, the initial species has absorption maximum at 340 nm, which decayed by unimolecular process ($k_1 = 1.5 \times 10^5\ s^{-1}$) to give a species having absorption maxima at 290 and two closely lying peaks at 390 and 410 nm. Rate constant for the reaction of OH radicals with 3-HBA was determined to be 2 x 10^9 dm^3 mol^{-1} s^{-1} by following the build up of transient absorption at 340 nm.

Absorption spectrum of the transient species formed in the reaction of $N_3^{\cdot}$ radicals with 3-HBA was recorded

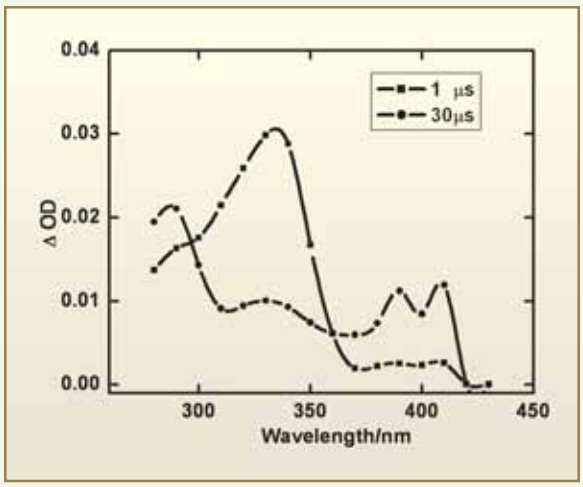

Fig. 1: Time resolved absorption spectra of the transient species formed on pulse radiolysis of N_2O saturated 1 x 10^{-3} mol dm^{-3} solutions of 3-HBA at pH 6.8.

in N_2O saturated 3-HBA solutions, containing 0.02 mol dm^{-3} NaN_3 and the same is given in Fig. 2.

Spectrum in Fig. 2 matches quite well with latter time window spectrum in Fig. 1. Thus it can be concluded that initial 3-HBA-OH adducts formed decay to give phenoxyl radicals of 3-HBA. Some proportion of OH radicals can react with 3-HBA by H-abstraction from

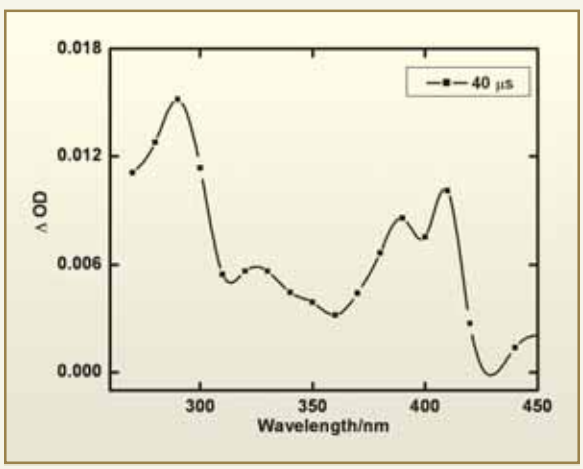

Fig. 2: Absorption spectra of the transient species formed on pulse radiolysis of N_2O saturated 1 x 10^{-3} mol dm^{-3} solutions of 3-HBA at pH 6.8 containing 0.02 mol dm^{-3} NaN_3.

–CH_2OH group giving radicals containing –C·HOH species which are reducing radicals. The yield of these radicals was determined by measuring the yield of methyl viologen radical cation which has strong absorption at 395 and 600 nm. It was estimated that 28% of the OH radicals react by H-abstraction from –CH_2OH groups.

At pH 6.8, experiments were carried out to investigate the dependence of decay rate of OH adducts on buffer concentrations. Equimolar concentrations of KH_2PO_4 and Na_2HPO_4 in the range 0.0005 mol dm^{-3} to 0.2 mol dm^{-3} were used. It was found that both the decay rate as well as rate of formation of phenoxyl radicals increases with buffer ion concentrations. Rate constant for the formation of phenoxyl radical varied from 4.2×10^4 s^{-1} at 0.001 M to 2.9×10^5 s^{-1} at 0.04 mol dm^{-3} buffer ion concentration. In Fig. 3, absorption traces obtained at 340 nm at different buffer ion concentrations are given. Traces showing the build-up of transient absorption at 410 nm due to phenoxyl radicals of 3-HBA are given in Fig. 4.

These traces clearly show that increase in the rate of formation with buffer is initially more pronounced and after certain concentration it reaches a plateau value. By making use of these traces, first order rate constant

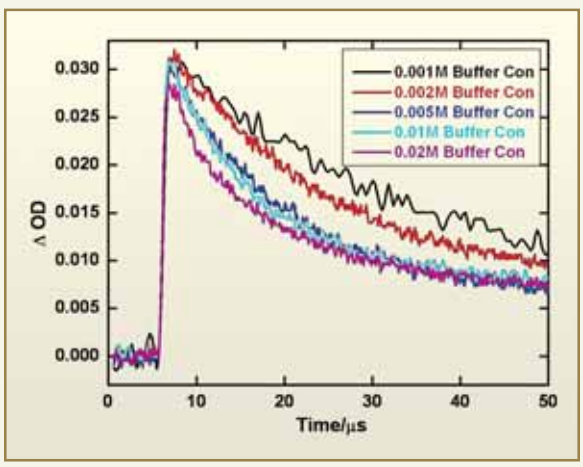

Fig. 3: Absorption traces obtained at 340 nm in N_2O saturated 1 x 10^{-3} mol dm^{-3} 3-HBA solution at various buffer ion concentations

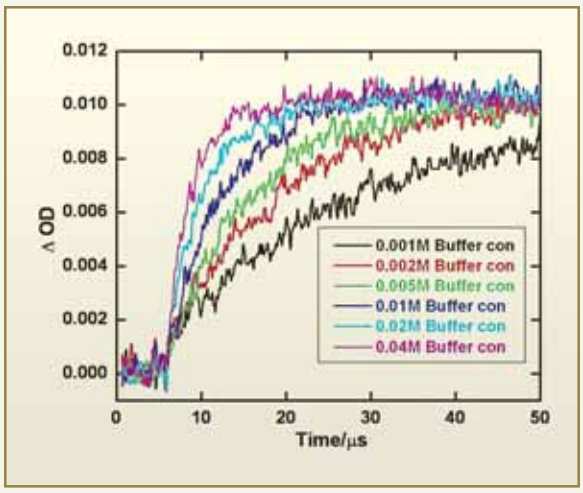

Fig. 4: Absorption traces obtained at 410 nm in N_2O saturated 1 x 10^{-3} mol dm^{-3} 3-HBA solution at various buffer ion concentations

values were determined and the same are plotted against buffer ion concentration in Fig. 5.

At pH 1, in O_2 satuarated solution reaction of OH radicals with 3-HBA radiolysis directly gave phenoxyl radicals.(Fig. 6). Spectra of the species formed was

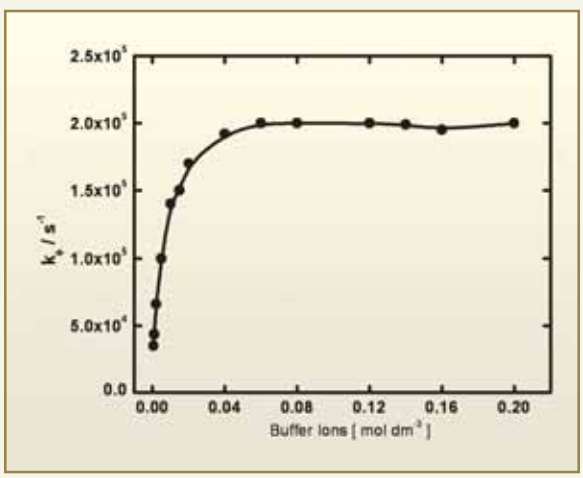

Fig. 5: Plot of first order rate constant for the formation of phenoxyl radical at 410 nm versus the buffer ion concentration

identical with that formed in the reaction of $Cl_2^{\cdot-}$ radicals with 3-HBA at pH 1. This showed that due to

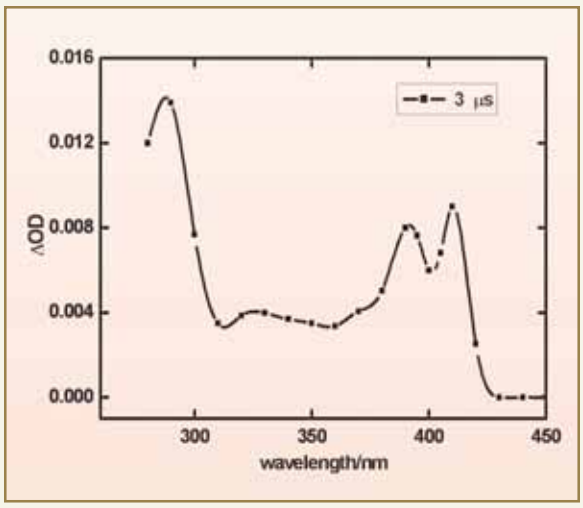

Fig. 6: Absorption spectrum of the transient species formed on pulse radiolysis of O_2 saturated 1 x 10^{-3} mol dm^{-3} solutions of 4-HBA at pH 1

higher reduction potential of OH radicals at pH 1 as compared to that at pH 6.8, it is able to oxidise 3-HBA quantitatively.

3-HBA has pKa 9.5 above which it exists in the deprotonated form. Reactions of OH radicals with 3-HBA were investiagtd at pH 10.5, with the aim to estimate the different pathways. Absorption spectrum of the transient species indicated, that there is direct formation of phenoxyl radicals. Electron transfer to methyl viologen showed that nearly 28% of the OH radicals abstract H-atom from –CH2OH group. Based on these observations, following Scheme 1 has been assigned for the reaction of OH radicals with 3-HBA at pHs 1, 6.8 and 10.5.

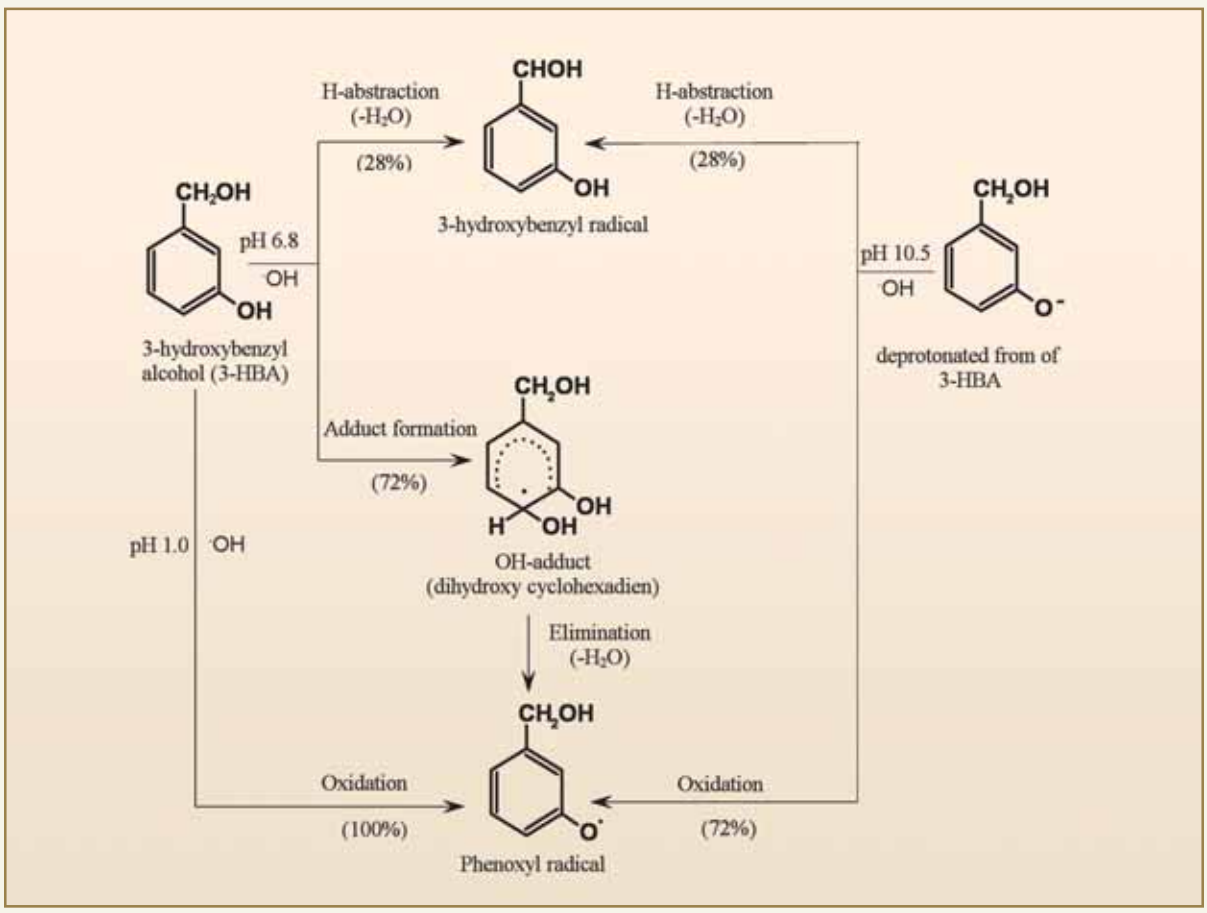

Scheme 1: Reaction pathways in reaction of OH radicals with 3-HBA at different pHs

Conclusions

Present study shows that hydroxyl radicals react with 3-hydroxybenzyl alcohol mainly by adduct formation reaction. Subsequent decay of the adduct to phenoxyl, depends very much on the phosphate buffer ion concentrations. Both with neutral and anionic forms of HBA, OH radical reaction give equal proportion of adduct as well as reducing radicals formed on H-atom abstraction from $-CH_2OH$ group.

Acknowledgement

The authors thank Dr. S.K. Sarkar, Head, Radiation & Photochemistry Division and Dr. T. Mukherjee, Director Chemistry Group, BARC for their support to this work.

References

1. Liu, J.; Mori, A. *Neuropharmacology* 1992, *31*, 1287.
2. Li, H-X.; Ding, M-Y.; Yu, L-Y. *J. Chromatogr. Sci.* 2001, *39*, 393.
3. Raghavan, N. V.; Steenken, S. *J. Am. Chem. Soc.* 1980, *102*, 3495.
4. Guha, S. N.; Kishore, K.; Moorthy, P. N.; Naik, D. B.; Rao, K. N. *Proc. Indian Acad. Sci. (Chem.Sci.)* 1987, *99*, 261.
5. Mukherjee, T. In: *Atomic, Molecular and Cluster Physics* S. A. Ahmad, (Ed.), Narosa: New Delhi, 1997, p. 299.
6. Fielden, E. M. In *The study of fast processes and transient species by electron pulse radiolysis*; Baxendale, J. H. and Busi, F. (Eds.), D. Riedel Publishing Co. Dordrecht Holland, 1982, p. 49-62.

ABOUT THE AUTHORS

Mr. S.B. Dhiman did his Post graduation in Physical Chemistry from University of Mumbai in 2003. Presently he is Senior Research Fellow under BARC-University of Mumbai Collaborative Scheme and doing research work in Radiation and Photochemistry Division of BARC. His research interests are in understanding the mechanism of free radical reactions in aqueous solutions involving biologically organic compounds. He was in Hahn Meitner Institute, Berlin, for nearly 3 months during 2007 and carried out studies concerning initial stages of silver nano particle formation in radiolysis.

Dr. D.B. Naik obtained is M.Sc. in Physical Chemistry from Karnatak University Dharwad. After successful completion of training from 27th Batch of BARC Training School, he joined the Chemistry Division of BARC in 1984. He was involved in setting up of pulse radiolysis facility in Chemistry Group. Using this facility he has carried out studies on a number of research topics of interest in Chemistry and Biology. In addition to this, he has also studied fast reactions in photo and radiation chemistry in homogeneous as well as microheterogeneous media. He obtained his Ph.D. from University of Mumbai in 1992. He was awarded Alexander von Humboldt Research Fellowship in 1993 and worked in Hahn Meitner Institute, Berlin. He has published nearly 70 research papers in peer reviewed journals. He is actively involved in the activities of Indian Society for Radiation and Photochemical Sciences (ISRAPS) as well as the Indian Chemical Society (Mumbai Branch) in various capacities.

बीएआरसी न्यूज़लेटर
BARC NEWSLETTER

SPECIATION OF METALS IN URANIUM MILL TAILINGS USING SEQUENTIAL EXTRACTION TECHNIQUE

Suchismita Mishra, Sunil Bhalke, B. Suseela, G.G. Pandit and V.D. Puranik
Environmental Assessment Division

This paper was awarded the Best Poster Presentation award (First Prize) at the National Symposium on Environment-XV (NSE-15) held at Coimbatore, during June 5-7, 2007

ABSTRACT

Mining sites contain residues from ore processing operations that are characterized by high concentrations of heavy metals. The form in which a metal exists strongly influences it's mobility and thus, it's effects on the environment. Operational methods of speciation analysis, such as the use of sequential extraction procedures, are commonly applied.

Investigation of the existing chemical forms and the concentrations of Mn, Pb, Cu, Fe, Zn and Natural U in uranium mill tailing samples from Jaduguda were carried out. The concentrations of Nat. U was found to vary from 81.05 to 120.21 $\mu g\ g^{-1}$ and most common mode of occurrence of Nat. U in the tailings is in association with exchangeable species, Fe-Mn oxides and residual form. The dominant chemical form of Nat. U in TP-2 was exchangeable species. The concentration of Mn, Pb, Cu and Zn ranged from 326.5-1395.86, 28.6-41.4, 214.97-508, 16.49-20.93 $\mu g\ g^{-1}$, respectively.

Introduction

Environmental pollution by heavy metals originating from mines, can become a very important source of contamination both in soil and water. Therefore, chemical as well as physical characterization of mining tailings is very important, to assess the risk of potential environmental mobility of toxic trace metals that are contained in this kind of waste. To assess the impact of trace elements on environment from uranium mill tailings, not only the total metal content, but also it's mobility and bio-availability should be considered. Uranium tailings are generated as solid and liquid wastes in uranium mining or milling operations. Since most of the uranium deposits in the world have low grades, millions of tonnes of such wastes are produced annually. The potential environmental hazards of uranium tailings arise, when the disposal site is abandoned after decommissioning of the uranium mill. Huge amounts of solid wastes as small particles of depleted ore remain in place. Water plays a dual role by triggering a sequence of reactions and by carrying contaminants away from the wastes site. The main concern during the operation of a disposal site, is the presence of radium in water. The leaching of toxic constituents however becomes effective, so long as

the tailings are in loose form. This is because of the acid generating properties of the pyrite, a substantial constituent of the tailings. Two types of contaminants tend to leave the solid and migrate to the pore water. These are the heavy metals and the radioactive elements. Pollution problems may arise if toxic heavy metals are mobilized into the soil solution and are either taken up by plants or transported in drainage waters to associated water supplies. The metals may then enter the human food chain through the consumption of such plants.

Extraction with specific reagents provides information on the association of metals in different phases and metal release when changes in geochemical conditions occur. However, the determination of specific chemical species or binding forms is difficult and often hardly possible. For this reason, experimental approach commonly used for studying the mobility, transport and bio-availability is the use of selective sequential extraction procedures. Sequential extraction procedures are commonly applied because they provide information about the fractionation of metals in different lattices of the solid sample which is a good compromise to give information on environmental contamination risk. Many of these schemes used are based on the five stages or it's modifications. These sequences are designed to differentiate between the exchangeable, carbonate, reducible (Fe / Mn oxides), oxidizable (sulphides and organic phases) and residual (mineral) fractions. Although the procedures are very tedious and time consuming, the results furnish detailed information about the origin, mode of occurrence, bioavailability, potential mobility and transport of metals in natural environment.

The objective of this work is to investigate the total metal content (Mn, Pb, Cu, Fe, Zn and U) and estimate phase-wise distribution of these metals, using sequential extraction technique proposed by Tessier et al, with slight modification in different operating conditions.

Experimental

Sampling Location

Tailing samples were collected from Jaduguda, where the tailing ponds are located in a valley surrounded on three sides with hills and man-made embankment on the fourth side. These tailing ponds are filled with effluent obtained after the ion exchange process of uranium removal and the fine particles obtained after the secondary filtration of barren liquor. Representative samples were collected by random sampling methods from the three tailing ponds. Among the three tailing ponds, tailing pond 3 is being utilized for tailing disposal at present.

Reagents

All reagents were of analytical reagent grade. Deionized water, further purified using a TKA water purification system (Germany), was used throughout. Aqueous certified Atomic Absorption Standards of elements were used. Electronic grade acids were used throughout the processing. All standards and reagent solutions were stored in thoroughly acid-cleaned containers.

Instrumentation

The concentration of Mn, Pb, Fe, Cu and Zn in different phases of uranium tailings after sequential extraction with specific reagents were analyzed using GBC-Avanta, Atomic Absorption Spectrophotometer. The concentration of Nat. Uranium in the processed samples was estimated by Adsorptive Stripping Voltammetric (AdSV) technique (Methrom, PG Stat Auto-20) with hanging mercury drop electrode.

A commercially available Microwave Sample Preparation System, Model MLS 1200 MEGA (Milestone) featuring programmable mineralization procedure parameters was used, for microwave digestion of tailing samples. pH measurements were performed with an Orion Research pH meter.

Total concentration of elements

The total Mn, Pb, Cu, Fe, Zn and Natural U concentrations in the uranium mill tailing samples were measured following microwave digestion of the tailing samples. About 1.0 gm of tailings was taken and digested using Nitric acid and HF (2:1) mixture in a microwave digester. To validate the method, IAEA-433 marine sediment standard reference material was measured. Observed and certified results are given in Table 1. All the metals (Mn, Pb, Fe, Cu and Zn) were analyzed using AAS and Nat. U was analyzed using DPASV in these processed samples.

Multi-step sequential extraction

The sequential extraction scheme applied to the samples with some modifications in different operating conditions. The extraction was carried out in microwave digestion system instead of shaking for a long time. There are a number of reports, suggesting that the extraction should be carried out at ambient temperature for fear that other phases could be leached at elevated temperatures. It was reported that no significant difference in extractability was evident, when microwave accelerated extraction was compared with the conventional procedure for the National Bureau of Standards (USA) SRM 1645 sediment sample. It was reported that extraction of the reducible fraction was not complete, if performed at ambient temperature. It has been recommended that the extraction times of the different steps in sequential extractions should be kept as short as possible, so as to minimize the opportunity for readsorption to take place. Considering all the facts, sequential extraction was carried out using microwave digestion system.

Approx. 6.00 gm of sample was dried in an oven at 60 °C for 24 hour in order to avoid, as far as possible, the transformation of some chemical forms (exchangeable and carbonate).This procedure includes five fractions. The extractants and operationally defined chemical fractions were as follows.

***Fraction 1* (F1):** Exchangeable and water soluble: Approx. 6 gm of sample was extracted with 60 ml of water twice, 30ml each time in ultrasonic bath for 2 hours. The supernatant was collected in a beaker and residue was extracted with 40 ml of 1M $MgCl_2$ at pH 5.0 using microwave digestion system. The $MgCl_2$ extract was centrifuged and mixed with water soluble extract.

Table 1: Observed values in IAEA-433 marine sediment certified reference material

Element	Unit	IAEA-433	
		Observed Conc.	Certified Conc.
Mn	$\mu g\ g^{-1}$	318 ± 14	316 ± 16
Pb	$\mu g\ g^{-1}$	26.5 ± 2.3	26 ± 2.7
Cu	$\mu g\ g^{-1}$	30.3 ± 2.2	30.8 ± 2.6
Fe	$mg\ g^{-1}$	41.2 ± 2.0	40.8 ± 1.9
Zn	$\mu g\ g^{-1}$	99.3 ± 6	101 ± 8
Nat. U	$\mu g\ g^{-1}$	2.5 ± 0.3	2.45 ± 0.24

***Fraction 2* (F2):** Elements associated with carbonates or specifically adsorbed: The residue obtained from first step was treated with 40 ml of 1M sod. acetate and acetic acid (pH 5.0) in microwave digester.

***Fraction 3* (F3):** Elements associated with Fe-Mn oxides: Residue from second step was treated with 40 ml of 0.04 NH_2OH. HCl in 25 % Acetic acid in microwave oven.

***Fraction 4* (F4):** Elements associated with organic matter and sulphides; Residue from step three was treated with 40 ml of H_2O_2 (30 %) and 0.02 M HNO_3 at pH 2 in microwave oven.

***Fraction 5* (F5):** Residual elements: It was treated with HNO_3 and HF (2:1) mixture in microwave digester. The multistage extractions were carried out for each fraction using microwave digester. The extract was centrifuged for 30 min. at 4000 rpm to collect the supernatant. The residue was washed with distilled water after each extraction and the washing was mixed with the respective fraction. After extraction each fraction was further digested with HNO_3 and $HClO_4$ mixture and the final solution was taken in 0.25 % HNO_3 and stored in glass containers until analysis, using AAS and DPASV.

Result and Discussion

Figs. 1 and 2 give the total metal content of tailings and pH of samples collected from different tailing ponds at Jaduguda. It shows that TP-1 and TP-2 are acidic and TP-3 is under neutral environment.

The concentrations of most of the metals are comparable with that of normal soil, with an exception of U and Cu. This is expected because the region belongs to highly mineralized area. Since the tailings are at a different environmental condition, there is always a possibility of change of state of these metals. Studying the impact of metals in environment, it is very important to know the different chemical form of the specific metal, which actually decides the mobility and bioavailability of the metal, under various conditions. For that, a five stage sequential extraction scheme was applied in these different tailing pond samples, to find out the partitioning of metal in different phases.

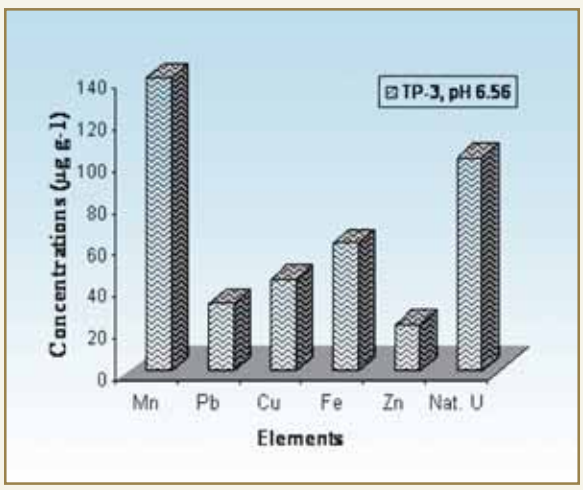

Fig. 2: Total concentration of metals in tailings at TP-3; (Fe is in mg g^{-1}; Actual values of Mn & Cu are 10 times more than the graph i.e., 1423 & 432 µg g^{-1} respectively).

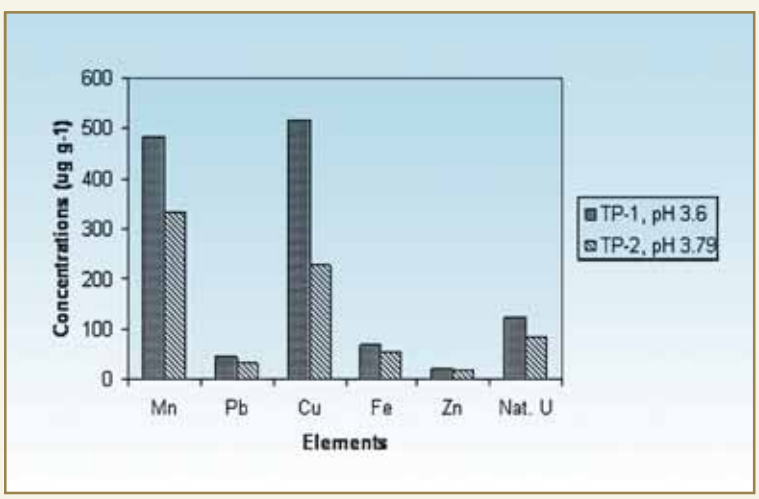

Fig. 1: Total concentration of metals in tailings at TP-1 and TP-2; (Fe is in mg g^{-1}).

Metal Speciation

In the sequential extraction scheme used in this study, the mobility and hence possible bioavailability of metals decrease, in the order of extracted fractions from readily exchangeable to residual. Table 2 gives the experimental results obtained for the five fractions in sequential extraction steps. The average percentage of total metals belonging to each fraction are represented in a bar diagram in Fig. 3. The important findings of this work are detailed in the following sections.

Fraction 1

The fraction comprises of water soluble and exchangeable part. All the metals are extracted significantly in this fraction except Fe. The extraction of Mn, Cu and U(Nat.) is more in TP-1 and TP-2 samples, 38 % - 50 %, 53 % -57 % and 24 % - 42 % respectively than TP-3, 32 %, 35 % and 18 % respectively which is currently in use. The acidic environment at TP-1 and TP-2 may favour these extractions.

But there is a deviation observed in the case of Pb. In TP-3 Pb extraction was 61 % where as in TP-2 and TP-3 the extraction limits were 9 % - 17 %. TP-3 showed Pb fraction higher in exchangeable fraction indicating more mobility of this metal and therefore most available for plant uptake and other release into the environment. TP-1 and TP-2 contains higher Pb fractions in residual fractions, which may be bound to SiO_2. for better conclusive more number of representative tailings samples would be required.

Fraction 2

The amount of metals released in the carbonate fraction represents a very low proportion of the total metal content and in most of the cases the concentration is found at below the detection limit. The sum of fractions 1 and 2 represents the bioavailability of the metal.

Table 2: Sequential extraction results for Uranium tailings

Element in TP-3	Unit	F1	F2	F3	F4	F5	Total
Mn	$\mu g\ g^{-1}$	454.3	9.13	288.47	56.58	587.35	1395.86
Pb	$\mu g\ g^{-1}$	17.67	<0.28	3.31	<0.068	7.63	28.6
Cu	$\mu g\ g^{-1}$	140.8	0.61	45.97	152.07	61.06	400.54
Fe	$mg\ g^{-1}$	0.623	<1.13	2.86	0.04	53.98	57.52
Zn	$\mu g\ g^{-1}$	4.4	<1.0	3.22	0.71	11.91	20.25
Nat. U	$\mu g\ g^{-1}$	18.5	4.05	28.43	4.14	49.34	104.54
Element in TP-2	**Unit**	**F1**	**F2**	**F3**	**F4**	**F5**	**Total**
Mn	$\mu g\ g^{-1}$	123.9	1.68	57.68	9.1	134.16	326.5
Pb	$\mu g\ g^{-1}$	5.83	<0.28	1.13	0.107	26.107	33.17
Cu	$\mu g\ g^{-1}$	123.05	<0.23	32.47	10.91	48.54	214.97
Fe	$mg\ g^{-1}$	1.82	<1.13	3.83	0.03	46.49	52.17
Zn	$\mu g\ g^{-1}$	2.66	<1.0	3.51	0.74	9.58	16.49
Nat. U	$\mu g\ g^{-1}$	34.01	3.16	18.23	11.84	13.8	81.05
Element in TP-1	**Unit**	**F1**	**F2**	**F3**	**F4**	**F5**	**Total**
Mn	$\mu g\ g^{-1}$	236.94	5.04	59.78	11.52	162.58	475.86
Pb	$\mu g\ g^{-1}$	3.89	0.86	<0.36	<0.068	36.64	41.4
Cu	$\mu g\ g^{-1}$	269.6	<0.23	44.34	11.52	182.53	508
Fe	$mg\ g^{-1}$	0.239	<1.13	3.68	0.009	60.175	64.1
Zn	$\mu g\ g^{-1}$	1.92	<1.0	2.81	0.32	15.89	20.93
Nat. U	$\mu g\ g^{-1}$	29.49	4.86	26.9	7.58	51.37	120.21

Fraction 3

Most of the metals extracted significantly (13-23 %) in Fe-Mn. Fe recovery in this fraction is higher than other fractions except residual fraction. These amounts of metals would be released under reducing conditions.

Fraction 4

Mostly metals associated with organic matter are extracted in this fraction. In most of the tailing samples, the association of metals was found to be very less in this fraction. This is because of less content of organic matter in tailings. The Loss Of Ignization (LOI) was found to be 0.16-0.098 %.

Fraction 5

It can be observed that the greatest part of the metals studied, especially heavy metals, was associated with the residual fraction. This fraction named "inert phase", corresponds to the part of the metals which cannot be mobilized. The amount of metals released in this fraction is Mn 34-42%, Nat. U 17-47 %, Pb 27-89 %, Cu 15-36 %, Fe 89-94 % and Zn 58-76 %. It is observed that under acidic environment more of lead is associated with this fraction (78 %) than neutral environment (27 %). Major portion of Fe (90 %) is extracted in this fraction.

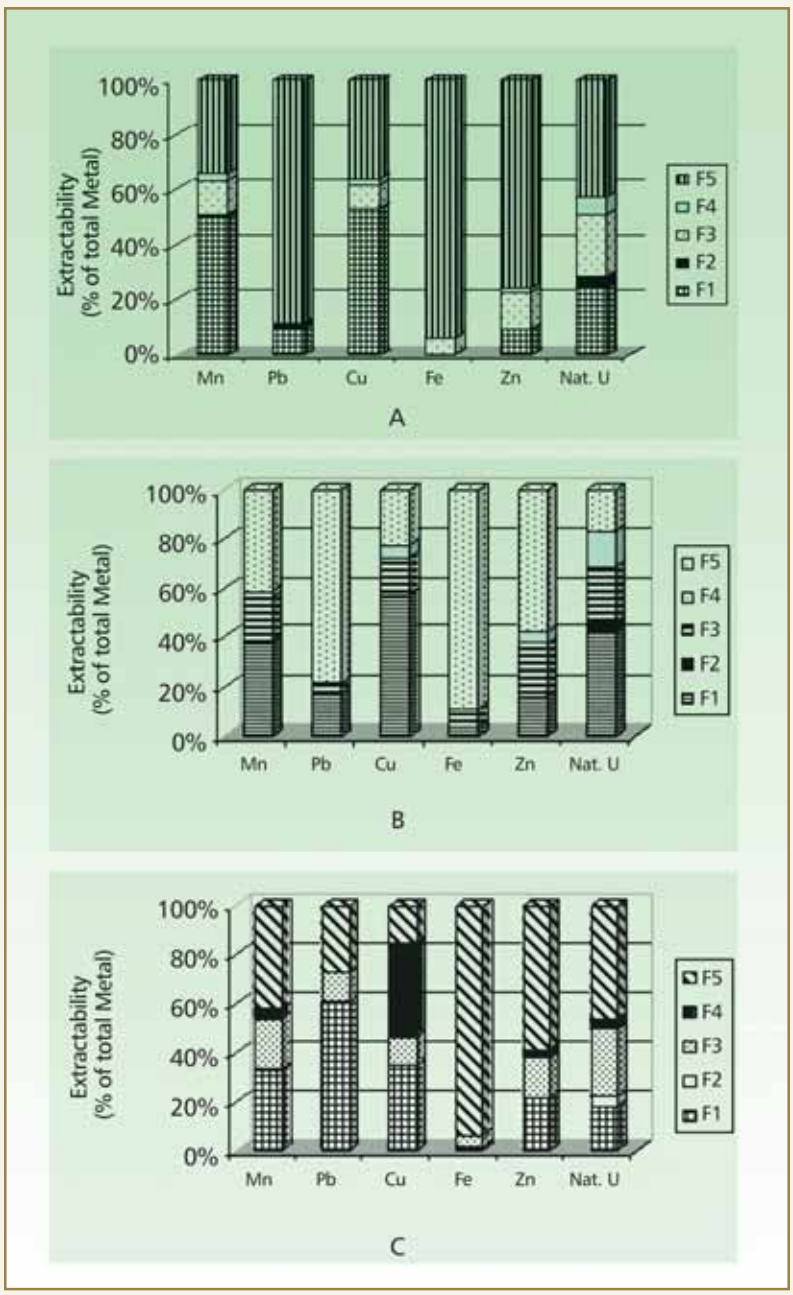

Fig. 3: Mean extractabilities of metals from tailings (A) TP-1, (B) TP-2 and (C) TP-3

Conclusion

The present study clearly shows the importance of metal partitioning in different phases. High extractability was observed for most of the metals in the residual fraction with an exception of lead. High extractability for Pb was observed in the exchangeable part in TP-3. At the same time more amount of Mn and Cu extracted in the exchangeable fraction under acidic condition i.e., at TP-1 and TP-2. So the mobility and bioavailability of metal is decided on the basis of at which form and environment it exists. In the present study few elements are selected considering the ease in analysis due to high concentration. The study can be extended for the major concern radiogenic contaminants due to uranium tailings i.e. Ra-228, Th-230, Po-210 and Pb-210 and non radiogenic contaminants but highly toxic like Cd, Cr, As and Hg.

ABOUT THE AUTHORS

Ms. Suchismita Mishra completed her M.Sc. (Chemistry) in 1997 from Utkal University, Orissa and joined the Environmental Assessment Division (EAD), BARC through the 41st Batch of BARC Training School (Chemistry Discipline) in 1998. Her fields of interest include characterization of heavy metals and radionuclides in environmental and biological matrices, speciation analysis, risk assessment and use of sorbents for removal of contaminants. Currently she is involved in characterization and speciation of metals in uranium mill tailings.

Mr. Sunil Bhalke after completing his B. Sc. from Rani Durgavati Vishwavidyalaya, Jabalpur, joined the Environmental Assessment Division, BARC through Sixth Batch of BARC Training Course on Health Physics in 1998. He completed his M.Sc. Chemistry (Organic) (By Research) from the Institute of Science, Mumbai University, 2003. His fields of interest include estimation, charecterization and speciation and of heavy metals, organo-polltants and radionuclides in various environmental and biological matrices using different analytical techniques.

Ms. B. Suseela joined the Department of Radiological Protection, BARC in 1971 and retired from Environmental Assessment Division, BARC in 2007. She was mainly engaged in trace metal analysis and radiochemical separation of low level actinides in various environmental and biological matrices.

Dr. (Ms.) G.G. Pandit joined BARC Mumbai in 1981 (24th Batch of Training School, Chemistry). Currently She is heading the Environmental Monitoring and Assessment Section of Environmental Assessment Division, BARC. Presently her research interests are assessment of long term impact from both radioactive and non-radioactive pollutants released to different compartments of the environment. She is the National Project Coordinator of UNDP/IAEA/RCA project on Characterization and source identification of particulate matter in Asian Region.

Mr. V.D. Puranik joined the 15th Batch of BARC Training School. He is looking after the safety of personnel and environmental monitoring of the front end fuel cycle facilities of the department and the radiation monitoring and networking programme in the country. Presently he is the Head, Environmental Assessment Division and his interests include radiological and chemical pollutants, their generation and dispersion in air and water and modeling of such processes.

PHASE-CONTRAST IMAGING USING X-RAY AND NEUTRONS AS PROBES

P.S. Yadav, Y.S. Kashyap, P.S. Sarkar, Tushar Roy and A. Sinha
Laser & Neutron Physics Section

This paper was awarded the Best Poster Award at the 52nd DAE Solid State Physics Symposium, held at University of Mysore, Mysore, during December 27-31, 2007.

ABSTRACT

Since the discovery of X-ray in 1895, the vast majority of radiographs have been taken and interpreted on the basis of absorption contrast of the object. In recent years, the possibility of utilizing phase-contrast effect has received considerable attention. In this paper, we present use of phase-contrast imaging for the examination of soft materials like carbon fiber, carbon-felt and pyrocarbon coated alumina micro-spheres using SYRMEP beamline at ELETTRA, Italy. Phase contrast imaging can also be done using neutrons and is quite effective in cases where X-rays are unable to penetrate. To explore such a possibility, we also present theoretical simulation of Pb & ZrH_2 objects with thermal neutron source using Kirchhoff integral formula.

Introduction

In recent years, phase contrast imaging with X-ray and neutrons has been the subject of significant research efforts. It helps to improve the image contrast as compared to conventional radiography. The contrast produced relies not only on differences in absorption, but also on differences in real part of the refractive index. The refractive index is given by $n = 1 - \delta - i\beta$, the real part (δ) of the refractive index is responsible for phase shift, while the imaginary part (β) determines absorption. The radiography with thermal neutrons, is a powerful non-destructive method, for the investigation of materials. We have carried out phase-contrast imaging with X-ray sources which have been published elsewhere, but, even X-ray phase imaging has limitations for imaging of high Z materials like Pb, Ti, ZrO_2 etc, as the X-ray absorption is very high for such materials. Unlike X-rays, neutrons interact with various materials with very specific cross-sections largely independent of atomic number (Z) of the material and neutrons can pass through many high Z materials. The neutron radiography also fails to yield good results, if neutron attenuation is too weak to be detected. Hence for objects of high Z materials, but with poor neutron absorption, phase imaging techniques should be used. With neutron phase imaging, it is possible to image minute quantities of these materials, in the specimen of materials having very weak neutron absorption properties. We have done theoretical simulation for materials like Pb with air bubble, ZrH_2 in zircaloy. This paper deals with

application of this technique for material science applications using X-ray and neutrons.

X-ray Phase Imaging at ELLETRA

We have carried out experiments at SYRMEP bending magnet beam-line Elettra, Italy. A CCD detector and fiber-optic combination having effective pixel pitch of 4.5 μm was used, for collecting high resolution images. Fig.1 shows the X-ray phase contrast image of carbon-felt taken at E=10 keV, exposure time=2 sec and object-detector distance (Z_2) =50cm. Fig. 2 (a) shows the phase contrast image of pyrocarbon (PyC) coated alumina micro-spheres with a diameter of 500 µm, which was taken at E=16 keV, t=1.6 sec and Z_2=50 cm. The coated sample was prepared in a high temperature graphite vessel. These kinds of materials are important for nuclear science applications. We have determined the average PyC coating thickness to be 60 µm on alumina micro-spheres. This technique is found to be very useful in visualizing and determining coating thickness of PyC, uniformity of the coating and optimization of coating parameters.

Fig. 1: X-ray phase-contrast image of carbon-felt

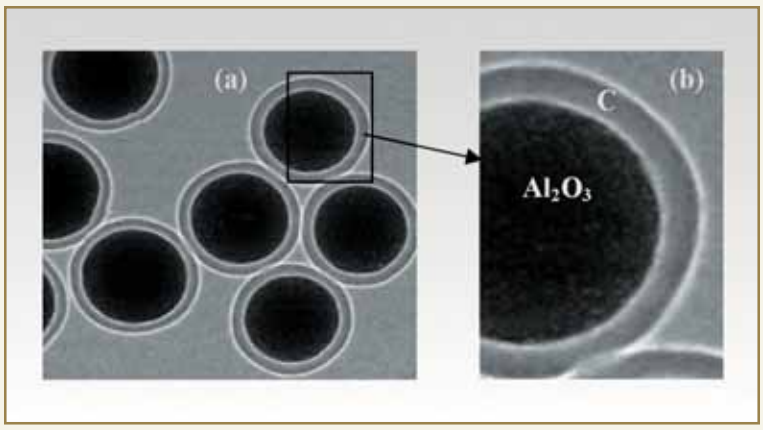

Fig. 2: (a) X-ray phase-contrast image of PyC coated alumina micro-spheres. (b) Magnified phase contrast image of the black-rectangle portion revealing the coatings

Simulation of Phase-contrast with Thermal Neutrons

We have used Fresnel-Kirchhoff integral formula [4] of parallel wave for simulation, to calculate the wave function and the intensity of the image at the detector plane:

$$f(x;zod)=\left(\frac{i}{\lambda z}\right)^{1/2}\exp(-ikzod)\int q(X)\times\exp\left(\frac{-ik(x-X)^2}{2zod}\right)dX$$
$$k=\frac{2\pi}{\lambda}$$
$$I(x;zod)=|f(x;zod)|^2 \quad (1)$$

Where x is the position coordinate within the image plane, zod is the object to image distance, I(x; zod) is the intensity of the object and q(X) is the transmission function of the object. The phase shift ϕ of a neutron with a wavelength λ on it's way through the object, with regard to propagation in free space, is given by

$$\phi=-\frac{2\pi}{\lambda}\int_s \delta ds=-\frac{\lambda}{2\pi}\int_s a_{coh}\rho ds\ ,\ \delta=\frac{\lambda^2}{2\pi}a_{coh}\rho \quad (2)$$

Where a_{coh} is the bound coherent scattering length and ρ is the average number of atoms per unit volume.

For X-rays, the phase difference is given by

$$\phi = -\frac{2\pi}{\lambda}\int_s \delta ds = -\frac{\lambda}{2\pi}\int_s r_e \rho f_r ds$$
$$\delta = \frac{\lambda^2}{2\pi} r_e \rho f_r \qquad (3)$$

For calculation of contrast (C) we have used formula [5], C = (Imax – Imin) / (Imax + Imin), where Imax (maximum value of intensity) and Imin (minimum value of intensity) are values obtained from the 1-D plot of radial distance and transmitted intensity of the object. Table1 shows the cases where the use of X-rays is impractical, because of their high attenuation. Table 2 shows the differences in d values of Pb, ZrO_2 and ZrH_2 for X-rays and thermal neutrons and contrast values for neutrons. Eqs. (2) and (3) show that the phase difference is proportional to wavelength for both X-rays and neutrons. For neutrons there is more scope to increase sensitivity by using longer wavelengths without a significant increase in attenuation. However, for X-rays, attenuation prevents the use of longer wavelengths (>2 Å) and limits sensitivity. We have solved eq. (1) using FFT technique, to simulate the ideal phase-contrast imaging conditions. The objects were assumed to be circular ZrH_2 (r = 40 mm) in cylindrical ZrO_2, (r = 80mm), circular lead (radius, r, = 100 mm) with air bubble (r = 20 mm and the thermal neutrons was assumed to be monochromatic radiation with a wavelength of 1.81Å (E = 25meV). Figs. 3 and 4 show the result of the simulation, with object to detector distance of 11 and 25 cm respectively. The presence of primary maxima along with secondary maxima is a characteristic feature of phase contrast imaging. Figs. 3(a) and (b) show the phase contrast image of ZrH_2 in ZrO_2 with X-ray, the ZrH_2 is not visible in this image, due to high X-ray absorption. However, it is clearly visible in the neutron phase contrast image, even though it has low neutron absorption. It shows the importance of phase-contrast imaging with neutrons for these types of materials.)

Table 1: A comparison of the linear attenuation coefficient in Pb, ZrO_2 and ZrH_2 for X-rays and neutrons

Object name	Neutron and X-ray energy	Neutron and X-ray wavelength (Å)	Neutron linear attenuation coefficient (cm^{-1})	X-ray linear attenuation coefficient (cm^{-1})
Pb	25 meV	1.81	0.38	58.933
ZrO_2	58.5 keV	0.2120	0.21	16.658
ZrH_2	-	-	2.39	21.713

Table 2: Real part delta (δ) differences in lead, ZrO_2 and ZrH_2 for X-rays and neutrons

Object name	ρ($\times 10^{28}$) (m^{-3})	Neutron & X-ray λ(Å)	X-ray δ(rad) ($\times 10^{-7}$)	Neutron δ(rad)	Neutron Contrast (C)
Pb	3.3031	1.81	5.4306	1.6177×10^{-6}	0.8281
ZrO_2	8.2211	0.2120	9.3280	8.0336×10^{-6}	0.9817
ZrH_2	10.884	-	9.2794	1.802×10^{-7}	0.9850

Acknowledgements

The authors would like to acknowledge the contribution of Dr. D. Sathiyamoorthy, Head, MSD for many helpful discussions and for providing samples.

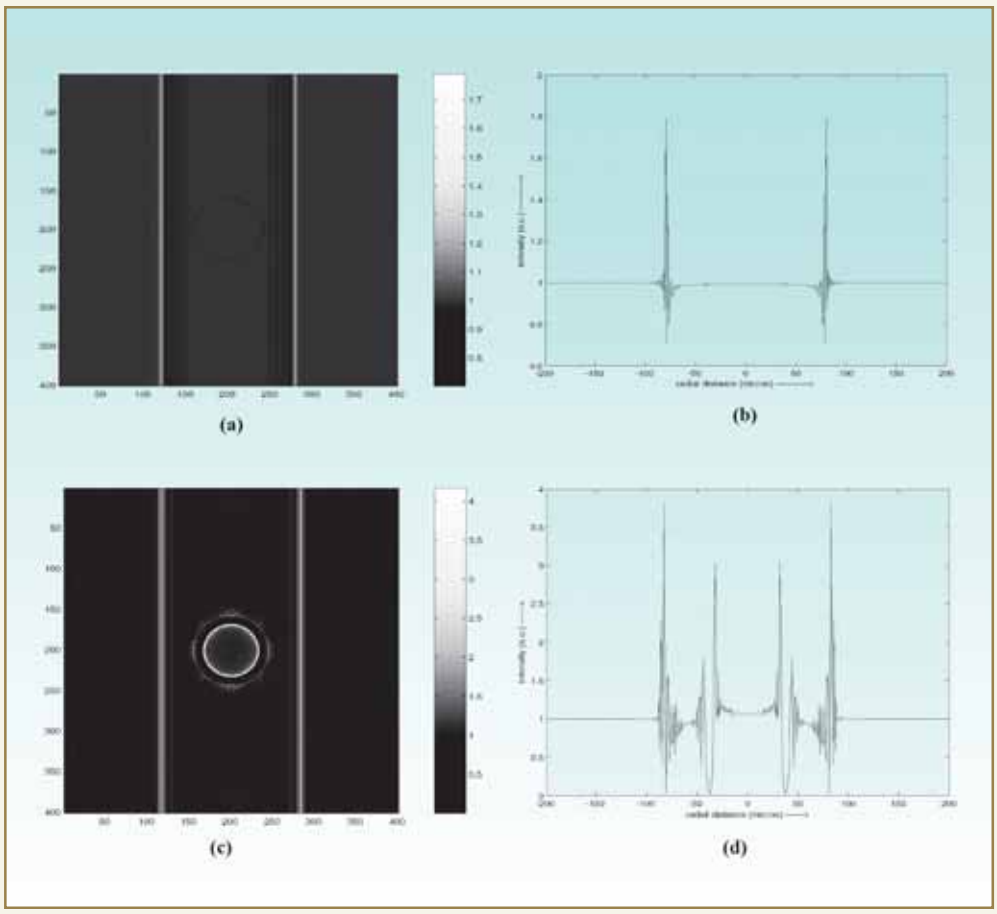

Fig. 3: (a) Phase-contrast image of ZrH_2 in ZrO_2 with X-ray at E= 58.5keV, (b) intensity profile of (a), (c) phase-contrast image of ZrH_2 in ZrO_2 with neutrons at E= 25meV and (d) intensity profile of (c).

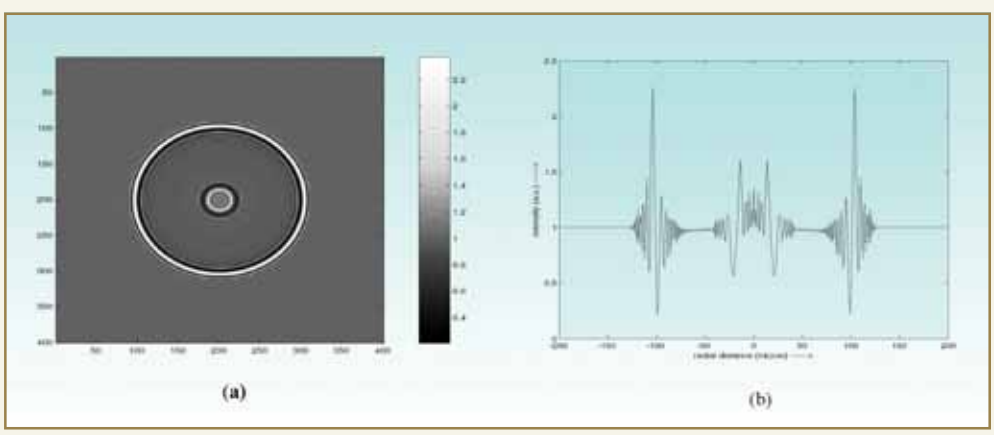

Fig. 4: (a) Phase-contrast image of Pb with air bubble using neutrons at E= 25meV & (b) intensity profile of (a).

ABOUT THE AUTHORS

Ms. Poonamlata S. Yadav is involved in activities related to phase-contrast X-imaging studies, using lab based X-ray Microfocus source and Synchrotron Radiation source on low Z (soft) materials like carbon composites, carbon fibers, polymers and soft tissues for early detection of tumour, cancer etc. She has carried out experiments at Electra Synchrotron source. Her recent work is on the pyrocarbon coated zirconia and alumina micro-sphere using phase-contrast X-ray imaging technique at the ELETTRA (SYRMEP) Synchrotron beam line (Italy).

Mr. Y. S. Kashyap obtained M. Sc. Degree in Physics from I.I.T. Kanpur. He graduated from the 44th Batch of Training School. He joined the Radiation Imaging Section, Laser & Neutron Physics Section, BARC. He is involved on the projects for the development of X-rays and neutron imaging techniques such as X-ray holography, tomography, phase-contrast imaging etc. He has worked on the setting up of laboratory-based phase contrast technique at Purnima Labs, BARC. He is also involved in design and development of Imaging beamline at the Indus-II and neutron imaging beamline at CIRUS.

Mr. P. S. Sarkar graduated from the 43rd Batch of Training School and joined the Laser & Neutron Physics Section, BARC. He has performed two phase flow visualization experiments through neutron radiography at APSARA reactor. He has also performed X-ray radiography based experiments for visualization of coal dust fluidized bed for void fraction determination. He has also been involved in the development of 3D X-ray Cone Beam tomography system, Digital Medical Imaging System – a multipurpose system for diagnostic purposes in hospitals and Battery based X-ray portable baggage inspection unit for *in-situ* inspection or checking of any suspected or unattended baggage/materials. He is at present working on experimentation on phase contrast imaging, development of portable imaging units and X-ray microtomography.

Mr. Tushar Roy obtained M. Sc. Degree in Physics from University of Allahabad. After graduating from the 48th Batch of Training School, he joined the Radiation Imaging Section, Laser & Neutron Physics Section, BARC. He has been involved in developing algorithm and computer simulation codes for emission tomography. He has also been associated with studies related to phase contrast imaging and microtomography. At present he is involved in the setting up of prototype experimental setup for emission tomography.

Dr. Amar Sinha graduated from the 20th Batch of BARC Training School. He has worked extensively on neutron and x-ray imaging research, in particular on the development of x-ray phase imaging, 3D x-ray and neutron tomography, real time imaging systems for basic and applied research etc. He and his team have been responsible for designing Phase contrast imaging setup, a digital medical imaging system and a Microtron-based neutron source at Mangalore University. He obtained his Ph.D. on the design of spallation neutron source for the simulation of radiation damage in fusion materials. He has published more than 70 papers.

बीएआरसी न्यूज़लेटर
BARC NEWSLETTER

SORPTION OF NEPTUNIUM BY HEMATITE COLLOIDS

Aishwarya Jain, Neetika Rawat, Sumit Kumar, B.S.Tomar and V.K. Manchanda
Radiochemistry Division

and

S. Ramanathan
Materials Science Division

This paper was awarded the Best Poster Prize at the DAE-BRNS Symposium on Nuclear and Radiochemistry (NUCAR-2007) held at M.S. University, Vadodara, during February 14-17, 2007.

ABSTRACT

Sorption of Np(V) on hematite colloids has been studied, at varying pH values (3-10) in the absence and presence of humic acid using ^{239}Np as a tracer. The results show negligible sorption of Np(V) on hematite colloids at lower pH <5, beyond which it was found to increase, sharply reaching ~ 90% at pH 10. In the presence of humic acid (2mg/L) the Np(V) sorption on hematite decreased at higher pH values while at lower pH the effect was found to be negligible. Using the binary interaction data, linear additive modeling of the sorption data of ternary system of Np(V) - humic acid - hematite was carried out, which suggested the role of non-additive factors. The experiments on ternary system of neptunium – hematite- humic acid under reducing conditions show reduction of Np(V) to Np(IV), causing increased sorption of neptunium at all pH values.

Introduction

^{237}Np is one of the most important radionuclides present in High Level Waste (HLW) which is generated during the reprocessing of spent nuclear fuel. The long half life ($T_{1/2} = 2.14 \times 10^6$y) and alpha activity of ^{237}Np make it one of the most hazardous contaminants in the geosphere in the long term. This is particularly due to the fact, that compared to plutonium and americium, it is more mobile in the aquatic environment, owing to the dominance of pentavalent state (NpO_2^+) under aerobic conditions [1]. Adsorption of radionuclides on colloids like silica, alumina and iron bearing colloids (hematite, magnetite, goethite) is the common mode of transport in the aquatic environment, which in turn is influenced by the presence of humic substances in the aquatic system. Presence of humic acid was found to facilitate the transport of neptunium as humic colloid bound species, which was attributed to the reduction of Np (V) to Np (IV) and formation of stronger Np (IV) - HA complexes [2]. There is no literature on the effect of HA on the sorption of neptunium on hematite colloids, which are one of the most common minerals present

in aquatic system. With this in view, we studied the influence of humic acid on the sorption of neptunium on hematite colloids, both in the absence and presence of humic acid at varying pH values (3-10). From the binary interaction data of Np (V), humic acid and hematite system, the sorption data on ternary system has been deduced, using the linear additive model. The measurements were also carried out on the ternary system, under reducing conditions, by using sodium dithionite (as a reducing agent).

Experimental

Hematite colloids were synthesized in the laboratory as described in [3]. The IsoElectric Point (IEP) of hematite colloids was found to be 6.57. ^{239}Np, the short lived (2.35 days) gamma-emitting isotope of neptunium was prepared by irradiating U_3O_8 in APSARA reactor and separating ^{239}Np, from uranium and fission products, by anion exchange method. The eluate solution was evaporated to dryness and then fumed with 1M $HClO_4$ thrice and finally dissolved in 0.1M $NaClO_4$ solution to prepare 10^{-11} M stock solution having pH ~ 6. Solvent extraction with 0.5M TTA in xylene, showed negligible extraction of neptunium indicating the predominant oxidation state to be Np(V). 100 µL of the stock solution was used in the sorption studies, so as to give the neptunium concentration of 10^{-13} M. All the solutions were prepared in de-ionized millipore water. Batch sorption experiments were carried out by equilibrating ^{239}Np solution at varying pH with hematite colloids. 30 mg of hematite powder was suspended in 10 mL of 0.1M $NaClO_4$ solution in polypropylene tubes. After leaving the suspension for two hours, it's pH was adjusted to the desired value, by addition of either dilute HCl or NaOH. Eight samples having pH in the range of 3-10 were prepared. After adding the ^{239}Np activity the suspensions were equilibrated for 48 hours. The details of measurement of sorption data are given in [4]. In another experiment, the batch sorption experiments on the ternary system of Np - HA - hematite were carried out under reducing conditions. 100 mL of 0.5 M sodium dithionite solution was added to the hematite suspension (3g / L) containing humic acid (2mg / L) so as to maintain the dithionite concentration as 5×10^{-3} M. The suspensions were purged with N_2 before adjustment of pH and again before keeping for equilibration. Np(V) is expected to reduce to Np(IV) under these reducing conditions, which may further be facilitated by the presence of humic acid.

Results and Discussion

Fig. 1 shows the sorption data of Np (V) on hematite colloids as a function of pH under aerobic conditions. The percentage sorption is very low till pH 5 (~10%), above which it increased sharply reaching the saturation value of 90 % at pH 9. This can be explained in terms of the decreasing zeta potential of hematite colloids with pH. In the presence of HA, the sorption is marginally lower in the pH range 3-6. On the other hand, at pH >7.0 the significant decrease in sorption in the presence of HA has been observed. Sorption behaviour of actinides on minerals has been explained on the basis of hard – soft, acid - base behaviour. Np (V) being a softer acid has lower interaction with bare mineral oxides, as compared to Th (IV), Pu (IV) and Am (III). Sakuragi et al [5] observed that HA enhanced the sorption of Am (III) on hematite colloids at lower pH and decreased the sorption at higher pH. This observation was attributed to strong sorption of HA on hematite at lower pH, which decreased with increase in pH. Thus the observations made in the present study, about the suppression of Np(V) sorption by HA at higher pH values, is explained by the formation of Np (V)-HA complex.

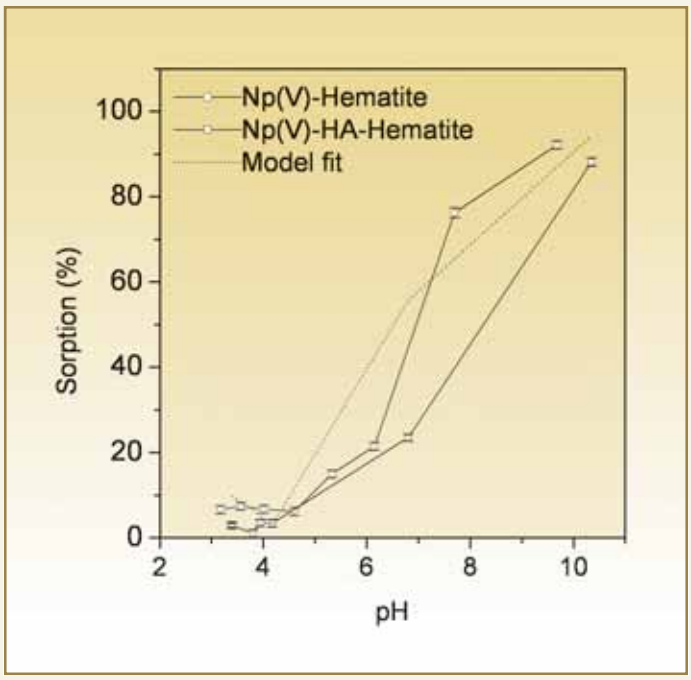

Fig. 1: Sorption of Np(V) on hematite: effect of humic acid

In order to simulate the sorption data of the ternary system involving Np(V), hematite and HA, we used the linear additive model modified by Samadfam et al [6]. The prediction of the linear additive model are shown in Fig. 4 as a dotted line, which shows increased sorption of Np(V) at intermediate pH and a slight decrease at higher pH values. The decrease in sorption at higher pH is in agreement with experimental results, though the decrease is not as much as observed experimentally. However, the predicted increase at pH 5-6 is not observed in the experiment, which suggests the influence of non-additive factors, such as, change in the surface charge density of HA-coated hematite particles with respect to bare hematite particles, or different value of stability constant for Np(V)-HA complex involving mineral bound and aqueous HA.

Fig. 2 shows the sorption data of ternary system of neptunium HA hematite under reducing conditions. The sorption of Np on hematite is significantly enhanced at all pH values, with respect to aerobic conditions. Under anaerobic conditions, Np(V) may be reduced to Np(IV) which being a hard acid, is expected to behave like Th(IV) and hence the sorption at lower pH is increased. However, it is not clearly explainable why the sorption of Np(IV) should increase at higher pH values in the presence of HA. As Np(IV)-HA complex has a much higher stability constant than Np(V)-HA, it is expected that the sorption of Np(IV) on hematite will reduce at higher pH, contrary to the observations of this work. This indicates that reduction of Np(V) to Np(IV) may not be complete at alkaline pH. Secondly Fe^{3+} released by dissolution of hematite may re-oxidise Np(IV) to Np(V).

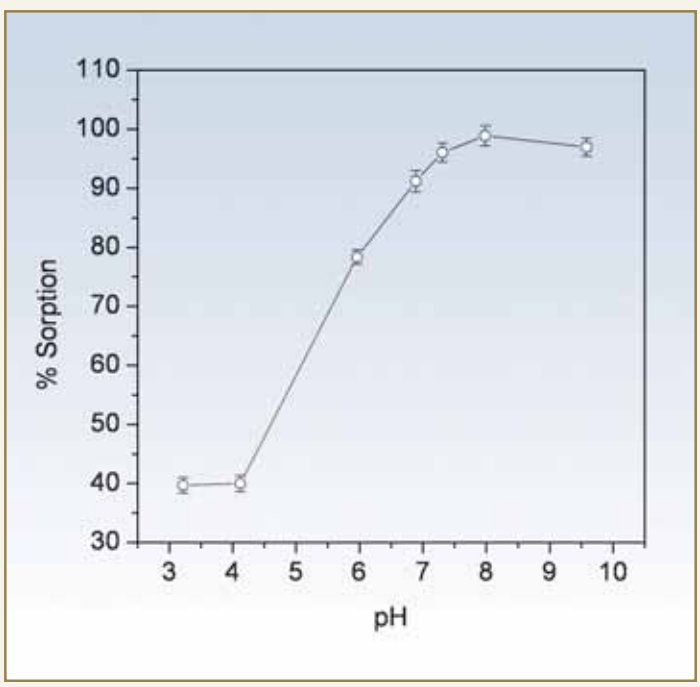

Fig. 2: Sorption of Neptunium on Hematite in presence of HA in reducing condition

Conclusions

The present study showed that HA decreases the sorption of Np(V) on hematite colloids at higher pH. Under anaerobic conditions, sorption of neptunium on hematite was found to be enhanced in the presence of HA, which was attributed to reduction of Np(V) to Np(IV) and stronger complexation of the latter by HA.

References

1. J.I. Kim, in Handbook on the Physics and Chemistry of Actinides eds A.J. Freeman and C. Keller, Elsevier Science 1986, p413.
2. R. Artinger, C.M. Marquardt, J.I. Kim, A. Seibert, N.Trautmann, J.V. Kratz, Radiochim. *Acta* 88, 609 (2000).
3. S. Kumar, N. Rawat, B.S. Tomar, V.K. Manchanda, S. Ramanathan, *J. Radioanalyt. Chem*., (In Press).
4. S. Kumar, B.S. Tomar, V.K. Manchanda, S. Ramanathan, *Radiochim. Acta* 94, 369 (2006).
5. T. Sakuragi, S. Sato, T. Kozaki, T. Mit'sugashira, M. Hara, S. Yoshimit'su, *Radiochim. Acta* 92, 697 (2004).
6. M. Samadfam, T. Jintoku, S .Sato, H.Ohashi, T. Mit'sugashira, M. Hara, Y. Suzuki, *Radiochim. Acta* 88, 717 (2002).

ABOUT THE AUTHORS

Ms. Aishwarya Jain is from the 48th Batch of BARC Training School. After successful completion of one year Orientation Course in Nuclear Science and Engineering, she joined the Radiochemistry Division in September 2005. Her research area is actinide speciation. She has been working on the colloid assisted transport of actinides and initiated spectroscopic work on actinide speciation.

Ms. Neetika Rawat obtained her M.Sc. from the Indian Institute of Technology, Delhi. She joined the Radiochemistry Division, in 2002 after completing one year orientation course in chemistry from BARC Training School (45th Batch). Her area of interest includes thermodynamics of complexation of actinides and fission products with various processes and environmentally important ligands.

ABOUT THE AUTHORS

Mr. Sumit Kumar joined the Radiochemistry Division, BARC, in 2003 after graduating through one-year training programme on Nuclear Science and Technology of BARC Training School. His research interests are application of Radioanalytical techniques in various scientific problems and Actinide Speciation in environment.

Dr. B.S. Tomar joined the 25th Batch of the BARC Training School in 1981 and won the Homi Bhabha Prize. Subsequently he joined the Radiochemistry Division in 1982. His areas of research include Nuclear Chemistry in general and Nuclear Fission, Nuclear reactions, Perturbed angular correlation, Ion beam analysis and speciation of actinides and fission products in particular. Presently he is heading the Actinide Chemistry Section of Radiochemistry Division, BARC.

Dr. V.K. Manchanda joined the Radiochemistry Division, BARC in 1969 after graduating from BARC Training School. His research interests include; Thermodynamics and kinetics of complexes of macrocyclic ligands with lanthanides and actinides, Design and synthesis of novel extractants of actinides relevant in the back end of the fuel cycle, Chemical quality control of Pu based fuels and Speciation of actinides in aquatic environment. He has about 170 publications in international journals. He currently heads the Radiochemistry Division of BARC.

Dr. S. Ramanathan joined BARC through the 19th Batch of Training School and works on processing of advanced ceramic materials for a wide variety of applications in the department. He worked on the development of solid oxide electrolyte materials for oxygen sensor application. Currently he works on synthesis of nano-crystalline oxide powders by gel combustion technique and their processing for applications such as SOFC, catalysis, absorption etc. Characterization of micro and meso porosity in treated nano-crystalline powders by Small Angle Neutron Scattering (SANS) is yet another area of his specialization. He has developed slurry-based tape casting process for formation of thin sintered tapes (100 to 500 μm thick) of electrodes and electrolytes for solid oxide fuel test cell studies. He also specializes in synthesis of controlled morphology colloidal powders by sol-gel technique for studies on absorption behaviour of radioactive nuclide on the surface.

NEW AUTOIONIZATION RESONANCES OF URANIUM BY THREE-COLOR RESONANCE IONIZATION SPECTROSCOPY IN HOLLOW CATHODE DISCHARGE TUBE

M. L. Shah, Vas Dev and B. M. Suri
Laser and Plasma Technology Division

This paper received the Best Poster Award at the 7th DAE-BRNS National Laser Symposium (NLS-7), held at M.S. University of Baroda, Vadodara , during December 17-20, 2007

Introduction

Multistep Resonance Ionization Spectroscopy (RIS) is a powerful tool, to study and identify high-lying atomic states. Especially studies on autoionization states, which are quasi-bound states of an atom, lying above the ionization threshold of the outer valence electron, have been of great importance because of their role in knowing efficient routes for resonance ionization, apart from addition to fundamental knowledge in Atomic Physics. The usual scheme for multistep photoionization, consists of excitation of an atom from low lying energy levels to intermediate upper excited states, with a sequence of lasers and subsequent ionization of the excited atom by another laser. Normally, most of this information is acquired by employing the multistep Resonance Ionization Spectroscopy (RIS) in the atomic beam setup. For refractory elements such as uranium, atomic beam set up is very complex. Some researchers have recorded three colour, three-photon optogalvanic spectra of uranium in a simpler device, the Hollow Cathode Discharge Tube (HCDT), where it is used as a source of atomic vapours as well as a photoion detector and was found to be in reasonably good agreement with the spectra recorded in an atomic beam set up. Single colour three-photon ionization spectra of uranium in the cathode dark space have been reported. Recently using the same technique, single colour three-photon as well as two-color three photon photoionization spectroscopy of uranium have also been studied. The major advantage of this technique is it's ease in implementation. Fig. 1 shows homemade HCDT along with the routinely used complex atomic beam setup. Researchers further extended it's use investigations of autoionization states. The even parity autoionization spectra of calcium were investigated by some researchers, using two colour two-step excitation. Others have studied the autoionization states of Lutenium, Praseodymium and Samarium using two colour optogalvanic spectroscopy.

We have studied the autoionization states of uranium by optogalvanic spectroscopy, using three-colour three-photon RIS in a U-Ne HCDT in the energy region 52850-53180 cm^{1}. We have identified 40 new

autoionization states of uranium and assigned their J values. Some of the autoionization states were also accessed through different excitation routes.

Experimental Setup

Experimental setup used for these studies is shown in Fig. 2. It consists of three Nd-YAg pumped dye lasers (spectral width 0.05 cm^{-1}, repetition rate 20 Hz, pulse width 7 nsec), a see-through type home-made U-Ne HCDT(cathode length 30 mm, diameter 8 mm), digital oscilloscope for signal monitoring and a box car averager for further signal processing. HCDT was operated at ~50 mA current. Spatially overlapped and temporally synchronized three dye lasers beams (~ 5mm diameter) are made to pass through the centre of the HCDT and optogalvanic signal was detected across a 4 KΩ ballast resistance.

Results and Discussion

Three-colour optogalvanic spectrum has been recorded and analyzed using the following excitation scheme

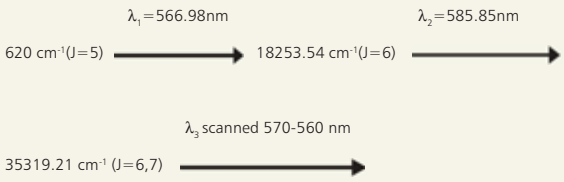

In these experiments first and second step laser wavelengths (λ_1 and λ_2) were fixed by observing the first and second step resonant optogalvanic signals and photoionization spectra along with Fabry-Perot Etalon (FPE) fringes were recorded, by scanning the third laser wavelength (λ_3) in the energy region of interest as shown in Figs. 3a and 3c.To obtain high signal-to-noise ratio and avoid single color non-resonant excitation, first and second step dye lasers powers were attenuated significantly. Three-colour three-photon autoionization spectrum recorded by this technique, consists of resonant single-colour (λ_3), two-color ($\lambda_1+\lambda_2$), and three-colour ($\lambda_1+\lambda_2+\lambda_3$) optogalvanic features. To extract the three-color autoionization features from this complicated spectrum, the experiment was repeated

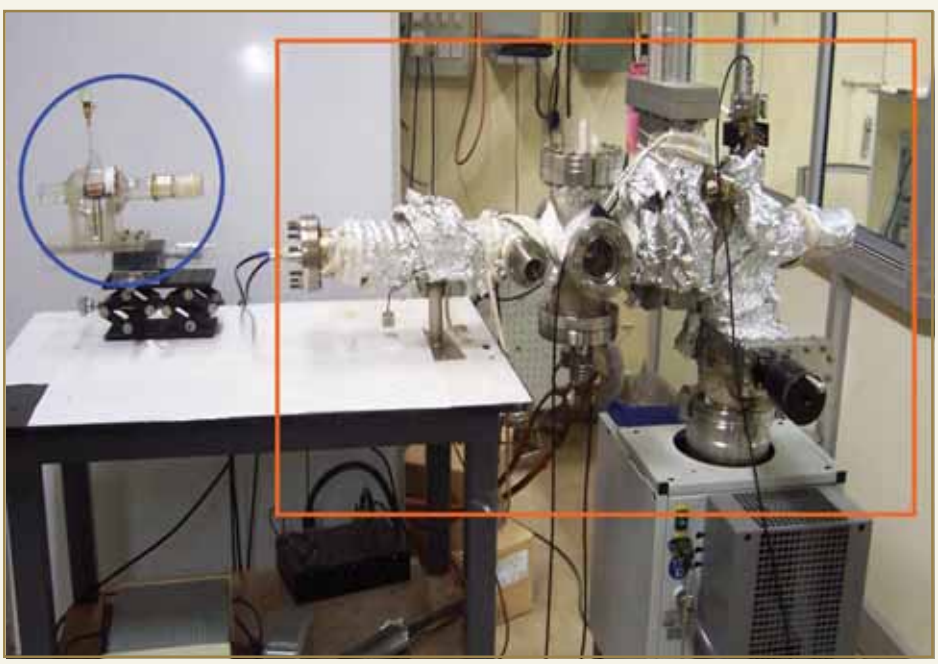

Fig. 1: Front view of home-made hollow cathode discharge tube (in circle) which is used instead of traditional atomic beam chamber (in rectangle).

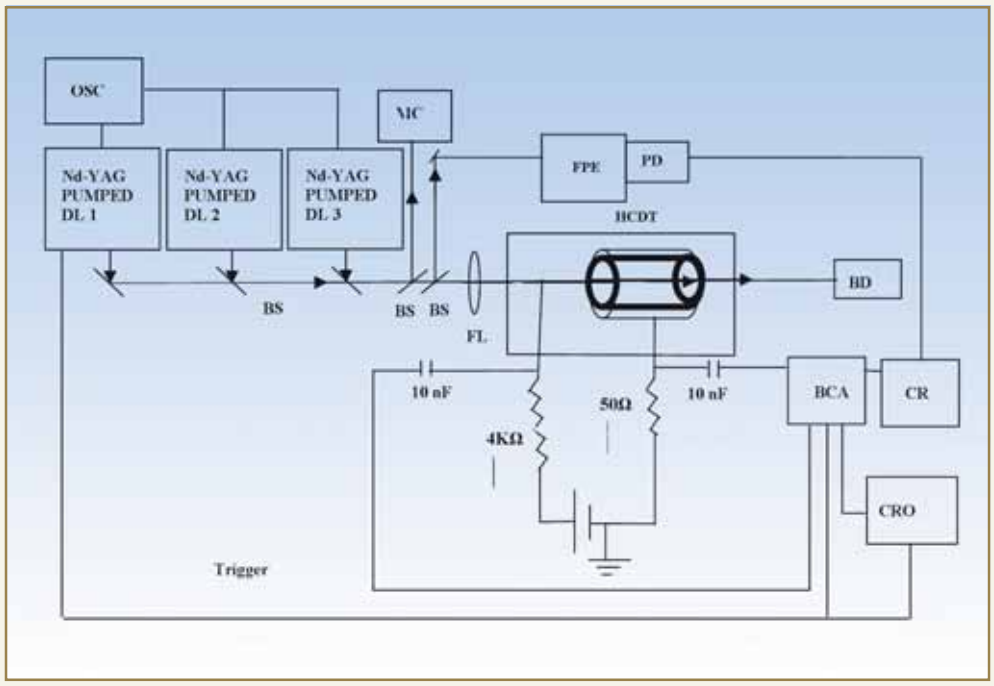

Fig. 2: Experimental setup

FPE-Fabry perot etalon, PD- Photodiode, OSC-Oscillator, MC-Monochromator, DL-Dye laser, BD-Beam dump, HCDT-Hollow cathode discharge tube, FL-Focusing lens, BCA-Box car averager, CR-Chart recorder

with the second laser (λ_2) blocked. The resultant optogalvanic spectrum consists of single-colour (due to λ_3) and two-colour (due to $\lambda_1+\lambda_3$) optogalvanic features only (see Fig. 3b). On comparison of three-color spectrum with the two-color spectrum, we have identified 40 autoionization resonances in the energy range 52850-53180 cm[1].

A list of all these resonances with their proposed J- values is given in Table1. Most of the three-colour features are broad as compared to single and two colour features with Full Width Half Maximum (FWHM) varying from 0.3 cm^{-1} - 4 cm^{-1}. To the best of our knowledge, the above mentioned energy region is not explored by any researcher so all resonances reported here are new autoionization resonances. A part of the above mentioned energy region was also accessed using the following excitation scheme:

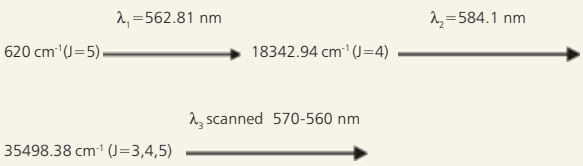

Autoionization resonances 29 and 30 as shown by asterisk in Table 1 have also been observed through the above-mentioned route. It has not only further confirmed our observation of autoionization resonances seen through the first scheme but also reduced their J value ambiguity from 5-8 to 5, 6.

Conclusion

The autoionization states of uranium have been studied by optogalvanic spectroscopy using three-colour three-photon RIS, in a simpler device, a U-Ne HCDT in the energy region 52850-53180 cm[1]. We have

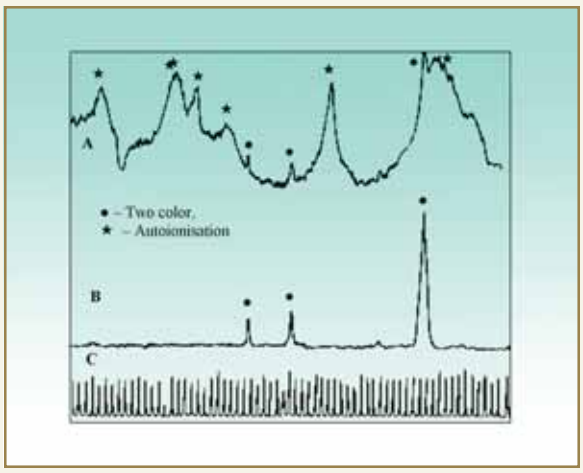

Fig 3a: A portion of three-colour, three- photon autoionization spectrum of uranium observed in HCDT with λ_1 =566.98, λ_2= 585.85 and λ_3 scanned from 561-562 nm in the energy region 53107-53140 cm^{-1}.
3b: Repeat of 1A with second step laser blocked
3c: Fabry-perot etalon fringes

identified 40 new autoionization states of uranium and assigned their J values. Part of this energy region has also been studied using different excitation scheme. The autoionization resonances identified by both the schemes reduced J value ambiguity form 5-8 to 5, 6.

Acknowledgement

The authors are thankful to Dr. L. M. Gantayet, Associate Director, BTDG and Dr. A. K. Das, Head, L&PTD, BARC, for their encouragement and support. Authors are also thankful to Mr. G. R. Zende for preparing hollow cathode discharge tube.

Table 1: Autoionization resonances

SN	Energy Levels (cm^{-1})	Proposed J Values
1	52870.75	5-8
2	52888.75	5-8
3	52894.25	5-8
4	52915.25	5-8
5	52924.00	5-8
6	52937.25	5-8
7	52946.75	5-8
8	52958.25	5-8
9	52958.75	5-8
10	52960.25	5-8
11	52961.75	5-8
12	52982.75	5-8
13	52988.75	5-8
14	53009.19	5-8
15	53011.19	5-8
16	53012.69	5-8
17	53015.69	5-8
18	53019.19	5-8
19	53021.19	5-8
20	53033.19	5-8
21	53037.69	5-8
22	53048.19	5-8
23	53059.19	5-8
24	53060.69	5-8
25	53064.44	5-8
26	53079.69	5-8
27	53082.69	5-8
28	53088.69	5-8
29*	53098.19	5-8
30*	53100.94	5-8
31	53112.19	5-8
32	53114.19	5-8
33	53117.19	5-8
34	53125.69	5-8
35	53134.69	5-8
36	53155.19	5-8
37	53160.19	5-8
38	53164.69	5-8
39	53170.69	5-8
40	53177.69	5-8

ABOUT THE AUTHORS

Mr. Mukesh Lal Shah joined the Laser and Plasma Tech. Division of BARC in 2000, through the 9th M. Tech. Batch (Orientation Course for Engineering Postgraduates) of Training School. Prior to that, he obtained his M.Sc. in Physics from Kumoun Univ. Nainital and M. Tech. in Optoelectronics from G S Institute of Tech. and Science, Indore. He has been involved in laser spectroscopy of various materials of interest. His other interests include development of optical fibre based systems for laser spectroscopy applications.

Dr. Vas Dev joined the Multi Disciplinary Research Section of BARC after graduating from the 26th Batch of Training School. His work on development of a frequency stabilized CO_2 laser and studies on dynamic instabilities led to completion of his Ph.D. degree from University of Mumbai in 1991. His recent research interest includes lasers and laser spectroscopy of lanthanides and actinides in small quantities. He has published more than 40 research papers.

Dr. B. M. Suri joined the erstwhile MultiDisciplinary Research Section, BARC in 1975 after completing one-year orientation course in Physics. Presently he is Head of Applied Spectroscopy Section in Laser & Plasma Technology Division. He has been involved in setting up Laser spectroscopy laboratory and related research and development. He was involved in pioneering development of Resonance ionization laser ion source for ultra-trace analysis applications. His current interests include laser spectroscopy and ultra-trace analysis. He has published about eighty papers.

बीएआरसी न्यूज़लेटर
BARC NEWSLETTER

PERFORMANCE CHARACTERISTICS OF REMOTELY TUNABLE, HIGH REPETITION RATE, COPPER VAPOUR LASER PUMPED SINGLE LONGITUDINAL MODE DYE LASER

Sunita Singh, G. Sridhar, V. S. Rawat, N.O. Kawade, A.S. Rawat, S. K. Mishra and L. M. Gantayet
Laser & Plasma Technology Division

This paper was adjudged as one of the Best Poster papers at the DAE-BRNS National Laser Symposium (NLS-07) in the category "Physics and Technology of Lasers", held at M. S. University, Vadodara during December 17-20-2007

ABSTRACT

We report the performance characteristics of grazing incidence grating, single longitudinal mode pulsed dye laser, pumped by 6 kHz Copper Vapour Laser developed indigenously in our lab. The linewidth and energy conversion efficiency obtained are ~375MHz and 2.3 % respectively with an ASE of 0.027 %.

Introduction

Pulsed tunable, high repetition rate (>6kHz), single longitudinal mode dye lasers are of interest to atomic laser isotope separation, trace analysis and precision nonlinear laser spectroscopy. For certain applications, mode hop free scanning over a wide wavelength range is required. Various resonator configurations have been reported in literature to obtain single longitudinal mode pulsed dye laser. In this paper, we report the performance characteristics of a remotely tunable grazing incidence grating, single longitudinal mode pulsed dye laser, pumped by 6 KHz Copper Vapour Laser (CVL), developed in our lab. Mode hop free scanning over 70GHz is reported.

Single Longitudinal Mode (SLM) Dye laser

The SLM GIG dye laser developed in our lab, is a short cavity laser (length ~5 cm) based on the design of Littman. The cavity comprises an indigenously designed flow through dye cell (5 mm x 1 mm cross section), high reflectivity (R > 99 %) end mirror, GIG grating (2400 lines/mm groove density) and a tuning mirror (R>99 %). The output of the dye laser was obtained from the zeroth order of the grating.

The axis of rotation of the tuning mirror, passes through a geometrically located point, known as pivot point. The surface planes of the tuning mirror, end mirror and grating intersect on this pivot point (Fig. 1).

The emission wavelength of the laser is determined by the relation,

$$m\lambda = d\,(\sin\theta_i + \sin\theta_d) \qquad (1)$$

Where m is order, d is groove density, θ_i incidence angle, θ_d diffraction angle, l is the wavelength. The cavity wavelength $N\lambda/2 = AB + BC$ (cavity length),

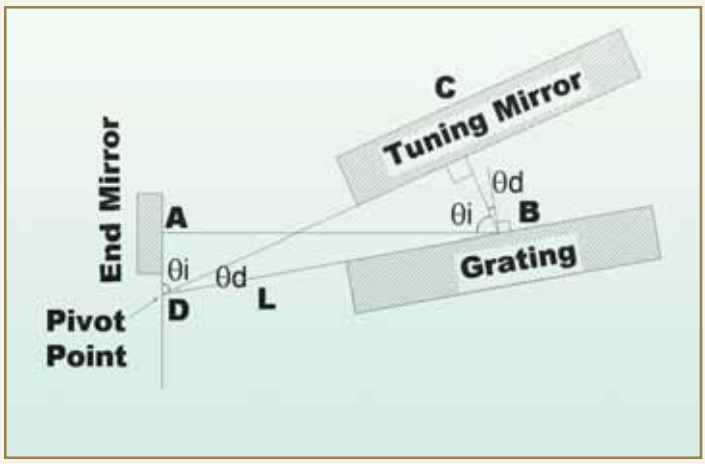

Fig. 1: Schematic of cavity configuration

where N is the longitudinal mode index number.

$AB = L \sin \theta_i$, $BC = L \sin \theta_d$

$N\lambda/2 = L (\sin \theta_i + \sin \theta_d)$ (2)

From equation (1) & (2)

$N = 2mL/d$ (3)

Equation (3) indicates that the longitudinal index number (N) does not depend on the diffraction angle θ_d and lasing wavelength λ and hence does not change, while rotating the tuning mirror. This implies that there will not be any mode hop while tuning the laser, if we match the cavity pivot point carefully.

The end mirror was fixed with epoxy adhesive to a PieZoelectric Transducer (PZT) stack, which provides a maximum displacement of 10mm at a drive voltage of 1 kV. The tuning mirror is fixed on a two-stage rotational table with coarse and fine tuning mechanisms. The first stage provides coarse movement with a minimum resolution of 25.92 arc-sec with a stepper motor of 50,000 micro-steps per revolution. The second stage is used for fine motion. It gives a minimum resolution of 0.0014 arc-sec. A 20 μm PZT with a drive voltage of 1 kV was used in series with a motorized mike at the tuning arm of length 100 mm.

A part of the SLM laser beam was used for beam diagnostics such as linewidth, wavelength and ASE measurement. The schematic of the laser is shown in Fig. 2.

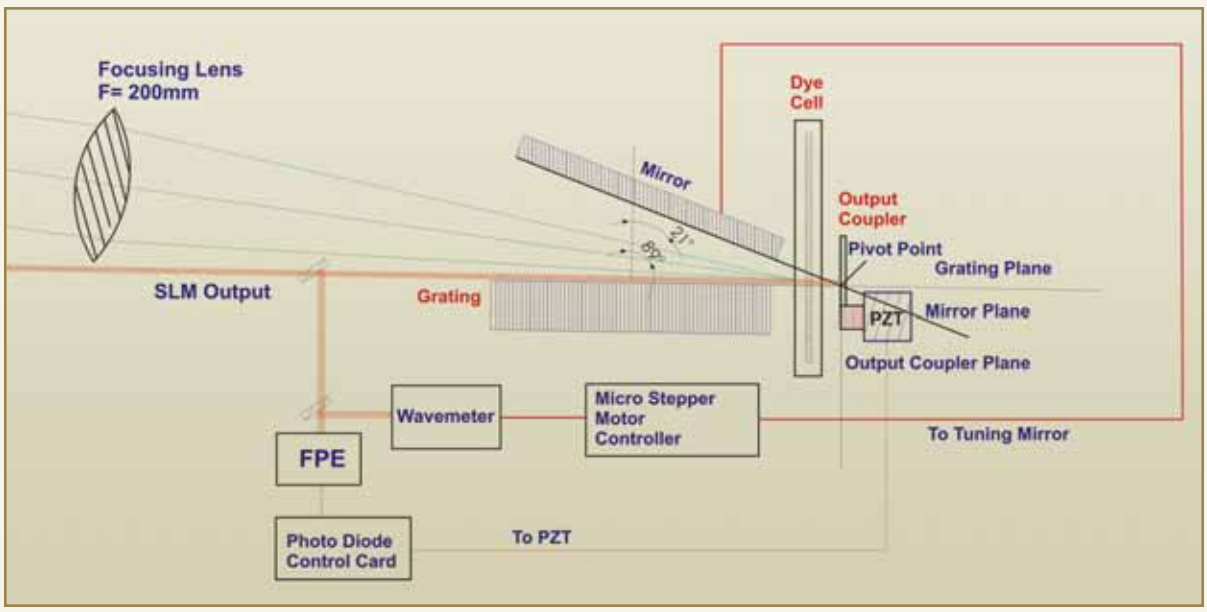

Fig. 2: Schematic of the SLM dye laser

Single Longitudinal Mode Selection

The SLM cavity is a short one, so that, the longitudinal mode spacing exceeds the single pass bandwidth of the laser. The cavity length of 50 mm gives a cavity mode spacing of 3 GHz. Grating is kept at an angle of incidence of 89 ^{0} to provide high dispersion for the laser.

The single pass line width of the grating mirror pair is given by

$$\Delta\lambda = \frac{\sqrt{2}\lambda^2}{\pi l(Sin(\theta)+Sin(\phi))} \quad (4)$$

The single pass line width is calculated to be 1.5 GHz for grating length l=62.5 mm. Since the single pass line width is half of the mode spacing, single longitudinal mode is selected by the cavity. For SLM mode operation, single transverse mode is achieved by the focal spot of pump beam, as it acts as an aperture for filtering higher order modes. The size of the focal spot should be optimum for SLM operation. Too small a spot size increases the diffraction losses and a larger spot size leads to multimode operation.

Experimental results

The SLM dye laser (Fig. 3) was longitudinally pumped with green component of the CVL beam. The green component (510.6 nm) of copper vapour laser operating at 6 kHz repetition rate, was focused into the gain medium with plano convex lens of focal length 200 mm. The size of the local spot in the gain medium is ~160 micrometers. The flow velocity of ethanol (2.55 m/sec) is sufficient to clear the flow with flow clearance ratio 2.5. The regions of concern are those with higher shear near the liquid solid interface where the average velocity varies from zero at the wall to the free stream velocity at some distance. We have carried out detailed computational fluid dynamics simulation, to design and fabricate flow through cells for the SLM dye laser, resulting in higher flow velocities without vortices and low pressure drop.

The linewidth of the laser spectrum was measured with Fabry Perot etalon of FSR 7.5 GHz and CCD camera. The Fabry Perot spectrum of SLM dye laser is shown in Fig. 4. The line width was reduced from 850 MHz to 510 MHz by increasing the incidence angle of grating from 88.5 ^{0} to 89.05 ^{0}. The SLM dye laser wavelength was tuned using central stepper motor and PZT, attached to tuning mirror through a 100 mm mechanical arm. Tuning range of SLM laser was varied between 556.4 nm to 568.5 nm using commercial wavelength meter. The smaller tuning range of 12 nm for SLM dye laser results from the GIG configuration with 89 ^{0} angle of incidence, which leads to high loss in the cavity. At this grating angle, the diffraction efficiency in the first order is around 1%, which is close to the efficiency of laser. Using a grating with higher diffraction efficiency will lead to higher energy conversion efficiency of SLM dye laser.

The Amplified Spontaneous Emission (ASE) was measured with monochromator grating and

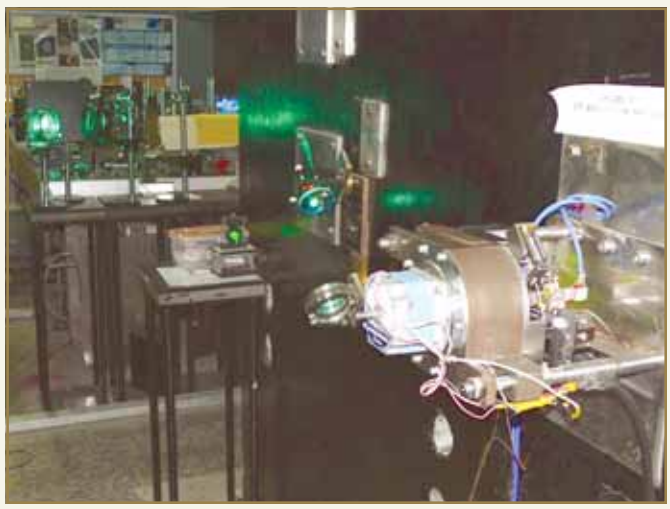

Fig. 3: Remotely tunable, wall mounted SLM dye laser

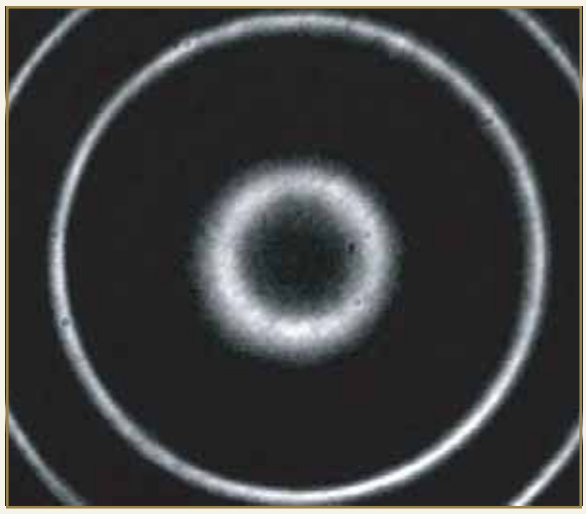

Fig. 4: Fabry Perot spectrum of SLM dye laser

photodiode. The ASE was reduced from 0.5 % to 0.027 % by increasing the angle between pump beam and dye laser beam to 4.7 ^{0}. Since the laser beam is obtained from the zeroth order of grating, the angle between the dye laser axis and pump beam axis is a critical parameter for minimization of ASE.

The FWHM of the SLM dye laser pulse was measured to be 20 ns for pump pulse duration of 30 nsec. The dye laser beam divergence was measured to be 0.648 mrad. SLM laser output of 16 mW was obtained with an efficiency of 1.6 %. The CVL beam size was telescopically reduced from 40 mm to 10 mm. The CVL beam was spatially filtered using a pinhole of diameter 700 μm. The SLM dye laser efficiency was improved from 1.6 % to 2.3 % with an increased output power of 95 mW at 3.8W CVL green beam. Beyond this pump power, a second mode appeared on and off as expected from spatial-hole burning effect. The experimental results are tabulated in Table1.

Mode Hop Free Wavelength scanning of SLM dye laser

SLM dye laser was remotely tuned with the 20 μm PZT fixed on the tuning mirror arm by applying a slowly

Table 1: Performance characteristics of SLM dye laser

Minimum average linewidth of the SLM laser	375 MHz
Energy conversion Efficiency	2.3%
ASE	0.027%
Pulse duration (FWHM)	20 nsec
Tuning range	12 nm

varying voltage (ramp) from 0 – 1kV. The input signal was generated from the computer and fed to the high voltage amplifier of the PZT. The high voltage signal was fed to the PZT at the tuning mirror. Using this technique, mode hop free tuning over a wavelength range from 559.75556 nm to 559.74642 nm (~ 70 GHz) was achieved. Laser wavelength meter and FP etalon fringes monitored the mode hop free tuning of the SLM dye laser. The cavity mode spacing is 3 GHz (~ 3 pm) for 5 cm cavity length. While tuning the SLM laser, the sudden jump of 3 GHz (Cavity FSR) in the wavelength was not detected in the wavelength meter, indicating mode hop free tuning.

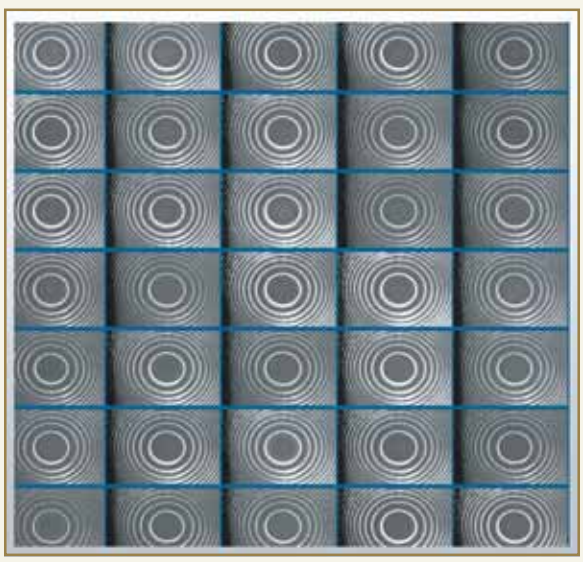

Fig. 5: Single shot fringes from fast CCD camera

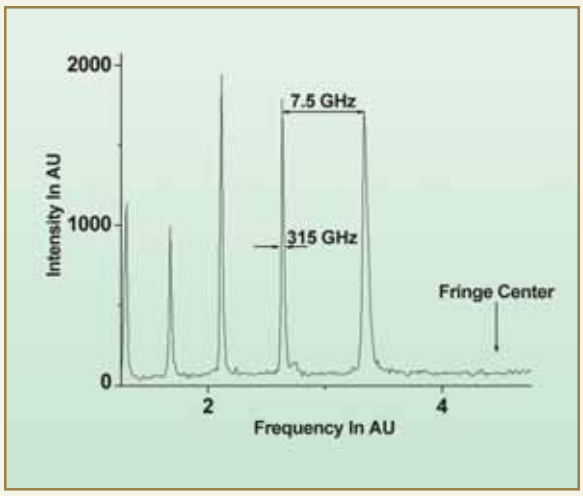

Fig. 6: Intensity pattern of interferogram for single pulse

Single pulse Spectrum

The bandwidth of SLM dye laser was measured with FP etalon of 7.5 GHz and wavelength meter (WS-7L).

A fast CCD camera was externally triggered, to measure the single shot, single pulse bandwidth of the SLM dye laser. Thirty-five frames of single shot, single mode FP fringes are shown in Fig 5. The time average bandwidth was measured as ~375 MHz and the single pulse bandwidth was 315 MHz as shown in Fig. 6.

Conclusion

A compact, short cavity, remotely tunable, high repetition rate grazing incidence grating single longitudinal mode dye laser with mode hop free scanning over 70 GHz has been developed. The average and single pulse bandwidths achieved were 375 MHz and 315 MHz respectively.

ABOUT THE AUTHORS

Dr. (Ms.) Sunita Singh heads the Visible Laser & Optics Section in L&PT Division of BARC. She has worked in the development of high and low power, pulsed, CW, polymeric dye lasers and electron optical imaging devices and streak cameras. Her current interests encompass design, development and delivery of tunable, single longitudinal mode, high power and high repetition rate dye laser facility for laser-based separation process.

Mr. G. Sridhar joined L&PTD in 1996 from the 39th Batch of Training School. He is involved in developing high power, high repetition rate CVL pumped Single Longitudinal Mode dye Oscillator- Amplifier systems. His field of interest includes theoretical and experimental studies of tunable lasers and associated systems, polymeric solid state dye lasers, laser atom interaction.

ABOUT THE AUTHORS

Mr. Vinod Singh Rawat received his M.Tech. in Instrument Technology from IIT Delhi in 1998. He joined L&PTD on 1st September 1999 after graduating from the 8th Batch of OCEP of Training School, BARC in 1998-99. His research interests are tunable laser systems particularly a Single Longitudinal Mode (SLM) pulsed dye laser, wavelength locking, designing of opto-mechanical components, optical instrumentation, optics design, laser beam diagnostic system, vibration analysis and flow visualization in dye cells.

Mr. Nitin O. Kawade received his M.Tech. in Instrument Technology from IIT Delhi. He joined BARC on 1st September 1998 after graduating from the 41st Batch of Training School, BARC. His research interests are laser-based Instrumentation and dye laser control, embedded, real time systems, PIV.

Mr. Aseem Singh Rawat is an Electronics engineer working in L&PT Division, BARC and is from 35th Batch of Training School. His field of interest is laser-based instrumentation. He has been involved in the design and development of laser scan dia gauge, laser surf check, laser velocity meter, Rebound velocity meter. He was involved in technology transfer of lascan dia-gauge, supply of laser surf-check to MPD,BARC and laser velocity meter to DMRL,DRDO, Hyderabad. Presently, he is working on flow visualization using PIV, distance and level measurement using optical triangulation technique and laser beam diagnostic instruments.

Mr. Suman K. Mishra is working in Laser & Plasma Technology Division, BARC, since 2004 in the field of Tunable Dye Laser systems pumped by Copper Vapour Lasers. He joined the Fuel Chemistry Division, BARC, in 2002. His areas of interest include Tunable Lasers, HPLC and Mass Spectrometry.

Dr. L.M. Gantayet is a Distinguished Scientist in the BTD Group of BARC. He has worked in the development of Separation Processes. His current research interest includes development of Laser-Based Separation Processes. He has contributed to new technologies required for such processes.

बीएआरसी न्यूज़लेटर
BARC NEWSLETTER

LASER SEPARATION OF SULPHUR – 33 ISOTOPE : A NOVEL TWO-STAGE APPROACH

P. Mathi, D.N. Joshi, P.K. Sahoo, A.K. Nayak and V. Parthasarathy
Laser & Plasma Technology Division

and

M.N. Deo
High Pressure Physics Division

and

S.K. Sarkar
Radiation & Photochemistry Division

This paper won the Best Poster Presentation Award at the National Symposium on Radiation & Photochemistry (NSRP–2007), held at the National Centre for Ultra-fast Processes, University of Madras, Chennai, during January 29–31, 2007

The element sulphur has four stable isotopes with the natural abundance $^{32}S : {}^{33}S : {}^{34}S : {}^{36}S = 95.0 : 0.76 : 4.22 : 0.014$ % respectively. Sulphur depleted in it's S – 32 content and enriched in S – 33 and S – 34 isotopes, is used as target material in a nuclear reactor for producing phosphorous – 33 (P-33), an important radioisotope in many biological applications. The ν_3 absorption features of the two prominent isotopic variants $^{32}SF_6$ and $^{34}SF_6$ are separated by an isotope shift of 17 cm^{-1}. However, the isotopic shift of minor isotopic species $^{33}SF_6$ is only 8.5 cm^{-1} from $^{32}SF_6$. Therefore, a considerable overlap occurs between the absorption bands of these species and the spectral features are not clearly resolved at room temperature. For such a reason, a high degree of enrichment in S – 33 can only be obtained, by a two-stage, InfraRed Multiple Photon Dissociation (IRMPD) process.

In stage 1, $^{32}SF_6$ is targeted and dissociated selectively, using a pulsed CO_2 laser tuned at an appropriate wavelength.

$$^{32}SF_6 \longrightarrow {}^{32}SF_5 + F \longrightarrow \text{Products}$$

The residual material is enriched in S –34 and S – 33 isotopes as compared to the initial natural abundance levels. In stage 2 of the process, recovered material can be selectively dissociated with respect to $^{34}SF_6$, so that the residual SF_6 is further enriched in S – 33 isotopes.

$$^{34}SF_6 \longrightarrow {}^{34}SF_5 + F \longrightarrow \text{Products}$$

Our studies on the IRMPD of natural SF_6 at room temperature with suitable scavengers showed, that it was possible to isolate residual SF_6 enriched in both S – 33 and S – 34 after stage 1 photolysis. However, at room temperature, the vibrational – rotational transitions of polyatomic molecules, spread out over a large frequency range, owing to the rotational structure and hot bands. This resulted in poor selectivity for both excitation and dissociation of the targeted species, leading to about 50 % loss of $^{33}SF_6$. By cooling the substrate gas during photolysis, these effects can

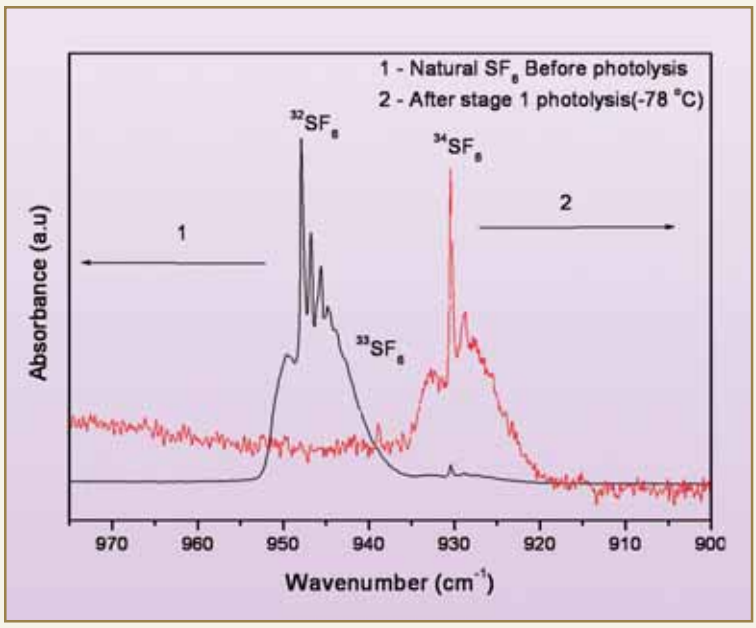

Photolysis results at - 78 °C: Stage1; Selective S-32 removal, Residual SF_6 composition

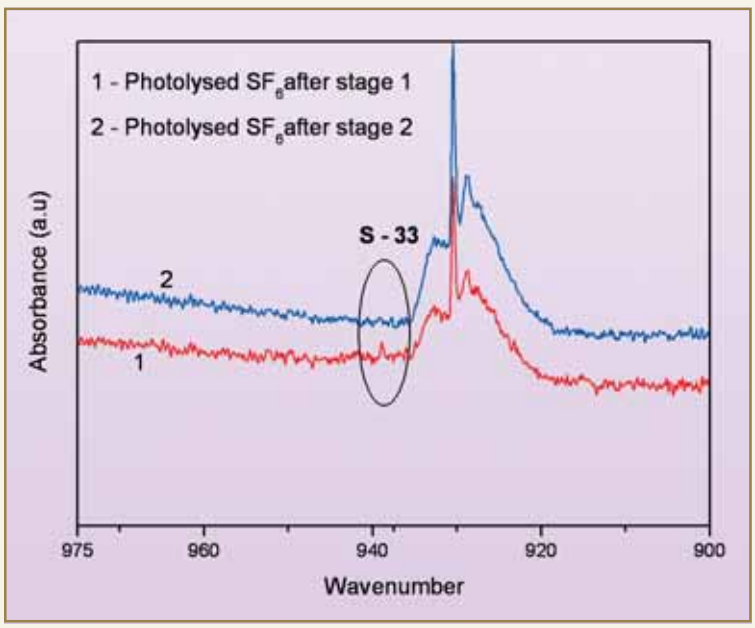

Photolysis results at - 78 °C : Stage 2 ; Selective S-33 removal in residual SF_6 from stage 1., $^{33}S:^{34}S$ = 92 : 8 % in the photo product SO_2F_2

be minimized to obtain better process selectivity. Therefore, successive stages of photolysis involving IR MPD of SF_6 were carried out at – 78 ^{0}C.

In the initial runs, $^{32}SF_6$ was dissociated first using 10 P (18) line of the CO_2 laser, followed by $^{34}SF_6$ removal using 10 P (38) or 10 P(40) line. Our efforts to obtain a final residual SF_6 highly enriched in $^{33}SF_6$ were not successful, as we ended up burning it completely during stage 2 removal of $^{34}SF_6$. From this important observation we realized, that it would be advantageous to selectively dissociate $^{33}SF_6$ in stage 2 rather than removing $^{34}SF_6$. Such an approach has two advantages, viz.,

(i) the inherent loss of S – 33 associated with the excitation of $^{34}SF_6$ using a red – shifted absorption frequency will be reduced

(ii) the line 10 P (26) required for $^{33}SF_6$ dissociation has better laser efficiency than 10 P (38) used for $^{34}SF_6$ removal.

Photolysis of natural SF_6 at ~ 0.3 Torr was done by 10 P (18) line in stage 1 and the residual, enriched sample was further irradiated in the same cell, in stage 2, at an appropriate laser wavelength with 100 ns tail free pulses. Further, we incorporated an isolation valve between the cell and the scavenger trap. This feature was very useful in controlling the exposure of the photolysed material to a scavenger, during the run as and

when required. In the first stage, for example, all the volatile photoproducts like SOF_2 / SOF_4 / SO_2F_2 were allowed to react with NaOH / trigol scavenger during the run and the only end product remaining in the gas phase was residual enriched SF_6. This novel idea helped in closing the chemical cycle between the two stages of irradiation as we could readily deploy the photoproduct (the residual SF_6 enriched in the minor isotopes) from stage 1 as feed material in stage 2, without any additional effort. During stage 2 photolysis with 10 P (26) line in the same cell, scavenger trap was kept isolated so that, formation of the end product SO_2F_2 highly enriched in S – 33 was facilitated. It can be seen from the figures, that there was an appreciable dissociation for $^{33}SF_6$ while $^{34}SF_6$ remained nearly unaffected. The relative percentage composition of ^{33}S: ^{34}S in the final product was estimated to be 92 : 8 % (see Figs.).

ABOUT THE AUTHORS

Ms. P. Mathi joined the Laser and Plasma Technology Division after graduating from the 44th Batch of BARC Training School. Her field of work is laser enrichment of isotopes of light elements at macroscopic levels.

Mr. D. N. Joshi joined BARC in 1969 and obtained his B.Sc. (Hons.) from Bombay University in 1973. He has specialized in vacuum technology and various optical coatings. Currently he is developing photolysis cells, suitable for use at both low and high temperatures.

Mr. P. K. Sahoo after graduation in Chemistry from Utkal University, joined the Laser & Plasma Technology Division in 2006.

ABOUT THE AUTHORS

Dr. Akshya Kumar Nayak obtained his M.Sc. from Utkal University in 1980 and joined the Multi Disciplinary Research Section in 1982 after graduating from the BARC Training School. He got his Ph.D. from University of Mumbai in 1992. His Post Doctoral work (1993 – 1995) at the National Institute of Science and Technology, Gaithersburg MD, USA with Dr. A. Fahr, involved the measurements of UV-VUV absorption cross sections of hydrocarbon compounds. His current research interest includes the study of dynamics and collisional effects on multiphoton dissociation, determination of radical – radical and radical – molecule gas phase rate constants by kinetic absorption technique and laser isotope separation.

Dr. Venkatachari Parthasarathy joined BARC in 1976 after his Master's degree in Chemistry from IIT Kanpur. He received his Ph.D. degree from the University of Mumbai in 1986 and did his Post – doctoral fellowship at the Ecole Polytechnique Federale de Lausanne, Switzerland during 1987 – '88. As Head of the Molecular Isotopic Photochemistry Section of the L&PT Division, his current research is focused on laser enrichment of various light elements at macroscopic levels.

Dr. M.N. Deo obtained his M.Sc. from Banaras Hindu University in 1983. He got his Ph.D. from University of Mumbai in 1993. He was a Post – Doctoral fellow at the Institute of Atomic and Molecular Science, Taiwan during 1996-97. He did his Post Doctoral fellowship (1997 – 98) and held a Visiting Scientist position (2002) at the Nobeyama Radio Observatory, Japan. He has specialized in high resolution molecular spectroscopy.

Dr. Sisir K. Sarkar joined BARC in 1974 and heads the Radiation & Photochemistry Division, BARC. Dr. Sarkar did his Post-doctoral work at Columbia University, New York with Prof. J.W.Flynn in the area of chemical dynamics using high-resolution semiconductor diode laser. He has worked as a Visiting Scientist at the P.N.Lebedev Physical Institute & Institute of Spectroscopy, Russia, Kyoto Institute of Technology, Japan and Institute of Chemical Process Fundamentals, Czech Republic, University of Heidelberg, Germany with various laser systems including Free Electron Laser. His research interest includes laser selective photophysics and photochemistry in nuclear fuel cycle, chemical dynamics, spectroscopy and laser development.

बीएआरसी न्यूज़लेटर
BARC NEWSLETTER

CALIBRATION OF AERODYNAMIC AND OPTICAL PARTICLE SIZING INSTRUMENTS WITH THE ELECTRICAL MOBILITY SIZER

Arshad Khan, P.S. Kothalkar, B.K. Sapra and Y.S. Mayya
Environmental Assessment Division

This paper received the 2nd Prize in the Poster presentation category at the Indian Aerosol Science & Technology Assoc. (IASTA-2007) conference, organized at the National Physical Laboratory, New Delhi, during November 14-16, 2007

Introduction

Particle sizing instruments are based on various principles which segregate the aerosol particles according to their size. Based on the classification technique, each instrument has a specified and limited size range. This study is aimed at comparing the size distributions obtained from various instruments in the overlapping size ranges, so as to assess their ability to generate continuous distributions in the entire particle size range (10 nm to 30 μm) (Peters et al 1993). In the present study, BARC developed PASS-LP (Sanjay et al, 2005) and GRIMM 1.108 Optical Particle Counter were compared with the GRIMM Scanning Mobility Particle Sizer (SMPS). The 11 stage Cascade Impactor has seven stages operating at normal pressure and four at low pressure (150 mm Hg). The operational flow rate is 10 lpm with the minimum cut off diameter of 0.1 μm. The GRIMM 1.108 Aerosol Spectrometer works on the principle of light scattering and gives number size distribution in 15 size channels from 0.3 μm to 20.0 μm. The GRIMM SMPS classifies particles based on their electrical mobilities in an applied field and hence can be regarded as a primary calibration system. The instrument segregates particles in 44 size channels ranging from 9.8 nm to 874 nm. However, the comparisons need to be made with caution, because while the impactor and the optical counter give the aerodynamic diameter and the optical diameter respectively, the SMPS estimates the mobility diameter. This calls for appropriate conversions and correction factors to be used, to arrive at near-accurate comparisons.

Experimental Setup

The study consisted of two sets of experiments: (1) Comparison of mass size distribution obtained from LP Impactor with number size distribution from SMPS and (2) Comparison of number size distribution from SMPS with the same obtained from OPC.

Study 1

In this study, test particles used were NaCl aerosols, generated by a compressed air nebulizer using 5 % salt solution. These were fed to a chamber of volume 27 litres with sampling port arrangements. For drying of generated aerosols, extra N_2 gas was continuously supplied @ 20 l min^{-1}. Parallel sampling was carried out with 11 stage LP-PASS impactor and SMPS. To measure the total particulate concentration inside the chamber, gross filter paper sample @10 lpm was taken. The mass-size distribution and the total

mass concentration were estimated, by subjecting the filter paper substrates of the impactor and the gross sampler respectively to both gravimetry as well ionic conductivity techniques. The overlapping size range of the two instruments being compared was 0.1-0.75 μm.

Study 2

In the second study, particle number concentrations obtained from the OPC were compared with those obtained from the SMPS in the overlapping range (0.3- 0.8 mm). The aerosols used in this study were ambient room aerosols and particles generated from a UV source lamp.

Results and Discussion

Study 1

The total mass concentration measured by gravimetry in all the 11 stages of the impactor (<21.3 μm) was found to be 44.06 mg/m^3, which was in good agreement with 40.1 mg/m^3 obtained from the gross filter paper sample. Using conductivity measurements, total concentrations were found to be 61.82 mg/m^3 and 57.25 mg/m^3 from impactor and grab sample respectively. The Mass Median Diameters (MMDs) estimated by gravimetry (with appropriate density corrections for NaCl aerosols) and conductivity measurements were found to be 1.14 μm (GSD= 3.2) and 1.24 μm (GSD= 2.6) respectively [Fig. 1 (a)]. Although the concentrations estimated by conductivity are 1.4 times higher than that estimated from gravimetry, the impactor estimated masses are consistent with the gross filter results by both the techniques.

The number concentrations obtained from the SMPS, were converted to the mass size distributions, assuming the density of NaCl particles as 2.16 gm/cm^3. In case of the impactor data, care was taken to convert the aerodynamic diameters, to the physical diameters, using the density corrections so as to make the data amenable to comparison with the SMPS data. The SMPS data gave a Count Median Diameter (CMD) of 0.064 μm with a GSD of 2.07 (in the sizes below 0.75 μm) which corresponds to a Mass Median Diameter (MMD) of 0.33 μm. This is in close agreement with the MMD value of 0.38 mm, GSD=2.8) obtained by fitting the impactor data in

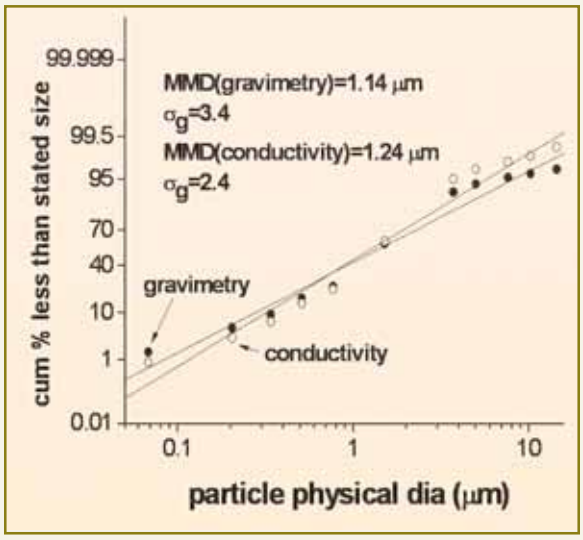

Fig.1(a): Impactor based mass size distributions: gravimetry and conductivity techniques

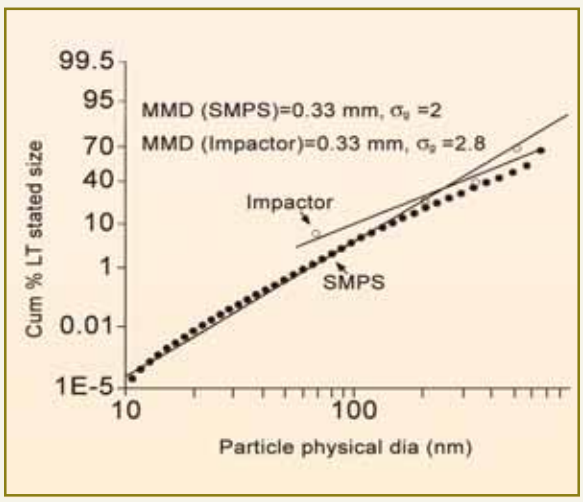

Fig.1(b): MMDs obtained from SMPS and low pressure impactor in common size ranges

the size range 0.77-0.06 μm to a lognormal distribution. [Fig.1(b)].

Interestingly, the total masses in the common size range (<0.75 μm) were also found to be fairly close; 10.42 mg/m^3 from the impactor and 8.15 mg/m^3 from SMPS.

Study 2

The number size distributions obtained by SMPS and OPC for ambient room aerosols in room environment were compared with each other. The instruments show good agreement in the common size channels [Fig. 2 (a)].

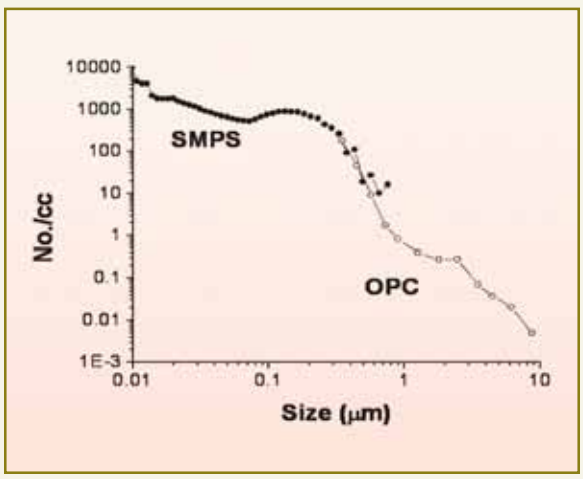

Fig. 2(a): Number size distribution recorded by SMPS and OPC for ambient room aerosols

As a second test involving very high particle concentrations, particles generated by UV source (known to generate particles in the 15-20 nm range) were used as test aerosols. In both the cases, the continuity and the trends of the size distributions were retained when the data from the two instruments was plotted together. Also, the data points of the two instruments in the overlapping size ranges were in close proximity [Fig. 2(b)].

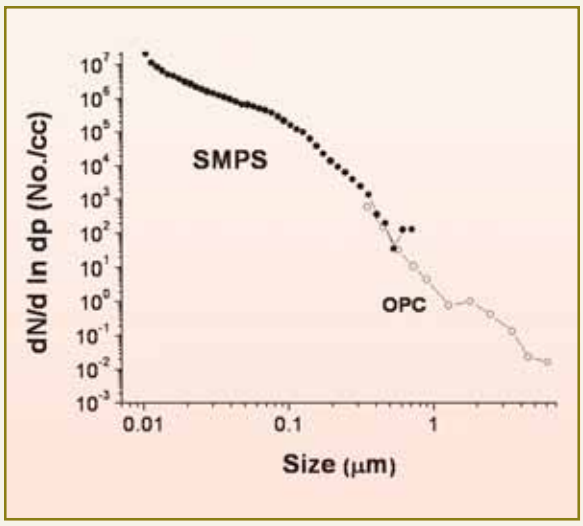

Fig. 2(b): Number size distribution recorded by SMPS and OPC for UV source generated aerosols

Conclusion

The experiments show that the size distributions obtained by the indigenous impactor and SMPS instruments, were in good agreement with each other. Measurements also indicate good agreement between SMPS and OPC in their overlapping size region.

References

1. Peters, T.M., H.M. Chein, D.A. Lundgren and P.B. Keady (1993), Comparison and combination of aerosol size distributions measured with a low pressure impactor, differential mobility particle sizer, electrical aerosol analyzer, and aerodynamic particle sizer, *Aerosol Sci. Technol.*, 19: 396-405.

2. Sanjay Singh, Arshad Khan, T. Das, B. K. Sapra, Pushparaja and Y. S. Mayya (2005), Indigenous development of an aerodynamic size separator for aerosol size distribution studies, *Current Science*, Vol. 88, no. 9: 1426-1433.

ABOUT THE AUTHORS

Mr. Arshad Khan is M.Tech. in Environmental Engineering and he joined the Environmental Assessment Division from the OCEP-8th Batch of Training School in 1999. He has specialized in the design, development and evaluation of aerosol measurement systems. He is associated with experimental studies on postulated reactor accidents and validation of reactor safety assessment aerosol behaviour codes. He has about 20 publications to his credit.

Ms. P.S. Kothalkar, Environmental Assessment Division, joined BARC through the10th Batch of Health Physics Training course. She did her B.Sc. in Physics from the University of Mumbai. She is actively engaged in the experimentation related to electromigration of aerosol and containment studies.

Dr. B.K. Sapra, Environmental Assessment Division, joined BARC through the 1988-89 (32nd) Batch of Training School. She did her M.Sc. and Ph.D. in Physics from University of Mumbai. She has specialized in aerosol studies vis-à-vis their generation, size characterization, deposition and mitigation. She has also carried out experimental and theoretical studies on the electromigration characteristics of aerosols. She is actively involved in studies on behaviour of aerosols in confined environments, especially relating to reactor containment studies under postulated accident scenarios. She has about 50 publications in journals and conference proceedings.

Dr. Y.S. Mayya has been working in the areas of aerosol physics, radon, thoron dosimetry, radiation epidemiology, since 1975. His contributions range from theoretical studies on particulate phenomenology to developing instruments and techniques for dosimetric applications. He has about 65 publications in refereed Journals. He is the head of Aerosol Monitoring and Simulation Section of the Environmental Assessment Division, Professor at Homi Bhabha National Institute and is a recognized Ph.D. guide of the University of Mumbai. He was the president of Asian Aerosol Research Assembly during 2005-2007, member of the Editorial Board of the Journal of Air Quality and Aerosol Research and is a member of the International Aerosol Awards Committee.

बीएआरसी न्यूज़लेटर
BARC NEWSLETTER

STUDY OF ULTRA-COLD ATOMS IN MAGNETIC AND OPTICAL TRAP

Swarupananda Pradhan
Atomic Physics and Quantum Optics Section
Laser and Plasma Technology Division

This paper received the Best Thesis Award at the National Laser Symposium, held at Vadodara, from Dec 17-20, 2007

Introduction

Experimental developments in the field of laser cooling and trapping have propelled Science & Technology into an exploratory regime, which has revealed numerous innovative and fascinating processes, playing at the edge of physical limits. The state-of-art technology has made it possible, to routinely prepare dense sample of atomic gases at ultracold temperatures, in the nano-Kelvin ranges. Innumerable applications of laser-cooled atoms in basic studies include: ultra-precision spectroscopy, physics of collisions mediated by long range interactions, cold molecule formation, ultra-cold plasmas, quantum optics, matter wave physics, quantum atom optics, degenerate quantum gases including bosonic and fermionic condensates. Experimental realization of Bose-Einstein condensation is, perhaps, the landmark accomplishment of ultra-cold atom research which has led to explosive growth of research in quantum degenerate gases, there by providing an opportunity to develop a lucid picture of cooper pairing, superfluidity, quantized vortices, Josephson junction, quantum phase transitions etc. The applications of laser-cooled atoms are equally fascinating and include, for example, precision atomic clocks, ultra-precise gravity gradiometer, atom lithography and quantum information processing.

The exciting and diverse applications of ultra-cold atoms can be accomplished, only if the contemporary techniques of laser cooling and trapping of atoms are developed in the laboratory, together with laser spectroscopic techniques, for characterization of ultra-cold atoms and their behaviour under collision and interaction with electromagnetic fields. This, however, is a nontrivial task involving a variety of disciplines and experimental systems. At the same time, there also exist a number of fundamental issues relating to the laser-atom and atom-atom interactions, in the very process of laser cooling and trapping of neutral atoms. In this article, experimental and relevant theoretical work dealing with these very subjects is summarized. For laser cooling and trapping studies, the most suitable candidates are alkali atoms owing to their simple valence shell structures, favourable cross-sections for the radiative and non-radiative processes and the availability of appropriate laser sources to access their resonance transitions. Atomic systems targeted in the present work are Cs and Rb, which are cooled and trapped and then subjected to a variety of investigations.

High resolution laser spectroscopy

Development of various high resolution laser spectroscopic techniques are inevitable tasks to be performed prior to commencing experiments, on laser cooling and trapping of atoms. These techniques play a crucial role in the characterization and manipulation of cold atoms. This involvement also arises from the requirement of stabilization of a single mode laser on a given atomic resonance, at a pre-determined red detuned frequency, with frequency stability of a few hundred KHz over a long duration of time [70-74], for efficient generation of a continuous source of cold atoms. Since the frequency stability is limited by the width of the atomic resonance line, it is preferable to lock the laser on a narrow spectral linewidth, obtained using a Doppler-free spectroscopic technique. Owing to its simplicity, the Saturated Absorption Spectroscopy (SAS) technique is the most frequently used Doppler-free technique in laser cooling and trapping experiments. The narrow linewidth (~20-30 MHz) SAS signal is used as frequency reference, for locking of the diode lasers on the respective transitions. Two independent frequency stabilization strategies are adapted, that rely on software control and hardware control of the error signal. The corresponding locking signal has been illustrated in Fig. 1. The software locking is the simplest scheme for frequency stabilization, however, it has limitation in controlling short-term frequency instability, due to the inherent slow response of the software. This shortcoming is circumvented by the use of hardware locking scheme, which has proven to be more accurate and reliable. The other minor advantage of hardware locking scheme is that, it overcomes the requirement of a dedicated computer system.

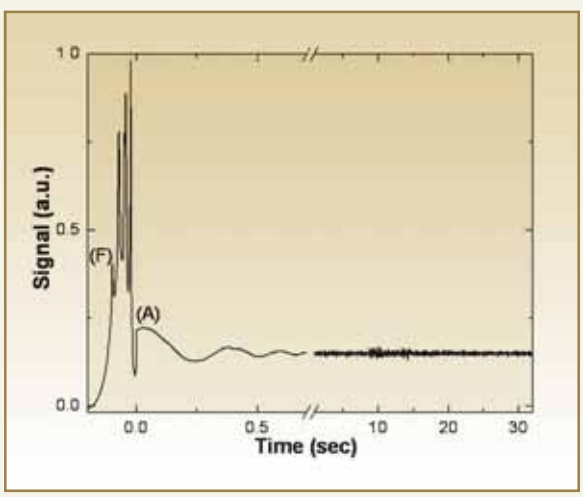

Fig. 1a: Practical realization of a diode laser locked to the red side of the cooling transition $6s_{1/2}$ F=4 → $6p_{3/2}$ F′ =5 [marked A] of Cs under software control. For convenience the transition on the other extreme, (F→F′)=(4→3), is marked [F]. The laser frequency is scanned up to the predetermined lock point, where it gets locked through software control. After enabling locking, the laser frequency undergoes a damped oscillatory motion and stabilizes within an accuracy of ± 1.2 MHz. The stabilization time is < 0.7 sec and the laser remains locked for hours.

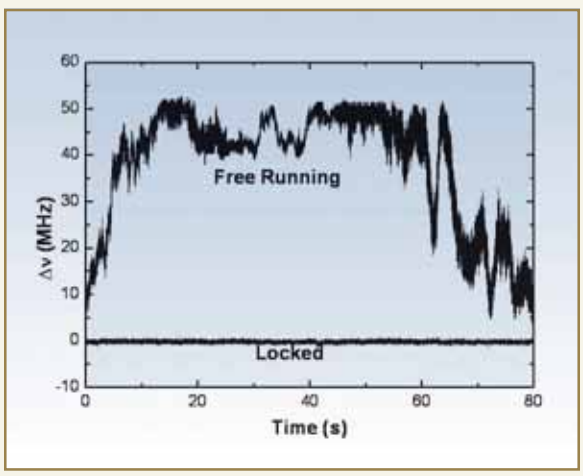

Fig. 1b: Frequency stability of a diode laser locked to the SAS signal of ^{87}Rb cooling transition, using hardware locking system. This system has the facility to lock on both sides of an atomic transition. It has been designed to work under the supervision of a computer and is isolated from the computer after enabling locking. The long term stability of the hardware lock is observed to be < ± 1 MHz. The frequency stability of a free running diode laser is shown for comparison.

Simply stabilizing the laser frequency is not a sufficient condition, as in many laser cooling experiments, it is often required to tune the laser frequency under locked condition, to ensure good frequency stability over a wide range of frequencies. This purpose is not served by directly locking to the saturation absorption profile, as in this procedure the capture range is limited by the change in the slope of the SAS signal. In situations such as those of ^{133}Cs and ^{85}Rb, the SAS signals do not provide good enough slopes for locking the laser frequency as desired by laser cooling experiment. This problem can be circumvented, by locking the laser at a different location, for e.g. a nearby crossover resonance having large signal strength, followed by either shifting the laser frequency using an Acousto-Optic Modulator (AOM) or shifting the reference SAS signal. We have developed a technique to shift the reference SAS signal utilizing Zeeman effect on the atomic hyperfine transitions.

The transmission of the probe beam in SAS is governed by the extent of absorption of the probe beam, which depends on the oscillator strength, the depth of the Bennett hole burning (depends on the oscillator strength and intensity of the pump beam) and the optical pumping to the other hyperfine ground level by optical transition, relaxation or combination of both. Here, we control the strength of various resonance peaks of SAS, by precisely manipulating optical pumping between Zeeman substate with the use of polarized laser beams and DC magnetic field. Fig. 2 illustrates such dependences, along with magnetic field dependent control shifting of SAS peaks, for specific configuration of pump-probe laser polarization. This set-up, facilitates linear tuning range of 400 MHz and 150 MHz for a lock on the peak of the cycling transition ($F = 4 \rightarrow F' = 5$) and the crossover resonance respectively. It may be noted here, that tuning of a side-lock exhibits nonlinearity with respect to the magnetic field, due to additional mechanism of Zeeman splitting assisted line broadening of SAS peaks.

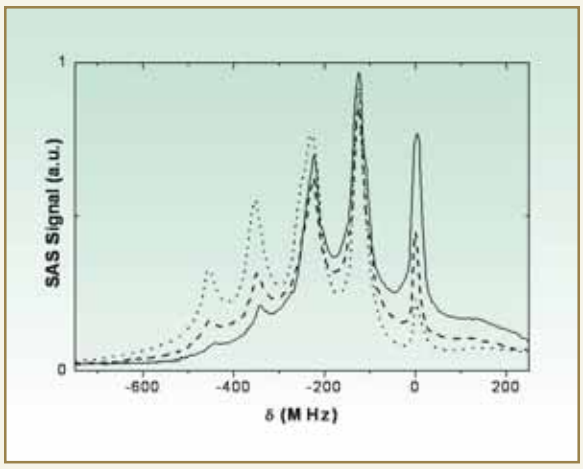

Fig. 2a: SAS signal of $6s_{1/2}$ F = 4 $\rightarrow$ $6p_{3/2}$ F' =3, 4, 5 transitions of Cs. The dotted curve is for plane polarized pump and probe beams and B=0. The dashed line is for pump and probe beam with (σ^+ - σ^- or σ^- - σ^+) and B=0. The solid line represents the signal taken with pump and probe beam (σ^+ - σ^- or σ^- - σ^+) configuration and $B \sim$ 4.7 G.

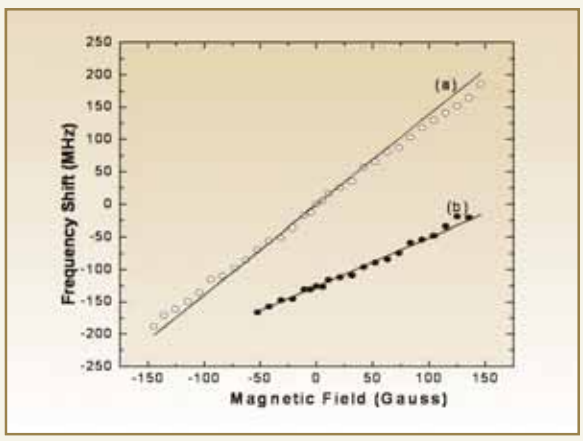

Fig. 2b: Zeeman shifting of the peak of cyclic (hollow circle) and crossover line (solid circle) measured from the field-free cyclic transition. Both the pump and the probe laser are right circularly polarized. Theoretically expected behaviour is shown by solid lines (a) and (b).

More involved Doppler-free techniques such as Degenerate Four-Wave Mixing (DFWM) and Nearly Degenerate Four Wave Mixing (NDFWM) finds use in the context of characterization of laser cooled atoms.

DFWM and NDFWM spectroscopy has been performed, on the $6s_{1/2}\, F = 4 \rightarrow 6p_{3/2}\, F' = 3, 4, 5$ transition of Cs atomic vapour. The novelty of the employed experimental configuration has resulted in several new observations. The DFWM signal, in the absence of a state preparation laser, is investigated for variation in laser power and polarization and the temperature of the vapour cell. In the presence of a state preparation laser, we observe an improvement in reflectivity, corresponding to the non-cycling transitions and also appearance of many new resonances. The origin of these new resonances has been explained, in terms of the conservation of population, due to the state preparation laser. In the NDFWM experiments, we observed resonances for $\delta = 0, \pm 2\Delta$, where Δ (pump detuning) and δ (probe detuning) are laser detuning from the field free resonance $6s_{1/2}\, F = 4 \rightarrow 6p_{3/2}\, F' = 5$ and from the pump frequency respectively. These resonances along with their characterization for a wide range of Δ are shown in Fig. 3. The origin of these resonances can be visualized, by considering the Bragg scattering of the forward pump beam and the backward pump beam from the grating structure, generated by the probe beam, with backward pump beam and forward pump beam respectively.

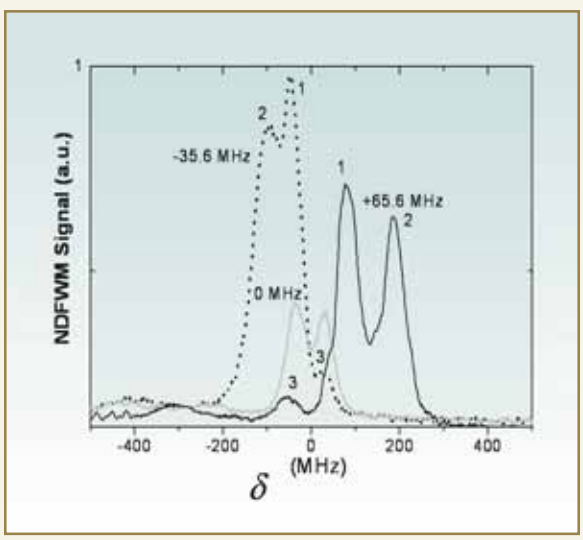

Fig. 3a: The profile shows the NDFWM signal for probe laser scanned across the $6s_{1/2}$ F = 4 → $6p_{3/2}$ F' = 3, 4, 5 hyperfine transitions and the pump beam stabilized at +65.6 MHz (black line), 0 MHz (gray line) and -35.6 MHz (dotted line) away from the $6s_{1/2}$ F = 4 → $6p_{3/2}$ F' = 5 transition. The first kind (1) and second kind (2) resonances arises due to the Bragg scattering of the backward pump beam and where as the third kind (3) resonance results from that of the forward pump beam. The broad structure seen at -200 to -500 MHz is due to interaction of the probe laser with the $6s_{1/2}$ F = 4 → $6p_{3/2}$ F' = 3, 4 hyperfine transitions.

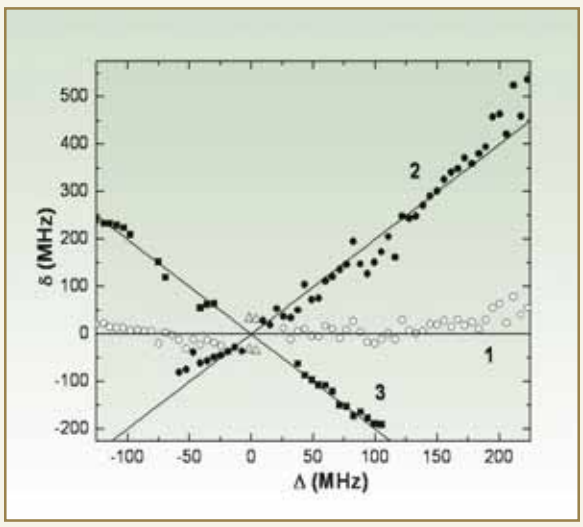

Fig. 3b: Variation of the frequency position of three kinds of resonances in the NDFWM as a function of Δ. The measurements, pertaining to the resonances of the first, second and third kind are shown by the hollow circles, solid circles and solid squares respectively. The solid line in each of these cases has slopes 0, +2 and -2 respectively. This proves that the resonances appear at probe detuning of Δ, 3 Δ and - Δ. For pump laser detuning ≤ 5 MHz, we observe two peaks (hallow triangle) where the three kinds of resonances converge, as for these pump detunings, the probe beams interact with nearly zero velocity group of atoms.

The relative strength of these resonances clearly illustrates the mechanism of thermal wash-out, operating in a thermal vapour cell environment.

Cooling and trapping of Cesium and Rubidium atoms

The development of MOT involves a variety of subsystems, consisting of optics and layout for the manipulation and transport of laser beams, ultra-high vacuum optical chamber, magnetic field, alkali metal reservoir and its characterization etc.; apart from the spectroscopic techniques, discussed in the context of high resolution laser spectroscopy. Further, the protocols for achieving laser cooling and trapping have to be developed, for obtaining cold atomic samples on demand, for experiments on hand. Here we present our work, on development of two independent MOT systems for cooling and trapping of Cs and Rb atoms.

The Cs MOT developed in our laboratory has a simple design and uses locally made low-cost equipment, except for the single mode diode lasers. It must be noted here, that this MOT is the first trap demonstrated in the country, for cooling and trapping of Cs atoms. The trap has many unique features : it uses an octagonal shaped ultra-high vacuum optical chamber, that is fabricated from a single metal piece thereby avoiding any vacuum joints, use of helicoflex seals for vacuum sealing, a continuous source of Cs vapour source along with online measurement of background density of Cs atoms, locally developed frequency stabilization unit and all the equipment has been set-up on an indigenously developed vibration isolation table of size 4 ft. x 3 ft. The development of the trap is also accompanied by concurrent development of simulation codes for magnetic coils and also a software scheme for frequency stabilization. This trap has served as a workhorse for a variety of experiments reported in this article.

The Rb MOT is a more involved experimental system, and has been developed to extend the work to pure magnetic trapping and optical dipole trapping of cold atoms, generated in a MOT. It's design is based on the experience generated in the work, on Cs MOT. In this trap, we have incorporated an optical isolator to protect the diode lasers against the optical feedback and acousto-optical modulators for very precise control, over the frequency detuning of diode lasers. The trap includes additional features such as use of Titanium sublimation pump, multiple alkali vapour sources, steering magnetic field and provisions for setting up integrated magnetic and optical dipole trap. The trap, in its MOT form, has been used to obtain cold clouds of both ^{87}Rb and ^{85}Rb.

In a typical MOT operation, we obtain $>10^7$ cold atoms trapped in a volume of $\sim 0.5 \times 10^{-3}$ cm^3, thereby reaching a density in the range of $\sim 10^{10}$ atoms/cm^3. Further, depending on the experimental conditions, the cloud can have a temperature in the range of 100 μK to several mK. These measurements required specialized diagnostic techniques, which are narrated in the subsequent section. While $>10^7$ cold atoms are sufficient for many interesting physics experiments, we may add here, that the Rb MOT has provisions to improve the number of trapped atoms further by two orders of magnitude. It is a crucial requirement for realization of degenerate quantum gas.

The cold atomic sample in the sub-Doppler cooling limit, has played an unparalleled role in revealing various issues in the foundations of Physics. In practice, such samples can be realized by transferring laser-cooled atoms in a MOT, to a pure magnetic trap or an optical dipole trap and subjecting these samples to evaporative cooling. In this context, we have made significant progress towards a far-off detuned optical dipole trap, using a single mode Yb:Yag laser. The dipole trap has been considerably explored and the specialized techniques developed include manipulation of the dipole trapping laser, absorption imaging, transfer of atoms from one hyperfine level to the other and sequential control operation of the MOT parameters.

Diagnostic techniques and characterization of cold atomic clouds

A cold cloud of atoms trapped in a MOT has three intrinsic characteristics: the steady state number of trapped atoms (N_{ss}), the atom density (n) and the temperature (T). Knowledge about these parameters is a must, for use of the cold atoms in any experiments and also for optimizing the trap, with respect to it's operating parameters, i.e. intensity of trapping beams, detuning of the cooling beam from the atomic resonance, detuning of the repumping laser beam, gradient of the quadrupole magnetic field and the density of background atoms. It is also important to have a precise knowledge of the rates of various kinetic processes, namely, the atom capture rate ($\boldsymbol{R}$), linear loss rate (α) due to collision with the background atoms and the quadratic loss rate due to cold-cold collisions (β). These kinetic processes in turn, determine N_{ss} and and also the lifetime (τ_M) of atoms in the trap. Measurement of these various attributes of the MOT, requires a variety of experimental techniques and data analysis procedures. Characterization techniques for a MOT are largely derived from the analysis of the fluorescence, originating from the cooled and trapped atoms. Consequently, the fluorescence spectroscopy in frequency, time and spatial domain, forms an indispensable tool in the development of the diagnosis and characterization techniques. Very similar techniques have been used for both Cs and Rb MOT.

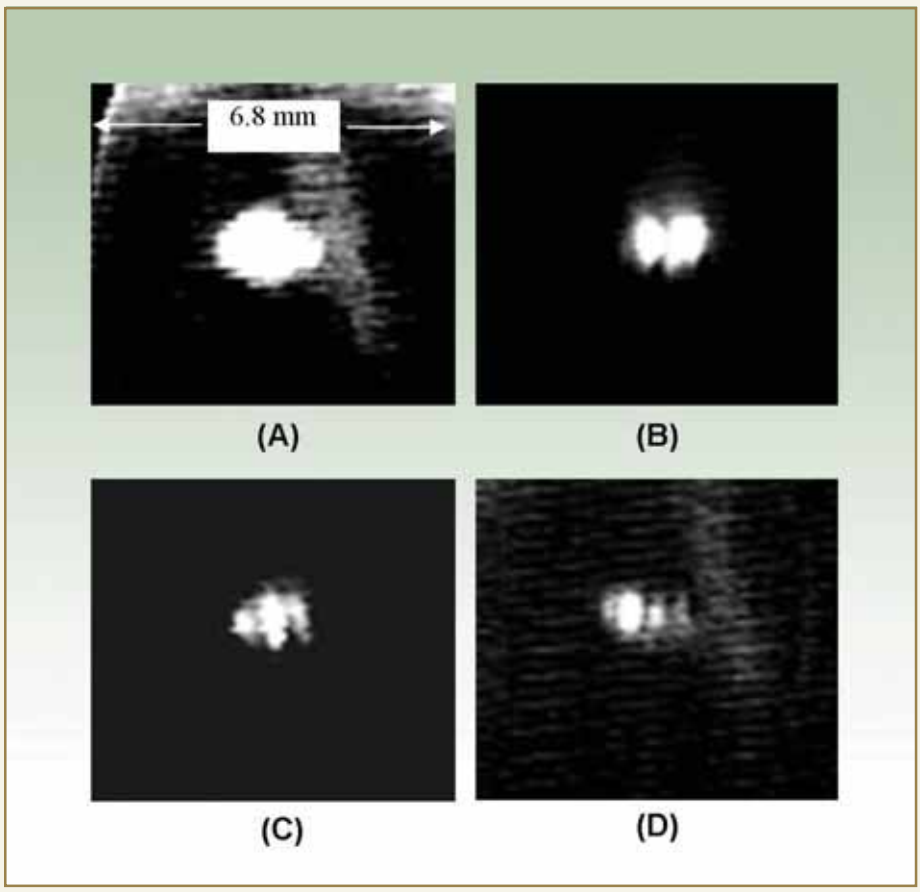

Fig. 4: The spatial distribution of the cold cloud in a Cesium MOT as observed by a CCD placed at 45^0 with respect to the radial beams. These multiplet structures are generated by changing the MOT alignment.

The steady state fluorescence from the cold atoms, trapped in the MOT is used, to quantify (N_{ss}), which is further optimized with respect to the trap parameters namely: the detuning and intensity of cooling/ repumping laser beams, the magnetic field gradient and the number density of background atoms. Under specific experimental conditions, we observe instabilities in N_{ss} when the fluorescence intensity is observed for a long duration and analyzed using Fourier transform technique. These studies gives a better insight in to the physical processes governing the trap dynamics. Another important steady-state characteristic of a cold cloud, is it's size and shape. We use here fluorescence imaging with a charge-coupled device to decipher this information. In general, we observe the cold clouds that are Gaussian in three dimension and that enables us to obtain the rms sizes and ω_x, ω_y and ω_z and thereby the effective volume of the cloud. Formation of cold clouds of various shapes, has been one of the interesting issues in the study of a MOT for a long time. In this context, we have explicitly demonstrated, formation of multiple cloud structures in a MOT, as shown in Fig. 4. The multiple clouds in our experiments appear to form by the change of the single well MOT potential, to multi-well caused by the changes in the alignment of the trapping beams.

For measurement of temperature of the cold cloud, we have implemented the release and recapture (R&R) technique. A primary requirement in the realization of R&R technique or for that matter, any technique for the measurement of temperature of the cold cloud, is an amplitude modulator, that generates the bright and dark intervals of unequal lengths by modulating the cooling beams. We have devised a very simple and effective amplitude modulator, that is based on a rotating optical shutter.

A noble, simple and reliable technique of temperature measurement, based on one dimension (1-D) expansion of the cold cloud in a MOT is developed. This technique is realized by switching off a pair of trapping beams in a MOT, which allows the cold cloud to expand in 1-D, in the presence of the orthogonal trapping laser beams. The 1-D expansion is followed in both spatial and temporal domains by fluorescence imaging using a charge-coupled device. We show here that in the time scale $0 \le t < 5$ ms, the 1-D expansion is essentially ballistic and the time variation of the rms size of the cloud in the expansion direction, provides the temperature of the cloud. This new technique offers several advantages: It avoids the use of a probe laser beam, since the orthogonal trapping beams are used, to illuminate the expanding cloud for fluorescence imaging. The use of optical shutter as amplitude modulator, avoids the employment of elaborate equipment and set-up. Further, the technique can be used for measurement of temperature, in any three orthogonal directions, by switching off the relevant pair of trapping beams. For switching off a pair of trapping beams in the horizontal plane, the cloud expands with virtually no effect of gravity. We show here explicitly, that the temperatures measured using this new technique, are consistent with those obtained with R&R technique and also with the temperature scaling law (Fig. 5). Finally we may note here, that this new technique provides directly the information on whether the cold cloud is in the temperature limited regime or multiple scattering regime, from the extent of contraction at zero time.

We have developed experimental technique for the studies on the MOT kinetics, to obtain the basic rates R, α and β. The reliability of the technique has been explicitly verified by observing the expected tendency of variation in R, α and β and therefore on N_{ss} with respect to the change in the background atom density. This technique along with its data analysis procedure, finds extensive use in the experimental work presented in this report. Finally, we may add here, that the developed diagnostic techniques, play a decisive role in many experiments, performed with the laser-cooled atoms.

Control laser-assisted enhanced loading of a MOT

Efficient capture of atoms in a MOT, to realize a large number of steady state atoms (N_{ss}) is the first and foremost step, in many experiments relying on laser-cooled and trapped atoms. In the normal course of operation of a MOT, there exist only a limited possibility of improving of N_{ss} due an unfortunate linkage between the large capture rate (R) and large loss rate (Γ),

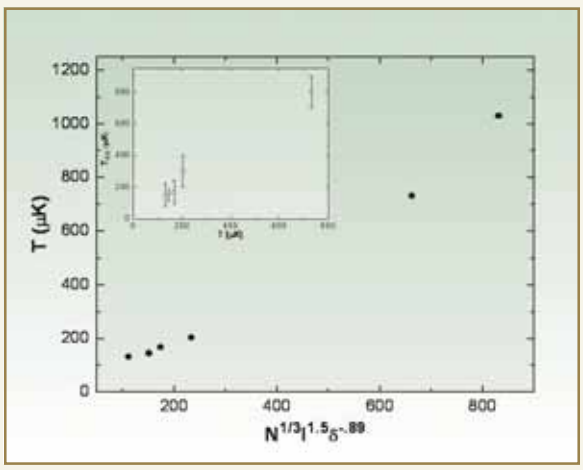

Fig. 5: The temperature T versus $N^{1/3} I^{1.5} \delta^{-0.89}$ for a few cold cloud of atoms, where T, N, I, and δ are the temperature measured with the one dimensional expansion technique, number of trapped atoms, intensity of cooling laser and detuning of the cooling laser respectively. The insert shows the comparison of T with the temperature measured with R&R method (T_{RR}).

i.e., a MOT parameter that enhances R inevitably enhances Γ, so that $N_{ss} = R / \Gamma$ remains essentially fixed. It is therefore required, to devise experimental strategies; those that either increase R or decrease Γ without affecting the other parameters. Multi-frequency MOT configuration is such an example, where additional laser beam, at further red detuned frequency from the cooling laser beams, are used to capture atoms from a larger velocity class and that gives rise to an improved R without affecting Γ.

In other experiments, using the optical shielding as the mechanism, the cold cloud is illuminated with a blue detuned 'catalysis' laser and that brings a decrease in the intra-trap collisions, thereby decreasing Γ, without affecting R.

Here, we have presented our new observations on a control laser-assisted enhanced loading, which are distinctively different from the multi-frequency MOT configurations and the optical shielding. We have demonstrated enhanced loading of a Cs MOT, by illuminating a small fraction of the capture region, with a control laser that is scanned over $6s_{1/2}\ F = 4 \rightarrow 6\rho_{3/2}\ F'=5$ cooling transition. Typical experimental data illustrating enhancement in N_{ss} , for various background vapour pressure, is shown in Fig. 6. The enhancement is observed to be a near-resonant phenomenon and is maximized when the laser is slightly blue-detuned. We further observe, that increase in the control laser is accompanied by increase

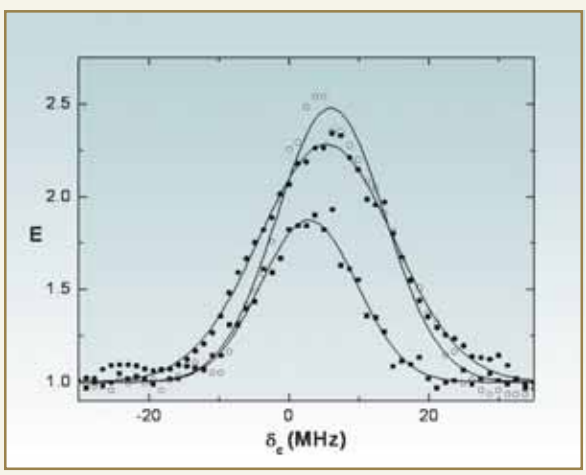

Fig. 6: Variation of the extent of enhancement (E) as a function of detuning (δ_c) of the control laser, where E denotes the relative increase in the number of atoms with respect to N_{ss}. Results are shown for Cs background atom densities, n_b = 8.2 x10^7 cm^{-3} (hollow circles), 3.3 x 10^8 cm^{-3} (solid circles) and 7.4 x 10^8 cm^{-3} (solid squares). The Gaussian fit to the data points is shown by the solid curve in each case.

in the cloud volume keeping the density constant, which demonstrates the cloud to be in the multiple scattering regime. We have studied the enhancement phenomenon, as a function of the detuning (δ_c), intensity (I_c), polarization and spatial position of the control laser beam. While the polarization is found to affect the enhancement marginally, the intensity of the control beam has a significant effect on the extent of enhancement (E_{max}). It is found that E_{max} increases with I_c, maximizes at $I_c = 1.7$ mWcm^{-2} and thereafter exhibits a sharp fall.

The kinetics of the MOT is investigated, to understand the mechanism underlying the enhancement. We obtain the MOT loading curves under the modulation of the cooling laser beam, for control laser locked at different detuning. The analysis of the MOT loading curve shows, that the control laser causes ~ two fold increase in R and that results in the proportional

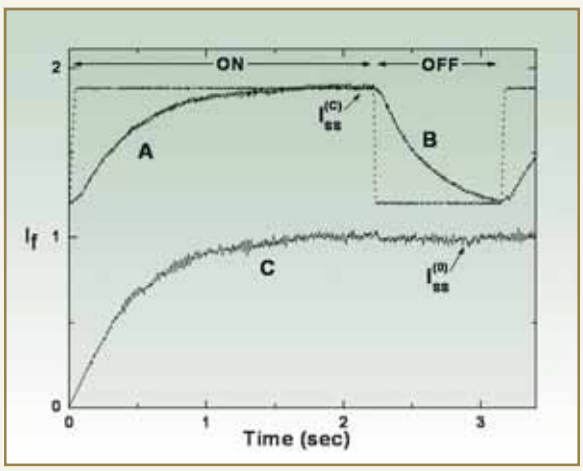

Fig. 7: MOT loading (A) and decay (B) curves under the modulation of control laser for control laser detuning δ_c ~1 MHz, n_b = 3 x 10^8 cm^{-3} and with fixed MOT beams. Loading curve (C) in the absence of the control beam is shown for comparison. I_f represents the fluorescence intensity in arbitrary units, and $I_{ss}^{(0)}$ and $I_{ss}^{(c)}$ are steady state values of fluorescence intensity in absence and presence of the control beam. The 'ON' and 'OFF' of the control beam is shown by the dotted curve.

enhancement in N_{ss}. It further pointed out that, the linear and quadratic loss rate are marginally changed, well within the experimental uncertainties. These results infer, enhanced loading as the mechanism behind observed enhancement and forbid any role of optical shielding in it. We have also investigated the MOT loading and decay curves, under the modulation of the control laser beams as shown in Fig. 7 and these results provide a direct proof for increase in N_{ss} caused by the control laser. Large time constants associated with these curves, rule out any possibility of increase in the MOT fluorescence intensity, without actual increase in N_{ss}.

A detailed explanation of the enhanced loading, requires consideration of interplay between Zeeman and Doppler shift and Rabi frequencies of various resonances. Further, the task is made difficult, by the complexities of laser-atom coupling in a multilevel atom, moving in a multifrequency optical field. However, we believe, that the possible mechanism responsible for enhancement, is the optical pumping of the inaccessible Zeeman states to the stretched state, caused by the control laser beam. Various experimental observations appear to support this conclusion. The present work, thus, provides a simple and interesting technique for increased efficiency in a MOT loading.

Optical control of a magneto-optical trap

The Magneto-Optical Trap (MOT) is a complex dynamical system that is rich in atom-field and atom-atom interaction processes. Application of a near-resonant auxiliary laser beam, can either enhance or suppress these basic processes and thereby, provide an optical control over the characteristics of the MOT; specifically the steady state number of trapped atoms (N_{ss}). Such studies are useful for various experiments in quantum optics, cold collisions, precision measurements etc., for understanding of the MOT dynamics and also for the development of deterministic atom sources. In the past, several studies

have been reported, where a near-resonant 'catalysis' laser has been used, to modify the collision dynamics of atoms trapped in a MOT and to yield an optical control over the inelastic collisions, responsible for the trap loss. In these experiments, the cold cloud of atoms in the MOT is illuminated by a catalysis laser, which enhances or suppresses the trap loss rate, depending on whether the laser is tuned to the red or blue of the cooling transition. However there exist only few examples where it has resulted in an increase in N_{ss}, as the catalysis laser simultaneously increases the light induced loss rate.

The enhancement phenomenon that we have discussed in section 5, illustrates enhanced loading of a Cs MOT, achieved by illuminating a small fraction of the capture region, with an auxiliary laser (control laser) that is scanned over $6s_{1/2}\ F = 4 \rightarrow 6\rho_{3/2}\ F' = 5$ cooling transition. The enhanced loading observed in these experiments, is caused, not by increase in the capture velocity as in the multi-frequency MOT configurations, but by removal of the Zeeman inaccessibility by the control laser beam, through optical pumping. These observations manifest the importance of the multi-level nature of the atoms, in the magneto-optic trapping of neutral atoms in multi-frequency optical fields and also point to the possibility of optically manipulating the capture rate and thereby of N_{ss} in a MOT.

A detailed parametric study shows that in general, the control laser can enhance or suppress N_{ss} depending on the choice of control parameters, thus providing a novel way of controlling N_{ss} in a MOT. We have found that the enhancement and suppression result from two distinct processes, that arise from the interaction of the control laser with two different groups of atoms, i.e., in the capture region and in the cold cloud. These processes combine to produce a general variation of N_{ss}, of which the results reported earlier in this article are only a special case. This general variation of N_{ss} is realized, by scanning the control laser over the entire $6s_{1/2}\ F = 4 \rightarrow 6\rho_{3/2}\ F' = 3,4,5$ hyperfine manifold, to involve an additional hyperfine level in the control dynamics for different positions and intensity of control laser, at various background vapour pressures. The observed experimental results are depicted in Fig. 8. These results presented in this section, demonstrate all optical manipulation of N_{ss} and they have implications in the development of deterministic cold atom sources. Thus, an auxiliary laser beam added to a Cs MOT and tuned over the $6s_{1/2}\ F = 4 \rightarrow 6\rho_{3/2}\ F' = 3, 4, 5$ hyperfine transitions, enables us to vary the number of cooled and trapped atoms. This variation is a result of the interplay of two distinct position dependent processes: one responsible for enhancement and the other for depletion. Interaction of the control beam with the atoms in the capture region, results in the enhancement in the number of trapped atoms. This is caused, by an increase in the capture rate and possible mechanism, involving optical pumping of inaccessible Zeeman states into the stretched states, by the control laser. Position and intensity dependence of the enhancement profiles provides evidence for participation of Zeeman levels in the interaction dynamics. Suppression occurs, when the control beam interacts with a part of the cold cloud and maximizes at frequencies that are blue, with respect to individual hyperfine resonances. This is attributed to the heating of the cloud by blue detuned frequencies, resulting in the expulsion of the atoms from the trap. These two processes, depending on the relative overlap of the control beam with the capture region and the cold cloud, combine to produce a general variation in the number of trapped atoms, which can be controlled by the position, intensity and frequency of the control beam. The ability to vary the number of trapped atoms without changing the MOT operating conditions, makes this study interesting and potentially useful, for controlling the number of trapped atoms, necessary for various experiments and also for studies of the dynamical and collisional properties of a MOT. Finally, the results presented here are also important in understanding

the space-dependent effects, in the magneto-optic trapping of atoms.

Velocity diffusion and radiation trapping force in a magneto-optical trap

A cold cloud of atoms trapped in a Magneto-Optical Trap (MOT) expands under the influence of gravity, when the trapping force is suddenly switched off. The study of this expansion in the spatial and temporal domains, has been extensively used for characterizing the temperature of cold clouds. An interesting situation arises, when the cold cloud is allowed to expand in the presence of near-resonant laser beams, that are orthogonal to the expansion direction. This section deals with the experimental and theoretical investigations of such an expansion of cold Cs atomic clouds, in a MOT. By suitably configuring the trapping beams of the MOT in time domain, we achieve 1-D expansion of the cold clouds in orthogonal 2-D laser beams and study their spatio-temporal evolutions. In a sense, this experimental configuration is similar to that used in the work on deflection of an atomic beam by resonant standing waves, where the laser beams are impinged from the orthogonal directions, on the atomic beam.

The primary motivation for our work, stems from it's intimate connection to the role of fluctuations of the radiation force, on the motion of atoms, which has been a subject of intense theoretical and experimental investigations, particularly in the context of laser cooling of atoms. It is well known, that the fluctuations originating from random atomic recoils accompanying spontaneous emission, give rise to diffusive spreading of velocities in optical molasses. In more general laser cooling situations, that deal with atoms with several Zeeman sub-levels, polarized laser beams and atom traps, there exist additional fluctuations, arising from the difference among the number of photons absorbed in each counter propagating laser beam, instantaneous dipole force, radiation trapping force and the magnetic force. These fluctuations make the evolution of the atomic momentum, look like a random walk. In analogy with the classical Brownian motion, it is then possible to define a diffusion coefficient, which is related to the steady-state kinetic temperature by well-known Einstein relation. There exist only a few experimental studies, on the measurement of the diffusion coefficient and these experiments pertain to optical molasses and collimated atomic beams. In comparison, the experimental scheme discussed in this paper, can provide a direct determination of diffusion coefficient, in a general MOT environment. The atomic random walks can be visualized conveniently in an expanding cloud and the phenomenon is elucidated with a theoretical model, based on Langevin formalism.

The other important issue that is related to the present study, is the radiation trapping force: the long-range repulsive force, that arises from multiple scattering of photons. It is well known that this force limits the steady state density in a MOT. The manifestation of the radiation trapping force in a MOT, has been observed in several other experiments, such as observation of spatial distributions, coherent backscattering, self-sustained oscillations and lengthening of the effective lifetime of $^2P_{3/2}$ level of Cs in a high density MOT; the last study perhaps provides a direct evidence of this force.

With these motivations, we have demonstrated that the 1-D expansion of a cold cloud of atoms, exhibits three distinct features in different time domains and these features are signatures of the basic processes, that are of fundamental interest to laser cooling and trapping. In that sense, the study reported here, provides a fresh insight into the issue of the motion of atoms in near-resonant radiation field. Sudden initial ($t=0$) contraction of the cloud, observed in our experiments, reveals the existence of the radiation trapping force in the MOT and the extent of contraction is found to be consistent with the Sesko-Walker-Wieman model. This is

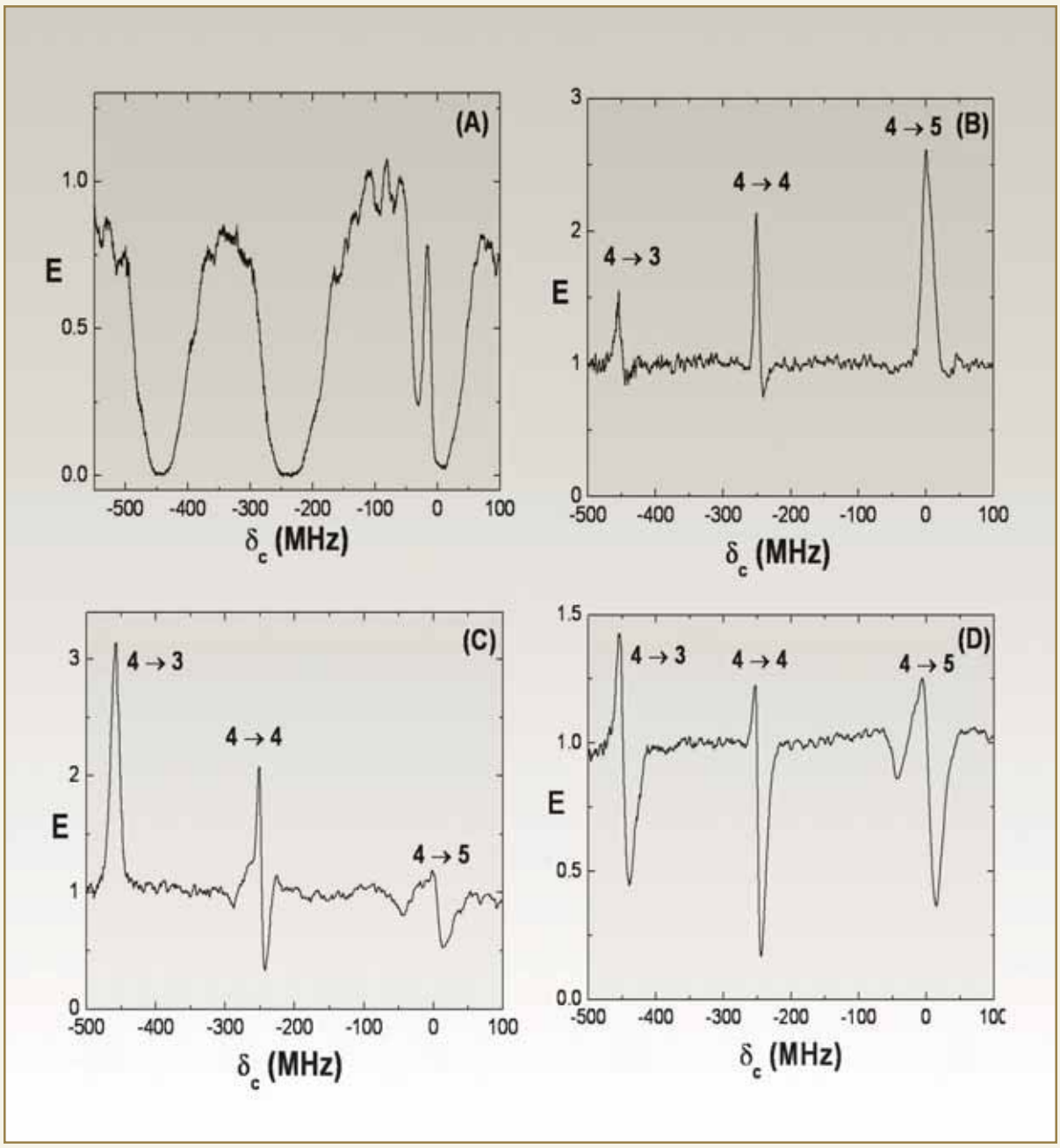

Fig. 8: Enhancement profiles $E(\delta_c)$ obtained with the control laser scanned over $6s_{1/2}\,F = 4 \rightarrow 6p_{3/2}\,F'=3$, 4, 5 transitions. The control laser detuning δ_c is measured from the cooling resonance and control laser intensity I_c = 4.2 mWcm^{-2}. Frame (A): s ~0 mm, n_b=3 x10^8 and $N_{ss}^{(0)}$ =7.6 x 10^6. Frame (B): s ~3 mm, n_b=1 x 10^8 and $N_{ss}^{(0)}$=9 x 10^5. Here s represents the distance of control laser from the centre of cold cloud. Observed δ_c^{max} = -454, -251 and +1 MHz for F' =3, 4 and 5 respectively. Frame (C): s~2 mm, n_b=1.5 x 10^8 and $N^{(0)}$=2 x 10^6. For F'=3, δ_c^{max} = - 454 MHz while for F'=4, 5, the set (δ_c^{max}, δ_c^{min}) = (-251, -242), (-2, 11) MHz respectively. Frame (D): s~2 mm, n_b=3 x 10^8 and $N_{ss}^{(0)}$= 1 x 10^7. (δ_c^{max}, δ_c^{min})=(-454, -439), (-251, -244), (-5, 11) MHz for F'=3, 4, 5 respectively.

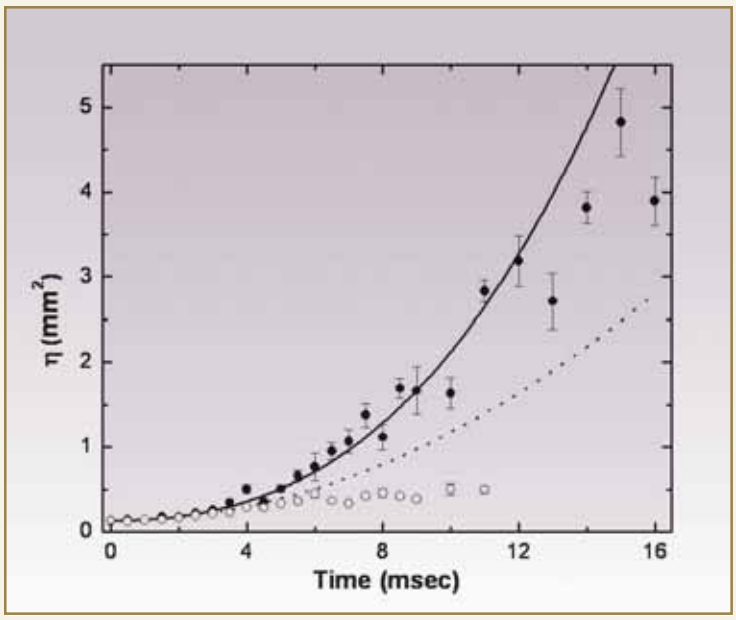

Fig. 9: One dimension expansion of cold atoms in presence of orthogonal photon field. Temporal evolution of the cloud size derived from the normalized centre line intensity η(*t*) (solid circles) and $\sigma_x^2(t)$ (hollow circles) of the expanding cloud. The η(*t*) fitted to $\sigma_x^2(t)=\sigma_x^2(0)+\frac{k_B T}{M}t^2+\frac{2}{3}D_v t^3$, where (*t*) is the temperature of the cloud and D_v is the velocity diffusion coefficient as shown by the solid line. The dashed line represents the behaviour of cloud under ballistic expansion, characterized by the temperature of the cloud as measured from R&R method. Both the derived and observed cloud size found to be following ballistic expansion for initial ~5 ms expansion time. The effect of super-ballistic expansion becomes evident for expansion time of more than 5 ms.

probably the most direct evidence of radiation trapping force, operating in a MOT environment. In the intermediate time scale, $0<t<5$ ms, the cloud expands essentially in the ballistic manner, as determined by the initial temperature of the cloud. In the third time domain, $t>5$ms, the ballistic expansion is overtaken by the stochastic heating of the cloud, arising from the fluctuations of the trapping force. This results in rapid dispersal of atoms from the cloud and eventually a super-ballistic explosive expansion at long times. Analytical expressions obtained from the Langevin formulation of the problem are used, to obtain velocity diffusion coefficient from the experimental data. Such a procedure is illustrated in Fig. 9. Observed diffusion coefficient is found to correlate well with the diffusion coefficient of the MOT. It may be noted here that this is the first ever report of super-ballistic expansion.

Conclusions

This report has briefly summarized the thesis work on "Study of ultracold atoms in magnetic and optical traps". In the course of this work, two independent magneto-optical traps were developed from the scratch, for laser cooling and trapping of Cesium and Rubidium isotopes. These atomic samples at unprecedented ultracold temperatures were subjected to a variety of investigations, facilitated by parallel development of numerous specialized diagnostic techniques. Sincere effort in this regard has witnesed several new spectroscopic observations along with the development of an innovative technique of temperature measurement, in a magneto-optical trap.The enhancement in the number of trap atoms of a cesium magneto-optical trap, has been demonstrated, by a novel arrangement of a control laser, illuminating a small fraction of capture region. The diagnostic techniques have assisted to reveal, the physical mechanism behind this observation. In a more general context, the control laser has been used to have an all-optical control, over the number of trapped atoms. This has paved a new approach for realization of the deterministic atom sources. An innovative method based on one dimensional expansion of cold atoms in a magneto-optical trap has been studied, both experimentally and theoretically. This has led to direct observation of radiation trapping force, operating in a magneto-optical trap environment, consistent with the

Sesko-Walker-Wieman model. It has also explored the first ever observation of super-ballistic expansion. Thus, the accomplished work has laid a solid foundation, to address several issues, pertaining to laser atom interaction and physics of ultra cold atoms.

Acknowledgements

I am very much thankful to my thesis supervisor Dr. B.N. Jagatap for his constant help and guidance in the course of this research work. I take this opportunity to express my gratitude to Dr. K.G. Manohar, Dr. A. Venugopalan, Dr. Y.S. Mayya and Dr. S.J. Gaur for their help and involvement in the reported work. It is my pleasure to sincerely thank Dr. A.K. Das, Head, L&PT Division for his kind help and guidance in many difficult situations. I am indebted to Dr. L.M. Gantayet, Associate Director, BTD Group, for his suggestions and stimulating encouragement.

ABOUT THE AUTHOR

Dr. Swarupananda Pradhan completed his Post graduation in Physics from Sambalpur University, Orissa. He pursued his Diploma in Advanced Physics from the Institute of Physics, Bhubaneswar. He is from the 42nd Batch of BARC Training School and is currently working in the Laser and Plasma Technology Division. Recently he completed his Ph.D. from the University of Mumbai. His research interest includes laser-atom interaction and quantum degenerate gases.

बीएआरसी न्यूज़लेटर
BARC NEWSLETTER

HETEROGENEOUS GROWTH OF DIAMOND FILMS: SOME KEY ISSUES RESOLVED

M. Roy
Chemistry Division

Dr. Roy is the recipient of the G.C. Jain Memorial MRSI Best Thesis Award -2007

ABSTRACT

Hot filament chemical vapour deposition technique, has been explored extensively, to solve few exciting problems associated with the heterogeneous growth of diamond thin films on silicon single crystals. Nucleation density was enhanced almost five orders of magnitude as compared to pristine silicon using novel slurry pre-treatment. Diamond films were doped *in-situ* with boron, using a non-toxic boron source over a very wide range of boron concentrations, starting from semiconducting to metallic domains. Formation of nanocrystalline diamond phase at the film surface was detected, using surface enhanced resonance Raman spectroscopy and finally performance of devices made from HFCVD diamond films were investigated, under different test conditions.

Introduction

Growing synthetic diamond today, is no big deal. But when it comes to making of diamond films with targeted and specialized applications, to exploit the unique and extreme properties of diamond, a number of serious and challenging issues, concerned with morphology and texture of the deposits, their mechanical, optical and electrical properties spring up, demanding immediate attention. In this report, we will discuss about some of the intriguing issues pertaining to heterogeneous growth of diamond films by Hot Filament Chemical Vapor Deposition (HFCVD) technique.

HFCVD Technique for Diamond Thin Film Deposition

HFCVD is the earliest and by far the most popular technique, used for the deposition of diamond thin films at sub-atmospheric pressures. It involves precipitation of carbon onto suitable substrates from the vapour state, under conditions where diamond is thermodynamically unstable with respect to graphite (see Fig. 1). Like any other CVD techniques for producing diamond films, HFCVD requires activating carbon containing precursor molecules present in the gas phase, which in this case is usually a hot filament made of refractory materials, such as tungsten, rhenium or tantalum maintained at ~2100 °C.

The substrate is maintained at temperature in the range 600-900 °C, in order to have an optimized sticking of the hot ad-atoms produced during gas-phase reaction and at the same time prevent them from getting transformed to graphite spontaneously, which usually takes place above 1300 °C. The distance between the substrate and the hot filament is usually kept constant

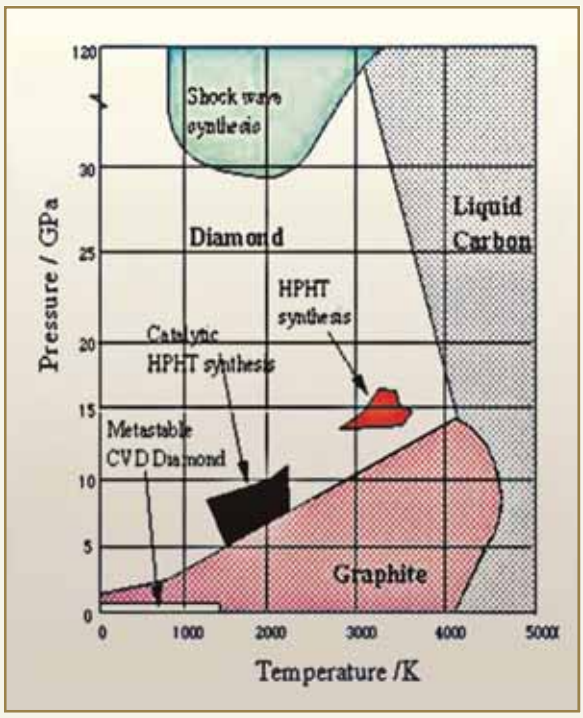

Fig. 1: Pressure-temperature phase diagram of carbon

at ~0.8 cm. Practically any carbon source such as methane, propane, ethane and even oxygen-containing organic materials including acetone, ethanol and methanol could be used, in conjugation with hydrogen for depositing diamond films. In fact, use of oxygen containing carbon sources widens the temperature range for diamond deposition. A wide range of substrates like tungsten, tantalum, molybdenum, zirconium, silicon, ceramics etc. have been used so far, for depositing diamond. On most substrate materials, except for diamond seeds, random nucleation of diamond particles leads to the formation of polycrystalline diamond films. The typical growth rate is ~1μm / h and substrates as large as 0.5 m^2 are reportedly known to have been coated, using this technique. Other deposition parameters viz. total chamber pressure, relative concentration of CH_4 with respect to H_2 in the feed gas etc. are also required to be optimized within a small window, for effective deposition of quality diamond films. In general, higher CH_4: H_2 ratio leads to higher growth rates, but poorer diamond quality. The total chamber pressure is maintained in the range 20-80 Torr, depending on the reactor design, substrate temperature and CH_4: H_2 ratio in the feed gas. Fig. 2 shows a schematic representation of a typical HFCVD reactor. It is however worthwhile to mention here, that the HFCVD technique suffers from certain inherent limitations. The hot filament constantly evaporates materials from it's surface that tend to contaminate the growing diamond surface, thereby limiting the quality of the film that can be grown by this technique.

This is in sharp contrast with the microwave CVD reactors, wherein optically transparent high-purity diamond films can be deposited at reasonably high deposition rates. Few years back, a state-of-the art MWCVD reactor (from Seiki, Japan) was installed in the Chemistry Division, BARC. However, all the issues that will be discussed subsequently in this report have been resolved, based on experiments carried out using a HFCVD reactor developed in-house.

Substrate Pre-Treatment

Some very recent and exciting applications of polycrystalline diamond thin films such as X-ray lithographic masks, Micro / Nano electro-mechanical systems (MEMS/NEMS) etc., require the films to be smooth, relatively defect and impurity free, continuous even at sub-micron thickness and at the same time be able to deposit on appropriate non-diamond substrates such as silicon etc. But owing to it's very high surface energy, nucleation density of diamond on pristine silicon is rather low ~10^4 particles / cm^2 under standard conditions of CVD deposition. This badly affects the properties, morphology and homogeneity of the deposited films, because it is only during the nucleation stage that the density of diamond particles, alignment of the crystallites and many such important properties are determined. Therefore, in order to improve such low nucleation, a variety of surface

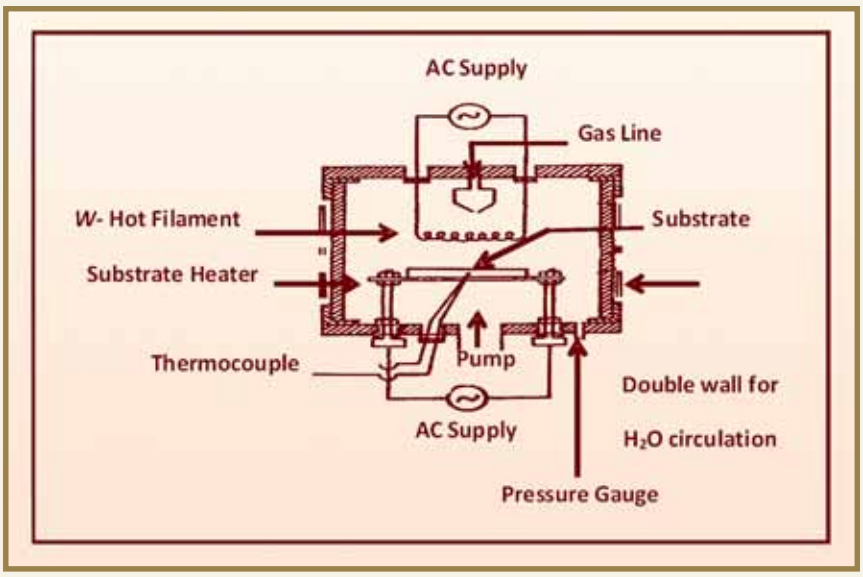

Fig. 2: Schematic representation of a typical HFCVD reactor

pre-treatments are given to the substrates, such as damaging the surface either by mechanical or ultrasonic abrasion with diamond or other hard powders, seeding with diamond grits, ion implantation, applying bias etc. Of the different methods employed for nucleation enhancement, ultrasonic pre-treatment using diamond slurry is most commonly used because of the ease of it's application to substrates, having all sorts of complex geometry and shape and also the homogeneity in morphology of the films, obtained upon deposition. It is reportedly known from literature that using a poly dispersed slurry composed of a mixture of diamond and metal particles, it is possible to attain very high nucleation densities and also nanometer rough films. Following the same recipe, we developed a novel slurry comprising of diamond (particle size <0.2 μm) and zirconium metal particles (particles size ~ 50 μm) dispersed in methanol and it was used for the first time as an abrasive, to enhance diamond nucleation on Si. Silicon substrates were first treated with HF to remove native oxide layer, then given the slurry pretreatment by ultra-sonication and finally used for diamond deposition. Zirconium was chosen because it forms a stable cubic carbide phase with lattice constant, close to that of diamond and is also an active catalyst with very high heats of hydrogenation. Besides, zirconium being a high density metal, it was presumed that hammering of the fine diamond particles by coarse metal particles during ultra-sonication, would lead to their sub-implantation providing the necessary diamond seeds for effective nucleation. Weight ratio of two particles was varied to find out it's effect on the properties of diamond films grown on the pre-treated substrates.

Results and Discussion

It has been observed from the AFM topographies of samples (Fig. 3) grown for $\sim$20 min on Si pre-treated with slurries comprising of different Zr: diamond ratio that nucleation density of the order of 10^9 particles/cm^2 (one of the highest reported) could be easily achieved in all the samples, which is five orders of magnitude higher as compared to the untreated pristine silicon substrate. It is to be noted that such high nucleation density could be achieved, in spite of the fact that the substrates were thoroughly cleaned by sonicating in methanol following slurry treatment. Moreover, for slurry containing Zr: diamond = 4, it was possible to obtain a continuous film with surface

roughness below 15 nm just within 20 min of deposition. The nucleation density of the samples has been found to increase and their roughness decrease monotonically, with increasing metal contribution in the mixed slurry. This has been attributed primarily to different inter-layer formation viz. ZrC for metal-rich and SiC for diamond-rich slurry pretreatment. However, one negative aspect of such slurry pre-treatment was that, the concentration of non-diamond carbon in the film increased, along with the number of grain-boundaries, ensuing leakage current and inferior electronic property due to damaged interface.

In-Situ Boron Doping Using Non-Toxic Precursor

To explore the feasibility of band gap engineering in diamond films, by virtue of boron doping using a non-toxic precursor was extremely challenging, both from scientific and technical aspects. Diamond films because of their unique properties, are promising semiconductor materials for the new generation electronic devices, that can operate at high temperatures, in very severe chemical environment and in radiation field. Doping of these films is one of the key steps in their fabrication. Moreover, by suitably doping the films they can be made to conduct electricity and hence, find tremendous applications in the form of diamond-coated electrodes with enhanced lifetime and stable characteristics, in harsh chemical solutions. Boron is regularly used to p-type dope diamond films. Due to it's small covalent radius, it is easily incorporated into the diamond lattice such that it's concentration in excess of 10^{20}/ cm^3 is possible. But the activation energy for the boron acceptors is quite high (~0.37eV) thereby limiting the percentage of carrier conversion. Both *ex-situ* and *in-situ* techniques have been used to dope diamond films with boron. But the *in-situ* techniques are found to be more effective in maintaining uniformity of the doping profile. Usually, a boron source is added along with the feed for diamond deposition. Gaseous boron hydride (B_2H_6) is the most conventionally used reagent for the process, but it is deadly poisonous even at

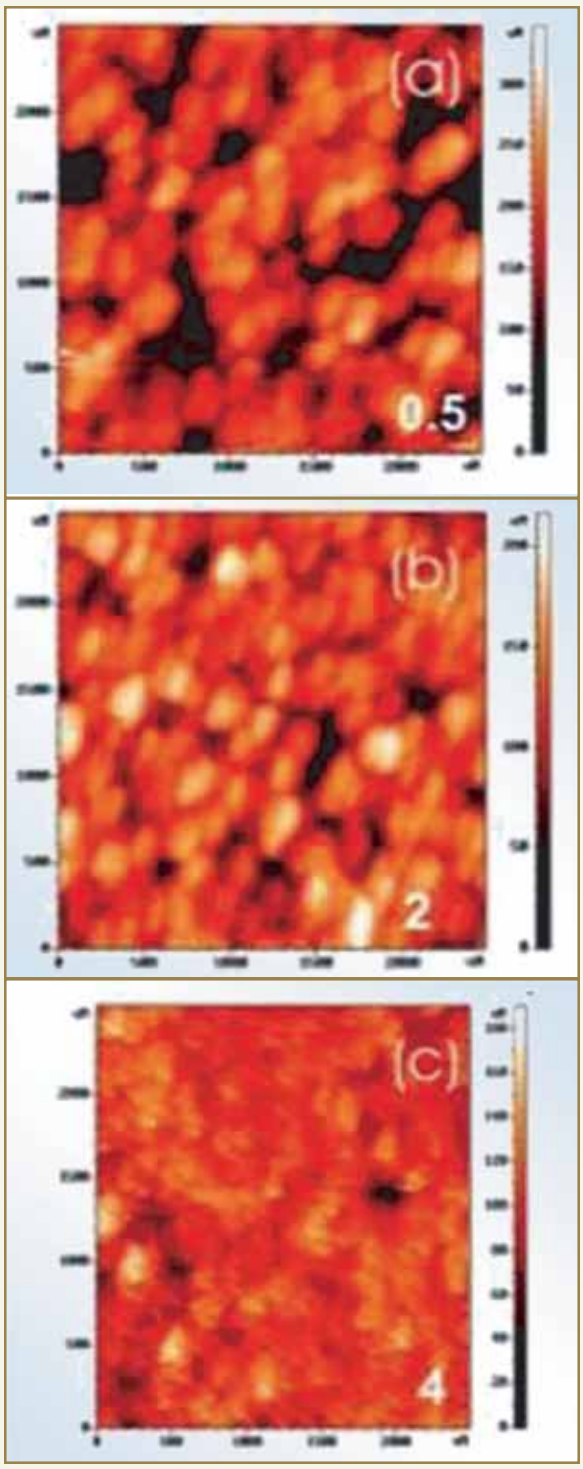

Fig. 3: AFM topography of diamond films deposited for ~20min after pre-treatment of the substrates with mixed diamond slurries containing zirconium: diamond weight ratio (a) 0.5, (b) 2 and (c) 4.

ppm level. We used H_3BO_3 instead, which is non-toxic in nature. H_3BO_3 was dissolved in CH_3OH from where vapours were transported along with feed gases, allowing *in-situ* doping of diamond as it grew. CH_3OH was chosen as a solvent, since it produced highly volatile ester upon reaction with boron according to the equation given below:

$$3CH_3OH + H_3BO_3 \leftrightarrow B(OCH_3)_3 + 3H_2O \quad \text{(i)}$$

However, few fundamental questions regarding the negative impact of oxygen on diamond films and the feasibility of controlled and heavy boron doping by this technique, needed to be answered. Besides, there were difficulties related to vapour transport that were eventually resolved, by devising a simple and unique bubbler fitted with a needle valve that allowed controlled and uninterrupted flow of vapours containing boron precursors. A series of samples were thus prepared with varying concentrations of H_3BO_3 in CH_3OH and analyzed.

growth of facets, that dictates different boron intake levels in the samples. Boron concentration is also found to vary along the film surface as is evident from the concentric circular patches of ~0.5 cm diameter with different contrasts.

Unintentional incorporation of oxygen during the growth process however, induced compressive stress in the films, that lowered diamond lattice constant well below the ASTM values.

Nanocrystalline Diamond at Film Surface: Detection by SERS

Opto-electronic properties of HFCVD grown diamond films, are strongly influenced by the presence of different allotropes of carbon. An important allotropic modification is nanocrystalline diamond. It is optically transparent, possesses smooth surfaces and displays low coefficient of friction and low electron emission threshold voltage. It has also been reported to exhibit totally different dielectric properties as compared

Results and Discussion

It could be successfully demonstrated from XPS, Raman and XRD studies, that by using this technique, controlled boron doping of diamond films is feasible over a very wide range of boron concentrations, starting from semiconducting to metallic domains (see Fig. 4), with nearly 1% of carrier conversion. Variation of boron concentration in the films with the molarity of H_3BO_3 in the feed solution as shown in Fig. 4 clearly demonstrates, the level of control that can be achieved on boron doping, using this technique. Formation of metallic phase at very high boron levels was confirmed from the Fano-deformation of Raman signals (see Fig. 5) and negative / zero activation barriers in temperature dependent I-V measurements (Fig. 6).

For the first time, cross-sectional Raman spectroscopy was put forward as a simple and non-destructive technique, for boron profiling in diamond films. The technique was proposed as a complementary technique to widely used Secondary Ion Mass Spectrometry (SIMS) which apart from being destructive in nature, requires stringent experimental conditions such as ultrahigh vacuum, high voltage, etc. and is often difficult to use, because of sample inhomogeneities and matrix effect. A small spread in the boron concentration is however observed, along the cross-section of the films due to the uncontrolled

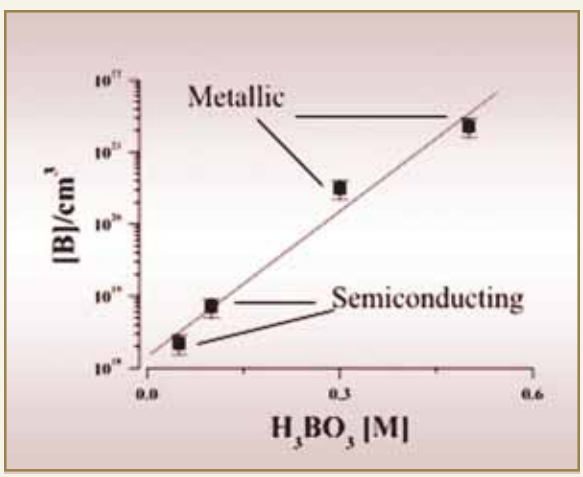

Fig. 4: Controlled boron doping

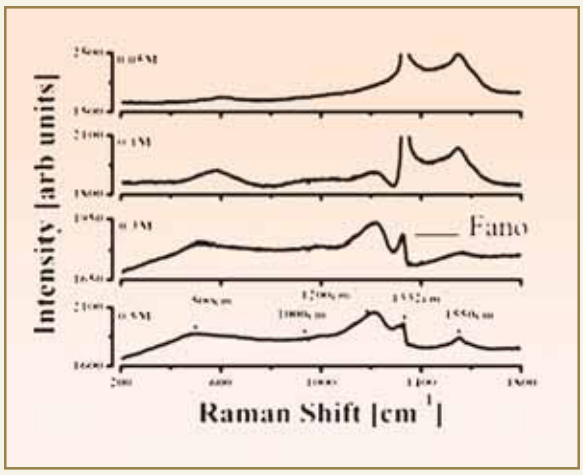

Fig. 5: Raman spectra of boron doped samples

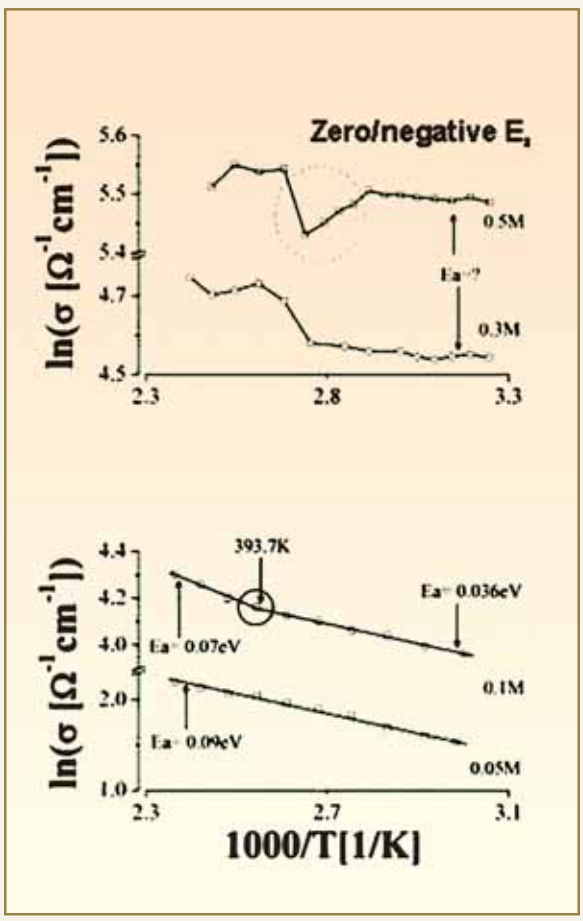

Fig. 6: I-V characteristics of boron doped samples

to the cubic phase and drastically modifies the optoelectronic properties of HFCVD grown films, if present in it. Thus, extensive characterization of such films is mandatory for the detection of all possible carbon allotropes present in the film, before planning for any specific application. For device applications, the film surface plays a very crucial role as it forms the interface between the metal and the film and hence, it is of utmost importance to know the different phases that constitute it, in order to exclude or exploit their properties to the maximum possible extent.

SERS in Brief

Surface Enhanced Resonance Raman Spectroscopy (SERS) is a state-of-the-art surface technique, that was used for the first time, to investigate exclusively the diamond thin film surface grown by HFCVD technique. By this technique it is possible to amplify Raman signals (often ~10^4–10^6 orders of magnitude) preferentially from the near surface region of the samples. The effect usually occurs at rough surfaces of free electron metals, for a broad range of laser exciting frequencies. Surface plasmons specific to rough metal surfaces are believed to be responsible, for such huge Raman amplification near the surface. Silver was already known to produce SERS on a large number of materials and hence was used for the present study.

Results and Discussion

For the first time it was found, that a nanocrystalline diamond layer is invariably formed at the surface of HFCVD grown diamond films. Phonon confinement in these nano-sized crystals, resulted in asymmetric broadening of the 1332 cm^{-1} diamond peak and appearance of a new peak at ~1240 cm^{-1} corresponding to a feature in the phonon density of states of diamond (Fig. 7). These features were observed only after depositing silver on diamond films, implying that signals are from film surface as a consequence of Raman amplification by surface-plasmons and are not from the bulk. The observations

were further corroborated by high-resolution SEM studies. Lack of coalescence among the crystallites and constant exposure to reactive atmosphere, are believed to have resulted in the formation of such surface nanophase. Further studies were conducted to investigate the formation dependence of such nanocrystalline diamond phase on the feed gas composition. It was found, that it's concentration increased with increase in CH_4:H_2 in the fed gas and decreased on introducing small amount of O_2 in the same (Fig. 8).

Fabrication of Device: Performance under Test Conditions

Metal-insulator-semiconductor type of structures was fabricated on HFCVD grown diamond films. Prior to metallization, the films were thoroughly cleaned using standard 'RCA cleaning technique', which removed the non-diamond carbon present in the films to a great extent. Aluminum or silver gates were then evaporated on top of the films and a coating of In-Ga paste was applied at the back. Often aluminum was also used as a back contact, instead of In-Ga paste. Fig. 9 gives a schematic representation of a typical device used for the study.

The devices so fabricated were then subjected to actual performance tests. It was observed, that the devices exhibited rectifying behaviour upon RCA cleaning as against near Ohmic behavior prior to that. This could be explained on the basis of large leakage current along the grain boundaries and via conducting impurities present in the as-grown diamond films. Removal of the non-diamond graphitic stuff from the films by RCA cleaning, made it to exhibit rectifying behaviour. The RCA cleaned diamond films were then subjected to H_2-plasma treatment, to study it's effect on the performance of the device. It was found from temperature-dependent current-voltage studies and also from deep level transient spectroscopy, that the plasma-treated samples exhibited homogeneous distribution of highly conducting surface states, having activation energy spread ~0.13 eV that dominated the transport mechanism below 290 K (Fig. 10). The surface states however vanished upon annealing the

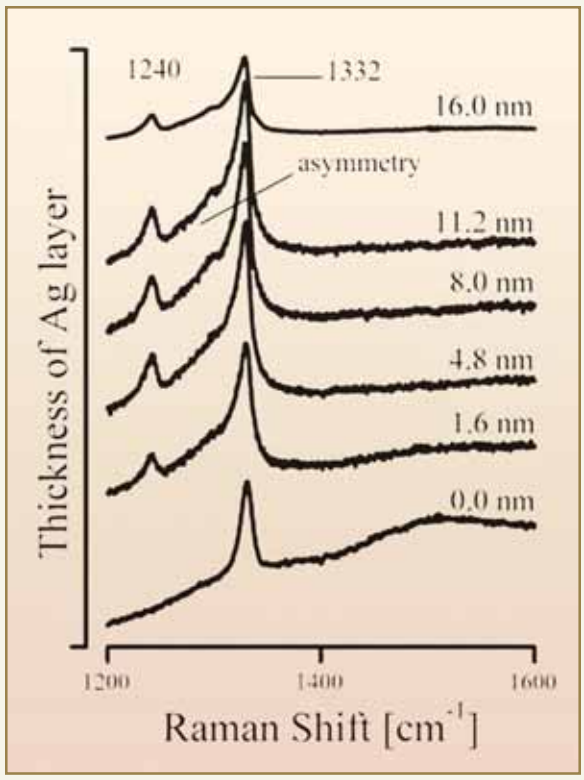

Fig. 7: Raman spectra of a typical sample as a function of silver deposition

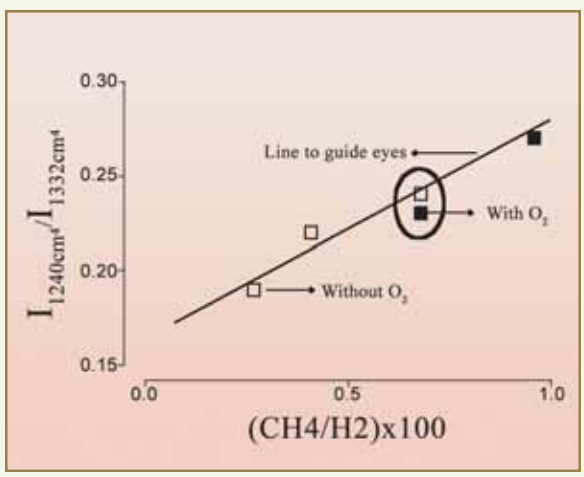

Fig. 8 : Growth of nano-diamond phase as a function of feed gas composition

samples at ~800 °C under vacuum as a result of H_2-desorption.

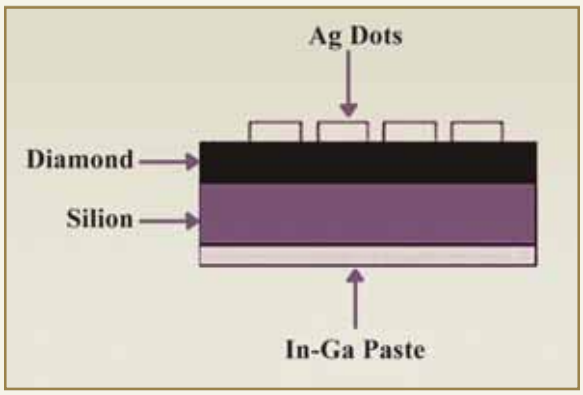

Fig. 9: Schematic diagram of a typical diamond thin film device

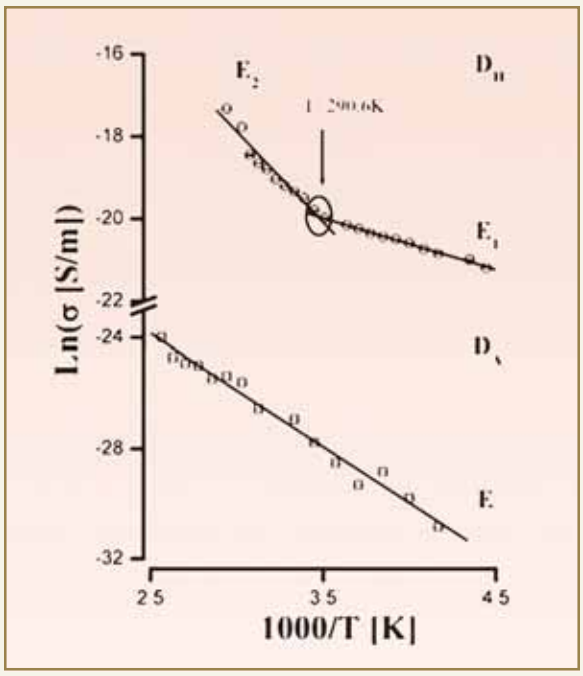

Fig. 10: Temperature dependence of electrical conductivity of the device after H_2-plasma treatment (D_H) and vacuum annealing (D_A)

Summary

It has been demonstrated that the hot filament chemical vapour deposition technique could be deployed successfully, to solve many advanced research problems in the field of diamond deposition. Using mixed slurry pre-treatment, diamond nucleation on silicon could be enhanced to almost five orders of magnitude, as compared to pristine silicon. P-type boron doping of diamond films was carried out, using a non-toxic solution of H_3BO_3 in CH_3OH, that enabled controlled doping over a wide range starting from semiconducting to metallic domains. For the first time, presence of nanocrystalline diamond phase was detected at the surface of HFCVD diamond films using state-of-the-art Surface Enhanced Resonance Raman Spectroscopy (SERS). Finally, devices were fabricated from HFCVD diamond films and their performance was tested under different thermal and chemical treatments.

ABOUT THE AUTHOR

Dr. Mainak Roy joined the Chemistry Division of BARC in 1999, after completing his B. Sc. in from the Burdwan University and graduating from the 42nd Batch of the BARC Training School. He completed his Ph.D. from the Mumbai University in 2005. His fields of interest are surface and interface of thin films, surface enhanced resonance Raman spectroscopy and Raman studies of carbon nanotubes, diamond and DLC. One of his significant works has been, the detection of nano-diamond phase at the surface of HFCVD grown diamond thin films using surface enhanced resonance Raman spectroscopy.

AUTHOR INDEX

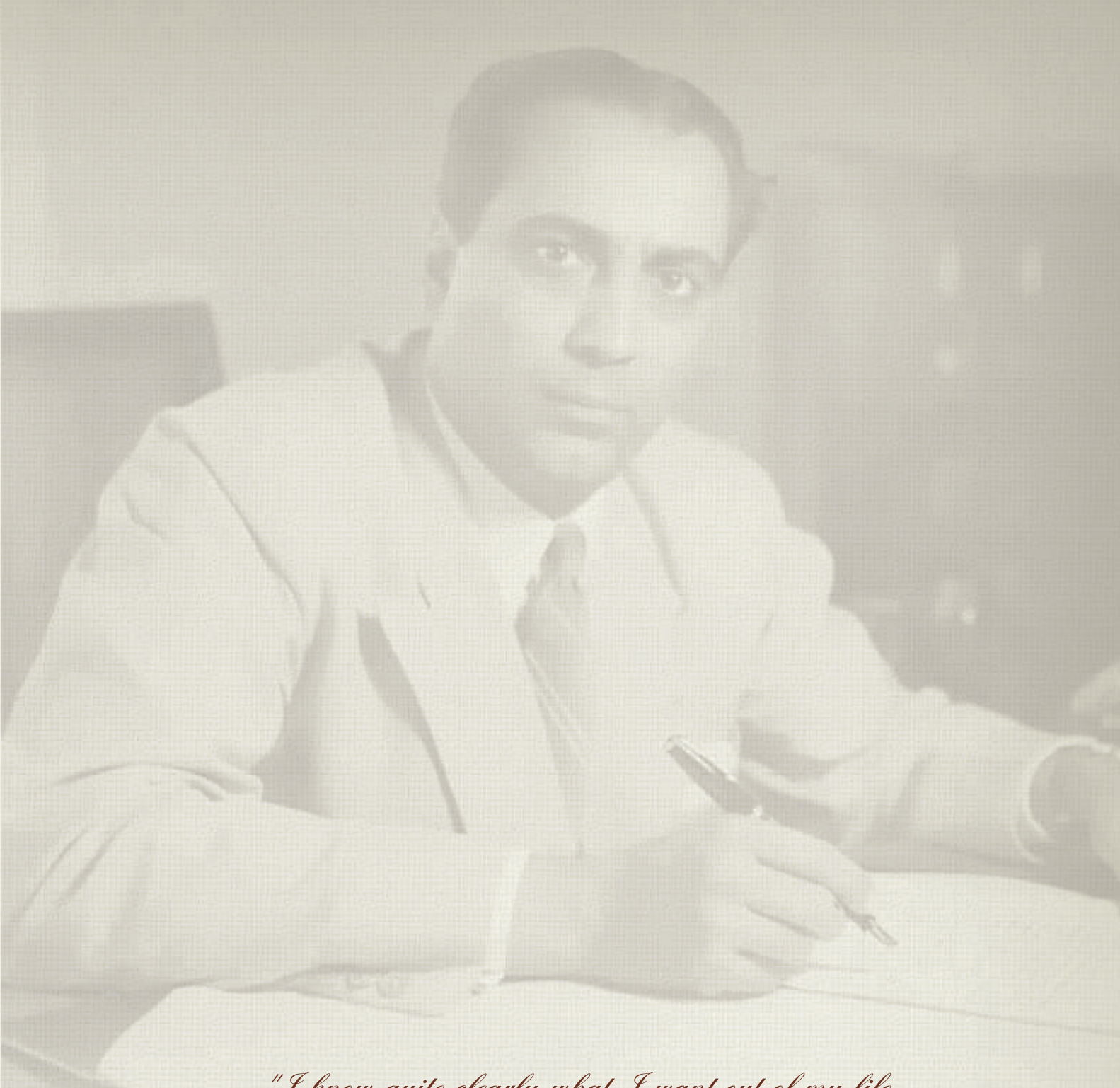

"I know quite clearly what I want out of my life.
Life and my emotions are the only things
I am conscious of. I love the consciousness of life
and I want as much of it as I can get. But the span of one's life is limited.
What comes after death no one knows. Nor do I care. Since therefore,
I cannot increase the content of life by increasing it's duration,
I will increase it by increasing its intensity. Art, Music, Poetry and
everything else that consciousness I do have this one purpose-increase the
intensity of my consciousness of life."

- *H.J. Bhabha*

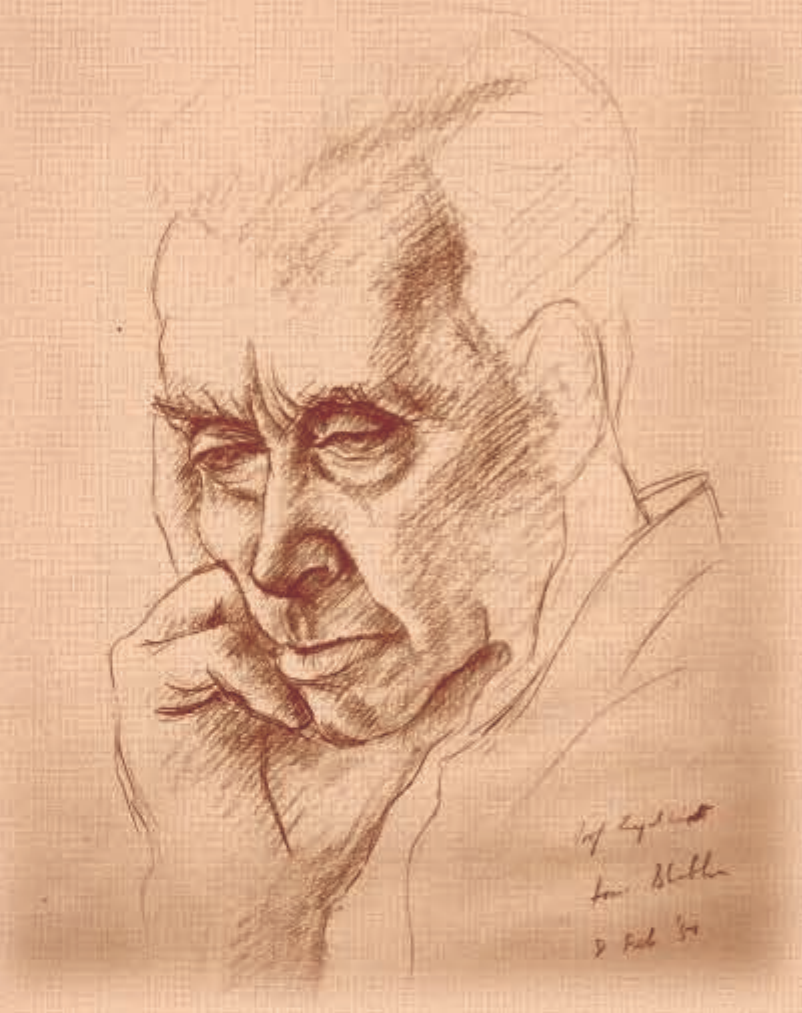

Edited & Published by:
Dr. Vijai Kumar, Associate Director,
Knowledge Management Group &
Head, Scientific Information Resource Division,
Bhabha Atomic Research Centre, Trombay, Mumbai 400 085, India.
Editorial Management : Dr. (Ms.) S. C. Deokattey,
Computer Graphics & Layout : N. Kanagaraj, SIRD, BARC
BARC Newsletter is also available at
URL : http://www.barc.gov.in